NASA Conference Publication 2185
DOE Publication CONF-810226

Wind Turbine Dynamics

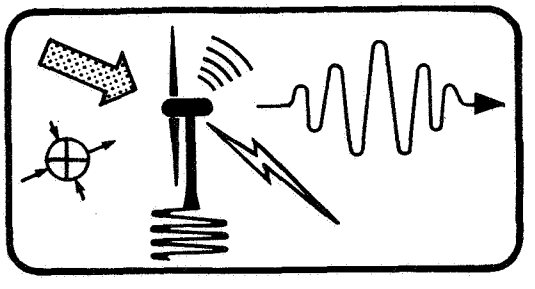

Proceedings for a workshop held at
Cleveland State University
Cleveland, Ohio
February 24-26, 1981

SERI/CP-635-1238

Printed in the United States of America
Available from:
National Technical Information Service
U.S. Department of Commerce
5285 Port Royal Road
Springfield, VA 22161
Price:
Microfiche $3.00
Printed Copy $ 14.50

UC Category: 60

NASA Conference Publication 2185
DOE Publication CONF-810226

Wind Turbine Dynamics

Robert W. Thresher, Editor
Oregon State University
Corvallis, Oregon

Proceedings of a workshop sponsored by
Department of Energy
Division of Wind Energy Systems, and
NASA Lewis Research Center and held at
Cleveland State University, Cleveland, Ohio
February 24-26, 1981

NASA
National Aeronautics
and Space Administration

Scientific and Technical
Information Office

1981

FOREWORD

The Second DOE/NASA Wind Turbine Dynamics Workshop was held in Cleveland, Ohio, on February 24-26, 1981. Over 200 persons met at Cleveland State University to hear papers on the dynamic behavior of large and small horizontal-axis and vertical-axis wind turbines. While the first DOE/NASA dynamics workshop (reference below) concentrated on structural dynamics, the present program contained 48 papers on a variety of topics, including:

- Aerodynamics
- Structural Dynamics
- Electrical System Dynamics
- Control Dynamics
- Acoustics

Papers were contributed by universities, manufacturers, government laboratories, and private research organizations.

The objective of this Workshop was to discuss and document recent progress in the analysis and prediction of the dynamic behavior of wind turbine generators. Discussions followed each technical session in which the participants were asked to focus on the following questions:

- Are state-of-the-art analysis tools satisfactory for designing the next generation of wind power systems?
- Are state-of-the-art analysis tools being used satisfactorily by designers?
- What important verifications of theory are lacking or inadequate?

Summaries of these informative discussions as well as the questions and answers which followed each paper are documented in the proceedings.

The Workshop Committee is appreciative of the many efforts of presenters, session chairmen, and reviewers which contributed to the success of this conference.

Reference: Wind Turbine Structural Dynamics, NASA Conference Publication 2034, DOE Publication CONF-771148, 1978

WORKSHOP COMMITTEE

Chairman: Dr. David A. Spera
Chief Engineer, Wind Energy Projects
NASA Lewis Research Center

Program Chairman: Dr. Robert W. Thresher
Professor of Mechanical Engineering
Oregon State University

Arrangements Chairman: Dr. Romualdas Kasuba
Department Chairman, Mechanical Engineering
Fenn College of Engineering
Cleveland State University

TABLE OF CONTENTS

SECOND DOE/NASA WIND TURBINE DYNAMICS WORKSHOP

Aerodynamics I

Session Chairman - J.M. Savino (NASA LeRC)

"Aerodynamic Potpourri"
R.E. Wilson
(Oregon State University)

"Aerodynamic Performance Prediction of HAWT's"
D. Jeng
T. Keith
A. Aliakbarkhanafjeh
(University of Toledo)

"Double-Multiple Streamtube Model for Darrieus WT's"
I. Paraschivoiu
(IREQ)

"The UTRC WECS Performance Analysis for HAWT's"
T.A. Egolf
(UTRC)

"The Velocity Field of a System of Unsteady Cycloidal Vorticies"
B.J. Young
(Young Energy Systems)

"Analytical Studies of New Airfoils for Wind Turbines"
W.H. Wentz
(Wichita State University)
J.T. Calhoun
D. Miller
(NASA LeRC)

"On the Wake of a Darrieus Turbine"
T.E. Base
P. Phillips
G. Robertson
E.S. Nowak
(University of Western Ontario)

"Recent Darrieus VAWT Aerodynamical Experiments at Sandia Laboratories"
P.C. Klimas
(Sandia Laboratories)

AERODYNAMIC POTPOURRI

Robert E. Wilson

Department of Mechanical Engineering
Oregon State University
Corvallis, Oregon 97331

ABSTRACT

Aerodynamic developments for vertical axis and horizontal axis wind turbines are given that relate to the performance and aerodynamic loading of these machines. Included are: (1) a fixed wake aerodynamic model of the Darrieus vertical axis wind turbine; (2) experimental results that suggest the existence of a laminar flow Darrieus vertical axis turbine; (3) a simple aerodynamic model for the turbulent windmill/vortex ring state of horizontal axis rotors; and (4) a yawing moment of a rigid hub horizontal axis wind turbine that is related to blade coning.

I. DARRIEUS FIXED WAKE THEORY

A fixed wake theory for the Darrieus Rotor has been developed and compared to test results (1). A comparison of theory and test results is shown below in Figure 1.

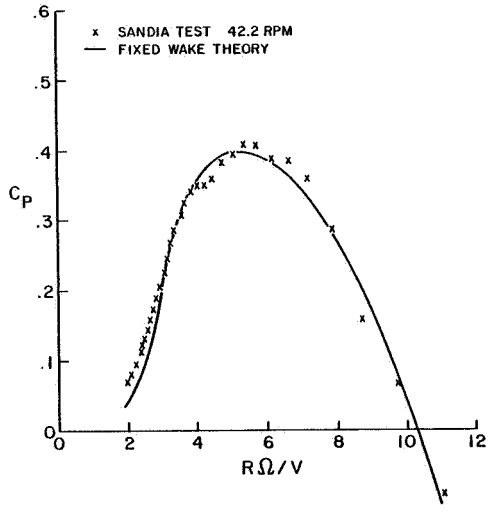

Figure 1. Fixed Wake Theory and Test Results for the Sandia 17 m Machine.

The induced velocities at the front and rear of the streamtube shown in Figure 2 are determined from the shed vorticity in the wake. For the front position (segment BC), a semi-infinite wake of strength directly proportional to the circulation at BC is developed. No effect from the rear position is felt along BC.

At the rear position, DA, the induced velocity is the result of the wake from the front blade which appears as an infinite wake and a semi-infinite wake of strength directly proportional to the circulation at DA. A point in the far wake is subject to infinite wakes from both the front and rear blade positions. If we denote the induced velocity by $\Delta U_F \equiv a_F V_\infty$ and $\Delta U_R \equiv a_R V_\infty$ where F stands for front and R for rear and we use Γ_F and Γ_R to represent the front and rear blade circulations, then we may write

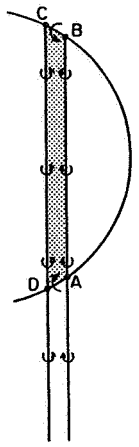

Figure 2. Fixed Wake Streamtube.

$$\Delta U_F = k|\Gamma_F| = a_F V_\infty$$

$$\Delta U_R = k[2|\Gamma_F| + |\Gamma_R|] = a_R V_\infty$$

$$\Delta U_{wake} = k[2|\Gamma_F| + 2|\Gamma_R|] = 2aV_\infty$$

Here the far-wake induced velocity is defined as 2a. Accounting for the sign of the circulation, these results may be put in the form

$$\frac{a_R}{a_F} = 2 - \frac{\Gamma_R}{\Gamma_F}, \quad a_R - a_F = a$$

These relations are exactly the same as developed by Holme (2). Momentum considerations yield an expression for the dimensionless induced velocity

$$a(1-a) = \frac{BcX}{8\pi R}\left[\frac{C_L W}{V_\infty}\bigg|_F - \frac{C_L W}{V_\infty}\bigg|_R\right]$$

where B is the number of blades, c is the chord, X is the tip speed ratio, C_L is the lift coefficient and W is the velocity relative to the blade. Both the lift coefficient and the relative velocity are determined from the local induced velocities. When the circulation is expressed in terms

of the lift coefficient, the above three equations can be used to determine a, a_R and a_F.

For idealized aerodynamics, $C_L = 2\pi m \sin\alpha$, the above relations can be solved in simple form. The results are:

$$a(1-a) = \frac{BcmX}{4R} \cos\gamma \sin\theta(1-a + \sqrt{1-2a})$$

$$a_F = \frac{1}{2}(1 - \sqrt{1-2a})$$

$$a_R = \frac{1}{2}(1+2a - \sqrt{1-2a})$$

where γ is the inclination of a blade element with respect to the vertical and θ is the blade angular position, 90° being directly upwind.

II. DARRIEUS DRAG COEFFICIENT MEASUREMENTS

During testing of the 5 meter and 17 meter Darrieus vertical axis turbines at Sandia Laboratories, data has been obtained at wind speeds below 1 mph (3). At such wind speeds, the tip speed ratio is 70 or above so that the blades are operating with very small angles of attack. In this mode of operation, power input is required to overcome blade drag, so that the power input, RPM and rotor geometry can be used to determine the blade drag coefficient C_{D_0}. Data from the Sandia Laboratories test site is reduced using the method of bins (4). The results for NACA 0015 blades are shown below. Each point represents over 400 samples using the bins method. Also shown are the results of a numerical prediction for the NACA 0015 airfoil. The computation method is described in Reference (5).

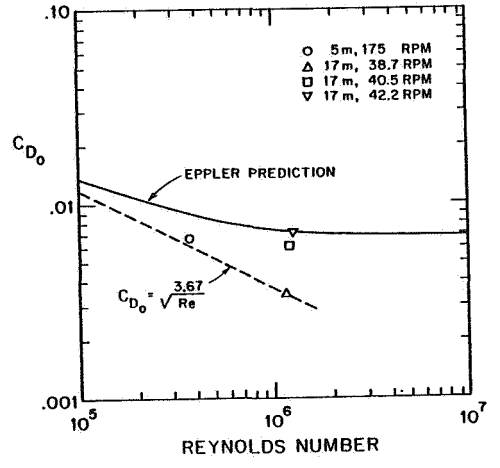

Figure 3. C_{D_0} versus Reynolds Number for the NACA 0015 Airfoil.

These few data points suggest that laminar flow may exist up to a chord Reynolds Number of $1.1 \cdot 10^6$ for the NACA 0015 extruded aluminum Darrieus vertical axis wind turbine blades. The test results for the 17 m at 38.7 RPM show a higher peak power coefficient (0.46) and lower peak power output ($K_{P_{max}} = 0.0080$) than achieved for operation at higher RPM. If laminar flow characteristics can be incorporated into the design of a vertical axis wind turbine, significant improvements can be made in the COE and reliability of a Darrieus Rotor.

III. TURBULENT WINDMILL/VORTEX RING STATE

Strip theory analysis of horizontal axis wind turbines determines local induced velocity by equating blade normal forces to the momentum change in a streamtube. Figure 4 below illustrates the operating states of a rotor expressed in terms of the thrust coefficient, C_T, and the induced velocity, a.

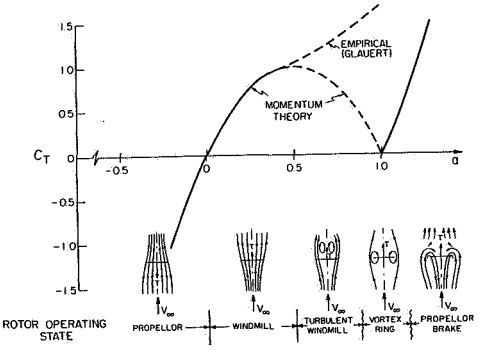

Figure 4. Rotor Operating States.

For operations at induced velocities greater than 0.5, it may be seen that there is a great difference in the value of C_T between the momentum and Glauert (6).

The aerodynamic loads and the performance predicted using the momentum and Glauert values of C_T show corresponding differences. The Glauert empirical curve is represented by an implicit algebraic equation, however, approximating the Glauert relation by a straight line gives a useful and accurate representation the local thrust coefficient for strip theory use. Using the expressions given below, strip theory calculations were made for a two-bladed rotor with NACA 0015 constant chord, untwisted blades. The local values of C_T used were

$$C_{T_L} = 4a(1-a) \qquad a < 0.38$$

$$C_{T_L} = 0.5776 + 0.96a \qquad a > 0.38$$

Test data (7) and calculations are illustrated in Figure 5 below. The measured value of $C_T)_{Rotor}$ increases with tip speed ratio for 0° and 2° blade pitch angle cases. The calculated flow for these cases are in the turbulent windmill state. Agreement between theory and test suggests the above relations can be used to predict the aerodynamic loads of horizontal axis wind turbines operating in the turbulent windmill state.

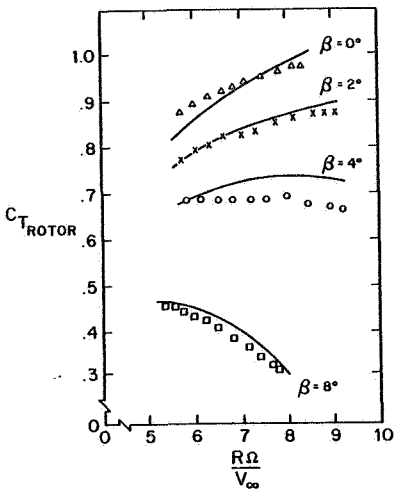

Figure 5. Measured and Predicted Rotor Thrust Coefficients at Various Blade Pitch Angles.

IV. YAW MOMENT FOR A HORIZONTAL AXIS WIND TURBINE

Downwind rigid-hub horizontal axis wind turbines derive their yaw stability from blade coning. The coning acts similar to dihedral in an airplane by increasing the velocity normal to the upwind blade. Yaw forces developed by rigid hub rotors are quite small so that the yaw moment controls yaw stability. The yaw moment can be expressed in terms of integrals over the blade length. Denoting the yaw angle as δ and the position of the ith blade by θ_i, as shown in Figure 6, the rotor yaw moment is the moment about the z axis. Considering the flow induced by rotor yaw, the yaw moment is obtained by the approach of Ribner (8) in which the yaw moment is determined from blade forces and momentum considerations.

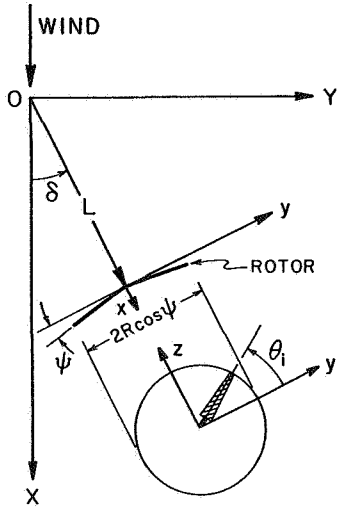

Figure 6. Wind Turbine in Yaw.

The results for a rotor with B blades is

$$C_{M_{Yaw}} \equiv \frac{M_z}{\frac{1}{2}\rho V_\infty^2 \pi R^3} = -\frac{\delta}{\pi} \sum_1^B \cos^2\theta_i \, \frac{I_1 I_{10}}{I_1 + I_4}$$

where

$$I_1 = \int_0^1 \left(\frac{\partial C_{T_L}}{\partial a}\right) \eta^2 d\eta$$

$$I_4 = \frac{B}{2\pi} \int_0^1 \eta^2 \cos\psi \, F_1 d\eta$$

$$I_{10} = \int_0^1 \eta \sin\psi \, F_1 d\eta$$

and $F_1 = \left(\frac{c}{R}\right)[2C_n(1-a) + C_{n_\phi} \eta X]$

and $C_n = C_L \cos\phi + C_D \sin\phi$

$$C_{n_\phi} = C_{L_\alpha} \cos\phi + C_{D_\alpha} \sin\phi - C_t$$

$$C_t = C_L \sin\phi - C_D \cos\phi$$

Here the local blade coning angle is ψ, the blade chord is c and ϕ is the angle between the local relative wind and the plane of rotation. The variable η is the radial position r divided by the rotor radius R. For a rotor with 3 or more blades, the yaw moment becomes

$$C_{M_z} = -\frac{B\delta}{2\pi} \frac{I_1 I_{10}}{I_1 + I_4}$$

The above relation has not been verified by comparison to test data, however, downwind free-yaw rigid rotors are observed to be stable in yaw and the above term has been found to be, by far, the largest stabilizing moment.

CONCLUSIONS

The material presented above should be of use in the design and design analysis of wind turbines. Three of the four developments have been compared with test data.

REFERENCES

1. Wilson, R.E., and Walker, S.N., Fixed Wake Analysis of the Darrieus Rotor, Oregon State University Report for Sandia Laboratories, Corvallis, Oregon, November, 1980.

2. Holme, O., A Contribution to the Aerodynamic Theory of the Vertical-Axis Wind Turbine, BHRA International Symposium on Wind Energy Systems, September 1976.

3. Worstell, M.J., Unpublished data.

4. Akins, R.E., Performance Evaluation of Wind Energy Conversion Systems Using the Method of Bins-Current Status, SAND77-1375, Sandia Laboratories, Albuquerque, NM, March 1978.

5. Eppler, R., Turbulent Airfoils for General Aviation, AIAA Journal of Aircraft, Vol. 15, No. 2, February 1978.

6. Glauert, H., The Analysis of Experimental Results in the Windmill Brake and Vortex Ring States of an Airscrew, British ARC R&M 1026, 1926.

7. Dugundji, J., Larrabee, E.E., and Bauer, P.H., Experimental Investigation of a Horizontal Axis Wind Turbine, Volume V, Wind Energy Conversion ASRL TR-184-11, MIT Department of Aeronautics and Astronautics, Cambridge, MA, 1978.

8. Ribner, N.S., Propellors in Yaw, NACA Report 820, Washington, D.C., 1948.

QUESTIONS AND ANSWERS

R.E. Wilson

From: T. Currin

Q: Effects of articulation on yaw forces and motions? Order of magnitude with coning?

A: *Professor Miller's paper, "On the Weathervaning of Wind Turbines," (Journal of Energy, Vol. 3, No. 5, Sept-Oct 1979, pp. 319-320), develops expressions for teetering and articulated rotors. His paper was the first to note the dihedral like effect of coning.*

From: J. Glasgow

Q: How did you get measurements for the power coefficient on Sandia machine?

A: *Data was obtained using the method of Bins (4) by Sandia (3).*

From: F. Perkins

Q: When will a wind turbine enter the vortex ring state, and what will the loads look like (steady state or not, large or small)?

A: *The blade normal loads as measured (7) are large. The time histories of these loads appeared to be steady.*

From: I. Paraschivoiu

Q: Did you calculate the loads distribution as a function of the azimuthal angle θ for a vertical-axis turbine?

A: *Yes, loads were calculated as a function of θ. As would be expected, the upwind blade positions experience the largest loads.*

From: L. Mirandy

Q: Vortex ring formula implies C_T can reach 1.5. I have never seen any data mech. over 1.0, have you?

A: *The data of Glauert (British Aeronautical Research Committee Reports & Memoranda No. 1026, Feb. 1926) has C_T up to 1.5 and above.*

AERODYNAMIC PERFORMANCE PREDICTION OF HORIZONTAL AXIS WIND TURBINES

D. R. Jeng, T. G. Keith and A. Aliakbarkhanafjeh

Department of Mechanical Engineering
The University of Toledo
2801 W. Bancroft Street
Toledo, Ohio 43606

ABSTRACT

The purpose of this work is to describe a new method for calculating the aerodynamic performance of horizontal axis wind turbines. The method, entitled the helical vortex method, directly calculates the local induced velocity due to helical vortices that originate at the rotor blade. Furthermore, the method does not require a specified circulation distribution.

Results of the method are compared to similiar results obtained from Wilson PROP code methods (Prandtl, Goldstein, NASA and no tip loss) as well as to existing experimental data taken from the NASA Mod-0 wind turbine. It is shown that results of the proposed method agree well with experimental values of the power output both near cut-in and at rated wind speeds. Further, it is found that the method does not experience some of the numerical difficulties encountered by the PROP code when run at low wind velocities.

INTRODUCTION

Recently there has been a renewed interest in wind turbines as a means of producing power. Considerable effort has been directed toward experimental and theoretical studies of wind turbine performance.

At present, the analytical method used in predicting aerodynamic wind turbine performance by the NASA Wind Energy research group utilizes a modified blade element theory [1] or Glauert vortex theory incorporated with Prandtl [2], Goldstein [3] and NASA [4] tip loss models. In the Glauert vortex theory, it is assumed that trailing vortices originate from the rotating blades and form a helical vortex system that passes down stream. This vortex system, in turn, induces velocities which alter the flow around the blade. However, in this method, the induced velocities are not determined directly due to the complexity of the method. Instead, an interference velocity is calculated as the induced velocity of this vortex system on any blade element. The calculation of these interference velocities is simplified by assuming that the rotor has an infinite number of blades. The latter assumption removes the complexity associated with the periodicity of the flow and permits momentum theory to be directly used to evaluate the interference velocities. However, for single and double bladed rotors, this assumption may be inadequate.

Consider a wind turbine, rotating with an angular velocity Ω about its horizontal axis of rotation, that is placed in a uniform stream of wind of velocity V_o parallel to the axis of rotation. The blade can be coned or tilted to an angle of ψ from the plane perpendicular to the axis of rotation. The velocity experienced by the typical blade is shown in Fig. 1. It can be seen from Fig. 1, that $V_o(1-a)\cos\psi$ is the wind free stream velocity minus the axial interference velocity normal to the blade surface. Further, $\Omega r(1+a')\cos\psi$ is the relative velocity of blade to the air velocity and accordingly is the angular velocity of the blade section plus the rotational interference velocity. The factors, a and a' are the axial and the rotational interference factors respectively.

In order to evaluate the local drag force and torque, the interference factors a and a' must first be determined. However, before presenting the equations for determining a and a', it may be helpful to review the tip and hub losses for a blade. It should be anticipated that the flow around a rotor blade of finite length will be disturbed at the tip and root or hub of the blade. These disturbances are due to the fact that the difference of pressure between the upper and lower sides of the blade disappear along the blade span and must therefore diminish to zero toward the tip and hub. An approximate method of estimating the effect of these radial disturbances has been given by Prandtl [2]. Later, a more accurate solution to this problem was developed by Goldstein [3]. Introducing a reduction factor, F, to account for the fact that only a fraction of the air between successive vortex sheets of the slip stream receives the full effect of the motion of these sheets, into the momentum equation for the flow at radius r and then equating the differential drag and torque equations obtained respectively from momentum and blade element theories, permits the writing of equations which must be satisfied by a and a'. These equations may be written as:

$$\frac{a}{1-a} = \frac{\sigma_L(C_L\cos\phi + C_D\sin\phi)\cos^2\psi}{4\,F\sin^2\phi} \qquad (1)$$

and

$$\frac{a'}{1+a'} = \frac{\sigma_L(C_L\sin\phi - C_D\cos\phi)}{4\,F\sin\phi\cos\phi} \qquad (2)$$

Expressions for the reduction factor F can be found in [2,3]. The tip loss method which has been used by NASA is the so-called "effective radius model". Due to the radial flow near the boundary of the slipstream, there is a drop of circulation which can be represented by an equivalent rotor with an infinite number of blades

and with the same drag force but with a smaller radius R_e, i.e., an effective radius is defined as

$$R_e = B_o \cdot R \tag{3}$$

where B_o is a constant tip loss factor.

Wilson and Walker [4] developed a computer program called PROP to evaluate the solution of eqs. (1) and (2). A preassigned tip loss factor (F = 1, no tip loss) was used and an iteration procedure for determining $\underline{a}$ and $\underline{a'}$ for a given differential element was employed. Once $\underline{a}$ and $\underline{a'}$ were determined, torque, drag and power could all be calculated from the appropriate equations. However, the value of the axial interference factor $\underline{a}$ has a limit. For a positive axial velocity V_o, the induced axial velocity of out flow near the rotor with a coning angle ψ is (V_o a cosψ), thus, from vortex theory, the induced axial velocity in the ultimate slipstream will be ($2V_o$a cosψ). Therefore, the trailing velocity of air far behind the rotor is [V_o(1-2a)cosψ]. Equations (1) and (2) are based on the notion that the axial velocity at any location is unidirectional, and, therefore, the analysis is valid only if $a \leq \frac{1}{2}$. If the rotor absorbs all the energy, i.e., $V_2 = 0$, then $\underline{a}$ would have a maximum value of $\frac{1}{2}$. Unfortunately, by using the PROP code to calculate $\underline{a}$, under certain operating conditions, particularly for large tip speed ratios (small wind velocities), the local value of the axial interference factor can exceed this limiting value for all tip loss models. Therefore, the equations cease to be valid. It was also found that the PROP code generally underestimated the performance [5, 6]. Accordingly, it is the purpose of this paper to develop a computational method for predicting aerodynamic performance of a horizontal axis wind turbine that avoids these difficulties. In this method, the induced velocity is directly calculated by integration of Biot-Savart's law under the assumption that a filament of the trailing vortices is helical in nature, extends infinitely downstream of the rotor, and has constant pitch and diameter. Of primary importance, the method does not use interference factors.

The predicted performance of wind turbines obtained by use of the present technique will be compared with those obtained from the PROP code and with some experimental data obtained from the Mod-0 100 kw wind turbine operated by NASA - Lewis Research Center in Sandusky, Ohio.

ANALYSIS

General Assumptions and Discription of the Problem

Two major assumptions upon which the present analysis is based may be stated as follows:

1.) The trailing vortex system is helicoidal with constant pitch and diameter, and extends infinitely far downstream from the blade.

2.) The relative velocity of a blade element to the medium is identical to that in two-dimensional motion if reference is made to the relative velocity between the element and the medium.

Unlike Goldstein theory, the helical vortex assumption does not restrict the circulation distribution along the blade. In the Goldstein theory, an optimum circulation distribution was used that corresponded to a rigid helicoidal vortex system moving backward with constant velocity. However, in both theories, it is assumed that the slipstream expansion may be secondary and thus neglected.

The physical model of the problem is illustrated in Fig. 2. The coordinate system, which is shown in Fig. 3 was chosen such that the z coordinate is the distance measured from the rotor to a segment of the trailing vortex parallel to the axis of rotation of the rotor and that the r axis is along the blade. The conning angle of blade is ψ. The induced velocities are computed in terms of the coordinate system in Fig. 3 as will be demonstrated in the next section.

Calculation of Induced Velocity

Suppose that circulation at a particular span location, say r, of the blade is Γ. The circulation at a nearby point, say r + dr is

$$\Gamma + \frac{d\Gamma}{dr}\, dr \quad .$$

The difference in these circulation values i.e., $\frac{d\Gamma}{dr}\, dr$, according to Helmholtz theory, the strength of a vortex that will spring out from the blade element of dr to form the trailing vortex, Fig. 2. The induced velocity normal to the resultant velocity W at a point r' due to the helical vortex filament originating from each of the blades and extending to infinity is determined, via the Biot-Savart' law [7] by,

$$w_n(\xi) = \int_{\xi_{hub}}^{1} \frac{\frac{d\Gamma}{d\xi}\, d\xi}{4\pi R\cos\psi} \sum_{k=1}^{B} \int_o^{\infty} \frac{N_1 + N_2}{D_1^{3/2}\, D_2^{1/2}}\, d\theta \tag{4}$$

where $N_1 = (\xi - \xi'\cos\theta_k)\xi\xi'$

$N_2 = [\xi(\theta\sin\theta_k + \cos\theta_k) - \xi']\lambda_o^2\cos^2\psi$

$D_1 = \xi^2 + \xi'^2 - 2\xi\xi'\cos\theta_k + \theta^2\lambda_o^2\cos^2\psi$

$D_2 = \lambda_o^2\cos^2\psi + \xi'^2$

$\theta_k = \theta + \frac{2\pi(B-k)}{B}$

$\lambda_o = \frac{V_o}{\Omega R\cos\psi}$

$\xi = \frac{r}{R}$

$\xi' = \frac{r'}{R}$

An expression similar to eq. (4) was employed by Plencner [8] for studying propeller characteristics.

The integration with respect to θ in eq. (4) is an arduous task. Furthermore, the form of the expression, as it stands, is inconvenient for practical use because the integral becomes infinitely great at the point $\xi' = \xi$ and $\theta = 0$. Clearly, this feature unless properly handled can cause considerable errors when calculating the induced velocity.

Moriya [7] proposed a method to remedy the problem. In his method, he introduced a so-called induction factor I which is defined as

$$I(\xi,\xi',\lambda_o) = (\xi-\xi') \sum_{k=1}^{B} \int_o^{\infty} \frac{N_1 + N_2}{D_1^{3/2} D_2^{1/2}} \, d\theta \qquad (5)$$

With this factor, the singularity at $\xi = \xi'$ can be shown to reduce eq. (4) to

$$w_n = \int_{\xi_{hub}}^{1} \frac{\frac{d\Gamma}{d\xi} \, d\xi \quad I}{4\pi R \cos\lambda \quad (\xi-\xi')} \qquad (6)$$

It should be mentioned that the induction factor, which is a continuous function of λ_o, ξ and ξ', is simply the ratio of the normal induced velocity for a helical trailing vortex system to the normal induced velocity for a straight trailing vortex system of the same strength. At a point $\xi' = \xi$, the induction factor I has a value of unity. In the following, the induction factor will be determined by numerical integration using 24 terms of a Lagurre-Gaussian Quadrature [9].

Governing Equation Formulation

The governing equation used in this study can be established from the fact that if the blade section is set at a geometrical angle of attack, α_g, relative to the incoming wind velocity, W, as shown in Fig. 4, its setting relative to W is α_g diminished by the downwash angle, α_i. This relation may be written as

$$\alpha_g = \alpha_e - \alpha_i \qquad (7)$$

where

$$\alpha_i = \tan^{-1} \frac{w_n}{W}$$

and α_e is an effective angle of attack. The negative sign appearing in eq. (7) occurs because the induced angle of attack, α_i, is itself a negative number. The geometric angle of attack can be obtained from Fig. 4 as

$$\alpha_g = \tan^{-1} \frac{\lambda_o \cos\psi}{\xi'} - \beta \qquad (8)$$

where β is the pitch angle of the blade element at ξ'.

The induced angle of attack may be expanded in series form in terms of $\frac{w_n}{W}$. Moreover, because the value of $\frac{w_n}{W}$ is usually small, it may be assumed that

$$\alpha_i \cong \frac{w_n}{W} = \int_{\xi_{hub}}^{1} \frac{I(\xi,\xi',\lambda_o) \frac{d\Gamma}{d\xi} \, d\xi}{4\pi\Omega R^2 \cos^2\psi \, D_2^{\frac{1}{2}} \, (\xi - \xi')} \qquad (9)$$

The circulation function, Γ, may be expressed as a Fourier-Sine series satisfying the following boundary conditions

$$\Gamma(\xi = 1) = \Gamma(\xi_{hub}) = 0$$

An expression that meets these conditions may be written as

$$\Gamma(\xi) = \sum_{m=1}^{\infty} A_m \sin m\pi \left(\frac{\xi-\xi_{hub}}{1-\xi_{hub}} \right) \qquad (10)$$

The relation between circulation and lift coefficient is given by the Kutta-Joukowski theorem for a two-dimensional airfoil as

$$\Gamma = \tfrac{1}{2} \, c \, W \, C_L \qquad (11)$$

where c is the chord length.

Using equations (5) and (7) through (11), the aerodynamic characteristics for a given blade element can be determined. The calculation involves an iteration process and requires that the series for Γ be truncated at N terms. A computer program has been developed for this iteration and proceeds according to the following logic:

1) Assume $\alpha_e = \alpha_g$ in the first iteration.

2) Find C_L from two-dimensional airfoil data such as that shown in Figs. (5) and (6). In the program, experimental data for C_L and C_D were curve fitted using polynomials and were stored in the program.

3) Calculate the local circulation $\Gamma(\xi)$ by employing eq. (11).

4) With the values of $\Gamma(\xi)$ known at each location ξ, the constant's, A_m, appearing in eq. (10) can be determined by solving a set of linear algebric equations.

5) Calculate local α_i by using eq. (9). This can be done by substituting eq. (10) into eq. (9) and integrating the resulting equation. However, in practice, the integral is broken into three separate integrals to remove the singularity as follows

$$\int_{\xi_{hub}}^{1} g(\xi)d\xi = \int_{\xi_{hub}}^{\xi'-\delta} g(\xi)d\xi + \int_{\xi'-\delta}^{\xi'+\delta} g(\xi)d\xi + \int_{\xi'+\delta}^{1} g(\xi)d\xi \qquad (12)$$

where δ is an arbitrarily small number, say $\delta = 10^{-5}$.

The first and the last terms on the right hand side of eq. (12) can be evaluated by using standard numerical integration procedures. The second integral on right hand side of eq. (12) contains a singularity, but, it can be shown that its value is very small, $0(10^{-4})$, and, thus, may be ignored in the calculation.

6) Calculate a new $\alpha_e = \alpha_g + \alpha_i$.

7) Obtain C_L from two-dimensional data using newly calculated α_e.

8) Compare the current C_L to the previous value of C_L, and if equal, stop, otherwise repeat the iteration by returning to step 3.

Power, Torque and Drag on Wind Turbine

Once the iteration process is successfully terminated and the effective angle of attack distribution calculated, the rotor thrust, torque and power can be calculated respectively from the following equations

$$\frac{dT}{dr} = \tfrac{1}{2}\rho BcW^2(C_L\cos\phi+C_D\sin\phi)\cos\psi$$

$$\frac{dQ}{dr} = \tfrac{1}{2}\rho BcW^2(C_L\sin\phi-C_D\cos\phi)r\cos\psi$$

Integration yields

$$T = \int_{\xi_{hub}}^{1} (\tfrac{1}{2}\rho BcW^2)(C_L\cos\phi+C_D\sin\phi)R\cos\psi d\xi \qquad (13)$$

$$Q = \int_{\xi_{hub}}^{1} (\tfrac{1}{2}\rho BcW^2)(C_L\sin\phi-C_D\cos\phi)R^2\cos\psi \; d\xi \qquad (14)$$

$$P = \int_{\xi_{hub}}^{1} (\tfrac{1}{2}\rho BcW^2)(R^2\Omega\cos\psi)(C_L\sin\phi-C_D\cos\phi)\xi d\xi \qquad (15)$$

RESULTS AND DISCUSSION

The proposed method has been used to calculate performance of two-bladed wind turbines. The particular blade and operating conditions, listed in Table 1 and used in the calculations, correspond to those of NASA's Mod-0, 100kw large wind turbine located in Sandusky, Ohio. Further description of this facility may be found in [10].

A circulation distribution corresponding to the operating condition tabulated in Table 1 is plotted in Fig. 8. As one can see, it is quite irregular and departs greatly from an eliptical shape generally used in aerodynamic studies in which the distribution of circulation is unknown.

An empirical expression, taken from [11], was used in the calculations to compare predicted to recorded alternator power. This expression accounts for drive train losses and is given as

$$P_G = 0.95\,(P_R - 0.075\,P_E) \qquad (16)$$

in which:

P_G ; generated electrical power, kw

P_R ; power produced by rotor, kw

P_E ; rated electrical power, kw (100 kw).

Predicted alternator power is plotted against wind speed in Fig. 9. Also shown are corresponding theoretical results obtained by using the PROP computer code and existing experimental data [12].

From these figures, it can be seen that there is a closer correlation between the values predicted by the present method and the experimental data than there is with the four PROP code methods of predictions. It is generally known that PROP code models underestimate performance compared with experimental data [5, 11, 13]. However, our results are 10 to 15% higher than are PROP code values for wind speeds ranging from 8 to 20 mph. There is excellent agreement between our data and the experimental values. Our data predicts a "cut-in" wind speed of 8 mph which agrees with the actual value reported in [5]. It is known that the "cut-in" speed is not predicted accurately by any of the methods found in the PROP code.

Other calculations have been made for the MOD-1 wind turbine (2MW). The operating conditions and the input data for these calculations are listed in Table II. The airfoil used for the blade construction is an NACA 4418 with a "half rough" surface condition and a variable twist angle along the blade span.

The chord and twist angle are tabulated in Table III.

The power coefficient C_p vs. tip speed ratio for MOD-1 is presented in Fig. 10. As can be seen, the results obtained from the PROP code are unlikely as the power coefficient has a saddle-like distribution. On the other hand, our results do not exhibit this behavior. It is believed that incorrect handling of the interference factors is the source of the difficulty.

ACKNOWLEDGEMENTS

The research project was sponsered by NASA Wind Energy Research Program under the contract number NCC3-5.

REFERENCES

[1] W. F. Durand, (Ed.) "Aerodynamic Theory" Chap. VII, Sec. 4, pp. 169-360.

[2] L. Prandtl, "Application of Modern Hydrodynamics to Aeronautics", NASA Report 116, 1921.

[3] S. Goldstein, "On the Vortex Theory of Screw Propellers", Proceeding of the Royal Society of London, Series A, 123, 1923.

[4] R. E. Wilson and S. N. Walker, "A Fortran Program for the Determination of Performance, Loads, and Stability Derivatives of Wind Tubeines", Department of Mechanical Engineering Oregon State University, Corvallis, Oregon, Oct. 1974.

[5] T. Richards, "Mod-0 Performance" NASA Lewis Research Center, Cleveland, Ohio, Wind Energy Project PIR No. 11, 1977.

[6] L. Viterna, "An Improved Aerodynamic Model for Wind Turbines", NASA Lewis Research Center, Cleveland, Ohio, Wind Energy Project PIR 144 1980.

[7] T. Moriya, "Selected Scientific and Technical Papers", University of Tokyo, Tokyo, Japan 1959.

[8] R. M. Plencner, "Numerical Analysis of Subsonic Propellers", Master Thesis of Aeronautical and Astronautical Engineering, University of Illinois at Urbana-Champaign, 1975.

[9] Shao, Chen, Frank, "Tables of Zeros and Caussian Weights of Certain Associated Laguerre Polynomials and Related Generalized Hermite Polynomials", IBM Technical Report TR00.1100, March 1964.

[10] R. L. Thomas and T. R. Richards, "ERDA/NASA 100 kw Mod-0 Wind Turbine Operations and Performance", ERDA/NASA/1028-7719, NASA TM-73825.

[11] L. Viterna, "Mod-0 Utility Pole Blade Performance", NASA Lewis Center, Cleveland, Ohio Wind Energy Project PIR 109, 1979.

[12] H. Neustadter and R. Wolf, "Mod-0 Hard and Soft Tower; Utility Pole Blades; Power, Flap Bending, Chord Bending and Horizontal Acceleration", NASA Lewis Research Center, Cleveland Ohio, Wind Energy Project PIR 106, 1979.

[13] L. Viterna, "An Improved Aerodynamic Model for Wind Turbines", NASA Lewis Research Center, Cleveland, Ohio, Wind Energy Project PIR 144, 1980.

NOMENCLATURE

a	axial interference factor
a'	rotational interference factor
B	number of blade
c	chord
C_D	drag coefficient
C_L	lift coefficient
C_p	power coefficient
L	lift
P	power
Q	torque
Q_c	torque coefficient
r	distance along the blade
r_L	r cos ψ
R	radius of rotor
Re	effective radius
T	thrust
V_o	wind velocity
w_n	normal induced velocity
W	vector sum of rotational and wind velocity
W'	vector sum of W and w_n
z	rearward distance from the rotor
α	angle of attack
α_e	effective angle of attack
α_g	geometric angle of attack
α_i	induced angle of attack
β	pitch angle
Γ	circulation
ρ	density
σ_L	solidity = $\frac{BC}{2 r_L}$
ψ	corning angle
Ω	rotational speed of blade

Table I - Operating Condition of the Utility Pole Wind Turbine

Root/Tip Chord	6.25/2.08
Chord Distribution	see Fig. 7
Percent Root Cut	23%
Blade Radius R, ft	62.5
Conning Angle, deg.	3.8
Solidity	0.033
Thickness to Chord Ratio	.24
Airfoil	NASA 230-24
Pitch Angle	0
Airfoil Surface	Rib Stitched, Fiberglass Cloth (half rough)
Operating RPM	32 and 33 rpm for 2 blade
Twist Angle	0

Table II - Input Data and Operating Condition for MOD-1 Wind Turbine (2MW)

Root/Tip Chord	12/2.82
Blade Radius R, ft.	100.8
Hub Radius	9.75
Percent Root Cut	10%
Conning Angle, deg.	9
No. of Blade	2
Airfoil	NASA 4418 (half rough)
Pitch Angle	0
Operating RPM	34.7
Solidity	0.042

Table III - Chord and Twist Angle

r/R	Chord ft.	Twist Angle degree
1	2.82	-3
.9	3.9	-1.85
.8	5.0	-0.62
.7	5.95	0.62
.6	6.95	1.85
.5	8.0	3.0
.4	9.0	4.28
.3	10.03	5.5
.2	11.03	6.69
.1	12.0	8.0

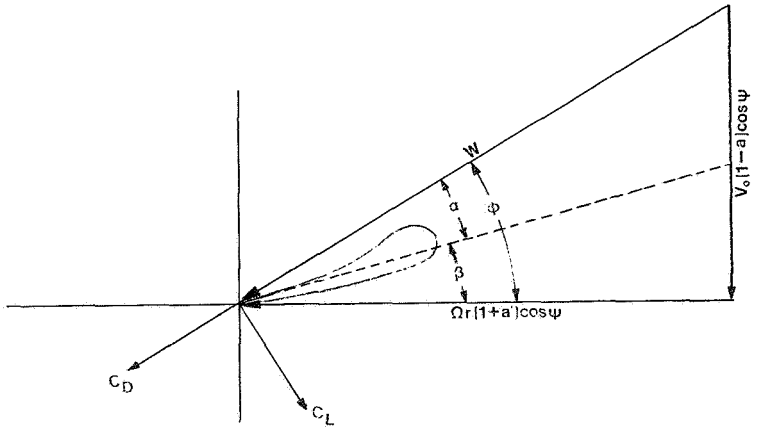

Fig. 1 - Force and velocity diagram for Glauert vortex theory.

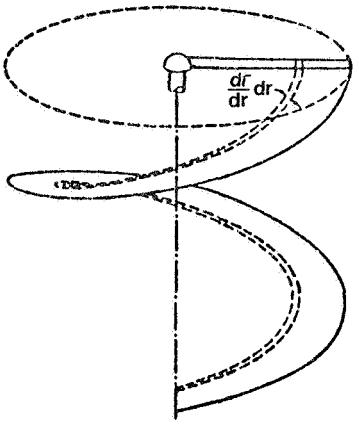

Fig. 2 - Physical model of the problem.

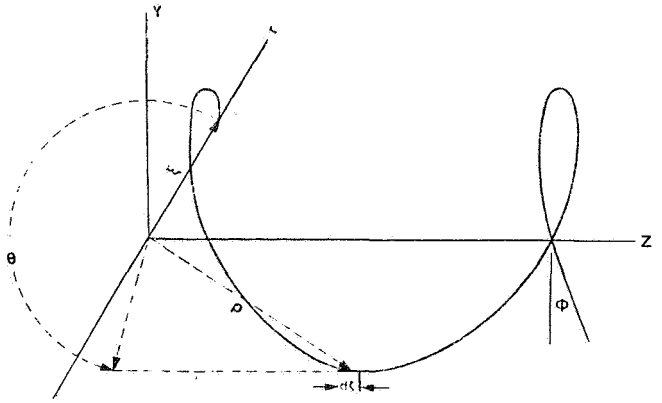

Fig. 3 - Helical vortex geometry and coordinate system.

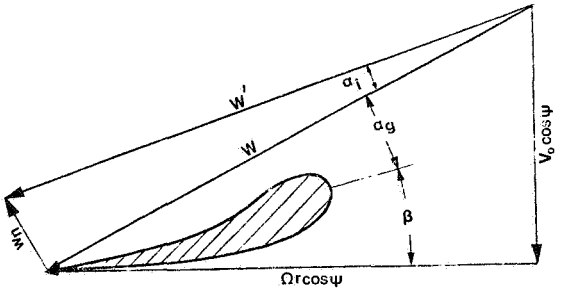

Fig. 4 - Velocity diagram showing the effect of induced velocity.

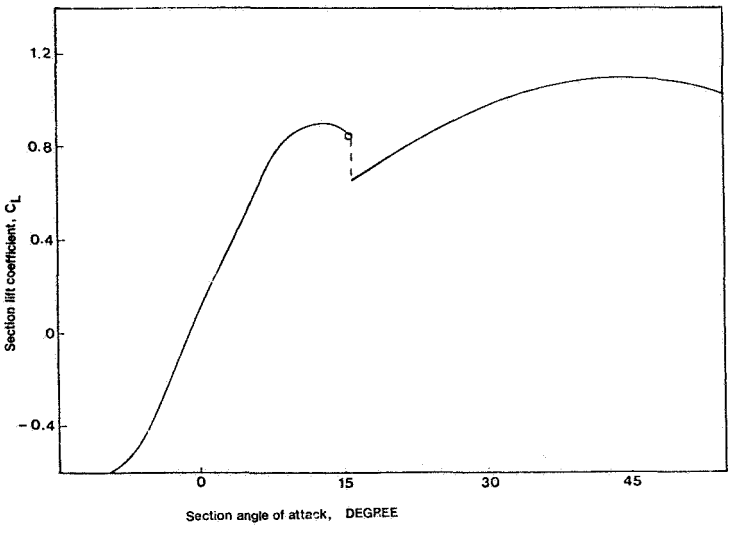

Fig. 5 - Lift coefficient vs. angle of attack for a half rough 23024 airfoil.

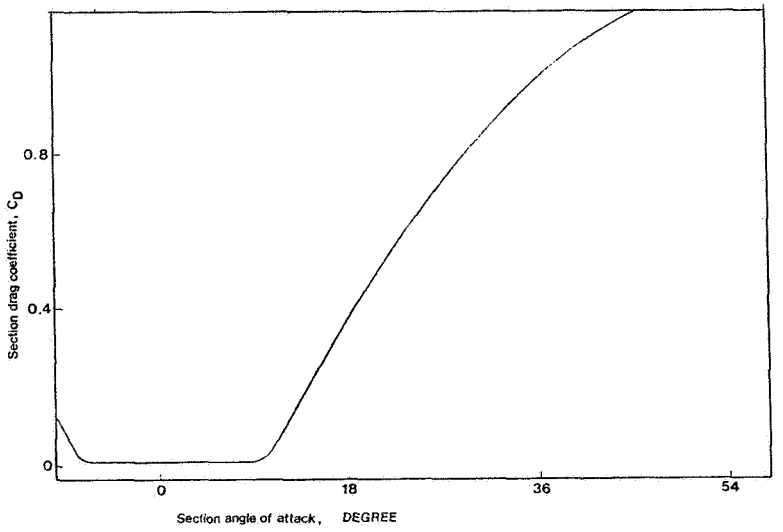

Fig. 6 - Drag coefficient vs. angle of attack for a half rough 23024 airfoil.

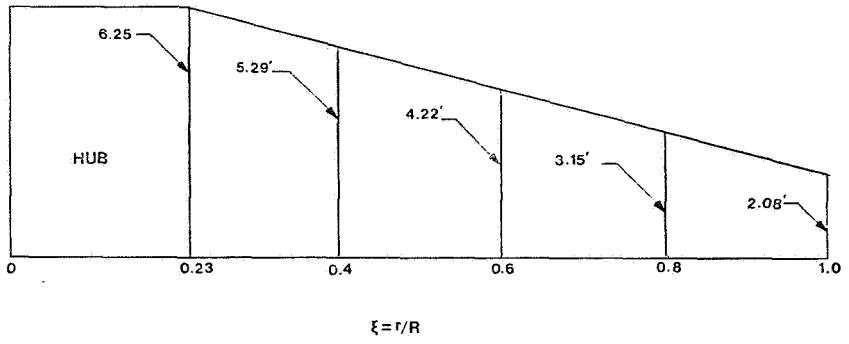

Fig. 7 - Chord distribution along the blade.

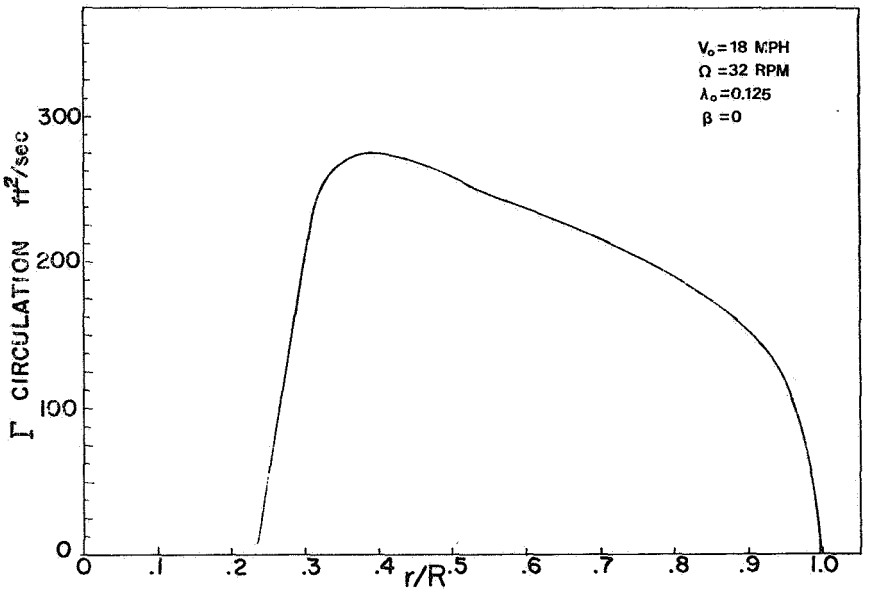

Fig. 8 - Circulation Distribution.

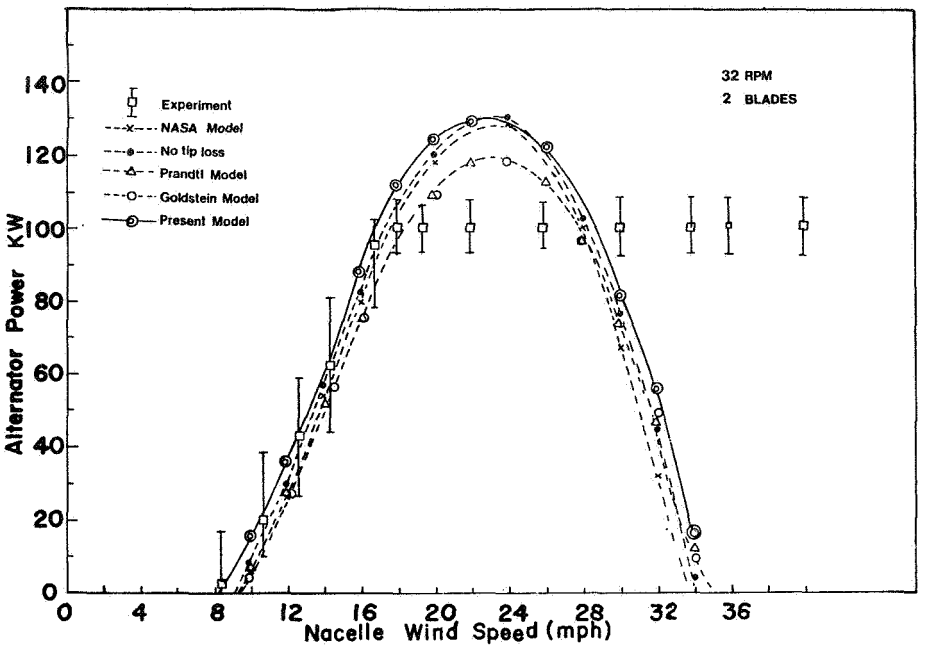

Fig. 9 - Alternator power vs. wind speed; zero pitch angle.

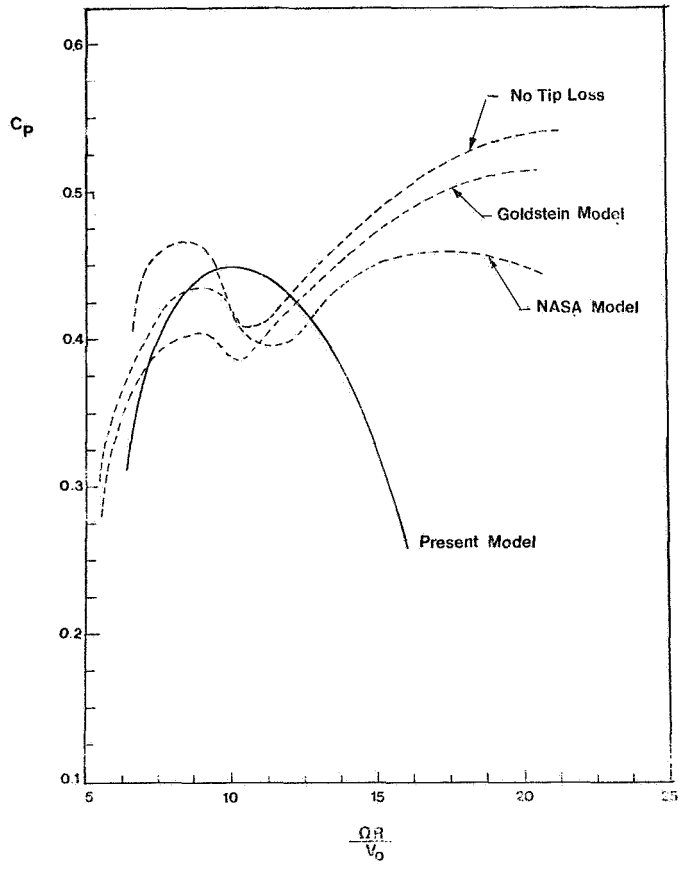

Fig. 10 - Cp vs. tip speed ratio, MOD-1 (NASA 4418 airfoil).

QUESTIONS AND ANSWERS

D. Jeng

From: Anonymous

Q: Can you comment on actual power being higher than predicted at high wind speed?

A: *Comparison between experimental and theoretical values is valid only between wind speeds of 8 mph to 18 mph. When the wind turbine reaches the rated power of 100 kW. Because the blade geometry for the theoretical calculation was not changed, the actual power and predicted power cannot be compared for wind speeds which exceed the rated value of 18 mph (Fig. 9).*

From: Anonymous

Q: Can any conclusion about aerodynamic correlation be drawn from cut in speed results which are largely dependent on mechanical friction and may vary from season to season?

A: *To obtain alternator power, the rotor power values were corrected for drive train losses by an empirical equation applicable for the MOD-0 wind turbine and given in the text. It is assumed that the power loss due to friction for this particular machine is 7.5 kW which is constant. By comparing the cut-in speed, we can compare the actual rotor power (alternator power is zero) and the predicted rotor power at the lowest wind speed.*

DOUBLE-MULTIPLE STREAMTUBE MODEL FOR DARRIEUS WIND TURBINES

Ion Paraschivoiu

Institut de Recherche d'Hydro-Québec
Varennes, Québec
Canada, J0L 2P0

ABSTRACT

An analytical model is proposed for calculating the rotor performance and aerodynamic blade forces for Darrieus wind turbines with curved blades. The method of analysis uses a multiple-streamtube model, divided into two parts: one modeling the upstream half-cycle of the rotor and the other, the downstream half-cycle. The upwind and downwind components of the induced velocities at each level of the rotor were obtained using the principle of two actuator disks in tandem.

Variation of the induced velocities in the two parts of the rotor produces larger forces in the upstream zone and smaller forces in the downstream zone. Comparisons of the overall rotor performance with previous methods and field test data show the important improvement obtained with the present model.

The calculations were made using the computer code CARDAA developed at IREQ. The double-multiple streamtube model, presented in this paper, has two major advantages: it requires a much shorter computer time than the three-dimensional vortex model and is more accurate than multiple-streamtube model in predicting the aerodynamic blade loads.

INTRODUCTION

The Darrieus-type vertical-axis wind turbine is one of the best wind energy conversion system. This curved-blade turbine is now under theoretical and experimental study in the U.S., at Sandia Laboratories (2-m, 5-m and 17-m turbines), for example, and in Canada at a larger scale with the 230-kW machine in the Magdalen Islands and, recently a new project for building a prototype of about 4000-kW for the end of 1983.

The first approach to modeling the aerodynamic performance of a Darrieus wind turbine was developed by Templin (ref. 1), who supposed that the rotor is enclosed in a single streamtube.

A more complex analytical model is the multiple-streamtube (ref. 2) in which the swept volume of the turbine is divided into a series of adjacent, aerodynamically independent, streamtubes. The blade element and momentum theories are then employed for each streamtube. This model assumes that the induced velocity varies over the frontal disk area, both in the vertical and the horizontal directions.

Rotor power, torque and drag are calculated by averaging the contributions from each streamtube. The multiple streamtube model is a good approach for predicting the overall performance and axial force of Darrieus turbines under conditions where the blades are lightly loaded and the rotor tip speed ratios are low, (refs. 2 and 3).

Other types of aerodynamic performance model for studying vertical-axis wind turbines are based on the vortex theory: these are the fixed-wake (ref. 4) and free-vortex models (refs. 5 and 6). Recently, Strickland (ref. 6) extended the free-vortex model to the curved-blade Darrieus turbine, using a concept of the three-dimensional vortex structure. He used a single lifting/line vortex theory to represent an airfoil segment.

Overall turbine performance in the form of drag, torque and power coefficient, have been reasonably predicted by streamtube models and the analytical results are in good agreement with experimental data. The performance values calculated with vortex model in the same conditions (stalled or unstalled blades) are not much better from this point of view. Although the vortex models have the major advantage of predicting the blade forces more exactly than the streamtube models but they have the disadvantage of requiring considerable computer time.

AERODYNAMIC MODEL

Induced Velocities

The calculation of the induced velocities through the rotor is based on the principle of the two actuator disks in tandem at each level of the rotor, as shown in Figure 1. This analytical method uses a multiple-streamtube model divided in two parts: one for the upstream half-cycle of the rotor and the other for the opposite half-cycle (downstream). The multiple-streamtube model has been extended to the flow field upstream and downstream of the rotor.

The upwind and downwind components which traverse each streamtube are considered separately and the variations in the freestream velocity are incorporated into the model. The freestream velocity profile is given by the following relation:

$$V_{\infty i}/V_{\infty} = \left(Z_i/Z_{EQ}\right)^{\alpha_w} \qquad (1)$$

The upwind velocity component is less than the local ambient wind velocity, $V < V_{\infty i}$, and in the middle plane between the upstream and the downstream zone there is an equilibrium-induced velocity, $V_e < V$; thus the induced velocity decreases in the axial streamtube direction so that the downwind component is less than the equilibrium velocity, $V' < V_e$. Figure 1 shows the velocities induced into a pair of actuator disks in tandem with Lapin's assumption, (ref. 7). For the upstream half-cycle of the rotor, the local

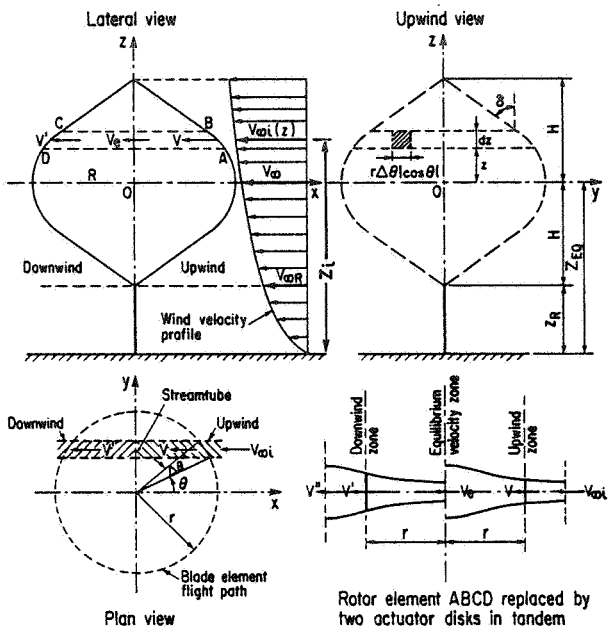

Figure 1 - Definition of rotor geometry for a Darrieus wind turbine. Two actuator disks in tandem.

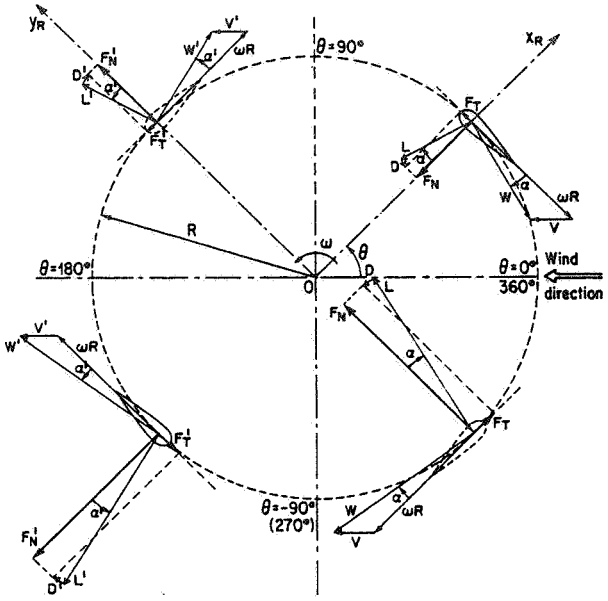

Figure 2 - Angles, force and velocity vectors at the equatorial plane.

wind velocity $V_{\infty i}$ decreases by an interference factor of $u < 1$ and the induced velocity becomes

$$V = uV_{\infty i} \tag{2}$$

Finally the equilibrium-induced velocity is

$$V_e = (2u-1)\ V_{\infty i} \tag{3}$$

For the downstream half-cycle of the rotor, V_e is the input velocity and, at the end of the streamtube, the induced velocity can be written

$$V' = u'\ (2u-1)\ V_{\infty i} \tag{4}$$

where $u' = V'/V_e$ is the second interference factor for this part of the rotor, $u' < u$.

Under these conditions, the streamtube induced velocity is calculated by a double iteration, one for each part of the rotor.

Upstream Half-Cycle of the Rotor

The local relative velocity for the upstream half-cycle of the rotor, $-\pi/2 \leq \theta \leq \pi/2$, is given by the expression:

$$W^2 = V^2\left[(X - \sin\theta)^2 + \cos^2\theta\ \cos^2\delta\right] \tag{5}$$

where $X = \omega r/V$ represents the local tip speed ratio. The definitions of the angles, and the force and velocity vectors at the equatorial plane of the rotor are given in Figure 2. The general expression for the angle of attack is:

$$\alpha = \arcsin\left[\frac{\cos\theta\cos\delta\cos\alpha_0 - (X-\sin\theta)\sin\alpha_0}{\sqrt{(X - \sin\theta)^2 + \cos^2\theta\ \cos^2\delta}}\right] \tag{6}$$

This Equation suggests the possibility of an asymmetrical section or a symmetrical section where the chord line is not tangent to the circle of rotation (or blade flight path), $\alpha_0 \neq 0$, here we supposed $\alpha_0 = 0$.

Using the blade element theory and the momentum equation at each streamtube and by equating the vertical variation of the induced drag coefficient of the rotor, we found:

$$F_{up}\ (V/V_\infty)^2 = \pi\eta\ (V/V_\infty)\left[(V_{\infty i}/V_\infty) - (V/V_\infty)\right] \tag{7}$$

or, in the terms of the interference factor,

$$F_{up}\,u = \pi\eta\ (1-u) \quad , \quad \eta = r/R \tag{8}$$

where F_{up} is the function that characterizes the upwind conditions

$$F_{up} = \frac{Nc}{8\pi R}\int_{-\pi/2}^{\pi/2}\left(C_N\frac{\cos\theta}{|\cos\theta|} - C_T\frac{\sin\theta}{|\cos\theta|\cos\delta}\right)\left(\frac{W}{V}\right)^2 d\theta \tag{9}$$

and

$$\begin{aligned} C_N &= C_L\cos\alpha + C_D\sin\alpha \\ C_T &= C_L\sin\alpha - C_D\cos\alpha \end{aligned} \tag{10}$$

The blade airfoil section lift and drag coefficients, C_L and C_D respectively, are obtained from NASA and Sandia Laboratories test data by interpolation using both the local Reynolds number and the local angle of attack.

Defining the blade Reynolds number as $Re_b = Wc/\upsilon_\infty$, for local conditions, Re_b is given by the following relation:

$$Re_b = \left(Vc/\upsilon_\infty\right)\sqrt{(X - \sin\theta)^2 + \cos^2\theta\ \cos^2\delta} \tag{11}$$

where c is the airfoil chord and υ_∞ is the kine-

matic viscosity. Introducing the turbine Reynolds number $Re_t = \omega Rc/\upsilon_\infty$, we obtain the relationship between Re_b and Re_t:

$$Re_b = \left(Re_t \eta/X\right)\sqrt{(X - \sin\theta)^2 + \cos^2\theta \cos^2\delta} \qquad (12)$$

For a given rotor geometry and rotational speed ω and a given velocity at each streamtube position from Equation (1), a value of induced local tip speed ratio X is chosen by assuming that the interference factor u is unity. Thus, Re_b and α will be evaluated in first approximation and the characteristics of the blade section profile C_L, C_D. Then, with Equations (10), the normal and tangential force coefficients are estimated, and Equation (9) allows us to evaluate the function F_{up}. With the first value of F_{up} we can calculate another value of the interference factor employing Equation (8) and the iterative process is repeated until successive sets of u are reasonably close. Convergence is fast with a maximum number of iterations at the equatorial streamtube, especially for high tip speed ratios, and the error is less than 10^{-4}. Once the true value of the induced velocity V has been calculated, we can obtain the local relative velocity W with Equation (5) and the effective angle of attack α with Equation (6).

Upstream Blade Forces and Performance

The streamwise blade force, normal and tangential components may be evaluated for each streamtube as functions of the blade position. Half-rotor torque, power and drag are resolved by averaging the contributions from each streamtube for the upstream half-cycle of the rotor.

For each blade in the upstream position, the nondimensional force coefficients as functions of the azimuthal angle Θ are given by:

$$F_N(\Theta) = (cH/S)\int_{-1}^{1} C_N\left(W/V_\infty\right)^2 (\eta/\cos\delta)\, d\zeta, \qquad (13)$$

for the normal force, and by:

$$F_T(\Theta) = (cH/S)\int_{-1}^{1} C_T\left(W/V_\infty\right)^2 (\eta/\cos\delta)\, d\zeta, \qquad (14)$$

for the tangential force, where $\zeta = z/H$ and S is the swept area of the rotor.

The torque produced by a blade element is calculated at the center of each element. By integration along the blade we obtain the torque on a complete blade as a function of Θ:

$$T_{up}(\theta) = \frac{1}{2}\rho_\infty cRH \int_{-1}^{1} C_T W^2 (\eta/\cos\delta)\, d\zeta \qquad (15)$$

The average half-cycle of the rotor torque produced by N/2 of the N blades is thus given by:

$$\overline{T}_{up} = \frac{N/2}{\pi}\int_{-\pi/2}^{\pi/2} T_{up}(\Theta)\, d\theta \qquad (16)$$

and the average torque coefficient will be:

$$\overline{C}_{Q_1} = \frac{NcH}{2\pi S}\int_{-\pi/2}^{\pi/2}\int_{-1}^{1} C_T\left(\frac{W}{V_\infty}\right)^2 \left(\frac{\eta}{\cos\delta}\right) d\zeta d\theta \qquad (17)$$

Thus the power coefficient for the upstream half-cycle of the rotor can be written:

$$C_{P_1} = \frac{\omega R}{V_\infty}\,\overline{C}_{Q_1} = X_{EQ}\,\overline{C}_{Q_1} \qquad (18)$$

Downstream Half-Cycle of the Rotor

For the second half-part of the rotor in the streamflow direction (or downstream half-cycle) the local relative velocity is:

$$W'^2 = V'^2\left[(X' - \sin\theta)^2 + \cos^2\theta \cos^2\delta\right] \qquad (19)$$

where $X' = \omega r/V'$
and the angle of attack is given by Equation (6) where X is replaced by X' with $\pi/2 \leq \theta \leq 3\pi/2$. The induced velocity in this part of the rotor V' is a function of both interference factors: upstream (u) and downstream (u'), and with the condition of continuity we can obtain one of the velocity components in terms of the others for a certain wind velocity $V_{\infty i}$, Equation (4).

Following the same logic used for the upstream half-cycle, we consider that the equilibrium used for the velocity given by Equation (3) is the input condition of the flow in the downstream half-cycle at each streamtube. Thus, the iterative process is initialized by u' = u, where u is the true value obtained for the first part of the rotor at each level.

The transcendental equation which contains the interference downstream factor u' becomes:

$$F_{dw}\, u' = \pi\eta\,(1-u') \qquad (20)$$

where the function F_{dw} is:

$$F_{dw} = \frac{Nc}{8\pi R}\int_{\pi/2}^{3\pi/2}\left(C'_N \frac{\cos\theta}{|\cos\theta|} - C'_T \frac{\sin\theta}{|\cos\theta|\cos\delta}\right)\left(\frac{W'}{V'}\right)^2 d\theta \qquad (21)$$

Downstream Blade Forces and Performance

The normal force coefficient as a function of θ, for a complete blade, is :

$$F'_N(\theta) = (cH/S)\int_{-1}^{1} C'_N\left(W'/V_\infty\right)^2 (\eta/\cos\delta)\, d\zeta \qquad (22)$$

and the tangential force coefficient of the blade as a function of θ is given by:

$$F'_T(\theta) = (cH/S)\int_{-1}^{1} C'_T\left(W'/V_\infty\right)^2 (\eta/\cos\delta)\, d\zeta \qquad (23)$$

The torque on a complete blade, in the downstream half-cycle, as a function of θ is:

$$T_{dw}(\theta) = \frac{1}{2}\rho_\infty cRH \int_{-1}^{1} C'_T W'^2 (\eta/\cos\delta)\, d\zeta \qquad (24)$$

The average half-rotor torque has the following form:

$$\overline{T}_{dw} = \frac{N/2}{\pi}\int_{\pi/2}^{3\pi/2} T_{dw}(\theta)\, d\theta \qquad (25)$$

and the average torque coefficient:

$$\overline{C}_{Q_2} = \frac{NcH}{2\pi S} \int_{\pi/2}^{3\pi/2} \int_{-1}^{1} C_T' \left(\frac{W'}{V_\infty}\right)^2 \left(\frac{\eta}{\cos\delta}\right) d\zeta d\theta \qquad (26)$$

The power coefficient for the downstream half-cycle of the rotor becomes:

$$C_{P_2} = \frac{\omega R}{V_\infty} \overline{C}_{Q_2} \qquad (27)$$

The power coefficient for the full cycle is the weighted sum of the coefficients for the half-cycles:

$$C_P = C_{P_1} + C_{P_2} \qquad (28)$$

RESULTS AND DISCUSSION

In order to verify this analytical model, we calculated the aerodynamic loads of the blades and torque as a function of the blade angular position as well as the power coefficient as a function of tip speed ratio, including the effects due to ambient windstream shear. The theoretical results obtained with the double-multiple-streamtube were compared with other analytical models such as multiple-streamtube and two-dimensional vortex theory, and with the experimental data for Sandia 5-m rotor (ref.8). The rotor of this turbine possesses two (or three) of the straight-line / circular-arc form, with a constant symmetrical airfoil NACA-0015, from hub to hub.

The double-multiple-streamtube model shows important retardation of the flow in the downwind zone of the rotor. The aerodynamic forces on the blades are considered as the nondimensional normal and tangential force coefficients for each element of the blade, separately, in the upwind and downwind positions. The elemental force coefficients were integrated along the length of the blade and the variation with the azimuthal angle was obtained with respect to a rotational-axis system, x_R 0 y_R where x_R has its initial position linked to blade No.1 in Figure 2.

Figure 3 shows the resultant of the normal force coefficient for two blades as a function of the blade position. For a tip speed ratio of X_{EQ}= 3.0, the zero value of F_N may be observed

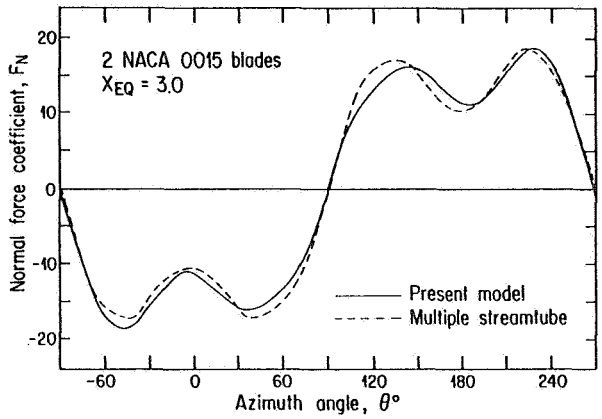

Figure 3 - Comparison between normal force coefficients calculated by the multiple-streamtube theory, and the present model.

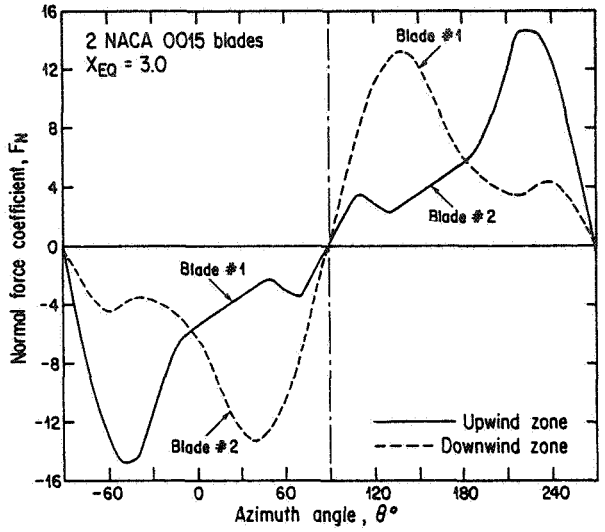

Figure 4 - Variation with azimuthal angle θ of the normal blade loading, for each blade, in the upwind and downwind zones.

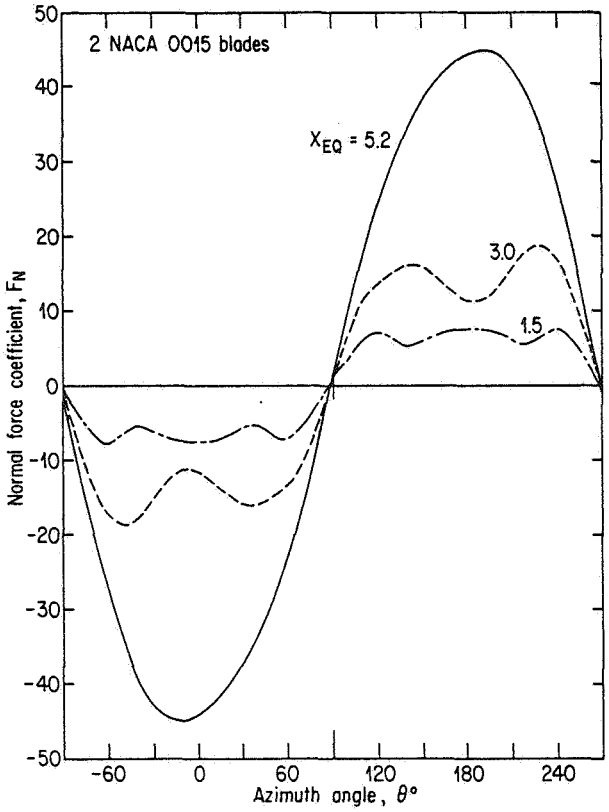

Figure 5 - Variation with azimuthal angle θ of the normal force coefficient, for two blades, at three tip speed ratios.

to occur at $\theta < 90°$ in contrast with $\theta = -90°$, as is the case of the multiple-streamtube model. The variation in the normal force coefficient with the blade position is shown in Figure 4 for each blade; the normal forces are smaller in the downwind than in the upwind zone. The effect of the tip speed ratio on the normal force is presented in Figure 5 for X_{EQ} = 1.5, 3.0 and 5.2.

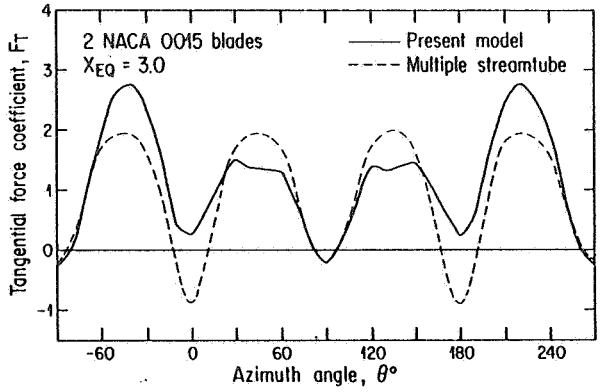

Figure 6 - Comparison between tangential force coefficients calculated by the multiple-streamtube theory and the present model.

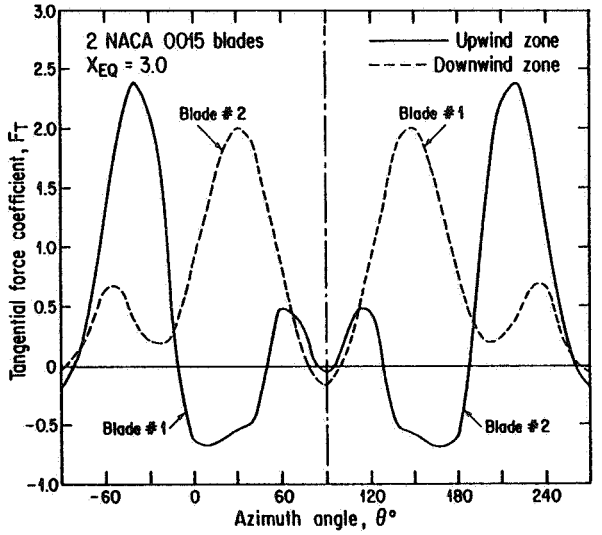

Figure 7 - Variation of the tangential blade loading with the azimuthal angle θ, for each blade, in the upwind and downwind zones.

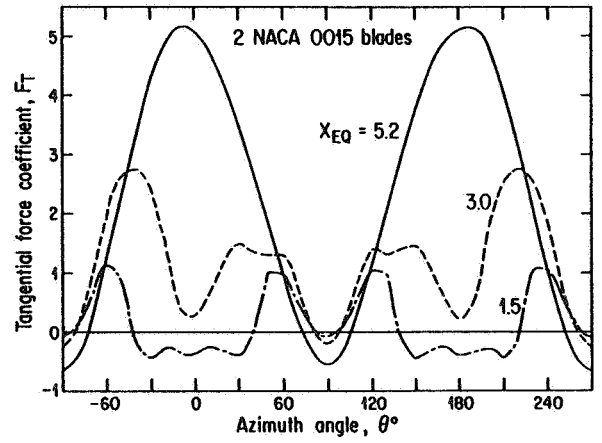

Figure 8 - Variation of the tangential force coefficient with the azimuthal angle θ, for the two blades, at three tip speed ratios.

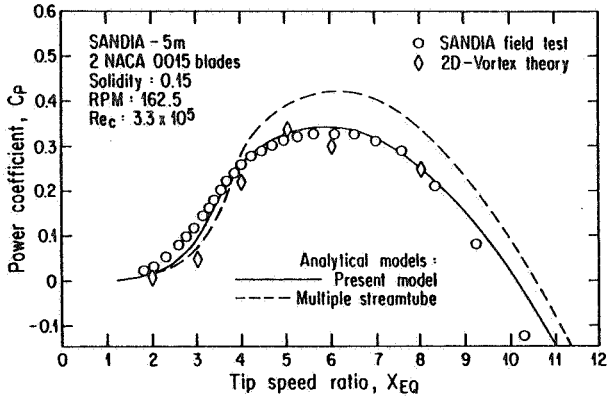

Figure 9 - Power coefficient as a function of the equatorial tip speed ratio. Comparison between analytical model results and field test data for the Sandia 5-m, two-blade rotor.

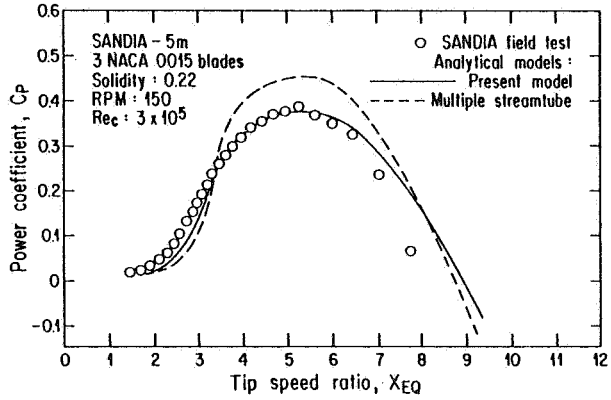

Figure 10 - Power coefficient as a function of the equatorial tip speed ratio. Comparison between analytical model results and field test data for the Sandia 5-m, three-blade rotor.

The tangential force coefficient for two complete blades as a function of the azimuthal angle is plotted in Figure 6 for a tip speed ratio of X_{EQ} = 3.0. The variation of this force calculated with multiple-streamtubes is similar on both half-cycles of the rotor. The tangential forces obtained with the present model are smaller on the downwind face of the rotor in comparison with the tangential forces on the upwind face, Figure 7. The effect of the tip speed ratio on the tangential force is given in Figure 8 for X_{EQ} = 1.5, 3.0 and 5.2.

Figure 9 presents a comparison of the power coefficient results from three analytical models: multiple-streamtubes, two-dimensional vortex theory and double-multiple-streamtubes with Sandia field test data for two NACA-0015 blades, 5-m rotor. We can see that the double-multiple-streamtube model is in good agreement with the experimental data for tip speed ratios of 3.5 to 8.5. The results of the present model are better than with other streamtube methods because the downwind blade sees the induced velocity differently from the upwind blade, $V' < V$. This concept can be improved by considering the effects

of the dynamic stall of the blades which is prevalent at low tip speed ratios and causes the torque to increase.

Figure 10 shows a comparison between the power coefficient obtained from the multiple-streamtube theory, the present model and the Sandia field tests for three NACA-0015 blades, 5-m rotor. There is a good agreement with test data up to tip speed ratio of about 7; for low speed ratios, $X_{EQ} \simeq 3.5$, the same phenomenon as with a two-blade rotor can be observed. There is a big difference between the multiple-streamtube results and experimental data, where the power coefficient reaches its maximum. The tip speed ratio for a maximum power coefficient decreases mainly with increasing drag and does not seem to be influenced by the number of blades. Retardation of the flow in both upstream and downstream zones intensifies with increasing rotor solidity; however, this effect is more significant in the downstream region of the rotor.

CONCLUSION

The present analytical model represents an extension of the multiple-streamtube model, which is capable of calculating the difference in the induced velocities at the upstream and downstream passes. This is possible if it is assumed that each element of the rotor is replaced by two actuator disks in tandem, in the wind direction. The aerodynamic characteristics for each element of the blade were therefore obtained independently for the upwind and downwind parts of the rotor by using both the local Reynolds number and the local angle of attack.

The double-multiple-streamtube model allows for variation of the aerodynamic loads and the torque with the blade position for each part of the rotor. The method is generally adequate for studying a Darrieus rotor with several curved blades. Field test data with a Sandia 5-m machine and comparisons with previous methods satisfactorily confirm the theoretical predictions for the overall performance parameters.

The present model could be improved by considering the effect of dynamic stall on the blades, which would enhance the ability to predict both loads and performance. This refinement is currently under way at IREQ and the results will be compared with those furnished by other analytical models as well as with Magdalen Islands field test data.

ACKNOWLEDGMENTS

This research was fully supported by IREQ. The author would like to acknowledge the contribution of his colleagues in the Wind Energy Program in the form of valuable remarks during the preparation of this paper.

We would like to point out that R.J. Templin of the National Research Council of Canada has dedeveloped a new version of the multiple-streamtube model, which allows for variation of induced velocities through the rotor. His work has not yet been published.

REFERENCES

1. Templin, R.J.: Aerodynamic Theory for the NRC Vertical-Axis Wind Turbine, NRC of Canada TR LTR-LA-160, 1974.

2. Strickland, J.H.: The Darrieus Turbine: A Performance Prediction Model Using Multiple Streamtubes, Sandia Laboratory Report SAND 75-0431, 1975.

3. Klimas, P.C.: Vertical Axis Wind Turbine Aerodynamic Performance Prediction Methods, Proceedings of the Vertical-Axis Wind Turbine (VAWT), Albuquerque, N.M., April 1-3, 1980.

4. Holme, O.: A Contribution to the Aerodynamic Theory of the Vertical-Axis Wind Turbine, International Symposium on Wind Energy Systems, Cambridge, England, September 1976.

5. Fanucci, J.B., and Walters, R.E.: Innovative Wind Machines: The Theoretical Performance of a Vertical-Axis Wind Turbine, Sandia Laboratory Report SAND 76-5586, p.III-61-93.

6. Strickland, J.H., Webster, B.T., and Nguyen, T.: A Vortex Model of the Darrieus Turbine: An Analytical and Experimental Study, Sandia Laboratory Report SAND 79-7058, 1980.

7. Lapin, E.E.: Theoretical Performance of Vertical-Axis Wind Turbines, ASME paper 75-WA/Ener-1, The Winter Annual Meeting, Houston, Texas, Nov. 30 - Dec. 4, 1975.

8. Sheldahl, R.E., Klimas, P.C., and Feltz, L.V.: Aerodynamic Performance of a 5-Metre-Diameter Darrieus Turbine with Extruded Aluminium NACA - 0015 Blades, Sandia Laboratory Report SAND 80-0179.

QUESTIONS AND ANSWERS

I. Paraschivoiu

From: Art Smith

Q: If the Darrieus produces a significant side force, is it not wrong to neglect the lateral component of velocity?

A: *No, because the effect of the lateral component of velocity is normally smaller than 10% of the freestream velocity (see Ref. 6); if the lateral component of velocity is considered the loads prediction will be better.*

The UTRC Wind Energy Conversion System Performance Analysis for Horizontal Axis Wind Turbines (WECSPER)

T. Alan Egolf
Research Engineer
and
Anton J. Landgrebe
Chief, Aeromechanics Research Section
United Technologies Research Center
East Hartford, Connecticut

ABSTRACT

The theory for the UTRC Wind Energy Conversion System Performance Analysis (WECSPER) for the prediction of horizontal axis wind turbine performance is presented. Major features of the analysis are the ability to: (1) treat the wind turbine blades as lifting lines with a prescribed wake model; (2) solve for the wake-induced inflow and blade circulation using real nonlinear airfoil data; and (3) iterate internally to obtain a compatible wake transport velocity and blade loading solution. This analysis also provides an approximate treatment of wake distortions due to tower shadow or wind shear profiles. Finally, selected results of internal UTRC application of the analysis to existing wind turbines and correlation with limited test data are described.

INTRODUCTION

The analytical capabilities required to accurately predict horizontal axis wind turbine rotor performance are varied and complex depending on the turbine design, operating conditions, and the desired computational accuracy. Such factors as rotor yaw angle, tower shadow, and wind shear create inflow profiles which are unsteady and nonuniform. Conditions where the turbine rotor wake is close to the rotor disk result in wake induced effects which can significantly affect performance predictions. Further complexities occur when rotor aeroelastic effects are considered. Many of these effects are generally neglected for wind turbine rotor performance predictions because the increased computational costs required to obtain the gain in predictive accuracy are not justifiable.

The UTRC Wind Energy Conversion System Performance Analysis (WECSPER) for horizontal axis wind turbine performance is capable of treating uniform wind conditions using rigid blade aerodynamics which include real airfoil section properties (lift and drag) for prescribed wake geometries. In addition, it can treat nonuniform inflow profiles for conditions which do not violate the assumptions of the analysis. The computer code is computationally very fast, highly modular, and well structured. This analysis is a logical extension and refinement of the UTRC Prescribed Wake Rotor Performance Method of Landgrebe (Refs. 1 and 2) for hovering helicopter rotors which has been adapted and applied to statically thrusting propellers (Ref. 3) and high speed propeller configurations (Ref. 4). This analysis (Ref. 2) and similar derivatives for helicopter forward flight applications have been expanded in capability and combined into a single comprehensive rotor inflow analysis, the UTRC Rotorcraft Wake Analysis (Ref. 5).

THEORY

General

Briefly, the method is derived utilizing blade-element lifting line theory and incorporates a prescribed wake model consisting of a finite number of trailing vortex filaments. The trajectories and positioning of these filaments are prescribed through internal equations or input coordinates. To reduce the computational time, the original analysis makes use of the fact that for zero yaw angle and steady uniform wind conditions the flow is steady with respect to the turbine rotor blades and has an axially symmetric wake. The analysis uses a cylindrical coordinate system axially aligned with the trajectory of the wake. All velocities and lengths are defined in the positive sense consistent with the right hand rule. Figure 1 illustrates this coordinate system. Figure 2 is an illustration of two types of prescribed wake models used for hovering helicopter rotors (similar representations are used for propellers). The classical model is the one generally used for wind turbine application and is used herein. This model is generally acceptable for wind turbine applications because the wake is transported rapidly away from the blades. A free wake analysis can be used to obtain a wake geometry which models the self-induced distortions; however, this is a costly computational procedure and is generally not warranted. Once the position of the wake is prescribed, a set of equations in terms of the unknown bound circulations is generated utilizing the Kutta-Joukowski and Biot-Savart relationships and the airfoil section lift characteristics. The solution for the blade bound circulation distributions is found and the corresponding induced velocity and section angle of attack distributions are calculated. With the use of the two-dimensional airfoil data the complete

blade loading distribution (lift and drag) and rotor performance (thrust and power) are then obtained.

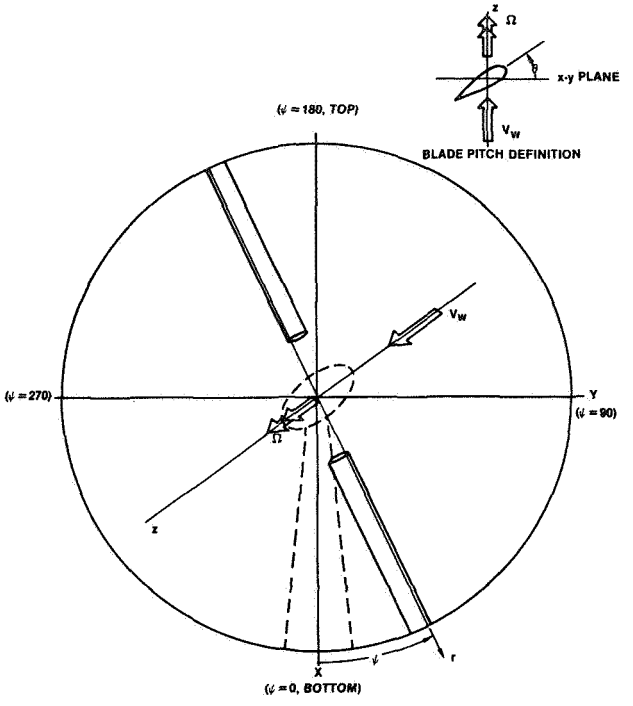

Figure 1. Coordinate System Used in the UTRC Horizontal Axis Wind Turbine Performance Analysis

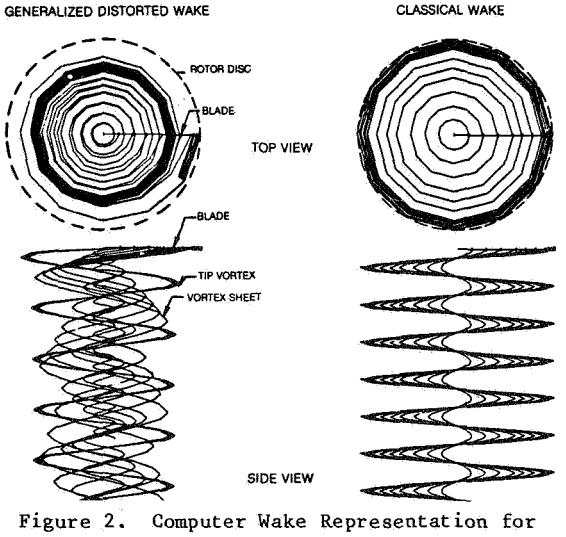

Figure 2. Computer Wake Representation for One Blade of a Hovering Rotor, Classical and Generalized Distorted Wake Models

Lifting Line - Wake Modeling

The concept of a prescribed wake, blade element, lifting line theory applied to wind turbine rotors assumes that each blade of the rotor is represented by a segmented bound vortex lifting line located along the rotor blade quarter chordline with a spanwise varying concentrated circulation strength proportional to the local blade lift (Kutta-Joukowski Law). The wake is assumed to be modeled by a system of discrete segmented trailing vortices shed from the junction points of the bound vortex segments. The circulation strength of these trailing segments is a function of the spanwise blade bound circulation gradients. A finite wake whose trailing filament segmentation is defined by a specified azimuthal step size ($\Delta\psi$), is used which is of sufficient length to approximate an infinite wake. Figure 3 is an illustration of this modeling procedure.

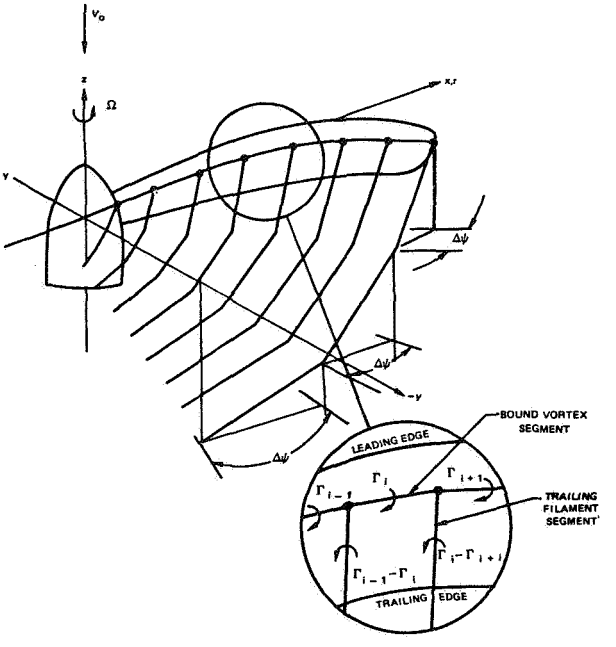

Figure 3. Representation of a Blade and Wake by Bound and Trailing Vortex Segments

The influence (induced velocity) of the bound and trailing vortex segments at any field point is computed by using the Biot-Savart Law for finite length, straight line segments of constant strength. The induced velocity of a filament segment due to a unit strength is called the geometric influence coefficient. The calculation of these coefficients is the most time consuming portion of the analysis.

Within this analysis it is possible to prescribe internally several different wake geometries or to input the wake geometry from an external source. Only the classical wake model which is currently used for wind turbine applications is described. The classical wake model is defined by the addition of the wind speed and the momentum induced velocity for the condition being investigated.

$$V_T = V_W + v_{imom} \quad (1)$$

No radial wake expansion or contraction is used. The resulting wake shape is a helix for which the pitch rate depends on the wind speed and thrust level (Fig. 2).

Vortex core effects are not modeled in this analysis because it is assumed that conditions for which the vortex core influence should be considered will not occur (i.e., close blade-vortex interactions). The roll-up of the vortex sheet into a tip vortex is modeled by prescribing the wake roll-up for the tip region if desired. Our experience has shown that for most wind turbine operating conditions, wake roll-up modeling is unnecessary for performance predictions, even though flow visualization studies have clearly shown the existence of a tip vortex.

Blade Element Aerodynamics

The modeling of the wind turbine blade by the lifting line approach defines the inflow and the effective angle of attack at each blade segment. This aerodynamic model is shown conceptually in Fig. 4. Tabulated linearized airfoil data are used to relate the effective angle of attack at each blade element segment to the local section lift, thus inherently accounting for the chordwise vorticity distribution and the Kutta condition. For this discretized system, the section bound circulation (Γ) is related to the local velocity (U), chord (c), and lift coefficient (C_ℓ) at a section through the Kutta-Joukowski Law.

$$\Gamma = \frac{1}{2} c\, C_\ell(\alpha) U \tag{2}$$

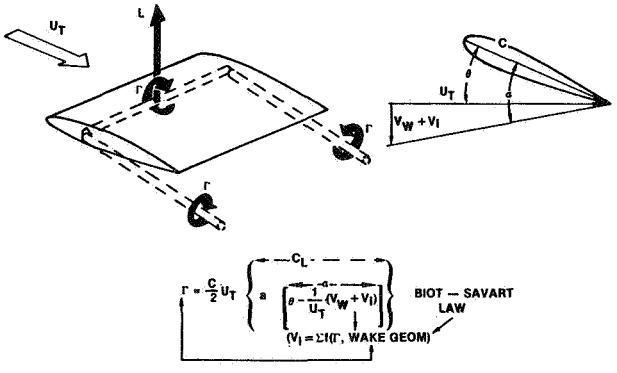

Figure 4. Lifting Line/Wake Aerodynamics - Linearized Model

The local velocity and effective angle of attack (α) are functions of the local tangential velocity (U_T), axial induced velocity (v_z), wind velocity (V_w), and blade pitch angle (θ).

$$U^2 = (U_T)^2 + (V_w + v_z)^2 \tag{3}$$

$$\alpha = \theta + \tan^{-1}\left[(V_w + v_z)/U_T\right] \tag{4}$$

The local axial induced velocity due to a given wake geometry is a function of the unknown bound circulation distribution and known geometric influence coefficients (GC) for the particular wake geometry.

$$v_z = \frac{1}{4\pi R} \sum_{j=1}^{N} GC_j\, \Gamma_j \tag{5}$$

These relationships (Eqs. 2-5) result in a system of simultaneous nonlinear equations in terms of the wake geometric influence coefficients (GC), the inflow and section properties at each blade element, the two dimensional lift coefficients, and the unknown blade circulation distribution.

Solution

The circulation solution is based on the linearization of the above relationships to form a system of linear equations whose solutions can be obtained and corrected for the actual nonlinearities of the problem using a lagged iteration procedure. For the linearized solution it is assumed that all angles are small, and that the local velocity (U) can be approximated by the local rotational velocity (U_T). The lift coefficient at each section is modeled by a linear lift curve slope (a) and effective angle of attack adjusted for the lift offset (α_o). With these assumptions and Eqs. (2-5), the section circulation can be expressed as:

$$\Gamma = \frac{1}{2}\, cU_T\, a\left(\theta - \alpha_o + \frac{V_w + v_z}{U_T}\right) + \frac{1}{2}\, ca\, C_f \tag{6}$$

where,

$$C_f = \frac{U\, C_\ell}{a} - U_T\left(\theta - \alpha_o + \frac{V_w + v_z}{U_T}\right) \tag{7}$$

is the correction to the linearized equations for the nonlinearities of the actual problem. Since the induced velocity is also a function of the circulation distribution, the equation at the ith blade section can be rewritten as

$$(D_i - GC_i)\Gamma_i - \sum_{j\neq i}^{N} GC_j \Gamma_j = 4\pi R(U_T\, \bar{\theta} + C_f)_i \tag{8}$$

where $\bar{\theta} = \theta - \alpha_o + \frac{V_w}{U_T}$ and $D = \frac{8\pi R}{ac}$

This equation can be written for each blade segment, resulting in a system of simultaneous linear equations if the correction term (C_f) is assumed known. This system of equations can be expressed in matrix form for the nth iteration as,

$$A\,\Gamma^n = b + C(\Gamma^{n-1}) \qquad (9)$$

where the correction vector $C(\Gamma^{n-1})$ is calculated based on the circulation solution from the previous iteration. When the solution procedure converges, the resulting circulation satisfies the original nonlinear relationships. Using the corresponding angle of attack (Eq. 4), the section lift and drag coefficients are obtained from tables of airfoil data for each segment. The lift and drag forces are then calculated and transformed to axial and rotational forces at each segment. The appropriate integrations of these forces yield the rotor thrust and torque.

Nonuniform Wind Conditions

As noted earlier, the inclusion of wind shear, tower shadow, and yawed wind direction introduce additional complexities into the problem of predicting the rotor performance. These nonuniform inflows create aerodynamic environments at the rotor blades which vary azimuthally and radially, and distort the wake geometry in a nonsymmetric manner. This dissymmetry in the wake and the azimuthal variation in the rotor inflow represent aerodynamic conditions for which the general formulation of the method described above is no longer valid since the solution is no longer independent of azimuth position. Rigorous treatment of the problem requires the use of a more sophisticated analysis which involves the wake dissymmetry and nonuniform rotor inflow. Such an analysis exists (the UTRC Rotorcraft Wake Analysis, Ref. 5), but it requires a significant amount of computer time to obtain the solution. In order to make use of the high computational efficiency of the above formulation, the WECSPER analysis includes an approximate treatment of the wake dissymmetry and azimuthal variation in the wind inflow. This treatment is broken into two portions; the wake geometry dissymmetry, and the azimuthal dependency.

Wake Dissymmetry

Comparisons made at UTRC between the predicted results using a Goldstein analysis and the WECSPER Analysis have shown that for most wind turbine operating conditions the wake induced influence at the turbine blade is strongly characterized by the immediate shed wake from that same blade. For these conditions the local wake displacement angle dominates the wake influence. The wake of the preceding blade is transported rapidly away from the rotor disk and does not have the strong influence on the following blade that is typically seen for hovering helicopters or statically thrusting propellers. Thus, to account for the wake dissymmetry due to the nonuniform inflow, a pseudo wake distortion method can be used.

To treat wake dissymmetry in a manner which makes use of the computationally efficient solution procedure for the symmetric wake problem the trailing wake filaments are regionalized in terms of their wake age into three regions; a near wake region, an intermediate wake region and a far wake region (Fig. 5). The near wake region is defined from the blade which shed the wake to one half of the blade azimuthal spacing behind the blade. The blade spacing is defined as the azimuthal spacing between blades. The extent of the intermediate region is from the end of the near wake region to one and one-half blade azimuthal spacings away from the blade.

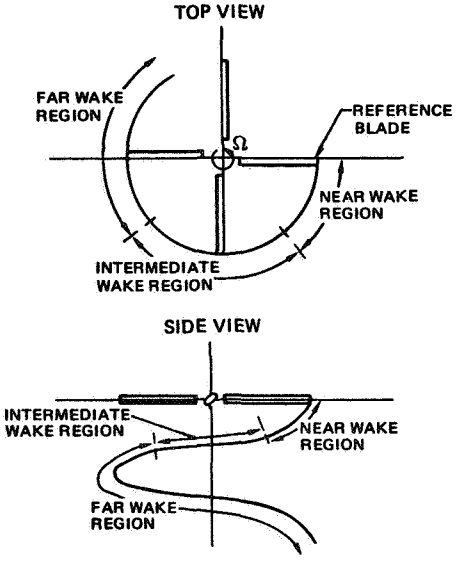

Figure 5. Wake Regionalization for a Tip Vortex Filament of a Four Bladed Rotor

The far wake region is the remaining portion of the wake. In the analysis, the geometric influence coefficients for all filaments are first calculated and stored according to the appropriate regions for the classical wake model. The near wake geometric influence coefficients of all filaments of a given azimuthal position are then scaled by the ratio of the cosines of the wake pitch angles defined by the uniform inflow definition and the local nonuniform inflow definition. The reason for scaling is that the local influence of the filament at the blade which shed the filament is characterized by the filament's orientation (Fig. 6). Geometric assumptions made to result in this simplified scaling factor have been investigated and the error introduced by the approximations were found to be insignificant for general wind

turbine applications. The intermediate wake geometry influence is computed based on corrections to the intermediate wake region geometric influence coefficients. These corrections are based on the change in axial location between the reference wake and the location of the displaced wake of this region (Fig. 6). In this region, changes in orientation are less significant than changes in axial location because of the strong inverse proportionality to displacement distance defined in the Biot-Savart Law.

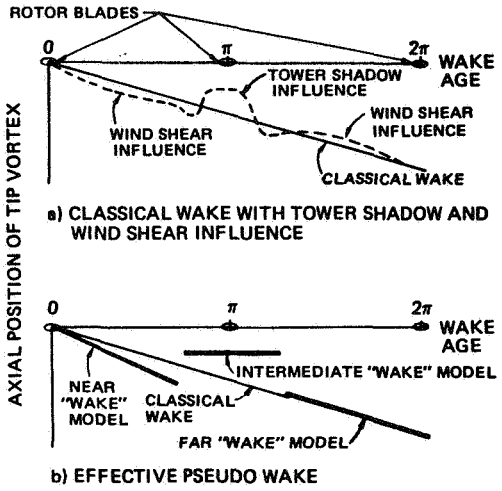

Figure 6. Pseudo Wake Distortion Model for a Tip Vortex of a Two Bladed Rotor

The far wake geometric influence coefficients are assumed to require no corrections since perturbations on the far wake geometry about a mean wake geometry tend to be felt as an average influence which is equal to the influence of the mean wake for small perturbations. With this scaling technique, the initial calculation of the classical wake geometries influence coefficients need only be done for one azimuthal position of the rotor.

Azimuthal Dependence

The performance solution for nonuniform inflow conditions such as wind shear and tower shadow is rotor azimuth dependent. The assumption of near wake dominance and quasi-steady aerodynamics allows for the uncoupling of the azimuthal dependence in the solution procedure. This in turn, allows for the original, computationally efficient, analysis solution procedure to be used.

The geometric influence coefficients are calculated by the pseudo-wake distortion procedure for the particular inflow condition at a specified rotor azimuth position and the circulation distribution and performance prediction are obtained. This is done for each azimuth position defining one revolution of the rotor and the performance is integrated over this time period to calculate the time-averaged wind turbine performance.

Using all of the azimuthally varying bound circulation distributions obtained above, the induced velocity distribution at the rotor blades is recomputed by multiplying the pseudo-distorted wake influence coefficients for each rotor azimuth position by the appropriate time-dependent circulation values. Using these induced velocity distributions at each azimuth position, the resulting time averaged performance prediction is made. This essentially computes an approximately coupled azimuthally dependent solution. A measurement of the accuracy of the assumption of the near wake's dominance of the rotor performance is obtained by comparing the approximately azimuthally dependent and independent performance solutions. If there is a significant difference, the operating condition is sufficiently extreme to invalidate the assumptions used and requires the use of a more technically sophisticated analysis.

Rigorous treatment of yawed flow requires an analysis which computes the skewed unsymmetrical wake influence and the resulting azimuthally dependent circulation solution (Ref. 5). In the WECSPER Analysis, the assumption of local wake dominance is assumed to allow the influence of small yaw angles to be treated as an effective reduction in the uniform axial inflow profile and neglects the associated wake dissymmetry.

Wake Iteration

Once the rotor performance prediction is obtained, additional iterations may be required. The wake geometry is defined by both the non-induced and induced flow velocity field, and the induced field is unknown at the onset of the analytical procedure. The method used in the WECSPER Analysis is to calculate the classical wake model based on the predicted momentum-induced inflow from the previous solution iteration. The first iteration value is specified by the user. The complete performance solution is then repeated for each iteration until a converged momentum induced velocity solution is obtained. The complete prediction procedure is diagrammed in the flow chart shown in Fig. 7.

Inflow Profile Models

The analysis is capable of treating several types of inflow profiles with the assumptions noted earlier. There are currently three types of profiles available in the analysis, each shown pictorally in Fig. 8. The conventional mode of analysis uses a uniform wind profile model (upper portion of Fig. 8) for conditions without azimuthal or radial variation in the wind inflow velocity. A wind shear profile model can be used in the time dependent

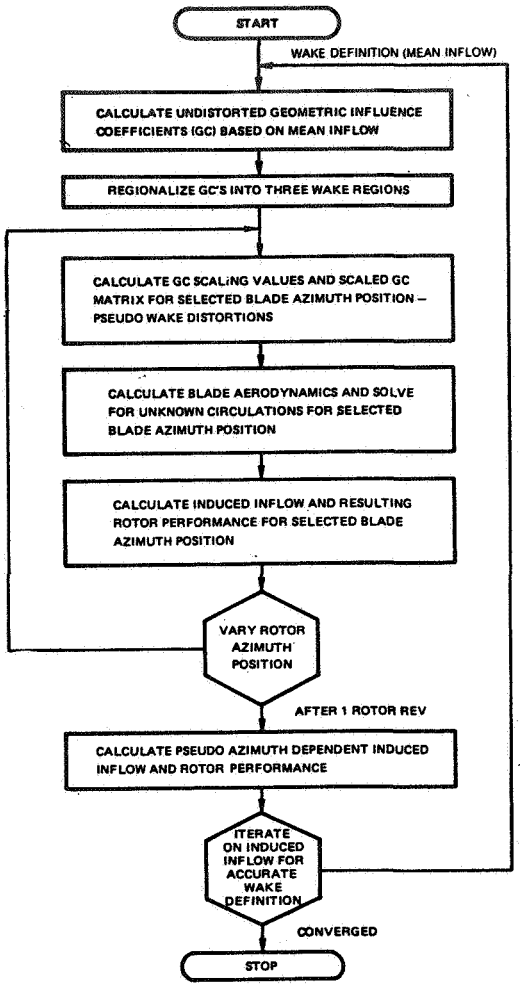

Figure 7. Simplified Flow Chart of Basic Structure for UTRC Wind Turbine Performance Analysis

mode of operation. This model is currently based on a user specified power law behavior (lower left portion of Fig. 8),

$$V_w = V_{ref} (h/h_{ref})^{\alpha} \qquad (10)$$

The influence of a tower support structure on the wind turbine performance is modeled by assuming that the tower influence is represented as a constant velocity deficit from the uniform value over a selected region on the rotor disk, centered about the tower centerline. This region is defined by a tapered column of selected width and taper on the rotor disk (lower right portion of Fig. 8).

APPLICATION

An application of the analysis to actual test conditions to validate the analysis is currently being funded by a DOE sponsored contract through Rockwell International. Results are currently not yet available; however, selected results of internal UTRC application of the analysis

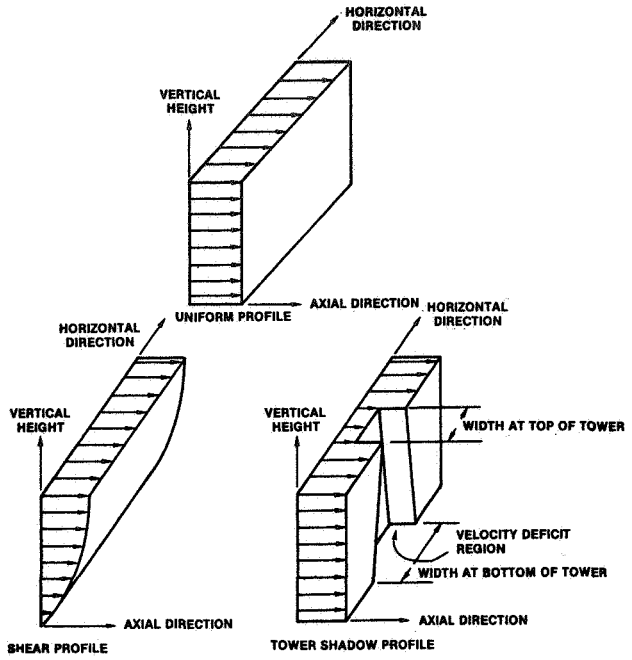

Figure 8. Wind Inflow Profile Models at Rotor Disk

are presented. Figure 9 presents a comparison of measured and predicted rotor performance at one blade angle in terms of power ratio versus velocity ratio for a 1/30 scale model of a Hamilton Standard 3.5 megawatt wind turbine tested in the UTRC main wind tunnel (Ref. 6). The low speed airfoil data used in this analysis was adjusted to reflect Reynolds number effects on the minimum drag coefficient and stall characteristics. These test results, presented for two different tip speeds, show some noticable differences in measured results near the peak power ratios. These differences with tip speed could be attributable to both Reynold's number and compressibility effects.

The predicted results show fair to good correlation for the lower tip speed results except at the higher velocity ratios. The difference between measured and predicted results could be due at least in part to the Reynold's number corrections used on the airfoil data and/or the accuracy of the test measurements and data reduction procedures used for these low power output operating regimes (high velocity ratio). In addition, the lower tip speed results have a measured power ratio data point at a velocity ratio of 7 which appears to be slightly inconsistent with the other results. In general, when one considers the accuracy of the corrected airfoil data used in the analysis, the correlation as presented is good.

The results of another application of this analysis to the UTRC 8 kW wind turbine (Ref. 7) are shown in Fig. 10. This figure presents measured and theoretical power output versus wind speed for data taken onsite on several different test dates. The scatter in this data

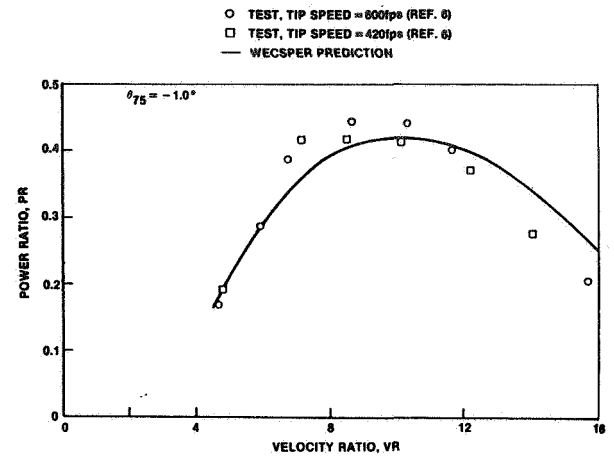

Figure 9. Comparison Between Measured Vs. Predicted Wind Turbine Performance For Rotor of Ref. 6

reflects the uncertainty in the measuring techniques associated with the fact that the actual site wind conditions are unsteady and that the wind shear profile is unknown. The theoretical results obtained were based on the uniform inflow model. The correlation is seen to be good except at the high wind speeds where the test data shows a distinct variation dependent on the particular test day.

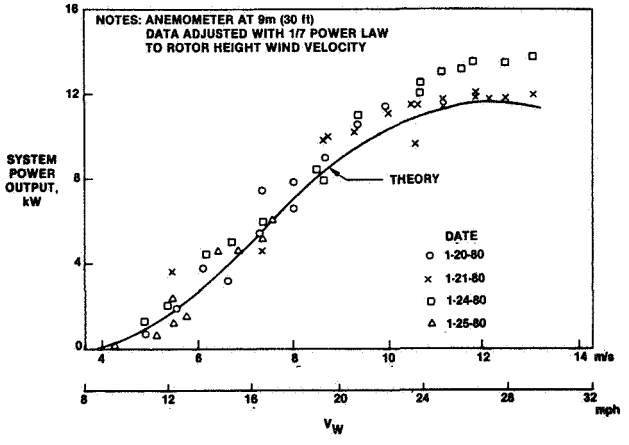

Figure 10. Power Output for UTRC 8 kW Rotor System

CONCLUDING REMARKS

The theory for the UTRC WECSPER Analysis has been presented, and selected results of the application of this analysis to existing UTC wind turbines, model and full scale, have been shown. These preliminary results indicate generally good agreement with measured test results. Discrepancies noted between test and theory may be related to the accuracy of the airfoil data and/or the accuracy of the test measurements. However, extensive validation of the analysis will require more data and comparisons to be made, such as that provided by the DOE funded validation activity noted above.

REFERENCES

1. Landgrebe, A. J.: An Analytical and Experimental Investigation of Helicopter Rotor Hover Performance and Wake Geometry Characteristics. United Aircraft Research Laboratories; USAAMRDL Technical Report 71-24, Eustis Directorate, U.S. Army Air Mobility Research and Development Laboratory, Fort Eustis, Virginia, June 1971, AD728835.

2. Landgrebe, A. J.: The Wake Geometry of a Hovering Helicopter Rotor and Its Influence on Rotor Performance. Journal of the American Helicopter Society, Vol. 17, No. 4, October 1972. (Also preprint No. 620, 28th Annual National Forum of the American Helicopter Society, May 1972).

3. Ladden, R. M. (Part I), D. C. Gilmore (Part II): Advanced V/STOL Propeller Technology. Volume II Static Thrust Prediction Method Development, AFFDL-TR-71-88 Volume II. Air Force Flight Dynamics Laboratory V/STOL Division, Air Force Systems Command, Wright Patterson Air Force Base, September 1971.

4. Egolf, T. A., O. L. Anderson, D. E. Edwards, and A. J. Landgrebe: An Analysis for High Speed Propeller-Nacelle Aerodynamic Performance Prediction, Volume I - Theory and Initial Application. June 1979. NASA Contract Number NAS3-20961, R79-912949-19.

5. Landgrebe, A. J. and T. A. Egolf: Rotorcraft Wake Analysis for the Prediction of Induced Velocities. USAAMRDL Technical Report 74-45, Eustis Directorate, USAAMRDL, Fort Eustis, Virginia, January 1976.

6. Wainauski, H. S.: Wind Tunnel Test of a 1/30 Scale Model of a 3.5 Megawatt Wind Turbine. HSER 7816, Hamilton Standard, October, 1978.

7. Taylor, R. B. and M. C. Cheney: Development of a 8 kW Wind Turbine Generator for Residential Type Applications. R80-915158-1 Final Report, UTRC (to be published).

QUESTIONS AND ANSWERS

T.A. Egolf

From: W.E. Holley

Q: Is it feasible to compute time varying induced velocity for turbulence inputs?

A: *Not with this analysis. The program assumes a quasi-steady flow aerodynamic to obtain solutions under "slowly" varying inflow conditions. Turbulence time scales are probably too small for application of this analysis.*

From: Anonymous

Q: Have you attempted to compare your code with other rotor prediction codes such as the efficient induction factor method of propeller theory?

A: *The analysis has been correlated in a limited manner with the Goldstein strip theory for W.T. applications. For helicopter applications (from which this analysis was originally derived) induction methods which do not recognize a wake model with significant wake distortion effects will not yield good performance prediction. For wind turbine applications this has not been shown to be the case, although neglecting the wake influence at high velocity ratio ($\Omega R/V$) may be a dangerous assumption.*

From: W.C. Walton

Q: Who funds this code development?

A: *The code development and the applications presented were funded internally by UTRC. There is a current validation activity being funded by DOE, through Rockwell International (Rocky Flats).*

From: F.W. Perkins

Q: Is the accuracy of your analysis significant with respect to uncertainties in the yaw response of wind turbines?

A: *The intent of this analysis is to predict integrated rotor performance (C_{p_0}, C_T) within the operating conditions for which the assumptions used are valid. The accuracy of the analysis with respect to small variations in yaw angles is probably quite good. The analysis treats the effect of your angle as a reduction in the wind inflow. Large yaw angles invalidate the assumptions of the analysis and require a more sophisticated analysis (currently available at UTRC).*

From: T.E. Base

Q: How do you justify using potential flow theories in a shear flow?

A: *The treatment of a lifting surface with potential flow models is well justified in the open literature for fixed wing, propeller and helicopter applications. The viscous effects in the flow field can be neglected for most of these applications. On the lifting surface, the specification of a Kutta condition artificially replaces the actual viscous phenomenon. In the UTRC WECSPER analysis the Kutta condition is handled inherently through the use of actual airfoil data. Other viscous phenomena such as close blade/vortex interactions do not occur for general HAWT application.*

From: J. Tangler

Q: On the Hamilton Standard correlation, what was the rotor's Re number and blade geometry? Is a model like this adequate for twisted, tapered, blades using a constant pitch wake?

A: *The HSD correlation was for tapered, nonlinearly twisted blades using a constant pitch wake model. The tip Reynolds number was approximately 500,000. The analysis will handle most reasonable combinations of twist, taper and variable airfoil section types.*

THE VELOCITY FIELD OF A SYSTEM OF UNSTEADY CYCLOIDAL VORTICIES

Bernard J. Young

Young Energy Systems
15 Cedar Lane; RFD #2
Dennisport, MA 02639

ABSTRACT

An essential difference between two-dimensional and three-dimensional models of cycloidal rotors is the presence of unsteady trailing cycloidal vorticies in the wake. The velocity induced by these vorticies is the primary mechanism producing flow retardation for low span/radius ratio, finite blade number rotors. An idealized rigid wake model of finite blade cycloidal rotors is used to investigate some cycloidal rotor problems.

INTRODUCTION

During the past decade a rekindled interest in energy conversion has stimulated the development of aerodynamic theories and numerical methods for analyzing rotors whose blades make cycloidal paths through the incident stream. Momentum theories and vortex theories appear in the literature. In the case of vortex theories, some noteworthy models of the wake have been presented by Holme and by Wilson in References 1 and 2.

Missing from these developments is information about the velocity seen by the blades of a three-dimensional, finite blade number cycloidal rotor as it moves about its orbit. Also missing is the answer to the question: "What is the optimum orbital load distribution?" There is good reason the latter question has gone unanswered: the problem is complicated. In spite of research spanning seven decades, no theory or method having engineering usefulness has emerged for cycloidal propulsors. The power of present computers may provide the means for pursuing this question further; it is hoped that this work may be a step in that direction.

DISCUSSION OF THE PROBLEM

The load distribution on the blades of a cycloidal rotor has components due to:

- -flat plate angle of attack
- -camber
- -unsteady angle of attack (pitch)
- -unsteady motion normal to stream (heave)
- -circulation induced by bound vorticity from other blades
- -circulation induced from shed vorticity in the wake.

Two-dimensional theory can be used to determine the load due to these components once the velocity at each orbital position and the character of the wake are determined.

An essential difference between the two-dimensional and three-dimensional models of cycloidal rotors is the presence of unsteady cycloidal vorticies in the wake. The velocity induced by these vorticies is the primary mechanism producing flow retardation for finite and low span/radius ratio, finite blade number rotors. It is for this reason that the author has chosen to investigate the velocity field of unsteady rigid cycloidal vorticies. The presence of unsteady bound and shed vorticity in the field between these vorticies is recognized. The computation of the velocity induced by unsteady bound and shed vorticity is not within the scope of this paper. A comparison of the results of this paper with the results of the two-dimensional method of Mendenhall and Spangler (Ref. 3) shows that the velocity induced by trailing cycloidal vorticies is several times that of the bound and shed vorticies.

The wake is assumed to be convected downstream at a constant velocity. It is further assumed that it does not deform. While such assumptions are not as defensible for cycloidal rotors as they are for helicoidal rotors, it can be argued that the induced velocity seen by the blade is primarily influenced by the portion of the cycloidal vortex filament which is nearest the blade.

The validity of the model investigated may not prove useful for the complete range of tipspeeds and rotor loadings. One would expect it to be valid for very low tipspeed ratios where the model reduces to a multielement airfoil system in rectilinear flow. One would also expect it to be valid for lightly loaded rotors. It should be less satisfactory for a cycloidal propulsor whera a contracting wake will cause blades in the downstream half of the orbit to cut rolled vortex sheets originating in the upstream half of the orbit. The expanding wake of the turbine should minimize such effects. As with many other developments in the theory of fluid mechanics, the ultimate usefulness can only be established when the complete induced velocity field is computed (including bound and shed vorticity effects) and when correlation with experimental data has been acheived.

THE INDUCED VELOCITY

We have in mind a discrete vortex lifting line model of a straight blade cycloidal turbine. We seek to evaluate the velocity induced at the blades of the

rotor by a system of cycloidal vorticies originating at different spanwise locations on the blades. One such vortex filament ant the coordinate system for this discussion are shown in Figure 1. The cycloidal curves followed by vorticies trailing from the i-th blade under rigid wake assumptions are parameterised in time by:

$$x_i = R\cos(\theta-\Psi_i+\omega t) + ut$$

$$y_i = R\sin(\theta-\Psi_i+\omega t)$$

$$z_i = z$$

where the scalar quantity R is the radius of the blade orbit; u is a characteristic velocity through the rotor;

$$\Psi_i = (i-1)2\pi/N$$

is the angular position of the i-th blade of an N-blade rotor when blade 1 is at position $\theta = 0$; ω is the rotor angular velocity; and t is time (less than zero) representing conditions which orinigated in the past.

According to the Biot-Savart law the velocity induced by a vortex filament is given by the following integral:

$$\hat{V} = 1/4\pi \int \Gamma \frac{\hat{R} \times d\hat{l}}{|\hat{R}|^3}$$

where Γ is the circulation along the vortex filament; R is the vector from the point (x_o, y_o, z_o) where the velocity is computed to the point (x_i, y_i, z_i) on the vortex filament; dl is the unit tangent vector along the vortex filament directed away from the bound vortex.

The circulation is a function of the spanwise position z, orbital position θ, and blade number i:

$$\Gamma_i = A(z)B_n \cos(n\theta - \Psi_i + \omega t + \phi_n)$$

where B_n and ϕ_n give the variation in circulation around the orbit and A(z) is a spanwise load function.

The velocity induced by this system has streamwise and sidewise components given by the following integrals:

$$u^*(\theta) = \sum_{i=1}^{N} -A(z)R\omega/4\pi \int_{-\infty}^{o} \frac{\cos(\theta-\Psi_i+\omega t+\phi)(z-z_o)\cos(\theta-\Psi_i+\omega t)\,dt}{\{(x-x_o)^2 + (y-y_o)^2 + (z-z_o)^2\}^{3/2}}$$

$$v^*(\theta) = \sum_{i=1}^{N} -A(z)R\omega/4\pi \int_{-\infty}^{o} \frac{\cos(\theta-\Psi_i+\omega t+\phi)(z-z_o)(\sin(\theta-\Psi_i+\omega t)-u/R\omega)\,dt}{\{(x-x_o)^2 + (y-y_o)^2 + (z-z_o)^2\}^{3/2}}$$

For a straight blade rotor parallel to the z-axis we are not interested in the spanwise velocity component. These integrals have been evaluated by numerical integration.

APPLICATION OF THE MODEL

A straight bladed cycloidal rotor having blade span/radius of 4/3 was divided into ten equal segments. A trailing cycloidal vortex system was modeled by eleven cycloidal vortex filaments originating at the ends of these segments. The velocity induced at the midpoints of these segments was computed for a local tipspeed ratio $R\omega/u = 2.85$. The circulation on the segments was taken as the integrated average over the length of the segment for an elliptical spanwise load distribution. The orbital load distribution was cosinusoidal (B_n, $\phi_n = 0$ for $n>1$).

The velocity induced at the midpoints of the two segments nearest the midspan of a one blade cycloidal rotor is shown in Figure 2. For the middle 60% os the span the induced velocity is nearly constant. Near the tips it is not for two reasons. First, the discrete vortex lifting line model with equal segments does not yield the correct induced velocity near the tips. In steady, rectilinear flow models the spacing is ususlly modified near the tips. Secondly, there is no apriori guarantee that the circulation specified will result in the same pitch for the cycloidal vorticies that was used in computing the induced velocities. In fact, one must modify the pitch of the cycloidal vorticies and the repeat the calculation. Such iteration is also required in solving the helicoidal rotor problem. The second iteration has not been caried out in the work reported here.

Another question arising from these results is: "How do we determine the characteristic velocity at which the wake moves downstream?" We want, of course, to make a choice which gives the most accurate results. This question remains open, but in this work the velocity at $\theta = 180^\circ$ has been used. This is done because we will eventually want to use more terms in the cosine series for orbital circulation in the attempt to produce a more uniform induced velocity in the wake and the a more optimal rotor.

The results in Figure 2 form the basis on which the strength of the circulation and/or the incident stream may be varied to produce the local velocity at the rotor (u(180°)) which matches the assumed local tipspeed ratio. If both are varied, a range of power coefficients is obtained. The largest then would be the optimum power coefficient for that local tipspeed ratio, or pitch, for that orbital and spanwise circulation distribution.

Figure 3 shows 1 and 3 blade rotor results of varying the circulation and adjusting the inflow velocity until a local tipspeed ratio of 2.85 was acheived. These power coefficients are not quantitatively exact since they do not account for induced velocities from shed and bound vorticity, and are not derived from a completed iteration of spanwise loading and wake pitch. They do exhibit qualitative results showing an increase in obtainable power coefficient with increased blade number and show that there is an optimal loading for each blade number.

CONCLUDING REMARKS

This method would be enhanced if a fast means of evaluating the induced velocity integral were found. Asymptotic series and a regression analysis of computed values seem reasonable approaches.

The induced velocity components for bound vorticity and shed vorticity must be included in the analysis.

The performance computation requires modifying the pitch of the trailing vorticies so that the wake motion is consistant with the prescribed inflow conditions and the induced velocities at the appropriate location. An iteration is required.

The results of the inviscid theory must be reckonned with the reality of the viscous fluid effects. Correlation with experimental data is the ultimate test of a fluid dynamic theory or method.

The method should be exercised in an attempt at the solution of the optimal orbital load distribution problem by including further terms in the circulation series. Assuming we can find the optimal load distribution, we must then see if it can be obtained by a technically feasible lifting surface.

With minor extensions, this method could be applied to curved blade rotors of the Darrieus type. This is appealing because of the greater number of units which exist and the abundant theoretical and experimental date which is available for comparison.

REFERENCES

1. Holme, O.: A Contribution to the Aerodynamic Theory of the Vertical-Axis Wind Turbine, International Symposium on Wind Energy Systems, BHRA Fluid Engineering, Cranfield, England, Sept. 1976

2. Wilson, R. E.: Vortex Sheet Analysis of the Giromill, J. of Fluids Eng., Vol 100, Sept. 1978, pp 340-342

3. Mendenhall, Michael R. and S. B. Spangler: Theoretical Analysis of Cycloidal Propellers, Nielsen Engineering and Research, Rept. TR 53, June 1973

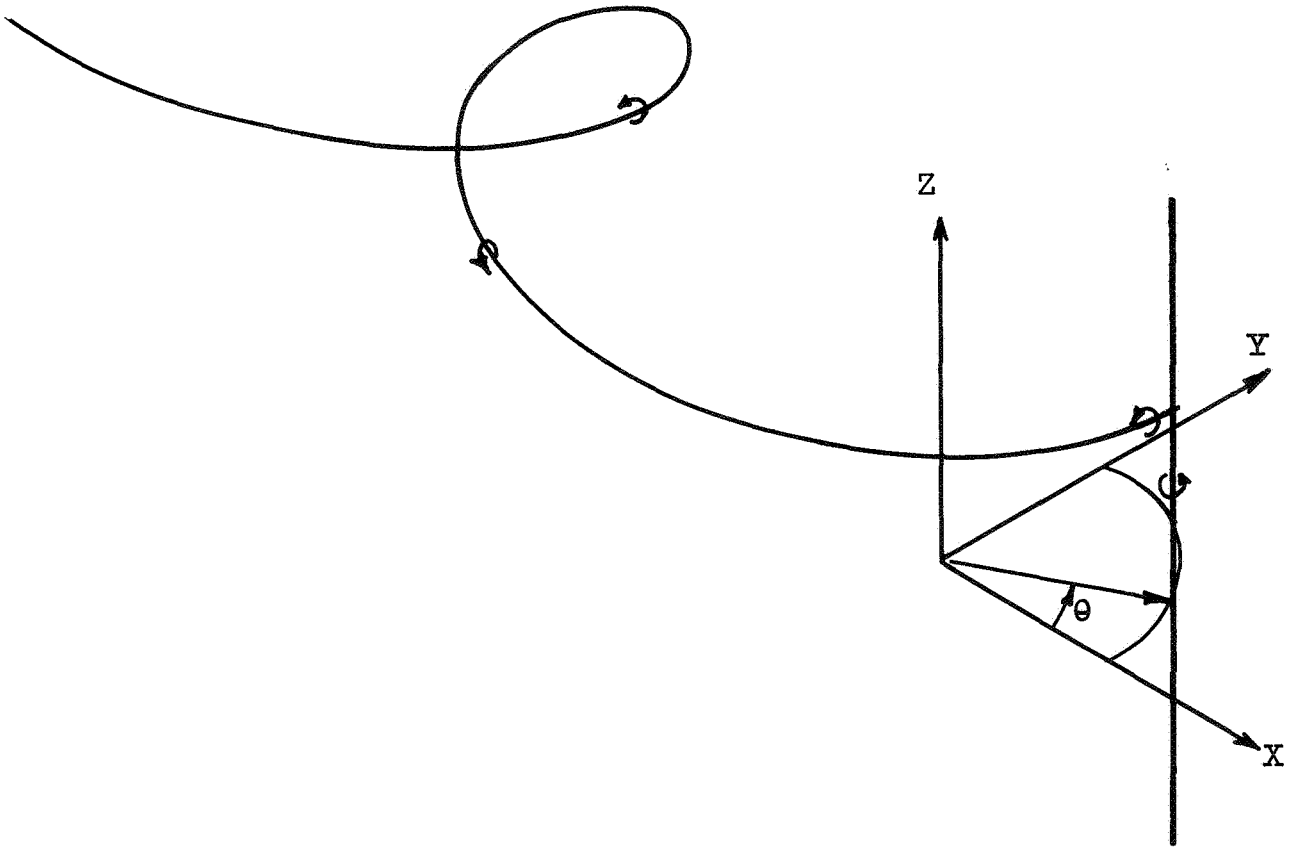

Figure 1- Coordinate System for the Analysis of a Cycloidal Vortex Filament

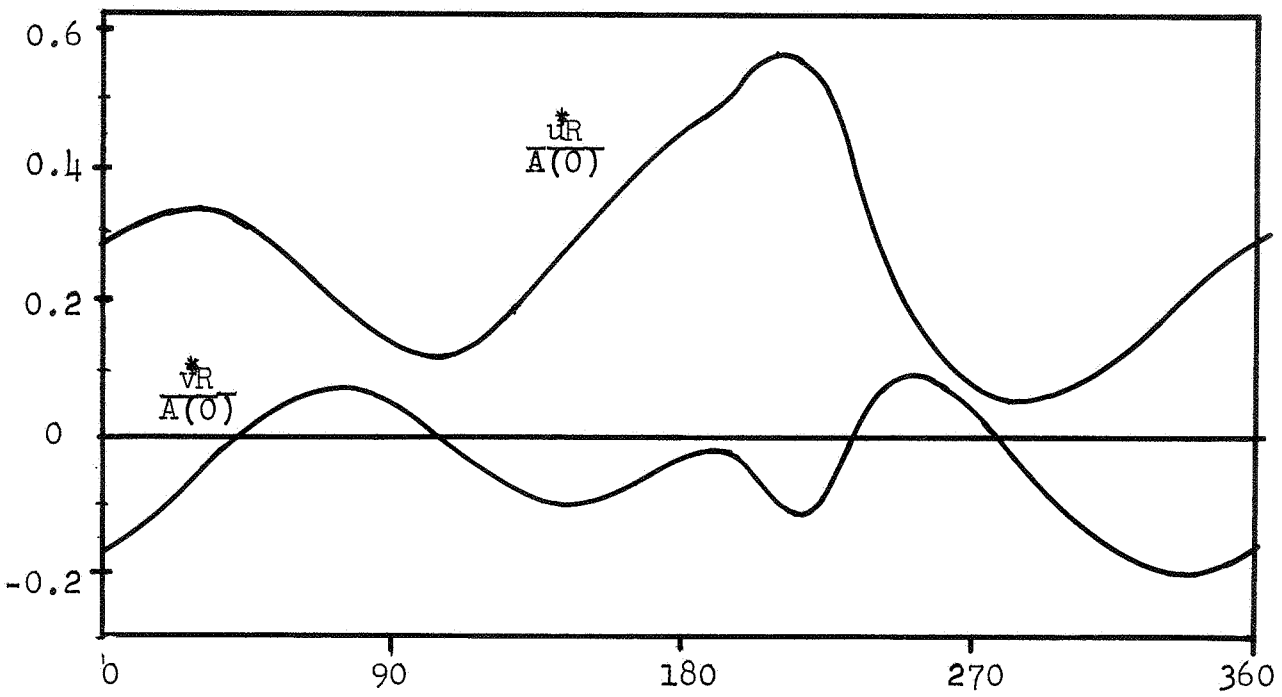

Figure 2- Streamwise and Spanwise Velocity Induced at Blade Midspan (Local Tipspeed Ratio R/u = 2.85) vs. Orbital Position

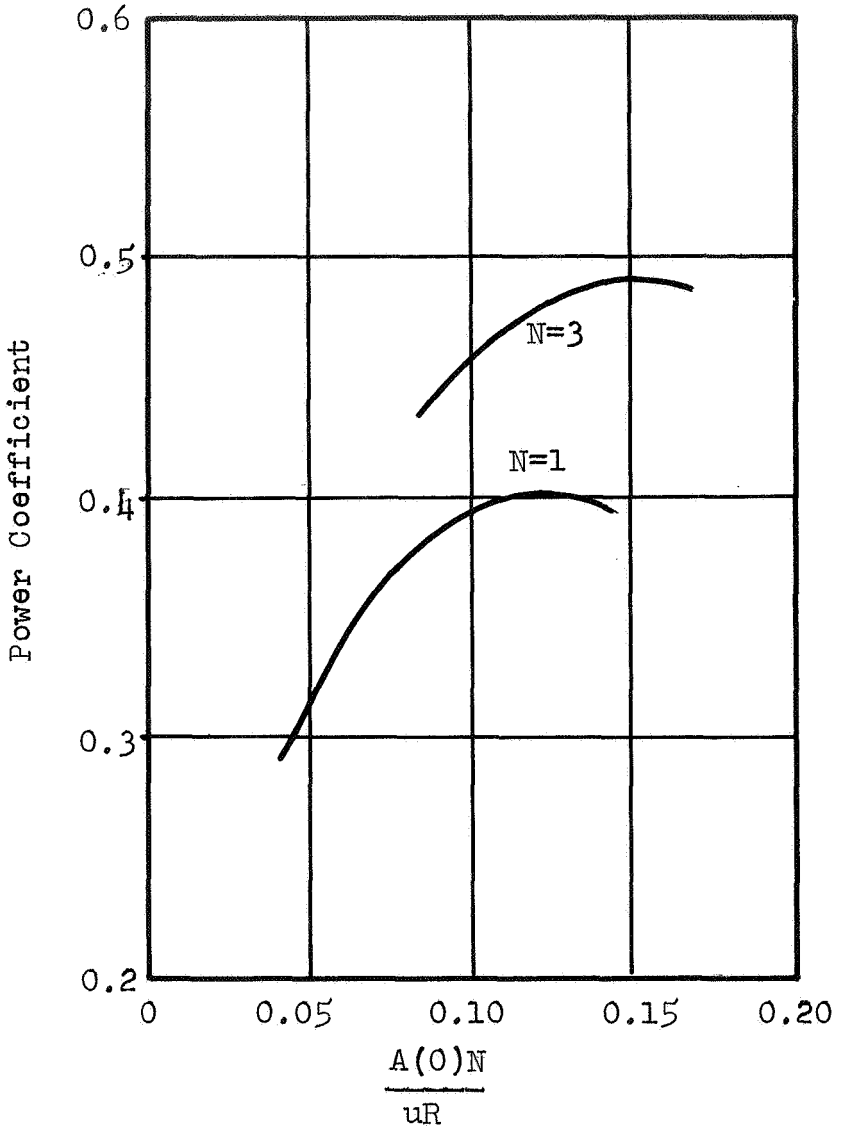

Figure 3- Power Coefficient vs. Circulation Parameter for 1 and 3 Blades

ANALYTICAL STUDIES OF NEW AIRFOILS FOR WIND TURBINES

W.H. Wentz, Jr., Wichita State University
J.T. Calhoun, Consultant

ABSTRACT

Computer studies have been conducted to analyze the potential gains associated with utilizing new airfoils for large wind turbine rotor blades. Attempts to include 3-dimensional stalling effects are inconclusive. It is recommended that blade pressure measurements be made to clarify the nature of blade stalling. It is also recommended that new NASA laminar flow airfoils be used as rotor blade sections.

INTRODUCTION

Studies of new airfoils for wind turbine applications are being conducted at Wichita State University, in cooperation with the NASA Lewis Research Center. Current wind turbines utilize airfoil sections designed in the 1930's and 1940's from the familiar NACA airfoil series documented in reference 1. Beginning about 1975, computational techniques for fluid dynamic analysis reached a state of development which permitted rapid, low cost analysis of airfoil shapes. This capability has resulted in a number of computer designed low-speed airfoil development programs in addition to the recent better known transonic airfoil developments. Examples of the new low-speed airfoils are documented in references 2, 3 and 4.

The purpose of the current studies is to determine whether the new airfoils or as yet undesigned airfoils offer significant advantages relative to the older airfoils for wind turbine application.

WIND TURBINE PERFORMANCE

Relationship Between Airfoil Characteristics and Wind Turbine Performance

In order to design a new airfoil for wind turbine application, it is essential to understand the relationships between airfoil characteristics and turbine performance. While it is perhaps obvious that high c_l and low c_d are desirable, the performance sensitivity of the turbine to these characteristics is not obvious.

The performance changes associated with wind speed changes for constant rpm can best be understood in terms of blade section angle of attack and section airfoil characteristics. For constant rpm operation, blade section angle of attack increases as wind speed is increased, as shown in figure 1. Thus the initial response to increasing wind speed is for blade lift coefficient and power to increase. As wind speed continues to increase, the angle for maximum lift coefficient is reached, and further increase in wind speed results in blade stalling, with rapid loss of lift and increase in drag, resulting in loss of power. Thus blade section stalling limits maximum power and the wind speed at which maximum power occurs.

These studies are being conducted utilizing a WSU-modified version of the "PROP" wind turbine performance computer code, which utilizes strip analysis combined with momentum (Betz theory). Earlier studies at WSU used a specially adapted version of this computer code to study aileron and spoiler control systems as alternatives to blade pitch control (ref. 5). The present paper is a status report of the airfoil studies, which are still in progress. These studies are based upon the 125 ft diameter NASA MOD-0 turbine, with untwisted blade utilizing the NACA 23024 airfoil section. Rotation rate is 33 rpm for all cases.

Swept Area Distribution and Blade Torque

Figure 2 illustrates the area distribution versus radius for a circle. It serves to highlight the significance of careful design of the outer portions of the rotor blade, since these portions sweep through the greatest area. Figure 3 shows calculated torque as a function of radius for several wind speeds. Even when tip loss effects are included, (as in the present case) the importance of the outer portion of the blade in producing power is evident. Thus if new aifoil sections for improved power output are to be designed for only a portion of the span, attention must be focused on the outer portion of the blade.

Parametric Studies of Airfoil Section Characteristics

Parametric variation of aerodynamic characteristics provide an excellent tool for increased understanding of the somewhat subtle relationships between airfoil characteristics and wind turbine performance. Airfoil characteristics can be summarized as follows. Lift coefficient depends primarily upon camber and angle of attack. In order to obtain good are aerodynamic performance, it is necessary to have unseparated flow. The camber of the section is the primary parameter which controls the lift coefficient at which separation and stalling occur, at least for medium thickness sections (10% t/c or more). Section lift curve slope is essentially independent of camber and thickness. For low Mach number conditions, maximum lift coefficient is obtained for sections having thickness ratios of about 12% to 15%. Section drag coefficient depends primarily on Reynolds number, thickness, portion of laminar flow (if the surface is smooth enough), camber, and lift coefficient.

Section Drag Coefficient Studies

Figure 4 shows the results of studies of wind turbine performance for parametric changes in airfoil section drag minimum drag coefficient. This figure shows that doubling the section minimum drag without changing the lift characteristics results in a power loss which is approximately constant for all wind speeds, about 16 kW for this machine. Reducing the minimum section drag

coefficient by 50% results in a nearly constant power increase of about 8 kW for this machine. These results illustrate that the "parasite power" of the turbine is essentially a function of blade area and rpm, and is therefore affected only slightly by wind speed.

These preliminary drag change studies were refined by calculating the drag changes associated with changes in airfoil thickness. Thickness affects section drag as shown in equation 1 from reference 6.

$$c_d = c_{d_{t=0}}(1 + 2\ t/c + 60\ t/c^4) \qquad (1)$$

This equation was used along with the basic 24% thick NACA 23024 data to calculate minimum section drag for a 12% thick NACA 23012. This result was used to make the computer runs shown in figure 5. Decreasing blade thickness to 12% over the full span results in a power increase of about 10 kW, while decreasing the thickness only from 70% radius to the tip results in about 8 kW power increase.

Section Lift Coefficient Studies

A series of runs were made in which a constant increment in lift was added to the standard airfoil characteristics. This study is designed to assess the importance of blade section camber on turbine performance. The results of this study are shown in figure 6. For moderate and high wind speeds, increasing the lift coefficient provides substantial power increases, as expected. At low wind speeds (6 m/s and lower), lift coefficient increments of 0.1 and 0.2 have little effect, while Δc_l values of 0.4 and 0.6 show substantial power gains. The gains in power at the very low wind speeds are surprising and are viewed with some skepticism. As a check on the computer results, a theoretical line for c_p = .59 (Betz limit) has been added to the graph. The computer results which exceed the Betz limit are invalid. Detailed printout for these runs shows that the slowdown factor (wind velocity reduction through the rotor) has not properly converged for cases for which the power coefficient has exceeded the Betz limit. At higher wind speeds, proper convergence in the slowdown factor iteration loop has been achieved, and the results are accepted with less skepticism. In reviewing the results of the drag and lift parametric studies, it becomes apparent that increases in camber (added c_l) are very promising.

Studies of Advanced Airfoils

To illustrate the potential gains in performance associated with advanced airfoils, computer studies have been conducted utilizing a new NASA-Langley low-speed airfoil designed to achieve a substantial portion of laminar flow. This airfoil has a high design lift coefficient, and has very low drag levels at lift coefficients from 0 to 1.2. The airfoil has a 15% thickness to chord ratio. A constraint on this particular airfoil design was to minimize penalties associated with loss of laminar flow due to surface roughness. This objective has been achieved to a remarkable degree, to the extent that with roughness applied to the airfoil, no loss in $c_{l_{max}}$ occurs, but only an increase in drag.

The appropriateness of selecting a laminar flow airfoil for application to wind turbine rotor is subject to question. Nevertheless, the authors believe that with blade fabrication techniques which insure a smooth, hard surface, proper finishing techniques, and occasional rotor washing on low-wind days to remove dirt and insect accretion, laminar flow can be achieved. The new-technology airfoils permit taking advantage of laminar flow when possbile, without the fear that a dirty or wrinkled blade will create intolerable performance penalties.

The predicted performance of the MOD-0 turbine based upon the new natural laminar flow airfoil is shown in figure 7. The performance gain associated with this airfoil seems quite remarkable, but are in fact consistent with gains illustrated earlier for similar levels of parametric section c_l and c_d variation. Even if laminar flow is not attained, the performance gains are quite large. Unfortunately, the problem noted earlier of computer calculation non-convergence for low wind speeds is again present.

Comparison Between Experiment and Theory

Since the primary objective of utilizing improved airfoils on wind turbines is to achieve performance gains, it is essential to have an analytical model which is capable of predicting actual performance with a reasonable degree of accuracy. Obtaining accurate experimental measurements is complicated by the need to test at full scale for proper Reynolds number matching and the problems associated with full scale field testing, such as: non-steady-state conditions, difficulties in obtaining accurage wind speed information, and uncertainties associated with generator efficiencies and drive train power losses.

A new technique for analyzing experimental full scale wind turbine data is being developed at NASA Lewis. This technique utilizes the method of bins for sorting the experimental samples, and special calibrations of the wind speed instrumentation from several sensors. This work is still in progress, and the results will be reported later. It is hoped that these studies will provide more definitive measurements of shaft power versus wind speed than are presently available.

Three-Dimensional Stalling Effects

Himmelskamp (ref. 7) performed experiments in which pressures were measured at a number of stations between 40% and 80% span on a rotating blade. His experiments (fig. 8) show that stalling tends to be delayed over most of the rotating blade relative to the two-dimensional case. This effect is attributed to centrifugal forces acting on the boundary layer flow. While Himmelskamp made no measurements beyond 80% span, extrapolation of his data indicates that characteristics at 90% span would correspond closely to the two-dimensional case, and stations from 90% to 100% span would have lower stalling angle and $c_{l_{max}}$ than the two-dimensional case.

In addition to the changes in stalling angle and $c_{l_{max}}$ which Himmelskamp observed, corresponding changes in drag must also occur. Unfortunately, Himmelskamp's drag measurements were not accurate enough to use for performance prediction for arbitrary airfoils.

In order to apply the Himmelskamp data to rotors of arbitrary geometry,it was necessary to extract a series of generalized characteristics from the Himmelskamp data. Parameters selected were the ratio of $c_{l_{max}}$ 3D to $c_{l_{max}}$ 2D, stalling angle in three dimensions to the stalling angle in two dimensions, and a series of parameters to model an assumed section drag coefficient behavior for three dimensions. The drag model assumes one parabolic form for the c_d vs alpha relationship prior to stalling, and a second parabolic equation for the drag curve from initial spearation to full separation. Initial separation angle, stalling angle and full separation angle become functions of radial station. Modeling the c_d relationship in three dimensions then becomes rather straightforward based upon modified angles for initial separation and stalling. The three-dimensional effects are treated as corrections to the two-dimensional data, so that the analytical model can be applied to any set of two-dimensional airfoil data in the PROP program.

Figure 9 shows predicted performance for the NACA 23024 airfoil section including the Himmelskamp three-dimensional effects. Figure 10 shows power predicted for the NASA MOD-0 turbine using the Himmelskamp three-dimensional stall prediction technique just described. This analysis shows that the predicted peak power has increased greatly, and now exceeds measured maximum power by a substantial amount. The discrepancy is so large that it casts doubt on all calculations with codes of this type which do not include 3-D stalling effects. It is very likely that the low-Reynolds number Himmelskamp experiments lead to over-prediction of the 3-D effects. Nonetheless, the potential effects are too large to be ignored. Even if the actual effects are only 50% of those predicted, the effects are still as large as the possible changes in performance between a poor (NACA 23024) airfoil and high-performance airfoil.

Need For Large Scale Blade Pressure Measurements

Further improvements in power prediction are not likely without determining power and wind speed with greater accuracy, and/or determining blade section stalling characteristics of a rotating turbine. Making blade pressure distribution measurements of a rotating full scale turbine would provide answers to the blade stalling questions, as well as providing checks on blade structural load prediction techniques, which rely on the same analytical models as the performance estimates. For these reasons, the authors are recommending that an experimental program be undertaken to measure pressures at a number of blade stations on the MOD-0 machine.

CONCLUSIONS

1. Analytical methods such as the PROP code need to be improved to provide proper convergence even for low wind speed, high section c_l cases.

2. Pressure measurements are needed on a large scale wind turbine to understand the nature of blade stalling in three-dimensions, and to aid in developing improved theoretical models.

3. Wind turbines should utilize advanced low-speed airfoils to take advantage of possible performance gains which do not add to blade cost.

REFERENCES

1. Abbott, I.H. and Von Doenhoff, A.E.: Theory of Wing Sections. Dover Publications, 1958.

2. Pierpont, P.K.: Bringing Wings of Change. Aero. and Astro. Magazine, October, 1975.

3. Anon.: Advanced Technology Airfoil Research. NASA CP 2045, 1978.

4. Liebeck, R.H. and Ormsbee, A.I.: Optimization of Airfoils for Maximum Lift. AIAA Journal of Aircraft, Sept.-Oct., 1970.

5. Wentz, W.H., Snyder, M.H. and Calhoun, J.T.: Feasibility Study of Aileron and Spoiler Control Systems for Large Horizontal Axis Wind Turbines. NASA CR-159856, 1980.

6. Hoerner, S.F.: Fluid Dynamic Drag. Published by the author, 1965.

7. Himmelskamp, H.: Profileuntersuchen an einem umlaufen Propeller. Dissertation, Goettingen, 1945. (Limited results presented in "Boundary Layer Theory" by H. Schlichting, McGraw-Hill, 1979.)

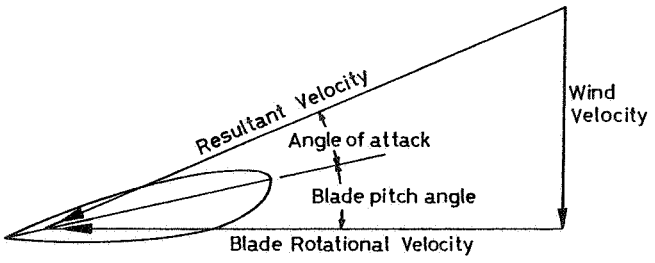

Fig. 1- Blade Section Angles.

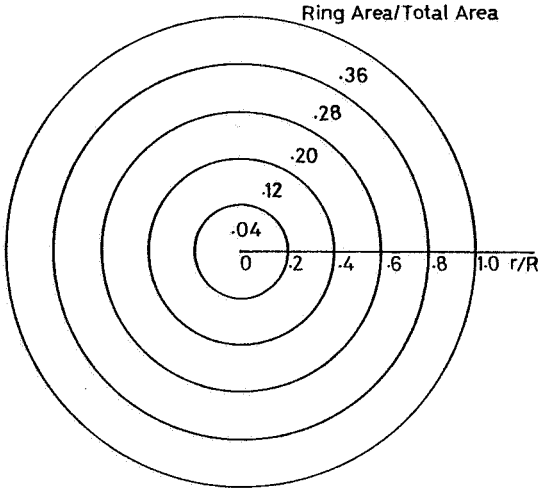

Fig. 2- Blade Swept Area Distribution.

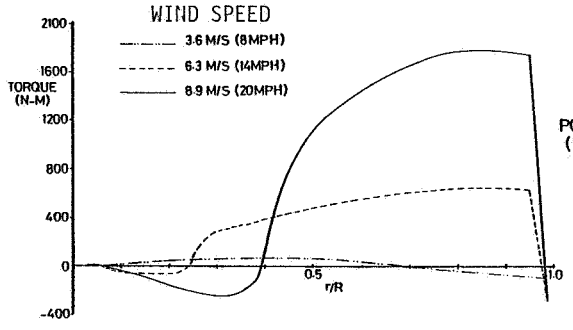

Fig. 3- Blade Torque Distribution.

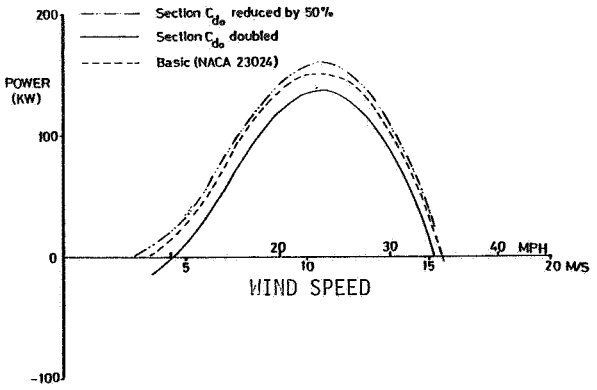

Fig. 4- Effects of c_{do} Changes on Wind Turbine Performance.

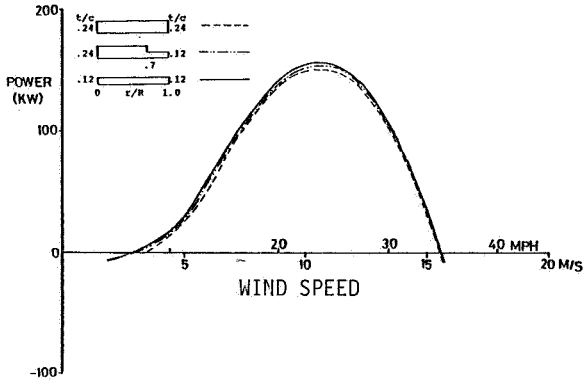

Fig. 5- Effects of Airfoil Thickness Changes on Wind Turbine Performance.

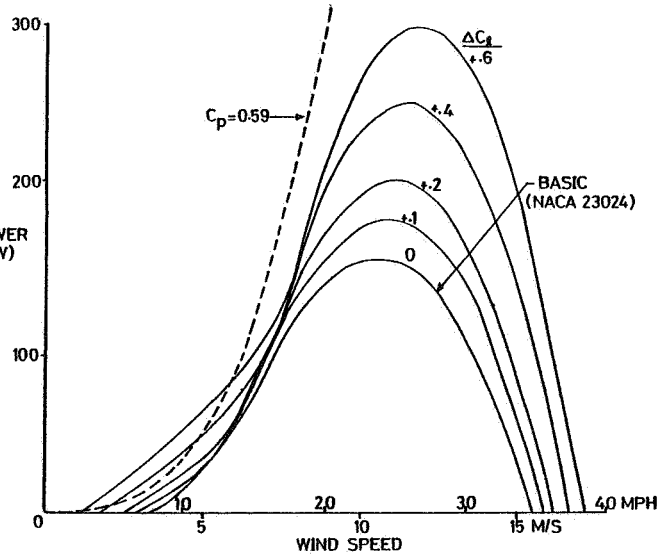

Fig. 6- Effects of Δc_l on Wind Turbine Performance.

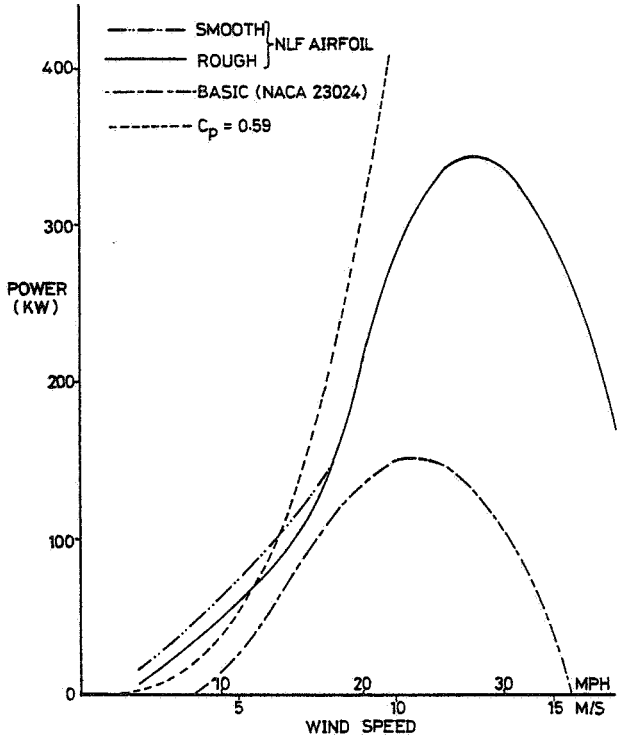

Fig. 7- Performance with New Laminar Flow Airfoil.

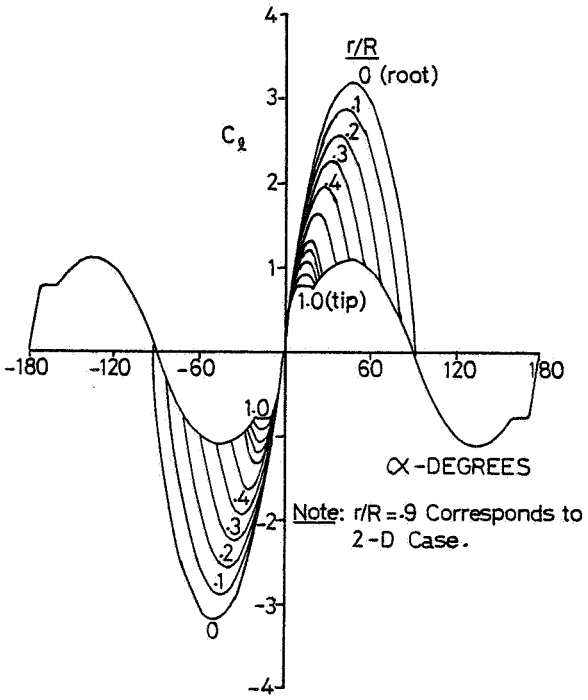

(a) Lift

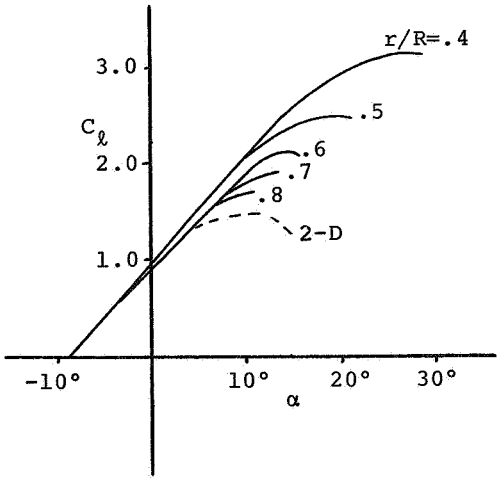

Fig. 8- Himmelskamp's Experiments.

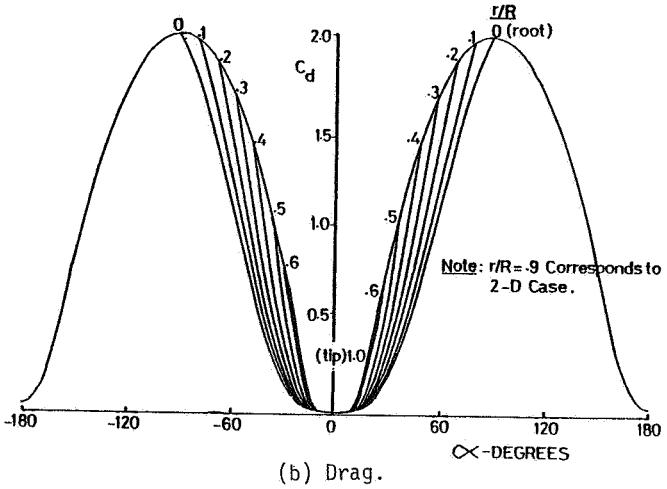

(b) Drag.

Fig. 9- Effects of 3-D Stalling on NACA 23024 Airfoil

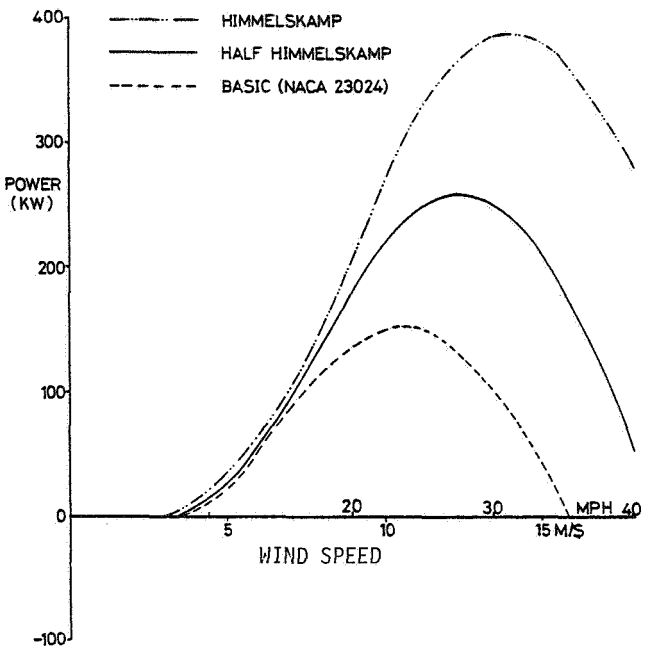

Fig. 10- Effects of 3-D Stalling on Wind Turbine Performance.

QUESTIONS AND ANSWERS

W.H. Wentz

From: A.D. Garrad

Q: Are you aware of Wortmann's work on laminar airfoils where he covers the section with a thin plastic sheet? This "bounces off" insects and dirt but remains smooth. This has been used successfully in realistic environmental conditions.

A: *I was not aware of Wortmann's specific work in this area, but have understood that materials are available which minimize "sticking" of bugs and other substances. These same surfaces are cleaned more easily than traditional materials.*

From: G. Beaulieu

Q: (Related to parametric study) - When you increased C_L, did you compute a proportional increase in induced drag before computing the power output in order to get realistic two-dimensional airfoil data?

A: *No. While this technique has been suggested by some researchers (I believe by Mr. Viterna of NASA Lewis Research Center), I do not believe that it has a theoretical basis. The induced velocity factors "a" and "a-prime" as used in the PROP computer code serve a purpose similar to calculating downwash on a finite span wing. Application of Glauert's momentum theory accounts for induced power in a manner analogous to Prandtl's induced drag factor for finite span wings. If some additional correction factor is needed to match experimental results, I would prefer to identify the factor as an empirical correction rather than obscure it as a theoretical correction, which it is not.*

From: T.E. Base

Q: In your figure, "Power - Flow Speed," do you exceed the Betz Limit with your laminar flow airfoil section if looked as if there was a 250% increase in performance?

A: *The laminar flow airfoil performance exceeds the Betz limit at low wind speeds, as shown in Figures 6 and 7. At wind speeds below, the "a" slowdown factor did not converge satisfactorily or exceed 0.5 which implies reverse flow in the far field. These are the limitations I tried to highlight in the presentation. For moderate and high wind speeds, convergence was satisfactory, and C_p values are well below the Betz limit.*

At speeds near cut-in, performance gains in excess of 100% will be possible (infinite, if we reduce the cut-in speed by reducing section C_{d_0}), but we need a code which will properly converge at these low wind speed, moderate C_l conditions.

From: A. Smith

Q: Did you consider radial variations in airfoil, camber, thickness, etc.?

From: M.P. Moriarty

Q: PROP has provision only to handle one airfoil section at a time. Have you modified PROP to accommodate varying sections and if so, how did you verify the code change?

A: (to both questions above). *We have modified the PROP code so that we can branch to different airfoil characteristic subroutines as a function of radial position. In this way, it is possible to charge airfoil characteristics as desired. We have used, at one time, a special model in which we calculate minimum C_{d_0} as a function of t/C. Ordinarily, it is necessary to insert the lift and drag characteristics of the specific airfoil you desired to study. These coding changes have been "verified" in the sense that we have made careful check runs with detailed printout at each radial station. From these runs, we check the C_l and C_d versus alpha at each station to insure that our airfoil coefficient tables have been properly input and are being properly called.*

From: T.A. Egolf

Q: Do you feel that for small WECS, improving airfoil performance is worthwhile from a Cost of Energy (COE) point of view?

A: *Yes. I am eager to see someone utilize the new airfoil technology on a small unit. It would be quite important to obtain accurate comparative performance data to establish the performance gains which the PROP code is predicting. One possible cost effective way to make such an evaluation, is to conduct "back-to-back" tests with standard and new blades. This should be possible on a small unit without excessive cost.*

From: Anonymous

Q: Is the technology to manufacture these blades presently available?

A: *Manufacturing techniques exist which are capable of providing surfaces which are both smooth enough and hard enough to give large areas of laminar flow, yet are neither highly exotic nor hard to use. Maintaining laminar flow under field conditions will require periodic cleaning. Whether periodic washing and waxing (?) is cost effective is a matter which I believe deserves attention.*

From: D. Cromack

Q: How does laminar flow affect the start-up (since it is often at such low Reynolds number)?

A: *Even though we have no wind tunnel data for Reynolds numbers corresponding to start-up, I see no reason that new laminar flow sections should be a problem. We have little or no data on the older (presently used) sections for these conditions, and they can be aerodynamically started. I do believe that a legitimate need exists for airfoils designed to operate at Reynolds numbers of less than 1 x 10^6, for small wind turbine application.*

From: F.W. Perkins

Q: What is the maximum power coefficient predicted under three-dimensional flow conditions by PROP?

A: *As indicated on Figures 6 and 7, for low wind speeds, the computer program predicted C_p values in excess of the 0.59 Betz limit. This did not occur for the baseline NACA 23024 airfoil, but was encountered for airfoils with substantial camber (higher C_d's at low angle of attack). In such cases, values of C_p in excess of 1.0 are frequently obtained. The paper by Professor Jeng seems to resolve this problem, and we plan to upgrade our computer code to incorporate his method.*

From: J. Landgrebe

Q: Do you really think that laminar flow can be maintained in the real wind environment (unsteady turbulent flow)?

A: *Under highly gusty conditions, laminar flow will not be possible. On the other hand, some atmospheric conditions and sites will permit periods of laminar flow, and the potential gains are attractive enough to pursue. Even if laminar flow is never attained with these airfoils, their performance as turbulent sections is excellent. Our studies on this matter are not yet complete, but I am having a hard time finding a better turbulent flow airfoil.*

From: J. Tangler

Q: What kind of laminar flow airfoil are you talking about? Do they depend on leading edge suction or aft camber?

A: *These airfoils do not require artificial powered suction, if that's what you are referring to. The laminar flow is achieved through pressure distribution control by means of the airfoil shape.*

From: D.C. Shepherd

Q: Are the results of your study presently published or must we wait for the proceedings of this workshop? Please identify any papers already published.

A: *Our earlier aileron control system studies were published in reference 5. This meeting is the first publication of application of new airfoils to wind turbines. Some of the airfoil data developed at the NASA Langley Research Center have not yet been published in the open literature, but I understand the data will be released soon, at least to U.S. based firms and agencies.*

ON THE WAKE OF A DARRIEUS TURBINE

T.E. Base, P. Phillips, G. Robertson and E.S. Nowak

Faculty of Engineering Science
The University of Western Ontario
London, Ontario, Canada N6A 5B9

ABSTRACT

In the paper, the theory and experimental measurements on the aerodynamic decay of a wake from high performance vertical axis wind turbine will be discussed. In the initial experimental study, the wake downstream of a model Darrieus rotor, 28cm diameter and a height of 45.5cm, was measured in the University Boundary Layer Wind Tunnel. The wind turbine was run at the design tip speed ratio of 5.5. It was found that the wake decayed at a slower rate with distance downstream of the turbine, than a wake from a screen with similar troposkein shape and drag force characteristics as the Darrieus rotor. The initial wind tunnel results indicated that the vertical axis wind turbines should be spaced at least forty diameters apart to avoid mutual power depreciation greater than ten per cent.

INTRODUCTION

An important aspect concerning the wake of a Darrieus rotor, is the interaction of such turbines in widespread arrays. For the production of cheap electrical power from the wind, it has been proposed that large wind turbines could be placed in 'clusters' or 'arrays'. An initial study of this problem by R.T. Templin (1974), concluded that if the spacing between individual power units was more than about 30 rotor diameters, the power reduction per machine would not exceed 5 to 10 per cent. However, if the spacing is further reduced, there is a rapid increase in the wake interference. The report treated the rotors as an array of large-scale roughness elements added to the terrain surface that was already rough, and hence, the individual wakes of the turbine rotors were 'smeared out' by the large-scale turbulence shear layer, well within the average spacing between adjacent machines. Since this first paper on the interaction of windmills in widespread arrays, several other studies have been made, notably by Craford (1975), Lissaman (1977), Newman (1977), Builtjes (1978), Bragg and Schmidt (1978), Faxén (1978), and Builtjes and Smit (1978).

In general, the development of the vortex wake downstream of a Darrieus rotor in the ambient boundary layer, may be divided into three regions. The first region represents the formation and rolling up of the concentrated vortex sheet shed from the rotating aerofoil blades, and then the decay of the coherent wake by vorticity amplification and molecular and turbulent diffusion and, finally, a turbulent wake uncorrelated with the initial disturbance. For a two-bladed Darrieus rotor when the vertical plane of the rotor is normal to the flow direction, the lift force on the blades is zero. For the time period for the rotor to rotate half a revolution, a closed vortex system is shed from the blades and is convected downstream, changing shape due to the mutual interaction, the effect of the ambient turbulent boundary layer, and the ground effect. In the case of the two-bladed Darrieus rotor, a 'packet' of vorticity is shed periodically.

The dominant factors involved in the description of the motion within the Darrieus rotor wake, are the initial properties of the wake, which governs the rate at which the wake entrains the surrounding atmosphere, and the rate and manner in which the entrained fluid is mixed into the wake. For example, it has been well illustrated (see Olsen, Goldburg and Rogers) that the two trailing vortices in the wake of an aircraft wing eventually break down to closed vortex configurations. The wake of the Darrieus rotor starts with a closed vortex structure. On the other hand, the wake behind a wire screen is already very turbulent, and shows very little evidence of any initial coherent vortex structure. It can be hypothesized therefore, that the wake of a horizontal axis wind turbine, which can be compared to that of an aircraft wing with the vortices forming a helix pattern, decays slower with distance downstream than the wake from a vertical axis wind turbine, when both turbines are tested at the same power coefficient and in the same turbulent boundary layer. This fact is important when discussing suitable spacing of turbines.

In the report, a vortex model of the near wake of the Darrieus rotor, will first be discussed, and finally, results of a study made on the simulation of the Darrieus wake by arrays of Troposkein shaped grids will be presented.

NEAR WAKE OF A DARRIEUS TURBINE - VORTEX MODEL

In the analysis, the Darrieus rotor troposkein shape was approximated by straight line elements. Since most of the torque is generated by the 'equatorial' element, the relevant theory will be discussed considering this element. In Fig. 1, a plan view of a typical straight bladed element is shown. The ambient airflow approaches from the right, and at the blade, the total velocity is the vector sum of the blade rotational speed and the free stream velocity corrected by a single inflow or blockage factor. The inflow factor takes into account the linear momentum change due to extraction of energy by the turbine.

Previous theory by Wilson and Lissaman (1974), and also by Base and Russell (1979) showed that the inflow factor (a) varied as the turbine solidity (σ) and Tip Speed Ratio (T_{SR}), so that it could be suitably represented by the following expression:

$$a = \sigma(T_{SR})\left|\sin\theta\right| \quad (\text{For } 4<T_{SR}<6) \qquad (1)$$

Where θ is the actual blade angle. By considering the geometry in Figure 1, then:

$$\text{Tan } \alpha = \frac{U \text{ Sin } \theta}{(U \text{ Cos } \theta + U_t)} \qquad (2)$$

Defining the Tip Speed Ratio and inflow factor by:

$$T_{SR} \equiv \frac{\Omega R}{U_\infty}$$

and $$U \equiv U_\infty(1-a)$$

Then: $$\text{Tan } \alpha = \frac{(1-a)\text{Sin } \theta}{(1-a)\text{Cos } \theta + \chi T_{SR}} \qquad (3)$$

For the equatorial element $\chi = 1$, and also substituting Equ. (1) into Equ. (3), then the following equation is obtained for the angle of incidence of the aerofoil:

$$\text{Tan } \alpha = \frac{(1-\sigma(T_{SR})|\text{Sin}\theta|)\text{Sin}\theta}{[(1-\sigma(T_{SR})|\text{Sin}\theta|)\text{ Cos}\theta + T_{SR}]} \qquad (4)$$

The aerofoil will experience a lift force whose magnitude will depend on the incidence of the total velocity vector and this lift force will be related to the circulation (Γ) developed about the aerofoil.

According to Lanchester's wing theory, line vortices may be considered to exist within the aerofoil. These are the so-called 'bound' vortices. However, the bound vortices for a finite wing cannot end in space, but become free trailing vortices ending downstream by a transverse vortex or the starting vortex. In plan view, the vortex array, in its simplest shape, is a rectangle with the trailing vortices linking the bound vortex to the starting vortex.

The concept of a line vortex is derived from a vortex tube by making the area of cross section of a vortex tube very small, while the circulation strength 'Γ' remains unaltered. Glauert (1946) discussed the line vortex and also the equation for the induced velocity at a point P of an element of a line vortex at a point Q, which is given by:

$$dq = \frac{\Gamma ds}{4\pi r^2} \text{ Sin } \theta \qquad (5)$$

where Γ is the circulation defined by $\oint_c \underline{V}.d\underline{r}$ the line integral of the velocity around a closed curve 'c' and for a potential vortex is constant. This is the Biôt-Savaart Law. The diagram below shows an element of the line vortex where 'r' is the distance between the field point P and the element at Q, and θ is the angle between the direction of the element and the line joining the element to the point P. The velocity dq is normal to the plane containing r and ds, and its 'sense' is the same as that of the circulation 'Γ' of the elemental vortex.

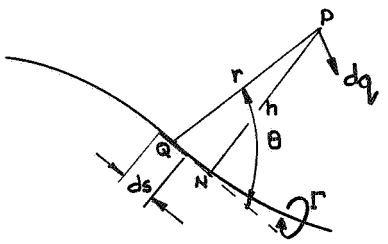

element of the line vortex

In general, the vorticity has the same geometrical properties as the velocity field. The streamlines of an incompressible fluid therefore, correspond to vortex lines of the rotational flow of which the direction at every point is that of the vorticity vector. An element 'ds' of a line vortex therefore, cannot exist independently and the Biôt-Savaart Law, for an element of vortex, should only be used as "building bricks" for more complicated closed vortex loops.

Another expression for the "elemental vortex" is given by:

$$dq = \frac{\Gamma h}{4\pi r^3} \qquad (6)$$

where 'h' is the length of the normal from the field point (P) to a line passing through the vortex line as shown in the Figure.

In the vortex model of a straight bladed vertical axis wind turbine, the aerofoil blade was assumed to start at $\theta = 0$ as shown in Figure 1, rotating at a speed of 'Ω' in a free stream of velocity 'U_∞' to achieve a particular Tip Speed Ratio. The lift coefficient of the aerofoil at this angle ($\theta = 0$) is zero, and hence, the first shed vortex from the aerofoil has zero circulation. As the aerofoil rotates, by considering the angle of the local flow incidence to the aerofoil derived in Section 3 and the lift-incidence curve for the aerofoil, the circulation of the shed vortex may be determined as follows. The circulation is related to the aerodynamic lift on the aerofoil element by the Magnus effect equation and:

$$\text{Lift Force} = \int_0^h \rho U_\infty \Gamma \, dz$$

Hence the lift force is given by the expression (assuming no tip losses)

$$L = \rho U_\infty \Gamma h$$

The lift coefficient is defined by the expression

$$C_L = \frac{L}{\frac{1}{2}\rho U_T^2 \, ch}$$

Where U_T is the total velocity of flow approaching the aerofoil and is the vector sum of the free stream velocity and the aerofoil blade rotation with allowance for the blockage factor. It can be shown that the aerofoil circulation is related to the aerofoil lift coefficient by the following expression:

$$\Gamma = \frac{C_L c U_\infty}{2} \left(\frac{U_T}{U_\infty}\right)$$

The variation of lift coefficient with incidence (α) is also known for the particular aerofoil section. Finally by previous theory (Equ. 4), the angle of incidence is related to the blade angle (θ), solidity (σ), and Tip Speed Ratio (T_{SR}).

and also: $$U_T = (1-\sigma(T_{SR})|\text{Sin}\theta|)U_\infty \frac{\text{Sin}\theta}{\text{Sin}\alpha} \qquad (7)$$

Figure 2 shows the initial rectangular vortex pattern and Figure 3 shows the complete vortex model. Further studies on this vortex model are currently in progress.

TESTS TO DETERMINE THE FAR FIELD WAKE

The main objective of this experiment was to model the interaction that occurs within a widespread two-dimensional array of Darrieus wind turbines. Figure 4 shows a sketch of a two-bladed turbine and some of the essential dimensions. The two-bladed turbine blades consisted of extruded aluminum airfoil section NACA 0012 which had the necessary high-lift, low drag characteristics, and were curved in the shape of a troposkein cantenary. The centre column served as a mounting point for the blades and also housed two low-friction roller bearings. This whole assembly was then mounted on a centre shaft which was braced by wires at the top to reduce turbine vibrations. Two vertical axis turbines used in the study were geometrically identical, being 45.5cm high, 28.0cm diameter, and with an aerofoil chord of 2.5cm. This gave a solidity which is defined as the ratio of blade area to wind turbine area of .36. Since the models used were operating with little load, the Tip Speed Ratio measured was approximately 5.5. The power coefficient for this Tip Speed Ratio and solidity was approximately 0.4. An important problem encountered when working with small models, is that bearing friction will often be greater than the power produced, and therefore, the windmill will not run. The Darrieus turbines used in this study were approaching the lower limit of geometric size. It is most difficult to construct working models of 2.5cm diameter, which would be required in the turbine array studies.

This particular experiment was an attempt to determine the spacial requirements for adjacent turbines, while allowing for a 10% drop in power. This 10% power loss applies to the last windmill of the array, so that if there were 10 rows of windmills, the windmill in the last row would be producing 10% less power than the windmill in the first row. In order to determine the power loss in a widespread array, it was necessary to model a large array, and then obtain velocity measurements downstream from the array. The power extracted by the turbine, is proportional to the velocity cubed, and so by obtaining the drop in velocity caused by the wind turbines, it was possible to calculate the percentage power loss.

In order to perform the experiment in the University Boundary Layer Wind Tunnel, with dimensions 2.4m x 1.8m x 24.0m, it was necessary to use very small models in order to obtain an array of acceptable size. It was not possible to construct working models of 2.5cm diameter, so 2.56cm screen discs were used.

A screen had to be selected, which had a porosity such that it would give the same effect on the momentum of the wind as the wind turbine itself. The following procedure was used to select the screen best suited for the experiment.

The two working models (28cm diameter) of the wind turbines were placed in the Boundary Layer Wind Tunnel, with one directly behind the other. Both were started, and their rotation speeds were measured, as the distance between them was varied from 4 diameters to 32 diameters. The rotational speed was measured with a Strobotac. Since the Tip Speed Ratio was constant for this particular turbine, the rotational speed "ω" was directly proportional to the wind velocity (U_∞).

Seven different types of screens, ranging from a very fine mesh to a quite heavy mesh, were then substituted for the upstream windmill.

The distance between the screen and the downstream wind turbine was then varied from 4 to 32 diameters. At each position, the rotational speed of the down wind turbine was measured. It was then possible to select the screen which modelled the wind turbine drag, and this screen had a porosity of 0.48. Twenty screens, each with a diameter of 2.5cm and troposkein shape, were then manufactured.
The drag ratio of the screen was measured using a small balance that was constructed and calibrated using a solid disc which had a known drag coefficient of 1.17. The drag coefficient for the wind turbine was estimated from the power coefficient value, and was found to be about .8 for the range in which the windmill was operating. The screen was then mounted on the balance, and its coefficient of drag determined to be approximately .75.

The correct screen had now been selected, and it had been established by two methods that this screen had the same effect on the wind momentum as a wind turbine. Therefore, if the 2.5cm screen discs were placed in an array, the effect on the wind velocity should be similar to the effect caused by an array of wind turbines.

Four sheets of masonite were placed in the tunnel and secured to the floor, and the array of screens were then placed in the Boundary Layer Wind Tunnel. The masonite had holes drilled every ten centimeters in each direction, so that the size of the array could be varied from 4 diameters to 36 diameters. In all cases, measurements were obtained using an array consisting of five rows perpendicular to the wind flow, and three parallel to the wind flow.

Velocity values were recorded downstream from the array as the distance between adjacent windmills was changed from 4 to 32 diameters. The velocity was measured at the location where the sixth row of the array would have been placed. The vertical height of the velocity measurements was equal to the mean height of the porous screen models. Measurements were taken every ten centimeters along the horizontal, by using transversing gear located in the Boundary Layer Wind Tunnel. By entering the required information into the computer, the data was automatically obtained for a sample time of 60 seconds. A hot wire anemometer was used to obtain the values of the velocity, which were compared to the values of velocity when no models were present. The value for no models present was obtained from the velocity profile which was taken at each location before the array was placed in the wind tunnel. The fact that the profiles taken at each location were similar, was also an indication of the fact

that the turbulent boundary layer did not deteriorate over the masonite.

DISCUSSION OF WAKES

In the analysis of the wake downstream of a Darrieus rotor, two distinct approaches may be used. In the near field, the decay may be considered to be that of an interacting discreet vortex array. For a single two-dimensional viscous vortex, the circulation (Γ) decays according to the following equation:

$$\Gamma = \frac{\Gamma}{2\pi r}\left[1\text{-EXP}\ (-r^2/4\nu t)\right]$$

and this would infer that for the vortex wake from a turbine, 'time' was more important in the decay process than distance, although both are related by the convection velocity of the vortices. Batchelor (1964) discussed the axial flow in trailing line vortices with application to trailing vortices from lifting surfaces. An important result of this study showed that the axial velocity defect varied as:

$$(U_\infty - u)_{max} \sim \frac{C_0^2}{\nu x} \log\left(\frac{xU}{\nu}\right)$$

Where C_0 is $(2\pi)^{-1}$ times the vortex circulation at large values of radius. For a turbulent wake downstream of a circular disc, using the mixing length theory (see Schlichting, 1968), the velocity deficit varies as:

$$(U-\bar{u}) \sim x^{-2/3}$$

Grainger (1966) studied three-dimensional vortex flow and approximated the vorticity by an infinite power series of the form:

$$\Omega(r,x) = f(x)\ e^{-f(x)r^2}$$

An interesting solution to the steady flow vorticity equation was then obtained, and in particular, the variation of the vorticity at the centre line of the vortex was shown to vary in the form of the elliptical function of the Weierstrass canonical form. One disadvantage of this type of solution when applied to the study of the decay of a vortex sheet shed from a Darrieus rotor, is that the mutual vortex effects which could also cause vorticity amplification, have been ignored. Another effect also excluded in these studies, which is important when considering the turbine wake decay, is the ground effect. At large distances downstream of the turbine, the vortex wake approaches an established turbulence flow state. Sforza (1970), Counihan (1971) and Lemberg (1973), considered turbulent wall wakes behind various shaped obstacles. The main conclusion of these studies, was that for a turbulent wake, the centre line velocity deficit varied inversely as the distance downstream of the turbine (x^{-1}). These established results for the decay of wakes, will be used for comparison with measured decay rates in the following section.

RESULTS

Near Wake

A vortex model describing the flow field about a Darrieus rotor was introduced. In the model, the flow field was assumed to consist of a regular intermittent coherent pattern of finite vortex elements, shed from the rotating blades every half a revolution. The circulation strengths of the vortices in the vortex model depended on the turbine parameters, such as Tip Speed Ratio, solidity, aerofoil blade section, and blade position relative to the incident airstream. The vortex model also satisfied Kelvin's theorem concerning continuity of vortices. Figures 2 and 3 show typical vortex arrays used in the model. In this initial study, it was shown that for a two-bladed Darrieus rotor, the vortices shed from the 'equatorial' element of the upstream blade intersected the downstream blade after 150^0 of rotation, when the rotor Tip Speed Ratio had a value of π. Further computer studies on this vortex model of the Darrieus rotor are planned in the future.

Far Wake

The first tests were to determine the correct screen with a given porosity, to model the Darrieus rotor operating at the design Tip Speed Ratio of 5.5. Two similar turbines were placed in a line parallel to the ambient air flow, so that the downstream turbine was affected by the wake of the upstream turbine. The downstream turbine was then moved downstream in increments of four diameters, and the various rates of rotation of the downstream turbine recorded. The forward turbine was then replaced by troposkein shaped screens of different porosity, and the rate of rotation was again recorded for the downstream wind turbine. Figure 5 shows the test results for the rate of rotation of the downstream turbine when initially a Darrieus turbine was upstream, creating blockage, and also with a screen with a porosity of 0.48, which was used in subsequent experiments placed upstream.

Tests were now made on an array of 'wind turbines' modelled by one inch diameter porous screens. Figure 6 shows the (3 x 5) array of fifteen screens in a square pattern array. The velocity measurements were made, as shown, in the sixth row. Figure 7 shows a typical wake traverse along the sixth row, when the screen array spacing was eight diameters. The maximum velocity deficit was taken as a measure of the wake effect. For example, when the square spacing was eight diameters and the free stream velocity 18.9 ft/sec., the velocity deficit was 4.4 ft/sec. This implied a percentage velocity deficit based on the free stream velocity of 23.3%, and a power deficit of 54.8%. Figures 8 and 9 show the estimated velocity and power deficits respectively, due to the wake effects of the five rows of screens, representing an array of Darrieus turbines for various square spacing, with the measurements being made in the sixth row position. Also in Figure 8, the wake decay is compared with the wake decay predicted by the various theories discussed in the previous section.

CONCLUSIONS

The theory and experimental measurements on the wake of a Darrieus turbine and an array of turbines were studied: In general, the development of the turbine wake may be classified into 3 regions: The first region consisted of the for-

mation and rolling up of the concentrated vortex sheet, and then the decay by molecular and turbulent diffusion. Finally, a homogeneous, fully developed turbulent state was achieved far downstream of the turbine. For a two-bladed Darrieus rotor or straight-bladed vertical axis turbine, when the vertical plane of the rotor was normal to the flow direction, the lift force on the blades was zero. At any other angle, the local incidence of the aerofoil blades at the 'equator' for instance, could be calculated by the following expression:

$$\text{Tan } \alpha = \frac{(1-\sigma\ T_{SR}\ |\text{Sin}\theta|)\text{Sin}\theta}{(1-\sigma\ T_{SR}\ |\text{Sin}\theta|)\text{Cos}\theta + T_{SR}}$$

For the time period for the rotor to rotate half a revolution, a closed vortex array was shown to be shed from the aerofoil blades, and was convected downstream, changing shape due to the mutual vortex interaction and the effect of the ambient air flow.

In the experimental study of the wake far downstream of an array of Darrieus wind turbines, represented by troposkein shaped porous screens, the results indicated that the 'turbines' should be spaced at least forty diameters apart to avoid mutual power depreciation greater than ten per cent. This predicted value of suitable spacing of turbines, compares favourably with the analytical estimates of Templin (1974).

ACKNOWLEDGEMENTS

The authors would like to acknowledge Mr. R.T. Templin, Head, Low Speed Wind Tunnel Laboratory, N.A.E., Ottawa, who initially suggested to Mr. P. Phillips, who was employed as a summer student at N.A.E., that wind tunnel experiments be made on arrays of wind turbines, represented by small screens, to possibly determine the spacing necessary to minimize interference.

REFERENCES

Base, T.E. and Russell, L.J., "The Flow Field About a Vertical Axis Wind Turbine", Alternate Energy Sources II, Ed. T. Nejat Veziroğlu, pub. Hemisphere Pub. Corp., N.Y. (1980).

Batchelor, G.K., "Axial Flow in Trailing Line Vortices", J.F.M., Vol. 20, Part 4, pp. 645-658 (1964).

Bragg, G.M. and Schmidt, W.L., "Determination of Optimum Arrays of Wind Energy Conversion Devices", J. of Energy, 2, 3, p.155 (1978).

Builtjes, P.J.H., "The Interaction of Windmill Wakes", 2nd Int. Sym. of Wind Energy Systems, Amsterdam, B.H.R.A., pp. B5-49-58 (Oct. 1978).

Builtjes, P.J.H. and Smit, J., "Calculation of Wake Effects in Wind Turbine Parks", Wind Engineering, 2, 3, p.135 (1978).

Counihan, J., "An Experimental Investigation of the Wake Behind a Two-dimensional Block and Behind a Cube in a Simulated b/l Flow", C.E.R.L. Report RD/L/N 115/71 (1971).

Craford, C., "An Estimate of the Interaction of a Limited Array of Windmills", Rep. DM-16, Univ. of Stockholm (Nov. 1975).

Faxen, T., "Wake Interaction in an Array of Windmills. Theory and Preliminary Results", 2nd Int. Sym. on Wind Energy Systems, Amsterdam, B.H.R.A., pp. B6-59-72 (Oct. 1978).

Glauert, H., "Elements of Aerofoil and Airscrew Theory", pub. C.U.P., 2nd ed. (1959).

Grainger, R., "Steady Three-dimensional Vortex Flow", J.F.M. (1966), Vol. 25, Part 3, pp. 557-576.

Lemberg, R., "On the Wakes Behind Bluff Bodies in a Turbulent Boundary Layer", Ph.D. Thesis, The Univ. of Western Ont. (1973).

Lissaman, P.B.S., "Energy Effectiveness of Arrays of Wind Energy Conversion Systems", AV FR 7058, Aero Vironment Inc., Pasadena, U.S.A. (May, 1977).

Newman, B.G., "The Spacing of Wind Turbines in Large Arrays", Energy Conversion, 16, 169 (1977).

Olsen, J.H., Goldburg, A. and Rogers, M., "Aircraft Wake Turbulence and its Detection", pub. Plenum Press, N.Y. (1971).

Schlichting, H., "Boundary Layer Theory", pub. McGraw Hill Bk. Co., 6th ed. (1968).

Sforza, P.M. and Mons, R.F., "Wall Wake: Flow Behind a Leading Edge Obstacle", AIAA J., 8, 12 (1970).

Templin, R.T., "An Estimation of the Interaction of Windmills in Widespread Arrays", NAE Technical Report, LTR-LA-171 (1974).

Wilson, R.E. and Lissaman, P.B.S., "Applied Aerodynamics of Wind Power Machines", Oregon State University (1974).

NOMENCLATURE

a	interference or blockage factor for vertical axis wind turbine
B	number of windmill blades
c	blade chord
C_0	vortex circulation times $(2\pi)^{-1}$
C_L	blade section lift coefficient
d	diameter of wind turbine
r	radius of a point in a vortex from the centre line or radius of a point on a turbine
h	height of blade element of wind turbine
t	time
T_{SR}	Tip Speed Ratio $(\Omega R/U_\infty)$
u_T	total local airspeed relative to blade
U_∞	ambient (approaching) wind velocity
α	angle of attack
x	distance downstream of turbine
θ	angle of blade rotation for vertical shaft windmill
ν	kinematic viscosity
ρ	density of fluid
σ	solidity (BC/2R)
Ω	blade rotational speed or vorticity

Γ circulation

Γ_0 initial circulation

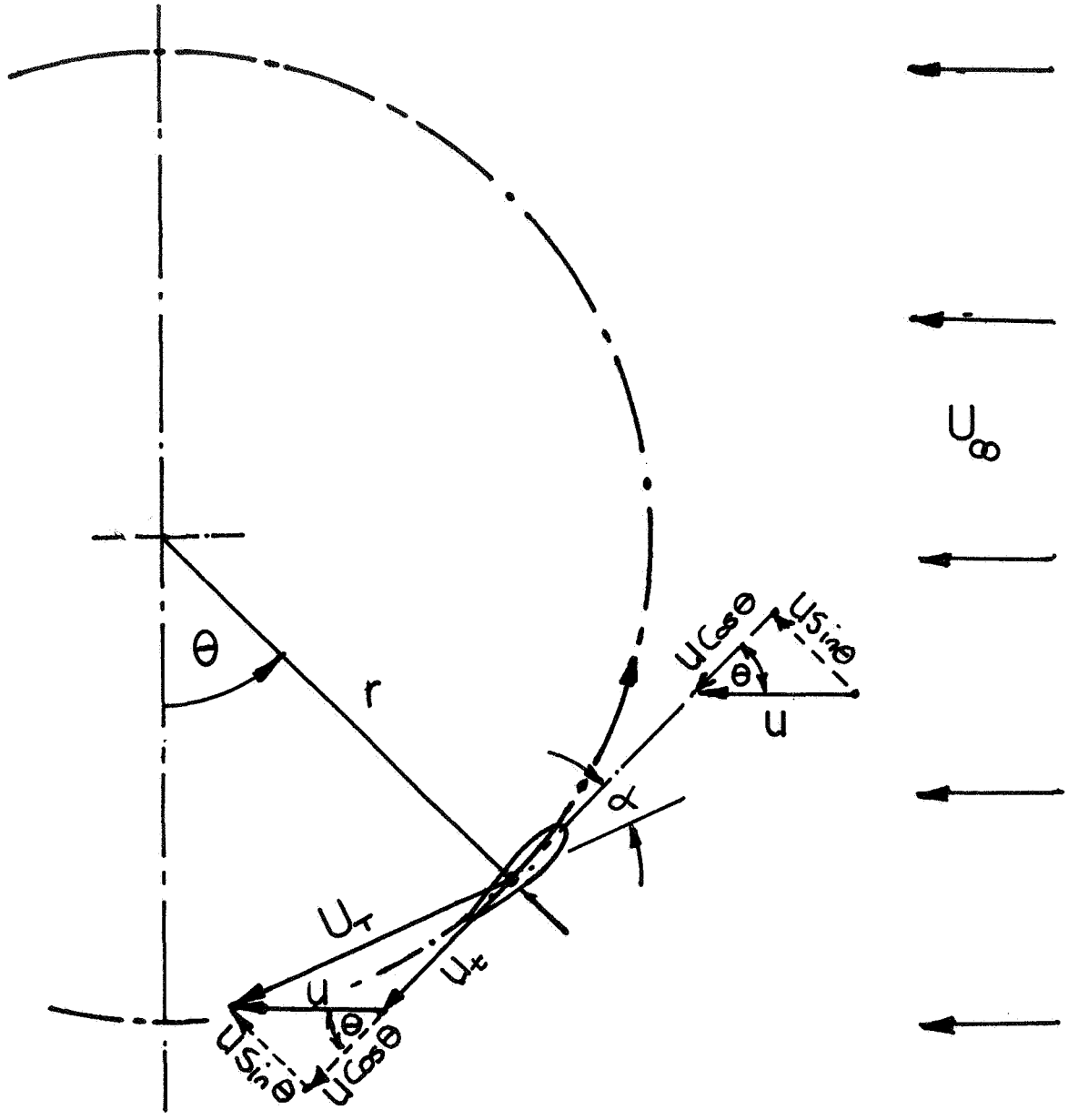

FIGURE1 VELOCITY DIAGRAM FOR ELEMENT OF DARRIEUS TURBINE BLADE.

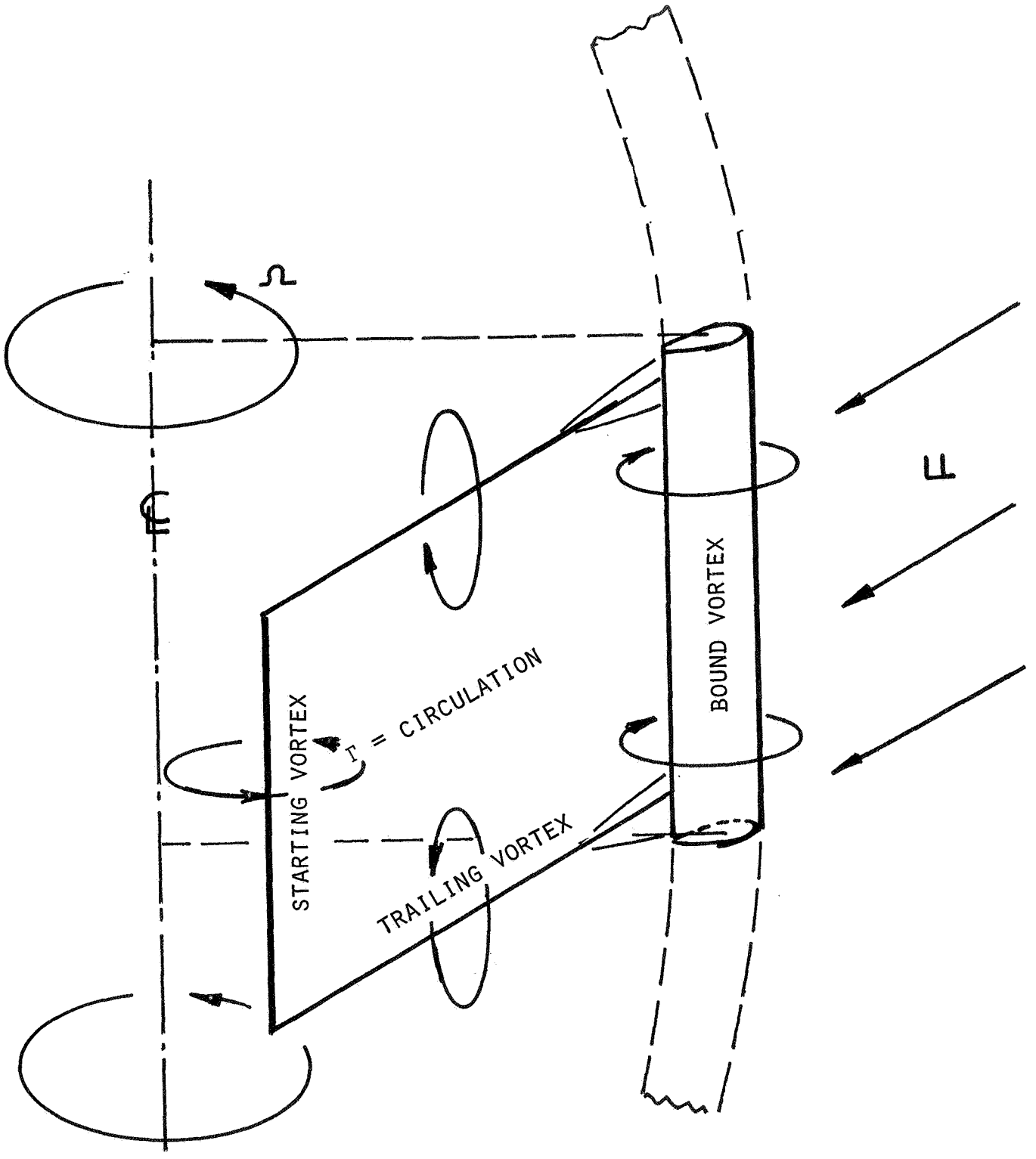

FIGURE 2 A SKETCH OF A RECTANGULAR VORTEX PATTERN SHED FROM A VERTICAL ROTATING AEROFOIL

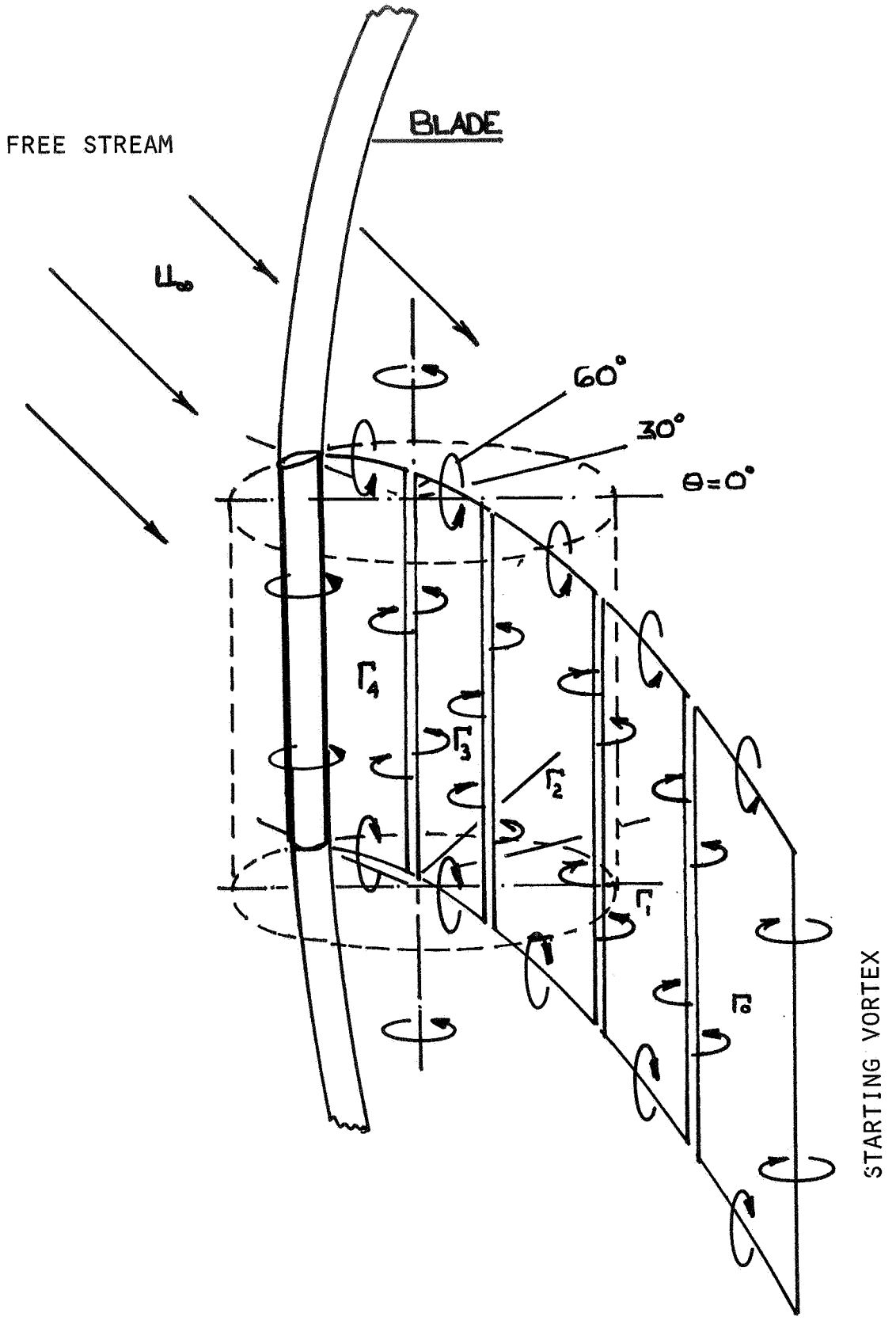

FIGURE 3 TRAILING RECTANGULAR VORTEX SYSTEM SHED FROM A SINGLE ROTATING AEROFOIL BLADE IN A CROSS FLOW

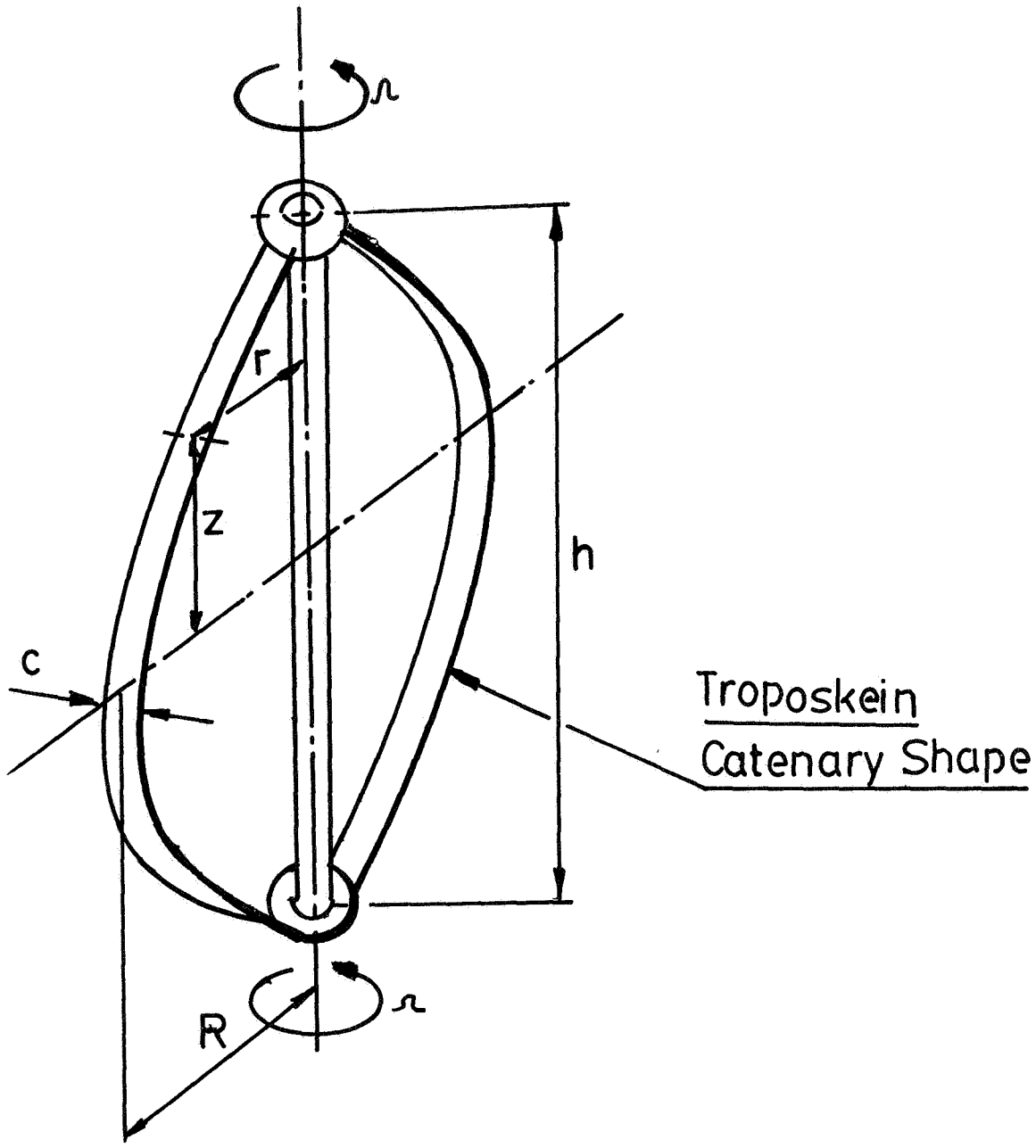

FIGURE 4 SCHEMATIC VIEW OF TWO BLADED DARRIEUS ROTOR

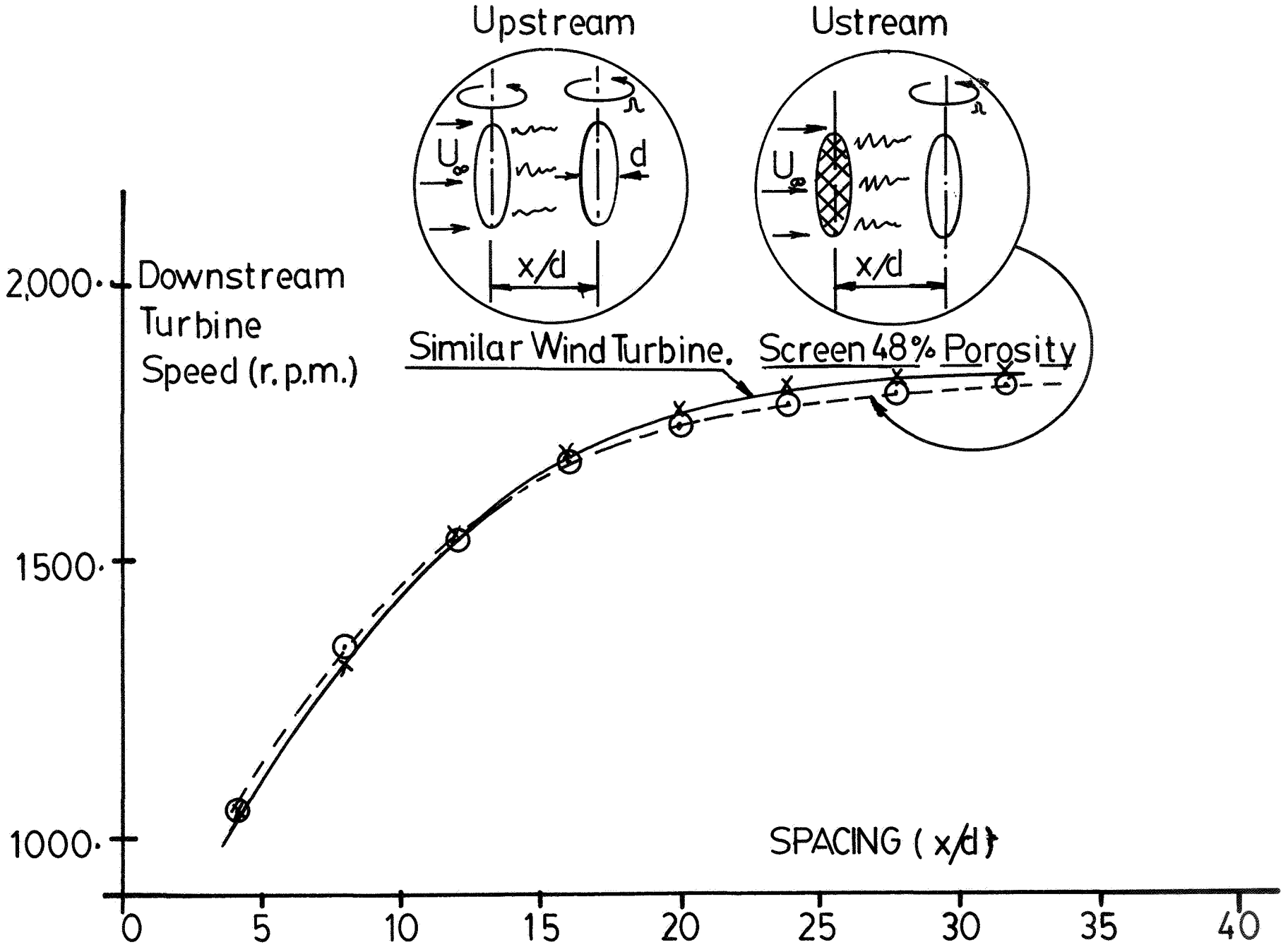

FIGURE 5 EFFECT OF AN UPWIND DISTURBANCE ON A TURBINE SPEED

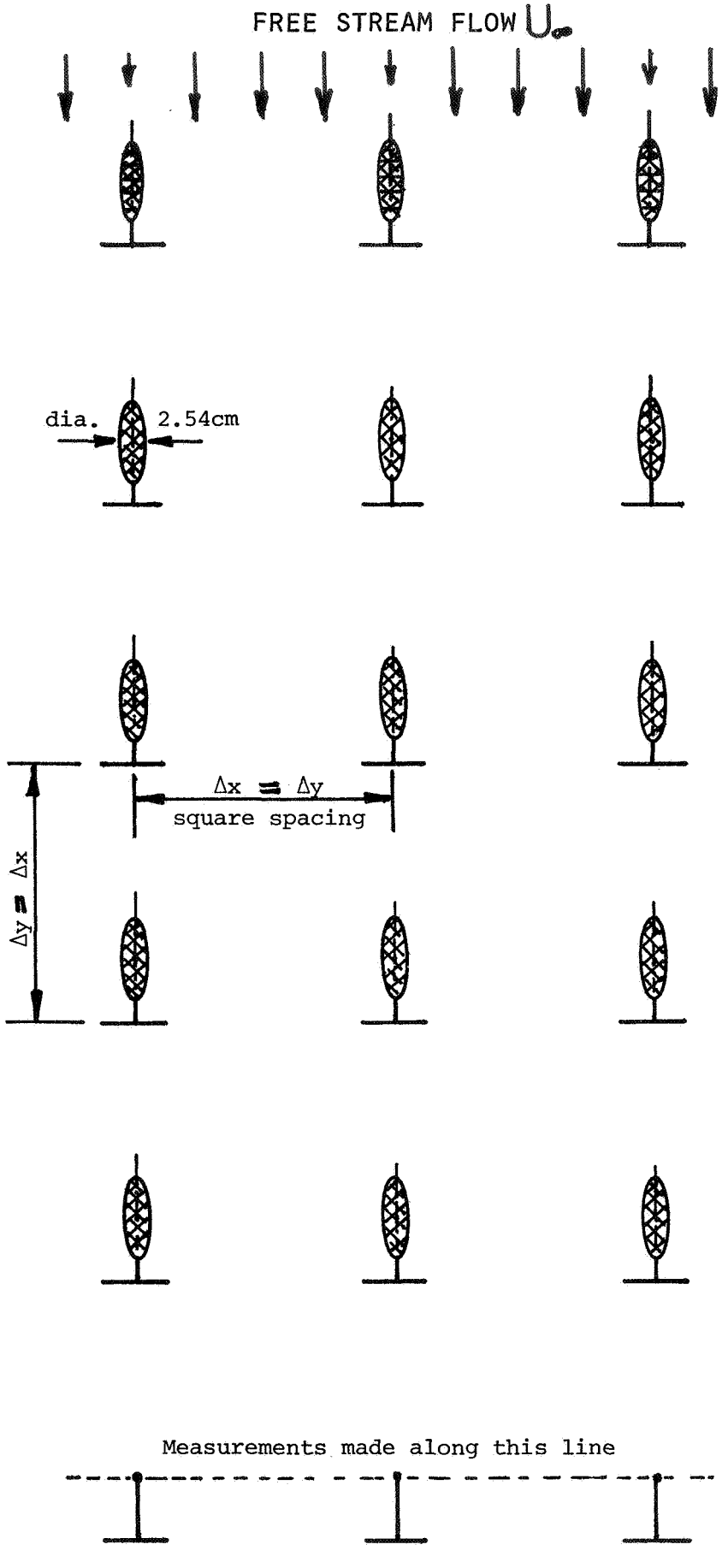

FIGURE 6 SCHEMATIC OF 'WINDTURBINE' SCREEN ARRAY

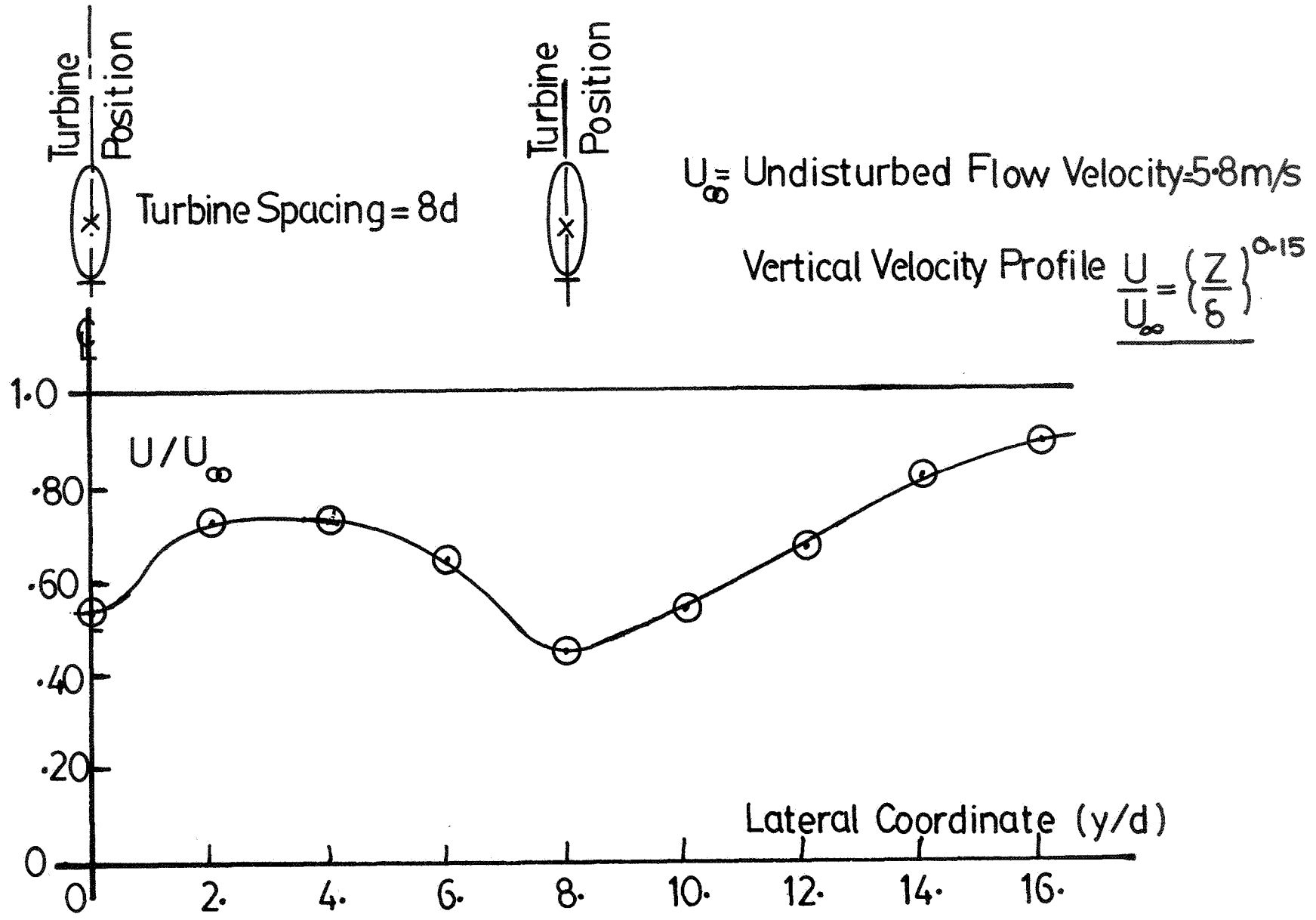

FIGURE 7 VELOCITY MEASUREMENTS AT SIXTH TURBINE ROW POSITION

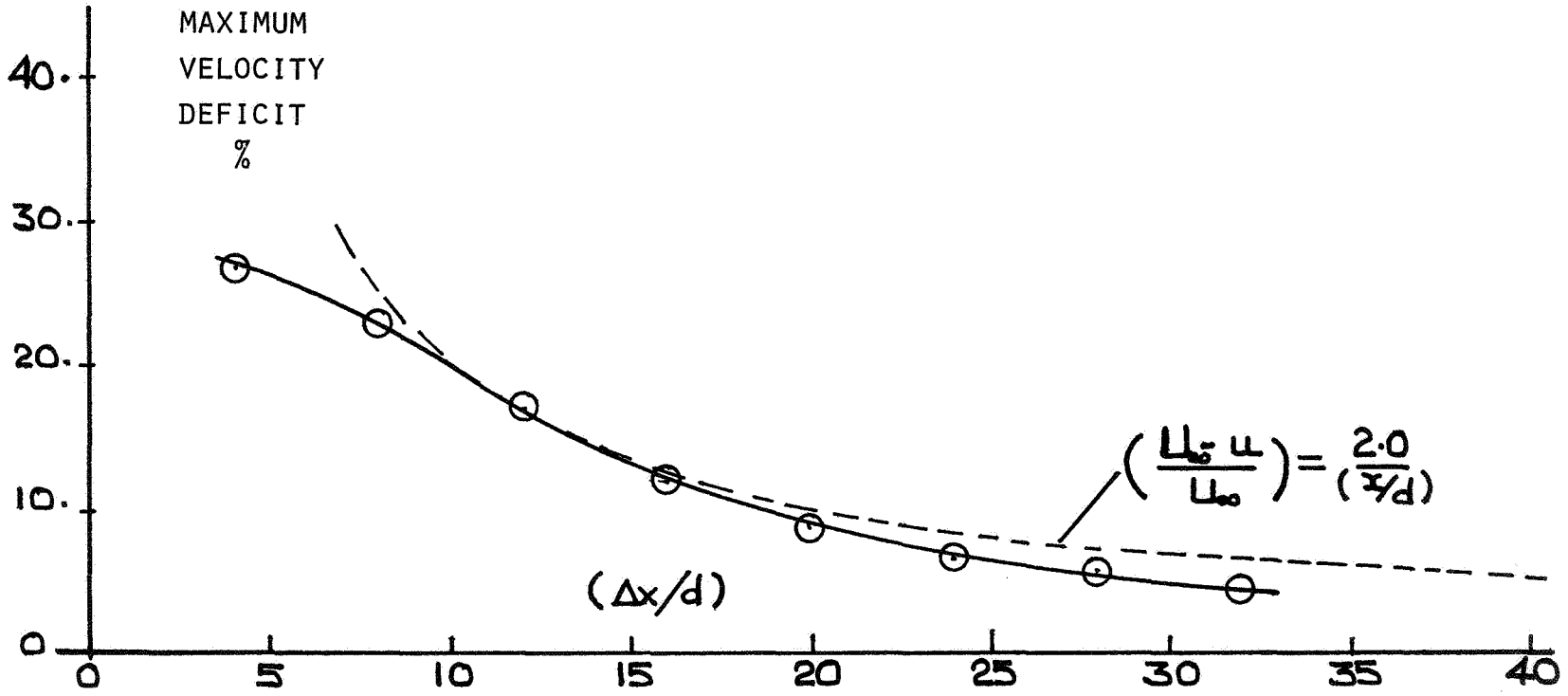

FIGURE 8 VELOCITY DEFICIT DUE TO TURBINE WAKES

MEASUREMENTS MADE IN SIXTH ROW

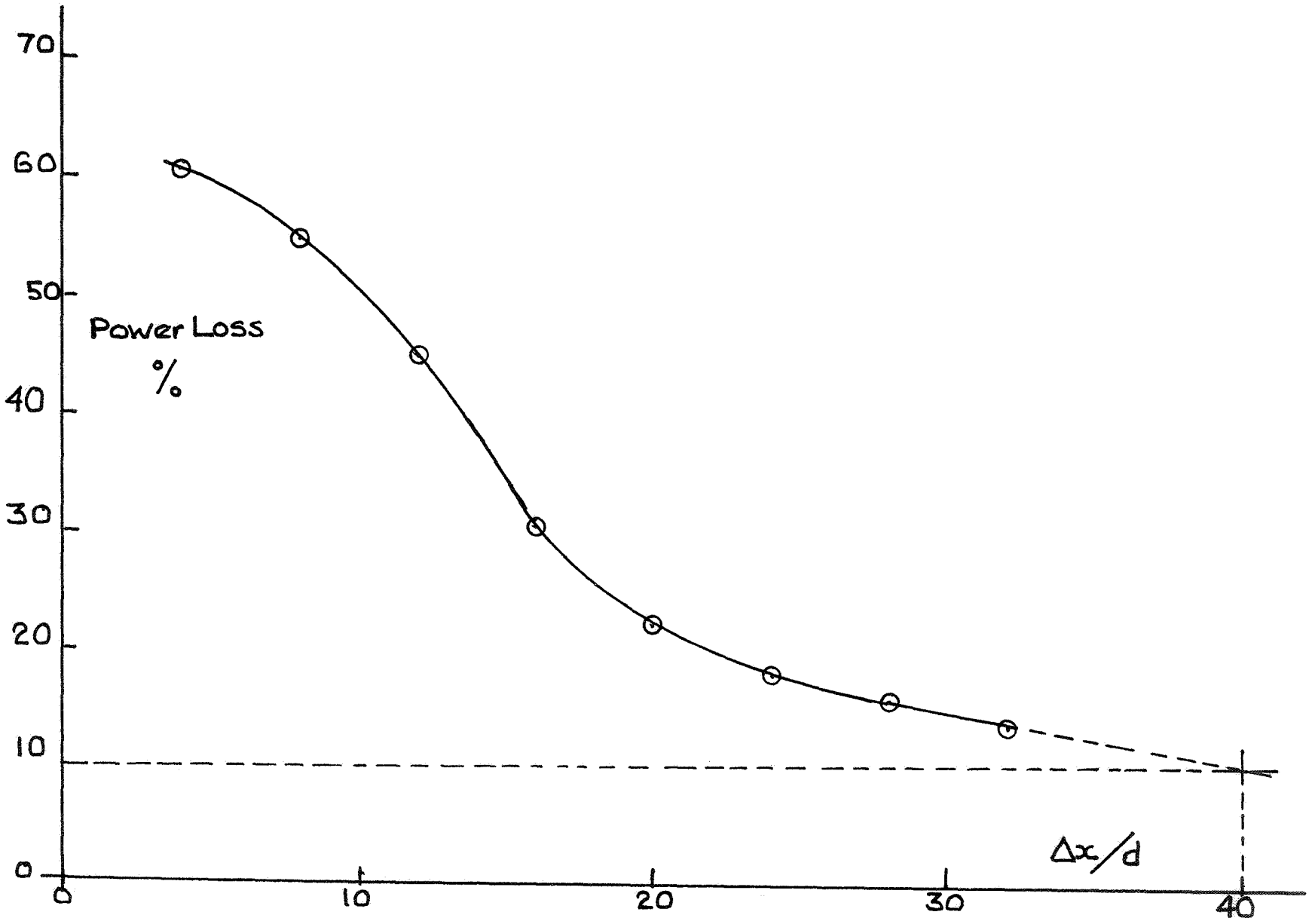

FIGURE 9 POWER LOSS DUE TO "TURBINE" WAKES

MEASUREMENTS MADE IN SIXTH DOWNSTREAM ROW

QUESTIONS AND ANSWERS

T.E. Base

From: T.A. Egolf

Q: Isn't it true that if you reduce your time step interval to a sufficiently small Δt, that the unsteadiness due to the blade impact with the shed vortex sheet is significantly reduced, and if unsteady aerodynamics were used, the effect would be further reduced?

A: *If the time increment is too short, the shed vortices from the blade will not be formed into a coherent structure.*

From: T. Sullivan

Q: How do you determine wake position for the near wake model? Are any measurements of this wake position available?

A: *The wake is shed from the wing and the subsequent position is determined from the induced flow field of the other vortex elements and are free stream, i.e.*

$$u_p = \sum_{i=1}^{No.\ Vortices} u_i + u_\infty$$

I do not know of any published detailed near wake velocity traces or vorticity distributions or flow visualization studies.

RECENT DARRIEUS VERTICAL AXIS WIND TURBINE AERODYNAMICAL EXPERIMENTS AT SANDIA NATIONAL LABORATORIES*

Paul C. Klimas
Sandia National Laboratories
Advanced Energy Projects Division
Albuquerque, New Mexico 87185

ABSTRACT

Experiments contributing to the understanding of the aerodynamics of airfoils operating in the vertical axis wind turbine (VAWT) environment are described. These experiments are ultimately intended to reduce VAWT cost of energy and increase system reliability. They include chordwise pressure surveys, circumferential blade acceleration surveys, effects of blade camber, pitch and offset, blade blowing, and use of sections designed specifically for VAWT application.

INTRODUCTION

It is anticipated that reduction in cost of energy for VAWTs can be effected through relatively simple departures from the current aerodynamic design. This existing design uses blades of symmetrical cross-section mounted such that the radius from the tower centerline is normal to the blade chord at approximately the 40% chord point. The departures from this configuration are anticipated to 1) lower cut-in windspeed, 2) increase maximum aerodynamic efficiency, and 3) limit maximum aerodynamic output power. All of these effects have been shown to increase energy capture for a given basic system and/or reduce system cost for a given annual energy output.[1] The airfoil section characteristics which would bring about these departures are 1) lower section zero lift drag coefficient, C_{do}, 2) higher maximum section lift-to-drag ratio, $(\ell/d)_{max}$, and 3) lower section maximum lift coefficient, $C_{\ell max}$, and higher drag coefficient at which $C_{\ell max}$ occurs, respectively. Mounting the blade at some point radically different from the 40% chord point mentioned above would also alter operating characteristics. This will allow a torque due to the section normal force to contribute (either negatively or positively) to the rotor turning torque. This paper describes certain experiments designed to both better understand the aerodynamics of an airfoil section operating as a VAWT blade element and bring about some of the changes in section characteristics already noted. The common goal of all of these experiments is to lower VAWT cost of energy and increase system reliability.

EXPERIMENTS

There are currently six experimental programs either currently underway or planned for the near future using the Sandia 5-m and 17-m diameter, height-to-diameter of one, test bed turbines. These include blade chordwise pressure distribution and acceleration surveys, blade cambering, blade offset and preset pitch (incidence), blade blowing, and the use of blade sections designed to operate specifically in the VAWT environment.

Blade Chordwise Pressure Distribution Survey

The VAWT blade operating environment is a complicated one. A blade element follows a circular path through space over which both the velocity magnitude and direction are constantly changing. A blade element may stall and recover twice in a single revolution. A blade element sees a range of Reynolds numbers in a single revolution. Operation at very high angles of attack is common. Knowledge of how blade forces are produced under these circumstances is sparse. A program has been designed and hardware is being procured to measure blade transient surface pressures at various chordwise locations as functions of time. Taken concurrently with these pressures will be local flow angularity and local airspeed information. The former will be measured with 29 Entran Devices, Inc. EPF 200-10 semiconductor transducers distributed chordwise near the equatorial section of one 61 cm chord blade of the Sandia 17-m turbine, 18 on both the upper and lower surfaces of the NACA 0015 section and one at the leading edge. The flow angularity and speed will be measured with a 1.27 cm diameter circular cylinder hemispherically tipped probe extending 14 probe diameters ahead of the equatorial blade section. Blade position relative to a fixed compass point will be measured by an AST/Servo Systems, Inc. 23CX6 synchro. Ambient windspeed and direction will be taken from a directional anemometer mounted 7 m above the turbine rotor. The two directional readings will give blade position relative to the ambient wind at any given instant in time. Using time as a common parameter, chordwise pressure distributions along with local flow angularity and local flowspeed may be constructed as functions of tipspeed ratio and blade

*This work supported by the U.S. Department of Energy under Contract No. DE-AC04-76DP00789.

circumferential location relative to ambient wind direction. It is expected that this detailed information will allow intelligent assessments of what is happening circumferentially locally in the generation of aerodynamic blade forces in the very complicated VAWT operating environment.

Blade Circumferential Acceleration Survey

An earlier 17-m experiment involved a limited circumferential survey of the blade equatorial section chordwise accelerations.[2] This information proved very valuable as it pointed out the existence of blade dynamic stall. It was noted that a more complete triaxial blade acceleration survey could be efficiently run simultaneously with the pressure survey described above. This survey will be taken using Schaevitz, Inc. LSMP1 (±1 g gravitational), LSMP2 (±2 g chordwise) and LSMP25 (±25 g normal) accelerometers. Accelerations will be measured as functions of time and related, as with the pressures, speeds and angularities, to tipspeed ratio and blade circumferential location relative to the ambient wind direction. These accelerations should prove helpful in evaluating the chordwise pressure data.

Blade Cambering

Blade section cambering has the potential for altering performance characteristics in two ways. The first one is to tailor section characteristics ($[\ell/d]_{max}$, $C_{\ell max}$, α_{stall}) to take advantage of the upwind-downwind and advancing-retreating rotor traverses. The upwind flowfield is relatively undisturbed and has the highest energy. The advancing portion of the trajectory has the highest relative airspeed. It may be possible to camber a blade element such that maximum efficiency is enhanced and a lower maximum power is achieved. The second idea is that a symmetrical blade section operating in a curvilinear flowfield acts like a cambered section, this being due to chordwise variations angle of attack stemming from the circular trajectory. The inverse of this concept is to add camber to any blade element (symmetrical or otherwise) such that the additional camber conforms to the trajectory of a point at the perpendicular intersection of a radial line from the axis of rotation to the element chord. This is postulated to reduce C_{do} and therefore decrease cut-in windspeed.

These two ideas are essentially independent but are both being investigated. Blades for the Sandia 5-m turbine were ordered extruded in the NACA (.85) 515 section with a 15.24 cm chord. This camber would cause the camber line to coincide with the trajectory of a point at the perpendicular intersection of a radial line from the axis of rotation to the equatorial blade element at its 50% chord location. Two sets of two blades each were bent to the straight line - circular arc - straight line troposkein approximation planform, one set with the camber concave outward from the axis of rotation and one concave inward. The first set was to investigate the first postulate stated while the second would address the second. Both blade sets were run, but it was found that the performance differences (from the nominal NACA 0015 geometry) measured fell within the measurement uncertainties of the 5-m data gathering system. In order to amplify these differences to discernable magnitudes, a second pair of blade sets were ordered extruded in the NACA (2.34)515 section. (Although the first blades were ordered with a 0.85% camber, they were actually extruded to a 1.17% value. The 2.34% camber of the second blade sets was chosen because it is double that of the first.)

Blade Offset and Preset Pitch

Mounting blades of symmetrical cross-section with some preset pitch or incidence angle (β) can also potentially take advantage of the upwind-downwind and advancing-retreating flowfield differences. Computer simulations[3,4] indicate that β's of only a few degrees ($< \pm 5°$) lead to large changes (up to 25% or so) in peak efficiency and peak output power. Varying the chordwise location where the position vector from the axis of rotation perpendicularly intersects the blade element can also utilize the flowfield differences. The mechanism here is to allow blade element normal forces to contribute (positively and negatively) to the turbine turning torque. Current design practice does not significantly include these contributions as the chordwise mounting point is very near the blade element center of pressure.

A parametric experimental series is currently being run on the Sandia 5-m turbine which combines both of these effects. It is implemented by mounting the blade ends on rack-like devices which allow the radius vector from the tower centerline to normally intersect the blade chord at chordwise locations of between 180% chord behind and 77% chord ahead of the blade leading edge in roughly 13% chord increments. This range corresponds to blade β's at the equatorial plane of -7° to +3° (see Fig. 1). Some preliminary results are given in Figs. 2 and 3. It can be seen that these offsets have a large effect on both peak power and peak efficiency.

A second series of preset pitch experiments is also planned. This series involves pitching only the circular arc portion of the turbine blade. Single hinge points located at the 30% chord

location at the extremeties of the curved portion will be oriented such that rotation of the curved portion about an axis parallel to the tower centerline is possible.

Blade Blowing

As mentioned previously, maximum rotor power is governed by maximum lift coefficient, $C_{\ell max}$, and the drag associated with operation at that condition. This may be governed actively as well as by the passive means described earlier. One scheme for active governing of maximum power is suggested by the fact that the hollow extruded aluminum blades when rotating act as centrifugal pumps. An experiment waiting to be run on the Sandia 5-m VAWT involves the use of blades into each of which have been drilled over 1000 circular holes of 0.13 cm diameter set 0.32 cm on center. These holes are placed on both sides of each blade at the 40% chord point and symmetrically distributed about the equatorial plane. By valving the ends of the blades, air volume flow through the holes may be controlled. At the maximum rotor power output operating condition, simple momentum and pumping power considerations indicate an 18% reduction in rotor power. Additionally assuming that 60% of each blade's lift is spoiled by this blowing suggests that the rotor will need to be externally powered in order to maintain rotational speed. Actual power loss will probably fall some place between these two extremes.

Blade Sections Designed Specifically for VAWT Application

Typical airfoil sections designed for aviation purposes exhibit low drag over a limited angle of attack range, high maximum lift coefficients, and gentle stall characteristics. This set of conditions is far from ideal when considering VAWT applications. Recently, attempts have been made to design an airfoil section which will exhibit low drag over a wider angle of attack range, a lower $C_{\ell max}$, and more abrupt stall than those sections currently available. Such profiles, when used as VAWT blade elements, will lower cut-in windspeed, raise peak efficiency, and lower maximum rotor power. Drag polars for an 18% thick laminar flow section intended to be used as a VAWT blade element is shown in Fig. 4. For comparison's sake, similar polars for the NACA 0015 airfoil is given in Fig. 5. Both sets were generated using the Eppler section characteristic synthesizer.[5] It is felt that typical VAWT flowfield turbulence levels are generally low enough that maintenance of laminar flow may be reasonably expected. It is currently intended to extrude a 15% thick profile having characteristics similar to the ones shown in Fig. 4 for testing on the Sandia 5-m turbine some time later in this year.

SUMMARY

A number of VAWT experiments, planned and ongoing, have been described which are intended to increase understanding of VAWT aerodynamics for the purposes of reducing VAWT cost of energy and increasing system reliability. Along with the analytical tools currently in use and under development, these experiments will hopefully provide the basis for the next generation of more cost-effective and reliable vertical axis wind turbines.

REFERENCES

1. Economic Analysis of Darrieus Vertical Axis Wind Turbine Systems for the Generation of Utility Grid Electrical Power -- Vol. 1: W. N. Sullivan, Executive Summary; Vol. 2: idem, The Economic Optimization Model; Vol. 3: R. D. Grover and E. G. Kadlec, Point Designs; and Vol. 4: W. N. Sullivan and R. O. Nellums, Summary and Analysis of A. T. Kearney and Alcoa Laboratories Point Design Economic Studies, SAND78-0962, Albuquerque, NM, Sandia National Laboratories, 1979.

2. McNerney, G. M.: Accelerometer Measurements of Aerodynamic Torque at the DOE/Sandia 17-m Vertical Axis Wind Turbine, Sandia National Laboratories, Albuquerque, NM, SAND80-2776, 1980.

3. Klimas, P. C.: "Vertical Axis Wind Turbine Aerodynamic Performance Prediction Methods," Proceedings of the Vertical Axis Wind Turbine (VAWT) Design Technology Seminar for Industry, Sandia National Laboratories, Albuquerque, NM, SAND80-0984, 1980.

4. Wilson, R. E. and Walker, S. N.: Fixed Wake Analysis of the Darrieus Rotor, prepared for Sandia National Laboratories under Contract 42-2967, November 1980.

5. Eppler, R.: "Turbulent Airfoils for General Aviation." Journal of Aircraft 15, No. 2 (1978), 93-99.

NOMENCLATURE

A_s	Turbine swept area
C	Blade Chord
C_ℓ	Blade airfoil section lift coefficient = $\ell/(1/2)\rho_\infty V_\infty^2 c$
C_d	Blade airfoil section drag coefficient = $d/(1/2)\rho_\infty V_\infty^2 c$
C_p	Power coefficient, $Q\omega/(1/2)\rho_\infty V_\infty^3 A_s$
d	Blade airfoil section aerodynamic drag
K_p	Power coefficient, $Q\omega/(1/2)\rho_\infty A_s (R\omega)^3 = C_p/X^3$
L	Blade length
ℓ	Blade airfoil section aerodynamic lift
Q	Turbine torque
R	Turbine maximum radius
Re	Chord Reynolds number, $\rho_\infty R\omega c/\mu_\infty$
V_∞	Freestream velocity
X	Turbine tipspeed ratio, $R\omega/V_\infty$
α	Blade section angle of attack
μ_∞	Freestream viscosity
ρ_∞	Freestream density

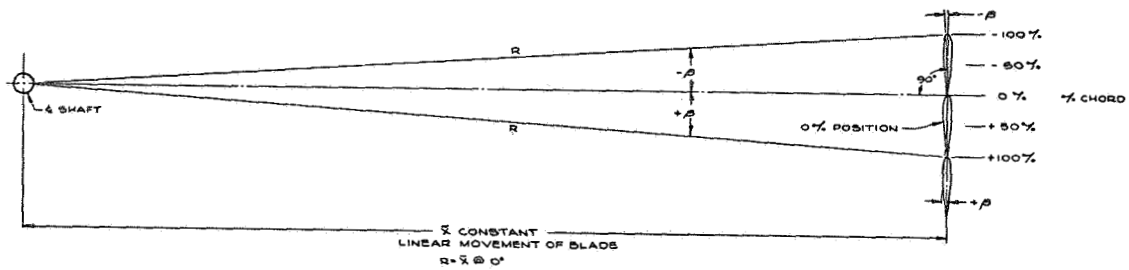

FIGURE 1. Definition of Blade Preset Pitch and Offset

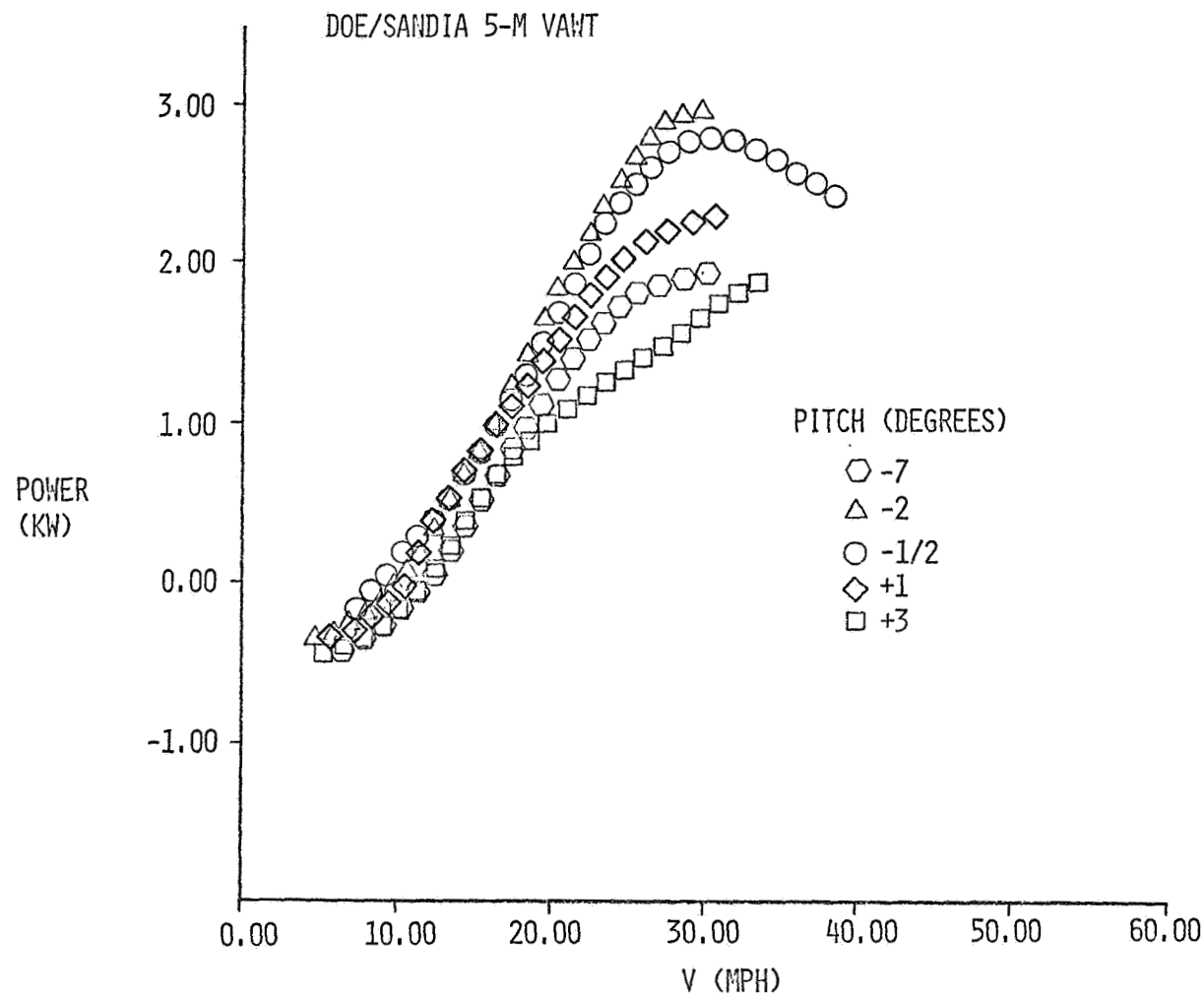

FIGURE 2. Preset Pitch/Blade Offset Rotor Power vs Windspeed, Sandia 5-m VAWT

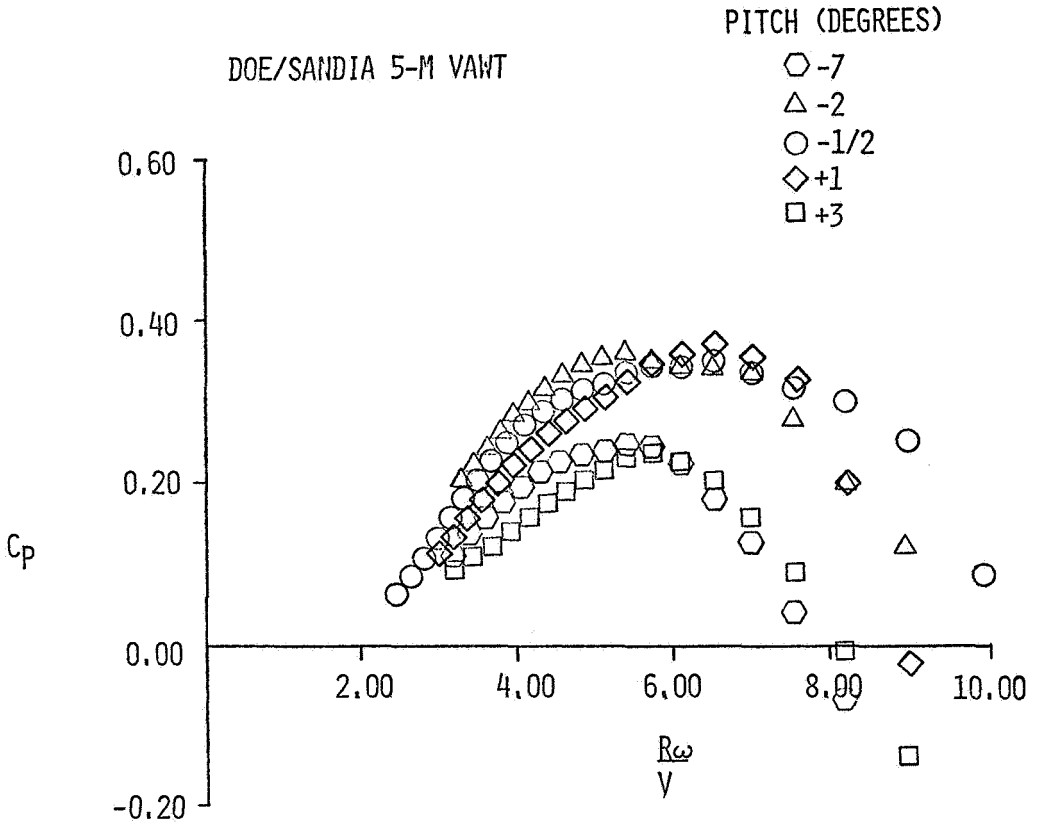

FIGURE 3. Preset Pitch/Blade Offset Power Coefficient vs Tipspeed Ratio, Sandia 5-m VAWT

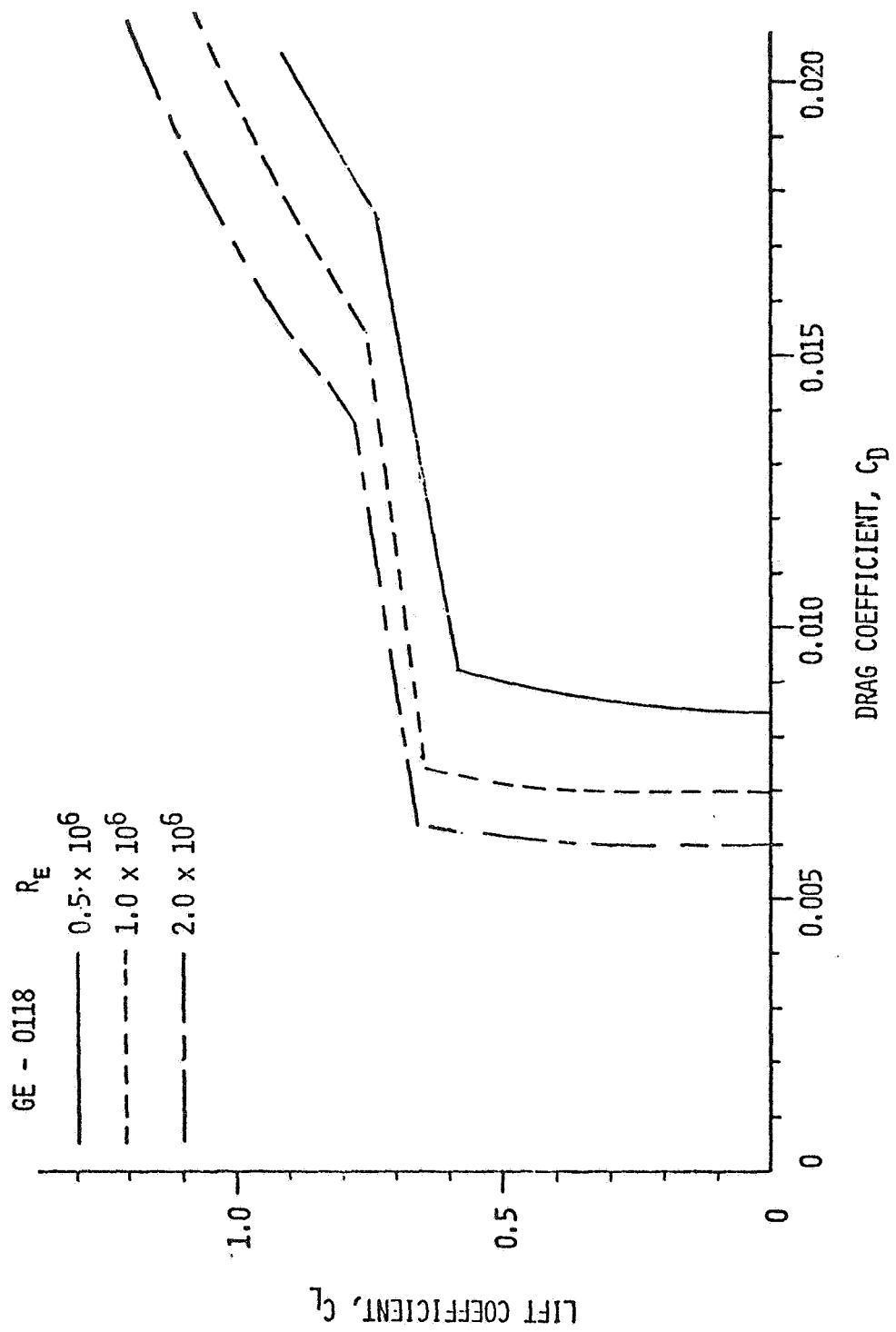

FIGURE 4. Predicted Drag Polars for 18% Thick Candidate VAWT Blade Element Section

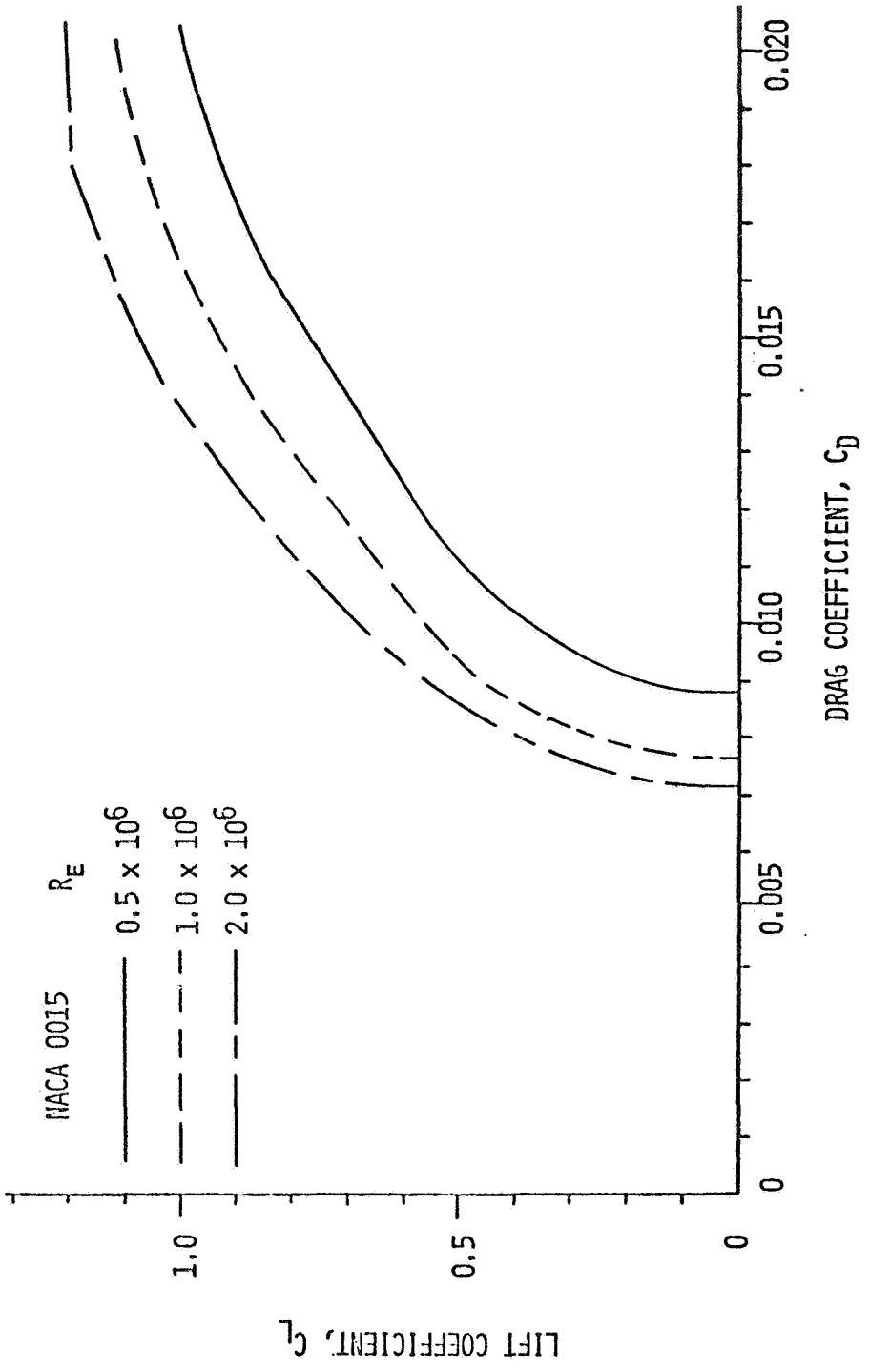

FIGURE 5. Predicted Drag Polars for NACA 0015 Airfoil Section

QUESTIONS AND ANSWERS

P.C. Klimas

From: J.A.C. Kentfield

Q: Have Sandia Labs. considered mounting a floating (i.e., trailing out in the wind) airfoil around the circular tube tower? This should reduce the tower wake on the downstream blade.

A: *This concept has been discussed at Sandia.*

From: N.H. Hubbard

Q: Will your blade pressure measurements include high frequency pressure fluctuations on the blade surface?

A: *I don't recall the frequency response specifications of the Entron, Inc., EPF 200-10 semiconductor transducers, but they are sensitive enough to see any fluctuations currently considered important. Each pressure will be sampled over a 20 millisecond interval.*

From: Anonymous

Q: At the beginning of your talk, you said you wanted to <u>decrease</u> C_{L_M} to move C_p curve to the right. Why?

A: *Decreasing $C_{L_{Max}}$ would <u>lower</u> the C_p curve by reducing output power. Since wind speeds corresponding to this point occur only for a low percentage of the time which the wind blows, cost reductions through lowering drive train requirements are proportionately greater than losses in annual energy, thus reducing cost of energy for the system. A second COE reduction comes through lowering drive train losses, these being proportional to rated power.*

From: J. Glasgow

Q: 1) How will you make Transient Pressure Measurements?

2) Comment in more detail what you expect to get from accelerometers with respect to dynamic stall.

3) Comment on wind speed measurements for Aero Performance Study = i.e. Distance Averaging Time, etc.

A: *1) Transient pressure measurements will be made with semiconductor type transducers which will be sampled for 20 millisecond time intervals.*

2) Hopefully the accelerometer measurements will help in interpreting the pressure measurements.

3) The wind speed measurements will be made by a directional cup anemometer located 7m above the turbine rotating tower. Using the well documented site wind shear profile the measured speed may be used to determine the ambient speed at any desired height.

From: Bill Wentz

Q: 29 transducers--how many chordwise points will you obtain? How many spanwise?

A: *The 29 transducers are all at one spanwise location. There are 14 on both the upper and lower surfaces and one at the leading edge.*

From: G.P. Tennyson

Q: Should you not also consider airfoil cambering as it relates to power optimization (or some such) in addition to symmetrical-about-the-arc-of-rotation cambered airfoils?

A: *Yes, this is currently being investigated.*

From: Art Smith

Q: Does increasing pitch narrow down the streamtube thereby increasing power available by increasing the velocity at the blade?

A: *Increasing pitch would narrow down the streamtube at some locations but increase it at others.*

SECOND DOE/NASA WIND TURBINE DYNAMICS WORKSHOP

Aerodynamics II

Session Chairman - J.C. Estes (NASA LeRC)

"Performance of WTG's in a Turbulent Atmosphere"
R.M. Sundar
J.P. Sullivan
(Purdue University)

"Wind Response of HAWT's"
R.W. Thresher
(Oregon State University)

"Wind Turbulence Inputs for HAWT's"
W.E. Holley
(Oregon State University)

"Rotor Thrust-Loading Spectra for the 200 kw MOD-0A Wind Turbine"
H.E. Neustadter
(NASA LeRC)

"An Overview of Fatigue Failure at the Rocky Flats Wind System Test Center"
C.A. Waldon
(Rocky Flats Plant)

"Performance Testing of a 50 kW VAWT in a Build-up Environment"
L.A. Schienbein
(DAF INDAL Ltd.)

"Calculation of the Guaranteed Mean Power of a WTG"
D.A. Spera
(NASA LeRC)

"The Hydraulic Windmill"
J.A. Browning
(Browning Eng. Corp.)

"Turbulence Modeling"
W. Frost

PERFORMANCE OF WIND TURBINES IN A TURBULENT ATMOSPHERE

R.M. Sundar and J.P. Sullivan

School of Aeronautics & Astronautics
Purdue University
West Lafayette, Indiana 47907

ABSTRACT

The effect of atmospheric turbulence on the power fluctuations of large wind turbines is studied. The significance of spatial non-uniformities of the wind is emphasized. The turbulent wind with correlation in time and space is simulated on the computer by Shinozukas method. The wind turbulence is modelled according to the Davenport spectrum with an exponential spatial correlation function. The rotor aerodynamics is modelled by simple blade element theory. Comparison of the spectrum of power output signal between 1-D and 3-D turbulence, shows the significant power fluctuations centered around the blade passage frequency.

INTRODUCTION

One of the considerations associated with the integration of large wind turbines into an electrical network is the fluctuation of output power/torque due to turbulence in the atmospheric wind. Information on the statistics of shaft power/torque fluctuations is essential for the design of control systems for large wind turbines.

The effect of one dimensional turbulence (i.e. only temporal variations about a uniform mean wind over the entire rotor plane) has been studied by Frost [Ref. 1] and der Kinderen et al [Ref. 2]. The one dimensional analysis shows how the high frequency oscillations in power due to the wind fluctuations can be attenuated by large rotor inertia.

In this paper we emphasize the significance of spatial turbulence on large diameter rotors. [See Fig. 1.] Observing the wind energy spectrum of turbulence in the atmosphere [Ref. 26] we see that the predominant energy is at the low frequency end. This low frequency is associated with large size eddies on the order of hundreds of feet. When the rotor diameter approaches the size of these eddies, then the effect of the blade chopping through this spatial turbulence is to produce fluctuations in the power output at the rotor frequency and its multiples. The study is subdivided into two distinct tasks.

(i) a suitable model to describe the turbulence in the atmosphere and the simulation of wind velocities conforming to this model.

(ii) a suitable rotor model to produce the fluctuating power output signal with the above wind input.

WIND MODEL

The objective of the wind model is to simulate the turbulent wind components. The model takes into account the structure of the atmospheric turbulence, and generates a turbulent wind signal appropriate to the terrain, the scale of turbulence and the mean wind velocity.

A comprehensive survey of the subject of atmospheric turbulence [Ref. 16,17,18,19,24,25,26,27] gives a good understanding of the mechanics of turbulence in the atmosphere and also empirical equations to describe the structure of turbulence close to the ground [13,14].

Later we will show that the horizontal component of wind turbulence makes the largest contribution to the output power fluctuations. Hence our attention is focused on the modelling of the horizontal component alone.

The Davenport Model

According to Davenport [14] the spectral density function for horizontal component is given by:

$$\frac{n\,S(n)}{C_T \cdot V_{M,33}^2} = 4\,\frac{x^2}{(1+x^2)^{4/3}} \qquad (1)$$

where: $x = 4000.\,\frac{n}{V_{M,33}}$

n = frequency (Hz)
$S(n)$ = Spectral density (m^2/s^2 per Hz)
$V_{M,33}$ = Mean Wind velocity at reference height of 10m(33') above ground (m/s)
C_T = Ground roughness factor (akin to roughness coeff. for pipe flow). Suggested values: 0.0005 for open sea, 0.050 for Urban area

The shape of this function [Fig. 2] conforms to observed general results of experimental measurements [Ref. 14]. The value of the constant C_T can be adjusted according to the terrain to give a model of the atmospheric turbulence at a particular site.

Davenports analysis of recorded data also shows that an exponential correlation between points in space agrees well with experimental results. The Spatial Correlation function is given by:

$$\text{Cor.} = \exp\left(\frac{-Cn\ell}{V}\right) \qquad (2)$$

where: V = Mean Wind velocity
C = correlation constant

This function is plotted in Figure 3 for C=6. Taking the Fourier transform of this function with respect to ℓ, we get a spectral description in terms of the wave number $k = \frac{2\pi}{\ell}$ (rads/m)

we get therefore, for spatial correlation:

$$S(k) = \frac{\alpha|\omega|}{\pi(\alpha^2\omega^2+k^2)} \qquad (3)$$

where: $\alpha = \frac{C}{2\pi V}$ (per m)

For a complete 3-dimensional simulation of the horizontal wind turbulence as a function of time and two spatial coordinates Y and Z in the plane of the rotor we use the composite spectral energy density function non-dimensionalized by mean wind velocity

$$\frac{S(n,k_y,k_z)}{V^2_{M,33}} = \frac{4.C_T}{\pi^2}\cdot\frac{x^2}{(1+x^2)^{4/3}} \cdot \frac{\alpha|\omega|}{(\alpha^2\omega^2+k_z^2)} \cdot \frac{\beta|\omega|}{(\beta^2\omega^2+k_y^2)} \qquad (4)$$

Where k_y, k_z are the wave numbers corresponding to the separation lengths in the y and z directions respectively. α and β are related to the correlation constant C. (Note: C could be different for correlation in y and z directions).

Simulation of Wind Velocities

A very comprehensive method of simulating a multi-dimensional multivariate process is described by Shinozuka [21]. A random process is simulated by a series of cosine waves at almost evenly spaced frequencies and with amplitudes weighted according to the spectral energy at the wave frequency.

For the simple case of a random function of time with spectral energy function $S(\omega)$ the process is simulated as:

$$F(t) = \sum_{j=1}^{N} [2.S(\omega_j)\Delta\omega]^{\frac{1}{2}}\cos(\omega_j t+\theta_j) \qquad (5)$$

where: $\Delta\omega = \frac{\omega_u}{N}$

ω_u = Upper cutoff frequency, above which $S(\omega)$ is practically zero.

$\omega_j = j\Delta\omega + \delta\omega$, $\delta\omega$ is randomly small quantity $<\Delta\omega/20$ is introduced to avoid a periodic repetition of the frequency ω_j

θ = Random phase angle $0<\theta<2\pi$

Shinozuka has shown that with as low as 50 frequencies one can obtain a fairly good representation of the spectrum. [Ref. 22] This procedure can be expanded to 3 dimensions as follows: [Ref. 21,22,23]

$$F(t,y,z) = \sqrt{2}\sum_{j=1}^{N_1}\sum_{k=1}^{N_2}\sum_{l=1}^{N_3}[S(\omega_j,k_{y_k},k_{z_l})\Delta\omega\Delta k_y\Delta k_z]^{\frac{1}{2}} \cos(\omega_j t+k_{y_k} y+k_{z_l} z+\theta_{jkl}) \qquad (6)$$

To obtain a good representation of the spectrum in the turbulent signal, the values of N_1, N_2, N_3 should be large. Direct evaluation of the above function turns out to be extremely time consuming computation.

By suitably rewriting the above equation the Fast Fourier Transform technique can be applied in place of the above triple summation. [Ref. 23]

For the present simulation the constants in the spectral density function are:

Mean Wind: $V_{M,33}$ = 32kmph(20 mph)

Terrain Roughness Factor = C_T = 0.005

Spatial Correlation Constants $\alpha=\beta=$ 0.098 per m(.03 per ft)

Cutoff Frequency n_u = 0.5 Hz

Cutoff Wave Number = k_u = 2 rads/m(0.628 rads/ft)(chosen to give a grid spacing of 1.5m(5ft).

After the simulation the turbulent wind data is stored as tabulated information. The table consists of 512 time planes at 1 sec intervals. In each time plane the wind velocities are tabulated at grid points 1.5m(5ft) apart in both y and z directions and covering a total area of 98x98m(320 x320 ft) in the y-z plane. (64 points in each direction)

Instead of generating the turbulent signal as a function of t,y,z by evaluating the triple series a table look up is done in the tabulated wind data with simple linear interpolation.

In the present work we evaluate the turbulent wind component at different radial stations on the wind turbine blade. Interpolation has been restricted to between time planes only. For turbulence at a particular spatial position we choose the value at the grid point closest to this position.

Details of the wind model and computational techniques are given in Ref.30.

An example of the accuracy of the simulation method is shown in Fig. 4 where a comparison between the Davenport Spectrum and a spectrum obtained by taking the Fourier Transform of a one-dimensional turbulent signal generated using Eq. 5, shows excellent agreement.

AERODYNAMIC MODEL OF ROTOR

All of the theories available for analyzing propellers are applicable for analysis of windmill rotors [3,4,12,13,14]. Based on the methods developed for propellers, the performance of windmills can be analysed [5,6,8,9,10,11]. Specific

method for analyzing the unsteady aerodynamics has also been developed [8,9]. The study by Barlow [3,4] presents a fairly comprehensive understanding of the forces on a propeller operating in a turbulent atmosphere. As pointed out earlier, this analysis can be equally adapted to the windmill rotor.

Simple Blade Element Theory

For the purpose of the present analysis a relatively simple model of the rotor is adequate. The Blade -element theory is adopted because of its simplicity and ease of computation. Instead of computing tip loss corrections, and induced velocities, we simply introduced an overall induced velocity factor.

The resulting expression for the power developed is very simple. Comparison of the results from this simple model with that of the Wilson-Lissaman program shows that the trend of the results is the same. By a suitable choice of the induced velocity factor one can attain a specific operating point defined by the tip speed ratio λ and the power coefficient C_p, for a particular pitch setting angle θ_p.

Although the model is very simple, it still retains all the nonlinear features of the wind input versus the power output.

In analyzing the effect of wind fluctuation on output power we are interested more in the fluctuating component of power, than in the exact reproduction of the actual power. If one is interested in the exact power at different operating points the more exact methods detailed above can be used.

Integration of the Wind Model & Rotor Model

The aerodynamic model of the rotor consists of calculating the forces and moments on each element of the rotor from the resultant velocity at that station. The free stream wind is modeled as the sum of the mean wind velocity including the effects of wind shear and the turbulence component as generated by the wind model. That is

$$\vec{V} = \vec{V}(z) + \vec{v}'(t,y,z) \qquad (7)$$

In terms of the freestream turbulent wind components u',v' and w' the fluctuating power coefficient is shown to be (Ref. 30)

$$C_p' = \int_0^1 \frac{C_{l\alpha}}{\pi} \frac{c(x)}{R} \frac{x^2}{(1+\lambda^2 x^2)} \left\{ \frac{-v'}{U}\sin\theta - \frac{w'}{U}\cos\theta + \frac{u'}{U}\lambda x \right\} x\,dx \qquad (8)$$

$\theta = \Omega t$ = angular position of rotor

$\lambda = \frac{\Omega R}{U}$ = tip speed ratio

From this equation we see the dominance of the $\frac{u'}{U}$ term which is multiplied by λ the tip speed ratio.

In the present model we only use the horizontal component of wind turbulence and treating the free stream wind velocity to be only in the axial direction we can easily find the resultant fluctuating wind input at each point along the rotor. As the rotor goes around in space each point on the rotor is at different spatial points at different times. Knowing the spatial point coordinates and time, the wind model can generate the turbulent velocity which then is added to the mean wind velocity to generate the resulting local wind velocity at that rotor station.

It can be observed, that the output power would be fluctuating even if the input wind has a frozen turbulence. That is, there is correlation with respect to space only. An analysis with frozen turbulence for a simple element of the rotor is presented in [Ref. 30].

RESULTS AND DISCUSSIONS

The aim of the present study is to show the important contribution of the spatial non uniformities of atmospheric turbulence on the output power fluctuations of a large wind turbine.

Using the Davenport spectrum and the exponential correlation function, with Shinozukas method of generating a random signal a complete table of turbulent wind data has been generated.

The next step is to input this wind model to the rotor model and analyze the resulting power output. In order to emphasize our point about the contribution from the spatial turbulence effects, we first study the simple one dimensional wind turbulence input.

In Fig. 5 is shown the unsteady power output with a one dimensional wind input. It must be pointed out here that the power output obtained is an ideal one. This is the direct power obtained from the aerodynamic forces acting on the blade. The inertia of the rotor and the flexibility of the shaft have not been considered. For such an ideal case observe the exact reproduction of the wind fluctuations in the power fluctuation.

Spectral analysis of the input one dimensional wind turbulence and the output fluctuating power is shown in Fig. 6. As expected from our observation of the time signals the spectra are identical in shape. Comparison of the Davenport spectrum of Fig. 3 with the spectrum of the wind turbulence Fig. 6 shows that the envelope of the peaks follows the Davenport spectrum. Although the simulated spectrum shows the correct shape, due to the finite length of the generated time signal the spectrum is not smooth at the low frequencies. This could be remedied by generating a longer time signal.

To show the effect of spatial turbulence we considered three different diameter rotors 30m, 60m, and 75m (100 ft, 200 ft, and 300 ft).

The results for the three different sizes of rotors are shown in Figures 7 to 9.* For comparison in each case is shown the power output with a one dimensional wind input and above it the power signal with a three dimensional wind input. (By three dimensional we mean the turbulent wind component as a function of time t, and spatial coordinates y and z in the planes of the rotor).

* All cases are for 2-bladed wind machines at the same tip speed ratio $\frac{\Omega R}{U} = 4.5$

Observe the high frequency fluctuations caused by the rotor chopping through the spatially non-uniform wind. The power spectrum of the time signals adequately show the important contributions from the spatial turbulence effects. Comparing the spectrum of the three different size rotors, observe how with increasing rotor diameter, the fluctuations caused by spatial turbulence dominate over the original Davenport spectrum due to the temporal fluctuations of the wind.

The blade passage is also indicated in the figure to show that the spatial turbulence effects are concentrated around the blade passage frequency.

Conclusion

The study conducted in the present simulation has shown the importance of spatial turbulence on performance of large wind turbines. This aspect of the fluctuations is an important consideration in the design of pitch control systems.

The above study can be easily extended to incorporate a more sophisticated rotor model, like the Wilson-Lissaman program or the vortex lattice method. In calculating the power output at the shaft the flexibility of the shaft and the rotor inertia can be introduced by writing the dynamic equilibrium equation for the entire rotor system in the presence of the applied aerodynamic torque and the torque load on the shaft. Solution of this dynamic equation will then provide the necessary shaft torque or power as a function of time. This extended model can be used to study the influence of rotor inertia and the flexibility of the shaft.

This complete dynamic model can then be merged into an overall simulation of a wind turbine power generation system as is done in Ref. 28 and 29.

ACKNOWLEDGEMENT

The authors wish to express their thanks to the Department of Energy for their financial support.

REFERENCES

1. Frost, Walter, "Analysis of the Effect of Turbulence on Wind Turbine Generator Rotational Fluctuations." University of Tennessee Space Institute, Atmospheric Science Division, Report ASD-1, April 1977.

2. der Kinderen, W.J.G.J., Von Meel, J.J.E.A., Smulders, P.T., "Effects of Wind FLuctuations on Windmill Behaviour." Wind Engineering Vol. 1, No. 2, 1977, pp. 126-140.

3. Barlow, J.B., "On the Forces and Moments on a Propeller Moving Axially Through Homogenous Turbulence." AIAA Atmospheric Flight Mechanics Conference. AIAA paper No. 70-549, May 1970.

4. Barlow, J.B., "Theory of Propeller Forces in a Turbulent Atmosphere." VTIAS Rep. No. 155, September 1970.

5. de Vries, O., "Fluid Dynamic Aspect of Wind Energy Conversion." AGARD-AG-243, July 1979.

6. Wilson, Robert, E., Lissaman, Peter, B.S., "Applied Aerodynamics of Wind Power Machines." PB238595, July 1974.

7. Preuss, R.D., Suiciu, E.O., Morino, L., "Two General Methods for the Unsteady Aerodynamic Analysis of Horizontal Axis Windmills." Proceedings of 12th IECE Conference.

8. Preuss, R.D., "Unsteady Potential Aerodynamics of Rotors with Application to Horizontal Axis Windmills." AIAA Journal, Vol. 18, No. 4, April 1980.

9. Third Wind Energy Workshop, Vol. 1, September 1977, CONF770921. (Sponsored by United States Dept. of Energy and Division of Solar Energy Technology).

10. AIAA, Collection of Technical Papers. AIAA/SERI, Wind Energy Conference, April 9-11, Boulder, Colorado.

11. Gaonkar, Gopal, Hohemsor, Kuh, H., "Flapping Response of Lifting Rotor Blades to Atmospheric Turbulence." Journal of Aircraft, Vol. 6, No. 6, November-December 1969, pp. 496-503.

12. Sullivan, J.P., "The Effect of Blade Sweep on Performance." AIAA Paper No. 77-716.

13. Chang, Li, Ko, "The Theoretical Performance of High Efficiency Propellers." Ph.d Thesis Purdue University, December 1980.

14. Davenport, A.G., "The Spectrum of Horizontal Gustiness Near the Ground in High Winds." Quarterly J. Roy Met. Soc.. Vol. 87, 1961, pp. 194-211.

15. Frost, Walter, Long, B.H., Turner, R.E., "Engineering Handbook on the Atmospheric Environmental Guidelines for use in Wind Turbine Generator Development." NASA TP-1359, December 1978.

16. Frost, Walter, Turner, RObert, E., "Summary of Atmospheric Wind Design Criteria for Wind Energy Conversion System Development." NASA TP-1389, 1979.

17. Fichtl, George H., Kaufman, John W., Vaugham, William W., "The Characteristics of Atmospheric Turbulence as Related to Wind Loads on Tall Structures." NASA Marshall Space-flight Center, Huntsville, Alabama.

18. Scroggins, J.R., "Wind Effects on Launch Vehicles." The Wind Field, AGARDOGRAPH 115.

19. Taylor, J., "Manual on Aircraft Loads." Chapter 2 Atmospheric Environment. AGARDOGRAPH 83.

20. Shinozuka M., Takeo Masaru, Vicaitis Rimas, "Parametric Study of Wind Loading on Structures." Journal of Structural Div. Proceedings of ASCE, March 1973.

21. Shinozuka, M., "Simulation of Multivariate Multi-Dimensional Random Process." Journal of Acoustical Soc. of America, Vol. 49, No. 1, part 2, 1971.

22. Shinozuka, M., "Digital Simulation of Random Processes and its Applications." Journal of Sound and Vibrations (1972) 25(1), pp. 111-128.

23. Shinozuka, M., "Digital Simulation of a Random Process with the aid of FFT Technique." Stochastic Problems in Mechanics. Univ. of Waterloo Press, 1976, pp. 227-286.

24. Lumley, John L., Panofsky, Hans, A., "The Structure of Atmospheric Turbulence." Monographs and Texts in Physics and Astronomy, Vol. Xii, 1964, Book.

25. Simiu, Emil, Scanlon, Robert H., "Wind Effects on Structures, An Introduction to Wind Engineering." Chapter 2, The Atmospheric Boundary Layer.

26. Sachs, Peter, "Wind FOrces in Engineering." 2nd Edition, Pergamon Press, 1978.

27. Etkin, Bernard, "Dynamics of Atmospheric Flight." Chapter 13, Flight in a Turbulent Atmosphere, Wiley, New York, 1972.

28. Krause, P.C., Man, D.T., "Transient Behaviour of a Class of Wind Turbine Generators During Electrical Disturbances." School of Electrical Engineering, Purdue University.

29. Wasuczuk, D., Man, D.T., Sullivan, J.P., "Dynamic Behaviour of a Class of Wind Turbines During Random Wind Fluctuations." School of Electrical Engineering, Purdue University.

30. Sundar, R.M., "Performance of Large Wind Turbines in Turbulent Atmosphere." M.S. Thesis. (To be published May 1981), School of Aeronautics & Astronautics, Purdue University.

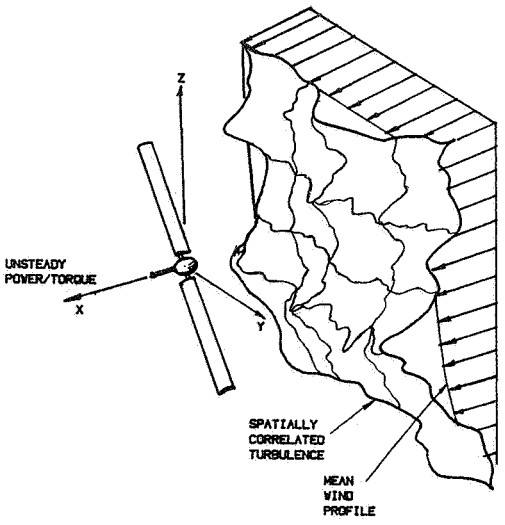

FIG. 1 THE PHYSICAL PROBLEM

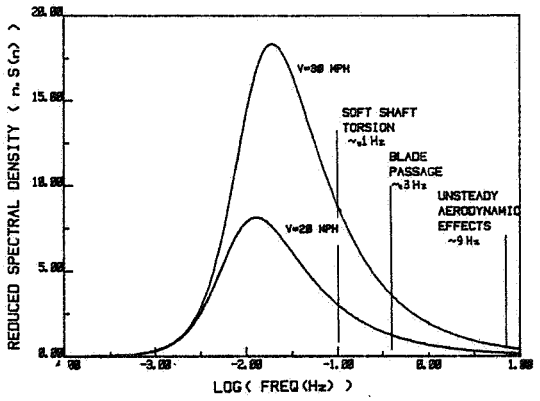

FIG. 2 DAVENPORT MODEL FOR SPECTRUM OF HORIZONTAL COMPONENT OF WIND TURBULENCE

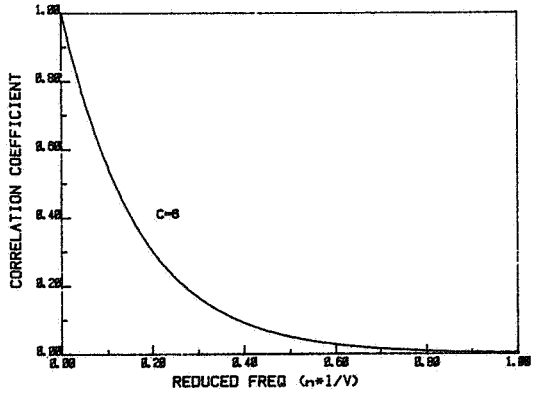

FIG. 3 CORRELATION FUNCTION FOR SPATIAL CORRELATION OF WIND TURBULENCE

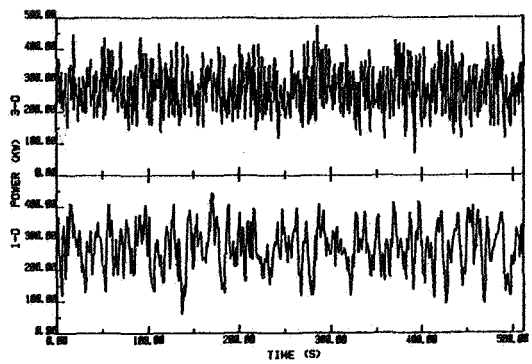

FIG. 8a UNSTEADY POWER OUTPUT WITH 1-D & 3-D TURBULENCE (D=200')

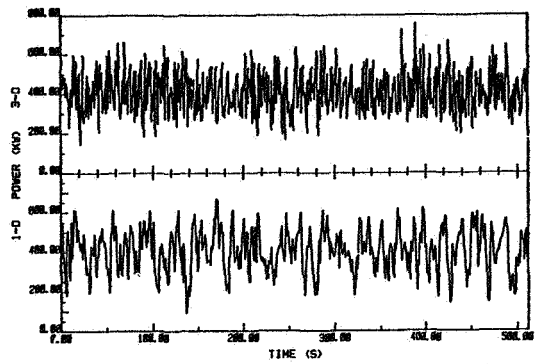

FIG. 9a UNSTEADY POWER OUTPUT WITH 1-D & 3-D TURBULENCE (D=300')

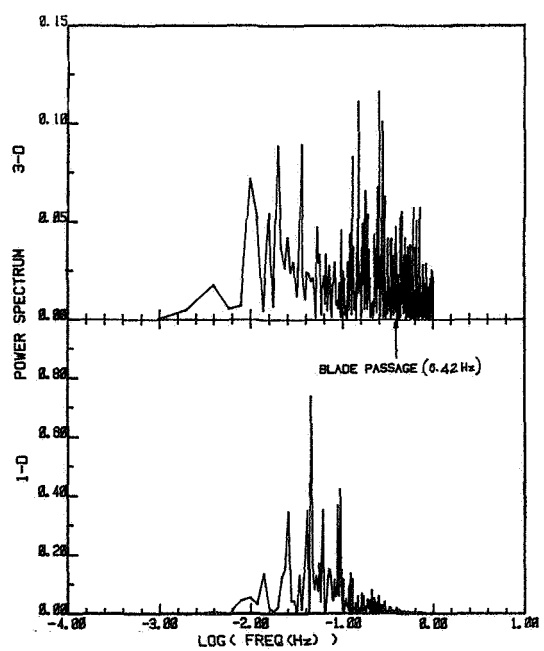

FIG. 8b SPECTRUM OF POWER OUTPUT WITH 1-D & 3-D TURBULENCE (D=200')

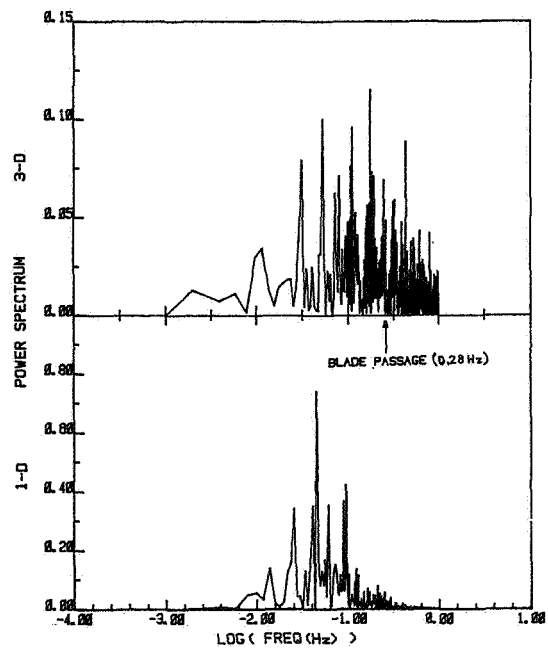

FIG. 9b SPECTRUM OF POWER OUTPUT WITH 1-D & 3-D TURBULENCE (D=300')

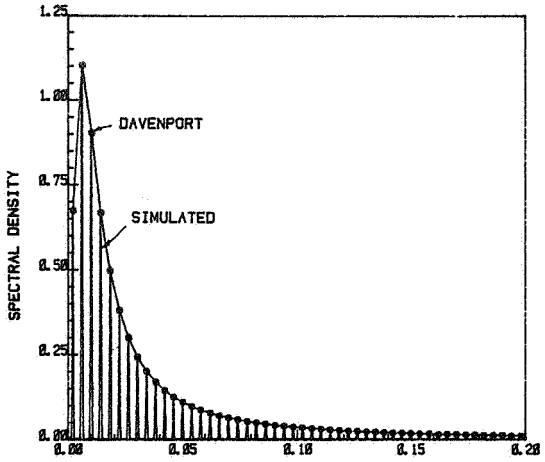

FIG. 4 COMPARISON OF DAVENPORT SPECTRUM WITH THAT OF 1-D TURB SIGNAL SIMULATED WITH 50 FREQUENCIES

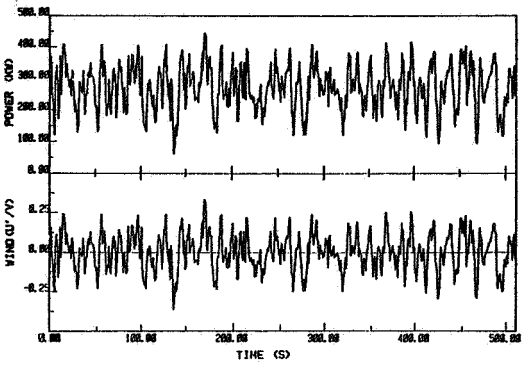

FIG. 5 UNSTEADY POWER OUTPUT WITH 1-D TURBULENCE

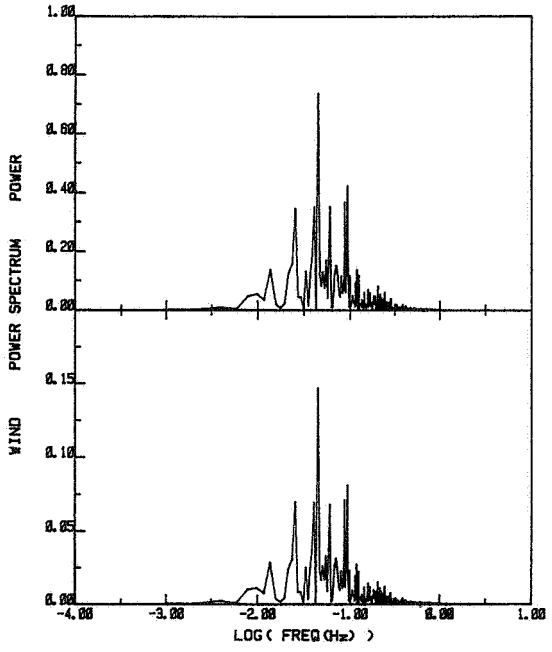

FIG. 6 SPECTRUM OF POWER AND 1-D TURBULENT WIND

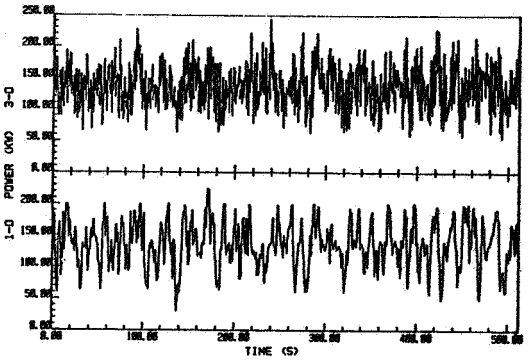

FIG. 7a UNSTEADY POWER OUTPUT WITH 1-D & 3-D TURBULENCE (D=100')

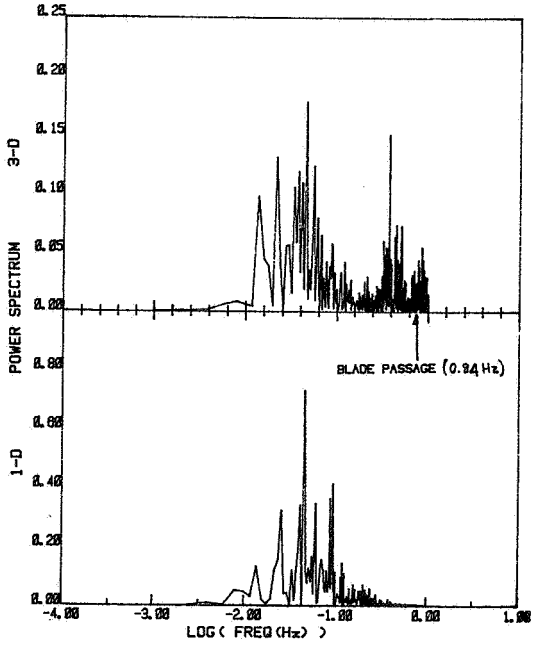

FIG. 7b SPECTRUM OF POWER OUTPUT WITH 1-D & 3-D TURBULENCE (D=100')

QUESTIONS AND ANSWERS

J.P. Sullivan

From: W.N. Sullivan

Q: Please comment on the effect of very soft drive trains on the output power spectra.

A: *A simulation of this problem is planned for the near future at Purdue.*

From: Walter Frost

Q: How is the coherence between frequencies of the wind simulated?

A: *With the exponential correlation function exp* $[-\frac{cn\ell}{V}]$ $c = 6$.

From: F.W. Perkins

Q: Why does the turbulence seem to drift in a preferred direction, low right to high left?

A: *I don't know, but it may be just a figment of color image processing.*

WIND RESPONSE CHARACTERISTICS OF HORIZONTAL AXIS WIND TURBINES

R.W. Thresher, W.E. Holley and N. Jafarey

Mechanical Engineering Department
Oregon State University
Corvallis, OR 97331

INTRODUCTION

The dynamic response of wind turbines to turbulent wind fluctuations has generally been modeled using only changes in the streamwise wind velocity as the disturbance which causes the varying aerodynamic forces and moments. Often these wind fluctuations are thought of, and modeled, as discrete wind gusts of specified shape and duration, which occur at some average rate. In addition, these wind fluctuations usually have been assumed to act uniformly over the entire rotor disk. In terms of the designer's needs, these models are used to generate design loads and expected control system actions.

It was the objective of the work reported here, and in the companion paper [1], to take a broader look at wind turbine dynamic response to turbulence, and attempt to ascertain the features of turbulence that wind turbines are most sensitive to. A statistical description of the wind input including all three wind components and allowing linear wind gradients across the rotor disk, was used together with quasi-static aerodynamic theory and an elementary structural model involving only a few degrees of freedom. The idea was to keep the turbine model simple and show the benefits of this type of statistical wind representation before attempting to use a more complex turbine model. As far as possible, the analysis was kept in the simplest form, while still preserving key physical responses.

From the onset of this work, it was felt that the results should be validated by comparison with test measurements. Due to the three-bladed rigid rotor used on the turbine and the limited degrees of freedom, comparison with data from one of the small systems under test at Rocky Flats would provide the most realistic comparison. At this time, the experimental comparison is incomplete.

The Turbine Model

The wind turbine model is shown schematically in Figure 1. Both the rotor and the nacelle are assumed to be rigid bodies which move in unison, except for the spinning rotor. Due to tower flexibility, the nacelle and rotor are free to translate in a plane parallel to the ground and rotate about the top of the tower in pitch and yaw. The yaw angle of the rotor axis is defined by the angle, ϕ, and the pitch angle by χ. The lateral translation, U, is in the x direction, while the V translation is in the y direction along the rotor axis. The rotor spin velocity is given by $\Omega + \dot{\Psi}$, where Ω is the mean rotation rate and Ψ is some small fluctuation. For the case of a turbine with a three-bladed rigid rotor, the basic principles of Newtonian mechanics and linear, quasi-steady aerodynamics give motion equations of the form

$$M_{ij}\ddot{X}_j + C_{ij}\dot{X}_j + K_{ij}X_j = F_{ij}V_j \qquad (1)$$

where M_{ij}, C_{ij}, K_{ij} and F_{ij} are the turbine system inertia, damping, stiffness and wind input coefficients. The five displacement coordinates already described are X_j, while the wind inputs are V_j.

The Tower

The wind turbine tower was modeled as a single finite element within which the tower displacements were expressed in terms of interpolating polynomials and the displacements at the top of the tower. Then the tower deformation, v(z,t), about one bending axis was written in the form

$$v(z,t) = P_V(z)V(t) + P_\chi(z)\chi(t) \qquad (2)$$

where P_V and P_χ are the interpolating functions which approximate the displacements within the tower. These are conveniently represented as cubic polynomials satisfying the necessary boundary conditions of a cantilever tower. Using this expression for the tower bending displacement, the stiffness and mass coefficients may be obtained by one of the numerous energy methods. In terms of the interpolating functions P_V and P_χ, the generalized stiffness and mass coefficients for the tower may be expressed as

$$k_{ij} = \int_0^L EI(z)P_i''(z)P_j''(z)dz \qquad (3)$$

$$m_{ij} = \int_0^L m(z)P_i(z)P_j(z)dz \qquad (4)$$

where EI(z) and m(z) are the stiffness and mass per unit length as a function of height. For additional detail concerning this technique, the interested reader should see Clough and Penzien [2]. Although the tower properties are the same in both bending directions, only one degree of freedom was desired for the x direction and therefore rotation of the nacelle about the rotor spin axis was neglected. The method of static condensation was used to eliminate the unwanted degree of freedom and obtain the desired x direction stiffness and inertia coefficients as

$$k_{UU} = k_{VV} = k^2_{V\chi}/k_{\chi\chi} \qquad (5)$$

$$m_{UU} = m_{VV} - 2(k_{V\chi}/k_{\chi\chi})m_{V\chi} + (k_{V\chi}/k_{\chi\chi})^2 m_{\chi\chi} \qquad (6)$$

In addition, the nacelle and rotor inertias add directly to the tower inertia coefficients, m_{ij}, to give the turbine system inertias. A detailed tabulation of the various terms in the inertia matrix is provided in the Appendix. There is also a gyroscopic coupling between the turbine

pitch and yaw motions. This coupling coefficient appears in the damping matrix and is given by

$$C_{\phi\chi} = I_r\Omega = -C_{\chi\phi} \tag{7}$$

where I_r is the total effective inertia of all the spinning mass connected to the turbine rotor. Using this simple model the structural stiffness and inertia coefficients for a particular wind turbine are numerically calculated using a TI-59 calculator code [3].

Aerodynamic Forces

The geometry of the three-bladed rigid rotor is illustrated in Figure 2. The blades are coned at an angle β_o, and are assumed to be twisted and tapered. The angle θ defines the pitch setting as the angle from the plane of rotation to the zero-lift-line of the airfoil at the blade tip.

For this analysis, quasi-static aerodynamics will be used to compute the forces acting on the blades due to the turbulent wind and structural motion. The wind input including turbulence is assumed to be made up of a steady mean wind, V_w, plus fluctuating components, $V_i(t)$, which at any instant are constant over the rotor disk and turbulence gradients $V_{i,j}(t)$, which vary linearly across the disk. Both $V_i(t)$ and $V_{i,j}(t)$ may be thought as disk averaged time dependent quantities. This allows the wind velocity to be written in a linear expansion as

$$\{V_\infty\} = \begin{Bmatrix} 0 \\ V_w \\ 0 \end{Bmatrix} + \begin{Bmatrix} V_x \\ V_y \\ V_z \end{Bmatrix} + \begin{bmatrix} V_{x,x} & V_{x,y} & V_{x,z} \\ V_{y,x} & V_{y,y} & V_{y,z} \\ V_{z,x} & V_{z,y} & V_{z,z} \end{bmatrix} \begin{Bmatrix} r\sin\Omega t \\ 0 \\ r\cos\Omega t \end{Bmatrix} \tag{8}$$

where r is the radial position in the rotor disk, and Ωt is the azimuthal location. Motivation for this particular form for the turbulence and discussion of its accuracy is presented in the companion paper, reference [1]. In this equation the mean wind direction coincides with the y axis of Figure 2. In addition, the spatial change in the y direction turbulence component due to the coning has been dropped in the above expression, which eliminates the effect of the turbulence gradients $V_{i,y}$.

Using the above wind representation and fundamental kinematic relationships provides the relative velocity as observed from the turbine blade. The relative velocity is made up of contributions from the wind, the moving structure and the induced velocity caused by aerodynamic action. In equation form this is

$$\vec{V}_{rel} = \vec{V}_\infty - \vec{V} - \vec{v}_i \tag{9}$$

In terms of the displacement coordinates, the relative velocity components parallel and perpendicular to the rotor disk rotational plane are given by

$$\begin{aligned} V_\mu/R\Omega = r\Omega/R\Omega + \{&r\dot{\Psi} + \cos\Omega t[-\phi(V_w-v_i) - \delta V_x \\ &+ \dot{U} - a\dot{\phi}] \\ &+ \sin\Omega t[-\chi(V_w-v_i) + \delta V_z \\ &- a\dot{\chi}]\}/R\Omega \end{aligned}$$

$$\begin{aligned} V_\nu/R\Omega = (V_w-v_i)/R\Omega + \{&\delta V_y + \cos\Omega t[-\beta_o\delta V_z + r\dot{\chi}] \\ &+ \sin\Omega t[\beta_o(\dot{U}-\delta V_x) \\ &- r\dot{\phi}]\}/R\Omega \end{aligned} \tag{10}$$

where the fluctuating part of the wind turbulence has been written as δV_i to shorten the expressions. These expressions have also been linearized assuming small displacements, and wind fluctuations; however, in some places the product of the static coning angle and the wind fluctuation were retained because of interest in their effect.

Referring to Figure 3, the aerodynamic forces parallel and perpendicular to the rotor plane may be written as

$$\begin{aligned} dA_\mu &= \tfrac{1}{2}\rho a' c\, d\xi\{-\eta V_\mu^2 - \theta V_\nu V_\mu + (1-\eta/2)V_\nu^2\} \\ dA_\nu &= \tfrac{1}{2}\rho a' c\, d\xi\{-\theta V_\mu^2 + (1+\eta)V_\nu V_\mu - \theta V_\nu^2/2\} \end{aligned} \tag{11}$$

where the lift and drag for a blade element have been calculated using the static formulas with the instantaneous velocities. In the above expressions a' is the slope of the sectional lift curve $dC_L/d\alpha$, c is the local airfoil chord, η is the ratio C_{D_0}/a', and ρ is the air density.

Using the wind input of Eq. (8), together with the velocity expressions of Eq. (10) and substituting into the aerodynamic force relationships gives

$$\begin{aligned} dA_\mu = \tfrac{1}{2}\rho a' c_t (R\Omega)^2 R\,dx\{&A' - B'[f_o + f_c\cos\Omega t + f_s\sin\Omega t \\ &+ f_{c2}\cos 2\Omega t + f_{s2}\sin 2\Omega t] \\ &+ C'[g_o + g_c\cos\Omega t + g_s\sin\Omega t \\ &+ g_{c2}\cos 2\Omega t + g_{s2}\sin 2\Omega t]\} \\ dA_\nu = \tfrac{1}{2}\rho a' c_t (R\Omega)^2 R\,dx\{&D' + E'[f_o + f_c\cos\Omega t + f_s\sin\Omega t \\ &+ f_{c2}\cos 2\Omega t + f_{s2}\sin 2\Omega t] \\ &+ F'[g_o + g_c\cos\Omega t + g_s\sin\Omega t \\ &+ g_{c2}\cos 2\Omega t + g_{s2}\sin 2\Omega t]\} \end{aligned} \tag{12}$$

where the primed quantities are the aerodynamic constants

$$\begin{aligned} A'(x) &= [(1-\eta/2)\lambda^2 - x(\eta x+\theta\lambda)]c/c_t \\ B'(x) &= [2\eta x+\theta\lambda]c/c_t \qquad C'(x) = [(2-\eta)\lambda-\theta x]c/c_t \\ D'(x) &= [(1+\eta)\lambda x - \theta(x^2+\lambda^2/2)]c/c_t \\ E'(x) &= [(1+\eta)\lambda - 2\theta x]c/c_t \\ F'(x) &= [(1+\eta)x - \lambda\theta]c/c_t \end{aligned} \tag{13}$$

with $x = r/R = (h+\xi)/R$, $\lambda = (V_w-v_i)/R\Omega$, and c_t is the chord at the rotor tip. Note that both the pitch setting, θ, and the blade chord, c, may be functions of x. In the above force equations the

subscripted f and g variables are combinations of the wind inputs and response variables and are defined as follows:

$$
\begin{aligned}
f_o &= r(\dot{\Psi} + \gamma_{zx})/R\Omega \\
f_c &= -\phi\lambda+(-V_x + \dot{U} - a\dot{\phi})/R\Omega \\
f_s &= -\chi\lambda+(V_z - a\dot{\chi})/R\Omega \\
f_{c2} &= -r\,\bar{\gamma}_{zx}/R\Omega \\
f_{s2} &= r\varepsilon_{zx}/R\Omega \\
\gamma_{zx} &= \tfrac{1}{2}(V_{z,x} - V_{x,z}) \\
\varepsilon_{zx} &= \tfrac{1}{2}(V_{z,z} - V_{x,x}) \\
g_o &= (V_y - \dot{V} - r\beta_o\bar{\varepsilon}_{zx})/R\Omega \\
g_c &= (r\dot{\chi} + rV_{y,z} - \beta_o V_z)/R\Omega \\
g_s &= (\beta_o(\dot{U} - V_x)-r\dot{\phi} + rV_{y,x})/R\Omega \\
g_{c2} &= -\beta_o f_{s2} \\
g_{s2} &= \beta_o f_{c2} \\
\bar{\gamma}_{zx} &= \tfrac{1}{2}(V_{z,x} + V_{x,z}) \\
\bar{\varepsilon}_{zx} &= \tfrac{1}{2}(V_{z,z} + V_{x,x})
\end{aligned}
\qquad (14)
$$

To obtain the aerodynamic coefficients for the total forces acting on the rotor hub, the appropriate components of the blade element forces, Eq. (12), are summed over the three blades and integrated with respect to radius for a specified induced velocity distribution. This gives the net thrust, torque, horizontal and vertical forces, and the yaw and pitch moments, which are to be added to the structural terms resulting in the final equations of motion, Eq. (1). A detailed list of these equations is provided in the Appendix.

The Induced Velocity

The aerodynamics of wind turbines involve highly complex flow phenomena, which require rather sophisticated theories in order to obtain accurate predictions. However, some fairly simple theories making relatively crude assumptions can often give reasonable estimates and generally can give excellent insight into the physical phenomena of interest. In this case two different wake models were used in an effort to gain insight into the significance of changes in the induced velocity field on wind turbine response to turbulence.

For the first wake model, the induced velocity was computed using blade element theory following the approach of Wilson [4], and performing a momentum balance neglecting wake rotation. This provided the induced velocity as a function of radius, under the assumption that the rotor axis was perfectly aligned with the wind direction. After the induced velocity distribution was computed for a given mean operating condition, it was assumed to be constant and independent of turbulent wind fluctuations. This model was named the "frozen wake model."

The second wake model was called the "equilibrium wake." For this model, the axial fluctuations in wind velocity are assumed to occur so slowly that the induced velocity is the steady state value for the instantaneous wind speed. In this situation, the axial flow will be not only time varying but nonuniform, because of the inclusion of the fluctuating wind gradient terms in the turbulence model of Eq. (8). These gradients could be thought of as slowly changing wind shears of arbitrary orientation, since their effect on the wind turbine would be similar. To obtain an approximation for the induced velocities of this "equilibrium wake," the "semi-rigid" wake model discussed by Miller [5] was used. Miller shows that the effect of including the induced velocity due to the nonuniform flow is to reduce the lift by a factor referrred to as the "lift deficiency" function.

For this analysis, assuming small velocity changes, the lift deficiency function was approximately

$$
\mathcal{L}_{d(x)} = \frac{1}{1+\tau_t F'(x)/x(2\lambda-\lambda_w)} \qquad (15)
$$

where $\lambda_w = V_w/R\Omega$ and $\tau_t = 3a'c_t/8\pi R$. In addition, the azimuthal change in the induced velocity distribution led to a change in the in-plane aerodynamic coefficients B'(x), where the change was

$$
\Delta B'(x) = \tau_t[B'(x)F'(x)+C'(x)E'(x)]/\{x(2\lambda-\lambda_w)\} \qquad (16)
$$

Because this change is small, it was tempting to neglect it, but all of the in-plane forces are small so it was retained. Finally, the wind fluctuations in the axial direction V_y, $V_{y,z}$ and $V_{y,x}$ are associated with a change in momentum in the streamwise direction which, for the assumptions of this wake model, change the equilibrium thrust. This added lift factor is approximately

$$
\mathcal{L}_a(x) = 1 + \lambda/(2\lambda-\lambda_w) \qquad (17)
$$

To incorporate these effects, the aerodynamic coefficients B'(x), C'(x), E'(x) and F'(x) of Eq. (13) were modified in the following manner to obtain the "equilibrium wake" coefficients:

$$
\begin{aligned}
B'_e(x) &= \mathcal{L}_d(x)\{B'(x)+\Delta B'(x)\} \\
C'_e(x) &= \mathcal{L}_d(x)C'(x) \\
E'_e(x) &= \mathcal{L}_d(x)E'(x) \\
F'_e(x) &= \mathcal{L}_d(x)E'(x) \\
C'_{ey}(x) &= \mathcal{L}_d(x)\mathcal{L}_a(x)C'(x) \\
F'_{ey}(x) &= \mathcal{L}_d(x)\mathcal{L}_a(x)C'(x)
\end{aligned}
\qquad (18)
$$

where the two coefficients C'_{ey} and F'_{ey} are specifically associated with the wind fluctuations V_y, $V_{y,z}$ and $V_{y,x}$. The aerodynamic coefficients A'(x) and D'(x) are related to the mean thrust and torque and are thus unaffected by wind fluctuations. Computationally, the influence of the wake model can be observed by changing the primed aerodynamic coefficients in the blade element force relationships Eq. (12).

Although both of these wake models were useful in developing an understanding of the influence of the induced velocity distribution on machine response to turbulence, it is unclear whether either model accurately approximates the real distributions and future work is needed to evaluate the effects of unsteady wake aerodynamics.

State Space Equations

The equations of motion Eq. (1) can be written in matrix form

$$[M]\{\ddot{X}\}+[C]\{\dot{X}\}+[K]\{X\} = \{Q_1\}+[F]\{u\} \qquad (19)$$

where

$\{X\}^T = (U,V,\phi,\chi,\Psi)$ = displacement coordinate

$\{Q_1\}^T = (0,T,0,Q,0)$ = steady state

$\{u\}^T = (V_x,V_y,V_z,V_{y,x},V_{y,z},\gamma_{xz},\varepsilon_r,\bar{\gamma}_r,\bar{\varepsilon}_{xz})$ = wind inputs

$\varepsilon_r = \varepsilon_{zx} \cos 3\Omega t + \bar{\gamma}_{zx} \sin 3\Omega t$

$\bar{\gamma}_r = -\varepsilon_{zx} \sin 3\Omega t + \bar{\gamma}_{zx} \cos 3\Omega t$

Furthermore, it is possible to model each of the nine turbulence inputs using a set of stochastic differential equations of the form

$$\{\dot{u}\} = [A_w]\{u\} + [B_w]\{w\} \qquad (20)$$

where the components of {w} are white noise of equal power spectral density, $[B_w]$ is the white noise input distribution matrix which is diagonal. The $[A_w]$ matrix is diagonal except for two elements

$$[A_w] = \begin{bmatrix} a_{11} & & & & \\ & \ddots & & & \\ & & a_{77} & 3\Omega & \\ & & -3\Omega & a_{88} & \\ & & & & a_{99} \end{bmatrix}$$

which arise as a result of the $\sin 3\Omega t$ and $\cos 3\Omega t$ in the ε_r and $\bar{\gamma}_r$ wind inputs. A more detailed presentation of the wind input model is presented in the companion paper [1].

Discarding the steady terms, it is convenient to transform the equations of motion given in Eq. (19) to the state space form, so that they are written as a set of first order equations similar to the turbulence inputs of Eq. (20). To further facilitate the computation of results, the state space form of Eq. (19) can be augmented with the turbulence inputs, Eq. (20), to form a single system of equations with white noise as the driving input. The five turbine displacements and their derivatives together with the nine turbulence inputs will form the state vector for this augmented system. The governing equations can then be written

$$\{\dot{x}\} = [A]\{x\} + [B]\{w\}$$

$$\{y\} = [c]\{x\} \qquad (21)$$

where

$$\{x\} = \begin{Bmatrix} \{X\} \\ \{\dot{X}\} \\ \{u\} \end{Bmatrix} \qquad [A] = \begin{bmatrix} [0] & [I] & [0] \\ -[M]^{-1}[K] & -[M]^{-1}[K] & [M]^{-1}[F] \\ [0] & [0] & [A_w] \end{bmatrix}$$

$$[B] = \begin{bmatrix} [0] \\ [B_w] \end{bmatrix} \qquad \{y\} = \begin{Bmatrix} F_x \\ F_y \\ M_z \\ M_x \\ \text{Power} \\ \{x\} \end{Bmatrix} = \text{outputs}$$

$$[c] = \begin{bmatrix} [K] & [0] \\ (00\ldots\Omega c_g\ldots 0) & \\ & [I] \end{bmatrix} = \text{response matrix}$$

With this formulation it is a relatively straightforward numerical procedure, to determine the complex eigenvalues of the A matrix and then to compute the modal matrix, which is made up of the associated eigenvectors. The modal matrix can then be used to decouple the equations of motion, so that transfer functions between any of the nine white noise inputs and any output, y_i, may be easily computed. These transfer functions account for differences in the energy level for the turbulence inputs, {u}, so that a comparison of the transfer function magnitudes provides a direct estimate of relative importance. The final result uses the central equation from random vibration theory, which states that the spectral density for any of the outputs {y} will be given by

$$\{S_y(\omega)\} = [|H_{yw}(\omega)|^2]\ \{S_w(\omega)\}$$

for uncorrelated inputs, where $\{S_y(\omega)\}$ is the spectral density of the outputs {y}, $[|H_{yw}(\omega)|^2]$ is the matrix of the transfer functions magnitude squared and $\{S_w(\omega)\}$ is the spectral density of the white noise driving inputs, which are all equal.

Results

To determine the influence of the turbulence inputs modeled in this work two wind systems of vastly different size were examined. The smaller machine, called the Mod-M, was an 8 kW turbine, with a three bladed rotor located downwind of the tower, and designed for free-yaw operation. The specific characteristics are as follows:

Mod-M

Rotor Characteristics:

Rotor Radius	16.67 ft
Blade Chord (constant)	1.5 ft
Coning Angle	3.5°
Blade Twist	0.0°

System Frequencies:

1st Bending (fore-aft)	15.1 rad/s
2nd Bending (fore-aft)	53.1 rad/s
1st Side to Side	15.9 rad/s

Aerodynamic Properties:

Lift Curve Slope	5.7
Drag Coefficient, C_{D_0}	.02
Stall not Modeled	

Operating Conditions Used:

Wind Velocity (mean)	16.63 MPH
Rotor Speed (mean)	73.35 RPM
Pitch Setting (to ZLL)	3.0°
Turbulence Length Scale	300 ft
Rms Turbulent Intensity	2.03 ft/s
Approximate Output	6 kW

Selected analysis results for this situation are shown in the power spectral density plots of Figures 4 through 6. The figures clearly illustrate the difference in response for the two wake models. For forces and moments which are highly dependent on the streamwise velocity such as thrust, the equilibrium wake assumptions give a larger response, as shown in Figure 4. This figure also indicates a significant response at the two system fore-aft bending frequencies. Figure 5 shows the yaw response, while Figure 6 gives the pitching moment response. These two figures indicate the degree of coupling between pitch and yaw for this free-yaw turbine. Notice that as the yaw response increases, there is a corresponding increase in the pitching moment. Figure 6 also shows a small response peak at 3Ω, which is the result of the sin3Ωt and cos3Ωt in the ε_r and $\bar{\gamma}_r$ inputs.

The second wind system to be analyzed in this study was a large turbine called the Mod-G. The Mod-G was 2.5 MW turbine with a three bladed rotor located upwind of the tower, and was designed for fixed-yaw operation. The specific characteristics of this system are:

Mod-G

Rotor Characteristics:

Rotor Radius	150 ft
Blade Chord (linear taper)	7.74 ft at hub to 3.15 ft at tip
Coning Angle	4°
Blade Twist (linear)	8°

System Frequencies:

1st Bending (fore-aft)	2.75 rad/s
2nd Bending (fore-aft)	12.8 rad/s
1st Side to Side	2.9 rad/s
2nd Side to Side	9.5 rad/s

Aerodynamic Properties:

Lift Curve Slope	5.73
Drag Coefficient, C_{D_0}	.008
Stall not Modeled	

Operating Conditions:

Wind Velocity	20 MPH
Rotor Speed	17.5 RPM
Pitch Setting at tip	-6.2°
Turbulence Length Scale	500 ft
Rms turbulent intensity	2.44 ft/s
Approximate Power Output	1.1 MW

Figures 7, 8 and 9 shows some typical results for the Mod-G. As was the case in the previous plots, the system frequencies are easily identified.

The primary objective of this work was to identify the features of turbulence which are most important in wind turbine design. In an effort to focus on these key features, the response at specific system frequencies was broken down into fractional contributions from each turbulence input. The most significant results of these calculations are tabulated in Tables 1 and 2.

From these results it would appear that the most important inputs are the three longitudinal turbulence terms, and in some instances, the two in-plane shear terms which have an effective frequency of 3Ω. An alternate means of presenting this same information is to plot power spectral density curves for the various outputs using only the turbulence input V_y, and then adding the two gradients $V_{y,x}$ and $V_{y,z}$. This has been done in Figures 10 through 15 for the outputs previously presented. As can be seen from these figures, a major contribution to the machine excitation is lost if the turbulence gradients are not included. However, neglecting the $\bar{\gamma}_r$ and ε_r appears to have only a local influence around the frequency 3Ω.

Conclusions and Recommendations

On the basis of the work done in this study, the longitudinal turbulence input, V_y, and the two gradients, $V_{y,x}$ and $V_{y,z}$ are of equal importance when computing the dynamic response of wind systems, and these three inputs together comprise the major excitation source for horizontal axis wind turbines. Because of the simplifying assumptions and approximations used in this analysis, it is imperative that the results and the technique be validated with experimental data, prior to use for design.

ACKNOWLEDGEMENTS

This research was supported by the Department of Energy through Battelle, Pacific Northwest Laboratory, under Contract DE-AT06-79ET23144. The authors would particularly like to thank Dr. J.R. Connell, the technical monitor, for his enthusiastic support, and the many valuable suggestions made by the PNL staff. The responsibility for the results and the opinions expressed rests with the authors and not the United States Government or Oregon State University.

REFERENCES

1. Holley, W.E., "Wind Turbulence Inputs for Horizontal Axis Wind Turbines," Second DOE/NASA Wind Turbine Dynamics Workshop, February 1981.

2. Clough, R.W. and Penzien, J., Dynamics of Structures, McGraw-Hill, 1975.

3. Jafarey, N., and Thresher, R., "Turbine System Natural Frequencies," Program Record for TI-59 Programmable Calculator, Program Records No. 101 and 102, Mech. Engrng. Dept., Oregon State University.

4. Wilson, R.E., and Lissaman, P.B.S., Applied Aerodynamics of Wind Power Machines, Oregon State University Report, NTIS PB-238-595, 1974.

5. Miller, R., Dugundji, J., Martinez-Sanchez, M., Gohard, J., Chung, S., and Humes, T, Aerodynamics of Horizontal Axis Wind Turbines, Volume II of Wind Energy Conversion, Report ASRL TR-184-8, Dept. of Aeronautics and Astronautics, MIT, Sept. 1978.

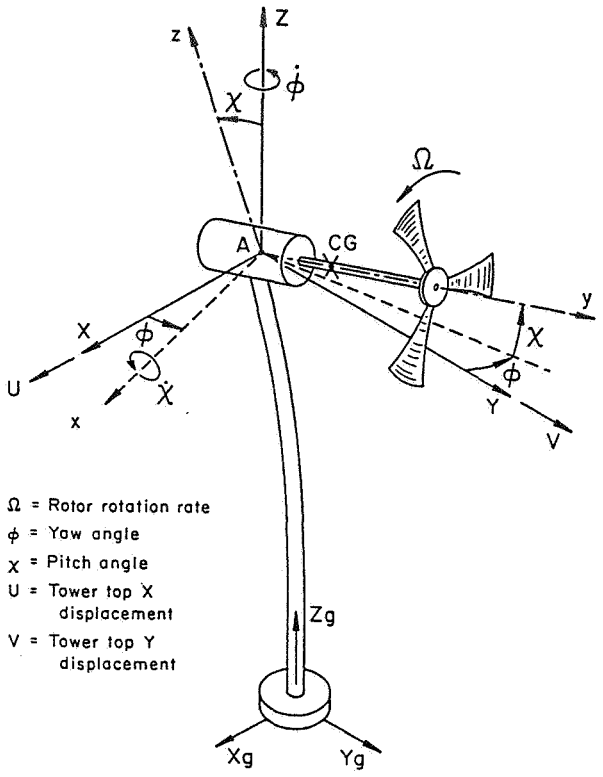

FIGURE 1. THE TURBINE MODEL.

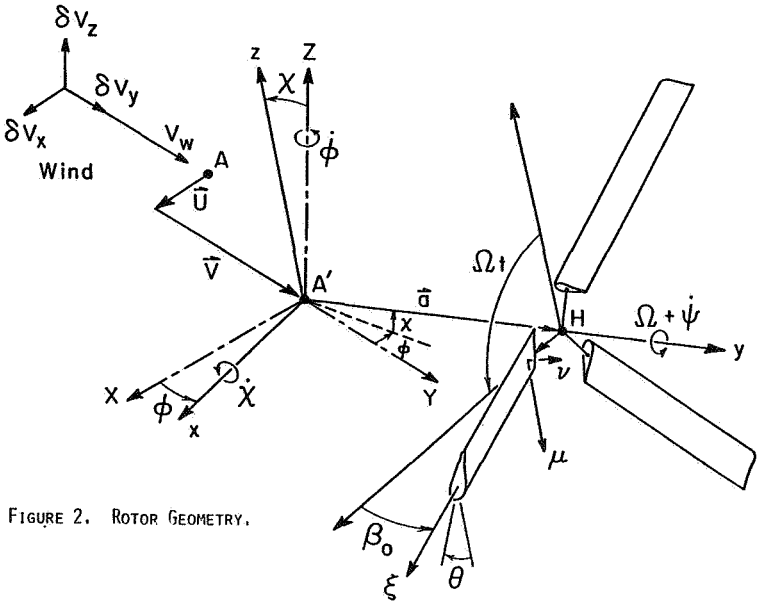

FIGURE 2. ROTOR GEOMETRY.

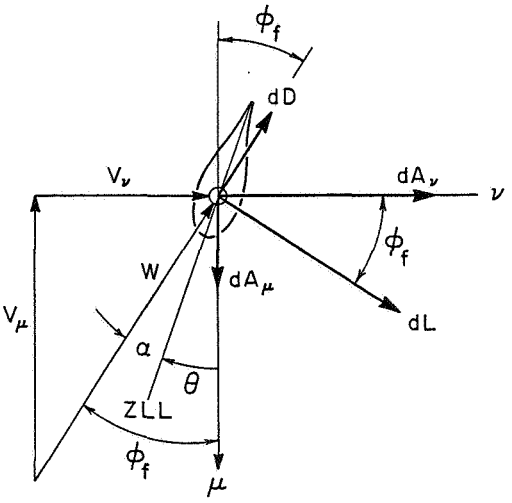

FIGURE 3. BLADE ELEMENT AERODYNAMIC FORCES.

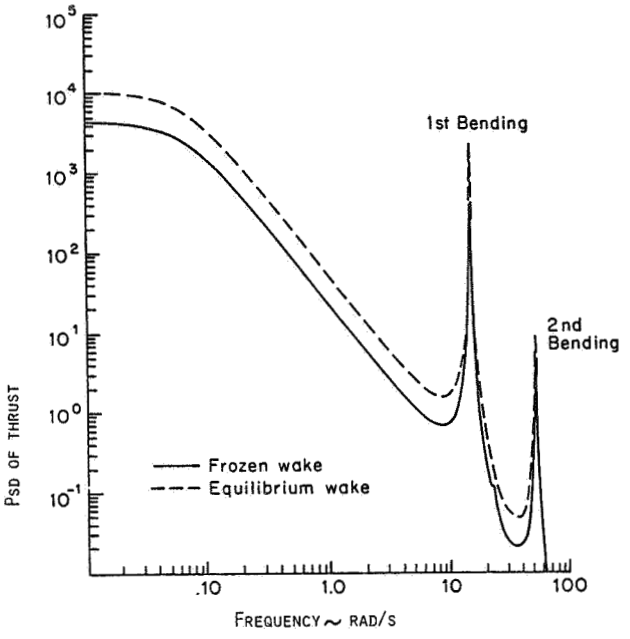

FIGURE 4. MOD-M POWER SPECTRAL DENSITY PLOT OF THRUST, F_Y.

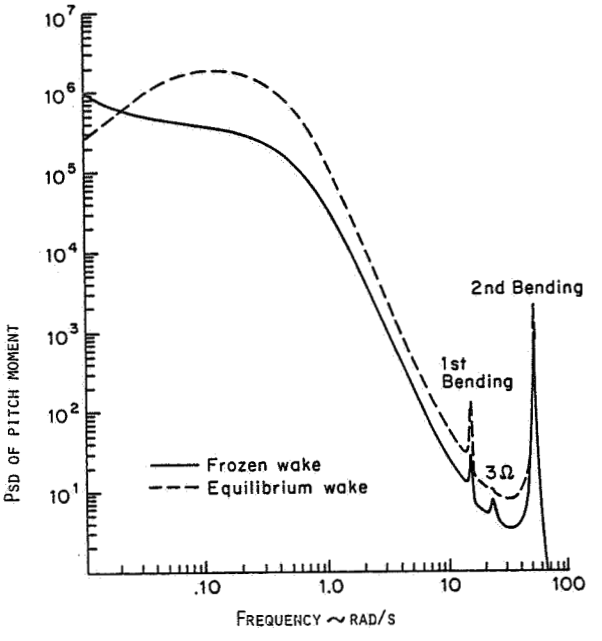

FIGURE 6. MOD-M POWER SPECTRAL DENSITY OF PITCH MOMENT, M_X.

ERRATUM: The power spectral densities shown in Figures 4-15 are incorrectly plotted. The ordinate, Psd, should be increased by exactly a factor of 10 to be correct.

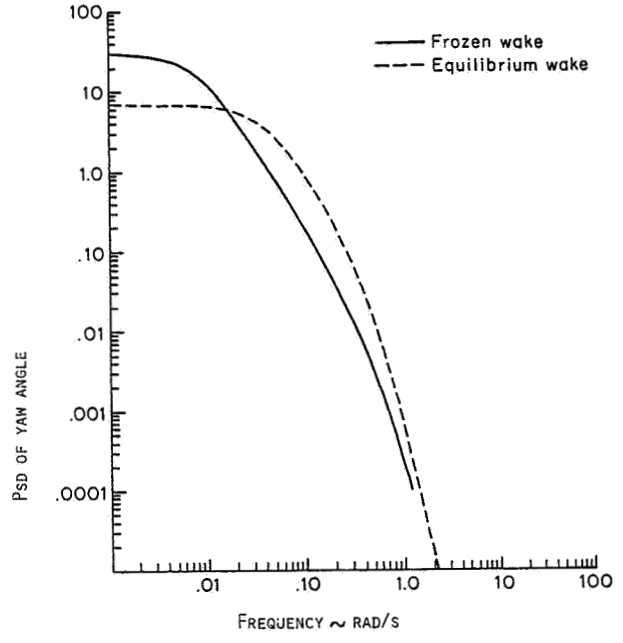

FIGURE 5. MOD-M POWER SPECTRAL DENSITY OF YAW ANGLE, Ø.

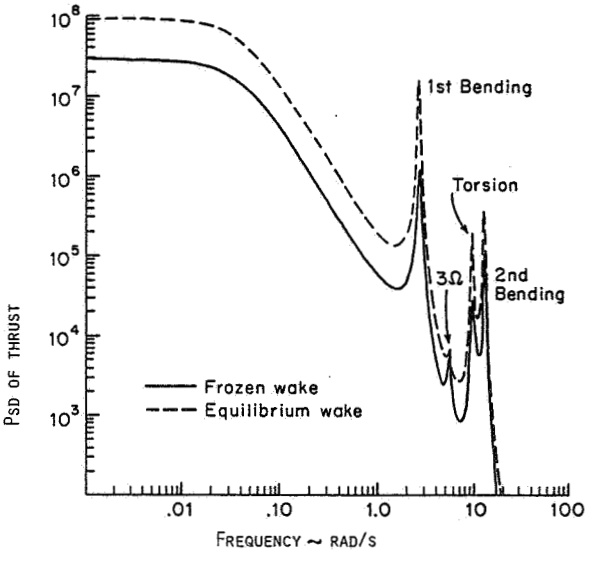

FIGURE 7. MOD-G POWER SPECTRAL DENSITY OF THRUST, F_Y.

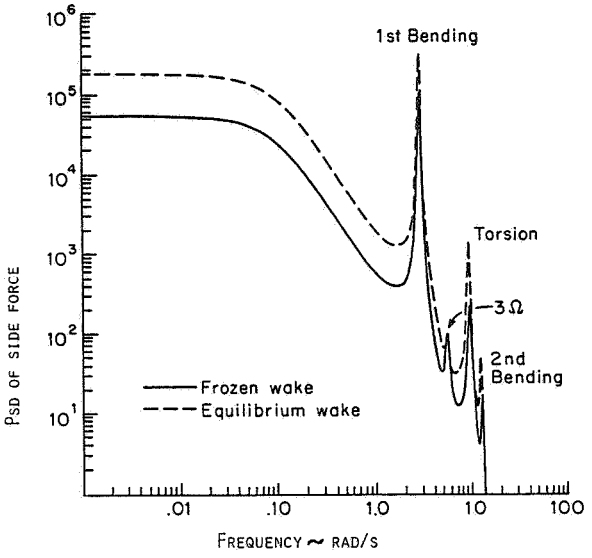

FIGURE 8. MOD-G POWER SPECTRAL DENSITY OF SIDE FORCE, F_X.

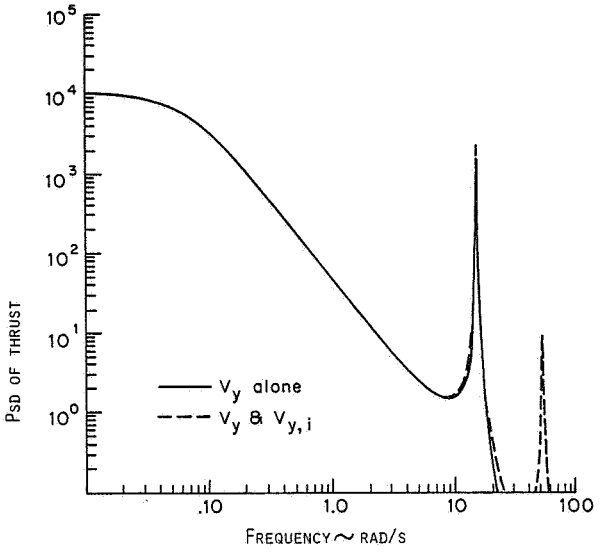

FIGURE 10. THE EFFECT OF THE GRADIENTS $V_{Y,X}$ & $V_{Y,Z}$ ON THRUST FOR MOD-M USING THE EQUILIBRIUM WAKE.

ERRATUM: The power spectral densities shown in Figures 4-15 are incorrectly plotted. The ordinate, Psd, should be increased by exactly a factor of 10 to be correct.

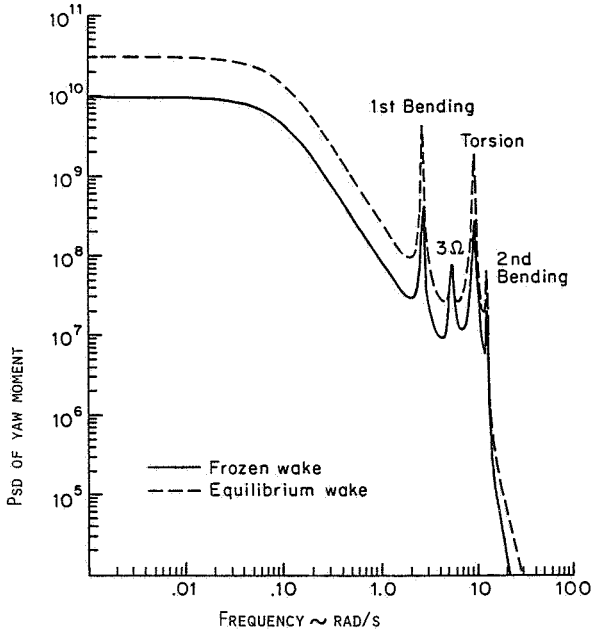

FIGURE 9. MOD-G POWER SPECTRAL DENSITY OF YAW MOMENT, M_Z.

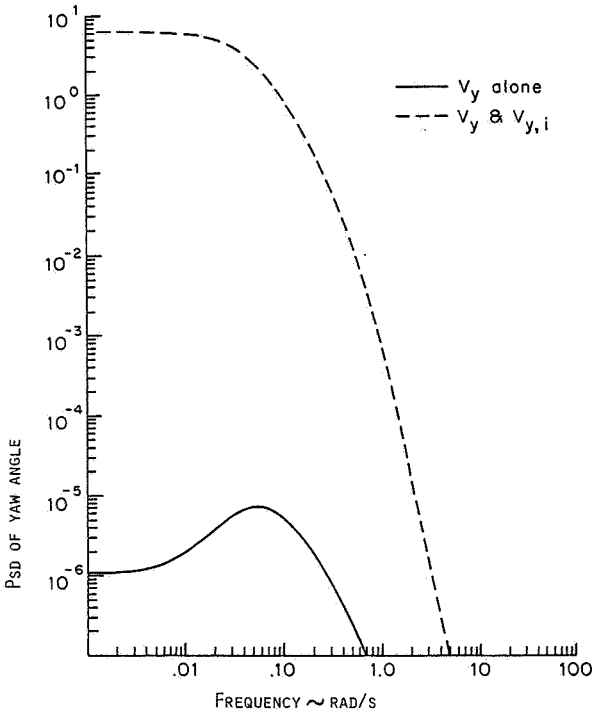

FIGURE 11. THE EFFECT OF THE GRADIENTS $V_{Y,X}$ & $V_{Y,Z}$ ON YAW ANGLE FOR MOD-M USING THE EQUILIBRIUM WAKE.

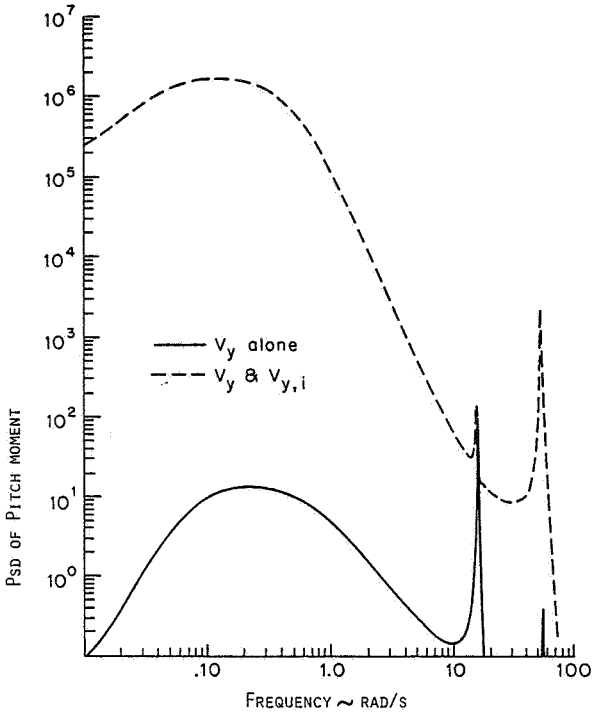

FIGURE 12. THE EFFECT OF THE GRADIENTS $V_{Y,X}$ & $V_{Y,Z}$ ON PITCH MOMENT FOR MOD-M USING THE EQUILIBRIUM WAKE.

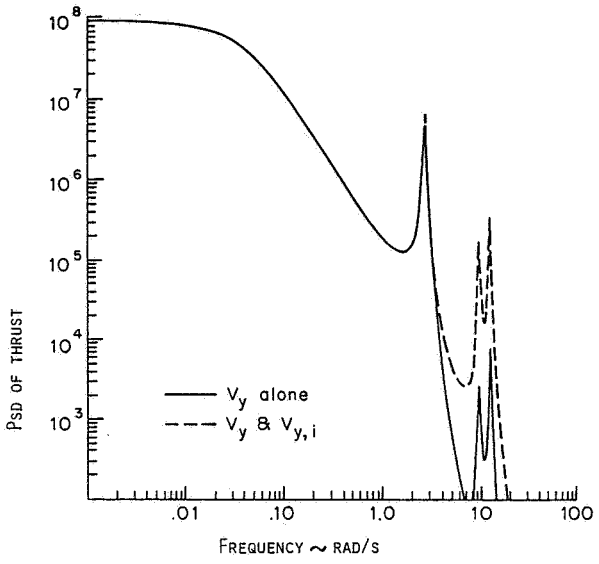

FIGURE 14. THE EFFECT OF THE TURBULENCE GRADIENTS $V_{Y,X}$ & $V_{Y,Z}$ ON THE THRUST FOR THE MOD-G USING THE EQUILIBRIUM WAKE.

ERRATUM: The power spectral densities shown in Figures 4-15 are incorrectly plotted. The ordinate, Psd, should be increased by exactly a factor of 10 to be correct.

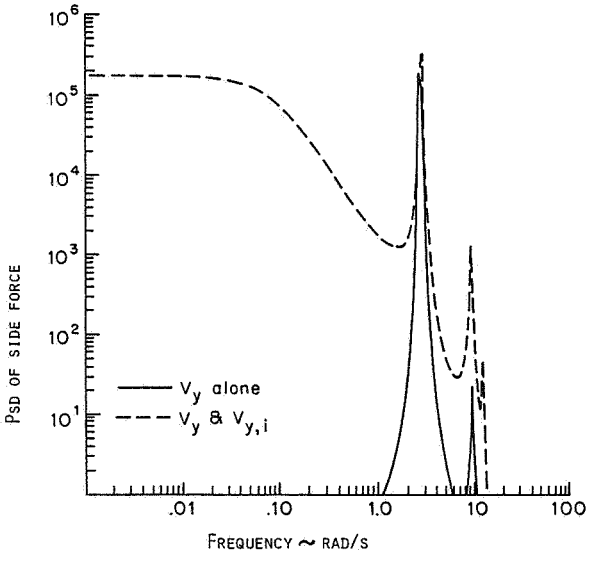

FIGURE 13. THE EFFECT OF THE GRADIENTS $V_{Y,X}$ & $V_{Y,Z}$ ON SIDE FORCE FOR THE MOD-G USING THE EQUILIBRIUM WAKE.

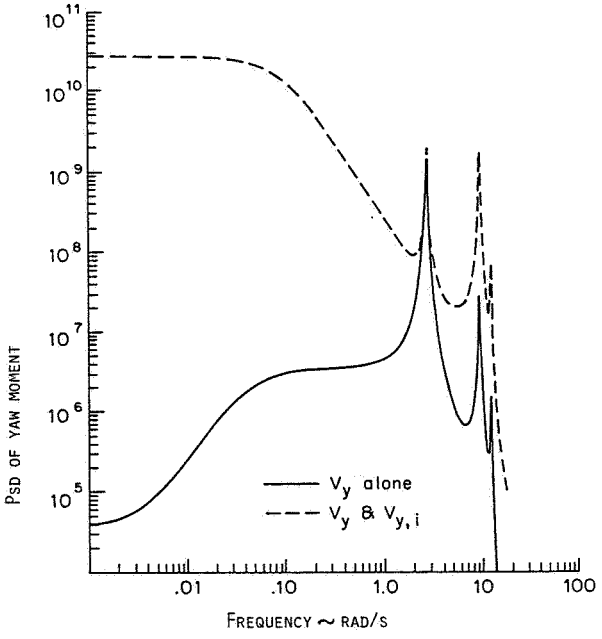

FIGURE 15. THE EFFECT OF THE GRADIENTS $V_{Y,X}$ & $V_{Y,Z}$ ON YAW MOMENTS FOR THE MOD-G USING THE EQUILIBRIUM WAKE.

Table 1. Fractional response contributions of the turbulence inputs for the Mod-M using the equilibrium wake.

Response/Input	V_y	$V_{y,x}$	$V_{y,z}$	ε_r	$\bar{\gamma}_r$	Other
Frequency ≃ 0						
Side Force, F_x	.0	.96	.0	.0	.0	.04
Thrust, F_y	1.0	.0	.0	.0	.0	.0
Pitch Moment, M_x	.0	.82	.12	.0	.0	.06
Frequency = 15.1 (1st Bending)						
Side Force, F_x	.33	.07	.56	.0	.0	.04
Thrust, F_y	.75	.06	.18	.0	.0	.01
Pitch Moment, M_x	.70	.07	.22	.0	.0	.01
Frequency = 3Ω = 23						
Side Force, F_x	.0	.02	.69	.14	.13	.02
Thrust, F_y	.32	.08	.52	.04	.04	.0
Pitch Moment, M_x	.0	.11	.77	.06	.06	.0

Table 2. Fractional response contributions of the turbulence inputs for the Mod-G using the equilibrium wake.

Response/Input	V_y	$V_{y,x}$	$V_{y,z}$	ε_r	$\bar{\gamma}_r$	Other
Frequency ≃ 0						
Side Force, F_x	.0	.06	.92	.0	.0	.02
Thrust, F_y	1.0	.0	.0	.0	.0	.0
Yaw Moment, M_z	.0	.97	.0	.0	.0	.03
Pitch Moment, M_x	.0	.0	.97	.0	.0	.0
Frequency = 2.76 (1st Bending)						
Side Force, F_x	.90	.02	.07	.0	.0	.01
Thrust, F_y	.77	.0	.22	.0	.0	.01
Yaw Moment, M_z	.77	.01	.21	.0	.0	.01
Pitch Moment, M_x	.76	.0	.23	.0	.0	.01
Frequency = 3Ω = 5.5						
Side Force, F_x	.01	.36	.07	.27	.27	.02
Thrust, F_y	.06	.05	.42	.22	.24	.01
Yaw Moment, M_z	.01	.29	.0	.35	.34	.01
Pitch Moment, M_x	.0	.05	.45	.23	.25	.02

APPENDIX

Governing Equations:

$$\begin{bmatrix} M_{11} & 0 & M_{13} & 0 & 0 \\ 0 & M_{22} & 0 & M_{24} & 0 \\ M_{31} & 0 & M_{33} & 0 & 0 \\ 0 & M_{42} & 0 & M_{44} & 0 \\ 0 & 0 & 0 & 0 & M_{55} \end{bmatrix} \begin{Bmatrix} \ddot{U} \\ \ddot{V} \\ \ddot{\phi} \\ \ddot{\chi} \\ \ddot{\Psi} \end{Bmatrix} + \begin{bmatrix} C_{11} & 0 & C_{13} & C_{14} & 0 \\ 0 & C_{22} & 0 & 0 & C_{25} \\ C_{31} & 0 & C_{33} & C_{34} & 0 \\ C_{41} & 0 & C_{43} & C_{44} & 0 \\ 0 & C_{52} & 0 & 0 & C_{55} \end{bmatrix} \begin{Bmatrix} \dot{U} \\ \dot{V} \\ \dot{\phi} \\ \dot{\chi} \\ \dot{\Psi} \end{Bmatrix} + \begin{bmatrix} K_{11} & 0 & K_{13} & K_{14} & 0 \\ 0 & K_{22} & 0 & K_{24} & 0 \\ 0 & 0 & K_{33} & K_{34} & 0 \\ 0 & K_{42} & K_{43} & K_{44} & 0 \\ 0 & 0 & 0 & 0 & 0 \end{bmatrix} \begin{Bmatrix} U \\ V \\ \phi \\ \chi \\ \Psi \end{Bmatrix}$$

$$= \begin{Bmatrix} 0 \\ T \\ 0 \\ 0 \\ Q \end{Bmatrix} + \begin{bmatrix} F_{11} & 0 & F_{13} & F_{14} & F_{15} & 0 & F_{17} & F_{18} & 0 \\ 0 & F_{22} & 0 & 0 & 0 & F_{26} & 0 & 0 & F_{29} \\ F_{31} & 0 & F_{33} & F_{34} & F_{35} & 0 & F_{37} & F_{38} & 0 \\ F_{41} & 0 & F_{43} & F_{44} & F_{45} & 0 & F_{47} & F_{48} & 0 \\ 0 & F_{52} & 0 & 0 & 0 & F_{56} & 0 & 0 & F_{59} \end{bmatrix} \begin{Bmatrix} V_x \\ V_y \\ V_z \\ V_{y,x} \\ V_{y,z} \\ \gamma_{zx} \\ (\varepsilon_{zx}\cos 3\Omega t + \bar{\gamma}_{zx}\sin 3\Omega t) \\ (-\varepsilon_{zx}\sin 3\Omega t + \bar{\gamma}_{zx}\cos 3\Omega t) \\ \bar{\varepsilon}_{zx} \end{Bmatrix}$$

Inertia Matrix

$M_{11} = m_{11} + m_n + m_r$; $M_{13} = M_{31} = -(m_n + m_r)q$

$M_{22} = m_{22} + m_r + m_n$; $M_{24} = m_{24} = M_{42}$; $M_{33} = m_{33} + I_{zz}$

$M_{44} = m_{44} + I_{xx}$; $M_{55} = I_r$; m_r = mass of rotor ; m_n = mass of nacelle

q = distance from C_L tower to nacelle-rotor C.G. ; I_{xx} and I_{yy} = mass moment of inertia of nacelle-rotor system about x and y axes ; I_r = rotor effective spinning inertia ; m_{ij} = tower inertia coefficients of Eq. (4), where for a uniform cantilever tower,

$m_{11} = 99\, m_t/420$, $m_{22} = 156\, m_t/420$, $m_{24} = 22\, m_t L/420$

$m_{33} = I_m L/3$, $m_{44} = m_t L^2/105$, m_t = tower mass , I_m = tower polar inertia

Damping Matrix

$C_{11} = 3f(B_o+\beta_o^2 F_o)/2R\Omega$; $C_{13} = -3f(\bar{a}B_o+\beta_o F_1)/2\Omega$; $C_{14} = -3f(C_1+\bar{a}\beta_o E_o)/2\Omega$

$C_{22} = 3fF_o/R\Omega$; $C_{25} = -3fE_1/\Omega$; $C_{31} = -3f(\beta_o\{F_1+B_1^*\}+\bar{a}\{B_o+\beta_o^2 F_o\})/2\Omega$

$C_{33} = 3fR(\{F_2+\beta_o\bar{a}B_1^*\}+\bar{a}\{\bar{a}B_o+\beta_o F_1\})/2\Omega$; $C_{34} = 3fR(\{E_1\bar{a}+\beta_o C_2^*\}+\bar{a}\{C_1+\bar{a}\beta_o E_o\})/2\Omega+I_r\Omega$

$C_{41} = 3f(\{E_1+\beta_o^2 C_1^*\}+\bar{a}\beta_o\{C_o+E_o\})/2\Omega$; $C_{43} = -C_{34}$; $C_{44} = C_{33}$

$C_{52} = 3fC_1/\Omega$; $C_{55} = 3fRB_2/\Omega+C_g$; C_g = Generator torque coefficient

Stiffness Matrix

$K_{11} = k_{11}$; $K_{13} = -3fG_o/2$; $K_{14} = -3f\beta_o H_o/2$; $K_{22} = k_{22}$; $K_{24} = k_{24}$

$K_{33} = k_{33} + 3fR(\beta_o G_1^*+\bar{a}G_o)/2$; $K_{34} = 3fR(H_1+\beta_o\bar{a}H_o)/2$; $K_{42} = K_{24}$

$K_{43} = -K_{34}$; $K_{44} = k_{44} + 3fR(\beta_o G_1^*+\bar{a}G_o)/2$

where k_{ij} = tower structural stiffnesses from Eq. (3), and for a uniform cantilever tower $k_{11} = 3EI/L^3$; $k_{22} = 12EI/L^3$; $k_{24} = 6EI/L^2$; $k_{33} = GJ/L$; $k_{44} = 4EI/L$

Wind Input Matrix

$F_{11} = 3f(B_o+\beta_o^2 F_o)/2R\Omega$; $F_{13} = -3f\beta_o(C_o+E_o)/2R\Omega$; $F_{14} = -3f\beta_o F_1/2\Omega$

$F_{15} = 3fG_1/2\Omega$; $F_{17} = -3f\beta_o(C_1-E_1)/2\Omega$; $F_{18} = -3f(-B_1+\beta_o^2 F_1)/2\Omega$

$T = 3fD_o$; $F_{22} = 3fF_o/R\Omega$; $F_{26} = 3fE_1/\Omega$; $F_{29} = -3fF_1\beta_o/\Omega$

$F_{31} = -3f(\beta_o\{F_1+B_1^*\}+\bar{a}\{B_o+\beta_o^2 F_o\})/2\Omega$; $F_{33} = 3f(\{E_1+\beta_o^2 C_1^*\}+\bar{a}\beta_o\{C_o+E_o\})/2\Omega$

$F_{34} = 3fR(F_2+\beta_o\bar{a}F_1)/2\Omega$; $F_{35} = -3fR(\beta_o C_2^*+\bar{a}C_1)/2\Omega$

$F_{37} = -3fR(\{E_2-\beta_o^2 C_2^*\}-\bar{a}\beta_o\{C_1-E_1\})/2\Omega$; $F_{38} = 3fR(\beta_o\{F_2-B_2^*\}+\bar{a}\{-B_1+\beta_o^2 F_1\})/2\Omega$

$F_{41} = F_{33}$; $F_{43} = -F_{31}$; $F_{44} = F_{35}$; $F_{45} = -F_{34}$; $F_{47} = -F_{38}$; $F_{48} = F_{37}$

$Q = 3fRA_1$; $F_{52} = 3fC_1/\Omega$; $F_{56} = -3fR\,B_2/\Omega$; $F_{59} = -3R\beta_o C_2/\Omega$

where $f = \frac{1}{2}\rho a' R c_t (R\Omega)^2$. The single subscript capitalized coefficients A_n through H_n are integral aerodynamic coefficients of the form

$$A_n = \int_{\bar{h}}^{1} A'(x)\, x^n\, dx \qquad \text{where } n = 0,1,2$$

with A' through F' defined as given in Eq. (13) for the "frozen wake" or Eq. (18) for the "equilibrium wake". In addition, $G'(x) = \lambda B'(x)$ and $H'(x) = \lambda E'(x)$, while the coefficients with stars are $B_{\bar{n}}^* = B_n - \bar{h}B_{n-1}$, $C_{\bar{n}}^* = C_n - \bar{h}C_{n-1}$ and $G_{\bar{n}}^* = G_n - \bar{h}G_{n-1}$, and $\bar{h} = h/R$, $\bar{a} = a/R$.

QUESTIONS AND ANSWERS

R.W. Thresher

From: B.J. Young

Q: Your results show a substantial excitation which is continuous down through zero frequency, while J.P. Sullivan's results were zero at zero frequency. Any comment on differences?

A: *Professor Sullivan used the Davenport model for the horizontal component of wind turbulence which vanishes at zero frequency. We used the model suggested by Von Karman which is finite at zero frequency; therefore, this excitation difference at low frequency is due to the turbulence models.*

From: K.H. Hohenemser

Q: How should you expect the results to change for hinged (teetering) blades?

A: *I have not done the analysis, so I do not know exactly. I would expect the magnitude of the forces and moments to decrease significantly.*

From: Anonymous

Q: What is the effect of damping on the first and second blade bending power spectra spikes?

A: *The blade is rigid so there are no blade resonances. The bending resonances illustrated in the plots are for the tower. The only damping in the model is aerodynamic damping, but if structural damping were added, the response near resonance points should be reduced.*

From: R. E. Wilson

Q: Do you plan to treat teetering rotors?

A: *I would like to add teetering to the model, but at this time, our sponsor has not indicated a strong interest in adding this additional degree of freedom. Perhaps after the model is validated this will be possible.*

WIND TURBULENCE INPUTS FOR HORIZONTAL AXIS WIND TURBINES

W.E. Holley, R.W. Thresher, and S-R. Lin

Department of Mechanical Engineering
Oregon State University
Corvallis, OR 97331

1. INTRODUCTION

In order to predict wind turbine response characteristics in the presence of atmospheric turbulence, two major modeling steps are required. First, the important atmospheric sources for the force excitations felt by the wind turbine system must be identified and characterized. Second, a dynamic model must be developed which describes how these excitations are transmitted through the structure and power train. The goal of this paper is to establish the first modeling step, that of quantifying the important excitations due to the atmospheric turbulence. The dynamic modeling of the second step is undertaken in the accompanying paper (1).

Fluctuations in the aerodynamic forces on a wind turbine blade are generated by the relative motions of the air with respect to the blade. These relative motions are comprised of two parts: the motions of the blade and the motions of the air. The motions of the air can further be divided into the undisturbed turbulent flow and the "induced flow" due to the presence of the wind turbine wake. The terms comprising the undisturbed flow will be characterized in this paper. More precisely, for a horizontal axis wind turbine, the aerodynamic forces are determined by the instantaneous air velocity distribution along each of the turbine blades. These blades in turn are rotating through the turbulence field which is being convected past the turbine rotor disc. It is thus necessary to characterize the wind turbulence field by a three-dimensional velocity vector which varies randomly with time and with the position in space. A complete statistical description of this turbulent velocity field requires the determination of all possible joint probability distributions between different velocity components at different times and positions in space. Clearly, such a description will not be possible without considerable simplification. The validity of the resulting simplified model will depend upon a comparison of the characteristics predicted by the model and those observed in the atmosphere and more importantly, those observed in actual wind turbine field tests. In this paper we will describe the assumptions and the analytical steps used to arrive at the simplified model. In the accompanying paper the model is used to predict wind turbine response charactertistics. It is hoped that these results will be verified in the near future by direct comparison with the results of actual field tests.

2. MODEL ASSUMPTIONS AND APPROXIMATIONS

The first assumption relates to the type of statistical information which is necessary to describe the net aerodynamic forces and moments acting on the turbine rotor. Several authors (2,3) have indicated that the quantities needed for wind turbine design can be obtained from the mean and second-moment statistical characteristics of the various system responses. For stationary processes this information is contained in the mean and power spectral density. In this type of analysis, the mean and power spectral density are characterized by a set of parameters. Rice's theory (4) for computing the frequency of level crossings or peaks is then used with the observed parameter probability densities to obtain the desired response statistics. In this paper, we will strive to determine the power spectral density characteristics of the turbulence. When they are combined with the machine dynamic model, we will assume that the resulting response statistics will be useful for machine design.

The next simplification assumes that the variation in the turbulent velocity observed at a stationary point is due primarily to the convection of the turbulent eddies past the tower. Known as Taylor's frozen field hypothesis (5), this assumption is widely used in reducing fixed-tower, wind turbulence data and correlating these results with data from spatially separated points (6).

The following assumptions which are often used in analyses involving aircraft flying through turbulence are more questionable when applied to turbulence observed in the atmospheric boundary layer. First, when the mean velocity field is subtracted from the total instantaneous velocity field, the resulting turbulent velocity is assumed to be locally homogeneous. Thus, when vertical separations between points are as large as the disc diameter, the correlations are not explicitly height dependent. Second, the field is assumed to be isotropic for all separations for which it is homogeneous. The latter assumption is known not to be precisely correct since the variance of the vertical component is less than the horizontal components (7) and the vertical and downwind components are correlated due to the boundary layer shear of the mean flow (8). However, no model currently exists for predicting the three-dimensional, nonisotropic correlations between velocity components at points separated in space. In the absence of a better model, the isotropic model will be used with the understanding that the results may need adjustment when more complete experimental results are available.

With the previous assumptions (and assuming incompressible flow), Batchelor (9) has shown that the correlation tensor between velocity components at spatially separated points has the form

$$R_{ij}(\vec{\xi}) = \sigma^2[f(\xi)\delta_{ij} + \frac{1}{2}\xi f'(\xi)(\delta_{ij} - \frac{\xi_i\xi_j}{\xi^2})] \quad (2.1)$$

where $R_{ij}(\vec{\xi}) \equiv E[v_i(\vec{x} + \vec{\xi})v_j(\vec{x})]$

$v_i(\vec{x})$ = ith velocity component at position $\vec{x}$

ξ_i = ith component of the separation $\vec{\xi}$

$\xi = \sqrt{\xi_1^2 + \xi_2^2 + \xi_3^2} = |\vec{\xi}|$

δ_{ij} = 1 for i = j and 0 for i ≠ j

$f(\xi)$ = longitudinal correlation function

σ^2 = variance of the turbulent velocity components

Von Karman (10) suggested the form for the longitudinal correlation function

$$f(\xi) = b\left(\frac{\xi}{aL}\right)^{1/3} K_{1/3}\left(\frac{\xi}{aL}\right) \qquad (2.2)$$

where a = 1.339

b = 0.5925

L = integral scale $\triangleq \int_0^\infty f(\xi)d\xi$

$K_{1/3}(\cdot)$ = modified Bessel function of order 1/3

This function results in Kolmogorov's (11) -5/3 power law for the inertial subrange in the longitudinal power spectral density.

At this point, a very useful approximation due to Etkin (12) is introduced. The power of this approximation is that it separates the computation of the aerodynamic responses into two tractable pieces. In the first, the spatial variation of the turbulence is locally approximated by an expansion. The various time varying turbulence components are then multiplied by standard aerodynamic influence coefficients to obtain the required aerodynamic responses. These influence coefficients are the same as those that would be computed in the absence of turbulence. The results of this procedure are extensively used in aircraft response calculations for flight through turbulence (13). The results for the airplane case, however, cannot be applied directly to the wind turbine problem because of major differences in the geometry. The aerodynamic surfaces of an airplane lie in a nearly horizontal plane while the blades of a horizontal axis wind turbine lie in a vertical plane nearly perpendicular to the mean wind. It is necessary then, to rederive the results in a form which is compatible with the wind turbine geometry.

3. DERIVATION OF THE TURBULENCE MODEL

The coordinate definitions used in this paper are shown in Figure 1. In the vicinity of the rotor disc, the turbulent velocity is expressed locally by the approximation

$$\hat{v}_i(r,\theta,t) = V_i(t) + V_{i,x}(t)\, r\sin\theta + V_{i,z}(t)\, r\cos\theta + \text{higher order terms} \qquad (3.1)$$

In this approximation, the spatial randomness of the turbulence is accounted for by the time varying random quantities $V_i(t)$, $V_{i,x}(t)$, $V_{i,z}(t)$ and higher order terms. While this approximation appears to be a Taylor series expansion, it is not. Because of the random nature of the spatial variations, the samples from the statistical ensemble do not have the usual continuity and differentiability properties necessary for a true Taylor expansion. The expansion, however, can be thought of as a functional approximation. Here, the object is to choose the terms in the expansion so as to minimize some measure of the approximation error. When dealing with random functions, a reasonable error measure is its variance. It will be understood that convergence of the approximation series means that the error variance approaches zero as more and more terms are included. Convergence in variance further implies that the series converges in probability (14), i.e.,

$$\lim_{n\to\infty} \Pr\{|e_n| > \varepsilon\} = 0 \quad \text{for all } \varepsilon > 0$$

where e_n is the approximation error including only the n^{th} order terms.

At any given time, the terms V_i, $V_{i,x}$, and $V_{i,z}$ are chosen to minimize the criterion

$$\varepsilon = \frac{1}{A}\int_A \Sigma_i (\hat{v}_i - v_i)^2\, dA \qquad (3.2)$$

where A = rotor disc area

$\hat{v}_i = V_i + V_{i,x}\, r\sin\theta + V_{i,z}\, r\cos\theta$

$v_i = v_i(r,\theta,t)$

The necessary conditions for the minimization are

$$\frac{\partial\varepsilon}{\partial V_i} = \frac{2}{A}\int_A (\hat{v}_i - v_i)\, dA = 0$$

$$\frac{\partial\varepsilon}{\partial V_{i,x}} = \frac{2}{A}\int_A (\hat{v}_i - v_i)\, r\sin\theta\, dA = 0 \qquad (3.3)$$

$$\frac{\partial\varepsilon}{\partial V_{i,z}} = \frac{2}{A}\int_A (\hat{v}_i - v_i)\, r\cos\theta\, dA = 0$$

which in turn require that

$$V_i(t) = \frac{1}{A}\int_A v_i(r,\theta,t)dA$$

$$V_{i,x}(t) = \frac{1}{I_x}\int_A v_i(r,\theta,t)\, r\sin\theta\, dA \qquad (3.4)$$

$$V_{i,z}(t) = \frac{1}{I_z}\int_A v_i(r,\theta,t)\, r\cos\theta\, dA$$

where $A = \pi R^2$ the disc area

$I_x = I_z = \frac{\pi R^4}{4}$ the area moments about the x and z axes.

Thus, if the statistics of the turbulence field are known, then the statistics of V_i, $V_{i,x}$ and $V_{i,z}$ and any higher order terms can be determined. For example the autocorrelation function for the uniform, through-the-disc component is expressed as

$$R_{V_y}(\tau) \triangleq E\,[V_y(t+\tau)V_y(t)] = \frac{1}{A^2}\int_A\int_A E[v_y(r,\theta,t+\tau)v_y(\rho,\phi,t)]dA_1 dA_2 \qquad (3.5)$$

Using Taylor's hypothesis yields

$$R_{V_y}(\tau) = \frac{1}{A^2}\int_A\int_A R_{22}(\xi_1,\xi_2,\xi_3)dA_1dA_2 \qquad (3.6)$$

where $\xi_1 = r\sin\theta - \rho\sin\phi$

$\xi_2 = V_w\tau$

$\xi_3 = r\cos\theta - \rho\cos\phi$

$dA_1 = rdrd\theta$

$dA_2 = \rho d\rho d\phi$

and V_w = mean wind speed

In the isotropic case,

$$R_{22}(\xi_1,\xi_2,\xi_3) = \sigma^2[f(\xi) + \frac{1}{2}\xi f'(\xi)(\frac{\xi^2 - V_w^2\tau^2}{\xi^2})] \qquad (3.7)$$

where $\xi^2 = \xi_1^2 + \xi_2^2 + \xi_3^2$

$= r^2 + \rho^2 - 2r\rho\cos(\theta-\phi) + V_w^2\tau^2$

Even for the simple exponential correlation function

$$f(\xi) = e^{-\frac{\xi}{L}} \qquad (3.8)$$

it is doubtful that an analytical expression for $R_{V_y}(\tau)$ exists. Hence, numerical integration procedures were employed to perform the required computations. Details of these procedures are found in the Appendix.

At this point, it is convenient to rearrange the gradient terms for the in-plane components. This form is chosen because the resulting terms naturally appear when the velocity is expressed in components which rotate with the turbine blades. These terms can be interpreted as local fluid rotations and strain rates. Thus, the following terms are defined

$$\left.\begin{aligned} \gamma_{xz} &= \frac{1}{2}(V_{z,x} - V_{x,z}) \quad \text{swirl} \\ \bar{\gamma}_{xz} &= \frac{1}{2}(V_{z,x} + V_{x,z}) \\ \varepsilon_{xz} &= \frac{1}{2}(V_{z,z} - V_{x,x}) \end{aligned}\right\} \text{shear strain rates} \qquad (3.9)$$

$$\bar{\varepsilon}_{xz} = \frac{1}{2}(V_{z,z} + V_{x,x}) \quad \text{dilation}$$

Typical fluid streamlines giving rise to positive terms are shown in Figure 2.

Retaining the uniform and gradient terms in the expansion results in the following nine terms which vary randomly with time: V_x, V_y, V_z, $V_{y,x}$, $V_{y,z}$, γ_{xz}, $\bar{\gamma}_{xz}$, ε_{xz}, $\bar{\varepsilon}_{xz}$. The correlation statistics of these terms can be computed using double-area integral expressions similar to Eq. (3.6). Because of the statistical isotropy, it is easily shown that all nine terms are mutually uncorrelated. Thus, all second moment statistics will be determined by the autocorrelation functions or the power spectral densities of the nine terms. Using the scaling parameters in Table 1, nondimensional power spectral density curves can be plotted. These curves will be a one parameter family depending on the ratio of turbine size to turbulence integral scale (R/L). Example curves are shown in Figures 3 and 4.

Table 1. Scaling Parameters for Nondimensional Curves.

Variables	Scaling Parameter
Turbulent velocity, V_i	σ
Velocity gradient, $V_{i,j}$	σ/R
Frequency, ω	V_w/L

Also shown in Figures 3 and 4 are approximate spectra derived from an exponential autocorrelation function. These approximate spectra match the computed spectra at low frequency and have the same total variance. Stationary, random processes with exponential autocorrelation functions can be conveniently represented by stochastic differential equations of the form

$$\dot{x} + ax = bw \qquad (3.10)$$

where x = random process

w = white noise with flat PSD = q

The autocorrelation function and power spectrum are

$$R_x(\tau) = \frac{b^2q}{2a}e^{-a|\tau|} \qquad (3.11)$$

$$S_x(\omega) = \frac{b^2q}{a^2+\omega^2} \qquad (3.12)$$

respectively, from which the parameters a and b can be determined

$$a = \frac{2R_x(0)}{S_x(0)} \qquad (3.13)$$

$$b = \frac{2R_x(0)}{\sqrt{qS_x(0)}} \qquad (3.14)$$

For the wind turbulence it is convenient to choose the white noise, power spectral density

$$q = \frac{\sigma^2 L}{V_w^3} \qquad (3.15)$$

Nondimensional parameters can thus be defined

$$a_* \triangleq \frac{La}{V_w} = \frac{2LR_x(0)}{V_wS_x(0)} \qquad (3.16)$$

$$b_* \triangleq \begin{cases} \dfrac{Lb}{V_w^2} = \dfrac{2\left(\frac{R_x(0)}{\sigma^2}\right)}{\sqrt{\frac{V_w S_x(0)}{L\sigma^2}}} & \text{uniform terms} \\ \dfrac{RLb}{V_w^2} = \dfrac{2\left(\frac{R^2 R_x(0)}{\sigma^2}\right)}{\sqrt{\frac{V_w R^2 S_x(0)}{L\sigma^2}}} & \text{gradient terms} \end{cases} \tag{3.17}$$

which will depend only on the ratio R/L. As an example of the computational procedure, consider the turbulence component V_y. In this case,

$$\frac{R_x(0)}{\sigma^2} = \frac{1}{A^2}\int_A\int_A g\left(\frac{\xi}{L}, 0\right) dA_1 dA_2 \tag{3.18}$$

and $$\frac{V_w S_x(0)}{L\sigma^2} = \frac{2}{A^2}\int_0^\infty\int_A\int_A g\left(\frac{\xi}{L}, \frac{V_w\tau}{L}\right) dA_1 dA_2 \left(\frac{V_w}{L}\right) d\tau \tag{3.19}$$

where $$g\left(\frac{\xi}{L}, \frac{V_w\tau}{L}\right) = f(\xi) + \frac{1}{2}\xi f'(\xi)\left(\frac{\xi^2 - V_w^2\tau^2}{\xi^2}\right)$$

$$\xi = \sqrt{r^2 + \rho^2 - 2r\rho\cos(\theta-\phi) + V_w^2\tau^2}$$

$$dA_1 = r\,dr\,d\theta$$

$$dA_2 = \rho\,d\rho\,d\phi$$

and $f(\cdot)$ is the isotropic correlation function.

The results of numerical computations for these integrals are shown in Figures 5-8 for all of the turbulence components.

In summary, each of the turbulence terms are modeled by stochastic differential equations of the form

$$\dot{x} = ax + bw \tag{3.20}$$

where x = instantaneous value of one of the terms V_x, ..., $V_{y,x}$, ..., γ_{xz}, etc.

w = nondimensional white noise with power spectral density $q = \sigma^2 L/V_w^3$

$$a = \frac{V_w}{L} a_* \tag{3.21}$$

$$b = \begin{cases} \dfrac{V_w^2}{L} b_* & \text{for uniform terms} \\ \dfrac{V_w^2}{LR} b_* & \text{for gradient terms} \end{cases} \tag{3.22}$$

The nondimensional terms a_* and b_* are found from Figures 5-8 as appropriate and depend on the ratio of turbine size to turbulence scale (R/L). Power spectral densities can be obtained if desired from the equation

$$S_x(\omega) = \frac{b^2 q}{a^2+\omega^2} \tag{3.23}$$

4. MODEL ERROR DISCUSSION

Three levels of approximation are introduced in this paper. In the first, the turbulence is modeled as locally homogeneous and isotropic with correlations given by the Von Karman model. This assumption probably introduces the largest amount of error in the model. Several authors (15,16) indicate that the horizontal velocity components have a variance which is approximately three times the variance of the vertical component. If we assume that the turbulent velocity predicted by the isotropic model has a vertical component which is $\sqrt{3}$ times too large, but is otherwise statistically correct, then the velocity error magnitude introduced has a variance

$$\begin{aligned} \varepsilon &\triangleq E\left[\sum_{i=1}^{3}(\hat{v}_i - v_i)^2\right] \\ &= E\left[(\sqrt{3}\,v_3 - v_3)^2\right] \\ &= (\sqrt{3}-1)^2\left(\tfrac{1}{3}\sigma^2\right) \\ &= 0.18\,\sigma^2 \end{aligned} \tag{4.1}$$

where σ^2 = variance of horizontal components.

The second level of approximation occurs in truncating the higher order terms in the spatial expansion. Thus, at any point on the rotor disc, the turbulent velocity is approximated by

$$\hat{v}_i(r,\theta,t) = V_i(t) + V_{i,x}(t)r\sin\theta + V_{i,z}(t)r\cos\theta \tag{4.2}$$

Since the velocity component through the rotor, V_y, produces the greatest aerodynamic force, consider the error variance produced by the approximation of this component

$$\varepsilon_1(r,\theta) = \frac{1}{\sigma^2} E[(\hat{v}_y(r,\theta,t) - v_y(r,\theta,t))^2] \tag{4.3}$$

Averaging over the rotor disc gives

$$\bar{\varepsilon}_1 = \frac{1}{A}\int_A \varepsilon_1(r,\theta)\,dA \tag{4.4}$$

Using the relations for terms $V_y(t)$, $V_{y,x}(t)$ and $V_{y,z}(t)$ given by Equations 3.4 yields the useful relation

$$\int_A (\hat{v}_y - v_y)\hat{v}_y\,dA = 0 \tag{4.5}$$

and hence

$$\bar{\varepsilon}_1 = \frac{1}{A\sigma^2}\int_A E[\hat{v}_y^2]dA - \frac{1}{A\sigma^2}\int_A E[\hat{v}_y v_y]dA$$

$$= 1 - \frac{1}{\sigma^2}E[V_y^2] - \frac{I_x}{A\sigma^2}E[V_{y,x}^2] - \frac{I_3}{A\sigma^2}E[V_{y,z}^2] \quad (4.6)$$

which finally gives

$$\bar{\varepsilon}_1 = 1 - \frac{R_{V_y}(0)}{\sigma^2} - \frac{1}{4}\frac{R^2 R_{V_{y,x}}(0)}{\sigma^2} - \frac{1}{4}\frac{R^2 R_{V_{y,z}}(0)}{\sigma^2} \quad (4.7)$$

This quantity can be interpreted as a measure of the total variance of the part of the turbulent velocity that is not included in the model. Thus, the averaged error, $\bar{\varepsilon}_1$ is zero if the approximation is "perfect",

and $\bar{\varepsilon}_1 = 1$ if the trivial approximation $\hat{v}_y = 0$ is used.

In a similar fashion the quantity $\bar{\varepsilon}_0$ can be defined when only the uniform terms are retained and $\bar{\varepsilon}_2$ when uniform, gradient, and quadratic terms are retained. Table 2 shows the effect of increasing rotor size relative to the turbulence scale.

Table 2 - Relative Approximation Error Variance

$\frac{R}{L}$	$\bar{\varepsilon}_0$	$\bar{\varepsilon}_1$	$\bar{\varepsilon}_2$
.01	.044	.026	.023
.054(Mod M)	.135	.081	.070
.1	.201	.121	.105
.3(Mod G)	.397	.250	.218
.5	.527	.348	.304
1.0	.724	.527	.465
2.0	.889	.737	.663

Observing the results given in this table, a significant improvement is obtained when the gradient terms are included along with the uniform term. However, only a small improvement is obtained when the quadratic terms are also included. This leads to the conclusion that the unmodeled portion of the turbulence is highly disorganized and probably has a negligible effect on the forces and moments felt at the hub.

To investigate this effect further, the following aerodynamic model was assumed for a light, rigid blade cutting through the turbulent velocity field

$$f(t) = \frac{3C}{R^3}\int_0^R r\sqrt{R^2-r^2}\; v_y(r,\Omega t,t)dr \quad (4.8)$$

where f = the net blade force (torque or thrust deviation from nominal)
C = the aerodynamic influence coefficient
Ω = rotation rate of the rotor
and $v_y(r,\theta,t)$ = instantaneous turbulent velocity.

Note, for a steady, uniform velocity, the force is constant and given by

$$f = C\, v_y$$

Now, let the approximate force be the result of the uniform and gradient terms in the model. Thus,

$$\hat{f}(t) = \frac{3C}{R^3}\int_0^R r\sqrt{R^2-r^2}\;\hat{v}_y(r,\Omega t,t)\,dr \quad (4.9)$$

where $\hat{v}_y = V_y(t) + V_{y,x}(t)r\sin\Omega t + V_{y,z}(t)r\cos\Omega t$

Integrating along the blade yields

$$\hat{f}(t) = C[V_y(t) + \frac{3\pi}{16}R(V_{y,x}(t)\sin\Omega t + V_{y,z}(t)\cos\Omega t)] \quad (4.10)$$

The relative error variance is given by

$$\varepsilon_1 = \frac{E[(\hat{f}-f)^2]}{E[f^2]}$$

$$= \frac{E[\hat{f}^2] - 2E[\hat{f}f] + E[f^2]}{E[f^2]} \quad (4.11)$$

Substituting Equations 4.10 and 4.8 into these variance terms gives

$$E[\hat{f}^2] = C^2[R_{V_y}(0) + (\frac{3\pi R}{16})^2(R_{V_{y,x}}(0)\sin^2\Omega t + R_{V_{y,z}}(0)\cos^2\Omega t)] \quad (4.12)$$

$$E[f^2] = \frac{9C^2}{R^6}\int_0^R\int_0^R r\rho\sqrt{(R^2-r^2)(R^2-\rho^2)}\;R_{22}(\xi_1,0,\xi_3)dr d\rho \quad (4.13)$$

where $\xi_1 = (r-\rho)\sin\Omega t$

$\xi_3 = (r-\rho)\cos\Omega t$

$R_{22}(\cdot,\cdot,\cdot)$ = turbulent velocity correlation function

$$E[\hat{f}f] = C^2(I_0 + I_1) \quad (4.14)$$

where

$$I_0 = \frac{3}{\pi R^5}\int_0^R\int_A r\sqrt{R^2-r^2}\;R_{22}(\xi_1,0,\xi_3)dA dr$$

$$I_1 = \frac{9}{4R^6}\int_0^R\int_A r\sqrt{R^2-r^2}\;\rho\cos(\phi-\Omega t)R_{22}(\xi_1,0,\xi_3)dA dr$$

$\xi_1 = r\sin\Omega t - \rho\sin\phi$

$\xi_3 = r\cos\Omega t - \rho\cos\phi$

$dA = \rho d\rho d\phi$

The normalized error variance, ε_0, defined by neglecting the gradient terms in the approximate velocity, is determined in a similar way. Table 3 shows the results of these computations

Table 3 - Relative Blade Force Error Variance

$\frac{R}{L}$	ϵ_0	ϵ_1
.01	.024	.009
.054(Mod M)	.076	.030
.1	.116	.046
.3(Mod G)	.248	.104
.5	.350	.157
1.0	.536	.278
2.0	.753	.488

Comparing the results of Table 3 and Table 2, it is seen that only half the unmodeled velocity variance is observed as unmodeled force variance. This result is due to the averaging effect of the integration along the blade. If the blade were more realistically modeled with inertia it is expected that little of the remaining unmodeled variance would be transmitted to the hub.

The third level of approximation involves the use of the stochastic differential equation (Equation 3.20) to model the uniform and gradient turbulence components. The accuracy of this approximation depends on how close the spectral form

$$S_x(\omega) = \frac{b^2 q}{a^2 + \omega^2}$$

is to the spectra computed by integration. Figures 3 and 4 show two examples of such a comparison. The parameters a and b are chosen so that the total variance and the low frequency spectrum for the model are correct.

Considering the results of these error calculations, it is reasonable to expect that the turbulence inputs described statistically by the model will approximate the effect of the true turbulence on the wind turbine. Realistic evaluation of the modeling error, however, can only be accomplished by comparison with experimental data. It is hoped that such a comparison can be made in the near future.

5. AERODYNAMIC FORCE ON ROTATING WIND TURBINE BLADE

As an illustration of how the turbulence interacts with a rotating turbine blade, consider the previous example of a rigid blade rotating in the turbulent velocity field. Using the approximate turbulence model, the blade force is given by

$$f(t)=C[V_y(t)+\tfrac{3\pi}{16} R(V_{y,x}(t)\sin\Omega t+V_{y,z}(t)\cos\Omega t)] \quad (5.1)$$

Defining the three components of the dynamic state vector

$$\left.\begin{aligned} x_1(t) &= V_y(t) \\ x_2(t) &= \cos\Omega t\, V_{y,z}(t) + \sin\Omega t\, V_{y,x}(t) \\ x_3(t) &= -\sin\Omega t\, V_{y,z}(t) + \cos\Omega t\, V_{y,x}(t) \end{aligned}\right\} \quad (5.2)$$

yields the stochastic differential equations

$$\dot{x}_1 = -a_1 x_1 + b_1 w_1 \quad (5.3)$$

$$\dot{x}_2 = -a_2 x_2 + \Omega x_3 + b_2 w_2 \quad (5.4)$$

and $$\dot{x}_3 = -\Omega x_2 - a_2 x_3 + b_2 w_3 \quad (5.5)$$

Since the original white noise inputs are uncorrelated with identical power spectral densities, it can be shown that w_2 and w_3 are also uncorrelated white noise processes with the same power spectral density. This yields the following matrix form for the stochastic differential equations

$$\begin{aligned} \{\dot{x}\} &= [A]\{x\} + [B]\{w\} \\ \{f\} &= [C]\{x\} \end{aligned} \quad (5.6)$$

where the matrices are given by

$$\left.\begin{aligned} [A] &= \begin{bmatrix} -a_1 & 0 & 0 \\ 0 & -a_2 & \Omega \\ 0 & -\Omega & -a_2 \end{bmatrix} \\ [B] &= \begin{bmatrix} b_1 & 0 & 0 \\ 0 & b_2 & 0 \\ 0 & 0 & b_2 \end{bmatrix} \\ [C] &= [C,\ C\,\tfrac{3\pi}{16} R,\ 0] \end{aligned}\right\} \quad (5.7)$$

Using these equations the output power spectral density is given by the well known expression (17)

$$S_f(\omega) = [H(i\omega)][Q][H^T(-i\omega)] \quad (5.8)$$

where the row matrix of transfer functions is given by

$$[H(i\omega)] = [C][i\omega I - A]^{-1}[B] \quad (5.9)$$

Since the elements of the noise vector are uncorrelated and have identical power spectral densities

$$[Q] = \begin{bmatrix} q & 0 & 0 \\ 0 & q & 0 \\ 0 & 0 & q \end{bmatrix} \quad (5.10)$$

which gives

$$\begin{aligned} S_f(\omega) &= q[H(i\omega)][H^T(-i\omega)] \\ &= q \sum_k |H_{jk}(i\omega)|^2 \end{aligned} \quad (5.11)$$

For the case at hand,

$$[H(i\omega)] = \left[\frac{Cb_1}{a_1+i\omega},\ \frac{C\,\frac{3\pi}{16} R\, b_2(a_2+i\omega)}{(a_2+i\omega)^2+\Omega^2},\ \frac{C\,\frac{3\pi}{16} R\, b_2\Omega}{(a_2+i\omega)^2+\Omega^2}\right] \quad (5.12)$$

and

$$S_f(\omega) = \frac{(Cb_1)^2 q}{a_1^2+\omega^2} + \frac{(C\,\frac{3\pi}{16} R\, b_2)^2(a_2^2+\Omega^2+\omega^2)q}{(a_2^2+\Omega^2+\omega^2)^2-(2\Omega\omega)^2} \quad (5.13)$$

Using the non-dimensional terms defined in Equations 3.16 and 3.17 yields the result

$$\frac{V_w S_f(\omega)}{C^2\sigma^2 L} = \frac{b_{*1}^2}{a_{*1}^2+\omega_*^2} + \frac{(\frac{3\pi}{16} b_{*2})^2(a_{*2}^2 + \Omega_*^2 + \omega_*^2)}{(a_{*2}^2 + \Omega_*^2 + \omega_*^2)^2-(2\ \Omega_*\omega_*)^2} \tag{3.14}$$

where the non-dimensional frequencies are defined by

$$\omega_* = \frac{L\omega}{V_w} \quad \text{and} \quad \Omega_* = \frac{L\Omega}{V_w} \tag{3.15}$$

The non-dimensional, power spectral density from Equation 3.14 is plotted in Figure 9. The parameters for these blades were selected to correspond to two typical wind turbines of vastly different size. Table 4 provides the key parameters for these two turbines.

Table 4 - Parameters for Typical Wind Turbines

	Mod M	Mod G
Radius, R (ft)	16.67	150
Rated Power	8 kW	2.5 MW
Windspeed, V_w (m.p.h.)	16.63	20
Rotation Rate, Ω (rpm)	73.35	17.5
Turbulence Scale, L (ft)	300	500

It is clear from Figure 9 that the effect of blade rotation is to concentrate the variance due to the turbulence gradient components at a frequency equal the rotation rate. This effect can be understood by considering the blade to be slicing through a slowly varying velocity gradient. As the blade encounters the higher velocity on one side of the rotor disc the force is increased. As it moves through 180° the force reaches a minimum giving a fluctuating force at the rotor frequency. The importance of this effect can be seen by comparing the relative contributions of the uniform and gradient components to the total variance of the blade force. Table 5 shows these results.

Table 5 - Relative Contributions to Blade Force Variance

	Uniform Term	Gradient Terms
Mod M (8 kW)	96%	4%
Mod G (2.5 MW)	85%	15%

Clearly for the larger blade, 15% of the variance at the relatively high rotor frequency could cause more fatigue damage than the 85% for the uniform component at the lower frequencies.

6. CONCLUSIONS

In this paper, we have formulated a theoretical model for the wind turbulence as it affects horizontal axis wind turbines. The model includes the effect of variations in the turbulent velocity across the rotor disc. An indication of the approximation error in the model has also been given. It is expected that the model will be useful for determining how important the different turbulence effects are for given machine responses. This type of study has been made in the accompanying paper (1). While we believe that the model will give qualitatively correct results, it is important that experimental verification and any necessary model adjustments be made before it is used for design purposes.

ACKNOWLEDGEMENT

This research was supported by the Department of Energy through Battelle, Pacific Northwest Laboratory, under contract DE-AT06-79ET23144. The authors wish particularly to thank Dr. J.R. Connell, the technical monitor, for his enthusiastic support and the PNL staff for their many valuable suggestions.

APPENDIX

Numerical Procedures Utilized in Model Development

A.1 Area Integration Over Rotor Disc

Two Gaussian quadrature formulas (18) were utilized to perform area integrations over the rotor disc. The distribution of points is shown in Figure 10 and given in Tables 6 and 7.

Table 6 - Sixteen Point Formula

r_i	C_i
.21132487	.19634954
.78867513	.19634954

Table 7 - Sixty-four Point Formula

r_i	C_i
.26349923	.03415057
.57446451	.06402420
.81852949	.06402420
.96465961	.03415057

The quadrature formulas have the following form:

$$\int_A f(r,\theta)dA = \sum_{i=1}^{n} \sum_{j=1}^{4n} C_i f(r_i,\theta_j)$$

$$\theta_j = \frac{\pi j}{2n}$$

A six-point formula was also developed to reduce the computational load. In this case, the radius was adjusted until the best match between computations using the sixty-four-point formula and the six-point formula was achieved and resulted in r = 0.69. For all computations, comparison was made between two formulas to verify accuracy to within five percent.

A.2 Integration Along Radius

An eight-point Gaussian quadrature formula (19) was utilized for radial integrations where required without angle dependence.

$$\int_0^1 f(r)dr = \sum_{i=1}^{n} C_i f(r_i)$$

The weights and absissas are given in Table 8.

Table 8 - Radial Quadrature Formula

r_i	C_i
.0198550717	.0506142681
.1016667612	.1111905172
.2372337950	.1568533229
.4082826787	.1813418916
.5917173212	.1813418916
.7627662049	.1568533229
.8983332387	.1111905172
.9801449282	.0506142681

A.3 Fourier Transforms

For calculation of power spectral densities the Fourier transform defined by

$$S(\omega) = \int_{-\infty}^{+\infty} e^{-i\omega\tau} R(\tau)d\tau$$

was numerically computed from the autocorrelation function using the finite approximation

$$S(\omega_k) = \frac{T}{2n}\left(2\mathrm{Re}\left[\sum_{j=0}^{n} R(\tau_j)e^{-i\omega_k\tau_j}\right]-R(o)\right)$$

where $\omega_k = \left(\frac{4\pi n}{T(n+1)}\right)k$

$$\tau_j = \left(\frac{T}{2n}\right)j$$

The fast Fourier transform techniques of the IMSL (20) library routine FFTRC were utilized. Several different time intervals were chosen to give overlapping spectra over the different frequency decades.

A.4 Semi-Infinite Time Interval

To calculate the zero frequency power spectra, a Gaussian quadrature formula (21) was utilized.

$$\int_0^{\infty} e^{-x} f(x)dx = \sum_{i=1}^{n} C_i f(x_i)$$

The absissas and weights for the sixteen points are given in Table 9.

Table 9 - Semi-Infinite Interval Quadrature Formula

x_i	C_i
.087649	.206152
.46270	.331058
1.14106	.265796
2.12928	.136297
3.43709	.473289 E-01
5.07802	.113000 E-01
7.07034	.184910 E-02
9.43831	.204272 E-03
12.21422	.148446 E-04
15.44153	.682832 E-06
19.18016	.188100 E-07
23.51591	.286235 E-09
28.57873	.212708 E-11
34.58340	.629797 E-14
41.94045	.505047 E-17
51.70116	.416146 E-21

A.5 Von Karman Correlation Function

Central to all of the previous numerical integration procedures is the need to compute the integrand. In this case the integrand will involve the evaluation of

$$f(\mu) = b\left(\frac{\mu}{a}\right)^{1/3} K_{1/3}\left(\frac{\mu}{a}\right)$$

and

$$g(\mu) = \frac{1}{2}\mu f'(\mu)$$

where $K_{1/3}(\cdot)$ = Modified Bessel function order of 1/3

These functions are evaluated by the subroutine VK developed by Holley and Bryson (22). The method utilizes spline interpolation and asymptotic expansion giving a result accurate to six significant figures over a wide range of arguments.

REFERENCES

1. Thresher, R.W., Holley, W.E. and Jafarey, N., "Wind Response Characteristics of Horizontal Axis Wind Turbines," Proc. Second DOE/NASA Wind Turbine Dynamics Workshop, Cleveland, Ohio, Feb. 24-26, 1981.

2. Frost, W., Long, B.H. and Turner, R.E., Engineering Handbook on the Atmospheric Environmental Guidelines for Use in Wind Turbine Generator Development, NASA Technical Paper 1359, Dec. 1978, p. 4.10-4.42.

3. Powell, D.C. and Connell, J.R., Definition of Gust Model Concepts and Review of Gust Models, Battelle, Pacific Northwest Laboratory, PNL-3138, June 1980, Section 4.

4. Rice, S.O., "Mathematical Analysis of Random Noise," Bell System Technical Journal, V. 24, n. 1 (1945), pp. 46-156.

5. Taylor, G.I., "Eddy Motion in the Atmosphere," Phil. Trans. of the Royal Soc., London, .. V. A215 (1915), pp. 14-22.

6. Kaimal, J.C., "Turbulence Spectra, Length Scales and Structure Parameters in the Stable Surface Layer," Boundary Layer Meteorology, V. 4 (1973), p. 300.

7. Panofsky, H.A., et. al., "The Characteristics of Turbulent Velocity Components in the Surface Layer Under Convective Conditions," Boundary Layer Meteorology, V. 11 (1977), pp. 355-361.

8. Busch, N.E., "The Surface Boundary Layer," Boundary Layer Meteorology, V. 4 (1973), pp. 213-240.

9. Batchelor, G.K., The Theory of Homogeneous Turbulence, Cambridge, 1953, pp. 169-187.

10. Von Karman, T., "Sur la Theorie Statistique de la Turbulence," Comptes Rendus des Seanies de l'Academie de Sciences, V. 226 (1948), pp. 2108-2111.

11. Kolmogonov, A.N., "The Local Structure of Turbulence in Incompressible Viscous Fluid for Very Large Reynolds Numbers," Doklady Acad. of Science, USSR, V. 30 (1941), p. 301.

12. Etkin, B., Theory of Flight of Airplanes in Isotropic Turbulence, AGARD Report 372, 1961.

13. Chalk, C.R., et. al., Background Information and User Guide for MIL-F-8785B, AFFDL-TR-69-72, Aug. 1969.

14. Melsa, J.L. and Sage, A.P., Estimation Theory with Applications to Communications and Control, McGraw-Hill, 1971, p. 35.

15. Panofsky, 1977, loc. cit.

16. Counihan, J., "Adiabatic Atmospheric Boundary Layers: A Review and Analysis of Data from the Period 1880-1972," Atmospheric Environment, V. 9 (1975), pp. 871-905.

17. Goodwin, G.C. and Payne, R.L., Dynamic System Identification, Acad. Press., 1977, pp. 229-232.

18. Pierce, W.H., "Numerical Integration Over the Planar Annulus," J. Soc. Indust. Appl. Math., V. 5 (1957), pp. 66-73.

19. Stroud, A.H. and Secrest, D., "Gaussian Quadrature Formulas," Prentice-Hall (1966), p. 256.

20. IMSL, Inc., IMSL Library Ref. Manual, 7500 Bellaire Blvd., Houston, TX 77036, p. FFTRC-1.

21. Stroud (1966) loc. cit.

22. Holley, W.E. and Bryson, A.E., Wind Modeling and Lateral Aircraft Control for Automatic Landing, Dept. of Aeronautics and Astronautics, Stanford University, SUDAAR #489 (1975), pp. 78-80.

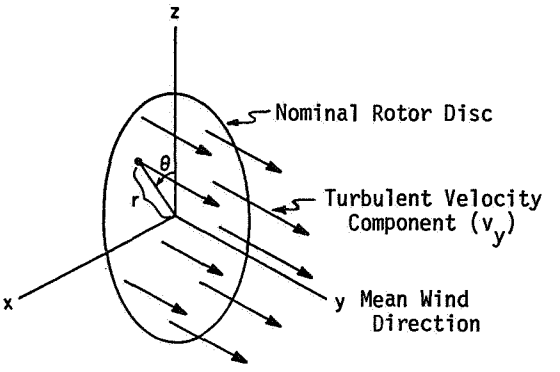

Figure 1: Rotor Disc Coordinates

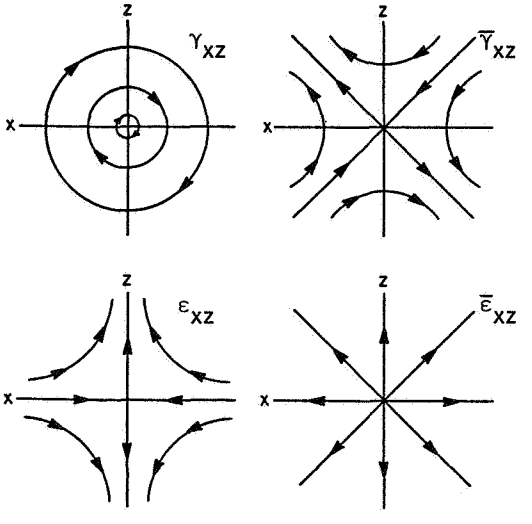

Figure 2: In-Plane Velocity Gradient Terms

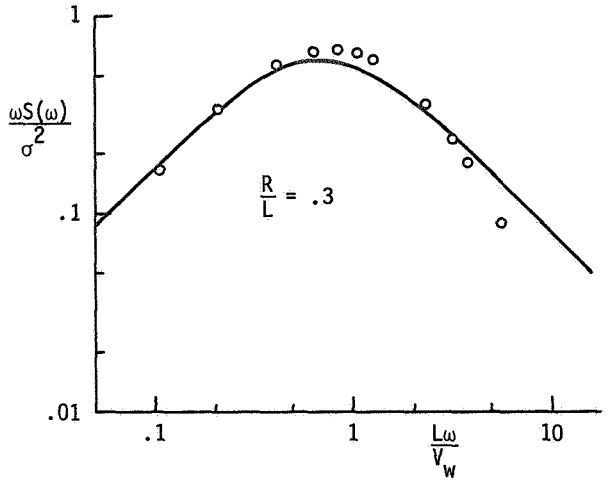

Figure 3: Dimensionless Spectrum for Uniform V_y Turbulence Component

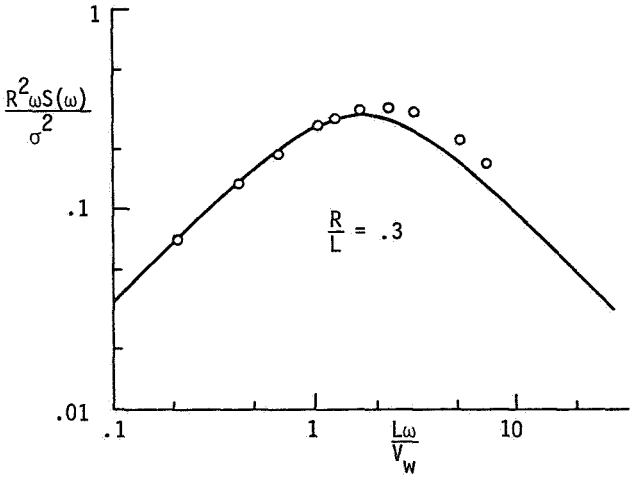

Figure 4: Dimensionless Spectrum for Gradient $V_{y,x}$ Turbulence Component

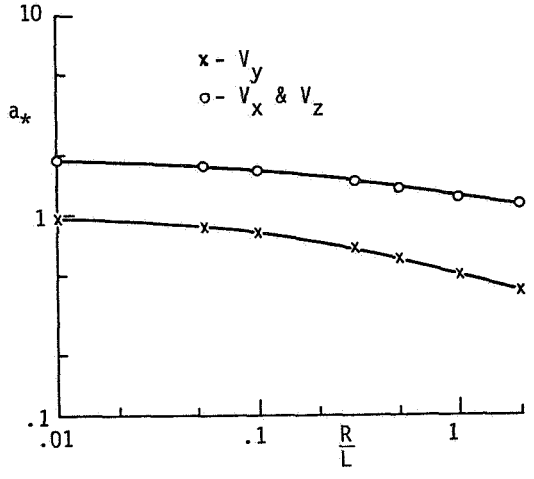

Figure 5: Dimensionless Parameter a_* for Uniform Turbulence Terms

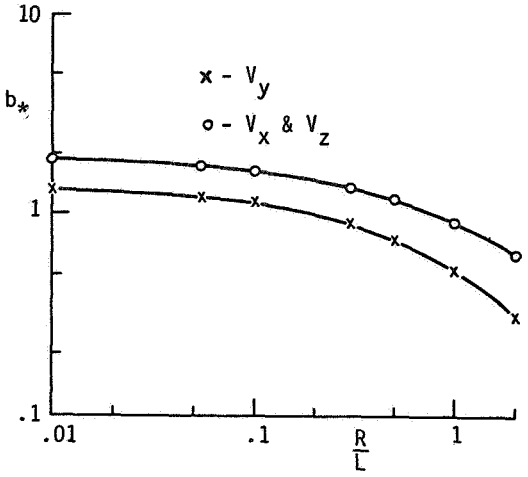

Figure 6: Dimensionless Parameter b_* for Uniform Turbulence Terms

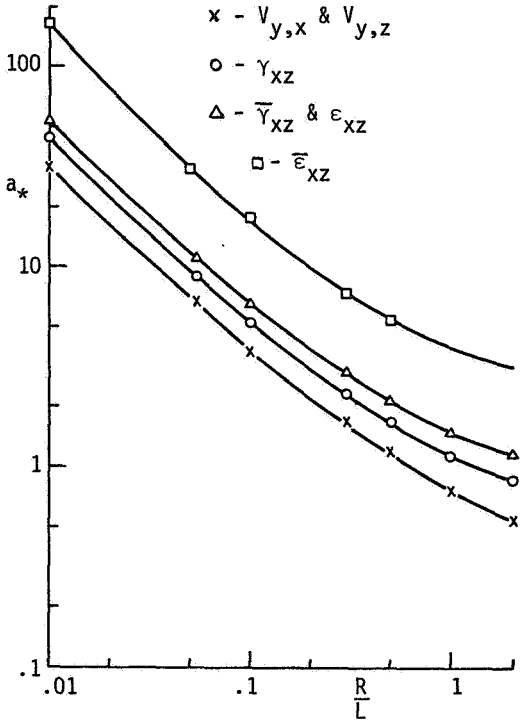

Figure 7: Dimensionless Parameter a_* for Gradient Turbulence Terms

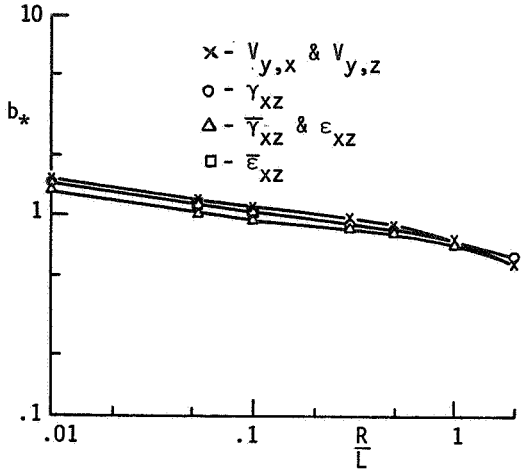

Figure 8: Dimensionless Parameter b_* for Gradient Turbulence Terms

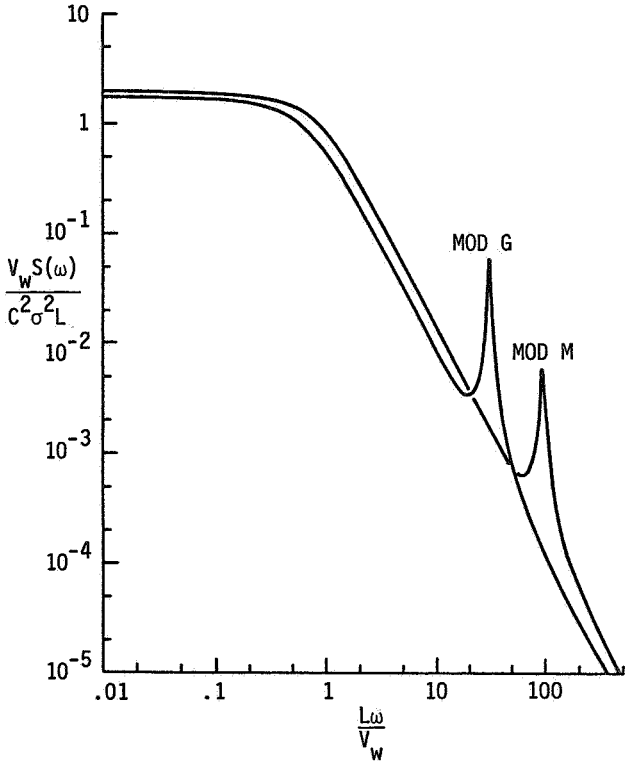

Figure 9: Dimensionless Spectrum for Rotating Blade Force

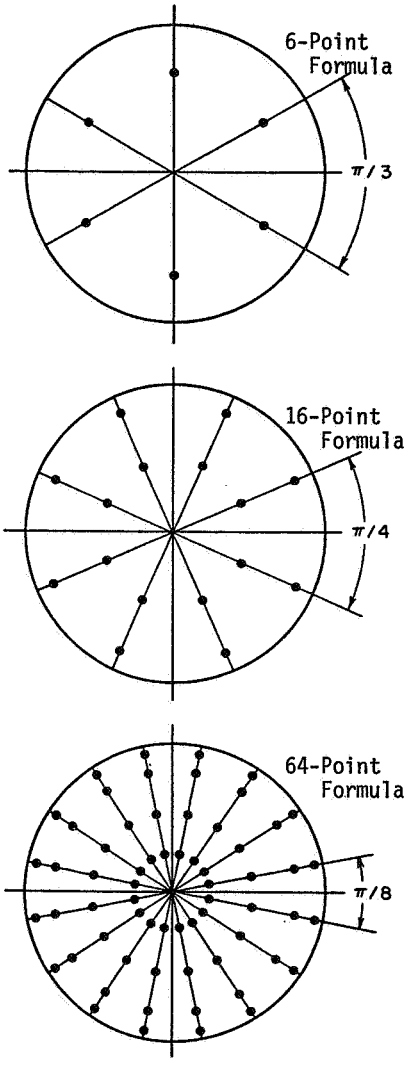

Figure 10: Unit Circle Point Distribution for Disc Area Integration

QUESTIONS AND ANSWERS

W.E. Holley

From: L.P. Rowley

Q: How would you propose verifying your model?

A: *We intend to compare the statistical results predicted by the model with results gained from a planar anemometer array. This comparison can be accomplished using results developed in system identification theory. We also would like to compare model predictions with wind turbine field data.*

From: T.E. Base

Q: Does your turbulence model satisfy the conservation equation, i.e., continuity?

A: *Yes, the Von Karman correlation function satisfies the constraint imposed by the continuity equation. To the degree that the model approximates the Von Karman correlation function, it also satisfies continuity.*

From: L. Mirandy

Q: Is the only spatial effect in your model due to rsin θ, rcos θ terms (gradients $V_{i,x}$, $V_{i,z}$ depend only on time) or do you have a spatial correlation like Dr. Sundar?

A: *The spatial variation effect includes only rsinθ and rcosθ effects. Other more disorganized spatial variations are ignored. These higher order terms are the source of the error discussed in the paper.*

APPLICATIONS OF THE DOE/NASA WIND TURBINE ENGINEERING INFORMATION SYSTEM

Harold E. Neustadter and David A. Spera
National Aeronautics and Space Administration
Lewis Research Center
Cleveland, OH 44135, (216)433-4000

ABSTRACT

The NASA Lewis Research Center manages for the Department of Energy, the technology and engineering development of large horizontal axis wind turbines. In support of this activity each wind turbine has a variety of information systems used to acquire, process and analyze data. In general four categories of data systems, each responding to a distinct information need, can be identified. The categories are: Control, Technology, Engineering and Performance.

The focus of this report is on the information that can be extracted by statistical analysis of data obtained from the Technology and Engineering Information Systems. These systems consist of the following elements: (1) sensors which measure critical parameters (e.g., wind speed and direction, output power, blade loads and component vibrations; (2) remote multiplexing units (RMUs) on each wind turbine which frequency-modulate, multiplex and transmit sensor outputs; (3) on-site instrumentation to record, process and display the sensor output; and (4) statistical analysis of data at the NASA-Lewis Research Center in Cleveland, Ohio.

Two examples of the capabilities of these systems are presented. The first illustrates the standardized format for application of statistical analysis to each directly measured parameter. The second shows the use of a model to estimate the variability of the rotor thrust loading, which is a derived parameter.

INTRODUCTION

The U.S. Government has established a Wind Energy Program within the Department of Energy (DOE) to encourage the development and promote commercialization of wind energy systems. One phase of this program is being managed by the NASA Lewis Research Center (LeRC). An agreement with DOE stipulates that LeRC shall manage both the Technology and Engineering Development for large (100 kW) horizontal axis wind turbines (ref. 1). Four wind turbine projects, designated the Mod-0 (ref. 2), Mod-0A (ref. 3), Mod-1 (ref. 4), and Mod-2 (ref. 5), are part of the current development program. In addition to these projects, efforts aimed at achieving lower machine costs have been initiated. These include advanced multi-megawatt (Mod-5) and 200 to 500 kW (Mod-6) wind turbine projects. With regard to all these machines, LeRC has the responsibility to monitor, and report on their performance.

Despite the diverse characteristics of these machines, we can nonetheless identify four distinct information/user categories that are common to all wind turbines; namely, operations/the wind turbine itself; technology/field operations personnel; engineering/system and component designers; performance/dispatchers or investors. The requirements for each category, as seen in Figure 1, are sufficiently disjoint that separate data systems have evolved to meet each need.

At one extreme, with the highest sampling rates, are the computer based control systems which govern the routine operation of each wind turbine generator. The data portion of the control system provides information regarding adequacy of the wind, status of all critical systems, machine alignment with the wind, etc., and often monitors more than 100 sensors. For certain critical parameters the control system must be capable of responding within milliseconds. This system is considered to be an integral part of the wind turbine and varies significantly from one design to the next.

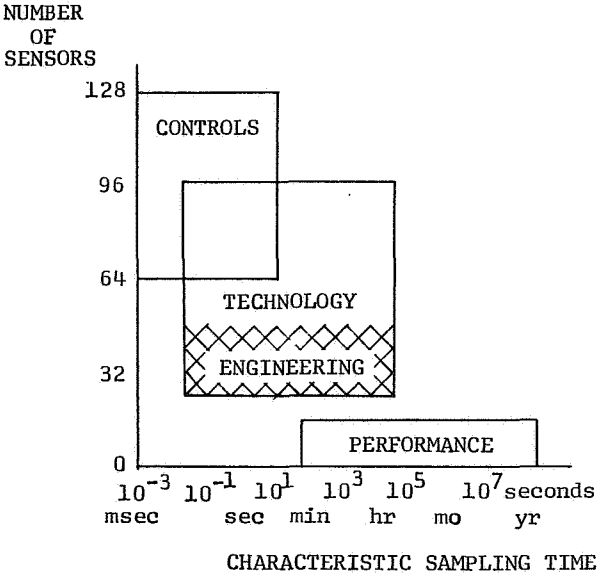

Figure 1 - The approximate relationship between the number of sensors, characteristic sampling time and the function of a data system.

At the other extreme, with the lowest sampling rate, is the performance system to provide information for evaluation of a wind turbine's availability, reliability and energy production. These data requirements are generally limited to meteorological, electrical and structural parameters with time scales ranging from one hour to the lifetime of the machine.

The two remaining information systems, Technology and Engineering, are discussed in greater detail in the remainder of this report. The next section deals with signal conditioning, data acquisition and display and the subsequent routine digital pre-processing. The third section provides an example of the standardized statistical analyses. The fourth section presents a technique to estimate variability in the rotor thrust, which itself is not measured directly but is derived from the flatwise bending moment.

TECNOLOGY AND ENGINEERING INFORMATION SYSTEMS

The Technology Information System has three functionally (and spatially) distinct components, as seen in Figure 2(a). The data signals from the sensors move through the system in the sequence: signal conditioning, acquisition/display, and statistical analysis. Physically, these three functions occur: on the wind turbine, at or near the base of the wind turbine tower and at LeRC, respectively. As was seen in Figure 1(a), the Engineering Information System is a subset of the Technology Information System in that fewer sensors are monitored. In addition, the Engineering System uses significantly less electronic equipment at each wind turbine site. As a consequence, if a statistical analysis is desired, some further processing and display is performed at the Plum Brook Station as illustrated in Figure 2(b).

The wind turbines monitored by LeRC vary considerably in their size, location, blade composition and design. Despite, and to some extent because of, this variability, it was decided that all data system implementations should have the same (or functionally equivalent) hardware and software.

Signal Conditioning

Signal conditioning is performed by a Remote Multiplexing Unit (RMU) (ref. 6). As input, an RMU can accept up to 32 low-level or high-level data signals from a variety of transducers. Each RMU contains reference junctions for thermocouples as well as the necessary electronics for excitation and bridge completion of strain gauges. Each DOE/NASA wind turbine has one RMU located in the hub, another in the nacelle and a third unit at the base of the tower in the control room. A listing of all the transducers monitored during the initial testing of Mod-1 has been reported elsewhere.(ref. 7)

After a signal is received at the RMU it is conditioned (scale and/or offset, amplification or attenuation) to a common range and frequency multiplexed for output. Each RMU can generate two multiplex groups. Each multiplex group consists of up to 16 FM signals (+ 125 Hz centered at 500 Hz intervals from 1000 Hz thru 8500 Hz) plus a precise reference tone at 9500 Hz. Other significant features of the RMU include a 4-pole active Butterworth low-pass filter, end-to-end system calibration capability (upon command from an external source) and one kilometer signal transmission via coaxial cable.

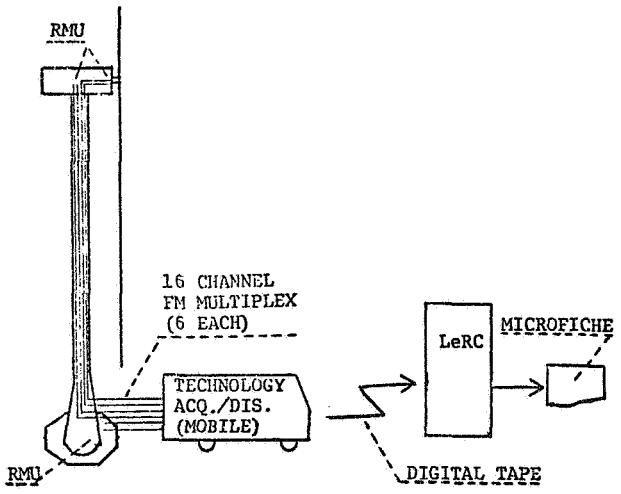

2(a) Technology Information System

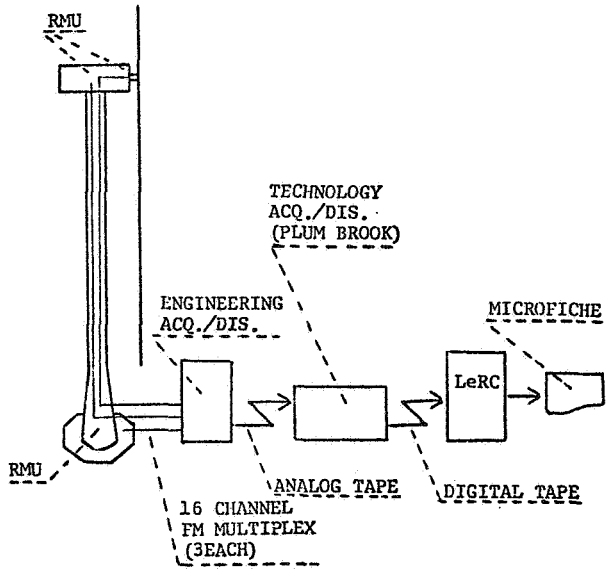

2(b) Engineering Information System

Figure 2 - Schematic representation of the DOE/NASA Wind Energy Technology and Engineering Information Systems.

Acquisition/Display

LeRC has two functionally equivalent Technology Acquisition/Display units. One unit is installed in a mobile van and is used to support field engineers, at wind turbine sites, thru assembly, check-out and initial operation of the first unit of each new wind turbine design. It is presently located at the Mod-2 site in Goodnoe Hills, Washington. The other unit is installed at the LeRC Plum Brook Station, Sandusky, Ohio. In addition to processing analog tapes received from those wind turbine sites equipped with Engineering Acquisition/Display units, it is also used in the Supporting Research and Technology program based on the Mod-0 machine.

A schematic representation of the electronic data processing capability of the mobile unit is shown in Figure 3(a). All RMU-generated FM multiplexes entering this unit are, with the addition of a time code, recorded in direct analog form. This recording capability is independent of any other equipment or processing activity within the unit. Simultaneously, the data can also be routed thru a bank of six sets of 16 discriminators which de-multiplex the signals and generate analog (±5V) signals. Any or all of these 96 analog signals can be digitized and routed thru the mini-computer. From there they can be processed for real-time digital display on the CRT and/or for transmittal on digital tape to LeRC for further analysis. In addition, any 24 of the 96 analog signals may be selected for display on strip charts and any single analog signal may be routed to a spectrum analyzer for frequency content evaluation. All the components shown with a stippling in Figure 3(a) can be set up and run under computer control at the discretion of the unit operator via the control terminal. This unit was designed with sufficient capacity to simultaneously support up to three wind turbines at a single site.

Even after the initial check-out of a new wind turbine design, LeRC retains the responsibility to monitor and report the wind turbine's performance. However, the Technology Acquisition/Display unit is too elaborate and expensive for long term monitoring at each site. Therefore, we have identified a functional subset, the Engineering Acquisition/Display unit, which is installed in the control area of each wind turbine. This latter unit provides on-line analog display on strip chart (eight channels per wind turbine) and continuously records 48 signals (as three FM multiplexes) plus time code on four tracks of analog magnetic tape. The analog magnetic tape recorder operates in either of two modes, depending on local conditions and requirements. At some sites it records until the tape is full (32 hours) and then automatically rewinds (10 minutes) and restarts, erasing old data as new data are recorded. At other sites the recorder operates for 96 hours (by making three passes thru the tape using a total of 12 tracks) and then automatically turns off. It remains off until the tape is replaced and the unit is manually restarted.

Large volumes of data are often of little value in their raw form. Even after processing, they may well be of negligible value if the end product is overwhelmingly voluminous, inadequately disseminated, or excessively delayed. To preclude these occurrences we routinely perform statistical analyses of both the technology and the engineering data. Condensed summaries are provided in both graphic and tabluar form, using microfiche as the distribution medium.

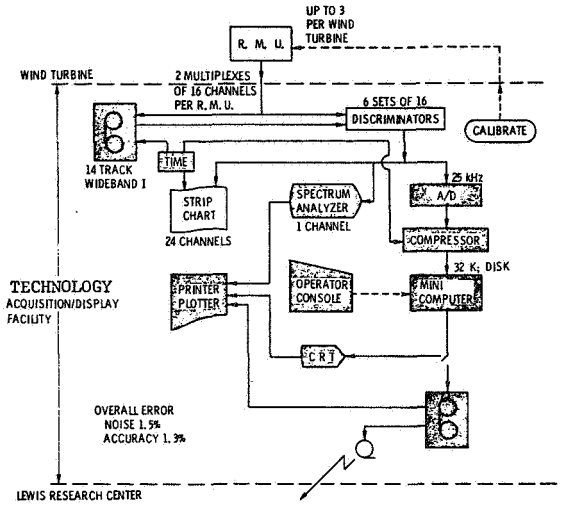

3(a) Technology Acquisition/Display Unit

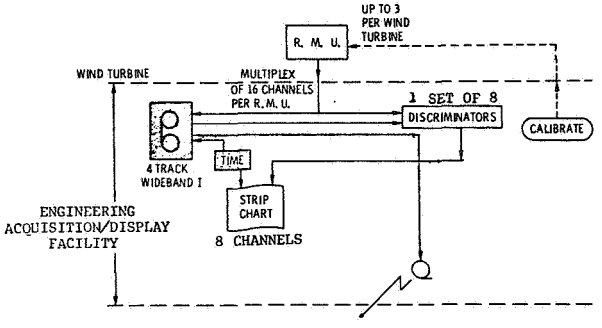

3(b) Engineering Acquisition/Display Unit

Figure 3 - Schematic representation of the electronic data processing in the Teccnology and Engineering Acquisition/ Display Units. In the Technology Unit, each device shown with stippling can be controlled by the operator from the console.

Digital Pre-Processing

Digital magnetic tapes can be generated at either of the Technology Acquisition/ Display units. The digital data consist of 11 readings per parameter per (nominal) revolution and are stored as a tightly packed, randomly sequenced record. Each datum is accompanied by an identifying tag. Time markers (to nearest millisecond) are merged with the data.

As the first step on the LeRC main frame system, these data tapes are transferred to disk for short term storage. During the transfer process, the internal representation is transformed (in software) from ASCII to EBCDIC. The next step compacts this initially large dataset ($5x10^6$ data values + $5x10^6$ tags + $1x10^6$ time markers) into a more manageable form, as follows. The rotor shaft position is used to mark the start of each rotation. These markers are then combined with the associated time markers and processed to give rotor speed (rpm) as a function of time. Then, the data from approximately 30 sensors of general interest are screened to yield maximum and minimum values for each parameter for each revolution of the rotor. This smaller data set ($5x10^5$data values) is stored on disk and is the data base for all further processing. In the final step, this latter data set is processed onto a microfiche containing the time history and statistical summary of each parameter of general interest. This entire process is shown schematically in Figure 4.

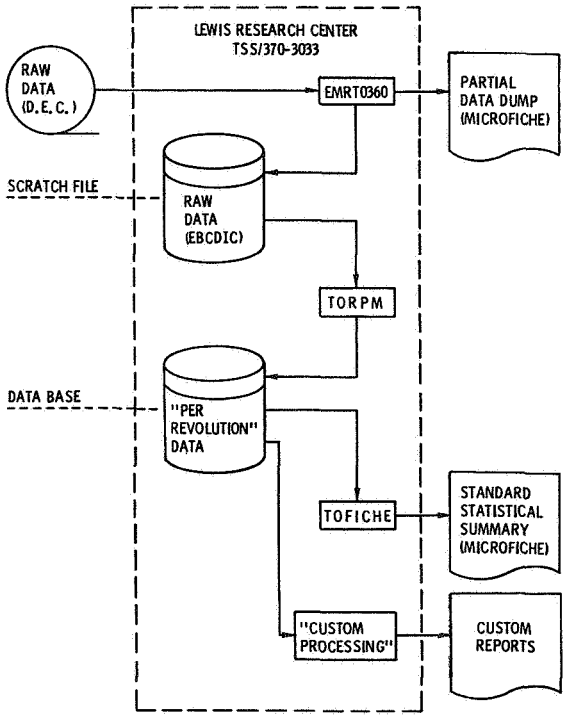

Figure 4 - Schematic represenatation of the final step in information processing using the LeRC main computer facility.

EXAMPLE 1: STANDARD STATISTICAL ANALYSIS

While the specific set of sensors and their associated scale factors will vary from machine to machine, nevertheless, a single analysis procedure and a common presentation format is applied to all data from all machines.

The data, which are stored in the data base as maximum and minimum values for each revolution, are transformed to represent the midpoint and cyclic values for each revolution. The transformation equations are:

$$\text{midpoint} = (\text{maximum} + \text{minimum}) / 2$$

and

$$\text{cyclic} = (\text{maximum} - \text{minimum}) / 2) \times (1 + f(\text{rpm}))$$

where,

$$f(\text{rpm}) = 2x10^{-5} (\text{rpm})^2.$$

The correction function, f(rpm), is introduced to compensate for the consistent underestimation of cyclic values resulting from the data sampling rate of 11 per (nominal) revolution.

The results of the analysis of each sensor are displayed as two frames, one graphical and one tabular on the microfiche card. An example of the graphical output is shown in Figure 5 and of the tabular output in Table I. These data were recorded by the on-site Engineering Acquisition/Display unit on January 5, 1981, and cover more than 12,000 consecutive revolutions of continuous machine operation.

The first frame for each sensor contains three graphs. On each graph there are two plots, one of the midpoint values with circles as symbols and the other of the cyclic values with diamonds as symbols. The three graphs are:

1. Time history. The top graph smooths and summarizes the information that one associates with a continuous trace on a strip chart recorder. One plot is of the average, over 30-second intervals, of the midpoint values. The other plot is of the corresponding cyclic values.

2. Partitioned distributions (ref. 8). The abscissa for this center graph is the wind speed midpoint value as measured at hub height. These wind speed values are used as the basis for sorting the data from the sensor of interest. These latter values are grouped into subsets such that for each subset all the sensor data values were obtained at approximately the same measured wind speed. Then the data values within each subset are separately ranked in ascending order. The 16th and 84th percentile for each such sequenced subset are displayed as horizontal tabs at the end of a vertical bar. We also estimate the confidence interval (at the 0.95 level) for significant differences of the median[8] and display it as an interval (denoted by a pair of circles or diamonds) on the same vertical bar. This entire process is performed separately for the midpoint (circle) and cyclic (diamond) data values.

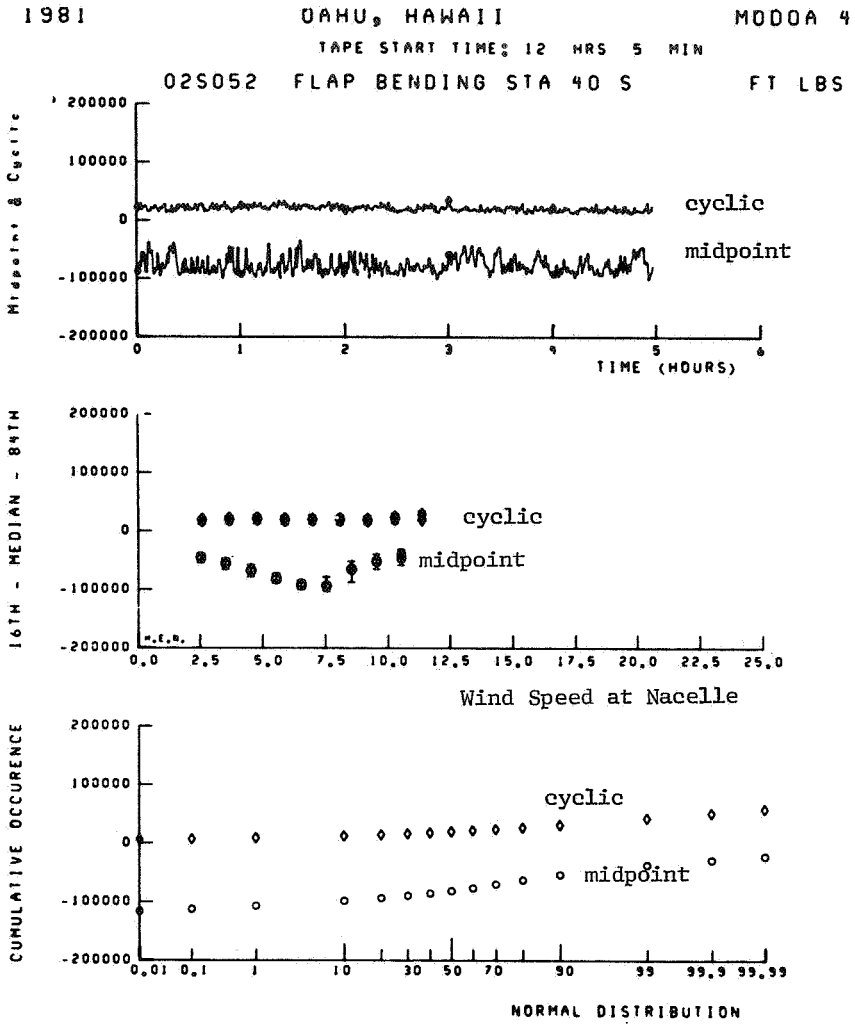

Figure 5. - Sample frame showing the three graphs produced by the standardized statistical processing for each parameter. The above graphs comprise over 12,000 rotor revolutions and were recorded by the on-site Engineering Acquisition/Display Facility. (nt-m = 1.356 ft-lb).

Table I. Distributional Information from Figure 5, in Tabular Form

1981 OAHU, HAWAII
TAPE START TIME: 12 HRS 5 MIN
02S052 FLAP BENDING STA 40 S FT LBS

---------- SEGMENTED DISTRIBUTIONS ----------

MIDPOINT						CYCLIC					
WIND	MINIMUM	16TH PCTL	MEDIAN	84TH PCTL	MAXIMUM	WIND	MINIMUM	16TH PCTL	MEDIAN	84TH PCTL	MAXIMUM
2.5	-7.1E 04	-5.3E 04	-4.42E 04	-3.8E 04	-3.0E 04	2.6	8.4E 03	1.3E 04	1.83E 04	2.4E 04	4.3E 04
3.5	-9.1E 04	-6.4E 04	-5.36E 04	-4.6E 04	-2.8E 04	3.7	6.2E 03	1.4E 04	1.97E 04	2.7E 04	5.0E 04
4.5	-1.0E 05	-7.7E 04	-6.63E 04	-5.6E 04	-3.4E 04	4.8	6.5E 03	1.5E 04	2.07E 04	2.9E 04	5.9E 04
5.5	-1.1E 05	-8.7E 04	-7.96E 04	-7.1E 04	-4.7E 04	5.9	5.3E 03	1.3E 04	1.90E 04	2.3E 04	5.7E 04
6.5	-1.1E 05	-9.8E 04	-9.03E 04	-8.3E 04	-4.5E 04	7.0	5.5E 03	1.4E 04	1.99E 04	2.9E 04	5.2E 04
7.5	-1.2E 05	-1.0E 05	-9.20E 04	-7.7E 04	-4.9E 04	8.1	6.0E 03	1.3E 04	1.95E 04	2.8E 04	5.7E 04
8.5	-1.1E 05	-8.5E 04	-6.36E 04	-5.0E 04	-2.8E 04	9.2	6.3E 03	1.4E 04	1.89E 04	2.7E 04	5.9E 04
9.5	-1.1E 05	-6.3E 04	-4.99E 04	-3.8E 04	-1.6E 04	10.3	1.0E 04	1.5E 04	2.25E 04	3.1E 04	4.8E 04
10.5	-7.3E 04	-5.6E 04	-4.12E 04	-3.0E 04	-2.5E 04	11.4	2.0E 04	2.0E 04	2.42E 04	3.6E 04	4.7E 04

--------- CUMULATIVE DISTRIBUTION ----------

FREQUENCY	MIDPOINT	CYCLIC	MAXIMUM	MINIMUM
0.0001	-114862.8	5476.3	-98162.8	-156445.8
0.0010	-111229.9	6500.0	-94183.0	-149613.9
0.0100	-105859.9	8684.0	-88825.9	-136587.9
0.1000	-97175.9	12358.0	-78638.9	-120388.9
0.2000	-92332.9	14529.0	-72793.9	-113875.9
0.3000	-88157.9	16199.0	-67784.0	-109032.9
0.4000	-84149.9	17869.0	-63108.0	-104857.9
0.5000	-80142.0	19706.0	-57931.0	-100683.0
0.6000	-75299.0	21543.0	-52587.0	-95840.0
0.7000	-68786.0	23714.0	-46909.0	-89160.0
0.8000	-61438.0	26553.0	-39895.0	-80643.0
0.9000	-52253.0	30895.0	-31545.0	-70623.0
0.9900	-36054.0	42214.5	-13008.0	-53255.0
0.9990	-27704.0	50447.7	4026.0	-44571.0
0.9999	-21330.6	57404.9	13337.6	-40255.1

3. Cumulative distribution. The bottom graph corresponds to a normal distribution, i.e., the abscissa is in units of normalized standard deviations and segmented with tick marks labelled by percentiles. Such a graph has the attribute that if the plotted data have a normal (i.e., gaussian) distribution, the plot will be linear. For this graph the entire set of all midpoint values is sequenced and plotted by percentile. This process is repeated, separately, for the cyclic values.

The second frame (see Table I) for each sensor presents tabular listings of the plotted data points from both distributional graphs. Some additional (non-plotted) data are also tabulated. Because some of these are extreme values (i.e., maxima and minima), these latter tabulated values must be addressed with caution as they might represent spurious noise.

EXAMPLE 2: ROTOR THRUST STATISTICS

As an example of using these data systems to obtain information about non-measured parameters, consider a calculation procedure which can be applied to estimate the variability in the rotor thrust from the measured flatwise bending moment data of a wind turbine blade. First an anlysis is made of the changes in the flatwise bending moment, which is a measured parameter. Then the changes in flatwise bending moment are related to changes in rotor thrust, which is a derived parameter, and developed as a normalized "range" (i.e., variability) coefficient.

Flatwise (Midpoint) Moment Range

The first step is to produce a pseudo-spectrum for the flatwise bending moment. The procedure starts with a data set consisting of the midpoint values (as defined in the previous section and as shown in figure 5) of the measured bending moment for each of some large number, n, of rotor revolutions. From these data, the range, i.e., the maximum minus the minimum, is calculated repeatedly over successively doubled time intervals. That is to say, the calculation of range values is made over every two cycles, again over every four cycles, again over every eight cycles, etc. This procedure yields n range values of the midpoint flatwise bending moment.

These range values are sorted in ascending order and plotted as a standard normal probability graph, as shown in Figure 6, using the scale shown to the left. The data for this particular calculation are the same data as seen earlier in Figure 5. The flatwise bending moment was measured near the root end of the blade at approximately five percent of the span, i.e., 100 cm from the axis of rotation. The median of the range of the flatwise bending moment data is 8,800 N-m and the 84th percentile is 24,400 N-m.

These same data are replotted in Figure 6 for the same abscissa, but using as the ordinate the logarithmic scale to the right of the graph. The fit of the straight line to these data from the 50th to the 99th percentiles indicates a log-normal distribution that is truncated at the very high end. When the same analysis is made on data which include start-up/shut-down sequences, there is no truncation of the distribution and log-normality prevails to the uppermost extent of the data set (ref. 9). In either case the results in the region from the 50th to 99th percentile are essentially the same. Therefore, the information extracted is drawn from the central region of the distribution which is, in statistical jargon, more robust.

Rotor Thrust

The conversion from mean flatwise bending moment to mean rotor thrust is made by using the MOSTAB-WT (ref. 10) simulation program to determine the ratio, C, of the change in thrust to the change in flatwise bending (N/N-m). For wind speeds below the rated wind speed (11 m/s) C = 0.016, and for wind speeds above the rated wind speed, C = 0.011. Since both conditions occurred during the machine operation and the calculations described above do not distinguish between these two cases, an average of the two cases, C = 0.013, is acceptable for this analysis. Applying this average value to the flatwise moment range data in Figure 6, we obtain the average results shown in Table II. The median value of the range of the rotor thrust is 1600 N and the 84th percentile is 4400 N. This information can be normalized by the rotor thrust at rated wind speed (32,000 N) and restated as a dimensionless parameter. This gives the dimensionless values of 0.05 at the 50th percentile and 0.14 at the 84th percentile for the ratio of the range of rotor thrust to the rotor thrust at rated wind speed.

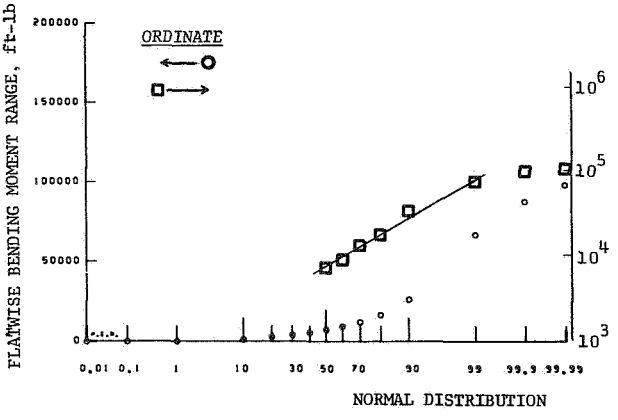

Figure 6 - Normal probability plots for the range of variability in the flatwise bending moment, based on the same data as in Figure 5.

Table II Rotor Thrust Varability for Mod-0A

$$\frac{\text{change in rotor thrust}}{\text{change in flatwise bending moment}} = 0.013m^{[1]}$$

rotor thrust at rated wind speed= 32,000 nt

Parameter	Median	84th Percentile
flatwise moment range (midpoint), nt-m	8,800	24,400
rotor-thrust range, nt-m	1600	4400
$\frac{\text{rotor thrust range}}{\text{rotor thrust at rated wind speed}}$	0.05	0.014

CONCLUDING REMARKS

Two related data systems, one for technology development and the other for engineering evaluation, have been identified and described. Typical data, in this instance six consecutive hours of flatwise bending moment data were presented. The description of the extraction of information thru the application of statistical analyses included both the standardized analysis procedure and an analysis specific to evaluating rotor thrust.

REFERENCES

1. Wind Energy Systems Program Summary, Raytheon Service Company, DOE/CS/20097-01, 1980.

2. Glasgow, J. C. and Birchenough, A. G., Design and Operating Experience on the U.S. DOE Experimental Mod-0 100 kW Wind Turbine, NASA TM-78915, 1978.

3. Glasgow, J. C. and Robbins, W. H., Utility Operational Experience on the NASA/DOE Mod-0A 200 kW Wind Turbine, NASA TM-79084, 1979.

4. Puthoff, R. L.; Collins, J. L. and Wolf, R. A.: Installation and Checkout of the DOE/NASA Mod-1 2000 kW Wind Turbine Generator, NASA TM-81444, 1980.

5. Mod-2 Wind Turbine System; Concept and Preliminary Design Report, Boeing Engineering and Construction, NASA CR-159609, 1979.

6. DOE/NASA Wind Turbine Data Acquisition System (Part 1: Equipment), EMR Data Systems, NASA CR-159779.

7. Neustadter, H.: Data Acquisition and Analysis in the DOE/NASA Wind Energy Program, NASA TM-81603, 1980.

8. McGill, R.; Tukey, J. W. and Larsen, W. A.: Variations of Box Plots, The American Statistician, Vol. 32, No. 1, P. 12-16, 1978.

9. Hoffman, J. A.: Wind Turbine Analysis Using the MOSTAB Computer Program, Mechanics Research Incorporated, MRI 2690-1, 1974.

10. Preliminary Calculation of Pseudo-Spectra for Mod-0A Rotor Thrust Loading , Lewis Research Center, Wind Energy Project Office, Internal report, PIR 167, 1980.

QUESTIONS AND ANSWERS

H.E. Neustadter

From: G. McNerney

Q: How extensive is the data base for each site, (sample rates, total time, and channels sampled), and is the data available in raw form for dissemination outside NASA?

A: *The raw form of the data is analog recording of FM encoded data and is not available for general distribution. For digital analysis the sampling rate is 11 times per revolution for up to 48 channels over a six hour duration for each analysis performed. There are about 100 analyses currently on microfiche and the production rate is, nominally, one per machine per week.*

From: W.N. Sullivan

Q: What is the turnaround time on creation of engineering information data sets?

A: *Under ideal circumstances it could be 2 or 3 days. Typical turnaround is 7 to 12 days.*

From: P.C. Klimas

Q: 1) Does your data system measure rotor C_p? If so, is the data available?

2) What is the time interval used for the measurements which you "bin"?

A: *1) Not yet, because most sites do not have free-stream wind data available.*

2) The values which are "binned" are the midpoint and cyclic values for a revolution. The time interval depends on the rotor speed.

AN OVERVIEW OF FATIGUE FAILURES AT THE ROCKY FLATS WIND SYSTEM TEST CENTER

C. A. Waldon
Rockwell International
Wind Systems Program
P.O. Box 464
Golden, Colorado

INTRODUCTION

Initially, wind energy state-of-the-art advancements involved the quantity and quality of the power produced by small wind energy conversion systems (SWECS). As wind energy commercialization increases, however, SWECS manufacturers must rapidly adopt rigid reliability programs. Wind machines must not only meet design performance specifications, but they must also perform without costly component or structural failures to assure continued market growth.

This paper is intended to identify potential SWECS design problems and thereby improve product quality and reliability. Mass produced components such as gearboxes, generators, bearings, etc., are generally reliable due to their widespread uniform use in other industries. The likelihood of failure increases, though, in the interfacing of these components and in SWECS components designed for a specific system use. Problems relating to the structural integrity of such components are discussed and analyzed in this report with techniques currently used in quality assurance programs in other manufacturing industries.

SUMMARY OF FAILURES

One of the prime objectives at the Rocky Flats Small Wind Systems Test Center (WSTC) is to determine the operational characteristics of a SWECS over a range of wind speeds up to at least 85 miles per hour (mph). At some point in the testing, most SWECS experience at least one wind storm with 85 to 120 mph winds, and the severe loading on SWECS components has been sufficient to cause failures. In some cases, the entire SWECS is lost due to a critical component failure. At least 40% of the SWECS tested have experienced one or more fatigue-related failures and of all the failures experienced, at least 65% were obvious fatigue (see Table 1). The failures attributed to fatigue have been substantiated by the Rocky Flats Plant Metallurgical Group. Since most of these failures were caused by high short-term stresses, some SWECS that survived conceivably contain parts with fatigue-related damage which has degraded the materials to the point where failure is imminent even though not apparent.

Even though the Rocky Flats wind environment is severe, the accumulative damage from lower wind speeds has also been sufficient to generate a fatigue caused failure. For example, an aluminum hub on one SWECS failed during a storm with a peak velocity of 28.6 m/s (64 mph). The SWECS had previously sustained higher wind speed loadings which apparently initiated or accelerated crack growth.

From the investigations of the failures the following causes have been identified:

1. Loadings higher than expected;
2. Vibrational loading excited within operational range;
3. Thin material was unsupported;
4. Sharp edges and threads caused stress risers;
5. Poor quality assurance on fabrication, welding, handling;
6. Voids or cracks in cast parts (no x-rays made by manufacturer).

DISCUSSION OF FATIGUE FAILURES

High Loadings

The wind energy industry includes the "garage" inventors as well as high technology research companies. Load analysis of SWECS designs range from trial-and-error methods to detailed computer programs. Regardless of the degree of design sophistication, the designer must use common sense and a spatial visualization of conditions that may be detrimental to the survival of a SWECS.

Testing has uncovered such basic problems as skin material of insufficient thickness to sustain high wind loading (Figure 1). Cyclical loading of the

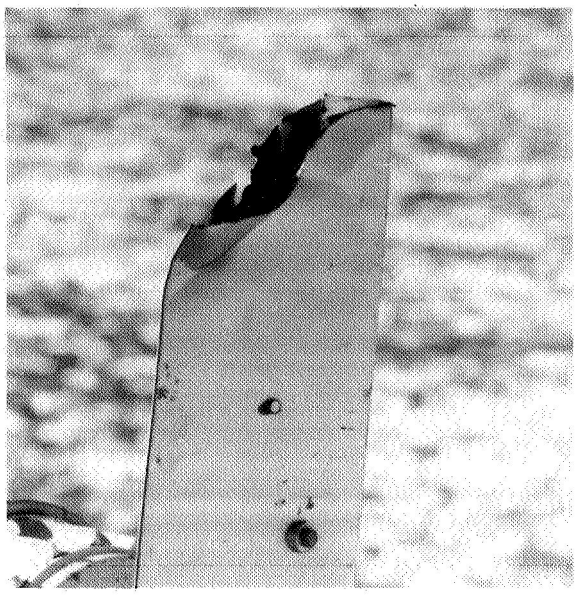

Figure 1 - Blade Skin, Fatigue Failure due to High Loading and no Support Structure.

TABLE I - SUMMARY OF WSTC FAILURES

SWECS NAME	DATE	FAILURE (PARTS & NATURE) AND REFERENCE
Dunlite 81/02550	12/04/78	Blade buckling, fatigue, and ductile fracture; tail boom and hardware fatigue; high wind - 94 mph; RFP-3028/3533/79-12.
Grumman W/S 25		None at WSTC; bolt failure and subsequent hub loss in Wyoming (modified by manufacturer).
Zephyr 15	08/14/78 01/28/78	Weld cracking from high vibration; blade failure (tied) during high winds; RFP-3041/3533/79-13.
Electro WV50G	12/04/78	Yaw shaft - coarse fatigue - multiple cracks in weld heat affected zone; RFP-3004/3533/79/7-1.
Altos 8B	03/25/79	Hub - porosity, sharp edges, hoop stresses led to rapid fatigue during gusts to 64 mph; had experienced higher; RFP-3035/3533/79-10.
American Wind Turbine AWT-16	12/04/78 12/05/78	Rotor (tied) bent in half (12/4/78),breakup (12/5/79); tail - failure still being investigated
Pinson C2E	12/04/78	Hub plates fatigue cracks from vibration; blade skins (3) fatigue cracks from vibration.
Millville 10-3 IND	12/04/78 12/05/78	Blade skins - buckling and fatigue; Weld - cracking from severe cut-in torque; Coupling - fracture from severe cut-in torque. Blade skins - buckling, fatigue and rivet pull through; RFP-2992/3533/79-3.
Parris-Dunn Free-Lite	12/05/79	Hub nut - unscrewed; Rotor shaft keyway - fracture on side; hub collar fracture; 119 mph wind storm.
UTRC (1/3 scale)	09/20/79	Caught upwind, tried to cut-in, and fractured coupling.
Dakota SI-4	12/05/79	Eye bolt weld - fracture - report not released; Blade - fractured on contact with tail boom; tail boom weld - fracture from blade strikes.
Whirlwind A240	04/06/80	Came off tower - cause unknown; Blade - fracture from high rpm and vibration.
Enertech 2 kW HR-1	12/21/79	Lightning rod - fatigue from high vibration.
North Wind 2 kW HR-1	11/79	Rotor shaft - bent, load unknown.
Windworks 8 kW Proto	03/80	Blade - ground contact fractured tip (metal to fiberglass); hub collars - fatigue in corner to porosity; bolts - cracks in threads - fatigue to failure. Report in preparation.
ASI/Pinson 2 kW HR	03/80	Cracks in welds - noted prior to testing.

blade in this example created fatigue cracking and eventual failure. This created high vibration loadings in other components and contributed to their failure as well (Figures 2 and 3).

SWECS which have induction generators must accurately control the rotor rpm and the electrical connection to the grid. The reverse torque from a cut-in at too high a rotor rpm can lead to severe damage to couplings (Figure 4). Secondary damage can be suffered by the rotor and nacelle support structure.

The fact that a SWECS is undergoing maintenance does not eliminate the possibility of damage. A rotor shaft was accidentally bent during a manual manipulation of the rotor system. The bend was discovered when machine operation revealed high rotor vibrations. The associated frequencies were close to other component frequencies and their excitation was also noted. An unbalanced rotor can have the same effect and lead to fatigue failures in several components. The shaft, in this instance, was loaded to the design stress or beyond.

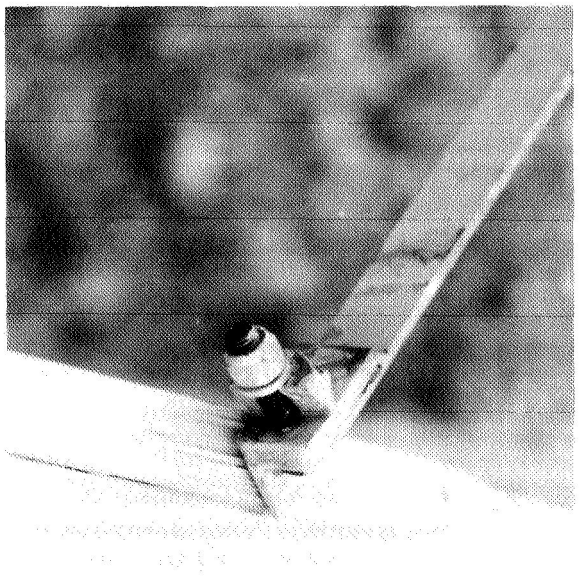

Figure 2 - Tail boom, Attachment fatigue due to high stress and vibration.

VIBRATION

SWECS vibration is often generated during operation of the rotor. The wind loads on the

Figure 3 - Tail boom, Fatigue emanating from attachment holes.

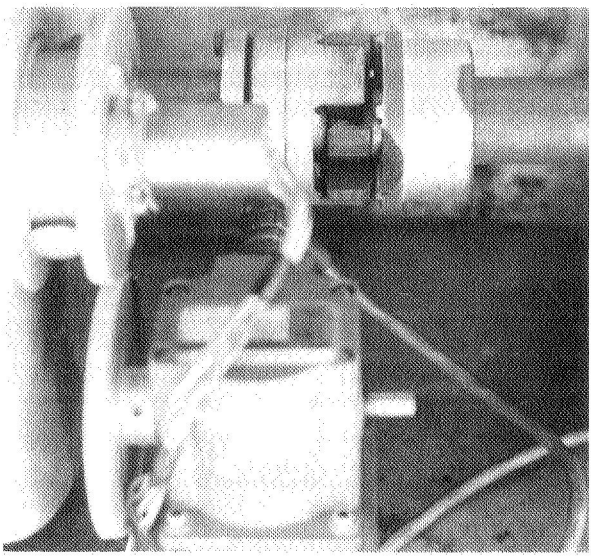

Figure 4 - Coupling, Failure from high torque cutin.

rotor occur with somewhat random frequencies. The frequency durations are short and system damping usually prevents excitation from creating high loadings. The critical points are when SWECS operational frequencies (i.e., rotor rpm) coincide with the fundamental frequencies of the system components. The rotor blades, in particular, are critical because their excitation is transmitted throughout the system and may cause other component excitation.

The rotor vibrations of interest are: 1 per revolution (1P), 2P, and 3P; 1st, 2nd, 3rd fundamental flapwise; 1st torsional; and 1st chordwise blade frequencies. The 1P, 2P and 3P are directly related to operational rpm and are excited by rotor imbalance or aerodynamic loading (i.e., tower shadow) generic to some SWECS configurations. The critical point is where the operational frequency coincides with a blade fundamental frequency.

A typical high vibrational loading failure is shown in Figures 5 and 6. The SWECS underwent a high energy 3P rotor excitation at a frequency where the SWECS and tower interacted (4.5 Hz). The vibrational motion was termed "violent" and led to rapid fatigue growth of cracks in the blade skins and welds at the rotor shaft and support plate joint. In this case, the skin design should have eliminated the stress risers (sharp corners) and firmly attached the skin around the joint to the support arms. However, movement in the skin under operational loadings caused fatigue cracking (Figure 5), and weld cracking (shown in Figure 6) was initiated by severe motions of the rotor and tower. The welds were found to be of good quality, pointing out the need for proper SWECS and tower matching. Modal analysis was conducted after the failure and after installation of a new unit on a different tower. The tests confirmed that first tower and SWECS interacted. They also predicted the new configuration would pass through the rotor 3P excitation, with greatly reduced energy at a frequency of 2.5 Hz of the tower. A new 1P excitation was felt to be a possibility (corresponding to rotor imbalance) but has not been seen to date.

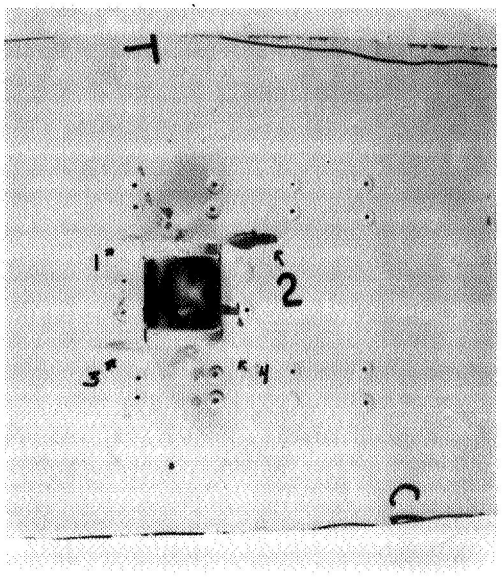

Figure 5 - Overall view of cracks in the skin of a blade. The numbers indicate the cracks.

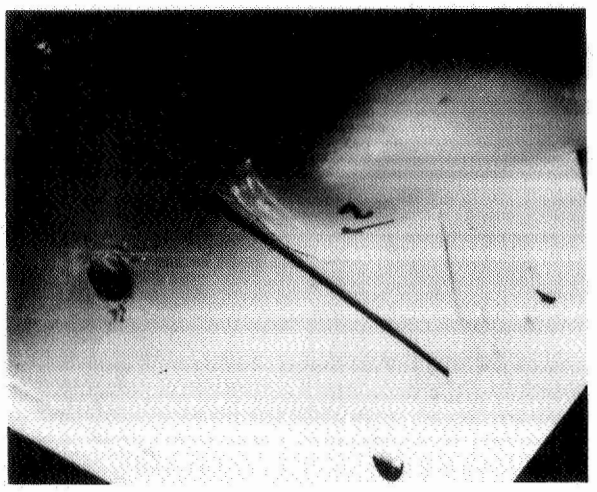

Figure 6 - Overall view of one of the cracks in a plate on the rotor shaft.

Figure 7 shows a 2-minute visicorder trace of a SWECS rotor system with a fundamental 1st bending frequency of approximately 7 Hz. During the modal analysis, it was discovered that two sharp frequency peaks existed, one at 6.6 Hz and the other at 7.2 Hz. Figure 7 shows there is a notable increase in amplitude of the bending and torsion between the corresponding rpm's noted on the trace. An rpm of 396 represents 6.6 Hz and 420 rpm represents 7 Hz. Modal analysis of the loadings that generated this trace confirmed that the fundamental bending and torsional frequencies were present.

Several changes could be made to the system to rectify this problem, but the problem should have been originally noticed in a Fan Diagram and designed out as an undesirable operating point. A typical Fan Diagram is shown in Figure 8. It should be noted that if the diagram is generated by theoretical analysis, it must be substantiated

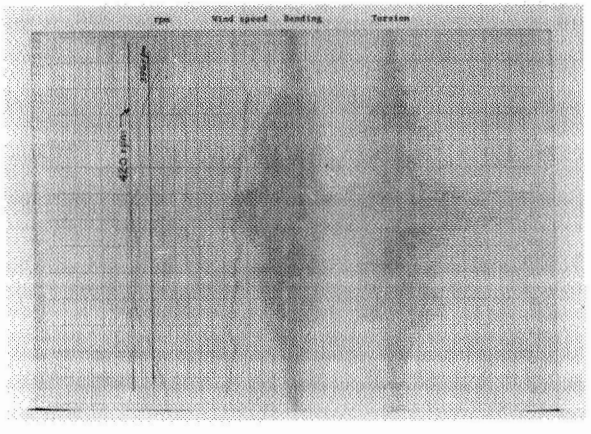

Figure 7 - Visicorder trace of bending and torsional vibration excitation on North Wind Prototype # 1 blade.

for component compliance with predictions, which is sometimes beyond the manufacturer's capability. One possible design change is to modify the blade fundamental frequencies, in this case upward, as 420 rpm is near maximum for the machine. Another change might be to alter the rpm control and not allow the critical rpm to be reached. Both of these changes would have to be checked for interference frequencies with other components prior to implementation.

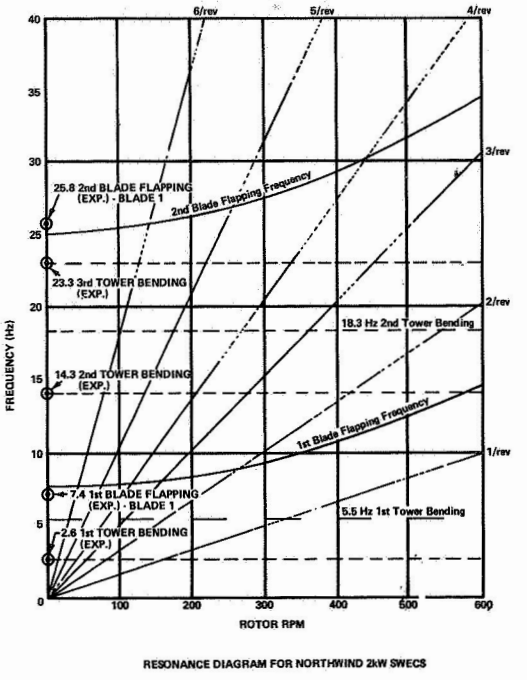

Figure 8 - Typical fan diagram.

Thin Material Loading And Attachment

When SWECS have metal blades, it is common to use a thin skin covering to create the airfoil shape. The substructure could include ribs, stringers and spars. The combination of these parts must be lightweight, yet strong enough to carry the loads. Part interfacing and placement are the areas in which problems normally arise.

The first case in point involved a SWECS that experienced a windstorm while in a maintenance orientation. The blades (which consisted of a main spar, ribs and skin) experienced buckling of the skin between the ribs. The buckling created highly stressed areas which fatigued rapidly. Figure 9 shows the buckled areas and the resulting fatigue cracking. It should be noted that the cracking also propagated along the leading edge, which was due to a tight-bend radius creating residual stresses in a material which was not sufficiently ductile. The leading edge crack was secondary, but design changes were still required to correct the problem. The blade skin between the ribs was unsupported and when bending was sufficient on the compression side of this airfoil, the skin buckled. This is commonly

known as "oil canning." The redesign included the addition of stringers between the ribs that attach to and support the skin, changing the leading edge radius and adding a leading edge spar. A material change was also made which helped to reduce the residual stresses and microcracks that are present in tight radius bends in brittle materials. These changes increased the survival rating by approximately 30%.

The blade failure in Figure 1 was of a similar type, except the rotor was operating and the wind exceeded the survival rating. Since the manufacturer has a different blade for high wind speed sites, no redesign was made.

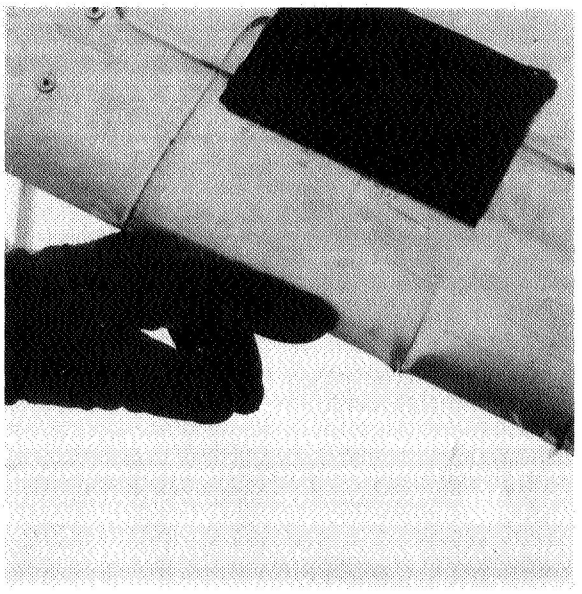

Figure 9 - View of Blade skin buckling and cracking in unsupported area. Note leading edge cracks and skin peeling.

Another blade skin problem which potentially leads to fatigue (Figure 10) is the attachment of skin sections to the ribs, where the thin skin is a load-carrying component. Riveting alone is often insufficient to transfer the loads. The movement between the skin and ribs tends to elongate the holes until rivet pullthrough occurs, which increases the stress at the remaining rivets. This movement also causes galling and fatigue cracking. Using skin doublers in this area (possibly with a bonding substance) will clamp the skins to the rib, and load can be transferred by friction between the layers as well as the rivets. Care must be taken in selecting similar materials which do not create galvanic action, and in making joints aerodynamic so that blade performance is not reduced.

Stress Risers

Stress risers are not totally avoidable. However, a few simple considerations should be reviewed to avoid spontaneous loadings and failures.

Holes represent a stress concentration factor of approximately 3. A much higher factor is possible if: 1) the hole is not deburred; 2) improper edge distances are used; or 3) the hole has sharp corners (i.e., a square hole). Figure 5 shows cracks beginning at sharp corners. Burrs in the holes can cause premature failure of the fastener as well as the surrounding metal. Scratches and notches have the same effect and precautions should be taken to avoid them.

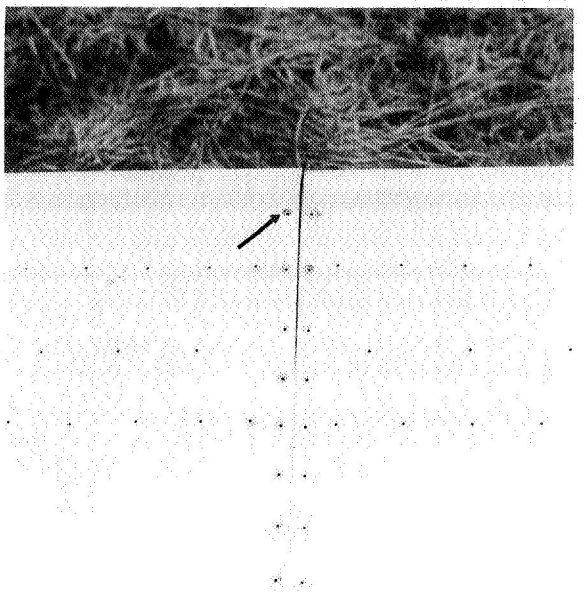

Figure 10 - An example of how skin movement caused rivet pullthrough. (arrow)

Bolts contain stress risers in the threaded area and when used in high stress areas or bending it is imperative that no threads are in the bend area. Bolts should also be of good quality, even if rolled threads are required.

It is also important to consider the environment and materials being used. Corrosion from salt water spray or galvanic action may create stress risers that lead to rapid failure. Anodized coatings and the use of bonding compounds can help avoid problems.

When parts are machined, it is important to cut proper radii and break all sharp edges. The intersection of two holes should be checked for stress risers and such intersections should be avoided as much as possible.

If the part is cast, x-rays should be taken to assure that no voids exist. Figure 11 shows an example of a cast part which contained voids. The machined hole penetrated the voids, and a fatigue crack developed which led to the failure. It is possible that the void alone may have been sufficient to cause the failure.

The heat affected zone surrounding a weld can be an area containing microcracks and residual stresses sufficient to cause fatigue cracking and eventual failure. Figure 12 shows a fractured weld in a highly stressed area of a SWECS yaw column. This failure led to the loss of the machine, which fell from the tower. Such welded areas should be designed away from the high stress areas or should be heat-treated to reduce residual stresses. Proper welding practices must be followed, and the services of a certified welder should be obtained whenever possible. Proper removal of slag and even the grinding of a small portion of the weld surface can help prevent fatigue cracking. Where multiple weld passes are necessary, the weld area may have to be "back ground" to insure integrity. Making sure of sufficient weld material and a reasonable "factor of safety" will also help prevent unwanted failure. X-rays of welds are prudent.

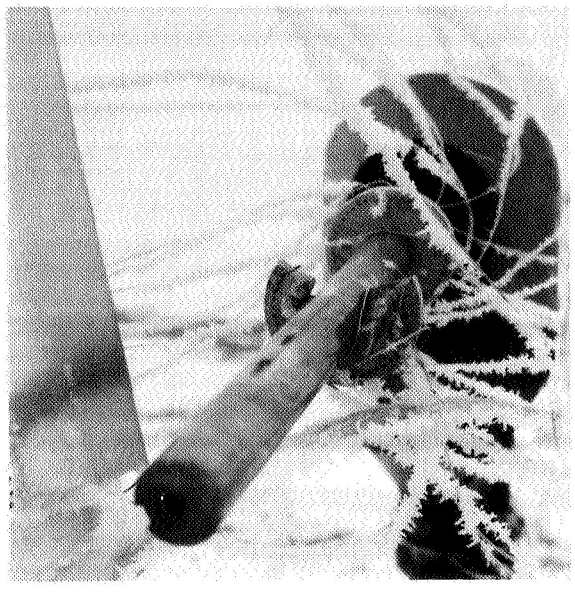

Figure 11 - View of hub which fatigued from area of casting voids.

Quality Assurance

The manufacturer has a basic responsibility to assure the SWECS is manufactured, handled and delivered to the dealer without undue degradation to the life of the components or system. The use of x-rays to check for casting voids and cracking in a welded area was discussed in the previous sections. Material handling is important from the initial fabrication to the final installation of the SWECS. Materials must be kept free from damage or alterations of the planned design. Fabrication discrepencies located in a highly stressed area could lead to premature failure and costly replacement. Figure 13 shows three variations of the forming of a blade trailing edge. If the deformities had been more pronounced, they conceivably could have affected rotor dynamics and caused vibration which could have led to fatigue failure. Figure 14 shows a similar deformity problem and also a crease which is the type of damage that initiates and accelerates fatigue cracking.

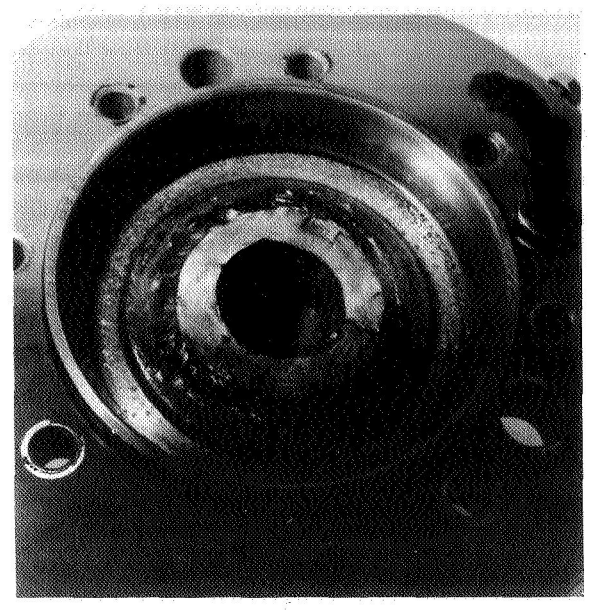

Figure 12 - View of yaw column fatigue in weld.

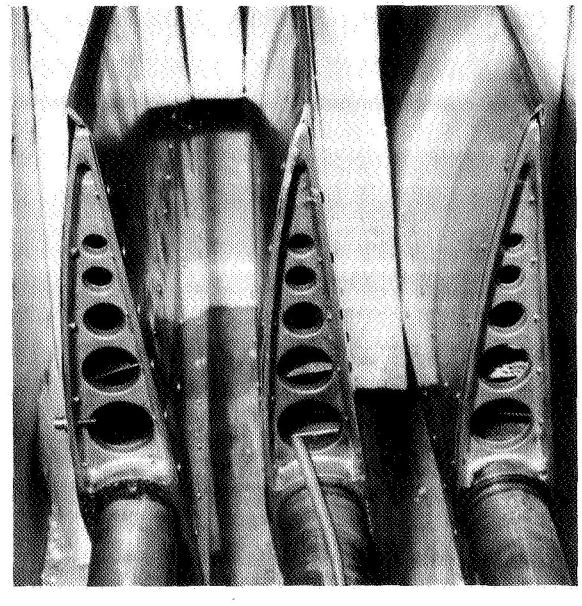

Figure 13 - Variations in manufacturing the trailing edge can lead to aerodynamic instability.

Shipping the SWECS to a buyer's site can be costly if the packaging is insufficient to protect the components. Figure 15 shows a crate which was destroyed during shipping, resulting

in blade skin damage (arrow) which required replacement at the manufacturer's expense. Figure 13 shows how the blades were subsequently shipped in a box with plywood sides and foam dividers between the blades and the sides. While this method of shipping is more costly, it will probably be cheaper than replacing damaged parts.

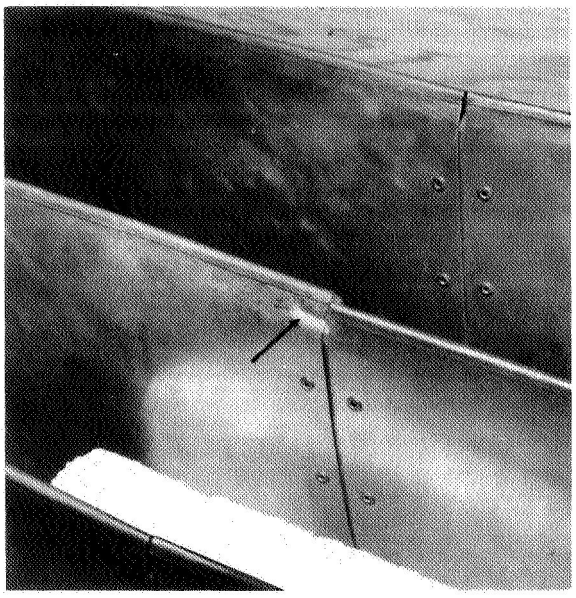

Figure 14 - View of blade manufacturing damage. (arrow)

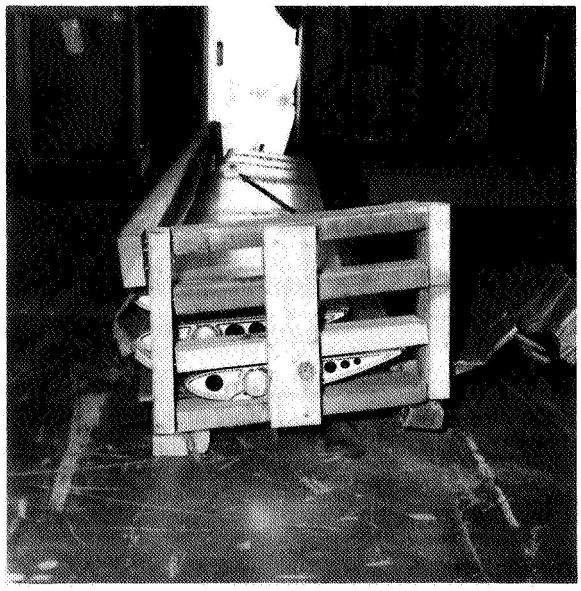

Figure 15 - View of packing crate damage and damaged blade skin. (arrow)

CONCLUSIONS

Prevention of fatigue failures is within the capability of even the most financially restricted companies. The reliability and safety of a system depend on doing the best designing, manufacturing, and installing possible. Where long-range survivability predictions are needed, component and system testing becomes necessary. While manufacturers do conduct tests, limited funds and equipment usually restrict such tests. Computer programs are available which may aid those designers and manufacturers who suffer these restrictions. In addition, the WSTC plans to perform fatigue tests on SWECS components under atmospheric loading conditions, and Rocky Flats personnel are available to discuss fatigue problems and aid in analysis.

REFERENCE

1. Waldon, C.A., "Wind Machine Fatigue Analysis and Life Prediction", Rockwell International April 1980, RFP-3135/3533/80/19.

QUESTIONS AND ANSWERS

C.A. Waldon

From: G.P. Tennyson

Q: The presentations (not just yours) indicate what the manufacturers did to contribute to problems and failures. Will there be similar presentations concerning the DOE/Rockwell contributions?

A: *Some of the DOE/Rockwell contributions to failures are included in Table I, but since they were not characteristic of fatigue, they were not discussed (i.e., AWT (TIED) rotor failure). This is a good lesson from a big mistake we made and reported. It will be brought up again and presented in the Reliability and Safety Program output.*

From: W. Frost

Q: a) Are the statistics and causes of failure reported and available to the public? If so, how does one get a copy?

b) How were the 120 mph (or 94 mph) winds you mentioned measured and where were they measured relative to the WTG?

A: *a) All failures are reported, including the mistakes made during the testing. All are considered useful lessons and specific requests should be made to Mr. Darrell Dodge, Rockwell, Int., P.O. Box 464, Golden, CO 80401 - Attn: Wind Systems Program or call 303/441-1351.*

b) The winds were measured by Propvane anemometers located upwind of the SWECS tower. Anemometer height was 5 ft below rotor centerline and approximately 5 rotor diameters upwind.

From: F.W. Perkins

Q: What do you consider "acceptable" failure behavior for prototypes? Are any failures acceptable? What RFP initiatives could reduce failures, e.g., extended contractor testing?

A: *Failures are costly, but may be a useful data point if verification of design ultimate strength is desired. Failures outside of "testing" are hurting the entire industry. Extended testing is part of the Rocky Flats Plant (RFP) plan for prototype, manufacturer testings.*

From: W.C. Walton

Q: Would you agree that the failures you have shown stem from deficient detail structural design techniques? If so, why do you connect them so strongly with aerodynamics?

A: *Most of the failures are structural in nature, but it is the difference in theoretical to actual which appears to create a failure for an otherwise adequate design. Analysis should look at nonoperating conditions and be verified for all conditions.*

PERFORMANCE TESTING OF A 50 kW VAWT IN A BUILT-UP ENVIRONMENT.

Lawrence A. Schienbein

DAF Indal Ltd.
3570 Hawkestone Road
Mississauga, Ontario
Canada. L5L 2V8

ABSTRACT

The results of performance tests of a DAF Indal 50 kW vertical axis wind turbine carried out at the Company's plant near Toronto, Canada, are presented. Results of limited free stream turbulence and vertical wind shear measurements at the site are also presented. The close agreement between measured and predicted energy outputs, required to verify the wind turbine power output performance relationship, was not attained. A discussion is presented of factors that may have contributed to the lack of better agreement.

INTRODUCTION

Free stream performance testing of a DAF Indal 50 kW vertical axis wind turbine was carried out at the Company's plant in Mississauga, Ontario, Canada under contract to the National Research Council of Canada. The wind turbine was erected at the plant in February, 1980, for pre-delivery trials.

The installation site (Figure 1) did not exhibit unobstructed exposure or strong and steady winds. In addition, the time available for testing was limited because the "windy" season usually ends in April. However, the urgent need for reliable performance data and the advantage of immediate access to the wind turbine weighed heavily in the decision to proceed with performance testing.

WIND TURBINE

The DAF Indal 50 kW vertical axis wind turbine (Figure 2) was designed as a demonstration machine for parallel operation with electrical power networks. The characteristics of the unit tested are given in Table I.

The induction generator can be operated in both the wye and delta winding configurations to take advantage of the reduced generator losses in wye at low power outputs. The control system commands a change from wye to delta when the power output exceeds about 30% of the rated generator output. The control system also disconnects the generator from the network when the rotor speed drops below the synchronous speed, to minimize motoring. The control functions described were overridden during performance testing so that data could be gathered for operation in both wye and delta, above and below the power production threshold wind speeds.

TEST SITE

The test site is shown schematically in Figures 3 and 4. The location of the wind turbine was determined by the fact that the guy anchor footings had to be on the Company's property. The base of the wind turbine rotor was at approximately the same elevation as the roof of the DAF Indal plant building.

The plant is located in a light industrial and warehouse area. Most of the buildings are between four and 10 meters high, and many have floor areas of several thousand square meters. The DAF Indal plant is 10m high and occupies an area of almost 10,000 square meters.

The closest obstructions to the wind turbine were the plant building and the test platform building (approximately 7m high) as shown in Figures 1 and 3. Large buildings, about 10m high, were located approximately 120 meters northeast, 120 meters north and 80 meters northwest of the wind turbine. In addition, construction staging (16m high), that had been installed to gain access to the spoilers, remained in place during the tests, seven meters south of the rotor axis, just clear of the rotor.

The anemometer tower was installed 18 meters west-southwest of the rotor, in order to be generally upwind during the relatively strong wind periods in February, March and April, based on long term data for the nearby Toronto International Airport. At this distance, the upwind free stream should not be significantly influenced by the flow through the rotor (ref.1).

Anemometers were installed at 10.5m and 18.3m above the base of the tower. The upper anemometer, used exclusively for performance testing, was 1.9m above the rotor equator. The lower anemometer was used for wind shear measurements only.

INSTRUMENTATION

Wind turbine power output performance data, performance verification data and some data describing the characteristics of the free stream were gathered. An instrumentation schematic is shown in Figure 5.

A rotating disc watthour meter recorded the net energy output or consumption of the wind turbine. Wind speed was recorded by a wind histogram recorder, which measured two second average wind speed continuously and incremented the appropriate bin counter (0.5 m/s bin widths). One second average wind speed was also displayed digitally.

Both cup anemometers were identical and of research grade, with a manufacturer's quoted response distance constant of 1.52 meters.

TEST METHOD

Performance data were recorded when the anemometer was believed to be outside of the influence of the flow through the rotor. Although the anemometers were positioned to be upwind of the rotor for the predicted strong wind directions, it turned out that during the period of testing, the strongest winds blew over one half the time from the directions such that either the anemometer was immersed in the rotor wake, or the wake of the main plant building. As a result, the periods during which performance data could be collected were very short. Most of the data were recorded during the passage of storms. Wind direction changes of about 15 to 30 degrees were commonly observed as strong gusts developed. Given these conditions, it is probable that some performance data, later used to define the performance curves, were acquired while the anemometer was influenced by the rotor wake, even though care was taken to eliminate such data.

The wind speed frequency distribution (or wind histogram) and the elapsed time were recorded for an exact number of watthour meter disc increment markers (100/rev.) to pass a reference mark. The elapsed time for each test run was typically between five and 25 seconds. Measurements were made when the disc speed was thought to be steady, and the wind speed and power output were thought to be reasonably well correlated. The method turned out to be tedious and time consuming.

The wind turbine performance could not be well defined for wind speeds in excess of about 14 m/s because operation was restricted to wind speeds less than 16 m/s pending the analysis of experimental blade stress data. (The wind turbine actually did operate at speeds in excess of 16 m/s for very short periods, during gusts).

Barometric pressure and temperature were recorded for each series of test data.

Performance verification data were recorded in the same manner as the performance data except that the test runs were several minutes, rather than several seconds, in duration.

Wind shear data were gathered by simultaneously recording the wind speed frequency distributions measured by the two anemometers for periods of between one half and four minutes. Alongwind turbulence data consisted of wind speed frequency distributions measured by the upper anemometer for periods of up to 15 minutes.

PERFORMANCE TEST RESULTS

A total of 416 and 212 useful data sets were acquired in the delta and wye generator configurations respectively. The wind histogram record for each set was reduced to the effective cubic weighted average wind speed for the test period (i.e. the steady wind speed having the energy equal to that represented by the actual wind speed frequency distribution for the test run). The average power output for each test run was proportional to the number of disc increments recorded, divided by the elapsed time.

Two random data analysis methods were used to determine the power output versus wind speed relationships.

(1) The method of bins (ref. 2 and 3). Here the data sets were grouped into wind speed bins (0.5 m/s width) and the average power was determined for each bin. The results for wye and delta are shown in Figures 6 and 7 along with best fit curves. These curves intersect at about 7.5 kW which is unexpectedly low. Data in the wye configuration were limited to power outputs below about 12 kW because the slip of the generator is such that at higher power outputs the wind turbine automatically shuts down due to overspeed.

    The test data were also binned by power; the results are shown in Figures 8 and 9. To the knowledge of the author, power binning has not been proposed previously. The results for power and wind speed binning are in good agreement except for delta configuration at power outputs greater than 30 kW.

The measured standard deviation is shown for each bin. These indicate the combined effects of the imperfect correlation between measurements of power and wind speed and the error in the individual power and wind speed measurements. The correlation effect dominates, since the power measurement error was estimated to be less than nine percent and the wind speed measurement error was estimated to range from 16 percent at two m/s to only three percent at 15 m/s.

(2) The method of frequency matching (ref. 3). Here the power curve is defined as the sets of measured power and wind speed points which have equal cummulative probabilities. The results of frequency matching are shown in Figures 10 and 11. There is seen to be good agreement between these data and the best fit curves for wind speed binning.

WIND SHEAR AND TURBULENCE TEST RESULTS

Alongwind RMS turbulence (gustiness) can be estimated using wind speed frequency distributions of several minutes duration. The ratio of the standard deviation to the average wind speed is a measure of the alongwind RMS turbulence intensity.

Data were recorded using the upper anemometer (18.3 m). Test runs were grouped by wind direction in order to investigate the effect of surrounding structures. The results of the data analysis, shown in Table II, are consistent with other published turbulence data for the same general surface features. There does not appear to be any significant correlation between turbulence intensity and wind direction (i.e. surrounding structures) at the measurement height of 18.3 meters. The turbulence intensity in the rotor wake, measured 18 meters from the rotor axis, is approximately twice that measured in the free stream.

The results of the wind shear data analysis are shown in Table III. The value of the power law exponent in each case was based on linear regression of the upper anemometer average wind speed on the lower anemometer wind speed.

The measured power law exponents appear to correlate with the proximity of the structures upwind of the anemometers. The exponent for northeast winds is the lowest of those measured, consistent with the unobstructed exposure for more than 120m upwind. The exponents for northwest winds are somewhat higher than those recorded for the northeast, indicating the effect of the building lying about 70 meters upwind. The exponents for south winds are the second highest recorded, clearly showing the influence of the west corner of the DAF Indal plant building lying about 50m upwind.

The measured power law exponents for southwest winds are unusually high, indicating the large shear in the near wake of the test platform building lying 10 meters upwind of the anemometers. Although 42 performance data points (wye and delta combined) were collected while the wind was from the southwest, it is believed that the overall effect on the performance curves was small.

POWER OUTPUT PERFORMANCE VERIFICATION

The validity of wind turbine power output performance curves is determined by comparing measured energy outputs (ideally for periods of at least several hours) to those calculated using the relationship.

$$E = T \int_{V_1}^{V_2} F(V) P(V) dV \text{ where}$$

F(V) is the measured probability density of wind speed, P(V) is the measured wind speed power output function, V_1 and V_2 are the wind speed limits for the test period, and T is the elapsed time.

Verification test runs were carried out for durations of several minutes only; the measured and calculated outputs are shown in Table IV. Calculated values are based on the curves shown in Figures 6 and 7. (Data from several performance verification test runs could not be used because the wind speed frequency distributions included wind speeds above which the performance curves are not defined).

The agreement between measured and predicted energy outputs is sensitive to the assumed best fit positions of the performance curves. However, it is probable that other factors contributed in part to the difference between the measured and calculated values.

(1) A significant portion of the test data used to define the performance curves could have been acquired while the anemometer was influenced by the rotor wake, even though care was taken to eliminate such data. The effect of a shielded anemometer is to shift the performance curves to lower wind speeds; therefore calculated energy outputs, based on these curves and the measured wind speed distributions, will be too high. Figure 12 shows data acquired with the anemometer known to be shielded. The effect of anemometer shielding is also shown in Table IV which includes the results of two performance verification test runs carried out with the anemometer in the wake of the rotor.

(2) The wind field at the test site would be perturbed because of the buildings surrounding the wind turbine (ref. 4 and 5). Therefore the wind speed distributions measured by the anemometer during the short performance verification test periods may have been significantly different than those experienced by the wind turbine.

The closest obstructions to the wind turbine were in the sector east to south-west of the rotor, which coincides with the two poorest performance verification test results. Power output and wind speed were frequently observed to be uncorrelated for periods of up to 10 seconds, except with the anemometer directly upwind of the rotor. The magnitude of the measured power output standard deviations confirms these observations (Figures 6 and 7). They are about ten times greater than those reported from tests of a Grumman Windstream 25 wind turbine (ref.3) at Rocky Flats, Colorado based on 30 second average data, and a DAF Indal 50 kW mechanically coupled vertical axis wind turbine near Bushland, Texas (ref. 6) based on 15 second average data. Both sites have unobstructed exposure.

It was also observed that the wind turbine power output did not follow wind speed fluctuations of two to three m/s having durations of five seconds or less (based on continuous one second averages) even with the anemometer upwind and taking into account a time delay. This suggests that, in the perturbed flow, a significant fraction of the wind energy was not captured because it was associated with frequencies above the wind turbine response cut off frequency (ref.7).

CONCLUDING REMARKS

The problems associated with wind turbine testing in a turbulent wind were amplified because of the effect of surrounding structures. Nevertheless performance curves for the DAF Indal 50 kW vertical axis wind turbine were obtained. The results of the performance data analysis, using the method of bins (wind speed binning) and the method of frequency matching are in good agreement. The close agreement between measured and predicted energy outputs required to verify the performance curves was not attained. The characteristics of the perturbed wind stream are believed to be partly responsible for the lack of better agreement.

The measured turbulence intensities (based on two second average wind histogram records) were consistent with other data for similar terrain features. The results of wind shear measurements did correlate with the position of surrounding structures and provided strong evidence of the effect of these structures on the wind stream seen by the wind turbine.

The benefit of wye to delta generator winding changes was found to be significantly less than expected. However, free stream wind turbine testing is an indirect technique for determining the loss characteristics of an induction generator. A small shift in the position of either the wye or delta performance curve will result in a significantly different point of intersection.

Although the wind and site conditions hampered data acquisition, the manual data acquisition method that was used may be more successful at other unobstructed test sites experiencing strong and steady winds.

REFERENCES

1. Akins, Robert E., "Wind Characteristics for Field Testing of Wind Energy Conversion Systems", Sandia Laboratories Report 78-1563, November,1979.

2. Akins, Robert E., "Performance Evaluation of Wind Energy Conversion Systems Using the Method of Bins - Current Status", Sandia Laboratories Report 77-1375, March, 1978.

3. Hansen, A.Craig., "Random Data Analysis in WTG Testing", Proceedings of the Workshop on Small Wind Turbine Systems, Boulder, Colorado, 1979, pp. 221-232.

4. Frost, Walter and Shieh, Chih Fang, "Wind Characteristics Over Complex Terrain Relative to WECS Siting" AIAA/SERI Wind Energy Conference, Boulder, Colorado,1980,pp.185-193.

5. Meroney, Robert N., "Wind in the Perturbed Environment: Its Influence on WECS", presented at the AWEA Spring Conference, May 11-14, 1977, Boulder, Colorado.

6. Personal Communication, R.N. Clark, U.S.D.A. South-Western Great Plains Research Center, Bushland, Texas.

7. Kirchoff, R.H., "Measurements of the Wind Field Interaction with the UMass 25 kW Wind Turbine", Proceedings of the Workshop on Small Wind Turbine Systems, Boulder, Colorado, 1979, pp. 179-188.

Table I

DAF Indal 50 kW Vertical Axis Wind Turbine
Description of the Unit Used for Performance Testing

Generic Description

Vertical axis wind turbine generator Darrieus Type. Troposkien blade shape.

Rotor

Number of Blades	2
Height	16.8 m
Diameter at Equator	11.1 m
Capture Area	121 m^2
Speed	80 rpm
Rotor Column	0.6 m dia. steel pipe
Weight	3100 kg
Struts	2

Blades

Material	Extruded aluminum alloy
Airfoil	NACA 0015
Chord	0.36 m

Transmission

Type: Single stage spur gear (bull gear) and pinion. Spray lubricated. Vertical shafts.

Ratio: 15

The bull gear also serves as the brake disc.

Generator

Type	Induction
Rating	56 kW
Voltage	575 V three phase
Speed	1200 rpm
Frequency	60 Hz

The generator also serves as the starting motor

Overspeed Control

Primary control by means of the rotor mounted automatic disc brake. Secondary control by means of aerodynamic spoilers mounted on the blades and deployed automatically

TABLE II

Alongwind Freestream Turbulence Test Results

Wind Direction	Total Number of Test Runs	Average Wind Speed at 18.3m (m/s)	Average Alongwind RMS Turbulence at 18.3m
NE	3	4.6	0.15
NNW	5	6.2	0.18
NW	11	9.5	0.18
SW	3	5.4	0.18
S	2	6.1	0.21
*NE	1	7.8	0.35
*NE	1	9.9	0.37
*NE	1	10	0.28
*NE	1	10.4	0.30

* Anemometer in the rotor wake.

TABLE III

Wind Shear Test Results

Wind Direction	Total Number of Test Runs	Range of Average Wind Speed for the Upper Anemometer (m/s)	Wind Shear Power Law Exponent Determined by Linear Regression
NE	10	3.4 to 5	0.14
NW	12	4.4 to 6	0.18
	15	6 to 8.5	0.23
	27	4.4 to 8.5	0.21
SW	15	4.2 to 6	0.32
	14	6 to 8.4	0.52
	29	4.2 to 8.4	0.47
S	5	2.6 to 6.1	0.22
	7	6.1 to 8.3	0.28
	12	2.6 to 8.3	0.26

Table IV

Performance Verification Test Results

Generator Winding Configuration	Duration Test Run (T) in Minutes	Wind Speed Range in m/s V_1	V_2	Wind Direction	Measured Energy in kWh*	Calculated Energy (E) in kWh**	Ratio of Measured to Calculated Energy
Wye	7.1	4.3	9.8	W	0.23	0.33	0.70
	19.8	2.8	9.8	S	0.23	0.40	0.58
	13.3	3.8	10.2	SW	0.53	0.85	0.62
	11.8	3.8	10.2	W	0.59	0.72	0.82
	5.2	5.8	10.2	NW	0.59	0.67	0.88
Delta	6.7	4.3	9.8	W	0.35	0.39	0.90
	7.1	3.8	11.3	NW	0.47	0.56	0.84
	7.0	4.3	9.8	NW	0.41	0.52	0.79
	6.0	4.8	10.7	NW	0.58	0.71	0.82
	5.8	5.3	10.7	NW	0.58	0.79	0.73
	12.9	4.8	13.7	NW	2.61	3.12	0.84
	29.2	3.8	13.2	NW	3.79	4.45	0.85
	*10.7	3.3	16.2	NE	4.60	2.12	2.17
	*11.6	3.3	16.2	NE	5.06	3.45	1.47

* Anemometer in the wake of the rotor.

** Determined using the curves in Figures 6 and 7.

* Corrected to freestream air density of 1.253 kg/m^3.

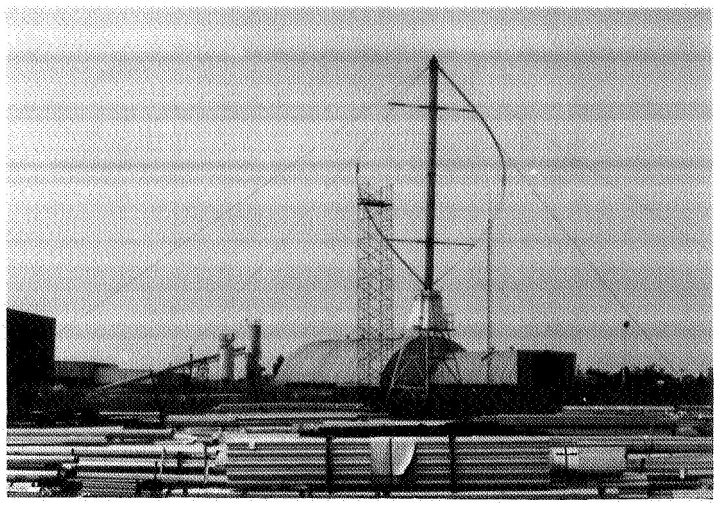

Figure 1 VIEW OF THE TEST INSTALLATION SITE LOOKING SOUTHWEST

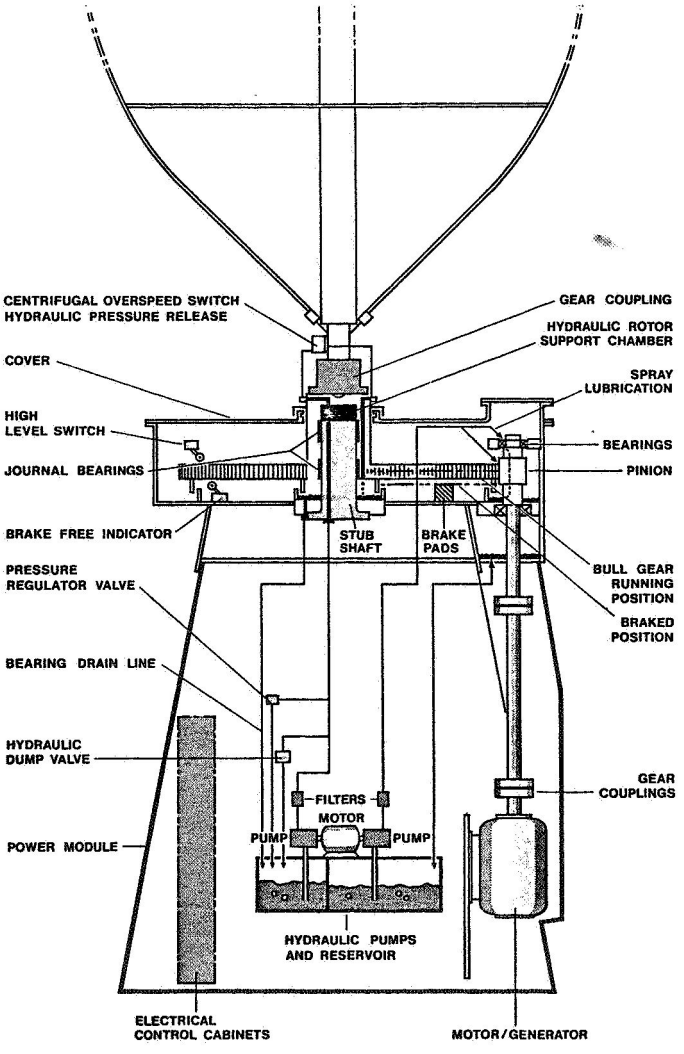

Figure 2 SCHEMATIC OF THE DAF INDAL VERTICAL AXIS WIND TURBINE

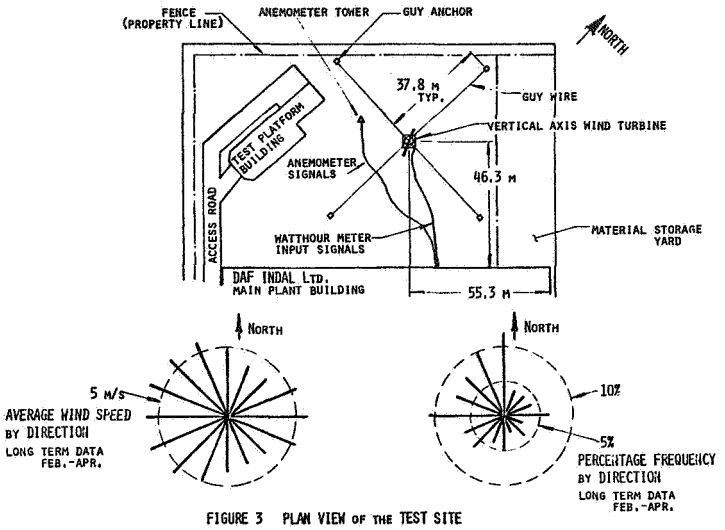

FIGURE 3 PLAN VIEW OF THE TEST SITE

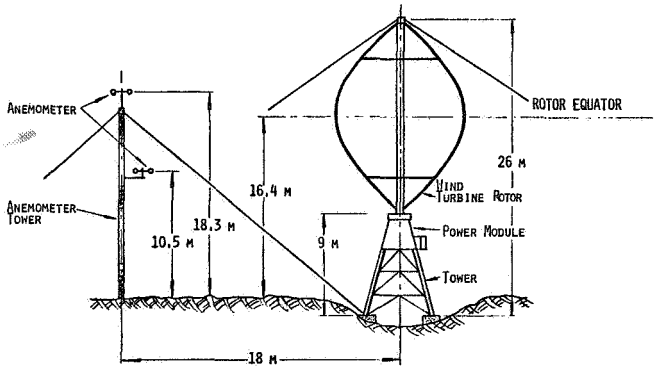

FIGURE 4 SCHEMATIC OF THE TEST INSTALLATION

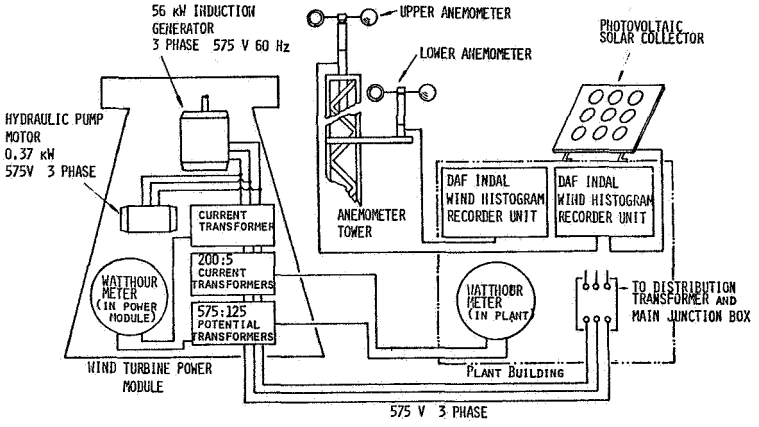

FIGURE 5 TEST INSTRUMENTATION SCHEMATIC

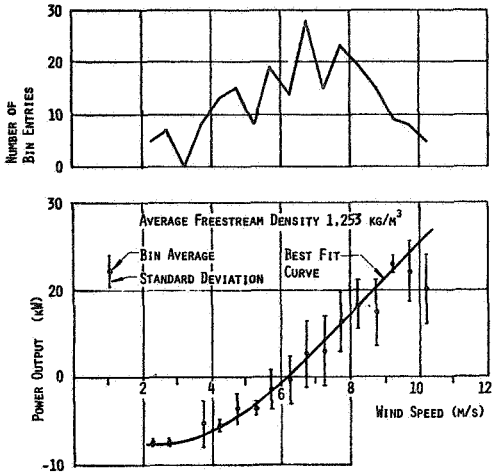

FIGURE 6 POWER OUTPUT IN WYE (WIND SPEED BINNING)

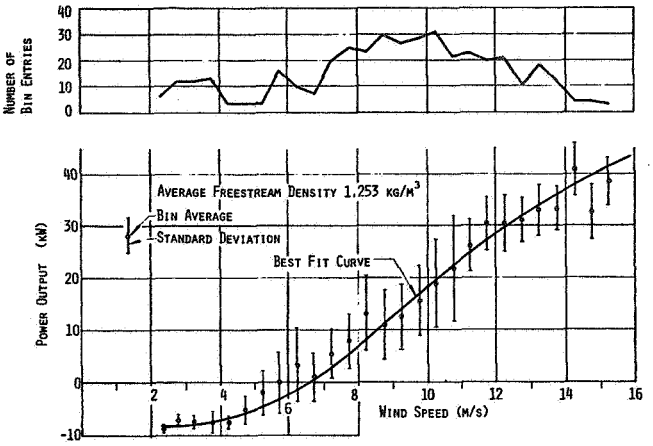

FIGURE 7 POWER OUTPUT IN DELTA (WIND SPEED BINNING)

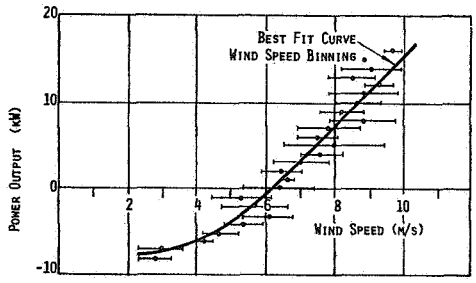

FIGURE 8 POWER OUTPUT IN WYE (POWER BINNING)

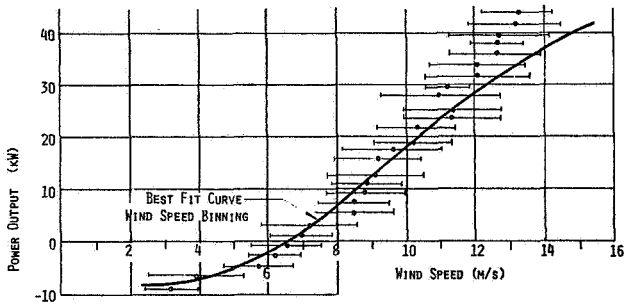

FIGURE 9 POWER OUTPUT IN DELTA (POWER BINNING)

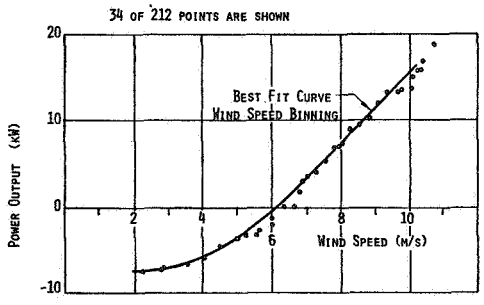

FIGURE 10 RESULTS OF FREQUENCY MATCHING OF WYE DATA

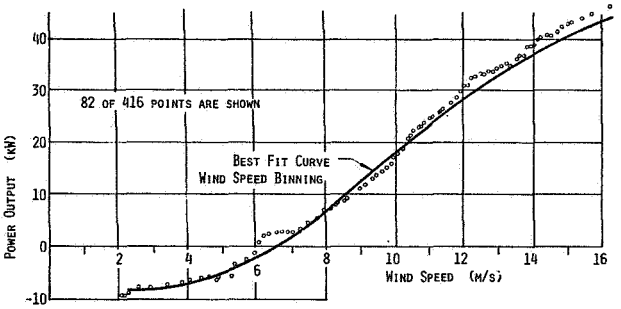

FIGURE 11 RESULTS OF FREQUENCY MATCHING OF DELTA DATA

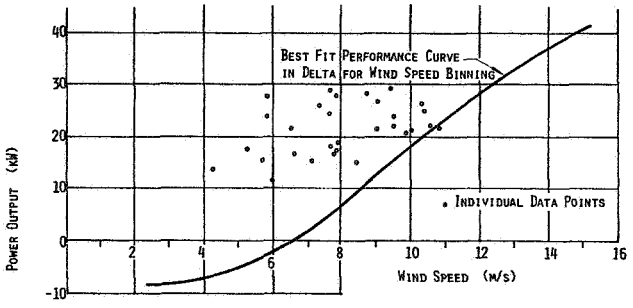

FIGURE 12 PERFORMANCE DATA SHOWING THE EFFECT OF ANEMOMETER SHIELDING

QUESTIONS AND ANSWERS

L.A. Schienbein

From: Bill Wentz

Q: How is your spoiler actuated?

A: *The spoilers are latched by electromagnets installed in the blades. When overspeed is sensed, the current to the electromagnets is interrupted and each spoiler deploys as the result of a combined aerodynamic and centrifugal moment.*

From: Tom Bellows

Q: Why did you not put the anemometer on top of the rotor tower?

A: *This was considered. We were advised by others who had mounted anemometers above the rotor, that anemometer maintenance was a problem and that anemometer life would be substantially reduced. Furthermore, given the nature of the test site, we believed that it would not be possible to reliably correct the measured wind speeds to the rotor equator height.*

From: R. Edkin

Q: During your wind turbine operation, did you experience any problems using an induction generator? With Wye or Delta connections?

A: *No to both questions.*

CALCULATION OF GUARANTEED MEAN POWER FROM WIND TURBINE GENERATORS

David A. Spera

National Aeronautics and Space Administration
Lewis Research Center
Cleveland, Ohio

ABSTRACT

Much research has been devoted to the nominal power generated by wind machines, but little work has been done on the subject of guaranteed power. Yet power guarantees will be part of the commercialization of wind energy systems. This paper describes in step-by-step fashion a proposed method for calculating the "guaranteed mean" power output of a wind turbine generator. The term "mean power" as used in this study refers to the average power generated at specified wind speeds during short-term tests. Extrapolation to an annual mean power, based on wind statistics, is beyond the scope of this paper. Guaranteed energy is not addressed. The DOE/NASA Mod-OA 200 kW plant in Clayton, New Mexico, is used as a sample case. Subjects discussed and illustrated are correlation of anemometers, the method of bins for analyzing non-steady data, the PROP Code for predicting turbine power, and statistical analysis of deviations in test data from theory. Guaranteed mean power density for the Clayton Mod-OA system was found to be 8 watts per square meter less than theoretical power density at all power levels, with a confidence level of 0.999. This amounts to 4 percent of rated power.

INTRODUCTION

As the commercialization of wind turbine generators progresses, there will be increased demands by purchasers for guarantees on power output. Such guarantees are common for thermal and nuclear power plants, and there is no reason to believe that wind power plants will be an exception. However, guaranteeing the performance of a wind energy system presents two major problems which sellers of conventional plants do not have to face. First, unlike conventional fuels, the energy content of the wind "fuel" is not easy to sample. Second, wind turbines normally operate in a transient state, unlike conventional plants which can be placed in a steady state in practice as well as in theory. Thus, the developers of wind energy systems are faced with both the requirement of guaranteeing system performance and substantial difficulty in satisfying that requirement.

Methods for predicting the nominal power output of a wind turbine have been studied extensively and reported in detail. A recent comprehensive review of almost 140 references on the aerodynamic behavior of wind energy systems is given in reference 1. However, the subject of a guaranteed power output does not seem to have been addressed in the literature. This is not surprising since guarantees imply commercialization, field test experience, and statistical analysis of data, all of which are rather recent additions to the wind energy field. The major purpose of this paper, then, is to stimulate discussion and publication of guaranteed as well as nominal performance data for wind energy systems. In addition, a proposed procedure is made available now to the analyst who is in the process of predicting wind turbine power for guarantee purposes.

The term "mean power" as used in this study refers to the average power generated at specified wind speeds during short-term tests. Extrapolation to an annual mean power, based on wind statistics, is beyond the scope of this paper. Guaranteed energy is not addressed. The proposed procedure for arriving at a guaranteed power will be described and documented by means of a sample case. The DOE/NASA Mod-OA 200 kW wind turbine generator will be used in this example. The design of this machine is described in detail in reference 2. While the Mod-OA is a large horizontal-axis wind turbine, procedures described in this paper may apply equally well to vertical-axis and small horizontal-axis wind turbine generators.

PROCEDURE

Most wind turbine generator systems can be represented by the schematic diagram shown in Figure 1. This idealized figure is the basis for many of the terms used later to describe measurements, calculations, and results. The system consists of a turbine, a transmission, and a generator, with a wind power input and wind, thermal, and electrical power outputs. For reference to measurement points, the system is divided by stations, in accordance with usual practice in analyzing fluid flow. Station 0 is along the turbine midline and far enough upwind to be undisturbed by the turbine. An anemometer is required at Station 0 to measure free-stream wind speed. An anemometer at Station 1 would measure turbine input wind speed, while turbine output wind speed would be measured at Station 2 on the midline. The turbine output shaft is also at Station 2, though it may actually be located upwind of the turbine. Stations at the output shafts of successive stages in the transmission are designated 2.1, 2.2, etc. Any of these shaft stations could be the location of torque and speed sensors. System electrical output and wind output occur at Station 3. Thermal output from power-train losses occurs between Stations 2 and 3. The station numbers in Figure 1 follow the usual notation for one-dimensional aerodynamic analysis.

Test Installation

Figure 2 illustrates the relative locations of the Mod-0A 200 kW wind turbine generator and its auxiliary anemometer tower, outside Clayton, New Mexico. The anemometer tower is approximately 50 meters to the southwest of the wind turbine in the direction of the prevailing wind. The anemometer at Station 0, at the 30 meter elevation on the turbine midline, measures the free-stream wind speed. A second anemometer is located just upwind of the rotor, at Station 1, and measures the turbine input wind speed. Turbine shaft torque and shaft speed are measured by sensors located at Station 2, between the turbine and the gearbox. Generator output is measured at Station 3, in the ground control enclosure.

Calculation Steps

The procedure for calculating guaranteed power will be divided into eight steps, as follows.

1. Correlation of free-stream and turbine input (or output) anemometers, located at Stations 0 and 1 (or 2), respectively.

2. Correlation of performance test data taken at various stations, such as wind speed at Station 1 with shaft torque and speed at Station 2, and with electrical power at Station 3.

3. Calculation of wind power input concurrent with test data, using the correlation obtained in step 1.

4. Calculation of theoretical turbine output power.

5. Analysis of deviations between measured and theoretical turbine output power.

6. Estimation of lower bound on the mean deviation from theory, for a specified confidence limit.

7. Analysis of power-train losses.

8. Calculation of guaranteed mean power output, for the turbine and the system.

Each of these steps is illustrated by means of a sample calculation for the Clayton Mod-0A wind turbine generator.

Method of Bins

Much of the data analysis in this study was done using the "method of bins", a statistical procedure (ref. 3) which has been used extensively to reduce wind turbine data (refs. 4, 5, and 6). For the purposes of this study, application of the method can be summarized as follows:

1. A "bin" is a data storage unit labeled with a nominal wind speed and containing a compartment for each sensor. Nominal wind speeds are selected to cover the operating range at intervals of 1.0 meter per second. In this study there are 15 wind speed bins each with four sensor compartments.

2. For each rotation of the turbine rotor (a period of 1.5 sec.) average readings from all sensors are stored in the same bin, in their respective compartments. The bin is selected according to the turbine input wind speed.

3. Median values are calculated for the contents of each compartment in each bin. Thus, the data set for this study was reduced to 60 compartment median values.

4. Compartment median values are assumed to be concurrent. No assumption is made concerning the concurrence of any data values other than the compartment medians.

The method of bins has been found to be particularly useful for the non-steady conditions under which wind energy systems operate. Correlation between data from sensors on the machine and data from anemometers placed away from the machine is generally improved when the method of bins is used in place of time coincidence.

CALCULATIONS, RESULTS, AND DISCUSSION

Step 1: Correlation of Free-Stream and Turbine Anemometers

With the wind turbine producing on-line power, simultaneous measurements of free-stream wind speed and turbine input wind speed were taken and analyzed using the method of bins. The resulting pairs of compartment median wind speeds were then cross-plotted as shown in Figure 3. Each data point in this figure represents one bin of data with a speed range of 1.0 meter per second, measured at the turbine input. Eight separate operating periods are included, totaling 26.4 hours and over 63,000 pairs of measurements. Bins at wind speeds more than 1.0 meters per second above rated have been eliminated because pitching the blades changes the trend of the data. Also, a correlation equation at wind speeds above rated is not required for efficiency calculations.

Regression analysis was used to fit a correlation line to the data in the following form:

$$V_0 = a + bV_1, \quad m/s \qquad (1)$$

V_0 and V_1 are the median values of bins of free-stream and turbine input wind speeds, respectively. The empirical constants for the Clayton Mod-0A wind turbine are as follows:

$a = 3.39$ m/s

and

$b = 0.667$

The scatter about the curve-fit line in Figure 3 can be attributed to variations in wind direction, yaw heading errors, and turbulence. This amount of scatter is to be expected, and therefore the data set must be large enough to randomize the variations. In addition, the machine must be operating as designed at all wind speeds, in order to produce the correct retardation in the free-stream wind speed.

Step 2: Correlation of Performance Test Data

Table I lists all the performance test data which were used in this study to calculate the guaranteed mean power of the Clayton Mod-0A wind turbine. These data were recorded during (a) 2.2 hours of on-line operation on January 10, 1978, (b) 4.6 hours of on-line operation on January 18, 1978, and (c) during a shop run-in test of a similar unit in December 1979. The latter data will be referred to during calculation of power-train losses.

The method of bins, as incorporated in the NASA data system (ref. 6), reduces a large data set to a concise summary while maintaining acceptable correlation and accuracy. Though Table I is brief, it contains bin compartment medians calculated from over 65,000 separate measurements. For each wind speed bin, 1.0 meter per second in range, the following median values of data in corresponding compartments are required for this analysis:

1. Turbine input wind speed V_1, measured at Station 1 (see Fig. 2 for stations).

2. Turbine shaft torque Q_2, measured at Station 2.

3. Turbine shaft speed Ω_2, measured at Station 2.

4. Generator output power P_3, measured at Station 3, in the ground control enclosure.

The bins are numbered for later reference in successive tables.

No special machine operations were performed to obtain the on-line data in Table I. Data were recorded during the initial 100-hr acceptance test of the machine, under normal utility operating conditions. Records 1 and 2 each contain at least one start-stop transient operation, which can be accommodated automatically by the data analysis system.

Step 3: Calculation of Wind Power Input

"Wind power input" refers to the power density of the free-stream wind at the turbine midline (Fig. 1), expressed in watts per square meter. All efficiency values are referenced to this wind power density, which is calculated according to the following fundamental equation:

$$P_0 = \frac{\rho}{2} V_0^3, \quad W/m^2 \qquad (2)$$

The free-stream wind speed V_0 in this equation is calculated for each bin using Equation (1) and the turbine input wind speeds V_1 from Table I. The results are listed in the second column of Table II.

The air density ρ in Equation (2) should be calculated from temperature and barometric pressure measurements made during the recording of power data. Use of Standard Atmosphere density data is not recommended. As shown in Figure 4, there is about a 5 percent difference between Standard Atmosphere density for the Clayton midline elevation and the actual densities at the time of the two test runs. This difference is too large for efficiency calculations. The average local air density of 1.101 kilograms per cubic meter was used to calculate the free-stream wind power densities listed in the third column of Table II.

Step 4: Calculation of Theoretical Turbine Output Power

The calculation of guaranteed mean power is essentially a calibration of a specified theory for predicting the aerodynamic performance of a wind turbine. As mentioned previously, there are a variety of such theories available (ref. 1). Without questioning the validity of various theories, it is clear that deviations between test data and theory will differ for different theories, leading to different calibrations. Therefore, it is important to specify the theoretical method used as a basis for predicting guaranteed mean power.

In this study, theoretical turbine output power was calculated by means of the PROP Code, described in references 7, 8, and 9. This code is in the public domain, and the references present the theoretical basis for the computational procedures in it. Quasi-static aerodynamic behavior is assumed. Data for the NACA 23000 series airfoils on the Mod-0A turbine were obtained from reference 10. Lift and drag coefficients for smooth and standard roughness airfoils were averaged, to approximate a NASA roughness condition.

The fourth, fifth, and sixth columns in Table II list the results of theoretical calculations of turbine output power for each bin. The tip-speed ratio is calculated from the equation

$$\lambda = R\Omega_2/V_0 \qquad (3)$$

in which the radial dimension R is 18.9 meters (including the effect of 7 degrees of coning), and the turbine shaft speeds Ω_2 are given in Table I.

Theoretical turbine efficiency is a function of λ and is independent of the air density. However, the turbine power density does depend on air density and is calculated as follows:

$$P_{2,th} = E_2 P_0, \quad W/m^2 \tag{4}$$

Step 5: Analysis of Deviations from Theoretical Power

Experimental turbine power densities are listed for each bin in the seventh column of Table II. To calculate turbine power density from the data in Table I, the following equation is used:

$$P_2 = Q_2 \Omega_2 / A, \quad W/m^2 \tag{5}$$

The constant A is the swept area of the turbine, equal to 1123 square meters for the Mod-0A rotor. Experimental turbine efficiency was then calculated by dividing turbine power output by wind power input, as follows:

$$\eta_2 = P_2 / P_0 \tag{6}$$

Experimental and theoretical peak efficiencies were found to be approximately the same and equal to 0.41.

Experimental turbine efficiencies are compared with theory in Figure 5. Theory is shown by the dashed line, and the solid line denotes a power output controlled to 200 kilowatts. The latter portion of the efficiency curve does not depend on theory. Therefore data at rated power have been deleted from Figure 5.

In general, the correlation shown in Figure 5 is good between experiment and theory. However, a quantitative measure of the correlation is required before guaranteed mean power can be calculated. To obtain this quantitative assessment, deviations from theoretical turbine power density are calculated as follows:

$$\delta P_2 = P_2 - P_{2,th}, \quad W/m^2 \tag{7}$$

The ninth column in Table II contains the power density deviations for the test data sets.

To simplify the statistical analysis which will follow, a random distribution of deviations is desirable. Two tests for randomness were performed. First, the deviations from theory in Table II were plotted versus the corresponding theoretical turbine power densities, as shown in Figure 6(a). No trend in the data was observed. Therefore, it is consistent with these test data to assume that deviations from theoretical power predicted using the PROP Code theory do not depend on power density, at least up to levels of 200 watts per square meter.

Next, the probability distribution of the deviations was calculated, leading to the results which are illustrated in Figure 6(b). A straight line on this graph indicates a normal distribution and random variation. The deviation data were found to be normally distributed, with a sample mean $\bar{X}$ of -0.7 watts per square meter and a sample variance of 24.8. The following equations apply:

$$\bar{X} = \frac{1}{n} \sum_{n} \delta P_2, \quad W/m^2 \tag{8a}$$

and

$$s^2 = \frac{1}{n-1} \sum_{n} (\delta P_2 - \bar{X})^2, \quad W^2/m^4 \tag{8b}$$

in which n is the number of bins, or 11 in this case.

In Table III, the data are listed on which Figure 6(b) is based. Deviations are first ranked from algebraically largest to smallest, and the number of bins exceeding a given deviation is calculated. One-half bin values result from the fact that the deviations given are median values for each bin. Probability of exceedance is then obtained by dividing each number in the third column in Table III by 11, the total number of bins in the sample.

In summary, statistical analysis of deviations from the PROP Code theory indicate the following:

1. Power density deviations from theory do not depend on power level, below 200 watts per square meter.

2. Sample mean deviation is -0.7 watt per square meter, with a variance of 24.8.

3. Correlation between experimental power output and theoretical power output is high.

Step 6: Estimation of Lower Bound on Mean Deviation from Theory

If a lower bound on the mean deviation from the power predicted using the PROP Code can be estimated with a high degree of confidence, then a guaranteed mean power can be established. A lower bound of this type can be calculated by conventional statistical methods from a sample mean $\bar{X}$ and a sample variance s^2. The applicable equation (ref. 11, for example) is as follows:

$$\mu(1 - \alpha) \geq \bar{X} - t(1 - \alpha, n - 1) \sqrt{\frac{s^2}{n}}, \quad W/m^2 \tag{9}$$

in which μ is the actual, but unknown, mean deviation, $(1 - \alpha)$ is the confidence level desired, and t is Student's factor which is tabulated in statistical references.

The level of confidence which should be used is a matter of judgment at this time. It should be high, to support a guarantee. For guidance, guaranteed minimum material properties usually imply a confidence level of 0.999. With this as a precedent, a confidence level of 0.999 was assumed for this study. Student's t-factor is 4.144 for a confidence level of 0.999 and a sample size of 11 units, which in this case are bins. Thus,

$$\mu(0.999) \geq -0.7 - 4.144\sqrt{\frac{24.8}{11}}$$

or

$$\mu(0.999) \geq -7 \text{ W/m}^2 \text{ (test conditions)} \quad 10(a)$$

A density correction is required to convert from test conditions to sea-level standard conditions, giving

$$\mu(0.999) \geq -8 \text{ W/m}^2 \text{ (standard conditions)} \quad 10(b)$$

Step 7: Analysis of Power-Train Losses

A general equation for power-train losses is needed before system output power can be calculated. The density of power-train losses, in watts per square meter, is listed for each bin in the last column of Table II and was calculated as follows:

$$p_{32} = \frac{1}{A}(P_3 - Q_3\Omega_2), \quad \text{W/m}^2 \qquad (11)$$

Because of a calibration error in the electrical metering equipment, a zero correction to the output power data is needed. The following procedure was used to make this correction: As shown in Figure 7, the power loss data without the zero correction were plotted versus turbine power density p_2, to obtain a slope of -0.050 and an apparent zero-loss at zero power density. The actual loss at zero power density was obtained during a run-in test of a similar unit (without blades) by measuring the power consumed by the auxiliary drive motor (Table I). This power was approximately 11 kilowatts, indicating a loss of -10 watts per square meter in the power train under zero load. Thus, the power-train loss equation for the Mod-0A machine becomes

$$p_{32} = -10 - 0.050\, p_2, \quad \text{W/m}^2 \qquad (12)$$

The zero correction to the output power data is therefore -11 kilowatts or -10 watts per square meter. Corrected output power densities are given in the third column of Table IV for each bin of test data, calculated using the equation

$$p_3 = \frac{P_3}{A} - 10, \quad \text{W/m}^2 \qquad (13)$$

Experimental system efficiences are listed in the fourth column, calculated as follows:

$$\eta_3 = p_3/p_0 \qquad (14)$$

The last column in Table IV gives the corrected output power data reduced to sea level standard conditions.

Step 8: Calculation of Guaranteed Mean Power Output

Guaranteed mean turbine power and guaranteed mean system power can now be calculated, using the lower-bound estimate on the mean deviation from theory, and the power-train loss equation. Results are listed in Table V. All calculations were made for sea-level standard conditions, with an air density of 1.225 kilograms per cubic meter.

First, the power density of the free-stream wind is calculated for wind speeds at convenient increments of 0.5 and 1.0 meter per second, using Equation (2). Next, theoretical turbine performance at these same wind speeds is calculated by means of the PROP Code and Equations (3) and (4). Results are listed in the third, fourth, and fifth columns of Table V.

Guaranteed mean turbine power density (column 6) is then calculated from the theoretical power density by adding the estimated lower bound on the mean deviation from Equation 10(b). Thus

$$p_{2,gm} = p_{2,th} - 8, \quad \text{W/m}^2 \qquad (15)$$

The confidence level on the guaranteed mean power is assumed to remain at 0.999, the assumed confidence level used in estimating the lower bound on the mean deviation. Guaranteed mean turbine efficiency values are listed in the seventh column, as calculated using Equation (6).

Guaranteed mean generator power data are tabulated in the last three columns of Table V. Equation (12) has been applied as follows:

$$p_{3,gm} = 0.950\, p_{2,gm} - 10, \quad \text{W/m}^2 \qquad (16)$$

Guaranteed mean system efficiency and generator output power are then easily calculated.

Figures 8, 9, and 10 show the data from Tables IV and V in graphical form. In Figure 8, turbine efficiencies are plotted versus tip-speed ratio. Guaranteed mean turbine efficiency peaks at 0.377, compared with a theoretical peak of 0.403. Figure 9 shows the variation of system output power with free-field wind speed, which is the format of most use to wind power system engineers. Guaranteed mean power and theoretical power curves are separated laterally by 0.3 meter per second at cut-in wind speed and less than 0.2 meter per second at rated. Vertically, separation is a constant 9

kilowatts or 8 watts per square meter. This is less than 5% of rated power and does not appear to be excessive, considering the high confidence level of 0.999.

Test data are also plotted on Figure 9 for comparison with both theoretical and guaranteed mean curves. Note that the data points at 47 kW and 69 kW fall below the solid curve, emphasizing that it is not a guaranteed minimum curve.

In Figure 10, the same system output data are displayed in terms of system efficiency versus free-field wind speed. This type of plot may be useful for selecting one or two points at which to guarantee system power output.

CONCLUSIONS

A method of calculating the guaranteed mean power output of a wind turbine generator has been described. The steps in the calculation procedure have been illustrated with data from the DOE/NASA Mod-0A 200 kW wind power plant in Clayton, New Mexico. On the basis of this analysis of performance test data, the following conclusions are drawn:

1. The PROP Code is a practical analytical tool with which the power from a wind turbine like the Mod-0A can be accurately predicted.

2. Deviations between measured and theoretical power do not appear to depend on power density up to 200 watts per square meter, and their distribution is random.

3. Subtracting 8 watts per square meter (9 kW) from the theoretical power output of the Mod-0A system gives a guaranteed mean power with a high degree of confidence.

4. Standard statistical analysis techniques and the method of bins are adequate for the calculation of guaranteed mean power from theory and test data.

REFERENCES

1. de Vries, O.: Fluid Dynamic Aspects of Wind Energy Conversion. AGARD-AG-243, 1979.

2. Andersen, T.S., et al: Mod-0A 200 kW Wind Turbine Generator Design and Analysis Report. DOE/NASA/0163-2, NASA CR-165128, 1980.

3. Tukey, J. W.: Exploratory Data Analysis. Addison-Wesley Publ. Co. (Reading, Mass.), 1977.

4. Akins, R. E.: Performance Evaluation of Wind Energy Conversion Systems Using the Method of Bins--Current Status. Sandia Labs., SAND-77-1375, 1978.

5. Richards, T. R., and Neustadter, H. E.: DOE/NASA Mod-0A Wind Turbine Performance. DOE/NASA/1004-78/13, NASA TM-78916, 1978.

6. Neustadter, H. E.: Data Acquisition and Analysis in the DOE/NASA Wind Energy Program. DOE/NASA/1028-28, NASA TM-81603, 1980.

7. Wilson, R.E.; and Lissaman, P.B.S.: Applied Aerodynamics of Wind Power Machines. Oregon State University, National Science Foundation Grant No. GI-41840, 1974.

8. Wilson, R.E., and Walker, S.N.: A Fortran Program for the Determination of Performance, Loads, and Stability Derivatives of Wind Turbines. Oregon State University, 1974.

9. Wilson. R.E.; Lissaman, P.B.S.; and Walker, S.N.: Aerodynamic Performance of Wind Turbines. Oregon State University, National Science Foundation Grant No. SER 74-04014 A03, 1976.

10. Abbott, H.; Von Doenhoff, A.E.; and Stivers, L.S., Jr.: Summary and Airfoil Data. NACA Report 824, 1945.

11. Gibra, I.N.: Probability and Statistical Inference for Scientists and Engineers. Prentice-Hall (Englewood Cliffs, New Jersey), 1973, pp. 323 and 563.

TABLE I

Performance Test Data From The
Clayton Mod-0A 200 kW Wind Turbine Generator
(Medians of Binned Data)

Bin no.	Turbine input wind V_1 m/s	Turbine shaft torque Q_2 N-m	Turbine shaft speed Ω_2 rad/s	Generator output power P_3 kW
(a) Record No. 1 (10 Jan 78, 2.2 hr on-line, air density = 1.104 kg/m^3)				
1	4.6	15,600	4.19	60
2	5.4	17,600	4.19	73
3	6.3	25,100	4.20	100
4	7.3	33,200	4.21	130
5	8.3	42,000	4.22	170
6	9.3	46,800	4.22	190
7	10.3	47,500	4.22	190
(b) Record No. 2 (18 Jan 78, 4.6 hr on-line, air density = 1.098 kg/m^3)				
8	3.7	12,200	4.19	45
9	4.6	13,600	4.19	54
10	5.6	21,700	4.20	84
11	6.5	27,100	4.20	110
12	7.5	35,200	4.21	140
13	8.5	42,000	4.22	170
14	9.5	46,100	4.22	180
15	10.5	47,500	4.22	190
(c) Shop Run-In (Dec 79, similar unit)				
--	---	0	4.19	-11[a]

a Auxiliary drive motor on transmission output shaft

TABLE II
Results of Performance Tests on the Clayton Mod-0A 200 kW
Wind Turbine Generator and Comparison with Theoretical Turbine Performance

Bin No.	Free-stream wind at turbine midline		Theoretical turbine output power (from PROP Code)			Turbine test results calculated from data in Table I			
	Speed V_0 m/s	Power density p_0 W/m^2	Tip speed ratio λ	Turbine efficiency $\eta_{2,th}$	Power density $p_{2,th}$ W/m^2	Power density p_2 W/m^2	Turbine efficiency η_2	Deviation from theory δp_2 W/m^2	Power train losses[a] p_{32} W/m^2
1	6.46	148	12.3	0.390	58	58	0.39	0	-4
2	6.99	188	11.3	.400	75	65	.34	-10	0
3	7.59	241	10.5	.405	98	94	.39	-4	-5
4	8.26	310	9.63	.399	124	124	.40	0	-8
5	8.93	393	8.93	.389	153	158	.40	5	-6
6	9.59	486	8.32	.375	182	176	.36	- b	-7
7	10.26	595	7.77	.333	198	179	.30	- c	-10
8	5.86	111	13.5	.351	39	46	.41	7	-6
9	6.46	148	12.3	.390	58	51	.34	-7	-3
10	7.12	199	11.1	.403	80	81	.41	1	-6
11	7 73	254	10.3	.404	103	101	.40	-2	-3
12	8.39	325	9.48	.397	129	132	.41	3	-7
13	9.06	410	8.80	.387	159	158	.38	-1	-6
14	9.73	508	8.20	.371	188	174	.34	- b	-7
15	10.39	618	7.68	.320	198	179	.29	- c	-10

a Zero correction required; deduct 10 W/m^2
b Not applicable; blades incorrectly pitched
c Not applicable; wind speed above rated

TABLE III

Probability Distribution of Deviations from Theoretical Turbine Power Density

Bin No.	Deviation from theory δp_2 W/m^2	Number of bins exceeded	Probability of exceedance %
8	7	0.5	4.5
5	5	1.5	13.6
12	3	2.5	22.7
10	1	3.5	31.8
1	0	4.5	40.9
4	0	5.5	50.0
13	-1	6.5	59.1
11	-2	7.5	68.2
3	-4	8.5	77.3
9	-7	9.5	86.4
2	-10	10.5	95.5

Sample mean: $\bar{X} = -0.7$

Sample variance: $s^2 = 24.8$

TABLE IV

System Output Power and Efficiency
Test Results for the Clayton 200 kW
MOD-0A Wind Turbine Generator

Bin no.	Free-stream wind speed V_0 m/s	Output power density, test conditions p_3 W/m^2	System efficiency η_3	Output power, sea-level standard conditions P_3 kW
1	6.46	44	0.30	55
2	6.99	55	.29	69
3	7.59	79	.33	99
4	8.26	106	.34	132
5	8.93	142	.36	177
6	9.59	159	---	---
7	10.26	159	---	---
8	5.86	30	.27	37
9	6.46	38	.26	47
10	7.12	65	.33	81
11	7.73	88	.35	110
12	8.39	115	.35	144
13	9.06	142	.35	177
14	9.73	157	---	---
15	10.39	159	---	---

TABLE V
Theoretical and Guaranteed Mean Power From a 200 kW Mod-0A
Wind Turbine Generator, Under Sea-Level Standard Conditions

Free-stream wind at turbine midline		Theoretical turbine output power (from PROP Code)			Guaranteed mean power (0.999 conf. level)				
					Turbine output		Generator output		
Speed V_0 m/s	Power density p_0 W/m^2	Tip speed ratio λ	Turbine efficiency $\eta_{2,th}$	Power density $p_{2,th}$ W/m^2	Power density p_2 W/m^2	Turbine efficiency η_2	Power density p_3 W/m^2	System efficiency η_3	Power P_3 kW
4.0	39	19.8	0.038	1	-7	-0.179	-17	-0.436	-19
4.5	56	17.6	.161	9	1	0.018	-9	-0.161	-10
5.0	77	15.9	.247	19	11	.143	0	.000	0
5.5	102	14.4	.314	32	25	.245	14	.137	15
6.0	132	13.2	.364	48	40	.303	28	.212	32
6.5	168	12.2	.393	66	58	.345	45	.268	50
7.0	210	11.3	.402	84	76	.362	62	.295	70
7.5	258	10.6	.403	104	96	.372	81	.314	91
8.0	313	9.91	.402	126	118	.377	102	.326	114
8.5	376	9.33	.396	149	141	.375	124	.330	139
9.0	446	8.81	.388	173	165	.370	147	.330	165
9.5	525	8.35	.377	198	190	.362	170	.324	191
10.0	612	7.93	.324	↓	198	.324	178	.291	200
11.0	815	7.21	.243		↓	.243	↓	.218	↓
12.0	1058	6.61	.187			.187		.168	
13.0	1345	6.10	.147			.147		.132	
14.0	1679	5.66	.118			.118		.106	
15.0	2066	5.29	.096			.096		.086	
16.0	2507	4.96	.079			.079		.071	
17.0	3007	4.66	.066			.066		.059	
18.0	3569	4.41	.055	↓		.055	↓	.050	↓

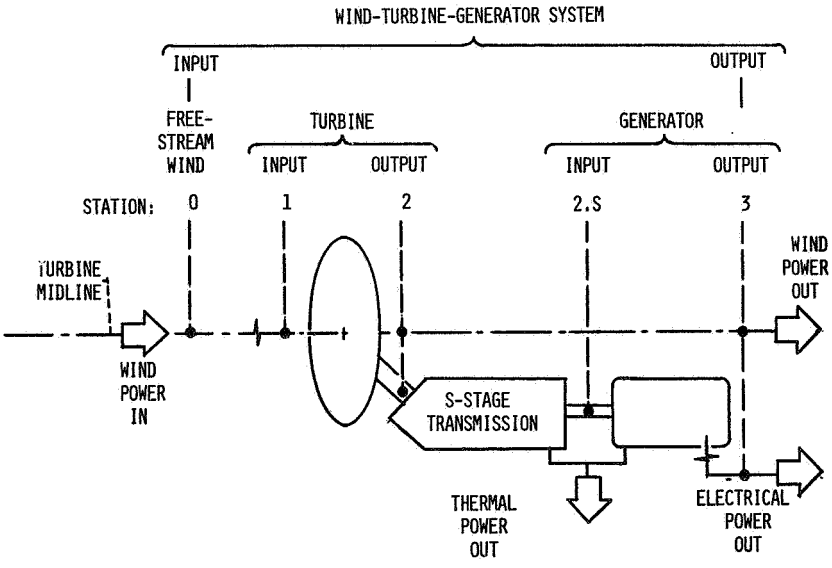

Figure 1. - Schematic diagram of a general wind turbine generator system, showing measuring stations and power flow.

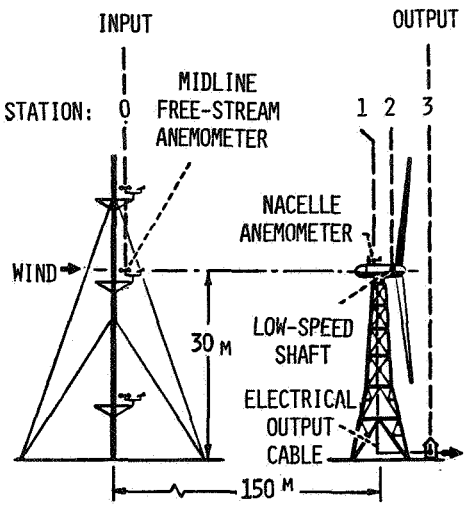

Figure 2. - Performance test installation at Clayton, New Mexico, showing the Mod-0A 200 kW wind turbine generator, the anemometer tower, and measurement stations.

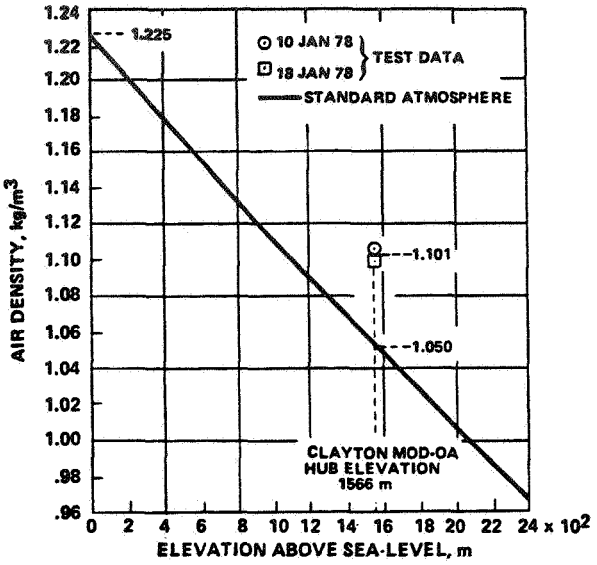

Figure 4. - Air densities during performance tests on the Clayton Mod-0A wind turbine, compared with Standard Atmosphere density.

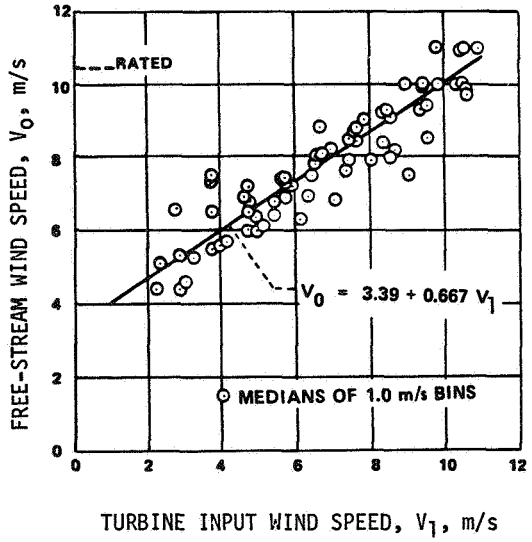

Figure 3. - Correlation of free-stream wind speed at hub height with turbine input wind speed, for the Clayton Mod-0A wind turbine.

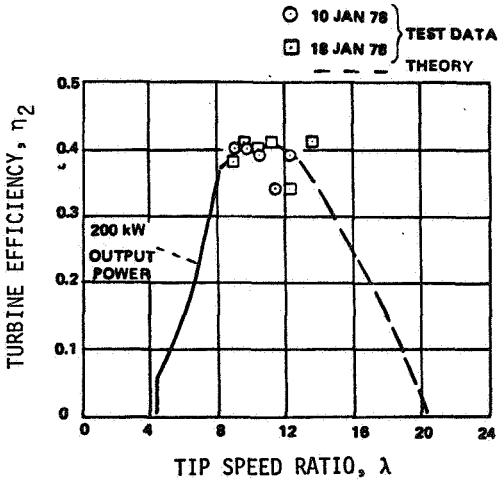

Figure 5. - Theoretical and experimental turbine efficiencies for the Mod-0A 200 kW wind energy system in Clayton, New Mexico.

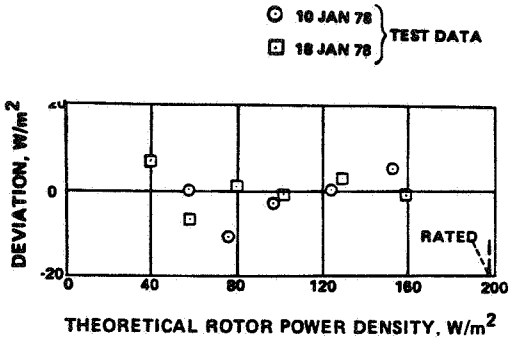

(a) Test for effect of power level

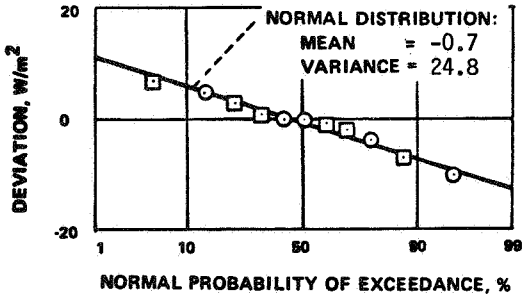

(b) Test for normal distribution

Figure 6. - Deviation of measured turbine power density from theoretical power density, calculated using the PROP Code.

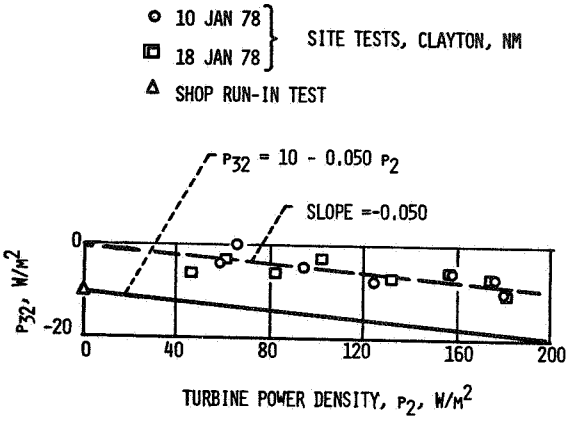

Figure 7. - Analysis of power-train losses in the Mod-0A 200 kW wind turbine system.

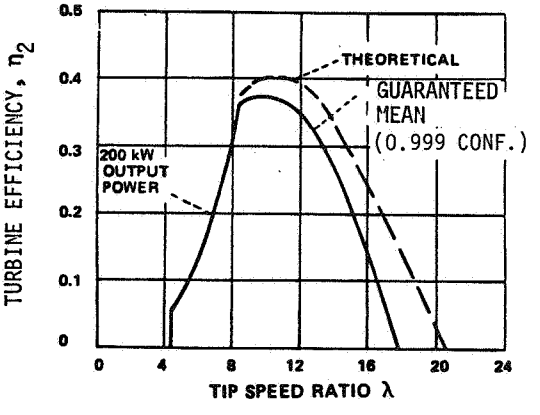

Figure 8. - Theoretical and guaranteed mean turbine efficiencies for the Mod-0A 200 kW wind energy system.

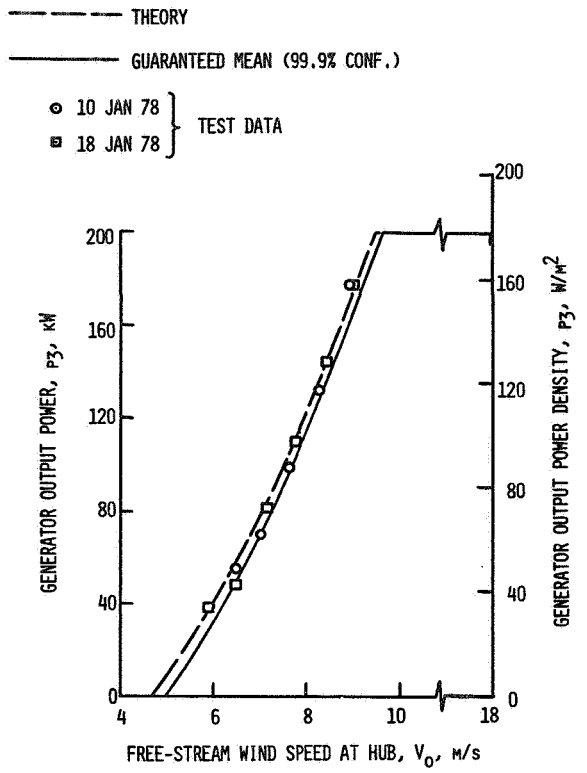

Figure 9. - Generator output power of the Mod-0A 200 kW wind energy system under sea-level standard conditions.

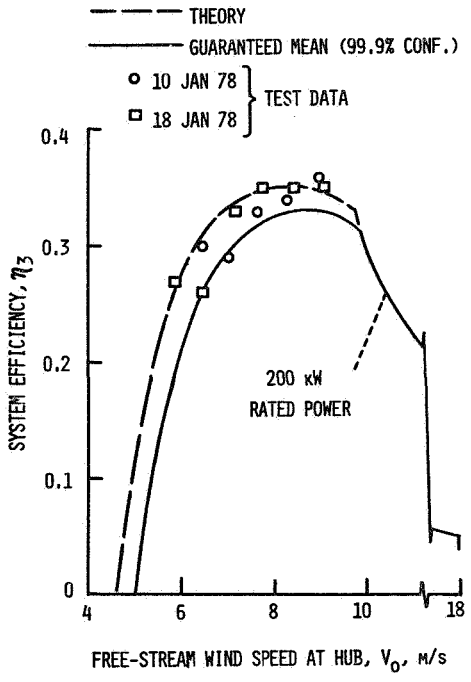

Figure 10. - Overall efficiency of the Mod-0A 200 kW wind energy system.

THE HYDRAULIC WINDMILL*

James A. Browning

Browning Engineering Corporation
P.O. Box 863
Hanover, New Hampshire 03755

ABSTRACT

The hydraulic windmill pumps pressurized oil from rotor shaft level to the ground where a motor-generator produces electricity. Alternatively, the useful output may be heat. Rotor speed is governed by a flow valve. Over pressure, the result of high wind velocity, rotates the tail to move the rotor blades out-of-the-wind. Loss of oil pressure causes a brake to close as well as to swing the tail to its maximum distance from the rotor plane.

DISCUSSION

Advantages of the hydraulic transmission principle lie in the simplicity of rotor speed control and the governing of power output in higher-than-design wind regimes. These functions can now be obtained at low cost and high reliability.

We have made and tested two prototype models of 16-Ft. and 31-Ft. rotor blade diameter. Power outputs were determined by measuring oil flow and pressure. Specific power levels were sufficiently high to warrent the construction of the 71-Ft., two-bladed, horizontal rotor axis machine presently undergoing tests on a high ridge in Lebanon, N.H. (see Figure 1).

We had, initially, selected a downwind rotor position. Later, due to information released by the N.A.S.A. concerning unduly high cyclical rotor shaft torque stresses, we switched to the upwind rotor position with conventional tail.

The design shown in Figure 2 provides a crank-arm at the end of the rotor shaft to power a double-acting hydraulic cylinder. Full-wave rectification of this flow is made by four check valves attached to cylinder ports. The oil passes through the vertical mast about which the windmill rotates to face the wind. The sole rotating seal is the cylinder piston. (In other cases other types of pumps could be used.)

The pressurized oil passes to the ground where pressure variations are damped by a high-pressure accumulator. The pressure-compensated flow control valve limits the maximum oil flow rate to provide a constant rotor speed. A properly sized hydraulic motor drives the generator at the correct speed. Several hydraulic windmills may be operated in-parallel to power a single generator.

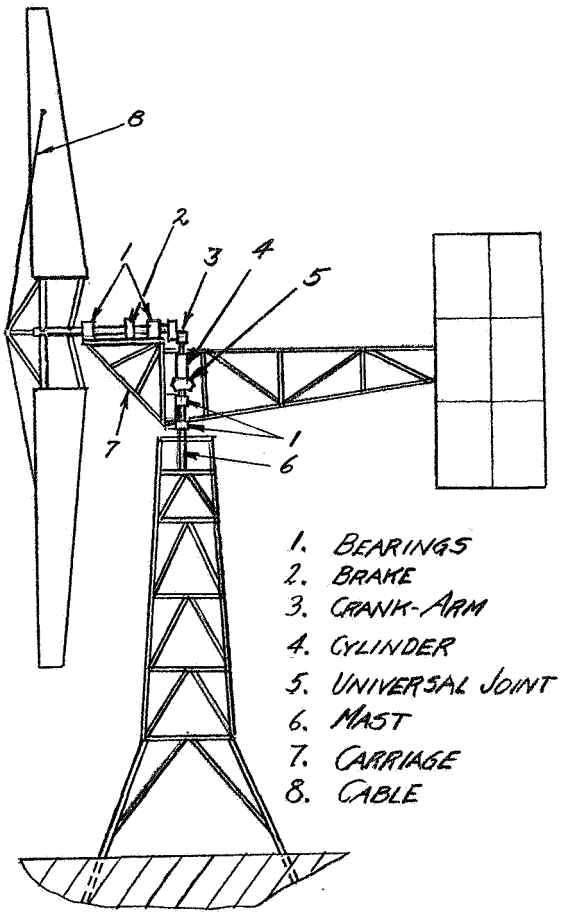

FIG. 1 - MAJOR ELEMENTS OF THE HYDRAULIC WINDMILL

From the motor the oil passes to a low-pressure accumulator pre-charged with nitrogen to a pressure sufficient to lift the oil to the cylinder and to power the tail-governor and safety devices.

Other components of the hydraulic circuit of Figure 2 include a manual shut-off valve which, when closed, assures an effective braking action to the allowable pressure rating of the hydraulic elements. Increase of pressure above this is limited by a pressure relief valve. A water pump

*The work of this program has been sponsored in part by the Department of Energy under Contract No. DE-FG01-80IR10320.

or other mechanically powered device may be substituted for the generator.

Figure 3 illustrates an alternative design which produces heat in place of mechanical energy. Rotor speed is limited by controlling the differential flow from the cylinder. The increased amount of flow on the piston down-stroke (equal to the rod displacement volume) must pass through the flow control. A desurger is required to provide smooth valve action. As accurate speed control is not necessary, the cost of a windmill producing heat is much less than that generating electricity. Efficiencies are much greater as losses in the circuit appear as useful output--heat. We estimate that a given size windmill will produce about 60% more energy when the output is heat rather than electricity.

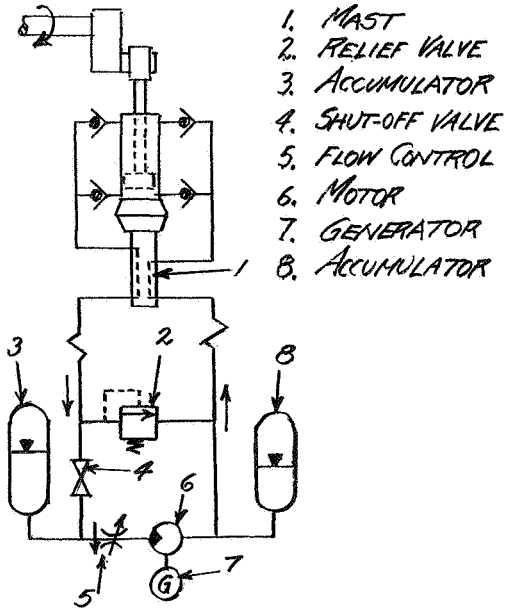

FIG. 2 — THE HYDRAULIC CIRCUIT FOR GENERATING ELECTRICITY

To make a windmill heat generator practical, means should be available for heat storage during the summer for cases where the heat is only utilized during cold months. Storage in the ground appears feasible. Several groups are studying the use of relatively non-permeable aquifers for heat storage.

In solid rock such as granite each 100 feet of 8-inch diameter well bore will accept over 5 KW of heat. Thus, 50 KW of heat can be "pumped" into rock using 5 wells each somewhat over 200 feet deep and spaced correctly apart. The total heat stored over a 7-month season by a 71-Ft. windmill in a region of adequate wind speeds amounts to nearly 80,000 KW-HR. It is thought that over 80% of this becomes available for later use. This is the equivalent of 2,000 gallons of oil burned in a boiler. To this should be added the heat generated during the 5 winter months.

Although this heat analysis is only speculative at this point, this use of wind energy must not be overlooked. In place of the heat equivalent of 2,000 gallons of oil the windmill would have produced about 50,000 KW-HR of electricity during the same 7-month period. At $1.20/Gal of oil the heat savings are $2,400. At $0.05/KW-HR the electric savings amount to $2,500. The heat-producing unit is less expensive than for electricity. Thus, heat generation could be the best use of the hydraulic windmill.

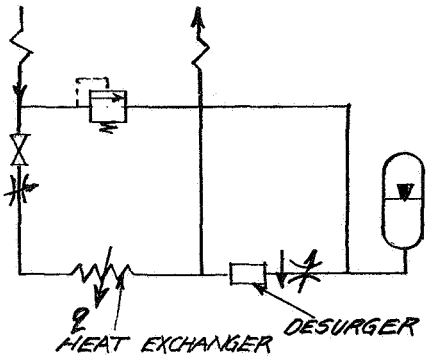

FIG. 3 - HYDRAULIC CIRCUIT FOR HEAT OUTPUT

Where speed control is governed by an impedance in the hydraulic circuit, maximum power output may be limited by matching the average peak oil pressure to a fixed pressure of lower value. This type of governor is sketched in Figure 4 where low and high-pressure cylinders are shown attached to the carriage. The tail support arm can move horizontally about a bearing mounted on the carriage. Oil pressure in the lower cylinder cavity is transmitted through a rifle drill hole.

The low-pressure cylinder "sees" the low-pressure accumulator pressure less the hydrostatic pressure drop in the oil column. A 4-inch diameter cylinder operating at a net pressure of 50 PSIG applies a force of 630 pounds against the movable tail. This force will keep the tail in the "running" mode until a greater counterforce is produced by the high-pressure cylinder. Selecting a cylinder having a 1-inch effective area on its rod side, an average operating peak pressure above 630 PSIG will commence to move the blades

out-of-the-wind. When this high maximum pressure drops due to a lowering of wind velocity the adjustable valve allows the tail to move toward its "running" position.

It is, of course, always possible that the hydraulic circuit could lose a large amount of oil by line leakage or damage to an element. The operation of both speed and power governors would cease. A "fail-safe" mechanism has been incorporated into the design. The tail rotates into its "running" position only when a set oil pressure value is exceeded. Below this, a counterweight (not shown in the figures) pulls the tail to its furthest position from the rotor axis. In addition, the brake mechanism is activated automatically. The brake is also designed to operate when undue vibrations are sensed by a weight held in unstable equilibrium.

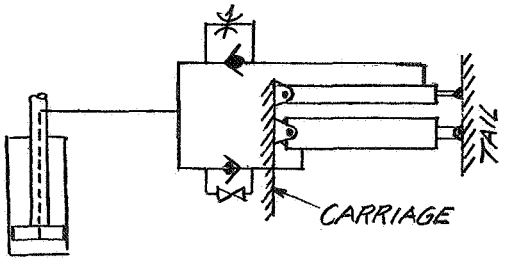

FIG. 4 - TAIL GOVERNOR

CLOSURE

The design of the 71-Ft. hydraulic windmill has attempted to reduce costs while maximizing reliability. These considerations preclude the use of feathering blades, limit the number of blades to two, and reduce communication between rotating structures and the ground to the oil column itself. Judgement of the relative success of these design parameters must await results of the testing period which is only now commencing.

QUESTIONS AND ANSWERS

J.A. Browning

From: J. Tangler

Q: For heating, how does your rotor load match compare to a system using a heat churn? Also, which approach do you consider more cost effective and why?

A: *Larger amounts of heat can be handled easily. In addition, positive speed control and overpower condition control are inherent. Mechanical output, or electric, is possible. I believe the hydraulic unit more cost effective.*

From: A.D. Garrad

Q: How lossy do you expect your hydraulic transmission to be?

A: *About 80% for a cylinder pump-to-motor combination for shaft power production. Nearly 95% for heat using generous amounts of thermal insulation.*

From: J.A.C. Kentfield

Q: What is the blade airfoil section? Do you require a high torque-at-low-speed characteristic?

A: *We have used a delta cross-section blade realizing higher efficiency would have resulted with other designs. It was simpler to construct. High torque-at-low speed characteristic is best.*

From: F.S. Stoddard

Q: Do you have any idea what the overall transmission efficiency is?

A: *Answered above.*

From: R. Shaltens

Q: What is blade construction? What diameter? kW output?

A: *Steel tube truss design with cross-bracing. Tubing covered with plywood which, in turn, has fiberglass-epoxy coating. The rotor diameter is 72 ft. We have designed for about 20 kW in a 15 mph wind.*

From: F.W. Perkins

Q: How much does the machine cost, especially compared to an electric machine?

A: *Considerably less. Speed control accuracy is not required. Also, the high-pressure accumulator, hydraulic motor, and generator are absent. Absolute cost figures for commercial designs in large quantities cannot, yet, be estimated.*

From: Anonymous

Q: What airfoil section is used for the rotor blades?

A: *Answered above.*

From: W.C. Walton

Q: Do you think the failures Waldron showed were due to lack of sophistication or to failure to apply basic engineering?

A: *Lack of sophistication probably results in lowering overall efficiency values--not to the failures reported. Basic engineering includes good design, model making and testing, and redesign. The large amount of funding (internal or external) has not been available to small, new organizations. Certainly a small windmill can achieve optimum design more easily than a large one. Sponsors have skipped this important step of a well thought out engineering program. Perhaps, they should have included this step rather than placing the blame elsewhere. Listening to the majority of the presentations it becomes evident that a major conceptual advancement can only come from the engineering entrepreneur.*

TWO-DIMENSIONAL TURBULENCE MODELS

Walter Frost* and Ming-Chung Lin

The University of Tennessee Space Institute
Tullahoma, Tennessee 37388

ABSTRACT

Two-dimensional turbulence models described in the NASA technical paper 1359, Engineering Handbook on the Atmospheric and Environmental Guidelines for Use in Wind Turbine Generator Development, are compared with experimental measurements made using an array of instrumented towers. Discussion of the spatial correlation coefficient, the two-point spectrum or cross spectrum, and the coherence function is given. The prediction techniques in general agree reasonably well with the experimental results. Measurements of the integral length scale however, do not correlate well with the prediction model recommended in the design handbook.

Introduction

Information relative to two- and three-dimensional turbulence scales is very important to the design of WTG control systems, to the experimental verification of WTG power output, to the loading of the rotor blades resulting from nonuniform gusts over the span of the rotor, and many other such problems. Some two-dimensional turbulence effects are illustrated schematically in Figures 1 through 3. Figure 1 shows that if the control sensor is located on top of the nacelle, variation in wind speed in a longitudinal direction can result in the sensor monitoring a positive gust, whereas the rotor experiences a negative gust. Therefore, in locating the sensor and computing the appropriate control network, one must have an estimate of how well the wind measured at the sensor location is correlated with the wind which occurs at the rotor. Also, the lag time between the large gusts passing the sensor and impacting upon the rotor is of design interest. Figure 2 illustrates the same sort of problem associated with monitoring wind upstream of a wind turbine generator and attempting to correlate this with the wind monitored at the rotor and the fluctuating power output. Figure 3 schematically illustrates how the spatial variation in wind speed for turbulent gusts across the rotor can create antisymmetric loads and, consequently, large bending moments. These and other problems related to the analysis of turbulent effect on WTG's are related specifically to the spatial variation which occurs in gusts making up the turbulent field.

Spatial wind fields are normally determined either by assuming Taylor's hypothesis or by measuring the wind with an array of towers. Since wind speed is normally measured as a time signal at a single point in space, it is generally converted to a spatial distribution with Taylor's hypothesis, i.e.,

$$x = \overline{W}t$$

This is also referred to as the frozen turbulence concept. Figure 4 shows a time history of wind speed measured at the 24-m level of a tower. The mean wind speed at this level is 6.64 m s^{-1}. The figure illustrates the temporal variation and the spatial variation based on the frozen turbulence concept. Taylor's hypothesis assumes that the velocity profile illustrated would be distributed in space according to the horizontal x-axis.

Spatial variation at two or more points in space can also be measured with one or more towers. The spatial variation in the vertical direction can be measured with a single tower instrumented at different levels and in the horizontal or lateral direction with an array of towers. Figure 5 shows the former case of longitudinal wind speed measured at the 24-m, 12-m, 6-m, and 3-m levels. Many interesting features of two-dimensional turbulence are contained in this figure, and these will be discussed in subsequent sections.

Quantitative estimates of the effect of spatial variation in the wind fields are provided by the three statistical quantities:

1. Correlation coefficient
2. Cross spectra or cross correlation
3. Coherence function

Definitions of these terms are given in References 1, 2, and 3.

The purpose of this paper is to describe these quantities physically and to review the models recommended in the Engineering Handbook on the Atmospheric Environmental Guidelines for Use in Wind Turbine Development [1] for predicting their values. Recent experimental data measured with an array of towers is then compared with the recommended prediction techniques.

Tower Array

The tower array is illustrated schematically in Figure 6. Full details of this Atmospheric Boundary Layer Test Facility, Atmospheric Sciences Division, Space Sciences Laboratory, NASA Marshall Space Flight Center, are given in Reference 4. The original purpose of the data measurements reported herein were to investigate the influence of a simulated block building on the wind field surrounding the building. The wind fields at the top of the towers (20 m in height) and well downstream of the building, however, were found to be insensitive to the presence of the building. Therefore, the upper level wind measurements

*Also, President, FWG Associates, Inc., Tullahoma, TN 37388.

represent essentially undisturbed flow and provide meaningful results for WECS design criteria comparisons.

Correlation Coefficients

The correlation coefficient is defined as

$$R_{ij}(r) = \overline{w_i(x)w_j(x + r)}/\sigma_i\sigma_j$$

This quantity is a measure of how fluctuations in the wind speed component, w_i, measured at the position, x, correspond or correlate with fluctuations in the wind speed component, w_j, at $x + r$. Two common mathematical forms of correlation coefficients are the Dryden and the von Karman [1]. Figure 7 is a plot of both the longitudinal and transverse von Karman correlations. The insert defines longitudinal and transverse correlation coefficients. The integral length scale, L_p, appearing in the correlations is discussed in a latter section.

Figure 8 shows the longitudinal correlation with wind parallel to the tower array. The top row of correlation values is plotted as solid circles on Figure 7. The measured correlation in the boundary layer is slightly lower than the theoretical curve. However, the agreement is reasonable considering that near the surface the flow will not be isotropic.

Some interesting properties of the correlation coefficient are observed in Figure 8. It can be seen that directly behind the block building there is very little correlation with the upstream position. This indicates a breakdown in the flow structure between the undisturbed flow upstream and the wake region behind the building. Also, as would be expected, the correlations in the free stream decrease with an increase in the distance separating the two points from which measurements were made. It should be noted that a correlation of unity indicates that the exact signal is felt instantaneously at the two points in question, and it is obvious that a point correlated with itself gives a value of unity (i.e., at the 20-m level on tower 1). A negative correlation between two points suggests a structured reverse flow region where a longitudinal fluctuation in the positive direction at one point results in a negative fluctuation at another point. If the correlation is equal to -1, then the velocities are equal in magnitude but opposite in sign. More experimental values of spatial correlations are given in References 4 and 5.

Integral Length Scale

Although the preceding correlations are based on the assumption of isotropic turbulence, which is a reasonable assumption at high altitudes (h > 300 m (1000 ft)), a technique frequently employed to adapt these isotropic relationships to low altitudes is to permit the integral length scale to vary with height, with surface roughness, and to be different for the longitudinal direction from what they are for the lateral and vertical directions. Relationships for the integral length scales recommended by Counihan [6] are shown in Figure 9. The mathematical definition of length scale is given in the insert. Measured values of L_{w_x} are shown in Figure 10. The scatter in the length scale values is very large and the results do not compare well with the theoretical results. Typically good correlations of measured length scales are difficult to achieve [6].

In theory, however, scale lengths are an indication of the size of the eddies. Figure 10 shows that the higher level usually has the larger length scale for the longitudinal gust, as predicted by the theoretical results shown in Figure 9. The vertical component of wind speed for the measured data [5] gives smaller length scales at a higher level. Conclusions from Figure 10 must be drawn with care since the presence of the building may influence the value of the length scales shown.

Two-Point Spectrum

The correlation coefficient provides a relationship between the correlation of fluctuations in the wind averaged over all values of gust sizes. In many cases, however, we are interested in the correlation between fluctuation in wind speeds of a prescribed frequency. In this case, the statistical quantity known as the two-point spectrum is useful.

Correlation of velocity over different spatial separations can be expressed by the two-point spectrum which has two parts--a real part, co-spectrum, and an imaginary part, quadrature spectrum. Also, this spatial variation in velocities can be expressed in terms of the dimensionless two-point spectrum. The latter form seems more manageable for wind loading applications and also has real and imaginary components as expressed below:

$$\hat{\phi}\left(x,x';\frac{\hat{n}}{\overline{W}}\right) = \frac{Co\left(x,x';\frac{\hat{n}}{\overline{W}}\right) + iQu\left(x,x';\frac{\hat{n}}{\overline{W}}\right)}{\left\{\phi\left(x;\frac{\hat{n}}{\overline{W}}\right)\phi\left(x';\frac{\hat{n}}{\overline{W}}\right)\right\}^{1/2}}$$

where $\hat{n}/\overline{W}$ is the wave number, x and $x' = x + r$ are two spatial coordinates, Qu is the quadrature spectrum (out-of-phase component) of the two-point spectrum, Co is the co-spectrum (in-phase component) of the two-point spectrum, and ϕ is the one-point spectrum.

For reasons of symmetry, the quadrature spectrum between similar velocity components is usually zero for points in the same horizontal plane. For vertical separations, however, Qu is nonzero, although usually not as significant as Co. The existence of the quadrature component can be taken to indicate a preferred orientation of eddies and therefore only occurs when there is asymmetry present in the flow. For example, there is no significant quadrature component in the horizontal direction crosswind spectrum between like components of velocity; however, in the vertical direction where there is strong asymmetry, the quadrature component is significant, and the maximum correlation in the horizontal wind speed at two different heights occurs not simultaneously but when the signal from the lower station is delayed by time roughly equal to $\Delta h/\overline{W}$. It is interesting to inspect Figure 5 in this regard where it has been illustrated that the delay time between eddies of the 24-m and 12-m level is

approximately $\Delta t = 1.7$ s whereas the calculated value of $\Delta h/\overline{W} = 1.9$ s. This means that in the vertical direction a signal hits the top of the tower before it hits the bottom because eddies lean into the wind as a result of wind shear.

Houbolt and Sen [7] have theoretically computed two-point spectra for vertical and longitudinal gusts in isotropic turbulence based on a von Karman correlation model. Their results for vertical fluctuations are plotted in Figure 11. This figure was developed for two-point spectra of nonuniform spanwise gusts on airfoils but has direct application to nonuniform spanwise gusts on WTG rotors.

Figure 12 illustrates the agreement of Houbolt and Sen's [7] theoretical model with experimental data. The model has a steeper slope at high frequencies and predicts less energy at low frequencies than the data show. Physically, this suggests that wind disturbances are more strongly correlated for small values of Δy but not as strongly correlated for intermediate values of Δy as predicted by the recommended design equations. In view of all the variables involved and of the fact that boundary-layer turbulence is not isotropic, however, the agreement with the prediction techniques is reasonably good.

Coherence

The coherence is defined as the absolute value of the two-point spectrum

$$\text{coh} = |\phi(x,x';n/\overline{W})|$$

and serves as a more useable form of the two-point spectrum.

Coherence is expressed by the relationship:

$$\text{coh} = e^{-a\hat{n}\Delta x/\overline{W}_{h=10m}}$$

where Δx is the spatial separation between the two points at which the wind speed is measured. The decay coefficient, a, is approximately equal to 7.5 for vertical separation and 4.5 for horizontal separation. These values represent an average of the decay coefficients reported in References 8, 9, and 10. The lateral decay coefficient is approximately equal to the vertical decay coefficient; hence,

$$a_x \simeq 4.5;\ a_y = a_z \simeq 7.5$$

The reader is cautioned that the values of a quoted are current state-of-the-art values and much research remains to be done before their value is confirmed. Moreover, it is known that a is dependent on terrain roughness, atmospheric stability, and spatial separation.

Measured lateral coherence functions are plotted as a function of reduced frequency, $\eta = \hat{n}\Delta y/\overline{W}_{h=10m}$ in Figure 13. The measured value of $a_y = 10.8$ is compared with the recommended value of $a_y = 7.5$.

The coherence function is a measure of the correlation of velocity fluctuations of frequency, $\hat{n}$, between spatial points separated by Δy.

CONCLUDING REMARKS

Comparisons of experimental data with the prediction models for two-dimensional turbulence design criteria given in [1] show that the models in predict the general trends in the data. The exception is length scales which show a very wide scatter in measured values.

The uncertainty in length scale however, does not impact the magnitude of the predicted statistical properties appreciable, and in general the guidelines recommended in [1] can be used for design with an appropriate safety factor.

ACKNOWLEDGMENTS

The authors are grateful for the use of NASA, Marshall Space Flight Center, Atmospheric Sciences Division, Space Sciences Laboratory, Atmospheric Boundary Layer Tower Array Facility under the guidance of Mr. D. W. Camp. Also, financial support to operate the tower array provided earlier by NSF under Mr. George Lea is acknowledged.

REFERENCES

1. Frost, W., B. H. Long, and R. E. Turner. NASA Technical Paper 1359, Engineering Handbook on the Atmospheric Environmental Guidelines for Use in Wind Turbine Generator Development, December 1978.

2. Bendat, Julius S., and Allan G. Piersol. Random Data: Analysis and Measurement Procedures, Wiley-Interscience (New York), 1971.

3. Lumley, John L., and Hans A. Panofsky. The Structure of Atmospheric Turbulence, Wiley-Interscience (New York), 1964.

4. Steely, Sidney L., and Walter Frost. NASA Contractor Report 3366, "Statistical Analysis of Atmospheric Turbulence About a Simulated Block Building", Contract NAS8-32692, January 1981.

5. Frost, W., and Ming-Chung Lin. "Statistical Analysis of Atmospheric Flow Perpendicular to a Line of Instrumented Towers," Final report under Contract NAS8-32692, in preparation.

6. Counihan, J. "Adiabatic Atmospheric Boundary Layers: A Review and Analysis of Data From the Period 1880-1972", Atmospheric Environment, vol. 9, Pergamon Press, 1975, pp. 871-905.

7. Houbolt, J. C., and A. Sen. "Cross-Spectral Functions Based on von Karman's Spectral Equation", NASA CR-2011, March 1972.

8. Brook, R. R. "A Note of Vertical Coherence of Wind Measured in an Urban Boundary Layer", Boundary Layer Meteorology, vol. 9, 1975.

9. Ropelewski, C. F., H. Tennekes, and H. A. Panofsky. "Horizontal Coherence of Wind Fluctuations", Boundary Layer Meteorology, vol. 5, 1973.

10. Davenport, A. G. "The Spectrum of Horizontal Gustiness Near the Ground in High Winds," Quart. J. Roy. Meteor. Soc., vol. 87, pp. 194-211, 1961.

NOMENCLATURE

h	Height above the surface
$\hat{L}$	Integral turbulence length scale
L_p	Longitudinal isotropic turbulence integral scale
L_{w_x}	Characteristic length scale of longitudinal wind fluctuation
L_{w_y}	Characteristic length scale of lateral wind fluctuations
$\hat{n}$	Frequency in cycles per second
R_{w_x}	Lateral correlation
r	Separation distance in turbulence correlations
t	Time
W_h	Wind speed at height h
W_x	Longitudinal wind speed
w_x	Longitudinal wind speed fluctuation about the mean
W_y	Lateral wind speed
w_y	Lateral wind speed fluctuation about the mean
W_z	Vertical wind speed
w_z	Vertical wind speed fluctuation about the mean
z_o	Surface roughness
η	Reduced frequency, $nh/\overline{W}$
$\overline{\zeta}$	Dimensionless two-point spectrum, $2\phi(\sigma,\overline{n})_{w_\alpha}/\sigma^2_{w_\alpha}$
σ_{w_α}	Standard deviations of the turbulence fluctuations where α represents x, y, or z, respectively
$\phi_{ij}(\hat{n})$	Two-point spectrum
$\phi_{w_\alpha}(\hat{n})$	Spectral density function for turbulence kinetic energy

Over Symbols

$(\overline{\ })$	10 min average or greater

Subscripts

α	Designates one of three wind vector component directions, x, y, or z

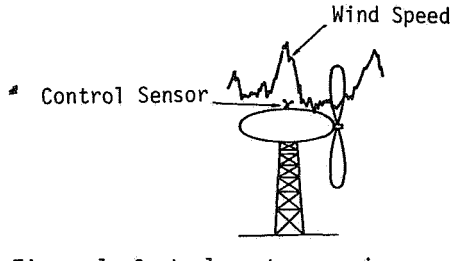

Figure 1 Control system requires correlation between wind speed at sensor and at rotor.

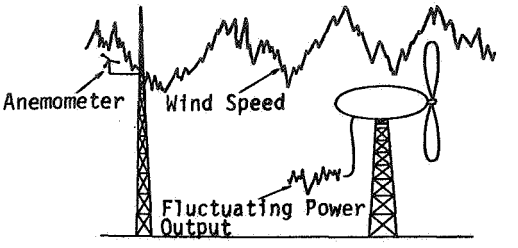

Figure 2 Correlation of wind speed at measuring tower with wind speed at rotor is needed for experimental verification.

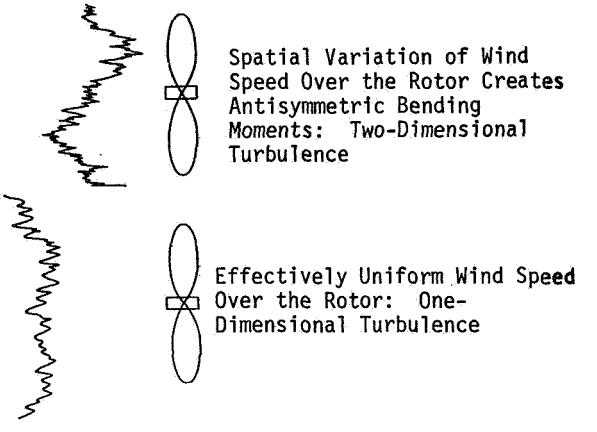

Figure 3 Wind speed fluctuation over the rotor.

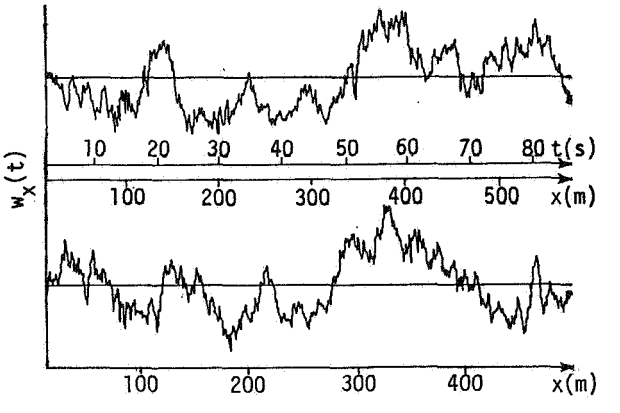

Figure 4 Illustrates Taylor's hypothesis (frozen turbulence) with data measured at 24-m and 12-m level.

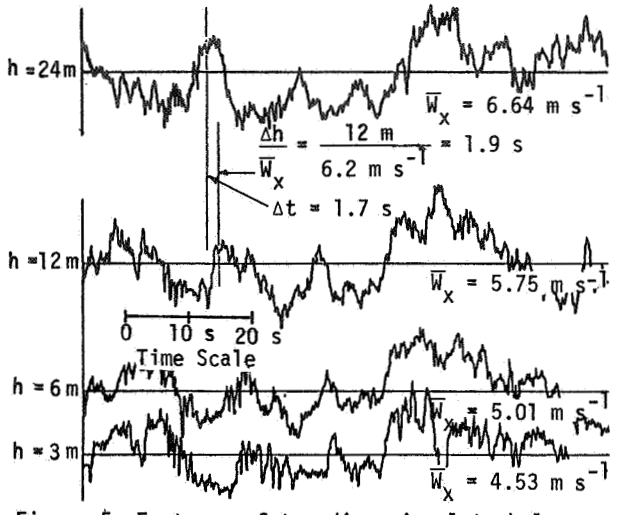

Figure 5 Features of two-dimensional turbulence measured with a single tower at 24-m, 12-m, 6-m, and 3-m level.

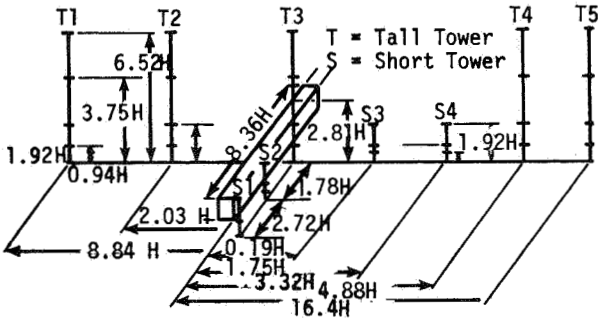

Figure 6 Schematic of the current configuration of the NASA Marshall Space Flight Center's Boundary Layer Facility. (Not to scale, H = 3.2 m.)

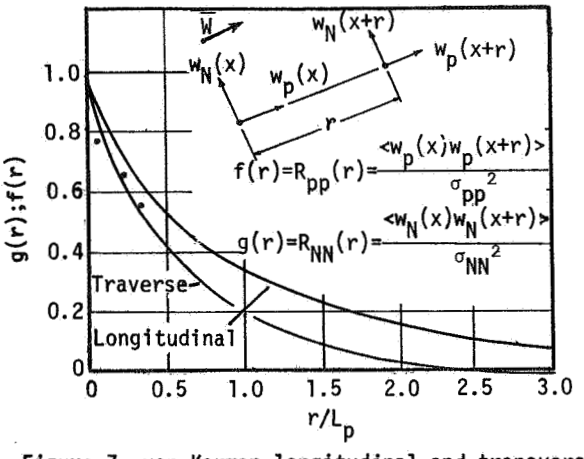

Figure 7 von Karman longitudinal and transverse fundamental correlation function for isotropic turbulence.

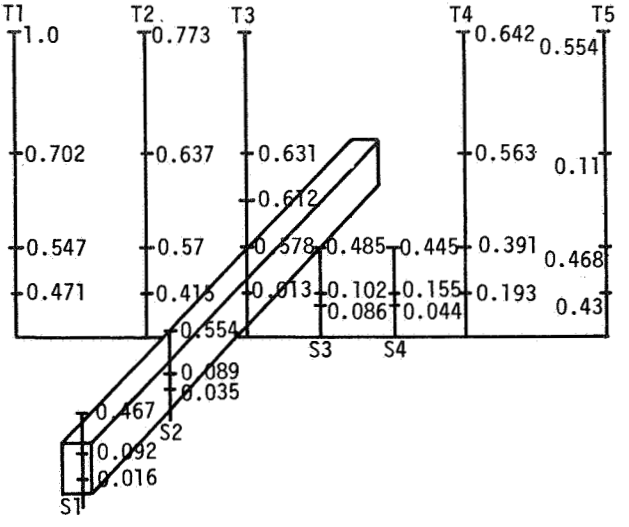

Figure 8 Spatial correlations of the longitudinal velocity component measured at the 20-m level on tower 1 with all other measuring stations [4].

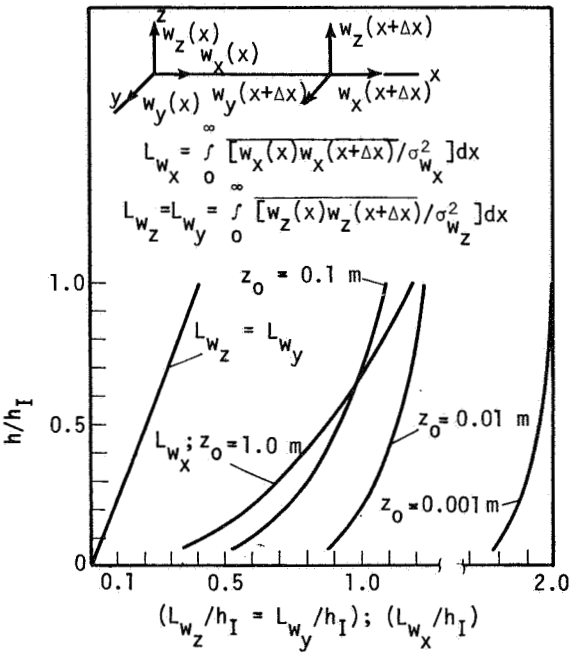

Figure 9 Integral scale length h_I = 250 m.

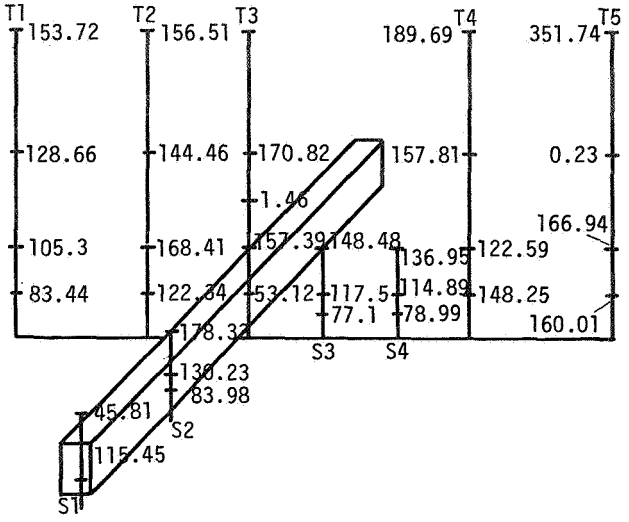

Figure 10 Integral length scale in meters for longitudinal component, L_{w_x}, wind perpendicular to array.

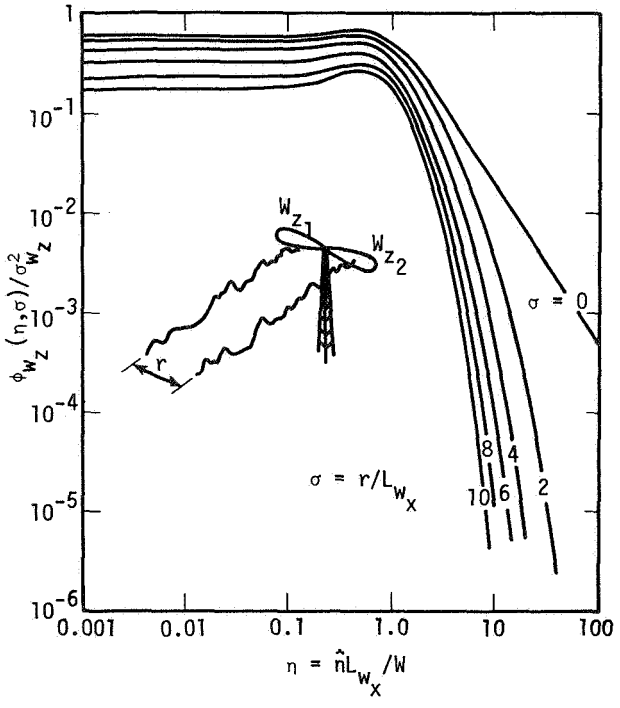

Figure 11 Theoretical two-point spectra for treatment of nonuniform spanwise gust.

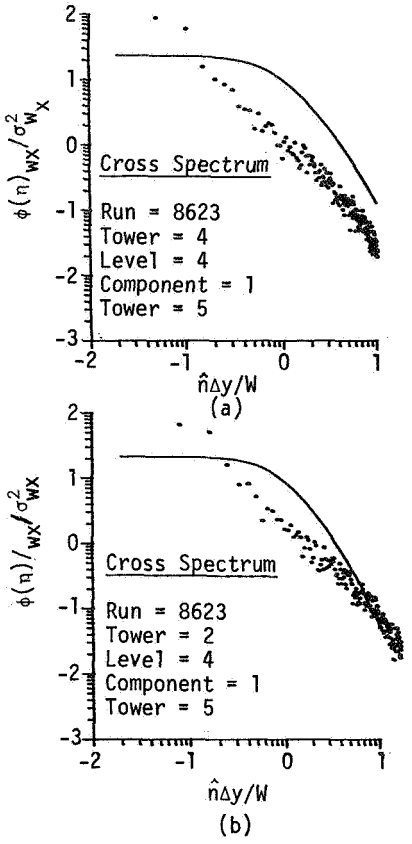

Figure 12 Comparison of theoretical two-point spectra with measured data.

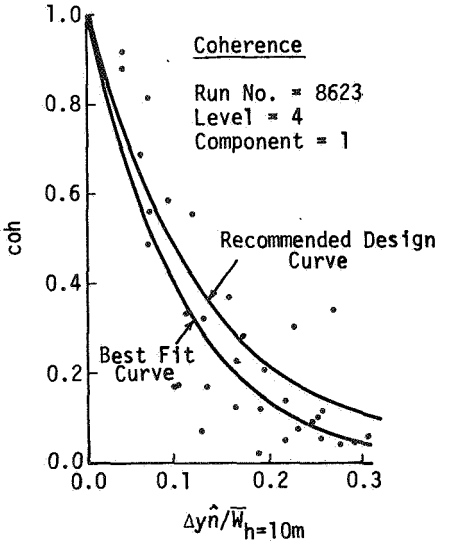

Figure 13 Experimental coherence function. Solid line is the best fit curve of $e^{-a\Delta yn/\overline{W}}$ where a = 10.8.

QUESTIONS AND ANSWERS

W. Frost

From: W.E. Holley

Q: Does the coherency = 1 at low frequency?

A: *Our data indicates that it does and, of course, the computation procedure forces it to unity when Δy goes to zero.*

From: D.C. Powell

Q: Why do you use length scale to calculate reduced frequency when you show that length scale is not a good parameter?

A: *Nearly all current prediction models use length scales as a scaling parameter. Personally I prefer the approach given in reference 1 of the paper which utilizes a characteristic reducing frequency and scales length with height above ground.*

SECOND DOE/NASA WIND TURBINE DYNAMICS WORKSHOP

Structural Dynamics

Session Chairman - T.P. Cahill (NASA LeRC)

"Review of Analysis Methods for Rotating Systems with Periodic Coefficients"
J. Dugundji
J. Wendell
(MIT)

"An Approximate Method for Solution to Variable Moment of Inertia Problem"
E.W. Beans
(University of Toledo)

"Computation of the Modes and Polar Moment of Inertia of the Blades of an HAWT"
D. Noisiux
G. Beaulieu
(IREQ)

"Dynamic Analysis of Darrieus VAWT Rotors"
D.W. Lobitz
(Sandia Labs.)

"Flutter of Darrieus Wind Turbine Blades: Correlation of Theory and Experiment"
N.D. Ham
(MIT)

"Whirl Flutter Analysis of a Two-Bladed Teetered Rotor on an HAWT"
D.C. Janetzke
K.R.V. Kaza
(NASA LeRC)

"WEST Analyzers Using Hybrid Simulation Techniques"
J.A. Hoffman
(Paragon Pacific, Inc.)

"Dynamics of the MOD-6H Wind Turbine: Experienced Based on the Use of MOSTAB-HFW Computer Code"
Yi-Yuan Yu
(Rockwell International)

"Comparison of Upwind & Downwind Rotor Operations of the DOE/NASA 100 kW MOD-0 Wind Turbine"
J. Glasgow
D. Miller
R. Corrigan
(NASA LeRC)

REVIEW OF ANALYSIS METHODS FOR ROTATING SYSTEMS WITH PERIODIC COEFFICIENTS

John Dugundji and John H. Wendell

Department of Aeronautics and Astronautics
Massachusetts Institute of Technology
Cambridge, Massachusetts 02139

ABSTRACT

The present article reviews two of the more common procedures for analyzing the stability and forced response of equations with periodic coefficients, namely, the use of Floquet methods, and the use of multiblade coordinate and harmonic balance methods. The analysis procedures of these periodic coefficient systems are compared with those of the more familiar constant coefficient systems.

INTRODUCTION

In dynamic analyses of rotating wind turbine systems, one frequently encounters equations of motion with periodic coefficients. Unlike systems with constant coefficients whose analysis techniques are well known and familiar, the analysis of these periodic coefficient equations are somewhat less familiar. The present paper reviews two of the more common procedures for analyzing the stability and response of these periodic coefficient equations, namely, the use of Floquet methods and the use of multiblade coordinate and harmonic balance methods. To put things in proper perspective and to make comparisons, the paper will briefly review the constant coefficient systems first. The paper is essentially based on Appendices A, B, C, and D of a recent report by the authors, (ref. 1).

CONSTANT COEFFICIENT SYSTEMS

Given a system of N linear differential equations with constant coefficients,

$$\underline{M}\,\ddot{\underline{q}} + \underline{B}\,\dot{\underline{q}} + \underline{K}\,\underline{q} = \underline{F}\,(t) \tag{1}$$

where $\underline{M}$, $\underline{B}$, and $\underline{K}$ are square matrices of order NxN, while $\underline{q}$ and $\underline{F}\,(t)$ are column matrices of order Nx1. These can be rearranged as,

$$\begin{bmatrix} \underline{M} & 0 \\ 0 & \underline{M} \end{bmatrix} \begin{Bmatrix} \dot{\underline{q}} \\ \ddot{\underline{q}} \end{Bmatrix} - \begin{bmatrix} 0 & \underline{M} \\ -\underline{K} & -\underline{B} \end{bmatrix} \begin{Bmatrix} \underline{q} \\ \dot{\underline{q}} \end{Bmatrix} = \begin{Bmatrix} 0 \\ \underline{F} \end{Bmatrix} \tag{2}$$

Then, multiplying through by the inverse of the mass matrix gives 2N first order equations,

$$\dot{\underline{y}} - \underline{A}\,\underline{y} = \underline{G} \tag{3}$$

where $\underline{A}$ is a square matrix of order 2Nx2N, while $\underline{y}$ and $\underline{G}$ are column matrices of order 2Nx1 given by

$$\underline{A} = \begin{bmatrix} 0 & \underline{1} \\ -\underline{M}^{-1}\underline{K} & -\underline{M}^{-1}\underline{B} \end{bmatrix}, \quad \underline{y} = \begin{Bmatrix} \underline{q} \\ \dot{\underline{q}} \end{Bmatrix}, \quad \underline{G} = \begin{Bmatrix} 0 \\ \underline{M}^{-1}\underline{F} \end{Bmatrix} \tag{4}$$

The above rearrangement, Eq. (3), is valid providing the mass $\underline{M}$ is not singular, which is usually the case with physical systems.

(a) Stability

To investigate stability, one sets $\underline{F} = 0$ (which gives $\underline{G} = 0$) in Eq. (3), to obtain a set of homogeneous equations. Then one seeks exponential solutions of the form $\underline{y} = \underline{y}\, e^{pt}$. Placing these into Eq. (3) leads to the standard eigenvalue problem,

$$\underline{A}\,\underline{y} = p\,\underline{y} \tag{5}$$

Eigenvalues p_k of the matrix $\underline{A}$ can be obtained by standard numerical eigenvalue routines. If any eigenvalue p_k is positive real or has a positive real part, the system represented by Eq. (3) or equivalently by Eq. (1) is unstable.

(b) Forced Response

Under steady-state conditions, the forces $\underline{F}\,(t)$ on a rotating system tend to occur periodically in multiples of the rotation frequency Ω. One can then express the force for a particular frequency $\omega_m = m\Omega$, in the form,

$$\underline{F}(t) = \mathrm{Re}(\underline{F}\, e^{i\omega_m t}) = \underline{F_R}\cos\omega_m t - \underline{F_I}\sin\omega_m t \tag{6}$$

The response $\underline{q}(t)$ is similarly of the form,

$$\underline{q}(t) = \mathrm{Re}(\underline{q}\, e^{i\omega_m t}) = \underline{q_R}\cos\omega_m t - \underline{q_I}\sin\omega_m t \tag{7}$$

Placing Eqs. (6) and (7) into the basic Eq. (1) and matching sine and cosine terms gives a set of 2Nx2N real equations,

$$\begin{bmatrix} \underline{G} & \underline{H} \\ -\underline{H} & \underline{G} \end{bmatrix} \begin{Bmatrix} \underline{q_R} \\ \underline{q_I} \end{Bmatrix} = \begin{Bmatrix} \underline{F_R} \\ \underline{F_I} \end{Bmatrix} \tag{8}$$

where one has the matrix elements,

$$\underline{G} = \underline{K} - \omega_m^2\,\underline{M}\,, \qquad \underline{H} = \omega_m \underline{B} \tag{9}$$

Given the amount of the m^{th} harmonic force present $\underline{F_R}^{(m)}$ and $\underline{F_I}^{(m)}$, Eq. (8) can be solved by simple inversion to find the response $\underline{q_R}^{(m)}$ and $\underline{q_I}^{(m)}$ for each harmonic. Then, one may sum up all the harmonics to give the total periodic response as,

$$\underline{q}(t) = \sum_{m=0}^{N} \underline{q_R}^{(m)}\cos\omega_m t - \sum_{m=0}^{N} \underline{q_I}^{(m)}\sin\omega_m t \tag{10}$$

Finding the response $\underline{q}(t)$ this way rather than by direct numerical integration, allows one to assess the effects of a particular harmonic on the

resulting response of the system.

FLOQUET METHODS

Assume the coefficients $\underline{M}$, $\underline{B}$, $\underline{K}$ in Eq. (1) or equivalently the coefficients $\underline{A}$ in Eq. (3) vary periodically in time, rather than being constants. For illustrating Floquet methods, it will be convenient to use the first order representation, namely 2N equations of the form,

$$\dot{\underline{y}} - \underline{A}(t)\underline{y} = \underline{G}(t) \tag{11}$$

where $\underline{A}(t)$ and $\underline{G}(t)$ are periodic over an interval T.

(a) Stability

The Floquet stability analysis described here follows that given by Peters and Hohenemser (ref. 2). To investigate stability, one sets $\underline{G}=0$ in Eq. (11) to obtain homogeneous equations. The Floquet theorem states the solution of Eq. (11) with $\underline{G}=0$ is of the form

$$\underline{y}(t) = \underline{B}(t)\left\{C_k e^{P_k t}\right\} \tag{12}$$

where $\underline{y}(t)$ and $\{C_k e^{P_k t}\}$ are $2N\times 1$ column matrices, and $\underline{B}(t)$ is a $2N\times 2N$ square matrix periodic over period T, that is, $\underline{B}(T)=\underline{B}(0)$. From the above, one can express

$$\underline{y}(0) = \underline{B}(0)\ \{C_k\} \tag{13}$$

$$\underline{y}(T) = \underline{B}(T)\left\{C_k e^{P_k T}\right\} = \underline{B}(0)\left\{C_k e^{P_k T}\right\} \tag{14}$$

Also, one can express $\underline{y}(T)$ as,

$$\underline{y}(T) = \underbrace{[\underline{y}^{(1)}\ \underline{y}^{(2)}\ \ldots]}_{[Q]} \begin{Bmatrix} y_1(0) \\ y_2(0) \\ \vdots \end{Bmatrix} \tag{15}$$

where $\underline{y}^{(1)}$ is the solution at t=T of Eq. (11) with $\underline{G}=0$, for the initial conditions $y_1=1$ and all remaining $y_i(0)=0$, $\underline{y}^{(2)}$ is the solution for $y_2(0)=1$ and all remaining $y_i(0)=0$, etc. The square matrix [Q] is called the "Transition Matrix." Equating Eq. (15) to (14) and introducing Eq. (13) gives,

$$[Q]\left[\left\{B(0)\right\}_1 C_1 + \left\{B(0)\right\}_2 C_2 + \ldots\right] = \left\{B(0)_1\right\} C_1 e^{P_1 T} + \ldots \tag{16}$$

Since C_k are independent, one must have

$$[Q]\ \{B(0)\}_k = \lambda_k \{B(0)\}_k \tag{17}$$

where $\lambda_k = e^{P_k t}$ are the eigenvalues of the [Q] matrix. One then has the relation

$$p_k = \frac{1}{T}\,\ell n\,\lambda_k = \alpha_k + i\,\omega_k \tag{18}$$

from which the real and imaginary parts of the stability exponent p_k are given as

$$\alpha_k = \frac{1}{T}\,\ell n|\lambda_k| = \frac{1}{2T}\,\ell n[(\lambda_k)_R^2 + (\lambda_k)_I^2] \tag{19}$$

$$\omega_k = \frac{1}{T}\tan^{-1}\left[(\lambda_k)_I/(\lambda_k)_R\right] \tag{20}$$

The real part α_k is a measure of the growth or decay of the response, as can be seen from Eq.(12). Values of $\alpha_k>0$ (or equivalently $|\lambda_k|>1$) indicate instability. The imaginary part ω_k represents the frequency. However, because $\tan^{-1}$ is multivalued, one can only obtain ω_k to within a multiple of 2π. To obtain the actual frequency and motion corresponding to the k^{th} root, p_k, one sets $C_k=1$ and all other remaining $C_i=0$ in Eqs. (12) and (13). Then, using the k^{th} eigenvector $\{B(0)\}_k$ from Eq. (17) as an initial condition, one would solve Eq. (11) with $\underline{G}=0$ by numerical techniques for the resultant motion.

Summarizing: To check for stability of a system of linear equations with periodic coefficients, obtain the eigenvalues λ_k of the "Transition Matrix" [Q]. If $|\lambda_k|>1$, one has instability. The traditional stability exponent p_k is related to λ_k through Eqs. (18) to (20). Two remarks on the above procedure should be noted. (1) The "Transition Matrix" [Q] can be formed by solving either the first order equations, Eqs. (11) with $\underline{G}=0$, or the second order equations, Eqs. (1) with $\underline{F}=0$ and periodic coefficients, whichever is more convenient for the integration scheme. (2) The above procedure will still apply even if the equations have constant coefficients. However, for such cases it is usually easier to form the matrix $\underline{A}$ given by Eq. (4) and obtain its eigenvalues p_k rather than to form the "Transition Matrix" [Q] and obtain its eigenvalues λ_k.

(b) Forced Response

Solutions of Eq. (11), or equivalently Eq. (1) with periodic coefficients, can be obtained by direct numerical integration using some convenient integration scheme. By proper choice of the initial conditions, one can eliminate all transients from the response and obtain the desired steady-state dynamic response by integrating through only one period T, instead of the very large number usually required to reach steady-state for lightly damped systems. A procedure for finding the proper initial conditions is given below.

Solutions of Eq. (11) are of the general form,

$$\underline{y}(t) = \underline{y}_H(t) + \underline{y}_P(t) \tag{21}$$

where $\underline{y}_H(t)$ is the homogeneous solution and $\underline{y}_P(t)$ is the particular solution. One can obtain a complete solution of Eq. (11) numerically for any given set of initial conditions. Call this solution $\underline{y}_E(t)$. One can add any number of additional homogeneous solutions $\Delta\underline{y}_H(t)$ having different initial conditions, to this solution. This would give a new solution to Eq. (11),

$$\underline{y}(t) = \underline{y}_E(t) + \Delta\underline{y}_H(t) \tag{22}$$

which would have different initial conditions than those for $\underline{y}_E(t)$.

One can obtain all the homogeneous solutions of Eq. (11) by solving Eq. (11) with $\underline{G}=0$ a total of 2N times, subject to the initial conditions $y_1=1$ and all remaining $y_i=0$, then $y_2=1$ and all remaining $y_i=0$, etc. In fact, this was done earlier to investigate stability and resulted in the 2N homogeneous solutions $\underline{y}^{(1)}(t)$, $\underline{y}^{(2)}(t)$, etc., respectively. Thus one may write

$$\Delta\underline{y}_H(t) = \underbrace{[\underline{y}^{(1)}(t)\ \underline{y}^{(2)}(t)\ \ldots]}_{[Q(t)]} \begin{Bmatrix} C_1 \\ C_2 \\ \vdots \end{Bmatrix} \tag{23}$$

where $[Q(t)]$ is the transition matrix at any instant of time, and C_1, C_2, ... are 2N arbitrary constants. The new solution Eq. (22) can be rewritten as

$$\underline{y}(t) = \underline{y}_E(t) + [Q(t)]\underline{C} \tag{24}$$

For a periodic solution over period $T=2\pi/\Omega$, one must have $\underline{y}(T)=\underline{y}(0)$. Placing Eq. (24) into this condition and solving for the arbitrary constants $\underline{C}$ gives,

$$\underline{y}_E(T) + [Q(T)]\underline{C} = \underline{y}_E(0) + [Q(0)]\underline{C}$$

$$\underline{C} = \left[\underline{1} - [Q]\right]^{-1} \left\{\underline{y}_E(T) - \underline{y}_E(0)\right\} \tag{25}$$

where it was noted that $[Q(0)]=\underline{1}$, and $[Q(T)]=[Q]$ is the "Transition Matrix" found earlier for the stability investigation. Placing these values of $\underline{C}$ back into Eq. (24), the initial conditions for insuring a periodic solution become

$$\underline{y}(0) = \underline{y}_E(0) + [\underline{1} - \underline{Q}]^{-1} \left\{\underline{y}_E(T) - \underline{y}_E(0)\right\} \tag{26}$$

One can then solve the basic Eq. (11) numerically with these initial conditions to obtain a periodic solution over one period. It should be noted that if one had chosen the initial conditions for $\underline{y}_E(t)$ as $\underline{y}_E(0)=0$, one would obtain simply

$$\underline{y}(0) = [\underline{1} - \underline{Q}]^{-1}\ \underline{y}_E(T) \tag{27}$$

This is a particularly convenient form for finding the initial conditions for periodic solutions.

An alternative form for determining the proper initial conditions for periodic solutions has been proposed by Friedmann and his coworkers (refs. 3 and 4) in their work on wind turbines, namely,

$$\underline{y}(0) = [\underline{1} - \underline{Q}]^{-1}\ \underline{Q} \int_0^T [Q(t)]^{-1}\underline{F}(t)dt \tag{28}$$

This is similar to Eq. (27), but does not use $\underline{y}_E$. It seems easier to obtain $\underline{y}_E(T)$ with initial conditions $\underline{y}_E(0)=0$ and use Eq. (27), rather than obtaining $[Q(t)]$ at every point and performing the indicated operations required by Eq.(28).

The general procedure described by Eqs. (21) to (27) may be extended to deal also with nonlinear equations,

$$\dot{\underline{y}} - \underline{A}(t)\underline{y} = \underline{F}(t, \underline{y}, \dot{\underline{y}}) \tag{29}$$

where the right hand side now contains nonlinear functions of the coordinates. An iterative variation of the previous linear procedure to obtain the initial conditions for periodic solutions of nonlinear equations is used by the MOSTAS Code (ref. 5). The procedure is as follows. First, a numerical solution $\underline{y}_E(t)$ is obtained to the nonlinear Eq. (29) for some estimate of the initial conditions $\underline{y}_E(0)$. Then each of the 2N elements of $\underline{y}_E(0)$ is perturbed a small amount ε_i and the resulting 2N solutions are obtained. This involves solving the nonlinear Eq. (29) subject to the initial conditions,

$$\underline{y}_E(0) + \begin{Bmatrix} \varepsilon_1 \\ 0 \\ 0 \\ \vdots \end{Bmatrix}, \quad \underline{y}_E(0) + \begin{Bmatrix} 0 \\ \varepsilon_2 \\ 0 \\ \vdots \end{Bmatrix}, \text{ etc.} \tag{30}$$

and will result in 2N responses of the form

$$\underline{y}^{(i)}(t) = \underline{y}_E(t) + \Delta\underline{y}_E^{(i)}(t) \tag{31}$$

where $\Delta\underline{y}_E^{(i)}(t)$ represents the effect of each perturbation ε_i, and is found by subtracting $\underline{y}_E(t)$ from each of the 2N resulting responses $\underline{y}^{(i)}(t)$. One can then express the total solution approximately as,

$$\underline{y}(t) = \underline{y}_E(t) + \underbrace{\left[\frac{1}{\varepsilon_1}\Delta\underline{y}_E^{(1)}, \frac{1}{\varepsilon_2}\Delta\underline{y}_E^{(2)}, \ldots\right]}_{[Q]} \begin{Bmatrix} \varepsilon_1 \\ \varepsilon_2 \\ \vdots \end{Bmatrix} \tag{32}$$

which is in the same form as Eq. (23). Then, again requiring the periodicity condition $\underline{y}(T)=\underline{y}(0)$ and following through as before, will result in the same relation Eq. (26) found previously. Because of the nonlinearities now present, the elements of $[Q]$ as found from Eqs.(32), (31), (30) may vary with the amplitude of the initial condition used, $\underline{y}_E(0)+\varepsilon_i$. This is in contrast to the linear case where $[Q]$ remains always constant. Hence, an iterative application of Eq.(26) with a new corrected $\underline{y}_E(0)$ should be done. If the nonlinearities are not too great, convergence to the required $\underline{y}_E(0)$ should be rapid.

It should be remarked that the numerical procedure for forced response described in this section, can also be used for the constant coefficient linear case, although it is probably easier there to obtain the solution by using Harmonic response methods given by Eqs.(6) to (10). However, for cases where there is some nonlinearity, the present iterative approach becomes attractive.

MULTIBLADE COORDINATES AND HARMONIC BALANCE

Given a rotor with N blades rotating with rotation speed Ω, attached to a flexible tower. Because the tower motions x_i are described in a fixed reference frame while the blade motions β_i are described relative to a rotating frame, the resulting equations may have mass, damping, or stiffness coefficients which are functions of the azimuthal position of the k^{th} blade ψ_k. A typical such set of equations is given, for example, in refs. 6 and 7 as,

$$M\ddot{x} + C_x\dot{x} + k_x x + S\frac{d^2}{dt^2}\sum^{k}\beta^{(k)}\cos\psi_k = F_x(t)$$
$$S\ddot{x}\cos\psi_k + I\ddot{\beta}^{(k)} + C_\beta\dot{\beta}^{(k)} + k_\beta\beta^{(k)} = F_\beta^{(k)}(t) \qquad (33)$$
$$(k = 1, 2, \ldots N)$$

where the azimuthal position ψ_k is,

$$\psi_k = \Omega t + (k-1)\,2\pi/N \qquad (34)$$

The first equation above represents force equilibrium for the tower motion x, while the remaining N equations represent force equilibrium for the motion of each of the N blades $\beta^{(k)}$. The above equations are readily generalized to more tower motions x_i, and more blade coordinates for each blade $\beta_j^{(k)}$.

(a) Stability

To examine Eqs. (33) for stability, one sets $F_x=0$ and $F_\beta^{(k)}=0$ to obtain homogeneous equations.

For rotors with 3 or more blades $N \geq 3$, one may eliminate the periodic coefficients in these equations by introducing new multiblade coordinates $b_o(t)$, $b_s(t)$, $b_c(t)$ such that

$$\beta^{(k)} = b_o(t) + b_s(t)\sin\psi_k + b_c(t)\cos\psi_k \qquad (35)$$

Substituting these into Eqs. (33), then multiplying the last N equations by $\sin\psi_k$, $\cos\psi_k$, and 1 respectively, then summing these last N equations and noting that

$$\left.\begin{aligned}
&\sum_{k=1}^{N}\sin\psi_k = \sum_{k=1}^{N}\cos\psi_k = 0 \\
&\sum_{k=1}^{N}\sin^2\psi_k = \sum_{k=1}^{N}\cos^2\psi_k = N/2 \\
&\sum_{k=1}^{N}\sin\psi_k\cos\psi_k = 0
\end{aligned}\right\} \text{ For } N \geq 3 \qquad (36)$$

results in a new set of differential equations in the variables x, b_s, b_c, b_o which now all have constant coefficients, namely,

$$M\ddot{x} + C_x\dot{x} + k_x x + \frac{N}{2}S\ddot{b}_c = 0$$
$$\frac{N}{2}\left[I\ddot{b}_s + C_\beta\dot{b}_s + (k_\beta - I\Omega^2)b_s - 2\Omega I\dot{b}_c - \Omega C_\beta b_c\right] = 0$$
$$\frac{N}{2}\left[S\ddot{x} + 2\Omega I\dot{b}_s + \Omega c_\beta b_s + I\ddot{b}_c + c_\beta\dot{b}_c + (k_\beta - I\Omega^2)b_c\right] = 0 \qquad (37)$$
$$N\left[I\ddot{b}_o + C_\beta\dot{b}_o + k_\beta b_o\right] = 0$$

These equations may then be investigated for stability using the standard constant coefficient techniques described earlier. For additional details and applications of multiblade coordinates, see Hohenemser and Yin (ref. 8). Multiblade coordinates were originally introduced by Coleman and Feingold (ref. 9) in their studies of helicopter ground resonance.

For rotors with 2 blades, N=2, the analysis is more difficult because the rotor disk no longer has polar symmetry. If the same multiblade coordinates given by Eq.(35) are used in the basic Eqs.(33), the periodic coefficients would not be entirely eliminated since now,

$$\sum_{k=1}^{2}\sin^2\psi_k = 1 - \cos 2\psi_1$$
$$\sum_{k=1}^{2}\cos^2\psi_k = 1 + \cos 2\psi_1 \qquad (38)$$
$$\sum_{k=1}^{2}\sin\psi_k\cos\psi_k = \sin 2\psi_1$$

instead of the convenient constant terms given by Eqs.(36). A rough estimate of the stability and response can be obtained by simply time-averaging the resulting $\cos 2\psi_1$ and $\sin 2\psi_1$ variations to zero and using only the constant coefficient terms. This is equivalent to setting N=2 in the multiblade transformed Eqs.(37).

For more accurate estimates for these 2-bladed rotors, one may use harmonic balance methods. This consists of first introducing new coordinates $b_T(t)$ and $b_A(t)$ for these two blades such that,

$$\beta^{(1)} = \beta_T + \beta_A\,, \quad \beta^{(2)} = \beta_T - \beta_A \qquad (39)$$

then summing and subtracting the last two equations of Eqs.(33) while noting that $\sin\psi_2 = -\sin\psi_1$ and $\cos\psi_2 = -\cos\psi_1$, then expanding each of the coordinates in a harmonic series,

$$x = x_o + x_{1S}\sin\Omega t + x_{1C}\cos\Omega t + x_{2S}\sin 2\Omega t + \ldots$$
$$b_T = b_{T0} + b_{T1S}\sin\Omega t + b_{T1C}\cos\Omega t + \ldots$$
$$b_A = b_{A0} + b_{A1S}\sin\Omega t + b_{A1C}\cos\Omega t + \ldots \qquad (40)$$

where x_0, x_{1S}, b_{T0}, b_{T1S}, ... are all functions of time. Placing these into Eqs.(33) and balancing out each harmonic term in each equation will yield a truncated series of constant coefficient differential equations. These equations may again be examined for stability using the standard constant coefficient techniques described earlier.

Often, depending on the form of Eqs.(33), the resulting constant coefficient differential equations will uncouple into several smaller coupled systems of equations which may be examined independently of one another. For example, for the case of Eqs.(33), one smaller coupled system would involve the variables x_0, x_{2S}, x_{2C}, b_{A1C}, b_{A1S}, ... while another would involve x_{1C}, x_{1S}, b_{A0}, b_{A2C}, b_{A2S}, ... For such systems, one could use an alternate extended form of the multiblade coordinate transformation Eq.(35) namely,

$$x = x_o + x_{2S} \sin 2\Omega t + x_{2C} \cos 2\Omega t + \ldots$$

$$\beta^{(k)} = b_{1S} \sin\psi_k + b_{1C} \cos\psi_k + \ldots \qquad (41)$$

together with the harmonic balance method to solve the problem. This works here, since the form given by Eq.(41) exactly duplicates the motion of the two blades given by the general case Eqs.(39) and (40), since $\sin\psi_2 = -\sin\psi_1$, $\cos\psi_2 = -\cos\psi_1$, and only x_0, x_{2S}, x_{2C}, b_{A1C}, b_{A1S}, ... would be present. However, in more general cases (for example, if the first equation of Eqs.(33) had an additional term $M_1\ddot{x}\cos\psi_1$ or $k_1 x \cos\psi_1$ present), the resulting equations would not split into two smaller groups, and the general harmonic balance method Eqs.(39) and (40) would have to be used.

Indeed, for the more general case mentioned above, one would also investigate the system for direct Mathieu equation type instabilities of half integer order $\Omega/2$, $3\Omega/2$, ... by introducing additional harmonic terms $\sin m\Omega t$ and $\cos m\Omega t$ where m=1/2, 3/2, 5/2, ... into Eqs.(40), and harmonically balancing as before. These terms would not couple in with the previous equations and can be solved independently of them. The primary instability region would result from the $\Omega/2$ terms. See Bolotin (ref. 10) for further details of the general harmonic balance method. Also see Sheu (ref. 7) for an application of the alternate extended form of the multiblade transformation Eq.(41), to a simple two bladed rotor in ground resonance.

(b) Forced Response

For rotors with 3 or more blades, $N \geq 3$, one uses the multiblade coordinate transformation Eq.(35) to eliminate the periodic coefficients in the basic equations of motion Eqs.(33), as described in the preceding section. The equations then reduce to the constant coefficient equations given by Eqs.(37), only now the right-hand-sides are

$$\text{R.H.S.} = \begin{Bmatrix} F_x(t) \\ \sum_{k=1}^{N} F_\beta^{(k)}(t) \sin\psi_k \\ \sum_{k=1}^{N} F_\beta^{(k)}(t) \cos\psi_k \\ \sum_{k=1}^{N} F_\beta^{(k)}(t) \end{Bmatrix} \qquad (42)$$

instead of the previous value of zero. Under steady-state conditions, the tower and blade forces generally occur periodically in multiples of the rotation frequency Ω, and can generally be expressed as,

$$F_x(t) = F_{x0} + F_{x1S}\sin\psi_1 + F_{x1C}\cos\psi_1 + F_{x2S}\sin 2\psi_1 + \ldots \qquad (43)$$

$$F_\beta^{(k)}(t) = F_{\beta 0} + F_{\beta 1S}\sin\psi_1 + F_{\beta 1C}\cos\psi_1 + \ldots$$

where $\psi_k = \Omega t + (k-1)2\pi/N$. Placing the above forces into Eqs.(42) and using the trigonometric identities and summations,

$$\sin m\psi_k \sin\psi_k = \frac{1}{2}\cos(m-1)\psi_k - \frac{1}{2}\cos(m+1)\psi_k$$

$$\cos m\psi_k \sin\psi_k = \text{etc.} \qquad (44)$$

$$\sum_{k=1}^{N} \sin m\psi_k = \begin{cases} N \sin m\psi_1 & \leftarrow m = N, 2N, \ldots \\ 0 & \leftarrow m \neq N, 2N, \ldots \end{cases}$$

$$\sum_{k=1}^{N} \cos m\psi_k = \begin{cases} N \cos m\psi_1 & \leftarrow m = N, 2N, \ldots \\ 0 & \leftarrow m \neq N, 2N, \ldots \end{cases}$$

one can obtain the right-hand-sides of Eqs.(37) in terms of either constants or harmonic functions of $m\Omega t$. The forced responses $x(t)$, $b_s(t)$, $b_c(t)$, $b_0(t)$ can then be found using the standard techniques for constant coefficient systems discussed previously. It should be noted that because of the multiblade transformation Eq. (35), the resulting responses for the tower motion and blade motions corresponding to the m^{th} harmonic $\omega_m = m\Omega$, would be of the form,

$$x = x_R \cos\omega_m t - x_I \sin\omega_m t$$

$$\beta^{(k)} = b_{0R}\cos\omega_m t - b_{0I}\sin\omega_m t + (b_{SR}\cos\omega_m t - b_{SI}\sin\omega_m t)\sin\psi_k + (b_{CR}\cos\omega_m t - b_{CI}\sin\omega_m t)\cos\psi_k \qquad (45)$$

The tower thus oscillates at frequency ω_m in the fixed frame whereas the blades may oscillate at frequencies ω_m, $\omega_m + \Omega$, $\omega_m - \Omega$ relative to the rotating frame.

For rotors with 2 blades, N = 2, the multiblade coordinate transformation Eq. (35) does not eliminate the periodic coefficients, but rather changes the $\cos\psi_k$ variations to $\cos 2\psi_k$ variations. A rough estimate of the response can be

obtained by simply time-averaging the resulting sin $2\psi_k$ and cos $2\psi_k$ variations to zero, and then proceeding with the remaining constant coefficient terms, as was done for the N≥3 case. The results are likely to be somewhat off for the second harmonic, sin $2\psi_k$ and cos $2\psi_k$ responses.

For more accurate estimates for these 2-bladed rotors, one can use the harmonic balance methods of the previous section. The steady-state periodic tower and blade forces given by Eqs. (43) are substituted into the basic equations of motions Eqs. (33). One then introduces the new coordinates given by Eqs. (39), then sums and subtracts the last two blade equations, then expands the tower and blade motions as given by Eq. (40), only now the coordinates x_0, x_{1S}, b_{T0}, b_{T1S}, b_{A0},...etc. are taken to be constants rather than functions of time. Harmonically balancing the various terms in each equation results in a truncated set of algebraic equations which can be solved to obtain the coordinates x_0, x_{1s}, b_{T0},... etc., corresponding to the given forcing excitations F_{x0}, F_{x1s}, $F_{\beta 0}$, $F_{\beta 1s}$,...etc. The resulting tower and blade motions are then given directly by Eqs. (40) and (39). The resulting set of algebraic equations will often uncouple into smaller coupled sets of equations which can be examined independently of one another. This procedure is similar to that for the constant coefficient forced response case Eq. (8), except now, the periodic coefficients couple the different harmonics together. Thus, the solution will consist of many harmonics mΩ even if only one forcing harmonic $F_{\beta 1s}$ were present alone.

ROTATING COORDINATES

As an addendum to the previous multiblade coordinates and harmonic balance methods, it should be mentioned that for some problems, the use of rotating coordinates is also convenient. For example, in the case of a 2-bladed rotor on isotropic tower supports (same tower mass, damping, and stiffness in two directions, x_1 and x_2), Eqs. (33) would read,

$$M\ddot{x}_1 + C_x\dot{x}_1 + k_x x_1 + S\frac{d^2}{dt^2}\sum^{k}\beta^{(k)}\cos\psi_k = F_{x1}(t) \tag{46}$$

$$M\ddot{x}_2 + C_x\dot{x}_2 + k_x x_2 - S\frac{d^2}{dt^2}\sum^{k}\beta^{(k)}\sin\psi_k = F_{x2}(t)$$

$$S\ddot{x}_1\cos\psi_k - S\ddot{x}_2\sin\psi_k + I\ddot{\beta}^{(k)} + C_\beta\dot{\beta}^{(k)} + k_\beta\beta^{(k)} = F_\beta^{(k)}(t) \qquad (k=1,2)$$

One can then express the tower motions x_1 and x_2 in terms of rotating coordinates ξ_1 and ξ_2 which rotate with the rotor, as

$$x_1 = \xi_1\cos\Omega t + \xi_2\sin\Omega t \tag{47}$$

$$x_2 = -\xi_1\sin\Omega t + \xi_2\cos\Omega t$$

where the rotation $\psi_1=\Omega t$ is taken from the x_2 axis towards the x_1 axis. Placing these equations into Eqs. (46), then multiplying the first two equations by $\cos\psi_1$ and $\sin\psi_1$ respectively and subtracting, then multiplying the first two equations by $\sin\psi_1$ and $\cos\psi_1$ and adding, then subtracting the third and fourth equations, then adding the third and fourth equations will result in a new set of differential equations in the variables ξ_1, ξ_2, b_A, b_T which now all have constant coefficients, namely,

$$M(\ddot{\xi}_1 + 2\Omega\dot{\xi}_2 - \Omega^2\xi_1) + C_x(\dot{\xi}_1 + \Omega\xi_2) + k_x\xi_1 + 2S(\ddot{\beta}_A - \Omega^2\beta_A) = F_{x1}\cos\Omega t - F_{x2}\sin\Omega t$$

$$M(\ddot{\xi}_2 - 2\Omega\dot{\xi}_1 - \Omega^2\xi_2) + C_x(\dot{\xi}_2 - \Omega\xi_1) + k_x\xi_2 - 4S\Omega\dot{\beta}_A = F_{x1}\sin\Omega t + F_{x2}\cos\Omega t$$

$$2S(\ddot{\xi}_1 + 2\Omega\dot{\xi}_2 - \Omega^2\xi_1) + 2I\ddot{\beta}_A + 2C_\beta\dot{\beta}_A + 2k_\beta\beta_A = F_\beta^{(1)} - F_\beta^{(2)}$$

$$2I\ddot{\beta}_T + 2C_\beta\dot{\beta}_T + 2k_\beta\beta_T = F_\beta^{(1)} + F_\beta^{(2)} \tag{48}$$

In the above, $\beta_T=(\beta^{(1)}+\beta^{(2)})/2$ and $\beta_A=(\beta^{(1)}-\beta^{(2)})/2$ are the same coordinates introduced earlier in Eqs. (33). These differential equations may then be investigated for stability and forced response using the standard constant coefficient techniques described earlier. Such analyses of a 2-bladed rotor on isotropic tower supports were also performed by Coleman and Feingold (Ref. 9) in their studies of helicopter ground resonance.

Rotating coordinates are often used in rotating machinery shaft critical speed problems, and are useful for dealing with problems of rotors with unsymmetrical mass, unsymmetrical damping, or unsymmetrical shaft stiffness supported on isotropic bearings. See for example, Bolotin (Ref. 11). For such problems, one can readily set up the equations of motion in the rotating frame directions, and the fixed supports will introduce no periodic terms because of their isotropic nature. For vertical axis wind turbines, such rotating coordinates for the blades are useful since the tower supports are generally isotropic due to the symmetrically arranged guy wires. For horizontal axis wind turbines, the tower supports are generally not isotropic, hence periodic coefficients will remain in the equations when using rotating coordinates. If the support anisotropy is not too large, one can again additionally introduce harmonic balance methods to eliminate the periodic coefficients, as was done in the previous section.

CONCLUDING REMARKS

The present article has reviewed two of the more common procedures for analyzing the stability and forced response of rotating systems with periodic coefficients, namely, Floquet methods and multiblade coordinate, harmonic balance methods. Also, the use of rotating coordinates was discussed.

The Floquet methods are based on a convenient numerical integration scheme and involves the computation of the "Transition Matrix," [Q], from which stability and the initial conditions for steady-state response solutions can be obtained. These methods seem attractive for large systems and can be modified to include nonlinearities in the equations.

The multiblade and harmonic balance methods involve first the introduction of multiblade coordinates in order to take out the periodic coefficients from the blades [Eqs.(35) for N≥3], or to obtain a better ordered system of equations [Eqs.(39) for N=2]. Then, harmonic balance methods Eqs.(40) are used to deal with any remaining periodic coefficients. These methods seem attractive for smaller systems and can give considerable insight into the origin and nature of instabilities and the various harmonics present in the forced response.

Rotating coordinates can also be used to effectively eliminate the periodic coefficients in problems involving unsymmetrical rotors on isotropic tower supports. These can often be used in rotating shaft critical speed problems and for vertical axis wind turbines. If the support anisotropy is not too large, harmonic balance methods may additionally be used to deal with any remaining periodic coefficients.

ACKNOWLEDGMENTS

The authors wish to acknowledge the support of NASA Lewis Research Center under Grant No. NSG-3303, administered by David C. Janetzke.

REFERENCES

1. Dugundji, J. and Wendell, J. H.: "General Review of the MOSTAS Computer Code for Wind Turbines," M.I.T. Aeroelastic and Structures Research Laboratory Report ASRL TR 197-1, July 1980.

2. Peters, D. A. and Hohenemser, K. H.: "Application of the Floquet Transition Matrix to Problems of Lifting Rotor Stability,: J. American Helicopter Society, Vol. 16, No. 2, April 1971.

3. Kottapalli, S.B.R., Friedmann, P.P., and Rosen, A.: "Aeroelastic Stability and Response of Horizontal Axis Wind Turbine Blades," AIAA J., Vol. 17, No. 12, December 1979, pp 1381-1389.

4. Warmbrodt, W. and Friedmann, P.P.: "Coupled Rotor/Tower Aeroelastic Analysis of Large Horizontal Axis Wind Turbines," AIAA J., Vol. 18, No. 9, September 1980, pp. 1118-1124.

5. Hoffman, J.A., Dreier, M.E., Williamson, D.R., and Henninger, W.C.: "Mathematical Methods Incorporated in the Wind Energy System Coupled Dynamics Analysis," Paragon Pacific Inc. Report PPI-1014-7, January 1977.

6. Miller, R.H., Dugundji, J., Chopra, I., Sheu, D.L., and Wendell, J.H.: "Wind Energy Conversion, Vol. 3: Dynamics of Horizontal Axis Wind Turbines," M.I.T. Aeroelastic and Structures Research Laboratory Report ASRL TR 184-9, U.S. Dept. of Energy Report COO-4131-T1 (Vol. 3), September 1978.

7. Sheu, D.L.: "Wind Energy Conversion, Vol. 7: Effects of Tower Motion on the Response of Windmill Rotor," M.I.T. Aeroelastic and Structures Research Laboratory Report ASRL TR 184-13, U.S. Dept. of Energy Report COO-4131-T1 (Vol. 7), September 1978.

8. Hohenemser, K.H., and Yin, S.K.: "Some Applications of the Method of Multiblade Coordinates" J. American Helicopter Society, July 1972.

9. Coleman, R.P. and Feingold, A.M.: "Theory of Self-Excited Mechanical Oscillations of Helicopter Rotors with Hinged Blades," NACA Technical Report TR 1351, 1958.

10. Bolotin, V.V.: The Dynamic Stability of Elastic Systems, Holden-Day, Inc., San Francisco, 1964.

11. Bolotin, V.V.: Nonconservative Problems of the Theory of Elastic Stability, MacMillan Co., New York, 1963.

QUESTIONS AND ANSWERS

J. Dugundji

From: P.R. Barnes

Q: The Singularity Expansion Method (SEM) introduced by Dr. Carl Baum of Kirkland AFB, Albuquerque, NM is another, perhaps better, approach to solving these problems. Do you know about SEM?

A: *No, I do not. I have just dealt here with two of the more common methods for dealing with these problems.*

From: W.E. Holley

Q: Are you aware of any treatments of stochastic problems with periodic coefficients?

A: *I have not dealt with that aspect of the problem, so I am not aware of them. I believe though that there is considerable literature on that subject.*

AN APPROXIMATE METHOD FOR SOLUTION TO VARIABLE MOMENT OF INERTIA PROBLEMS

E. William Beans
Associate Professor of Mechanical Engineering

The University of Toledo
Toledo, Ohio 43606

ABSTRACT

The "weathering vaning" motion of a wind turbine with a moving rotor is an oscillatory problem with a variable moment of inertia. The analysis of such a motion requires the solution of a non-linear differential equation. In this article an approximation method is presented for reducing the problem to an equivalent constant moment of inertia problem.

The method is based on the assumption that a moving rotor is an integrator and, therefore, the problem will behave as if it has an averaged moment of inertia. It is further assumed that this will be a valid solution to the problem if the rotating speed of the wind turbine is infinite. The method consists of determing the integrated average of the moment of inertia for a single rotation. This averaged value can then be used to determine equivalent natural frequency of the system and other dynamic properties.

The method is shown to be valid by solving the non-linear differential equation for various rotating speeds. It was found that the cycle time is the equivalent cycle time if the rotating speed is 4 times greater than the systems minimum natural frequency. The ratio of equivalent to minimum cycle time is

$$\bar{t}/to = (Imax/Imin)^{\frac{1}{4}}.$$

INTRODUCTION

The oscillatory motion of a system with a variable moment of inertia is complex. The analysis of such a motion requires the solution of a non-linear differential equation. In this article a method for reducing the problem to an equivalent constant moment of inertia problem is presented.

The application which generated interest in this problem is the "weather vaning" of a wind turbine with a moving rotor. The method established here is applicable to any problem in which the moment of inertia is a variable about the axis of rotation such as the roll of a helicopter.

The problem is illustrated in Fig. 1. It is desired to describe the motion of the system about the axis A-A while the rotor is moving. One can see from Fig. 1 that the moment of inertia about A-A varies from a minimum when the rotor is vertical (Position A) to a maximum when the rotor is horizontal (Position B). This variation is continuous and cyclic with each turn of the rotor.

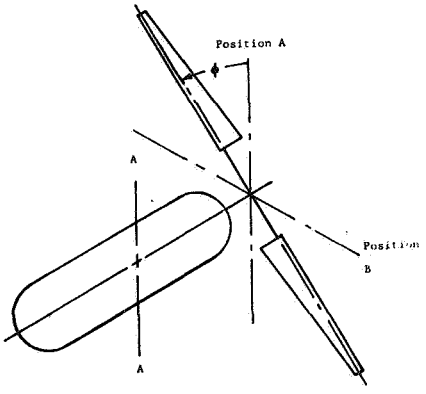

Fig. 1 - Problem Geometry

One can also see from Fig. 1 that the problem cannot be handled with a single initial condition. A different and unique motion is obtained for each initial position of the rotor. Hence, the problem has a stochastic nature.

ANALYSIS

At any rotor position, ϕ, the instantaneous moment of inertia of the rotor, I_i, about axis A-A is:

$$I_i = mr_k^2 \sin^2\phi = I_r \sin^2\phi$$

where m is the mass of the rotor. The terms r_k and I_r are the radius of gyration and the moment of inertia of the rotor about its axis of rotation, respectively. The moment of inertia of the rest of the system about A-A, which is constant, is:

$$I_o = I_c + mh^2$$

where I_c is the moment of inertia of the center-body and h is the distance from the center of the rotor to axis A-A. The expression for the total moment of inertia I is the sum of the constant and variable portions

$$I = I_o + I_i = I_o + I_r \sin^2\phi$$

or

$$I = I_o(1 + J\sin^2\phi) \qquad (1)$$

where $J = I_r/I_o$.

When the entire system is oscillating about axis A-A with a moving rotor, it is apparent that the rotor is acting as an integrator of moment of inertia. It is hypothesized that if the rotor has an infinite angular velocity the moment of inertia I behaves as a constant integrated average value. It is this hypothesis which is the basis of method presented here.

To establish the utility of the method, assuming for the moment that the hypothesis is correct, there are two questions which must be answered:

1) What averaging technique should be used?
2) How close must the speed be to infinite for the method to be useful? In other words, how fast is fast?

The hypothesis is proven by examining the simple harmonic motion of the system in Fig. 1. The proof is valid for more complex situations such as those including damping and forcing functions. In demonstrating the proof, the method of solving a variable moment of inertia problem will be established.

The equation for simple harmonic motion is:

$$\frac{d^2\alpha}{dt^2} = \frac{-K\alpha}{I} = -\frac{\omega_o^2\,\alpha}{1+J\sin^2(\omega t)} \qquad (2)$$

and

$$\omega_o^2 = K/I_o \qquad (3)$$

where K is the torsional constant and ω_o is defined in Eq. 3 as the reference frequency for the system. In writing Eq. 2, the moment of inertia I has been replaced by Eq. 1 and the rotor angle ϕ has been replaced by rotor angular velocity ω and time t.

Eq. 2 is dimensionalized by letting

$$\tau = t/t_o = \omega_o t$$

$$n = \omega/\omega_o$$

and $$\theta = \alpha/\alpha_o$$

where α_o is the initial angular displacement. Substituting these expressions into Eq. 2, one has

$$\frac{d^2\theta}{d\tau^2} = -\frac{\theta}{1+J\sin^2(n\tau)} = -k\theta \qquad (4)$$

The term k is defined as the natural frequency ratio

$$k = \frac{1}{1+J\sin^2(n\tau)} = \left(\frac{\omega_n}{\omega_o}\right)^2 \qquad (5)$$

and can be used to obtain the natural frequency of the system at anytime.

The hypothesis states that as the rotor angular velocity approaches infinity, the natural frequency ratio k approaches a constant integrated average value. The average value is obtained by integrating Eq. 5 over a quarter cycle

$$\bar{k} = \frac{2}{\pi}\int_o^{\pi/2} k\,d\phi = \frac{2}{\pi}\int_o^{\pi/2} \frac{d\phi}{1+J\sin^2\phi} = \frac{2}{\pi}\int_o^{\pi/2} \frac{d\phi}{(J+1)\sin^2\phi+\cos^2\phi} \qquad (6)$$

From a table of definite integrals*, one obtains

$$\int_o^{\pi/2} \frac{dx}{a^2\sin^2x+b^2\cos^2x} = \frac{\pi}{2ab}$$

$$\therefore\ \bar{k} = \frac{1}{\sqrt{J+1}} = \left(\frac{\bar{\omega}}{\omega_o}\right)^2 = \left(\frac{t_o}{\bar{t}}\right)^2 \qquad (7)$$

Eq. 7 is the answer to the first question. Since J + 1 is I_{max}/I_{min}, a more convenient form for Eq. 7 is

$$\bar{t}/t_o = (I_{max}/I_{min})^{\frac{1}{4}} \qquad (8)$$

The hypothesis is proven if it can be shown that the system oscillates at a cycle time defined by Eq. 7 as n increases. It should be noted in passing that the averaging method defined by Eq. 6 is the proper one. Initially, the following averaging was used which is incorrect.

$$J = \frac{1}{2\pi}\int(1+J\sin^2\phi)\,d\phi$$

The error the author made was that reciprocal of the average is not the average of the reciprocals.

Eq. 4 is a non-linear differential equation. It was solved numerically for a number of cases of n and J using the Continuous System Modeling Program (CSMP) which is standard IBM software.

The solution to the differential equation with time ratio τ is presented in Fig. 2 for J = 1. One can see that the frequency shifted significantly with increase in rotor speed from n = 0 to n = 1. Fig. 2 also shows a significant change in displacement with speed ratio n. In 3 reference frequency cycles, the solutions for other than n = 0 does not appear to be repeating indicating the stochastic nature of the problem.

*Handbook of Chemistry and Physics, Chemical Rubber Publishing Co.

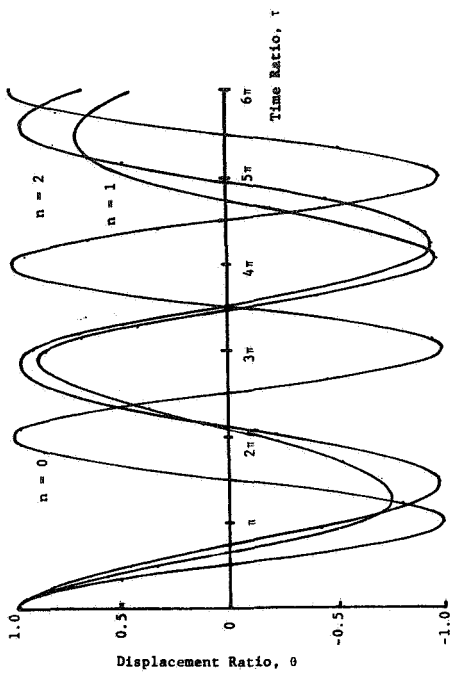

Fig. 2 - Displacement Response with Variable Rotor Speed

In Fig. 3 the time ratio τ for the first cycle is presented with increasing rotor speed ratio n. The limiting value as predicted by Eq. 7 is indicated in Fig. 3. One can see from Fig. 3 that the time ratio equals the limiting value when n > 4. Hence, the hypothesis is proven and the second question is answered.

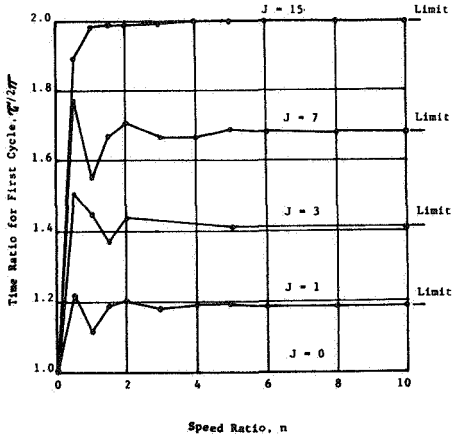

Fig. 3 - First Cycle Time Response

The curves in Fig. 3 are smooth even though the Fig. 3 does not indicate it. The curves all start at $\tau = 2\pi$ because the problem was always started with the system at minimum moment of inertia or with rotor at Position A. If the problem were started at maximum moment of inertia, the solution would have started at $\tau = 2\pi\sqrt{J+1}$. At any other position the solution would start anywhere in between. It is the variation in moment of inertia with rotor position that causes the oscillation of the first cycle time ratio in Fig. 3 before it "damps" down to the limiting value.

It appears from Fig. 3 that as J increases the first cycle time ratio approaches the limiting value more quickly. The reverse is also true. The solution for J = 0 is a constant horizontal line as indicated in Fig. 3. The speed ratio for utilizing the limit solution may maximumize with J.

CONCLUDING REMARKS

In conclusion, it can be stated that:

1) The hypothesis is true.

2) A variable moment of inertia problem can be analyzed as a constant moment of inertia problem if the rotor speed is 4 times the reference frequency, which is based on minimum moment of inertia.

3) The method of solution is to multiply the reference frequency by the fourth root of the minimum to maximum moment of inertia ratio to obtain the system's natural frequency.

4) If n > 4 the initial starting point is not important and the problem is deterministic.

QUESTIONS AND ANSWERS

E.W. Beans

From: T. Base

Q: When you set up your initial equations, why didn't you write them in form

$$\frac{d}{dt}(I\dot{\phi}) = \text{Applied Torques (including damping)}$$

so that: $I_M \frac{d\dot{\phi}}{dt} + \dot{\phi}\frac{dI_m}{dt} = \text{Applied Torques}$

then the rate of change of I_M with time could be used directly in the equations.

A: *The equation you wrote is not the one I wanted to solve. Your equation appears to have a velocity dependent term. Since dI/dt varies cyclic I would try to solve it using the averaging technique.*

From: Art Smith

Q: Do you plan to check your results with a more exact method?

A: *No. My results appear to satisfy application for which it was developed.*

From: G. Beaulieu

Q: You have considered rigid blade for your analysis; could the harmonic deformation of a vibrating blade significantly change the moment of inertia?

A: *Yes, if the mass center is displaced.*

From: Dan Schiff

Q: Does your solution account for dynamic effects, e.g., gyroscopic effects--or only static?

A: *No, but the method should be applicable to the solution of any equation with cyclic coefficients.*

COMPUTATION OF THE MODES AND POLAR MOMENT OF INERTIA OF THE BLADES OF AN HAWT

G. Beaulieu and D. Noiseux

Institut de Recherche d'Hydro-Québec (IREQ)
1800 Mtée Ste-Julie
Varennes, Québec, Canada, JOL 2PO

ABSTRACT

The numerical solution of the coupled differential equations of motion of the blades of an horizontal axis wind turbine is a more direct approach than the technique of finite elements, permitting the optimization of the design at relatively low cost. The procedure consists in transforming the equation of motion into a set of first order equations and solving them with fourth order Runge-Kutta integrators. This technique is applied to a twisted, tapered blade of variable cross section and stiffness including discontinuities. The first six natural frequencies and mode shapes are obtained.

This technique is extended to obtain the polar moment of inertia of the blades as a function of frequency and rotational speed.

A good match with the experimental results is achieved.

INTRODUCTION

The accurate determination of natural frequencies is of fundamental importance in the design of wind turbine blades. Similarly, the polar moment of inertia of the blades is required for the study of the torsional dynamics of the drive train.

Rotor dynamics is often studied with the use of large and specialized finite elements computer codes. However, the availability and cost of operation of these programs limit their use, and a more direct approach could be beneficial. The direct solution of the coupled differential equations of motion of the blade is such an approach, permitting optimization studies at low cost. This paper presents a model of a nonuniform, tapered, twisted cantilever wind turbine blade and a method of solution.

For the purpose of demonstrating the method, only the in-plane and out-of-plane bending modes are considered since the torsional modes occur at frequencies much higher than the bending modes because of the high torsional rigidity of the blade. The coupled differential equations of motion were transformed into a set of first order equations and solved with Runge-Kutta numerical integrators. The turbine blade under study has major stiffness dicontinuities. The blade is therefore considered as if made of adjoining segments, each one having a varying stiffness.

The first and second derivatives of the stiffness curves evidently have to be considered. The continuity of the shear forces and moments was imposed between each segments of the blade. With these variations of the Runge-Kutta method it is possible to obtain the resonant frequencies and the normalized distributions of displacement, bending moment and shear force for the first six bending modes. The coriolis forces and the tension force due to centrifugal loading are included. The modes of vibration are computed for a regime of rotational speed. The normal and tangential aerodynamic loading at each section of the blade could be included as extra terms in the differential equations; however, this paper considers only a rotor turning without the aerodynamic forces. These will be included in further studies dealing with the optimization of small capacity wind turbines.

An important extension to this model consists in the formulation of the polar moment of inertia of the rotor in terms of a couple at a frequency ω applied to the hub and the resultant angular acceleration of the rotor. A direct method using the shear forces and moments produced by each blade at the hub and an integral from using the in-plane displacements (mode shape) along the blades are formulated and the numerical results compared. The polar moment of inertia is then obtained as a function of frequency and rotational speed.

THE EQUATIONS OF MOTION AND THE TRANSFORMATION METHOD

Lets consider a turbine blade turning outside the aerodynamic and gravity field with its main axis perpendicular to the rotation axis mounted as a cantilever into a rigid hub. The tension in the blade due to centrifugal loading is included. If the blade elongation is assumed to be small relative to the transversal displacements, it can be demonstrated that the coriolis forces become negligeable. When only the in-plane and out-of-plane bending motions are considered, the coupled differential equations become:

$$\frac{\partial^2}{\partial z^2}\left[EI_{xy}\frac{\partial^2 v}{\partial z^2} + EI_{yy}\frac{\partial^2 u}{\partial z^2}\right] - \frac{\partial}{\partial z}\left[T\frac{\partial u}{\partial z}\right] = m\omega^2 u \qquad (1a)$$

$$\frac{\partial^2}{\partial z^2}\left[EI_{xy}\frac{\partial^2 u}{\partial z^2} + EI_{xx}\frac{\partial^2 v}{\partial z^2}\right] - \frac{\partial}{\partial z}\left[T\frac{\partial v}{\partial z}\right] = m\left(\omega^2 + \Omega_o^2\right) v \qquad (1b)$$

These equations are a subset of the equations of Houbolt and Brooks (ref. 1) and an extension of the equations of Canergie and Dawson (ref. 2) for a twisted blade. In these equations, the tension

T at any section of the blade is independent of the vibration frequency ω but proportional to Ω_o^2 and represented by:

$$T = \Omega_o^2 \int_z^L m(z) z \partial z \qquad (2)$$

Taking the first and second derivatives of the terms in braket while considering the moments of inertia I_{xx}, I_{yy} and I_{xy} as variable along the z axis, the system of equation (1) becomes:

$$EI_{yy}u^{IV} + EI_{xy}v^{IV} = -E\left[2\,I'_{xy}v''' + 2\,I'_{yy}u''' + I''_{xy}v'' + I''_{yy}u''\right] + Tu'' + T'u' + m\omega^2 u \qquad (3a)$$

$$EI_{xy}u^{IV} + EI_{xx}v^{IV} = -E\left[2I'_{xy}u''' + 2\,I'_{xx}v''' + I''_{xy}u'' + I''_{xx}v''\right] + Tv'' + T'v' + m\left(\omega^2 + \Omega_o^2\right)v \qquad (3b)$$

where ( )' and ( )"... indicate the first, second, ..., derivatives with respect to z. It is seen from these equations that the in-plane and out-of-plane bending are coupled through I_{xy} and its first derivative I'_{xy}.

The method of transformation of variables, first proposed by Canergie and Dawson (ref. 2) is generalized by applying it at any frequency of vibration and not exclusively to find the resonant frequency. The two fourth order equations are transformed into eight first order equations by the following substitutions:

$$\begin{aligned} Y_1 &= v''' & Y_5 &= v' \\ Y_2 &= u''' & Y_6 &= u' \\ Y_3 &= v'' & Y_7 &= v \\ Y_4 &= u'' & Y_8 &= u \end{aligned} \qquad (4)$$

By substitution and differentiation the following eight first order equations are obtained:

$$EI_{xy}\,Y'_1 + EI_{yy}\,Y'_2 = -E\left[2I'_{xy}\,Y_1 + I''_{xy}\,Y_3 + 2\,I'_{yy}\,Y_2 + I''_{yy}\,Y_4\right] + T\,Y_4 + T'\,Y_6 + m\omega^2\,Y_8 \qquad (5a)$$

$$EI_{xx}\,Y'_1 + EI_{xy}\,Y'_2 = -E\left[2\,I'_{xy}\,Y_2 + I''_{xy}\,Y_4 + 2\,I'_{xx}\,Y_1 + I''_{xx}\,Y_3\right] + T\,Y_3 + T'Y_5 + m\left(\omega^2 + \Omega_o^2\right)Y_7 \qquad (5b)$$

$$Y'_3 = Y_1 \qquad (5c)$$

$$Y'_4 = Y_2 \qquad (5d)$$

$$Y'_5 = Y_3 \qquad (5e)$$

$$Y'_6 = Y_4 \qquad (5f)$$

$$Y'_7 = Y_5 \qquad (5g)$$

$$Y'_8 = Y_6 \qquad (5h)$$

They can be conveniently represented by:

$$Y'_i = f_i\left(z, Y_1, Y_2, \ldots, Y_8\right)$$

$$i = 1, 2, \ldots, 8 \qquad (6)$$

Applying the appropriate boundary conditions, it is then possible to solve equation (6) with the use of Runge-Kutta numerical integrators.

The displacements and their first, second and third derivatives are then obtained. From these, one can compute the distributions of the shear forces and moments by the usual relations:

$$F_x = -E\left[I_{xy}v''' + I'_{xy}v'' + I_{yy}u''' + I'_{yy}u''\right] + Tu' \qquad (7a)$$

$$F_y = -E\left[I_{xy}u''' + I'_{xy}u'' + I_{xx}v''' + I'_{xx}v''\right] + Tv' \qquad (7b)$$

$$M_x = E\left[I_{xy}v'' + I_{yy}u''\right] \qquad (7c)$$

$$M_y = E\left[I_{xy}\,u'' + I_{xx}v''\right] \qquad (7d)$$

THE BOUNDARY CONDITIONS

Consider the turbine blade shown in figure 1. The longitudinal axis of the blade is the z axis and the rotor turns in the y-z plane. The x axis is the axis of rotation. The blade is mounted in a rigid hub at 6% of its span (ℓ) and has a total length of 4.95 meters (L).

Because the blade is rigidly mounted the boundary conditions are:

$$u = v = u' = v' = 0 \quad \text{at } z = \ell$$

that is $Y_i(\ell) = 0$ for $i = 5, 6, 7, 8$ (8)

At the free end the conditions are:

$$u'' = v'' = u''' = v''' = 0 \quad \text{at } z = L$$

since the moments and shear forces are zero;
that is $Y_i(L) = 0$ for $i = 1, 2, 3, 4$ (9)

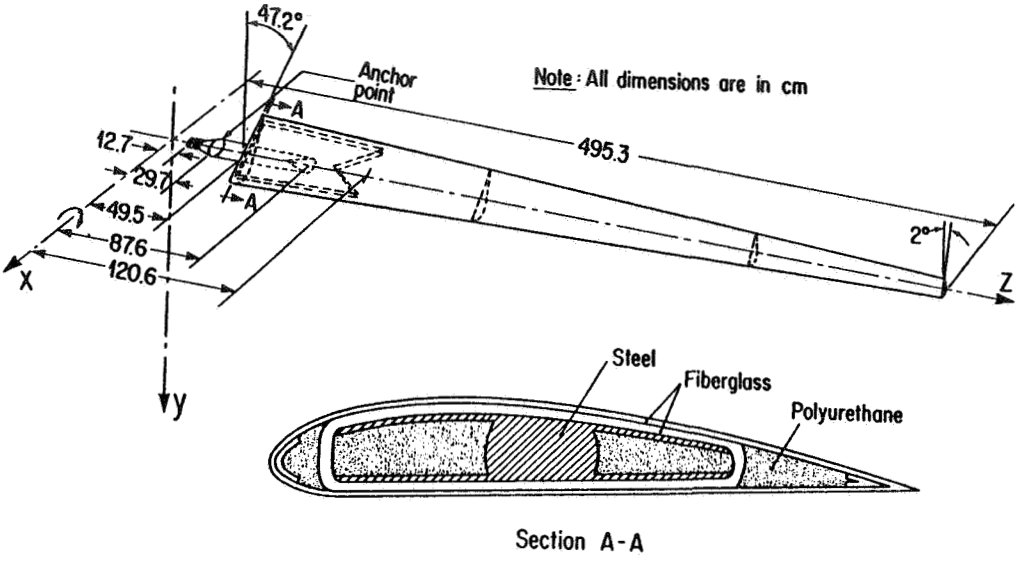

Figure 1 - Geometry of IREQ turbine blade

These boundary conditions apply to a stationary blade. When the hub is allowed to rotate around the x axis the conditions at the free end remain unchanged but the displacement v and its slope v' are different from zero at $z = \ell$. However, u and u' remain zero since the hub is assumed rigid. Therefore, if the rotor is allowed to spin and oscillate in the plane of rotation the boundary conditions at $z = \ell$ become:

$$\begin{aligned} u &= u' = 0 \\ v &= v(\ell) \\ v' &= v(\ell)/\ell \end{aligned} \qquad (10)$$

This last condition is the consequence of the rigid hub being displaced by an amount $v(\ell)$ at ℓ.

THE METHOD OF SOLUTION

The method of solving equation (5) is as follows:

1) A value is selected for the frequency ω;
2) The four known boundary conditions (equation 7) at the root are set and the four unknown conditions are given arbitrary values namely:

$$Y_1 = C_o,\ Y_2 = Y_3 = Y_4 = 0 \qquad (11)$$

3) From these eight boundary conditions at the root a solution is obtained with the use of fourth order Runge-Kutta integrators. Eight values, Y_1 to Y_8, are obtained for the free end:

$$Y_{i,r}(L) = F_{i,1} \quad (i = 1,2,\ldots,8)$$

$$(r = 1) \qquad (12)$$

where the subscript r = 1 indicates the solution with the first group of boundary conditions;

4) Step (3) is repeated by successively setting each of the unknown boundary condition to the arbitrary value C_o. In this way four sets of starting boundary conditions are obtained for $z = \ell$:

	Y_8	Y_7	Y_6	Y_5	Y_4	Y_3	Y_2	Y_1
(r)case	u	v	u'	v'	u"	v"	u"'	v"'
1	o	o	o	o	C_o	o	o	o
2	o	o	o	o	o	C_o	o	o
3	o	o	o	o	o	o	C_o	o
4	o	o	o	o	o	o	o	C_o

(13)

giving four sets of solutions for the free end:

$$Y_{i,r} = F_{i,r} \quad (i = 1,2, \ldots, 8)$$

$$(r = 1, \ldots, 4) \qquad (14)$$

5) The solution of equation (6) is a combination of these four solutions. Namely,

$$Y_i(z) = \sum_{r=1}^{4} a_r\, Y_{i,r}(z)$$

$$(i = 1, 2, \ldots, 8) \qquad (15)$$

However, the known boundary conditions at the free end are for a cantilever blade:

$$Y_i\,(L) = 0 \quad (i = 1,2,3,4) \qquad (16)$$

since the shear forces and moments must be zero. The right hand side of equation (15) can then be partitioned:

$$\sum_{r=1}^{4} a_r F_{i,r} = 0 \quad (i = 1,2,3,4) \qquad (17)$$

6) A non-trivial solution is possible if the determinant of the coefficients $F_{i,r}$ of equation (17) is equal to zero

$$\left\| F_{i,r} \right\| = 0 \quad (i = 1,2,3,4)$$

$$(r = 1,2,3,4) \qquad (18)$$

Therefore, the above steps are repeated with increased values of the vibration frequency ω until equation (18) is satisfied. That ω then corresponds to a resonant frequency.

7) Having found the resonant frequency a_1 is set to 1 and a_2, a_3 and a_4 are computed giving the four unknown boundary conditions at the anchor point.

8) The solution is repeated once more with the following initial conditions:

$$\begin{aligned} Y_1 &= a_1 & Y_5 &= 0 \\ Y_2 &= a_2 & Y_6 &= 0 \\ Y_3 &= a_3 & Y_7 &= 0 \\ Y_4 &= a_4 & Y_8 &= 0 \end{aligned} \qquad (19)$$

In addition to the displacement u & v the shear forces and moments are computed at each blade station with equations (7a) to (7d).

The method described above was first used by Canergie and Dawson (ref. 2) to find the natural frequencies of a straight constant section blade. Its application here is extended to twisted, tapered blade having discontinuity of rigidity.

TURBINE BLADE CHARACTERISTICS

The turbine blade used on the 40 kW, 10 meters IREQ wind turbine is a twisted, tapered composite blade made principally of steel and fiberglass. Figure 1 shows its construction. Its assymetric aerodynamic profile is NACA 4415. The chord is 44.45 cm at the root and 10.92 cm at the free end with a thickness varying from 7.11 cm to 1.78 cm. The twist angle β goes from 47.2 degrees to 2 degrees at the tip.

The principal moments of inertia I_{xx_s} and I_{yy_s} for a group of typical blade sections were computed from an engineering drawing of the blade and were transformed into the blade principal axis (in-plane and out-of-plane) by the usual relations:

$$I_{xx} = I_{xx_s} \cos^2\beta + I_{yy_s} \sin^2\beta$$

$$I_{yy} = I_{yy_s} \cos^2\beta + I_{xx_s} \sin^2\beta$$

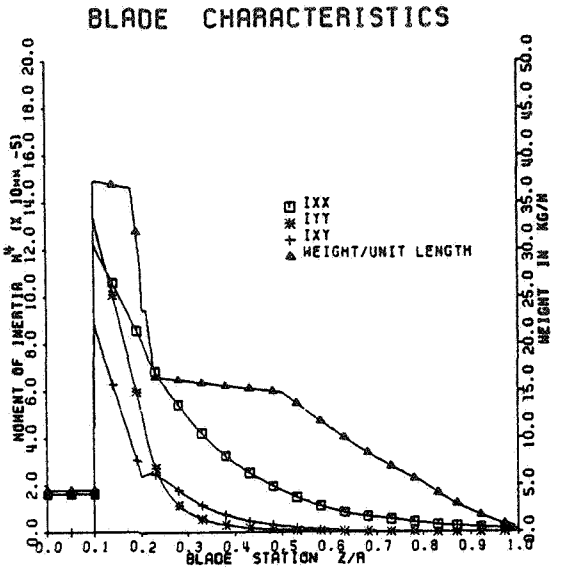

Figure 2 - IREQ turbine blade characteristics

$$I_{xy} = \frac{\left(I_{xx_s} - I_{yy_s}\right)}{2} \sin 2\beta$$

The I_{xx_s} and I_{yy_s} for each element of the blade section are equivalent moment of inertia based on the same reference modulus of elasticity E. The blade actual geometry was found to be significantly different from the drawing geometry. The moment of inertia I_{xx_s} and I_{yy_s} are then corrected to account for these manufacturing inaccuracies. The values used as input to the modal analysis program are shown in figure 2. The root sections of the blade is approximated by linear distributions while the all fiberglass section from the end of the steel insert to the blade tip was approximated by a polynomial computed from twelve input data points. The first and second derivatives of I_{xx}, I_{yy} and I_{xy} were numerically computed from the above distributions.

In order to take care of the discontinuities of stiffness, the blade is divided into three sections, the first from the anchor point to the blade root section, the second up to the end of the steel insert and the third to the tip of the blade.

The numerical integration is done from the anchor point to the tip of the blade in a continuous manner except that the values of four of the eight state variables (Y_1 to Y_4) are varied in a stepwise manner at the two major discontinuities of the blade. This is done because the state variables being integrated at each segment of the blade are the numerical derivatives of the displacements u and v, namely u', v', u", v", u"' and v"' and not the forces and moments in the blade. The physical quantities that must be continuous are the displacements, the slopes, the moments and the shear forces and the tension, not the derivatives. Therefore the continuity of the boundary conditions become:

$$
\begin{aligned}
u_- &= u_+ & M_{x_-} &= M_{x_+} \\
u'_- &= u'_+ & M_{y_-} &= M_{y_+} \\
v_- &= v_+ & F_{x_-} &= F_{x_+} \\
v'_- &= v'_+ & F_{y_-} &= F_{y_+} \\
T_- &= T_+
\end{aligned}
\qquad (20)
$$

The indices - and + represent the sections immediately to the left and immediately to the right of the discontinuity. Using equation (7a) to (7d) and equation (20), it is possible to find new values (the + values) for the derivatives u", v", u"', and v"' that will ensure the continuities of the forces and moments across the discontinuity. Performing the appropriate algebra on equations (7) and (20), we get:

$$
u''_+ = \frac{\left[\frac{M_{y_-}}{E} - \frac{M_{x_-} I_{xx_+}}{EI_{xy_+}}\right]}{\left[I_{xy_+} - \frac{I_{xx_+} I_{yy_+}}{I_{xy_+}}\right]} \qquad (21a)
$$

$$
v''_+ = \left[\frac{M_{y_-}}{EI_{xx_+}} - \frac{I_{xy_+} u''_+}{I_{xx_+}}\right] \qquad (21b)
$$

$$
u'''_+ = \frac{\left[\left(-\frac{F_{y_-}}{E} - I'_{xy_+} u''_+ - I'_{xx_+} y''_+ + \frac{T_+}{E} v'_+\right) - \frac{I_{xx_+}}{I_{xy_+}}\left(-\frac{F_{x_-}}{E} - I'_{yy_+} v'_+ - I'_{xy_+} + v''_+ + \frac{T_+}{E} u'_+\right)\right]}{\left[I_{xy_+} - \frac{I_{xx_+} I_{yy_+}}{I_{xy_+}}\right]} \qquad (21c)
$$

$$
v'''_+ = \frac{1}{I_{xy_+}}\left[-\frac{F_{x_-}}{E} - I'_{yy_+} u'' - I'_{xy_+} v''_+ + \frac{T_+}{E} u'_+ - I_{yy_+} u'''_+\right] \qquad (21d)
$$

It is clear that the shear forces and bending moments computed with this method are not exact in the immediate region of the discontinuities. However the distribution should not be affected in regions farther from the discontinuities.

FORMULATION OF THE POLAR MOMENT OF INERTIA

The polar moment of inertia J of an horizontal axis wind turbine rotor is required for the analysis of the dynamic torsional stability of the drive train. J varies with the vibration frequency ω and the rotational speed Ω_0. The variations of J are mainly caused by the transverse vibration of the blades. The polar moment of inertia of the rotor, excluding the hub, is defined at a frequency ω by:

$$
J = \frac{C_v}{-w^2\theta}
$$

where C_V is the amplitude of the couple applied by the hub at the frequency ω and $-\omega^2\theta$ is the angular acceleration of the hub. For a symmetrical three bladed rotor, J will be three times the polar moment of inertia of one blade computed with respect to the rotor hub.

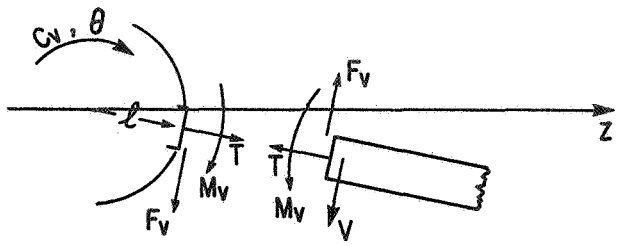

Figure 3 - Internal forces and moments at the blade anchor point.

When a blade vibrates at a frequency ω, an internal shear force and moment appear at the anchor point as shown in figure 3. The shear force and moment produced by the out-of-plane vibrations are reacted upon by the rigid hub and do not appear in the formulation of J. However, the hub is free to rotate around its axis and the in-plane vibrations will be reacted by the rotor hub in the form of a couple. The sign convention shown in figure 4 is introduced such that $F_V = -\partial M / \partial Z$. The external couple C_v, applied by the hub is then:

$$
C_v = -F_v(\ell)\,\ell - M_v(\ell) \qquad (23)
$$

The tension T, being purely radial at the hub, does not produce any couple. The external couple expressed by equation (23) is then introduced in equation (22) to give:

$$
J = \frac{-F_v(\ell)\,\ell - M_v(\ell)}{-\omega^2\, v(\ell)/\ell} \qquad (24)
$$

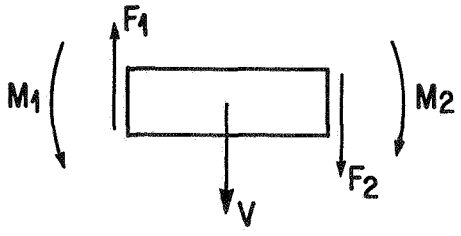

Figure 4 - Positive directions of shear forces and moments

Since T is radial at ℓ, F (ℓ) and M (ℓ) become:

$$F_v(\ell) = \left[- \frac{\partial}{\partial Z} \left(EI_{xx} v'' + EI_{xy} u'' \right) \right]_{z = \ell} \quad (25)$$

$$M_v(\ell) = \left[EI_{xx} v'' + EI_{xy} u'' \right]_{z = \ell} \quad (26)$$

If the blade section is uniform and symmetric at the anchor point (a circular section for the IREQ blade) we have:

$$I'_{xx}(\ell) = I'_{xy}(\ell) = I_{xy}(\ell) = 0 \quad (27)$$

and (25) and (26) become:

$$F_v(\ell) = -EI_{xx}(\ell)\, v'''(\ell) \quad (28)$$

$$M_v(\ell) = EI_{xx}(\ell)\, v''(\ell) \quad (29)$$

giving

$$J = \frac{EI_{xx}(\ell) \left[v''(\ell) - \ell v'''(\ell) \right]}{\omega^2\, v(\ell)/\ell} \quad (30)$$

In this last equation, the polar moment of inertia of one blade is expressed in terms of the forces and moments at the rotor hub.

Another representation of the polar moment of inertia is possible if one considers the in-plane displacements of the blade as it vibrates at a frequency ω. By using integration by parts on equations (1) and (7) and applying the appropriate boundary conditions, it can be demonstrated that

$$J = \frac{\ell}{v(\ell)} \int_{\ell}^{L} m\, v\, z\, dz \quad (31)$$

At a very low frequency, the blade is not deformed and moves as a rigid body; v(z) becomes a straight line

$$v(z) = v(\ell)\, z/\ell \quad (32)$$

and (31) takes the well known form of the static moment of inertia:

$$J_o = \int_{\ell}^{L} m\, z^2\, dz \quad (33)$$

Both equations (30) and (31) can be used to compute the polar moment of inertia but the integral formulation is inherently more exact from the numerical point of view because it only uses the blade in-plane displacements while equation (30) uses in addition the second and third derivatives of these displacements at the hub anchor point.

In order to compute the polar moment of inertia, the equations of motion of the blade must be solved in the manner described above except that a value is chosen for ω and the arbitrary value C_4 used as initial condition for Y_1 (v''') is varied until the determinant (equation 18) becomes zero. When a solution is obtained for that ω, equations (30) and (31) are used to compute J. This procedure must be repeated for each value of ω with the following boundary conditions at $z = \ell$:

	Y_8	Y_7	Y_6	Y_5	Y_4	Y_3	Y_2	Y_1
r (case)	u	v	u'	v'	u''	v''	u'''	v'''
1	o	C_o	o	C_o/ℓ	C_1	o	o	o
2	o	C_o	o	C_o/ℓ	o	C_2	o	o
3	o	C_o	o	C_o/ℓ	o	o	C_3	o
4	o	C_o	o	C_o/ℓ	o	o	o	C_4

(34)

These boundary conditions were explained earlier.

NUMERICAL RESULTS FOR THE MODES OF VIBRATION

The natural modes of vibration for the IREQ HAWT blade have been computed for the following conditions:

1) The first six modes of a stationary cantilever blade.
2) The first six modes of a cantilever blade at 100, 200 and 300 RPM.

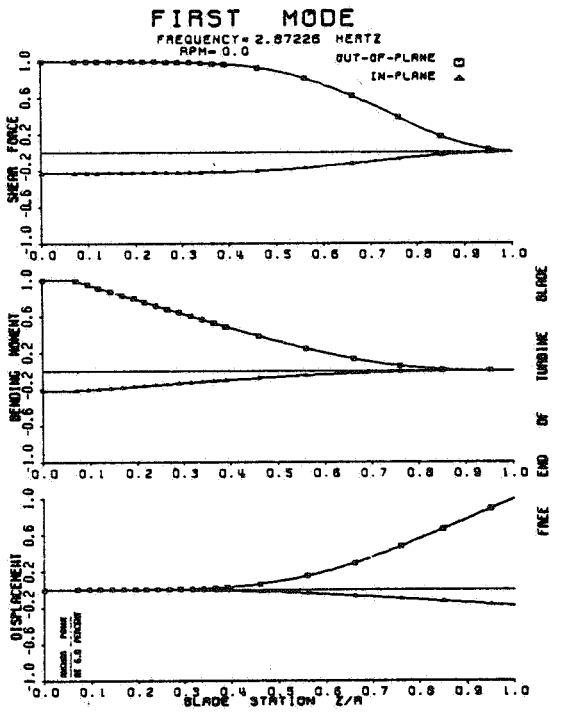

Figure 5 - First out-of-plane mode

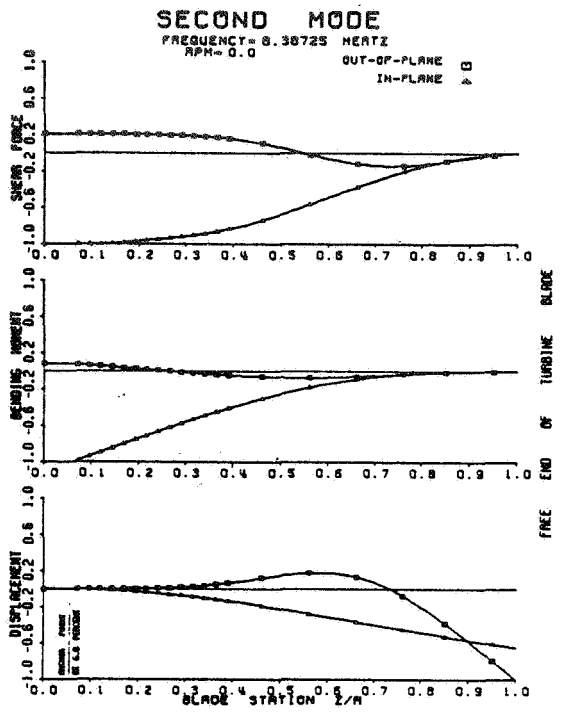

Figure 6 - Second out-of-plane mode

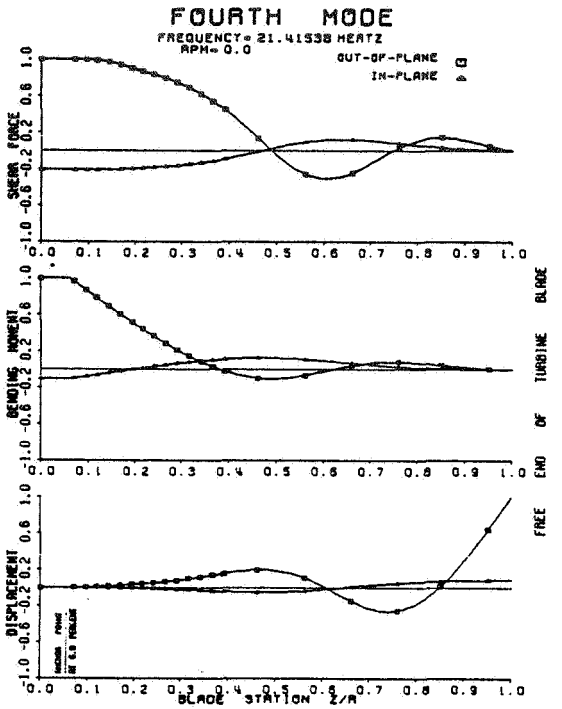

Figure 8 - Third out-of-plane mode

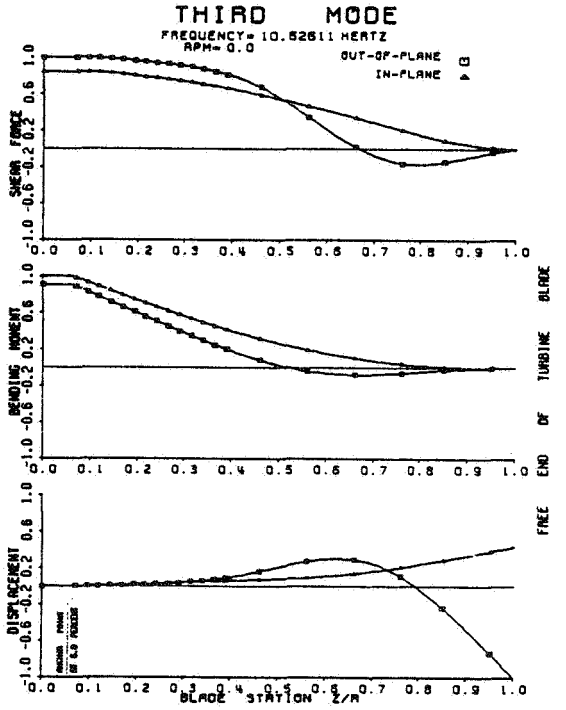

Figure 7 - First in-plane mode

For each of these cases, the following has been obtained:

1) The resonant frequencies (pôles). The zeros are also available from the polar moment of inertia curves.
2) The normalized in-plane and out-of-plane displacement curves or mode shape.
3) The normalized in-plane and out-of-plane shear force and bending moment distribution curves.

The results presented here are valid only for a blade mounted perpendicularly in a rigid hub. Only the coupled in-plane and out-of-plane bending modes are considered, torsion being neglected. One blade was tested experimentally in the laboratory for the stationary case only. The analytical and experimental frequencies are compared in table I.

MODES	ANALYTICAL	EXPERIMENTAL
1	2.872	2.80
2	8.387	8.00
3	10.627	10.99
4	21.415	18.66
5	31.384	27.39
6	37.474	30.77

Table I. Natural resonant frequencies in Hertz for a stationary blade.

It can be seen that the natural frequencies are in close agreement for the first few modes. The larger discrepancies for the higher modes are believed to be caused by some uncertainty in the construction causing local variations of mass and stiffness which would affect mostly the higher modes. Also, the fact that the blade support was not perfectly rigid, means that the observed frequencies would be lower than the one predicted under the cantilever assumption. Finally, the excitation of the blade was done with an electromagnetic exciter which requires some attachment hardware at the tip of the blade. This addition of mass at the tip, also tends to lower the frequencies.

The normalized mode shapes, shear forces and bending moments distribution curves are shown in figures 5 to 10 for a stationary blade. Coupling between the in-plane and out-of-plane modes is evident from the figures. It should be noted that the blade stiffness discontinuities at blade station 0.10 and 0.22 do not affect the continuity of the distribution of the bending moment and of the shear force.

The same computations were done for a rotating blade at 100, 200 and 300 RPM. Table II shows

MODE	RPM = 0	RPM = 100	RPM = 200	RPM = 300
1	2.872	3.728	5.421	7.183
2	8.387	8.649	9.099	9.594
3	10.626	11.228	13.031	15.703
4	21.415	22.143	24.161	27.117
5	31.384	31.593	32.206	33.143
6	37.474	38.206	40.246	43.486

Table II. Resonant frequencies of a rotating blade.

the resonance frequencies obtained. The effect of the rotational speed on the resonance frequencies for the three first modes is shown in figure 11. The agreement with some experimental results is good.

NUMERICAL RESULTS FOR THE POLAR MOMENT OF INERTIA

The polar moment of inertia of a three bladed rotor has been computed for vibration frequencies up to 70 radians/sec and rotational speed up to 200 RPM. The values of J_{F+M} obtained with the formula using the shear force and moment (equation 30) and the values $J_{\int}$ obtained with the integral formula (equation 31) give comparable results. However, as mentioned earlier the values of $J_{\int}$ are implicitly more accurate than the values of J_{F+M}. This fact is demonstrated numerically by observing that at very low frequencies, the value of $J_{\int}$ remains constant for all RPM used while the value of J_{F+M} shows small variations for each rotational speed considered.

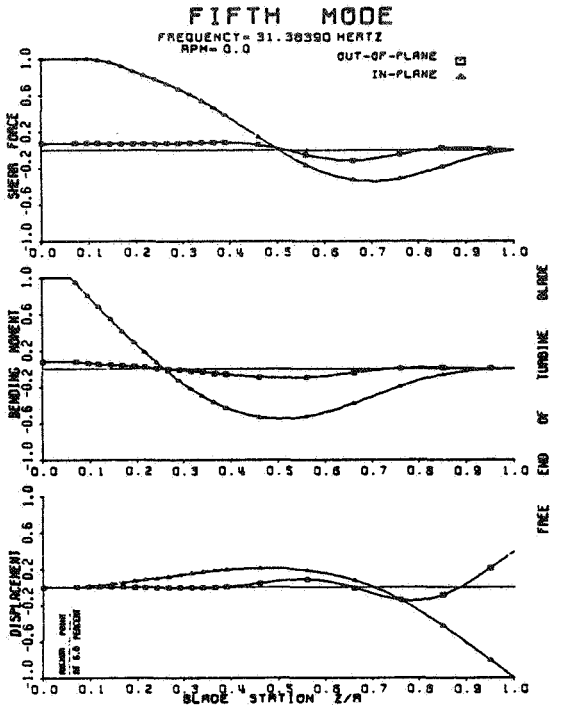

Figure 9 - Second in-plane mode

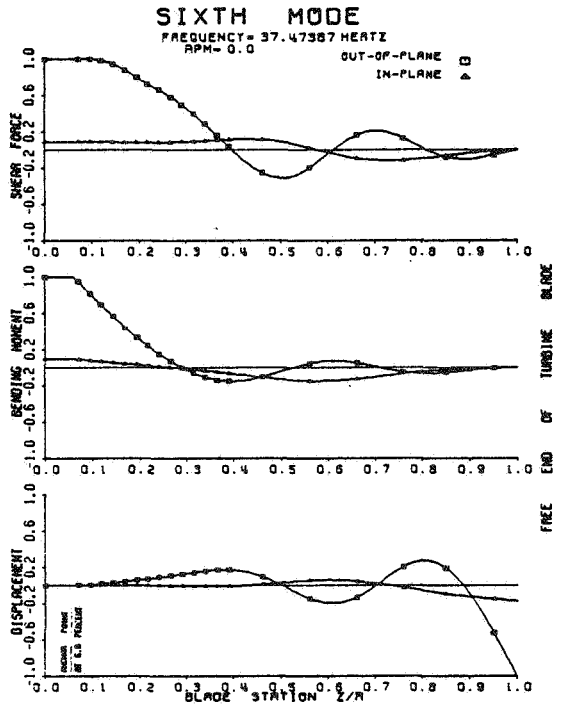

Figure 10 - Fourth out-of-plane mode

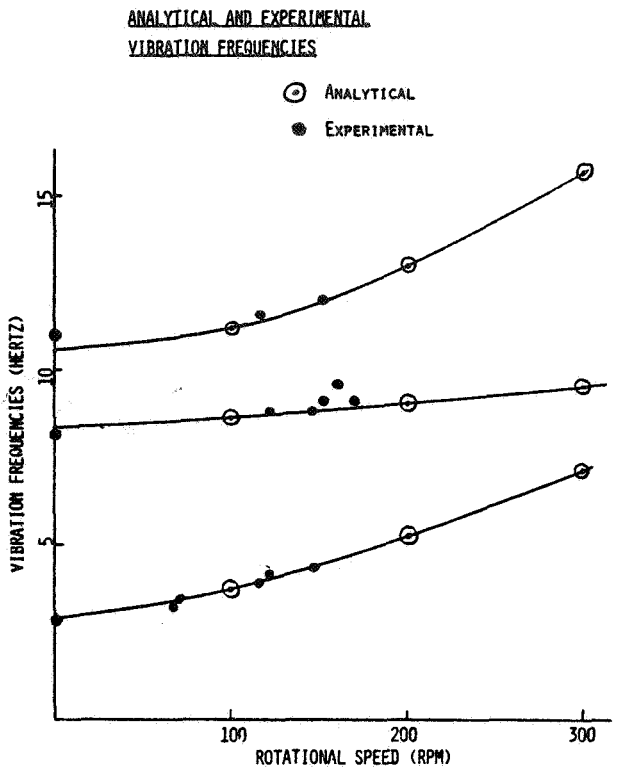

Figure 11 - Effect of rotational speed on vibration frequencies

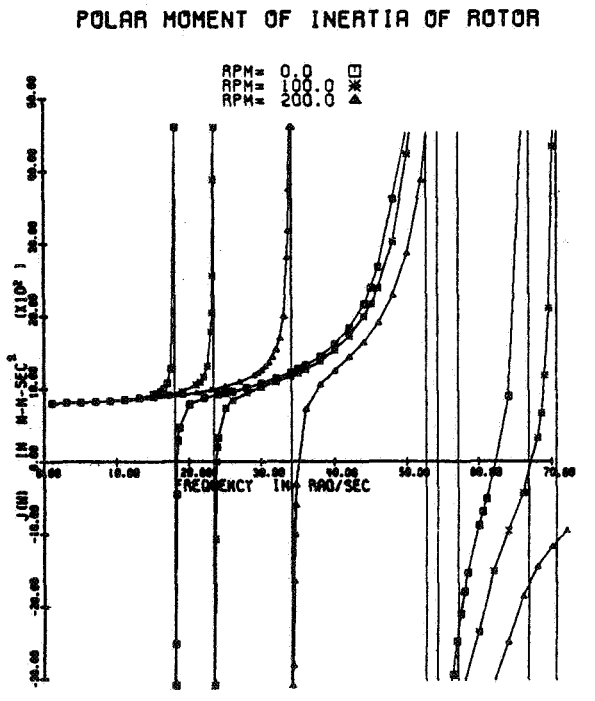

Figure 12 - Variation of polar moment of inertia in fonction of vibration frequency and rotational speed

The variation of the polar moment of inertia with the vibration frequency and rotational speed is presented in figure 12. Only the values of J_f are shown. The pôles (resonant frequencies) and the zeros can be seen on this graph. The numerical value of the zeros are presented in table III.

ZEROS	RPM = 0	RPM = 100	RPM = 200
1	2.916	3.789	5.588
2	9.912	10.689	-

Table III. Zeros of the rotor in Hertz

It can be seen that the value of J is relatively constant at low frequency and comparable (less than 0.47% at ω = 0.5 rad/sec) to the static value J_0. (The static value J_0 is 807.29 newton-meter-sec^2.)

If damping had been included in the equations the extreme variations of J at a pôle would be reduced, especially when a zero is very close to a pôle, as is the case for the first mode. With damping the pôle-zero doublet would produce only a small variation in J, its importance depending on the separation between the pôle and the zero.

CONCLUDING REMARKS

A mathematical model and its method of solution have been presented for a tapered twisted, cantilever wind turbine blade with discontinuous stiffness. The two fourth order differential equations representing the in-plane and the out-of-plane motion of the blade have been transformed into eight first order equations and solved with Runge-Kutta integrators. The blade discontinuities have been approximated by imposing the continuity of displacements, slopes, bending moments and shear forces. The centrifugal force is included in the model; the coriolis force was found to be negligeable. The polar moment of inertia of a three bladed rotor is formulated considering either the in-plane bending moment and shear force at the anchor point or the integral of the in-plane displacements for vibrating, rotating blades.

It has been demonstrated that the method is sufficient to compute the natural frequencies and mode shapes of a stationary or rotating wind turbine blade with large discontinuities in stiffness. The normalized distributions of bending moment and shear force are also computed. The polar moment of inertia has been computed as a function of frequency and rotational speed. Good agreement with experimental frequencies has been observed.

The computer program can be used efficiently for the structural optimisation of the blades of horizontal axis wind turbine. The computer time and memory requirements are relatively small (approximately 20 sec and 200 K with an IBM 370, for each mode) so that parametric studies are possible.

NOTE:

Numerical results of vibration frequencies and mode shapes for discontinuous turbine blades published by Lang and Nemat - Nasser (ref. 3) became known to us just recently, after the analysis presented here was completed. The accuracy of the method proposed here will be compared later with the results of reference 3.

ACKNOWLEDGMENT

The authors acknowledge the assistance of Bernard Saulnier, Ahmad Jamaleddine, Michel Gauthier, Yvan Sunderland and Dorien Marois, all of IREQ, for the experimental data.

REFERENCES

1. Houbolt, J.C., Brooks, G.W.: Differential Equations of Motion for Combined Flapwise Bending, Chordwise Bending and Torsion of Twisted Nonuniform Rotor Blades. NACA Report 1236, 1958.

2. Canergie W., Dawson B. Vibration Characteristics of Straight Blades of Asymmetrical Aerofoil Cross-Section. The Aeronautical Quarterly, May 69, pp. 178-190.

3. Lang K.W., Nemat-Nasser S.: An Approach for Estimating Vibration Characteristics of Nonuniform Rotor Blades. AIAA Journal, Vol. 17, No. 9, Sept. 79, pp. 995-1002.

4. Shampine L.F., Watts H.H.: Comparing Error Estimators for Runge-Kutta Methods. Mathematics of Computation, Vol. 25, No. 115, July 71.

5. Hull D.G.: Fourth-Order Runge-Kutta Integrations With Stepwise Control, AIAA Journal, Vol. 15, No. 10, October 77, pp. 1505-1507.

NOMENCLATURE

a_r	=	Coefficients in numerical solution
$C_o, C_1, \ldots, C_4$	=	Arbitrary constants used in numerical solution
C_v	=	Couple applied by hub at anchor point of the blade
E	=	Young's modulus
F_x, F_y	=	Shear forces in x and y directions
I_{xx}	=	Moment of inertia of blade about x axis
I_{yy}	=	Moment of inertia of blade about y axis
I_{xy}	=	Product of inertia
L	=	Total length of blade
ℓ	=	Distance between axis of rotation and anchor point of the blade
M_x, M_y	=	Bending moments about x and y axis
m	=	Mass of blade per unit length
RPM	=	Rotational speed in rev/min
T	=	Tension force in blade
u	=	Displacement along x axis
v	=	Displacement along y axis
x, y, y	=	Cartesian coordinates
$Y_1, \ldots, Y_8$	=	Variables of transformation
β	=	Twist angle of blade
θ	=	Angular displacement of rotor
Ω_o	=	Rotational speed of rotor
ω	=	Vibration frequency
$( )'$	=	First derivative with respect to z
$( )''$	=	Second derivative with respect to z
$( )'''$	=	Third derivative with respect to z
$( )^{IV}$	=	Fourth derivative with respect to z

QUESTIONS AND ANSWERS

G. Beaulieu

From: W.C. Walton

Q: Would you agree that the root support stiffness should affect the lower modes first so that this is probably not the explanation for higher mode errors?

A: *True. The support stiffness could explain the lower frequency in the first few modes, while unknown mass and stiffness distribution and the tip mass addition of the electromagnetic exciter could explain the deviations for the higher modes.*

From: W.N. Sullivan

Q: How were the experimental resonant frequencies shown measured on the turning rotor?

A: *Directly measured from strain gages recording on strip charts. We would have preferred magnetic tape recording and spectral analysis.*

From: A. Wright

Q: Why do the boundary conditions for edgewise displacements change if hub is free to rotate?

A: *When the hub is free to rotate, an in-plane displacement $v(\ell)$ is present at the anchor point and similarly the slope of this displacement is $v(\ell)/\ell$. If the hub would be fixed, v and v' would equal zero.*

From: Y.Y. Yu

Q: Could you elaborate further on the blade construction?

A: *Referring to Figure 1, we can see the stall shaft and plate insert near the root. The steel is bounded to the fiberglass box which is present for the complete span of the blade. The fiberglass box is bounded to the outside skin having a NACA 4415 profile.*

From: A.D. Garrad

Q: Do you have an estimate for the damping in the blade?

A: *No, but some stationary blade vibration tests are being done now and exponential decay will be measured to obtain an estimate of structural damping. Aerodynamic damping will not be measured.*

DYNAMIC ANALYSIS OF DARRIEUS VERTICAL AXIS WIND TURBINE ROTORS*

D. W. Lobitz

Sandia National Laboratories
Applied Mechanics Division
Albuquerque, New Mexico 87185

ABSTRACT

The dynamic response characteristics of the VAWT rotor are important factors governing the safety and fatigue life of VAWT systems. The principal problems are the determination of critical rotor speeds (resonances) and the assessment of forced vibration response amplitudes. The solution to these problems is complicated by centrifugal and Coriolis effects which can have substantial influence on rotor resonant frequencies and mode shapes. This paper will describe and discuss the primary tools now in use at Sandia National Laboratories for rotor analysis. These tools include a lumped spring-mass model (VAWTDYN) and also finite-element based approaches. The discussion will center on the accuracy and completeness of current capabilities and plans for future research.

INTRODUCTION

The primary goal at Sandia in the dynamic analysis of vertical axis wind turbines (VAWT) is to accurately predict vibratory and mean stress levels throughout the rotor system. In most VAWT designs to date, quasi-static analysis methods have been the primary tools utilized for dynamic analysis. This simple approach was motivated by the observation that the VAWT rotor is stiff relative to the excitation frequencies. However, experience has indicated that substantial resonances can and do occur for certain operating conditions in the VAWT rotor. There is clearly a need to construct relatively complete dynamic models to identify critical resonance conditions and, for near resonant operations, to predict dynamic amplification factors.

Techniques for predicting vibratory stress levels near resonance are hampered by uncertainties in the aerodynamic wind loading and structural damping. In the latter case, since the VAWTs encountered to date have all been very lightly damped (.1 to .5% of critical), near resonance, slight variations in the magnitude of the damping produce large variations in the vibratory stress levels.

Although techniques for predicting vibration amplitudes are still being pursued, the major effort is being expended on developing methods to identify critical resonances. With a knowledge of the natural frequencies of the turbine and the frequency content of the aerodynamic wind loading, both as a function of the turbine operating speed, one can identify possible turbine speeds which may produce resonance. Some of these critical speeds can be eliminated by considering the modal content of the wind loading as compared with the mode of vibration in question.

This all seems straightforward enough, but it is considerably complicated by the fact that the turbine modes and frequencies as well as wind forcing functions must be obtained relative to the rotating frame. Due to this added complexity and a scarcity of intuition for the behavior of rotating structures, experimental data have been relyed upon whenever possible to verify the mathematical models.

HISTORY

Originally at Sandia, finite element techniques which accounted only for the rotational effects of centrifugal stiffening were used to determine the spectral characteristics of VAWTs. A version of the SAP IV code, modified to include centrifugal stiffening, was utilized in this regard. It had also been determined, from symmetry arguments, that for two-bladed rotors, modes which involve axisymmetric motion about the turbine axis are driven only by even per rev excitations, whereas modes which involve lateral tower motion are driven by odd per rev excitations. A fan plot for the DOE/Alcoa low-cost 17 meter turbine which was generated with SAP IV is shown in Fig. 1.

The first revelation that this dynamic analysis technique was inadequate came when Alcoa's ALVAWT 6342 turbine was put into operation. A one per rev tower resonance, observed at the operating speed, was not predicted by the SAP IV analysis as all modes which involve tower motion crossed the one per rev excitation line well away from the operating speed. In an attempt to understand this apparent anomaly, closed form solutions of the whirling shaft problem were examined, whereupon the necessity of

*This work supported by the U.S. Department of Energy under Contract No. DE-AC04-76DP00789.

including all of the rotating coordinate system effects was immediately realized.

To include these effects, a simple, seven-degree-of-freedom, spring-mass model of a two-bladed VAWT, which is displayed in Fig. 2, was developed. In this model, the tower is represented by two rigid links joined together with a "U" joint. Torsional springs are mounted across the joint to account for the tower bending stiffness. The blades, which are also assumed to be rigid, are attached at the top and bottom of the tower through ball joints with torsional springs representing the blade lead-lag stiffness. Linear springs, which model the cable stiffness, are attached at the top of the tower, tending to restore it to its upright position. Torsional springs represent the drive train stiffness and blade aerodynamic loads are determined using a single streamtube aerodynamic model. The equations for the model are developed in a frame which rotates with the turbine, taking into account all low order rotating coordinate system effects. Solutions are obtained using time marching techniques developed for initial value problems. This analysis package, which goes by the name VAWTDYN, is covered in detail in a Sandia National Laboratories report.*

The dynamic behavior predicted by VAWTDYN differed markedly from that of the SAP IV model. This is shown in Fig. 3, where a VAWTDYN analysis of the DOE/Alcoa 17 meter is summarized. The natural frequencies of the turbine, which previously only increased with increasing rpm due to centrifugal stiffening, now varied in either direction reminiscent of the whirling shaft behavior. In addition to this, mode shapes which had been independent of each other became coupled. For example, modes which contained motion either in the plane of the blades or out of it, as predicted by SAP IV, now possessed both types of motion.

For verification purposes, VAWTDYN results were compared to the limited amount of experimental data available. VAWTDYN accurately predicted the tower resonance of the ALVAWT 6342 and, in fact, was relatively successful in all these verification tests. As a result, even though it is a relatively crude model, capable of representing only 3 or 4 rotor modes, a fair amount of confidence was developed in the VAWTDYN package.

However, after the erection of the DOE/Alcoa low-cost 17 meter turbine, a significant three per rev blade resonance was observed which VAWTDYN did not predict. And, in fact, no reasonable amount of variation in the parameters of the VAWTDYN model would produce the resonance or the associated mode of vibration. Speculating that the difficulty was associated with the crudeness of the model, a much more refined model, described in the next section was developed.

*D. W. Lobitz and W. N. Sullivan, "VAWTDYN - A Numerical Package for the Dynamic Analysis of Vertical Axis Wind Turbines," SAND80-0085, July 1980.

CURRENT METHODS

The model which is now used at Sandia for dynamic analysis of VAWTs is derived using finite element techniques. A coordinate system is employed, fixed in space at the base of the tower, which rotates at a constant angular velocity. Turbine motions within this system are assumed to be small. Manifestations of this rotating system appear primarily in the inertia terms of the equations of motion.

Due to the structural nature of VAWTs, the finite element equations need only be developed for beam elements and concentrated masses. In the case of the beam elements, for developing the inertia matrices, the displacements and velocities are assumed to vary linearly along the length of the element. Using the following equation for the total velocity at a point,

$$\underset{\sim}{v}_t = \dot{\underset{\sim}{u}} + \underset{\sim}{\Omega} \times (\underset{\sim}{r} + \underset{\sim}{u}) \ , \qquad (1)$$

where,

$\underset{\sim}{v}_t$ is the total velocity vector,
$\underset{\sim}{r}$, $\underset{\sim}{u}$, and $\dot{\underset{\sim}{u}}$ are the original position, the displacement, and the velocity vectors, respectively, as observed in the rotating coordinate system, and
$\underset{\sim}{\Omega}$ is the angular velocity vector of that system,

an expression for the kinetic energy of an elemental mass at that point can be developed. After substituting for $\underset{\sim}{r}$, $\underset{\sim}{u}$, and $\dot{\underset{\sim}{u}}$, their linear functional forms and integrating the kinetic energy along the length of the element, the total kinetic energy is obtained. The appropriate finite element matrices can now be developed using Hamilton's Principle. For the special case of $\underset{\sim}{\Omega}$ constant and directed along the "z" axis of the rotating system, i.e.,

$$\underset{\sim}{\Omega} = \begin{Bmatrix} 0 \\ 0 \\ \Omega_z \end{Bmatrix} \ , \qquad (2)$$

the various inertia matrices and their corresponding vector multipliers, for an arbitrary element, are given below:

Mass

$$\rho\ell \begin{bmatrix} 1/3 & 0 & 0 & 1/6 & 0 & 0 \\ & 1/3 & 0 & 0 & 1/6 & 0 \\ & & 1/3 & 0 & 0 & 1/6 \\ & & & 1/3 & 0 & 0 \\ & & \text{sym} & & 1/3 & 0 \\ & & & & & 1/3 \end{bmatrix} \begin{Bmatrix} \ddot{u}_{x_1} \\ \ddot{u}_{y_1} \\ \ddot{u}_{z_1} \\ \ddot{u}_{x_2} \\ \ddot{u}_{y_2} \\ \ddot{u}_{z_2} \end{Bmatrix}, \quad (3)$$

Coriolis

$$2\rho\ell\Omega_z \begin{bmatrix} 0 & -1/3 & 0 & 0 & -1/6 & 0 \\ 1/3 & 0 & 0 & 1/6 & 0 & 0 \\ 0 & 0 & 0 & 0 & 0 & 0 \\ 0 & -1/6 & 0 & 0 & -1/3 & 0 \\ 1/6 & 0 & 0 & 1/3 & 0 & 0 \\ 0 & 0 & 0 & 0 & 0 & 0 \end{bmatrix} \begin{Bmatrix} \dot{u}_{x_1} \\ \dot{u}_{y_1} \\ \dot{u}_{z_1} \\ \dot{u}_{x_2} \\ \dot{u}_{y_2} \\ \dot{u}_{z_2} \end{Bmatrix}, \quad (4)$$

Softening

$$\rho\ell\Omega_z^2 \begin{bmatrix} 1/3 & 0 & 0 & 1/6 & 0 & 0 \\ & 1/3 & 0 & 0 & 1/6 & 0 \\ & & 0 & 0 & 0 & 0 \\ & & & 1/3 & 0 & 0 \\ & & \text{sym} & & 1/3 & 0 \\ & & & & & 0 \end{bmatrix} \begin{Bmatrix} u_{x_1} \\ u_{y_1} \\ u_{z_1} \\ u_{x_2} \\ u_{y_2} \\ u_{z_2} \end{Bmatrix}, \quad (5)$$

Centrifugal Force

$$\rho\ell\Omega_z^2 \begin{bmatrix} 1/3 & 0 & 0 & 1/6 & 0 & 0 \\ & 1/3 & 0 & 0 & 1/6 & 0 \\ & & 0 & 0 & 0 & 0 \\ & & & 1/3 & 0 & 0 \\ & & \text{sym} & & 1/3 & 0 \\ & & & & & 0 \end{bmatrix} \begin{Bmatrix} r_{x_1} \\ r_{y_1} \\ r_{z_1} \\ r_{x_2} \\ r_{y_2} \\ r_{z_2} \end{Bmatrix}. \quad (6)$$

The subscripts x, y, and z refer to the vector components along the rotating coordinate system axes and the "1's" and "2's" denote the value at either the first or second node point of the element. The quantity, ρ, is the mass/unit length and ℓ is the length of the element.

Assembling the contributions from all the elements in the discretized model and denoting the total mass, Coriolis, and softening matrices by M, C, and S, respectively, the resulting finite element equations are given by

$$\ddot{M}\ddot{U} + C\dot{U} - SU + K\begin{Bmatrix} U \\ \theta \end{Bmatrix} = F_C + F_A. \quad (7)$$

The load vectors, F_C and F_A, respectively, represent the centrifugal force loading, which results from the element contributions detailed in Eq. (6), and blade loads caused by aerodynamic forces.

The matrix, K, is the usual assembled stiffness matrix for the beam elements, and consequently contains terms associated with rotations in addition to displacements, as indicated. In general, due to the stretching of the neutral axis, K is a function of the displacement. This introduces a nonlinearity in Eq. (7) which results in solution procedures of much greater complexity. To avoid this additional complexity, the stiffness matrix is developed commensurate with the quasi-static displacement field associated with the time-independent centrifugal loading only, neglecting variations which result from the time-dependent aerodynamic loads. With this approximation, K is constant, which eliminates the nonlinearity, and the equations represent small vibrations about a centrifugally prestressed state.

A critical factor in the development of this method is that at no time was it required to make vector transformations between stationary (groundbased) and rotating coordinate systems. For most VAWTs, the physical connections of the rotor to the ground occur through the tiedown cables and the tower base connection. Since the base of the tower is stationary, zero displacements exist in both systems. Furthermore, if there are three or more equally spaced tiedown cables with mass small relative to the rotor, identical in length, cross-sectional area, pretension, and angle of inclination, the restoring forces depend only on the displacement of the top of the tower from the vertical. These forces are directed toward the undisturbed vertical position of the rotor. Consequently, the tiedowns can be represented by massless linear springs which rotate with the turbine and are connected between its top and the vertical. To date, all turbines analyzed by this method have possessed this type of tiedown system.

In certain rotor designs, the restoring forces may also depend on the azimuthal angle of the turbine relative to ground (as in the case of unequally spaced cables, for example). In these situations, appropriate transformation must be implemented and time dependent coefficients appear in the stiffness matrix. Although the equations retain their linearity, the existence of these coefficients would require the current solution procedure to be extensively modified.

To obtain the modes and frequencies of the turbine as observed in the rotating system, a complex eigenvalue extraction procedure must be employed. For this purpose, Eq. (7) is reduced to the following form:

$$M\ddot{U} + C\dot{U} - SU + K\begin{Bmatrix} U \\ \theta \end{Bmatrix} = 0, \qquad (8)$$

with K corresponding to the pre-stressed state resulting from centrifugal loading, as discussed above. In the general case the damping matrix, C, produces complex eigenvalues and eigenvectors. However, in this case, where the C matrix represents Coriolis effects only and is consequently skew-symmetric, just the eigenvectors are complex.

Instead of developing a completely independent package for the eigensolution of Eq. (8), an existing code was modified. With this approach, duplication of such things as input, output, plotting, solution procedures, etc., is avoided. The MacNeal-Schwendler version of NASTRAN was selected here because the modification required was minimal and could be accomplished via DMAP programming, a feature which allows the NASTRAN user to modify the code without actually dealing with the FORTRAN coding. This version contains complex eigensystem solution procedures and also permits the stiffness, mass, and damping matrices to be modified through an input option. Thus, the special matrices required in Eq. (8), specifically the Coriolis (C) and softening (S) matrices, can be generated externally and read into NASTRAN as input. As the NASTRAN code handles non-symmetric as well as symmetric matrices, no special problems occur due to the skew-symmetry of the coriolis matrix. The mass (M) and stiffness (K) matrices are generated internally, complete with the effects of pre-stress in the stiffness matrix.

Although this method has been successfully tested with all available experimental data, the three per rev blade resonance which was observed in the DOE/Alcoa low-cost 17 meter turbine is of special significance, since it was not predicted by VAWTDYN. The fan plot shown in Fig. 4, which corresponds to the low-cost turbine, was developed using the current method. Note that the three per rev excitation line crosses the natural frequency line associated with the first in-plane mode very close to the 51.3 rpm operating speed, indicating the observed resonance. Moreover, at the operating speed, in addition to containing the observed three per rev blade edgewise motion, the first in-plane mode also contains the unusual tower motion which was measured. In this mode, even though the blade motion is predominantly out of the plane of the blades, reminiscent of flapping butterfly wings, the tower moves predominantly in the plane. This result, which tends to defy intuition, is a result of the rotating coordinate system effects.

The other tests, which have been used to verify the method, have involved experimental data taken from the Alcoa ALVAWT 6342 turbine and Sandia's 17 meter research machine. The method has also been tested against existing closed form solutions such as that for the whirling shaft problem. Although verification will continue as new tests become available, to date, no failures have been experienced.

The primary strength of this method is that a general class of VAWTs can be analyzed with it relatively easily and in much detail using the various NASTRAN modeling features. Additional blades, struts, concentrated masses, etc. can be analyzed simply through the preparation of the appropriate NASTRAN input.

FUTURE ACTIVITIES

Two major activities are planned for extension of the finite element package described in the previous section. In order to predict vibratory stress levels during turbine operation, a capability for the analysis of forced vibration will be developed. Time marching as well as modal superposition methods will be pursued. Using this capability, an effort will be made to establish a general categorization procedure with regard to severity for the various crossings of the frequency and excitation lines on the fan plot.

The other activity involves the inclusion of aeroelastic effects in the finite element equations. To implement these effects, modifications will be made to the mass, damping, and stiffness matrices to incorporate the corresponding aerodynamic matrices. The aeroelastic effects will be used both in forced vibration and flutter instability analyses.

In addition to these extensions, a major experiment is planned to provide a relatively comprehensive test of accuracy of this method in predicting turbine modes and frequencies in the rotating system. The test will consist of measuring these spectral data for the Sandia 17 meter research turbine while rotating. By conducting tests at several rotational speeds, a fan plot such as the one shown in Fig. 4 can be experimentally developed for comparison with predictions.

CONCLUSIONS

The sophistication of dynamic analysis methods for VAWTs has undergone steady improvement at Sandia. The current method provides a means to straightforwardly predict the spectral characteristics

of rotating turbines which have a significant degree of structural complexity. Verification tests have shown the accuracy of the method to be quite satisfactory. After completion of the planned activities identified in the previous section, a strong capability for dynamic assessment of VAWTs should be available. This should be achieved within the current calendar year and will significantly improve the capability to structurally design advanced VAWT systems.

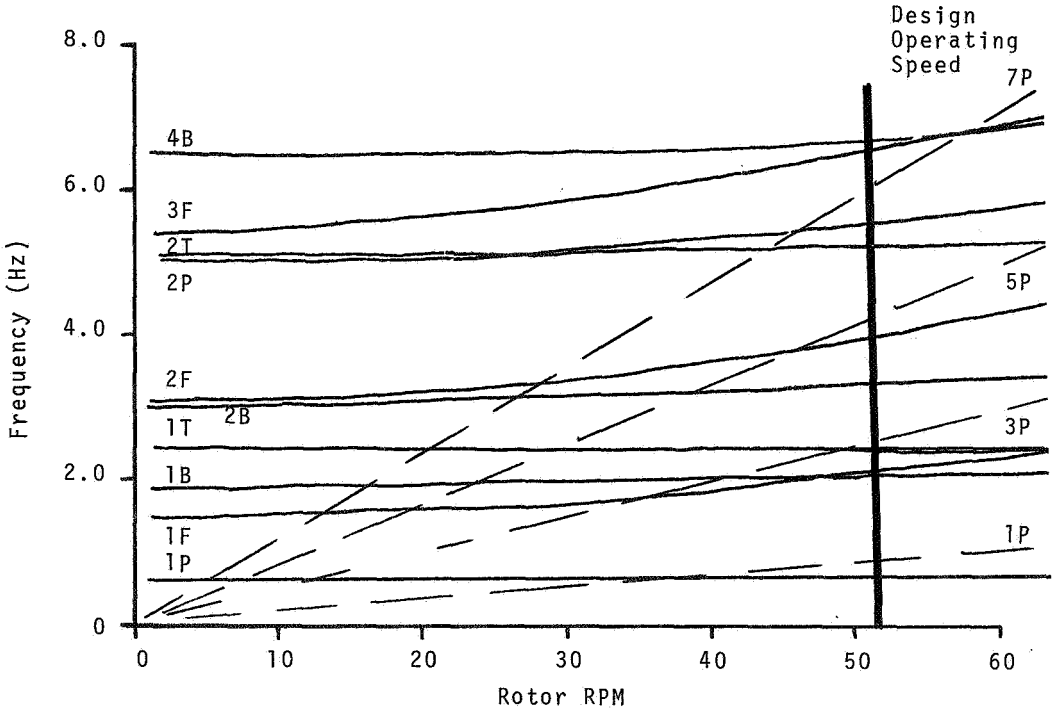

FIGURE 1: SAP IV Resonant Frequency Predictions for the DOE/Alcoa 17-m Rotor, Including Centrifugal Stiffening

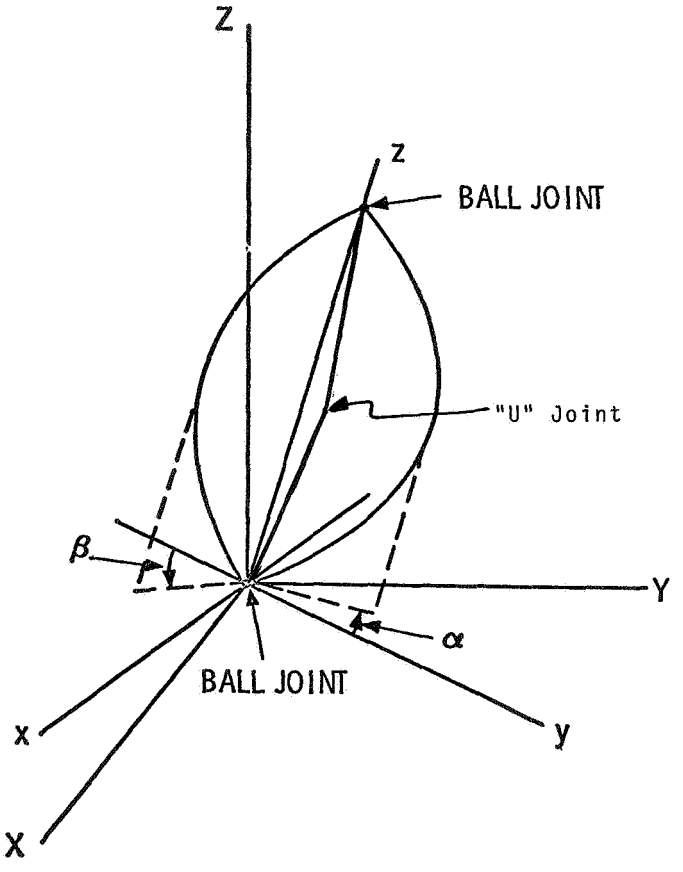

FIGURE 2: Blade and Tower Motions Included in the VAWTDYN Model

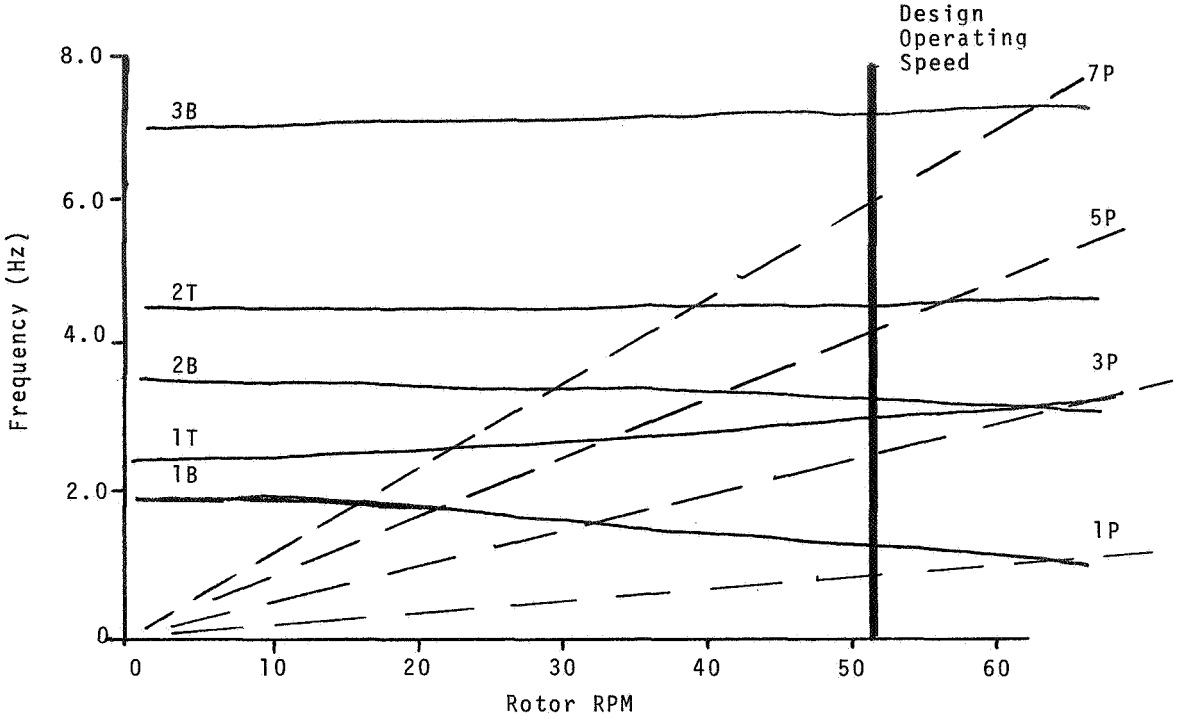

FIGURE 3: VAWTDYN Predictions of Resonant Frequencies for the DOE/Alcoa 17-m Rotor

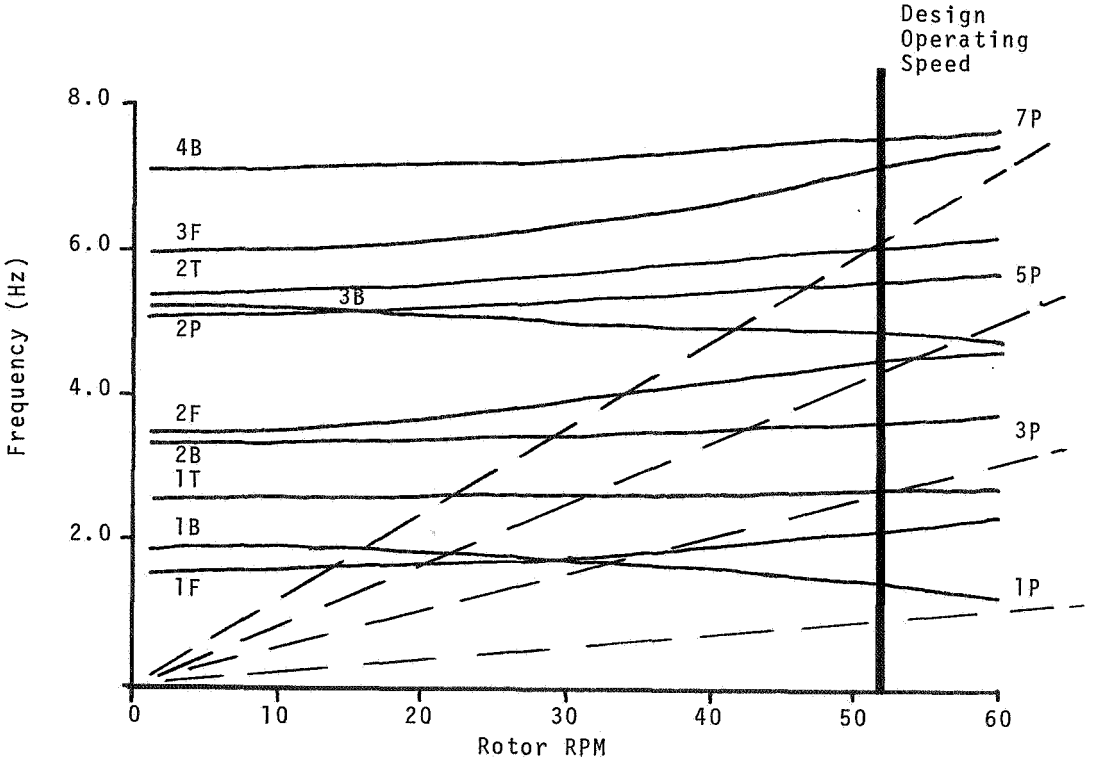

FIGURE 4: NASTRAN Resonant Frequency Predictions for the DOE/Alcoa 17-m Rotor, Including Rotating Coordinate System Effects

QUESTIONS AND ANSWERS

D.W. Lobitz

From: S.A. Shipley

Q: Is the Nastran modification applicable to HAWTS with N blades (including N = 2)?

A: *This modification is applicable to HAWT's of any number of blades under certain restrictions. These restrictions involve neglecting the inertia of the tower and modeling its stiffness by linear and rotational springs in the rotating system. These springs must be independent of the azimuthal position of that system. Of course, as with the VAWT's, the angular velocity of the rotating frame must be constant and motions within it, assumed small. For three or more bladed systems the multiblade coordinate transformation might yield an alternate NASTRAN approach. However, some method for affecting the equation manipulations would have to be developed. This approach would not be as restricted as the present one is.*

From: A. Wright

Q: How were centrifugal stiffening effects included in SAP-IV?

A: *Centrifugal stiffening effects are included in SAP-IV by internal modification of the stiffness matrix. These modifications are developed on the basis of a linear solution at 1 rpm. The alterations for other rpms is obtained by multiplication of the 1 rpm modification by the square of the desired rpm. Tests which involve a number of nonlinear iterations have shown this simple method to be quite accurate.*

From: G. Beaulieu

Q: How do you simulate the effects of the guy wires on the rotor into your NASTRAN model? Constant stiffness?

A: *The guy wires are modeled by a linear spring of constant stiffness which rotates with the turbine and tends to restore the turbine to its vertical position. As most of the cable systems we have dealt with are highly tensional, the sag contribution to the stiffness is minimal and the constant stiffness assumption is reasonably accurate. If the inertia of the guy wires was considered important and/or the spring constant was a function of the azimuthal position of the turbine, this NASTRAN solution procedure would be invalidated due to the introduction of non-constant coefficients. Fortunately, this has not been the case in the VAWT's encountered so far.*

From: Bill Wentz

Q: Please describe the "butterfly" mode.

A: *In a two-bladed VAWT system "butterfly" modes are characterized by lead-lag blade motions wherein the blades move simultaneously and equally in the same linear direction. The label "butterfly" is appropriate because when the turbine is viewed from the top, the motion is reminiscent of flapping butterfly wings. Three or more bladed systems also possess "butterfly" modes but of considerably greater complexity.*

From: W.C. Walton

Comment: Congratulations on the introduction of rotating effects in NASTRAN. We have also successfully used NASTRAN this way, though in a less complete and systematic way.

FLUTTER OF DARRIEUS WIND TURBINE BLADES: CORRELATION OF THEORY AND EXPERIMENT

Norman D. Ham

Department of Aeronautics and Astronautics
Massachusetts Institute of Technology
Cambridge, Mass. 02139

Acquisition of frequency data for the Alcoa 17-M LC and 1238229 wind turbines has permitted some limited correlation of the flutter analysis of Ref. 1 with experimental data for flutter of Darrieus blades from Ref. 2.

The natural frequencies of the non-rotating critical blade bending modes can be written as

$$\omega_{20} = \lambda_2 \sqrt{\frac{EI_F}{mR^4}} \text{ rad./sec.}$$

$$\bar{\omega}_{20} = \bar{\lambda}_2 \sqrt{\frac{GJ}{mR^4}} \text{ rad./sec.}$$

where λ_2, $\bar{\lambda}_2$ are frequency parameters, and

EI_F = blade flatwise bending stiffness, lb-ft^2

GJ = blade torsion stiffness, lb-ft^2

m = blade running mass, slugs/ft.

R = radius of circular arc portion of blade

Also, the effect of turbine rotational speed Ω is given by

$$\omega_2^2 = \omega_{20}^2 + K_2\Omega^2$$

$$\bar{\omega}_2^2 = \bar{\omega}_{20}^2 + \bar{K}_2\Omega^2$$

where K_2, $\bar{K}_2$ are Southwell coefficients.

Data provided by Alcoa has made possible the following tabulation for turbines of h/D = 1.5:

TABLE I

TYPE	λ_2	$\bar{\lambda}_2$	K_2	$\bar{K}_2$
17-Meter LC	5.72	23.7	2.74	4.57
1238229	10.0	23.5	4.32	3.99

The bracing struts of Type 1238229 appear to have a significant effect on the flatwise bending parameters λ_2 and K_2. It is suspected that significant mode shape variations may also be related to the clamping effect of the struts.

Experimental flutter data for wind tunnel models of Darrieus wind turbines of h/D = 1.5 are shown in Fig. 1 taken from Ref. 2. The correlating parameters are the reduced flutter speed

$$\frac{U_c \ell}{t} \sqrt{\frac{\rho_B}{G}}$$

where U_c = blade tangential velocity at flutter = $\Omega_F R_c$

ℓ = blade length

t = blade section maximum thickness

ρ_B = blade material density

G = blade material torsion modulus

and the density ratio

$$\frac{\rho_B A_B}{\frac{\pi}{4}\rho c^2}$$

where A_B = blade material cross-section area

ρ = air density

c = blade chord

These parameters were calculated for the 17-Meter LC and 1238229 wind turbines using their theoretical flutter speeds Ω_F of 108 rpm and 57 rpm respectively as calculated by the method of Ref. 1. The results are plotted in Fig. 1. The theory is seen to give a conservative prediction of flutter speed.

An attempt was made to predict the experimental flutter speed directly for the particular case of the aluminum blade of 0012 section of Fig. 1, using blade frequencies estimated by means of the parameters tabulated in TABLE I for the 17-Meter LC turbine, and the flutter parameter values $C_2 = -6.5$ and $m_\beta/m_\vartheta = 0.75$ for that strutless turbine. Again, the theoretical prediction is seen to be conservative.

Proceedings of the Second DOE/NASA Wind Turbine Dynamics Workshop, Cleveland, February 1981.

REFERENCES

1. Ham, N.D., "Flutter of Darrieus Wind Turbine Blades", from "Wind Turbine Structural Dynamics", NASA Publication CONF-2034, November 1977.

2. Templin, R.J. and South, P., "Canadian Wind Energy Program", Proc. of the VAWT Technology Workshop, SAND76-5686, Sandia Laboratories, Albuquerque, N.M., July 1976.

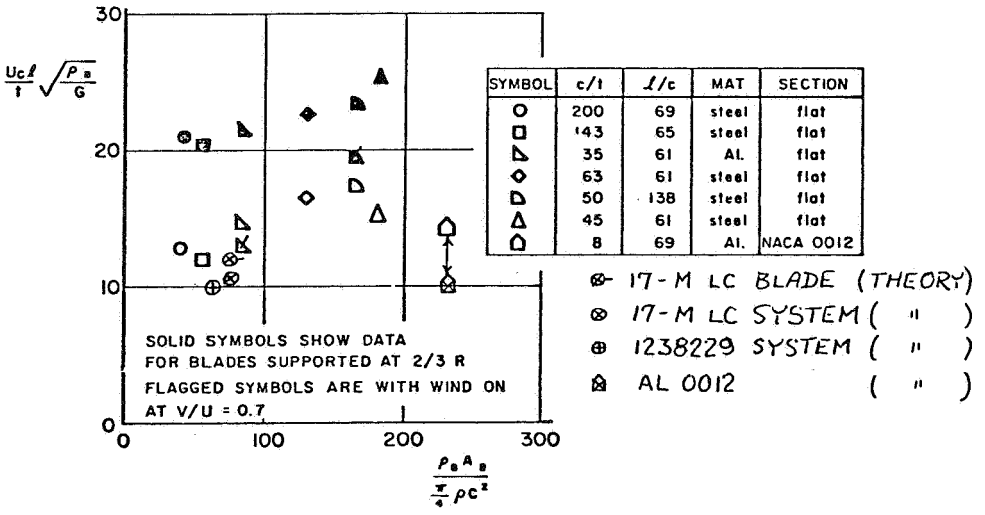

Fig.1. Variation of blade flutter parameter with density ratio for turbine with h/d = 1.5.

WHIRL FLUTTER ANALYSIS OF A HORIZONTAL-AXIS WIND TURBINE WITH A TWO-BLADED TEETERING ROTOR

David C. Janetzke
NASA Lewis Research Center
Cleveland, Ohio 44135

and

Krishna R. V. Kaza
The University of Toledo
and NASA Lewis Research Center

ABSTRACT

An investigation to explore the possibility of whirl flutter and to find the effect of pitch-flap coupling (δ_3) on teetering motion of the DOE/NASA Mod-2 wind turbine is presented. The equations of motion are derived for an idealized five-degree-of-freedom mathematical model of a horizontal-axis wind turbine with a two-bladed teetering rotor. The model accounts for the out-of-plane bending motion of each blade, the teetering motion of the rotor, and both the pitching and yawing motions of the rotor support. Results show that the Mod-2 design is free from whirl flutter. Selected results are presented indicating the effect of variations in rotor support damping, rotor support stiffness, and δ_3 on pitching, yawing, teetering, and blade bending motions.

INTRODUCTION

Recent horizontal-axis wind turbine (HAWT) designs such as the DOE/NASA Mod-2 wind turbine (ref. 1) include flexible towers in order to achieve significant weight and cost reductions. Experience with prop-rotors has shown that rotors with flexible supports have a potential aeroelastic instability known as whirl flutter. This form of instability involves the interaction of elastic, damping, gyroscopic, and aerodynamic forces. The whirl flutter problem is discussed in references 2-7 among others. In whirl instability, the rotor will precess in a whirl mode with an ever-increasing amplitude when the critical wind speed has been reached. That is, a point on the rotor hub will trace a divergent spiral as illustrated in Figure 1. The direction of the spiral rotation can be either the same as, or counter to, the rotor rotation. These two modes are referred to as forward and backward whirl modes, respectively. Continued operation of a wind turbine in the whirl flutter mode will quickly lead to failure of the supportive structure. This whirl instability is possible regardless of the presence of rotor teetering motions or blade out-of-plane bending motions. When these motions are included, they couple with the motions of the supportive structure. Then a whirl instability can occur in the whirl modes of the supportive structure and/or the rotor.

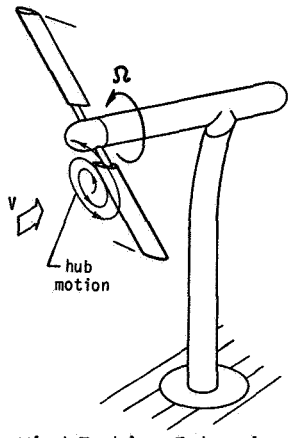

Figure 1. - Wind Turbine Rotor in a Forward Whirl Mode.

Most of the current large HAWT systems have rotors with two blades. The analysis of wind turbines with two-bladed rotors differs significantly from that with axisymmetric rotors. The properties of a two-bladed wind turbine change significantly as the blades rotate from a horizontal to a vertical position. As a result, the equations of motion of a two-bladed wind turbine system contain significant periodic coefficients.

In order to reduce blade bending loads, teetered rotors with pitch-flap coupling (δ_3) have been used in some HAWT systems. The pitch-flap coupling mechanically changes the pitch of the blades as the rotor teeters and thus is equivalent to an aerodynamic spring that restrains teetering motion. The effect of δ_3 on rotor motion stability was studied in refs. 6 and 8. A whirl flutter analysis for a prop-rotor on a flexibly mounted pylon was developed in ref. 6. That analysis may also be suitable for investigation of whirl flutter in HAWT systems. However, since most HAWT systems use rotor blades that are long and relatively flexible, the blade flexibility ought to be included in the formulation of a HAWT whirl flutter analysis.

Other analyses are available for the investigation of whirl flutter in HAWT systems. One is the MOSTAS computer code (refs. 9 and 10). However, it is very complex and uses a large amount of computer time. Hence, it is not well suited to parametric investigations.

Therefore, a simple model, encompassing only the pertinent degrees of freedom, is desired to study the possibility of whirl flutter in a flexibly mounted HAWT.

The primary purpose of this paper is to present the development of a simple model for exploring the possibility of whirl flutter in the DOE/NASA Mod-2 HAWT. Secondary purposes are to study the effects of pitch-flap coupling, rotor support stiffness, and rotor support damping on the response of the Mod-2.

A five-degree-of-freedom mathematical model is developed in the Appendix for a flexibly-mounted two-bladed teetering rotor. The degrees of freedom include the first out-of-plane bending mode for each blade, the rotor teetering motion, the rotor support pitching motion, and the rotor support yawing motion. The developed equations that have periodic coefficients are numerically integrated in the time domain using a standard Runge-Kutta method.

ANALYSIS METHOD

Mathematical Model

The mathematical model of a HAWT with two-bladed teetering rotor is shown in Figure 2. The rotor support is modeled by a rigid pylon of length h that is restrained at one end by two sets of rotational springs and dampers. These springs and dampers represent tower stiffnesses and dampings. The restraints allow only pitching and yawing motions, ϕ_x and ϕ_y, of the pylon. The teetering motion, γ, of the rotor hub with respect to the rotating shaft of the pylon is also restrained by a rotational spring and damper set. The angular velocity, Ω, of the rotor is assumed to be constant. The out-of-plane blade bending deflections are represented by w_1 and w_2. These deflections are, in turn, expressed in terms of the normal bending modes and the generalized coordinates. Since the blades are relatively stiff, only one mode is considered. This type of representation of the blade motion is referred to as a Rayleigh-type of analysis. As a consequence of this approximation of the blade motion, there are three degrees of freedom for the rotor, one for each blade, and one for teetering. Thus, with the pitching and yawing motions of the pylon, the wind turbine model has a total of five degrees of freedom. Only the out-of-plane bending motion of the blades is considered because it couples with the rotor teetering motion. Consideration of other motions such as tower translation, blade in-plane bending, and blade torsion are not difficult, but their inclusion would increase the complexity of the analysis. Furthermore, it is believed that these other motions do not have much effect on whirl flutter.

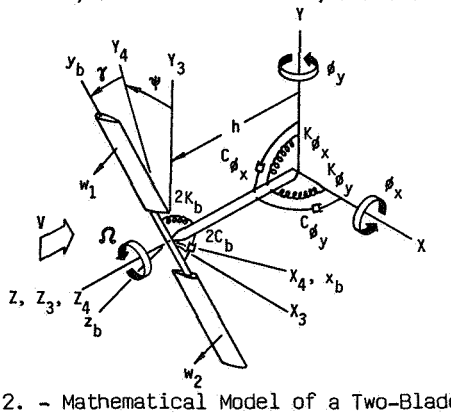

Figure 2. - Mathematical Model of a Two-Bladed Teetering HAWT.

Coordinate Systems

Several orthogonal coordinate systems are used in the derivation of the equations of motion. Those that are common to both the dynamic and aerodynamic aspects of the HAWT are described in this section.

1. Inertial system XYZ -- The Y-axis of this system, shown in Figure 2, coincides with the vertical axis of the HAWT tower and is positive upward. The Z-axis coincides with rotor axis and is positive into the wind.

2. Hub system $X_3Y_3Z_3$ -- This system is fixed to the hub center but does not rotate with the rotor. It is parallel to the XYZ system when the pod rotations are zero.

3. Rotor system $X_4Y_4Z_4$ -- This axis system is obtained by rotating the hub system about the Z_3 axis by the rotor position angle ψ ($=\Omega t$) as shown in Figure 2.

4. Blade system $x_by_bz_b$ -- This axis system is obtained by rotating the rotor system about the X_4-axis by the rotor teetering angle γ. The y_b axis is aligned along the blade quarter chord points and is also assumed to be the blade elastic axis. The x_b and z_b axes are also shown in Figure 3 along with the various blade element angles, relative velocities, and resultant aerodynamic forces.

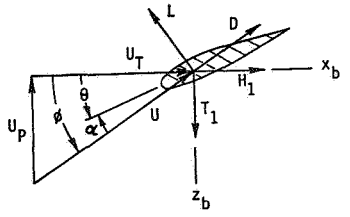

Figure 3. - Blade Element Velocity and Force Vectors for a Wind Turbine Rotor.

Computer Code

The equations of motion developed in the Appendix have timewise periodic coefficients. The stability of a HAWT must be determined by numerically integrating these equations or by using Floquet-Liapunov theory. To this end, a computer program called ASTER5 (Aeroelastic Stability of a TEetering Rotor with 5 degrees of freedom) was written to numerically integrate these equations. The ASTER5 program was first verified by several special cases obtained from ref. 6. The program was then used to investigate the possibility of whirl flutter in the DOE/NASA Mod-2 HAWT and the effect of variations in some of the Mod-2 parameters on its response.

The ASTER5 computer program was written in FORTRAN IV. The input includes the radial distributions of blade chord, twist angle, mass, and first out-of-plane bending mode; equivalent inertia, stiffness, and damping constants for the pylon; and aerodynamic data. The input allows part-span pitchable blades with pitch-flap coupling and cyclic pitch. The program uses a standard subroutine called DVERK, which solves a system of first-order differential equations with a Runge-Kutta method based on Verners fifth- and sixth-order pair of formulas.

RESULTS AND DISCUSSION

To verify the ability of the ASTER5 program to correctly predict whirl flutter, several cases of a prop-rotor, which was analyzed in ref. 6, were evaluated. The parameters for the prop-rotor are presented in Table I. Results are presented for two typical cases. In one case, the prop-rotor response exhibits whirl flutter, while in the other case it is stable. The whirl flutter case in which the pitching and yawing frequencies are 2.3 Hz and 5.0 Hz respectively, is shown in Figure 4. When the pitching frequency is raised to 3.3 Hz by increasing the pitch spring stiffness, the prop-rotor becomes stable, as shown in Figure 5. For comparison, the envelopes of the pitch motion amplitudes for the corresponding cases calculated in ref. 6 are also indicated in Figures 4 and 5. It is evident from these figures that there is agreement between the results of ref. 6 and the ASTER5 program. Thus, the ASTER5 program is capable of predicting whirl flutter. The quantitative differences evident in these figures may be due to differences in airfoil data and/or initial conditions. It should also be noted that ref. 6 does not account for the blade out-of-plane bending motions as does ASTER5. However, the blade frequency is assumed to be high for the input to ASTER5, and thus has a negligible effect on stability. The steady state pitch deflection, ϕ_x, evident in Figure 5, is due to the gravitational moment of the rotor, which is added to the pitching moment only for these verification cases.

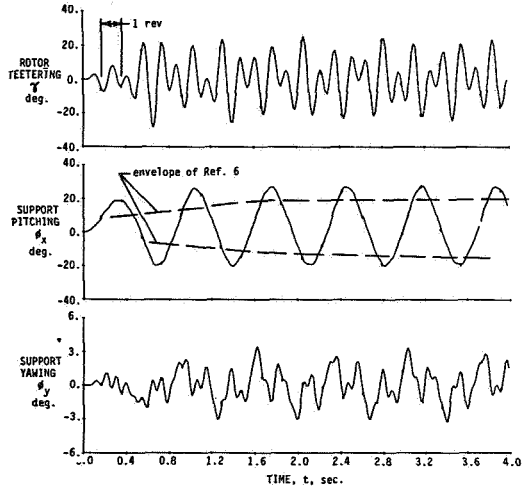

Figure 4. - Response of Prop-Rotor in Whirl Flutter Mode.

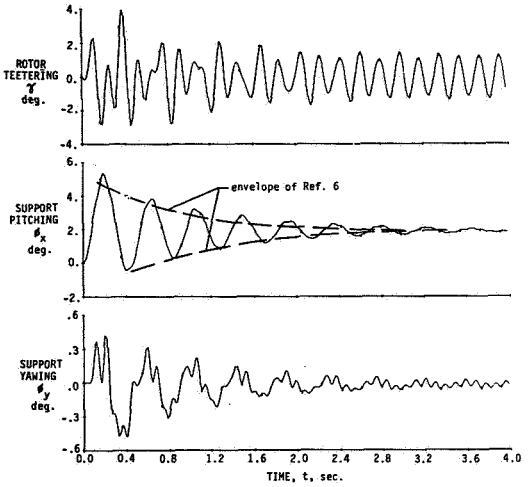

Figure 5. - Response of Prop-Rotor in Stable Mode.

The DOE/NASA Mod-2 HAWT was modeled to investigate the possibility of whirl flutter. The parameters for Mod-2 are presented in Table II. The response of the Mod-2 was calculated with the ASTER5 program. A baseline reference case of the Mod-2 parameters without structural damping was considered for an initial evaluation of its stability. The results of this case, given in Figure 6, show that the pitch, yaw,

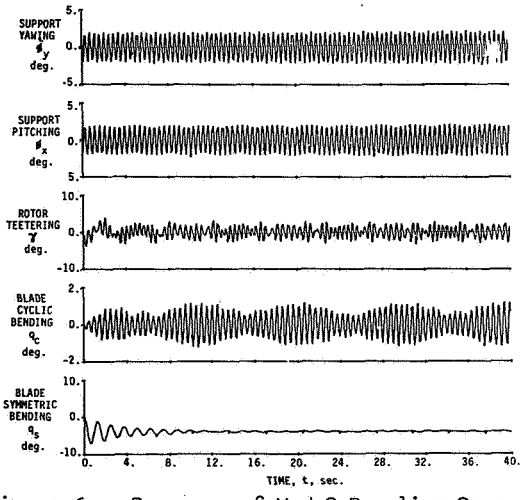

Figure 6. - Response of Mod-2 Baseline Case without Structural Damping.

teeter, and blade cyclic bending motions are neutrally stable. However, when a small amount of structural damping for the pitch and yaw motions is included, all motions are damped out as shown in Figure 7. Since damping exceeding this amount is expected in the actual system, it is concluded that the baseline Mod-2 is free from whirl flutter.

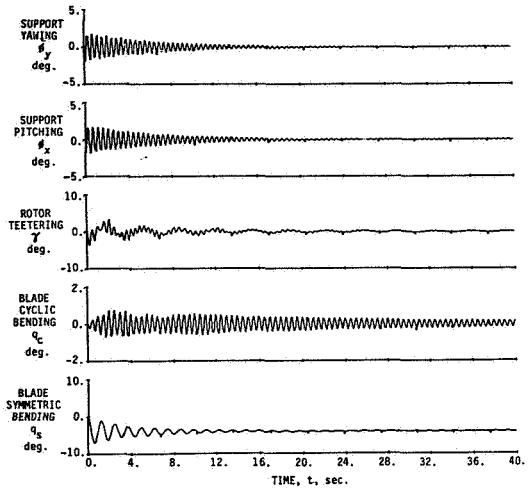

Figure 7. - Response of Mod-2 Baseline Case with Structural Damping ($\zeta_{\phi_x}=\zeta_{\phi_y}=.01$).

To study the effect of pitch-flap coupling on the response of the baseline Mod-2, several cases were calculated for values of δ_3 from -40^o to $+40^o$. The results indicate that only the blade cyclic bending motion as measured by q_c is affected by variations in δ_3. Figure 8 shows the change in maximum amplitude of q_c with δ_3. The results indicate that positive δ_3 has an adverse effect on blade cyclic bending motion.

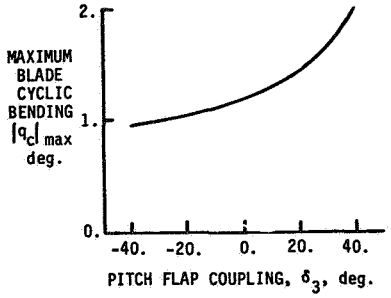

Figure 8. - Effect of Pitch-Flap Coupling, δ_3, on Blade Cyclic Out-of-Plane Bending Motion.

Other parametric studies were made to explore the possibility of whirl flutter over wide ranges of pylon spring stiffnesses, pylon dampings, rotor rotational speeds, and wind speeds. Some selected results of these studies are presented in Figures 9-12. The possibility of whirl flutter can exist for Mod-2 if the yaw or pitch stiffness of the pylon were substantially reduced. For example, Figure 9 shows the response of Mod-2 when the yaw stiffness is decreased to 6.6% of its baseline value while the other parameters remain the same. These results indicate whirl flutter by the unstable response of the yaw and teeter motions. When the pylon pitch stiffness is also reduced to 7.3% of its baseline value such that the pitch and yaw frequencies are equal ($\omega_{\phi_x}=\omega_{\phi_y}=3.665$ Hz), then the response of the pitch motion is also unstable as shown in Figure 10. The whirl motion of the pylon for this case is best illustrated by a cross-plot of the pitch and yaw motion in Figure 11. The figure shows that the system is in a forward whirl mode. From these results, it can be concluded that the stability of a HAWT is highly dependent on the rotor support stiffnesses.

As demonstrated earlier, the stability of a HAWT is sensitive to the presence of structural damping. To further illustrate this fact, a nominal amount of damping ($\zeta_{\phi_x}=\zeta_{\phi_y}=.04$) was added to the unstable case of Figures 10 and 11. The results, shown in Figure 12, indicate that a reasonable amount of structural damping has stabilized all motions of a previously unstable system.

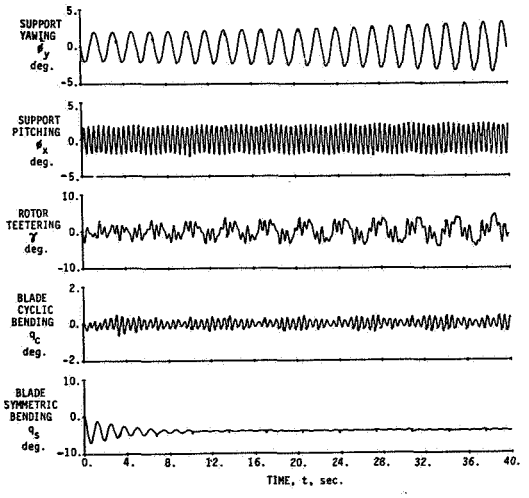

Figure 9. - Response of Mod-2 with Reduced Yaw Stiffness ($\omega_{\phi_y}=3.665$ Hz).

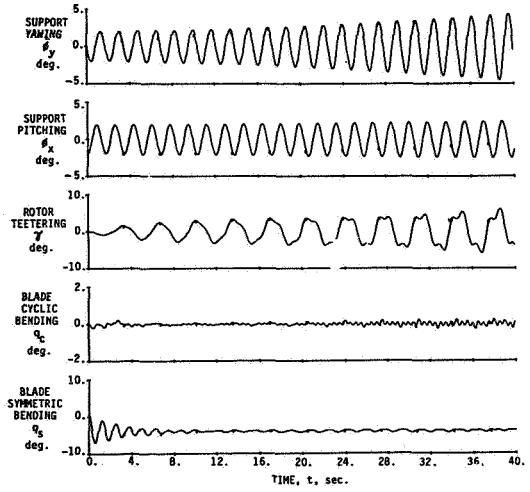

Figure 10. - Response of Mod-2 with Reduced Pitch and Yaw Stiffness ($\omega_{\phi_x}=\omega_{\phi_y}=3.665$ Hz).

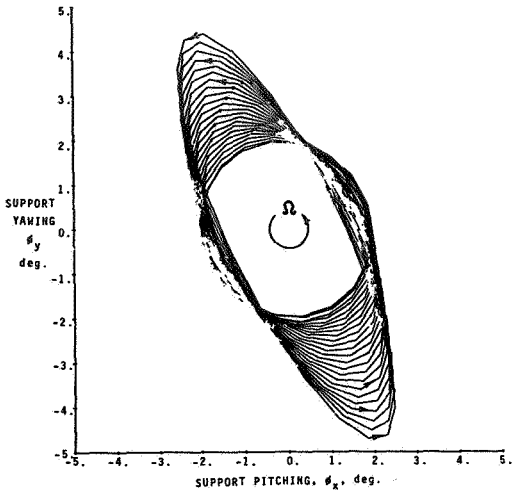

Figure 11. - Hub Motion of Mod-2 with Reduced Pitch and Yaw Stiffness ($\omega_{\phi_x}=\omega_{\phi_y}=3.665$ Hz) in Whirl Flutter Mode.

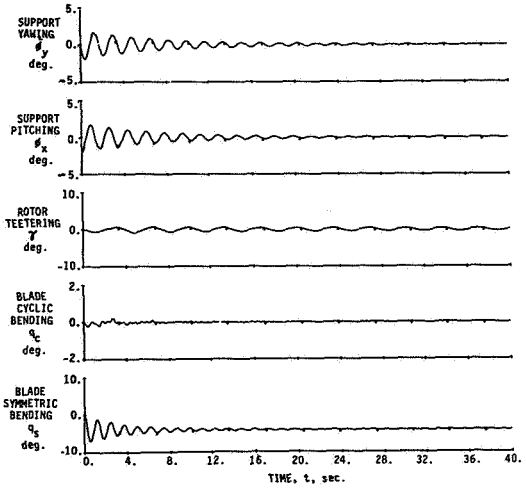

Figure 12. - Response of Mod-2 with Reduced Pitch and Yaw Stiffness ($\omega_{\phi_x}=\omega_{\phi_y}=3.665$ Hz) and Structural Damping ($\omega_{\phi_x}=\omega_{\phi_y}=.04$).

CONCLUSIONS

An investigation was conducted to explore the possibility of whirl flutter in a large HAWT. A five degree-of-freedom mathematical model and its associated computer program were developed and verified. The program was used to study the possibility of whirl flutter in the DOE/NASA Mod-2 wind turbine and the effect of parametric variations in pitch-flap coupling, rotor support stiffnesses, and structural damping on its response. Based on these limited studies, the following conclusions were obtained.

1. The ASTER5 program is capable of predicting whirl flutter for two-bladed teetering rotor systems.

2. The baseline design of the Mod-2 HAWT is free of whirl flutter.

3. Positive δ_3 has an adverse effect on cyclic blade out-of-plane bending motions for the Mod-2 design, whereas negative δ_3 has little effect.

4. Reduction in rotor support stiffness or structural damping increases the possibility of whirl flutter.

REFERENCES

1. Anon., Mod-2 Wind Turbine System Concept and Preliminary Design Report - Volume II Detailed Report, DOE/NASA 0002-80/2, NASA CR-159609, July 1979.

2. Reed, W. H., Review of Propeller-Rotor Whirl Flutter, NASA TR R-264, July 1967.

3. Kaza, K. R. V., The Effect of Steady State Coning Angle and Damping on Whirl Flutter Stability, J. Aircraft, Vol. 10, November 1973, pp. 664-669.

4. Kvaternik, R. G., Studies in Tilt-Rotor VTOL Aircraft Aeroelasticity, Ph.D. dissertation, Case Western Reserve University, Cleveland, Ohio, June 1973.

5. Johnson, W., Dynamics of Tilting Proprotor Aircraft in Cruise Flight, NASA TN D-7677, May 1974.

6. Hall, W. Earl, Jr., Prop-Rotor Stability at High Advance Ratios, J. Am. Helicopter Society, Vol. 11, No. 2, April 1966, pp. 11-26.

7. Baker, K. E.; Smith, R.; and Toulson, K. W., Notes on Propeller Whirl Flutter, Canadian Aeronautics and Space Journal, Vol. 11, October 1965, pp. 305-313.

8. Gaffey, T. M., The Effect of Positive Pitch-Flap Coupling (Negative δ_3) on Rotor Blade Motion Stability and Flapping, paper no. 227, Am. Helicopter Society, 24th Annual National Forum Proceedings, Sheraton Park Hotel, Washington, D.C., May 8-10, 1968.

9. Hoffman, J. A., Coupled Dynamic Analysis of Wind Energy Systems, NASA CR-135152, February 1977.

10. Kaza, K. R. V; and Janetzke, D. C., MOSTAS Computer Code Evaluation for Dynamic Analysis of Two-Bladed Wind Turbines, AIAA J. Energy, Vol. 4, No. 4, July-August 1980, pp. 162-169.

NOMENCLATURE

c	blade chord length
C_b, C_w, C_{ϕ_x}, C_{ϕ_y}	damping coefficients of rotor teetering, blade out-of-plane bending, pylon pitch and yaw motions, respectively
D	profile drag per unit length of blade element

h	pylon length
H	total rotor shear force, Eq. (A20)
H_1, H_2	rotor shear force per unit length of blade 1 and 2, respectively
I_b	mass moment of inertia of the blade defined in Eq. (A9)
I_{p_x}, I_{p_y}	mass moments of inertia of the pylon about the X and Y axes
K_b	half of the teeter spring stiffness
K_c, K_w	effective blade spring stiffnesses defined in Eq. (A11)
K_{ϕ_x}, K_{ϕ_y}	pylon spring stiffnesses
L	circulatory lift per unit length of blade element
M_b, M_{b_2}	mass properties of the blade defined in Eq. (A9)
q_c, q_s	cyclic and symmetric coordinates for blade out-of-plane bending motions defined in Eq. (A9)
q_{w_1}, q_{w_2}	generalized coordinates for out-of-plane bending motions of blades 1 and 2
r	radial distance along blade elastic axis
R	radial length of blade
S_{b_1}	mass property of blade defined in Eq. (A9)
t	time
T	total rotor thrust force, Eq. (A20) also kinetic energy
T_1, T_2	rotor thrust force per unit length of blade 1 and 2
U	resultant aerodynamic velocity, also potential energy
U_P, U_T	components of U, Figure 3
v	induced velocity
V	wind velocity
w_1, w_2	out-of-plane bending deflections of blade 1 and 2
x_b, y_b, z_b	blade coordinate system
X, Y, Z	inertial coordinate system
X_3, Y_3, Z_3	hub coordinate system
X_4, Y_4, Z_4	rotor coordinate system
α	blade angle of attack
γ	rotor teeter deflection angle
δ_3	pitch-flap coupling angle Eq. (A22)
ζ_b, ζ_w, ζ_{ϕ_x}, ζ_{ϕ_y}	critical damping ratios, Eq. (A13)
θ, θ_t, θ_0 θ_{1C}, θ_{1S}	blade pitch, twist, collective pitch, and cyclic pitch angles
ρ	air density
ϕ	aerodynamic inflow angle
ϕ_x, ϕ_y	pylon rotational deflections
Φ	normalized blade mode shape
ψ	rotor position angle
ω_b	blade natural frequency
ω_w	blade out-of-plane bending frequency
ω_{ϕ_x}	pylon frequency ($=\sqrt{K_{\phi_x}/I_{\phi_x}}$)
ω_{ϕ_y}	pylon frequency ($=\sqrt{K_{\phi_y}/I_{\phi_y}}$)
Ω	rotor rotational speed
$(\dot{})$	time derivative
$\{\ \}$	column matrix
$[\ ]$	square matrix

TABLE I. PARAMETERS FOR PROP-ROTOR OF REF. 6

Air velocity, V	77.1 m/s
Rotor	
Radial length, R	3.505 m
Rotational speed,	320 RPM
Pitch-flap coupling, δ_3	20^0
Teeter spring stiffness, $2K_b$	0
Teeter motion damping, $2\zeta_b$	0
Blade	
Mass properties	
M_b	26.09 kg
M_{b_2}	16.96 kg-m^2
S_{b_1}	42.17 kg-m^2
I_b	118.9 kg-m^2
Stiffness, (K_c+K_w)	$.3821\times10^6$ N-m/rad
Damping, ζ_w	0
Airfoil	NACA 0015
Chord, c	.2794 m
Twist distribution, $\theta_t(r)$	
$0 < r/R \leq .45$	$.677-1.217r/R$ rad
$45 < r/R \leq 1.0$	$.419(.75-r/R)$ rad
Collective pitch, θ_0	.74 rad
Pylon Properties	
Inertias, $I_{p_x} = I_{p_y}$	21.60 kg-m^2
Stiffness,	
$K_{\phi x}$	29.71×10^3 N-m/rad
$K_{\phi y}$	140.3×10^3 N-m/rad
Damping, $\zeta_{\phi_x} = \zeta_{\phi_y}$	.04
Length, h	1.143 m

TABLE II. PARAMETERS FOR DOE/NASA MOD-2 HAWT

Wind velocity, V	12.2	m/s
Rotor		
Radial length, R	45.81	m
Rotatinal speed,	17.5	RPM
Pitch-flap coupling, δ_3	0	
Teeter spring stiffness, $2K_b$	0	
Teeter motion damping, $2\zeta_b$	0	
Blade		
Mass properties		
M_b	26021.	kg
M_{b_2}	$.9125\times10^6$	kg-m^2
S_{b_1}	3.368×10^6	kg-m^2
Stiffness, (K_c+K_w)	78.82×10^6	N-m/rad
Damping, ζ_w	0	
Airfoil	NACA 23018	
Chord distribution, c(r)		
$.1542 \le r/R \le .3455$	3.319-8.429(.3455-r/R)	m
$.3455 < r/R \le 1.0$	1.436+2.877(1-r/R)	m
Twist distribution, $\theta_t(r)$		
$.1542 \le r/R \le .27$	.03459-.155(.27-r/R)	rad
$.27 < r/R \le 1.0$	-.0698 + .143(1-r/R)	rad
Collective pitch, θ_b		
$.1542 \le r/R < .7006$	0	
$.7006 \le r/R \le 1.0$	-.05236	rad
Pylon		
Inertia,		
I_{p_x}	6.115×10^6	N-m^2
I_{p_y}	$.6210\times10^6$	N-m^2
Stiffness,		
K_{ϕ_x}	6.183×10^9	N-m/rad
K_{ϕ_y}	3.140×10^9	N-m/rad
Damping,		
ζ_{ϕ_x}	0	
ζ_{ϕ_y}	0	
Length, h	7.3152	m

APPENDIX

Derivation of Equation of Motion

The mathematical model of a horizontal axis wind turbine is shown in Figure 2. The degrees of freedom and the required coordinate systems are described in the main body of this paper. The equations of motion, herein, have been derived by using the Lagrangian approach. This formulation requires expressions for the position vectors of arbitrary points on the pylon and the blades. These expressions are obtained with the aid of a series of rotations. The order of the rotations, illustrated in Figure 2, is ϕ_x, ϕ_y, ψ, and γ. The position vector of a point on the pylon axis is

$$\bar{r}_p = [T_{\phi_x}][T_{\phi_y}]\begin{Bmatrix}0\\0\\s_p\end{Bmatrix} \tag{A1}$$

and that of the hub-pylon axis junction point is

$$\bar{r}_{ph} = [T_{\phi_x}][T_{\phi_y}]\begin{Bmatrix}0\\0\\h\end{Bmatrix} \tag{A2}$$

where

$$[T_{\phi_x}] = \begin{bmatrix}1 & 0 & 0\\ 0 & \cos\phi_x & -\sin\phi_x\\ 0 & \sin\phi_x & \cos\phi_x\end{bmatrix}$$

$$[T_{\phi_y}] = \begin{bmatrix}\cos\phi_y & 0 & \sin\phi_y\\ 0 & 1 & 0\\ -\sin\phi_y & 0 & \cos\phi_y\end{bmatrix} \tag{A3}$$

The position vector of a point on blade 1 can be written in the $X_3Y_3Z_3$ axis system as

$$\bar{r}_3 = [T_\psi][T_\gamma]\begin{Bmatrix}0\\r\\w_1(r,t)\end{Bmatrix} \tag{A4}$$

where

$$[T_\psi] = \begin{bmatrix}\cos\psi & -\sin\psi & 0\\ \sin\psi & \cos\psi & 0\\ 0 & 0 & 1\end{bmatrix}$$

$$[T_\gamma] = \begin{bmatrix}1 & 0 & 0\\ 0 & \cos\gamma & -\sin\gamma\\ 0 & \sin\gamma & \cos\gamma\end{bmatrix} \tag{A5}$$

Combining Equations (A2) and (A4), the position vector of a point on the axis of blade 1 expressed in the XYZ axis system is

$$\bar{r} = [T_{\phi_x}][T_{\phi_y}]\left[\begin{Bmatrix}0\\0\\h\end{Bmatrix} + [T_\psi][T_\gamma]\begin{Bmatrix}0\\r\\w_1(r,t)\end{Bmatrix}\right] \tag{A6}$$

where $w_1(r,t)$ is represented by a single elastic blade mode and is

$$w_1(r,t) = \Phi(r)q_{w_1}(t) \tag{A7}$$

The position vector of a point on the axis of blade 2 is obtained from Equations (A6) by replacing w_1, γ, and ψ by w_2, $-\gamma$, and $\psi+\P$ respectively.

The total kinetic energy of the pylon and the rotor is formed from the position vectors given by Equations (A1) and (A6) and is given by

$$
\begin{aligned}
T = \frac{1}{2}\Big\{ & \left[I_{\phi_x} + I_b(1 - \cos 2\psi)\right]\dot{\phi}_x^2 \\
& + \left[I_{\phi_y} + I_b(1 - \cos 2\psi)\right]\dot{\phi}_y^2 \\
& + \left[-4S_{b_1}\gamma q_c - 2I_b\gamma^2 + 2I_b\right]\Omega^2 \\
& + 2I_b\dot{\gamma}^2 + 2M_{b_2}\left(\dot{q}_s^2 + \dot{q}_c^2\right) + 2\dot{\phi}_x\dot{\phi}_y I_b \sin 2\psi \\
& + 4\dot{\phi}_x\Omega\left[S_{b_1} q_c \sin\psi + I_b\gamma \sin\psi\right] \\
& + 4\dot{\phi}_x\dot{\gamma} I_b \cos\psi + 4\dot{\phi}_x\dot{q}_c S_{b_1}\cos\psi \\
& - 4\dot{\phi}_y\Omega\left[I_b\phi_x + S_{b_1} q_c \cos\psi + I_b\gamma\cos\psi\right] \\
& + 4\dot{\phi}_y\dot{\gamma}\, I_b \sin\psi + 4\dot{\phi}_y S_{b_1}\dot{q}_c \sin\psi \\
& + 4S_{b_1}\dot{\gamma}\dot{q}_c\Big\}
\end{aligned}
\tag{A8}
$$

where

$$
\begin{aligned}
I_{\phi_x} &= I_{p_x} + 2M_b h^2 \\
I_{\phi_y} &= I_{p_y} + 2M_b h^2 \\
M_b &= \int_0^R m_b\, dr \\
I_b &= \int_0^R m_b r^2\, dr \\
S_{b_1} &= \int_0^R m_b \Phi\, r\, dr \\
M_{b_2} &= \int_0^R m_b \Phi^2\, dr \\
q_s &= (q_{w_1} + q_{w_2})/2 \\
q_c &= (q_{w_1} - q_{w_2})/2
\end{aligned}
\tag{A9}
$$

The quantities I_{p_x} and I_{p_y} are the pylon inertias about the X and Y axes, respectively.

The potential energy of the pylon and the rotor can be written as

$$
\begin{aligned}
U = \frac{1}{2}\Big[& K_{\phi_x}\phi_x^2 + K_{\phi_y}\phi_y^2 + 2K_b\gamma^2 \\
& + 2(K_w + K_c)(q_s^2 + q_c^2)\Big]
\end{aligned}
\tag{A10}
$$

where

$$
\begin{aligned}
K_w &= \int_0^R EI_{y_b y_b}\Phi''^2(r)\,dr \\
K_c &= \int_0^R T_c\Phi'^2(r)\,dr \\
T_c &= \int_r^R m_b\Omega^2 r\, dr
\end{aligned}
\tag{A11}
$$

The dissipation potential for the pylon and the rotor can be written as

$$
\begin{aligned}
U_D = \frac{1}{2}\Big[& C_{\phi_x}\dot{\phi}_x^2 + C_{\phi_y}\dot{\phi}_y^2 + 2C_b\dot{\gamma}^2 \\
& + 2C_w\left(\dot{q}_c^2 + \dot{q}_s^2\right)\Big]
\end{aligned}
\tag{A12}
$$

where

$$
\begin{aligned}
C_{\phi_x} &= 2\zeta_{\phi_x} I_{\phi_x}\omega_{\phi_x} \\
C_{\phi_y} &= 2\zeta_{\phi_y} I_{\phi_y}\omega_{\phi_y} \\
C_b &= 2\zeta_b I_b \omega_\gamma \\
C_w &= 2\zeta_w M_{b_2}\omega_b
\end{aligned}
\tag{A13}
$$

By substituting Equations (A8), (A10), and (A12) into Lagrangian equations of the form

$$
\frac{d}{dt}\left(\frac{\partial T}{\partial \dot{q}_i}\right) - \frac{\partial T}{\partial q_i} + \frac{\partial U}{\partial q_i} + \frac{\partial U_D}{\partial q_i} = Q_i \tag{A14}
$$

the following equations of motion for the wind turbine model are obtained

$$
[I]\{\ddot{q}\} + [C]\{\dot{q}\} + [K]\{q\} = \{Q\} \tag{A15}
$$

where

$$
\{q\} = \begin{Bmatrix} q_s \\ q_c \\ \gamma \\ \phi_x \\ \phi_y \end{Bmatrix}
\qquad
\{Q\} = \begin{Bmatrix} Q_{w1} + Q_{w2} \\ Q_{w1} - Q_{w2} \\ M_\gamma \\ M\phi_x \\ M\phi_y \end{Bmatrix}
$$

$$
[I] = \begin{bmatrix}
2M_{b_2} & 0 & 0 & 0 & 0 \\
0 & 2M_{b_2} & 2S_{b_1} & 2S_{b_1}\cos\psi & 2S_{b_1}\sin\psi \\
0 & 2S_{b_1} & 2I_b & 2I_b\cos\psi & 2I_b\sin\psi \\
0 & 2S_{b_1}\cos\psi & 2I_b\cos\psi & I_{\phi_x} + I_b(1 + \cos 2\psi) & I_b\sin 2\psi \\
0 & 2S_{b_1}\sin\psi & 2I_b\sin\psi & I_b\sin 2\psi & I_{\phi_y} + I_b(1 - \cos 2\psi)
\end{bmatrix}
\tag{A16}
$$

$$
[c] = \begin{bmatrix}
2C_w & 0 & 0 & 0 & 0 \\
0 & 2C_w & 0 & -4I_b\Omega\sin\psi & 4S_{b_1}\Omega\cos\psi \\
0 & 0 & 2C_b & -4I_b\Omega\sin\psi & 4I_b\Omega\cos\psi \\
0 & 0 & 0 & C_{\phi_x} - 2I_b\Omega\sin 2\psi & 2I_b\Omega(1 + \cos 2\psi) \\
0 & 0 & 0 & -2I_b\Omega(1 - \cos 2\psi) & C_{\phi_y} + 2I_b\Omega\sin 2\psi
\end{bmatrix}
$$

$$
[K] = \begin{bmatrix}
2(K_w + K_c) & 0 & 0 & 0 & 0 \\
0 & 2(K_w + K_c) & 2S_{b_1}\Omega^2 & 0 & 0 \\
0 & 2S_{b_1}\Omega^2 & 2K_b + 2I_b\Omega^2 & 0 & 0 \\
0 & 2S_{b_1}\Omega^2\cos\psi & 2I_b\Omega^2\cos\psi & K_{\phi_x} & 0 \\
0 & 2S_{b_1}\Omega^2\sin\psi & 2I_b\Omega^2\sin\psi & 0 & K_{\phi_y}
\end{bmatrix}
$$

The next step is to obtain expressions for Q_{w_1}, Q_{w_2}, M_γ, M_{ϕ_x}, and M_{ϕ_y}. The expressions are derived from the virtual work of the aerodynamic forces, which can be written as

$$\delta W_A = \sum_{n=1}^{2} \int_0^R (\bar{F}_A \cdot \delta\bar{r}) dr \tag{A17}$$

where $\bar{F}_A$ is the aerodynamic force vector per unit length. The components of $\bar{F}_A$ are illustrated in Figure 3 from which one can write

$$\{F_A\}_{\text{blade 1}} = \begin{Bmatrix} H_1 \\ 0 \\ T_1 \end{Bmatrix} \tag{A18}$$

By using a similar expression for blade 2, substituting it with Equations (A6) and (A18) into Equation (A17), and neglecting several higher order terms believed to be unimportant, one obtains

$$\begin{aligned} Q_{w_1} &= \int_0^R T_1 \Phi \, dr \\ Q_{w_2} &= \int_0^R T_2 \Phi \, dr \\ M_\gamma &= \int_0^R (T_1 - T_2) r \, dr \\ M_{\phi_x} &= -Hh \sin\psi + Th\gamma \cos\psi + M_\gamma \cos\psi \\ M_{\phi_y} &= Hh \cos\psi + Th\gamma \sin\psi + M_\gamma \sin\psi \end{aligned} \tag{A19}$$

where

$$\begin{aligned} H &= \int_0^R (H_1 - H_2) dr \\ T &= \int_0^R (T_1 + T_2) dr \end{aligned} \tag{A20}$$

The expressions for circulatory lift and profile drag per unit length can be written as

$$\begin{aligned} L &= \tfrac{1}{2} \rho U^2 c C_L(\alpha) \\ D &= \tfrac{1}{2} \rho U^2 c C_D(\alpha) \end{aligned} \tag{A21}$$

where, from Figure 3 and Equation (A6), the following expressions are obtained

$$\begin{aligned} U &= \sqrt{U_P^2 + U_T^2} \\ U_P &= V \cos\phi_x \cos\phi_y \cos\gamma + r\dot{\phi}_x \cos\psi \\ &\quad + r\dot{\phi}_y \sin\psi + r\dot{\gamma} + \dot{q}_{w_1}\phi + v \\ U_T &= V \cos\phi_x \sin\phi_y \cos\psi - V \sin\phi_x \sin\psi \\ &\quad + h\dot{\phi}_x \sin\psi - h\dot{\phi}_y \cos\psi + r\Omega \cos\gamma \\ \alpha &= \phi - \theta \\ \phi &= \tan^{-1}\left(\frac{U_P}{U_T}\right) \\ \theta &= \theta_0 + \theta_t(r) - \gamma \tan\delta_3 \\ &\quad + \theta_{1c} \cos\psi + \theta_{1s} \sin\psi \end{aligned} \tag{A22}$$

In the derivation of above expressions for U_P and U_T, several higher order terms, believed to be unimportant, are neglected. Also, circulatory lift, produced by the angular velocity of the local blade section about the y_b-axis due to blade out-of-plane bending and rotor teetering, is neglected in the expression of Equation (A21). The values of C_L and C_D are nonlinear functions of x and are calculated from airfoil data.

By resolving L and D in Figure 3, the expressions for T_1 and H_1 are

$$\begin{aligned} T_1 &= -L \cos\phi - D \sin\phi \\ H_1 &= -L \sin\phi + D \cos\phi \end{aligned} \tag{A23}$$

The expressions for T_2 and H_2 are the same but the values of L, D, and are obtained by replacing γ, ψ, and q_{w_1} by $-\gamma$, $\psi+\pi$, and q_{w_2}, respectively in the expressions of Equation (A22).

The induced velocity v in Equation (A22) is based on classical momentum theory and is

$$v = \frac{-V + \sqrt{V^2 + 2T/\rho\pi R^2}}{2} \tag{A24}$$

QUESTIONS AND ANSWERS

D.C. Janetzke

From: A. Wright

Q: What type of failures would result from severe whirl flutter?

A: *Fatigue failure or ultimate limit load failure.*

From: Bill Wentz

Q: How do you increase structural damping in design?

A: *I don't know.*

From: J.A. Kentfield

Q: What magnitude of structural damping can be expected in the pylon of MOD-2 or similar machines?

A: *The damping applied to the pylon in the model represents the equivalent damping of the entire rotor support system which includes the pod and the tower. The Mod-2 welded tower damping is about 2% of critical damping.*

From: Mr. Doman

Q: What influence has the absence of tower bending modes on results?

A: *The tower bending modes are represented by the pylon support stiffness.*

From: P. Anderson

Q: What time step size was used in the integration process? Have any sensitivity tests been carried out to optimize step size?

A: 1. *An initial time step equal to 36 steps per rotor revolution was arbitrarily chosen. The integration process could change the step size within the initial size as needed for convergence.*

2. *Several other step sizes were used, but no attempt was made to optimize the size.*

WIND ENERGY SYSTEM TIME-DOMAIN (WEST) ANALYZERS

Mark E. Dreier and John A. Hoffman

PARAGON PACIFIC, INC.
1601 E. EL SEGUNDO BLVD.
EL SEGUNDO, CALIF. 90245
(213) 322-9111

ABSTRACT

Using the latest hybrid electronics technology, a portable analyzer which simulates in real time the complex nonlinear dynamics of horizontal axis wind energy systems has been constructed. Math models for an aeroelastic rotor featuring nonlinear aerodynamic and inertial terms have been implemented with high speed digital controllers and analog calculation; this rotor model is then combined with other math models of elastic supports, control systems, a power train and gimballed rotor kinematics. The analyzer also features a stroboscopic display system graphically depicting distributed blade loads, motion, and other aerodynamic functions on a cathode ray tube. The viewer sees a clear picture of rotor dynamics in the start-up, shut-down, and trim states, as well as operation in special transient conditions such as gust and emergency shutdown. Limited correlation efforts have shown good comparison between the results of this analyzer and other sophisticated digital simulations; the digital simulation results have been successfully correlated with test data.

INTRODUCTION

This paper describes the second generation Wind-Energy System Time-Domain (WEST) analyzer system developed by Paragon Pacific, Inc. under contract with the NASA-Lewis Research Center, Cleveland, Ohio.

WEST2 GENERAL DESCRIPTION

The WEST2 simulator is a complete coupled wind turbine dynamics analysis unit. The analyzer contains nonlinear dynamic math models for all components of a wind energy generator system, including the aeroelastic rotor, power train, tower, electrical machinery and control system elements. These models are executed in the time domain at speeds exceeding the capabilities of conventional digital computers by factors of 1000 or more, using the Special Purpose Hybrid Computer (SPHYC) technology developed by Paragon Pacific, Inc. Because of the high speed analysis capability of the SPHYC technology, the WEST2 simulator is able to perform critical analyses in real time; analyses that are totally impractical using other available methods.

The heart of the WEST2 simulator is the complex aeroelastic rotor analysis subsystem. Under contract with the U.S. Army Electronics Command (ECOM) Fort Monmouth, New Jersey, Paragon developed a Special Purpose Rotorcraft Simulator (SPURS). The most fundamental subsystem of SPURS, the rotor analysis, is used (with nominal extension for wind turbine analysis) in WEST2.

WEST2, including the aeroelastic rotor math models, is a special purpose analyzer containing both digital and analog components. Conventional strip theory is incorporated in the rotor analysis, including all nonlinear inertial and aerodynamic loading phenomena. The aerodynamic and inertial loads are integrated along the blade span at extremely high speeds, using an analog aerodynamics math model for a blade of infinitesimal radius.

The same loads package is switched from blade to blade by the digital controllers, and swept along the span of each blade to compute all loads which excite blade-mode and shaft motion. The high-speed capacity of the analog subsystems in WEST2 makes real time analysis practical.

WEST2 features a stroboscopic display system which enables convenient viewing of distributed loads and blade deflections during analyzer operation. When the rotor blade enters a narrow azimuthal sector defined by the WEST2 operator using the front panel controls, the distributed functions are "painted" on an oscilloscope for all blades in the rotor. the specific function presented is selectable using a front panel switch. The list of display radial functions includes in-plane and out-of-plane aerodynamic loading, flapping motion, angle of attack, lift coefficient, and drag coefficients due to stall.

In addition to the special-purpose portion of WEST2, a general purpose simulation unit (GPURS) is incorporated for modelling those components of the wind generator system which may vary from time to time, as the designs of wind energy devices evolve. Examples of such variable systems are the control and power management systems.

Applications for WEST Systems

Because of their unique power for fast nonlinear analysis, and because of their dedicated architecture, the WEST units are ideal for analysis where

- Large amounts of data (i.e., time histories of loads and motions under varying conditions) are required at low cost;
- Nonlinearities such as blade stall and mechanical hysteresis are significant to the analysis results;

- Stochastic processes are involved (e.g., predicting fatigue lives of critical components in a statistically varying environment);
- Real-time operation is required (e.g., operator training in failure modes);
- High speed operation is required so the WEST can be used in conjunction with complex simulations of electrical power network dynamics;
- A coupled simulation is performed involving many wind turbines operating in concert with one power network.

In these and many other areas, the WEST concept is technically superior and much lower in cost than the alternative methods associated largely with general-purpose digital computer simulation.

THE NEED FOR AND CAPABILITES OF A WEST2 ANALYZER

A wind energy generator is a very complex dynamic system, representing an assemblage of individual elements, each with its own special dynamic characteristics. When the system is operating, the dynamics of all the components of the system couple together: all elements of the system move at the same time, and the overall symphony of these motions determines the performance, safety and longevity of the complete wind generator unit. The following coupled dynamic phenomena, for example , represent critical aspects of wind generator performance:

- Dynamic loads in the various structural components of the system, which determine fatigue life, and therefore substantially impact on overall operational cycle costs;
- Overall system stability - the property that prevents certain motions from growing without bound and leading to the ultimate destruction of machine components;
- System control, wherein the rotor and power machinery are properly controlled for fruitful average yields of electrical power, with acceptable quality for use in existing utility networks.

The wind generator is a tuned dynamic system that must be operated in all kinds of weather. The system component loads, stability properties, and control quality and effectiveness will need to be evaluated not only in conditions with steady benign winds, but also in the random environments that characterize those periods when wind speeds and, hence, energy content are highest.

The WEST2 analyzer simulates the complete nonlinear dynamic characteristics of a wind energy system at speeds which make realistic environmental analysis practical. Because it represents a complete nonlinear simulation of the wind generator system, the WEST unit is able to perform virtually any of the standard analyses currently used in wind turbine development. Such analyses address performance, blade loads, control system stability, response characteristics, etc. Because of its unique high-speed capabilities, however, WEST2 is also able to perform examinations of wind generator operations that are not generally considered practical for standard analyses. A few examples of such unique capabilities are:

- Design Parametric Synthesis, wherein key design parameters in the wind generator system are input from front-panel or adjustable internal controls. Parameters such as blade chord, rotor tip speed, blade modal frequencies, power train critical stiffness, and control system gains are examples of such adjustable system properties. Time-history plots of dynamic blade and power train loads, vibrations, electrical signal purity, and control system response are examples of outputs that are revealed instantly by the operating WEST analyzer.
- Statistical Analyses, performed using internal random environment generators in the WEST2 unit. Wind speed and directional random properties are synthesized by filtering white noise. The key properties associated with the filter spectra, amplitude and bandwidth are adjusted from the front panel. Time-history responses are instantaneous outputs from the WEST simulator. Additionally, panel meters reveal general operating parameters such as shaft torque, power output, rotor speed, and rotor thrust.
- Real Time Control System Synthesis can be performed using the WEST2 analyzer/synthesizer system. Control laws synthesized using the WEST2 analysis could be switched over for direct control of research wind energy systems. This capability will enhance the safety of wind energy research programs, since control system stability and performance can be evaluated with a high-fidelity system math model before a set of control laws is used in a real system.
- On-Site Confirmation of Analytic Models can be performed using the real-time capability of the WEST analyzer. The WEST system can be operated during wind turbine test activities for immediate comparison of test and analytic results. Indeed, instrumentation data (e.g., wind speed and direction vs time) taken at the site during test operations can be input directly to the WEST2 unit, and response comparisons then can be made. Adjustments to WEST2 math models can be made to achieve correlation with the results being recorded from the test.

TECHNICAL DESCRIPTION OF THE WEST2 ANALYZER

Figure 1 is an overall block diagram of a WEST2 system. For convenience, in describing the complete

system, two separate sections have been defined; the nonrotor system (NRS) and the aeroelastic rotor system. Because of the relative complexity of the rotor compared to other components of wind energy systems, Figure 2 has been provided as a more detailed block diagram of the rotor component.

The technical descriptions which follow address the math models incorporated in the NRS and rotor, the electronic methods used for solving the math models, and the hardware architecture of the WEST2 units. Methods for programming the simulators for specific wind turbine units, and calibration, testing and maintaining the analyzers, are also described.

The Nonrotor System (NRS)

Part of the NRS occupies the top tray or drawer of the special purpose section of WEST2. Other NRS models are programmed on the general purpose simulation (GPURS) subsystem of WEST2. Components of the NRS are described below:

Air Motion Models - The motion of the air in the vicinity of the rotor is affected by the wind direction and speed, windshear (windspeed change with altitude), aerodynamic interference of wind flow from the tower (shadow effect), and retardation of the wind by the rotor. Models for all of these phenomena are included in the NRS.

The nominal windspeed and direction with respect to the rotor are defined from front panel controls. Panel controls can also be adjusted to produce step or ramp gust functions for the wind. Speed, direction, and swirl (rigid-body motion about a vertical axis) can be distributed in this manner.

The variation of windspeed with altitude (windshear) is also adjustable from the panel - the variation is currently assumed to be a linear function of altitude.

The tower shadow phenomenon is modelled as a step change in windspeed when the blade is in an azimuthal sector behind (or in front of) the tower. Both the strength and the sector size of the shadow model are adjustable from the front panel.

Wind retardation by the rotor is modelled using the Glauert momentum model. Retardation, of course, is a function of rotor thrust, air density, and net windspeed at the rotor disk. Air density is adjustable from the panel to conveniently model the influence of altitude.

The WEST2 NRS tray also includes a random gust synthesizer. A pseudo-random white noise generator produces the basic random signal. Three low pass filters with adjustable gain and bandwidth filter this noise to model random changes in wind speed, direction, and swirl.

Power Train - In WEST2, a single degree of freedom power train model is incorporated in the GPURS system. The generator model in the power train produces a torque on the system proportional to the rotor speed or to the phase angle of the power train with respect to an electrical network phase angle. The power demand is input on a GPURS panel potentiometer, simulating a field current control.

Front panel galvanometers display the key power train variables: power ratio (ratio of produced power to wind turbine rated power), shaft torque and rotor speed.

Flexible Supports - WEST2 contains a single degree-of-freedom shaft support, implemented on GPURS. The WEST2 support allows the rotor hub to move laterally and to yaw as the tower and yaw-drive mechanism move under loads applied by the rotor. The natural frequency, damping, mass and geometrical characteristics of the flexible support model are adjustable. The model can be expanded to include additional degrees of freedom.

Control System - The control system determines the blade pitch angle. In WEST2, a two-mode control system is implemented on GPURS. The mode is determined by a GPURS front panel switch. The startup/shutdown mode causes blade feathering to be commanded by a blade-angle control potentiometer on the NRS tray panel. At moderate rotor speeds, or above, the mode can be switched to speed command, in which the control system, by suitably pitching the blades, strives to maintain a speed commanded by a front panel control. If too much power is demanded at a given windspeed, however, the controller fails to maintain the commanded speed, the rotor slows, and usually stops.

The nonrotor elements of the Wind Generator System use straightforward simulation techniques, and represent no particular deviation from usual procedures incorporated in hybrid analysis. The overall system arrangement enables "stand-alone" simulation capability, or integrated capability where WEST2 becomes part of a larger simulation test facility. In the stand-alone mode, WEST2 can be used for basic research, controls development, response qualities assessment, blade loads analysis, etc.

Aeroelastic Rotor Analysis

The aeroelastic rotor model in the WEST2 simulator is characterized by the simplified block diagram of Figure 2. The digital section is essentially an executive monitor and sequencer which controls the computational sequences of the analog sections. The high frequency analog section contains the nonlinear math models associated with a blade element of infinitesimal radius. This same model is used for all blades in the rotor. The low frequency section contains the equations for the blade elastic degrees of freedom and various coordinate transformations of loads and motion signals between the fixed and rotating frames of reference.

A full set of nonlinear equations comprises the math model for a blade infinitesimal radial element. Aerodynamic loads are calculated using an airfoil model valid over a full 360-degree angle of attack range; airfoil parameters in the model are fully adjustable to simulate use of different airfoil designs. Distributed inertial loads caused by gyroscopic effects, coriolis accelerations, etc., are also represented by a comprehensive set of nonlinear blade-element equations.

The shaft accelerations and velocities with respect to the inertial frame and the shaft velocity with respect to the local wind are inputs to the rotor models. A series of Eulerian transformations is then used to solve for the airspeed, angle-of-attack and inertial acceleration of the blade-element model, at a specified radial position.

The blade-element model produces the loads, which are then resolved to shaft axes to define the infinitesimal shaft force and moment contributions made by the element. The elemental loads are also multiplied by the blade eigenfunction or modeshape and integrated along the span, to define the generalized forcing function which excites aeroelastic motion.

The analog implementation of the aerodynamic and inertial models described above uses a "sweeping" process, whereby the radial position of the blade element is varied as a sawtooth function, and the distributed loading functions are integrated with respect to time to produce shaft and modal loads. (Hence, a substitution of variable is occuring in the models, where very short time intervals take the place of radius in the radial integrations of distributed loads.)

The digital sequencer first inputs the state variables and azimuth position of, for example, blade number i to the high frequency section, and then "sweeps" out the radius, using radial position as a sawtooth input function. As the sweep proceeds, integrands for the modal generalized forcing function and shaft loads are generated in the geometry section. These are simultaneously integrated by the radial integrator units. At the end of the sweep, the integrator outputs, which represent the generalized forcing functions and shaft loads for blade i, are transferred to sample/hold units. (The outputs of these units are summed for all blades to get the total shaft loads. They are also applied as forcing functions to the blade motion equations.) After the short duration required to set the sample/hold units, the digital section resets the radial integrators to zero, advances the multiplexors to treat blade number i + 1, and repeats the process.

As the sweeping process occurs, programmable radial function generators produce variable blade properties such as chord, modeshape, twist, and mass distribution; these properties are input to the blade-element aerodynamic and inertial math models.

Currently, the WEST2 simulator, uses a single degree-of-freedom modal representation for the rotor blade aeroelastic properties. The second-order equations in the blade mode generalized coordinates are implemented using standard analog techniques. These models respond to the generalized forcing function variables produced during the sweep integration. The resulting blade motion is then multiplexed back into the blade element models to include the influence of aeroelastic blade motions on the distributed aerodynamic and inertial loads.

Electronic System Architecture

Paragon Pacific, Inc. has developed an extensive library of printed circuit cards called computational module cards. Each card has a number of groups of electronic devices, each group performing a specific mathematical function. For example, the multiplier card has ten multipliers, each performing an independent analog multiplication. Analog, digital and hybrid functions are contained in the library. Analog functions include summers, integrators, sample/hold units, etc. Digital devices include gates, one-shots, flip/flops, Random access Memory (RAM) units, etc. Hybrid cards contain analog-to-digital (A/D) converters, digital-to-analog (DAC) converters, etc.

Two different techniques are used to combine these precision electonic computational modules into a full system such as WEST; special-purpose and general-purpose architecture are described below.

Special Purpose Systems

In special-purpose programming, the module cards are plugged into a standard card cage. Each card cage, or drawer, can receive 120 math module cards. The cards plug into an assembly called a "pin plane" which is horizontally situated near the bottom of the drawer. The pin plane receives the card edge connectors on its top side, and connects each card circuit to a gold-plated vertical pin emerging from the bottom of the plane.

Each pin plane contains 8,640 pins, whose positions are very precisely located within a matrix. The special purpose drawer is programmed to be a specific function, such as a WEST, by wiring these pins together, thereby connecting the math modules on the cards into the desired circuits. A process called "wire-wrapping" is used to do this. The small wires are stripped and wrapped very tightly on the pins to form the desired circuit. Up to 8,640 wires are placed in one pin plane.

The wire-wrapping is done by machine and is fully automated. Specialized computer programs are used to convert the sustem design information, produced originally in the form of diagrams, into a deck of punched data processing cards. The automatic wire-wrapping machine reads these cards and wires the entire tray without making an error. In essence, computers are now reproducing themselves.

The special purpose trays are inserted into a cabinet, where connectors on the rear panels engage a "gallery" installed at the rear of the cabinet. The gallery contains wiring that connects the drawers together and supplies them with power.

In WEST2, the top drawer is the NRS, the center tray is the rotor, and the bottom half-size drawer contains the power supply. The power supply drawer also contains the maintenance system called the Verification and Calibration Equipment (VACE), which is described later.

General Purpose System (GPURS)

The GPURS system uses the same computational module cards as those used in the special purpose systems, except that they are inserted into the left front panel card cage. The card edge connectors are connected to the removable patch panel, where they can be conveniently wired into any system.

GPURS is a very flexible system, since both its wiring and its architecture are variable. Wiring is changed at the patch panel, and architecture is varied by plugging in different computational module cards.

GPURS accepts 17 module cards, and contains its own power supply and front-panel functions (pots, switches, interface trunks). GPURS also has an internal card cage and rear panel trunking system for special interfacing functions.

GPURS can be configured as a pure digital system, pure analog system, or any combination of both because of its flexible architecture and because of the availability of the large array of module cards.

As mentioned previously, WEST2 incorporates a GPURS at this time. The WEST2 GPURS component currently includes models for the wind turbine flexible supports, power train and control systems, and a gimbal or teetering rotor support.

MOSTAB-HFAWM, described in general terms in Reference 1, has been validated with test data taken from the NASA/DOE Mod 0 experimental wind turbine located at Plum Brook Station, near Sandusky, Ohio. Results of MOSTAB correlation-efforts are documented in Reference 2.

Programability

Special Purpose Hybrid Computers can be programmed in two ways by selection of optional subsystems:

- Mechanical adjustment of trim potentiometers;
- Potentiometers and Random-Access Memory (RAM) units which are set automatically, by external user command.

The mechanical potentiometers provide the least expensive and most compact programming means, and, hence, this approach was selected for the WEST2 unit. When the user requires rapid programming capability, however, the digitally-controlled pot and RAM units can be installed, enabling fully automated programming from data stored on a floppy disk device.

A Digital Support System (DSS), using Paragon's Modular Stability Derivative Program (MOSTAB) as a key component, calculates all required programming data using standard MOSTAB input data. The DSS is run on a digital batch processor, and performs most WEST2 calculations which do not change with time during wind turbine simulation (e.g., mass integrals, initialization co-efficients, etc.). If the fully-automated programming capability is incorporated in lieu of the trim pots, the DSS creates the data on the floppy disk, with no user intervention required.

Self-Testing: The Automatic SPHYC Test and Calibration (ASTAC) System

The ASTAC system has been procured with the WEST unit. ASTAC is a fully automated test system. A micro-based controller and interface unit open and close electronic switches within the WEST circuits by command from data contained on a "floppy disk" storage device. Test signals are substituted into the open circuits, and resulting subsystem performance is measured. The measured performance is compared to theoretically-correct performance indices also contained on the floppy disk. Incorrect operation is flagged by ASTAC and printed, giving the WEST2 maintenance technician complete informaton required to repair the fault and confirm normal operation.

WEST2 Maintainance: Verification And Calibration Equipment (VACE)

Unlike most printed circuit cards incorporated in computers, the computational module cards do not contain the actual algorithms associated with system operations. These are contained in the pin planes and on the GPURS patch panel. Consequently, all inputs and all outputs from each computational element on each card leave the card through the card edge connector.

This unique characteristic permits the module cards to be externally maintainable, because each function can be externally tested for proper performance and calibration.

The VACE unit performs the function of connecting the modules on the computational cards into specialty circuits, for purposes of rapid performance verification, fault detection, and calibration.

The card to be tested is plugged into a card-edge connector on the VACE front panel. Two plug-in units, also inserted into the front panel, program the VACE to deal with the specific module card under test. A series of procedures is then executed using VACE panel switches, and prescribed measurements are made using standard test instruments (for example, a digital voltmeter and oscilloscope). The procedures for testing and calibrating each card are detailed in a comprehensive VACE manual. They are arranged so that personnel who have no electronics training can execute the tests, verify acceptable performance, identify specific components on the card that have failed, and fully calibrate each module on the card, if required.

The VACE unit is also used, in calibration mode, to program the cards for a specific system; i.e., for a specific wind energy system design in WEST2.

Validation of the WEST2 Analyzer

The primary approach taken to validate WEST2, during this initial development effort, involved the extensive use of the ASTAC system, described in the previous section. This validation effort

essentially involved an electronic system verification, which proved that each WEST electronic subsystem does indeed execute the intended equations. ASTAC reads the program equations in FORTRAN form, executes these on a general purpose digital computer to produce the theoretically correct calculation, and then compares the WEST2 subsystem performance to the theoretically correct results. In this manner, each WEST2 subsystem is summarily checked.

As a final verification, a dynamic check of WEST2 performance was made by comparing blade-load time histories produced by WEST2 to those produced by the MOSTAB-HFAWM digital analysis. The very good comparison is presented as Figure 3.

Additional Documentation

More details of the WEST2 system is presented in Reference 3. References 4 and 5 contain the full description of all equations and programming techniques incorporated in the system.

CONCLUSIONS

The fundamental conclusions of the WEST simulator work to date is that the Special Purpose Hybrid technology can solve the complex nonlinear equations associated with wind energy systems in real time. Additionally, such implementations solve these equations with sufficient accuracy to compare well with proven alternative analysis methods.

The WEST analyzer concept enables thorough examinations of wind energy systems, including statistical analysis in nonlinear operating regions and transient functions of special interest. Such studies are totally impractical using the slower and more costly digital simulation methods.

REFERENCES

1. Hoffman, John A. : Coupled Dynamics Analysis of Wind Energy Systems. NASA CR 135152, February, 1977

2. Spera, David A. : Comparison of Computer Codes for Calculating Dynamic Loads in Wind Turbines. NASA TM-73773, DOE/NASA/1028-78/16, September, 1977.

3. Hoffman, John A.: Development Report: Wind Energy System Time-Domain (WEST) Analyzers Using Hybrid Simulation Techniques. NASA CR 159737, Oct., 1979.

4. Hoffman, John A., and Thoren, Robert J.: Mathematical Models and Hybrid Program for the Wind Energy System Time-Domain (WEST) Simulator Baseline West Unit. PPI-1030-1, January, 1978.

5. Hoffman, John A.: Math Modelling and System Design Report Conversion of the Wind Energy System Time-Domain Simulator Unit 1 (WEST1) System Design to the WEST2 Design. PPI-1030-4, July 1979.

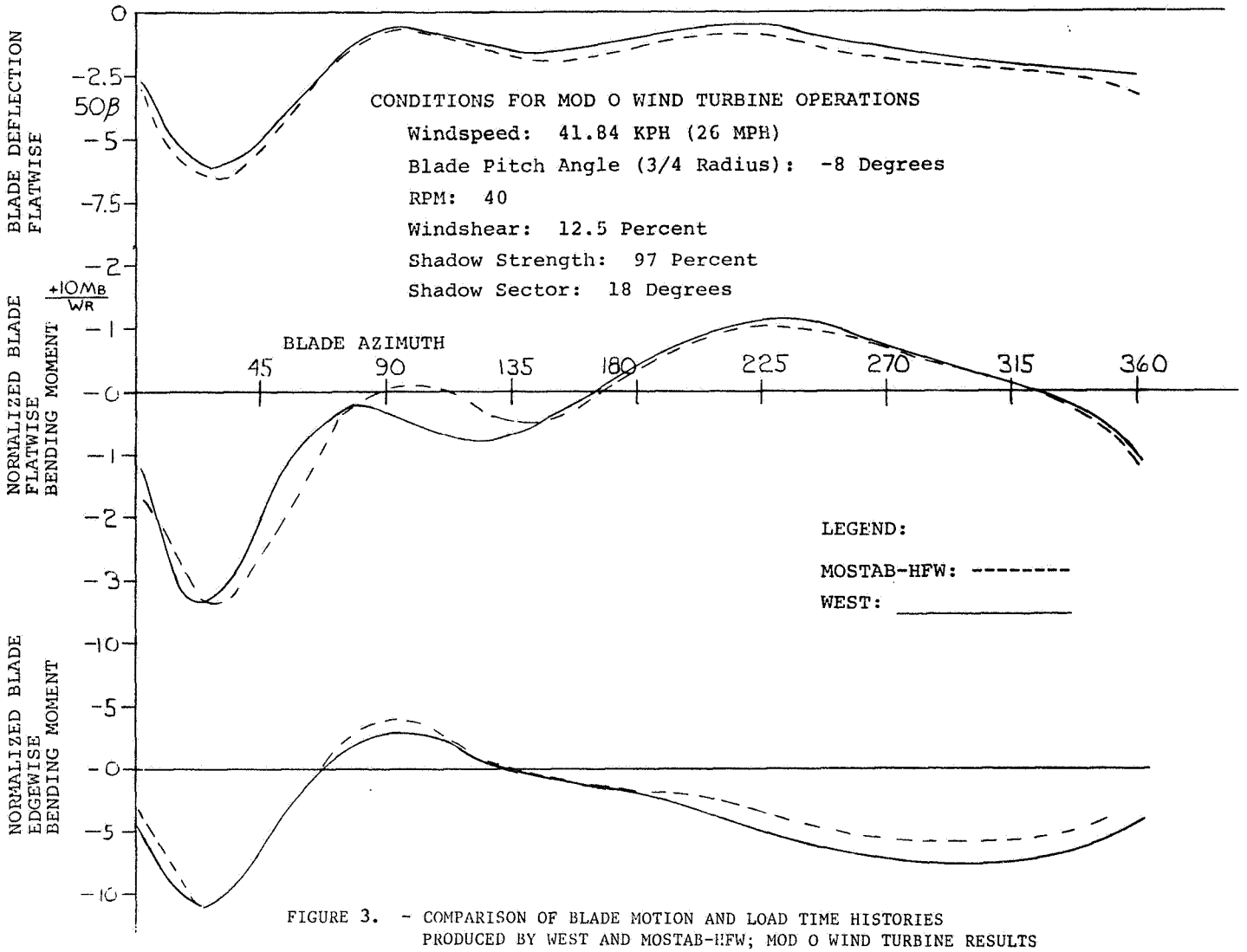

FIGURE 3. - COMPARISON OF BLADE MOTION AND LOAD TIME HISTORIES PRODUCED BY WEST AND MOSTAB-HFW; MOD O WIND TURBINE RESULTS

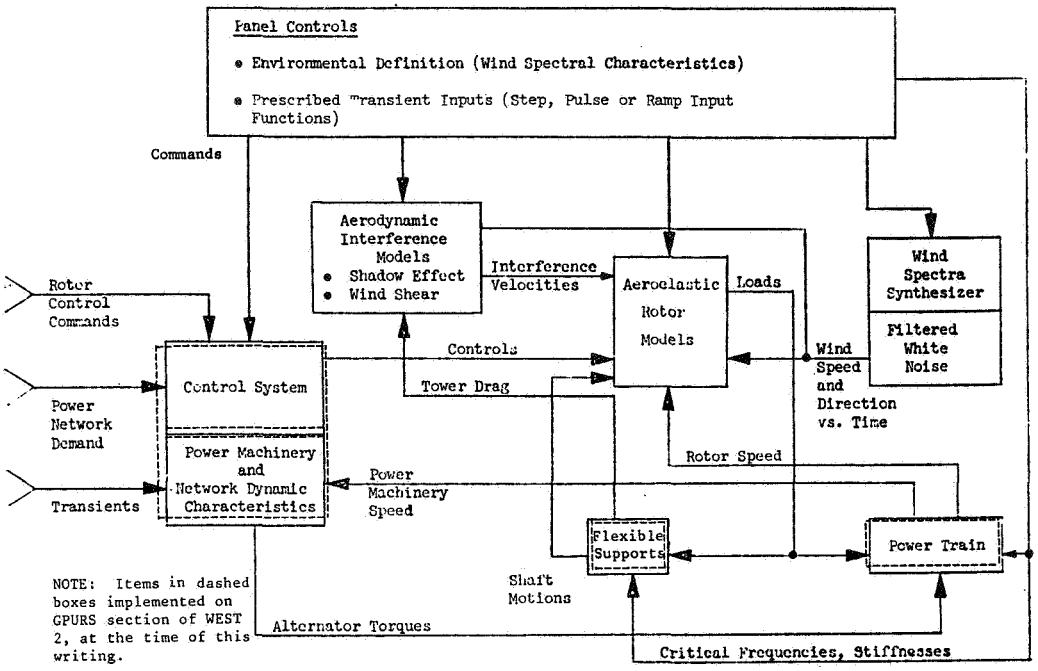

FIGURE 1. - WEST ANALYZER OVERALL SYSTEM DIAGRAM

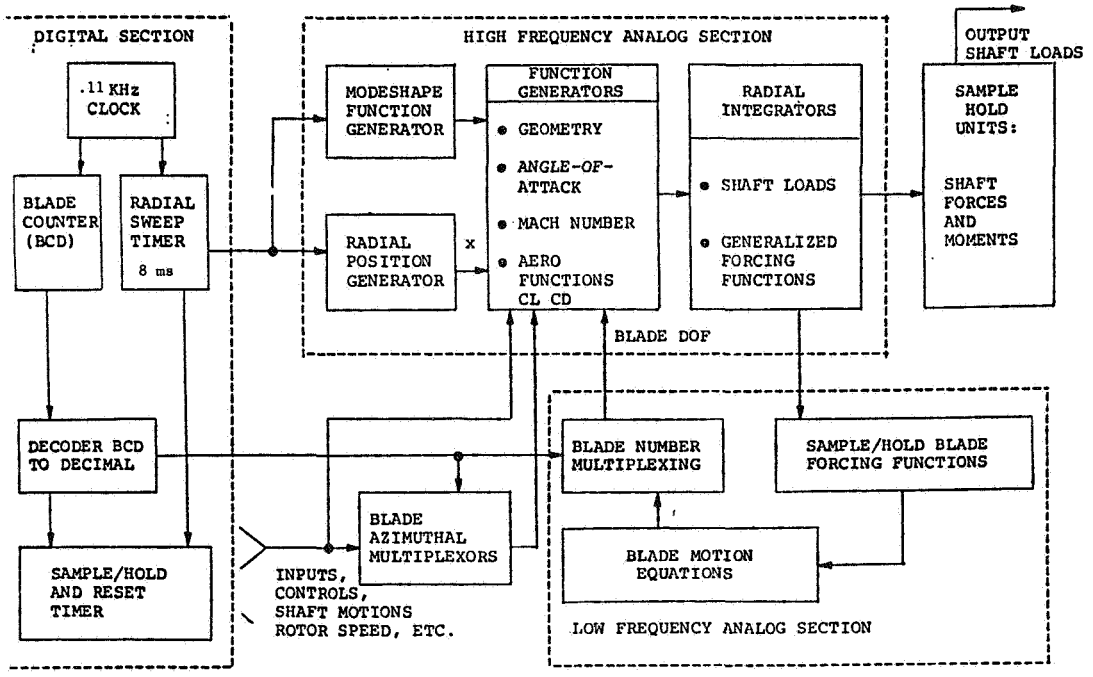

FIGURE 2. - WEST AEROELASTIC ROTOR MATH MODELS

QUESTIONS AND ANSWERS

J.A. Hoffman

From: W.E. Holley

Q: Suggest adding additional gust inputs to account for turbulence variations across rotor disc.

A: *The gust model is currently three-dimensional, providing for statistical variations in speed, direction and "vertical swirl" (the air rotating as a rigid body about a vertical axis). The swirl, of course, produces horizontal variations across the disk that would be associated with turbulent conditions.*

From: C. Rybak

Q: What is the cost of the WEST system?

A: *Between $80K and $120K depending on options.*

From: Anonymous

Q: How do you model the wake geometry to determine inflow and angle of attack?

A: *A Glauert (momentum) model is used for wake retardation caused by rotor thrust. Deviations from Glauert are superimposed to account for windshear and shadow phenomena.*

From: G. Beaulieu

Q: Do you have visual displays or what kind of output features do you use?

A: *Panel galvanometers are incorporated for basic data such as delivered power, shaft loads and tip-path deflections. Rear panel ports produce signals for digital data acquisition or for presentation on standard strip-chart recorders. These output signals are analog lines.*

EXPERIENCE ON THE USE OF MOSTAB-HFW COMPUTER CODE FOR HORIZONTAL-AXIS WIND TURBINES

Yi-Yuan Yu

Rockwell International
Energy Systems Group
Canoga Park, California 91304

ABSTRACT

Experience gained from the dynamic analysis of horizontal axis turbine rotors based on the use of the MOSTAB-HFW computer code is described. Three topics are covered, dealing with the frequencies of a rotating beam, the use of the fundamental mode of a uniform cantilever beam, and the analysis of resonance dwell. Immensely high peak loads were generated by the code for resonance dwell, indicating further need for including structural damping and for transient analysis capability. The effect of structural damping, newly incorporated in the code, is finally described.

INTRODUCTION

The MOSTAB-HFW computer code was developed by Paragon Pacific under support from NASA Lewis Research Center for the dynamic analysis of horizontal-axis wind turbine rotors. Experience on the use of the code is described in this paper. Three topics are covered.

FREQUENCIES OF ROTATING BEAM

The first topic deals with the frequencies of a rotating beam, which are needed as input to the MOSTAB-HFW code. Based on the numerical results of Yntema (Ref. 1), a simple expression has been derived relating the frequency of a rotating beam to that of the same beam without rotation. For wind turbine blades with commonly used dimensions, the expression is very convenient and accurate enough for preliminary design and analysis purposes. The derivation is presented below.

Yntema (Ref. 1) has given the frequency of a rotating beam by the equation

$$\omega_{Rn}^2 = \omega_{NRn}^2 + (K_{0n} + K_{1n} e)\,\Omega^2$$

where ω_{Rn} and ω_{NRn} are frequencies of the beam with and without rotation, respectively, K_{0n} and K_{1n} are dimensionless coefficients, the subscript n denotes the mode, e is the ratio between the offset and the beam length, and Ω the rotation speed. This equation is quite general and applicable to nonuniform beams with a large variety of mass and stiffness distributions. For linear mass and stiffness distributions Yntema calculated K_{0n} and K_{1n} for the first three modes of hinged and cantilever beams. The linear distributions vary from a beam with constant-mass and/or constant-stiffness to a beam whose mass and/or stiffness diminishes all the way down to zero at one end of the beam.

Yntema's results for K_{01} and K_{11} for the fundamental modes of cantilever beams deserve special attention, because these modes play an important role in the dynamics of wind turbine blades and are needed in the MOSTAB-HFW code. Such results are given in his Figs. 15 and 16. It is noteworthy that, for the wide range of linear mass and stiffness distributions these coefficients lie within limited ranges:

$$1.17 < K_{01} < 1.26, \quad 1.57 < K_{11} < 1.93$$

Thus, K_{01} already lies within a very narrow band. Although K_{11} does not, we note that the offset ratio e is seldom greater than 0.1 for wind turbines. Hence, by assuming a maximum value of $e = 0.1$, we have

$$0.157 < K_{11} e < 0.193$$

and, for $e \leq 0.1$

$$1.17 < (K_{01} + K_{11} e) < 1.45$$

This interesting result shows that $(K_{01} + K_{11} e)$ has only a limited variation for $e \leq 0.1$. Within 11 per cent accuracy we propose to take simply

$$(K_{01} + K_{11} e) = 1.31 \text{ for } e \leq 0.1$$

The fundamental frequency of a rotating cantilever beam is then given by

$$\omega_{R1}^2 = \omega_{NR1}^2 + 1.31\,\Omega^2$$

For some blades analyzed by the use of this equation, the accuracy on ω_{R1} has been found to be within 1 per cent.

USE OF FUNDAMENTAL CANTILEVER MODE

The next topic is associated with the natural modes of vibration of the blade which are also needed as input to the MOSTAB-HFW code. Although the code can accommodate coupled modes including flapwise and chordwise bending together with twisting of the blade, the use of the fundamental mode of a uniform cantilever beam for both flapwise and chordwise bending has been found to be satisfactory for quick calculation of the dynamic loads. This is essentially to apply the classical

Rayleigh procedure in structural dynamics to the computer computation.

The use of the fundamental cantilever mode simplifies the execution of the MOSTAB-HFW code greatly. The mode is well known and can be entered as input once for all, regardless of the values of the associated bending frequencies. The advantage of this is obvious, particularly during preliminary design and analysis of the rotor blade, when many changes may be needed.

The use of the fundamental cantilever mode in the code has been compared with the use of coupled modes in sample calculations. Differences between the resulting blade peak and cyclic loads ranged from 8 per cent for the twisting moment to 23 per cent for the flapwise bending moment. These are considered satisfactory, since the loads generated by the MOSTAB-HFW code can deviate from the test data by as much as 25 per cent, as reported by Spera (Ref. 2).

RESONANCE DWELL

The third topic in this paper deals with resonance dwell. This is when the ratio between a natural frequency of the blade and the rotor speed is an integer. Such a situation is naturally to be avoided in the design for the normal operation of a wind turbine. However, it cannot be avoided during a transient operation such as start-up, shut-down, or emergency shut-down, when the rotor speed varies and passes through resonances with the blade. Resonance dwell represents the limiting case of constant rotor speed or zero rotor acceleration and can be handled by the MOSTAB-HFW code, although the code does not treat the general transient case with a non-zero acceleration.

The importance of accommodating transient operations in the design of wind turbines cannot be overemphasized. Dynamic loads on the blades of the MOD-OA wind turbines were measured during actual transient operations and found to be four to five times the loads during normal operation (Ref. 3). High transient loads have also been reported by Dugundji (Ref. 4), who tested a small wind turbine model in a wind tunnel at MIT.

It had been hoped that, in the dynamic analysis of a wind turbine, results of trim analysis during resonance dwell based on the use of the MOSTAB-HFW code would shed some light on what might happen when the rotor speed was varying and passing through a resonance. Unfortunately, the peak loads generated by the code for resonance dwell turned out to be too high to be realistic. For instance, in one case of resonance dwell the code generated a maximum flapwise bending moment in the blade 36 per cent higher than that for normal operating speed, a maximum chordwise bending moment more than 5 times higher, and a maximum shaft torque more than 16 times higher.

The very high loads for resonance dwell given by the MOSTAB-HFW code were due to lack of structural damping in the code. The results reflect the extreme sensitivity of the structurally undamped dynamic system as treated by the original code. They point to the need for including structural damping and for transient analysis capability.

EFFECT OF STRUCTURAL DAMPING

In view of its apparent importance, structural damping was recently incorporated in the MOSTAB-HFW code by Paragon Pacific, in addition to the already present aerodynamic damping. The same case of resonance dwell mentioned before was analyzed again by means of the code, only now with 2 per cent of critical damping added for both the flapwise and chordwise bending modes. The maximum flapwise and chordwise bending moments in the blade and maximum shaft torque were found to be 69, 18, and 12 per cent, respectively, of their previous level for zero structural damping. The load reduction was, therefore, drastic.

REFERENCES

1. Robert T. Yntema, Simplified Procedures and Charts for the Rapid Estimation of Bending Frequencies of Rotating Beams, NACA Technical Note 3459, June 1955.

2. David A. Spera, Comparison of Computer Codes for Calculating Dynamic Loads in Wind Turbines, NASA TM-73773, September 1977.

3. Project Information Release No. 158, Wind Energy Project Office, NASA Lewis Research Center, 1980.

4. J. Dugundji, E. E. Larrabee, and P. H. Bauer, Experimental Investigation of a Horizontal Axis Wind Turbine, Wind Energy Conversion, Vol. V, ASRL TR-184-11, Aeroelastic and Structures Research Laboratory, Department of Aeronautics and Astronautics, MIT, 1978.

QUESTIONS AND ANSWERS

Y.Y. Yu

From: G. Beaulieu

Q: Does your constant K values consider the reducing stiffness of the cantilever blade? If not, your resonant frequencies will be shifted.

A: *The values of K_{on} and K_{ln} given by Yntema cover a large variety of linear stiffness (as well as mass) distributions. The final approximate frequency equation in the paper therefore applies to cantilever blades with such stiffness variations.*

From: T. Currin

Q: After rough approximations of input, is using a large code, i.e., MOSTAB, justified?

A: *The use of approximate frequencies and mode shapes as indicated in this paper saves time for preparing input during the early stage of design when a number of configurations may be considered and many changes needed. When the design is narrowed down, such approximations are replaced by more accurate values while many other inputs to the code remain the same. The use of the code at an early stage therefore does not add much to the analysis work.*

From: Jack Landgrebe

Q: Does your sensitivity demonstration indicate that you can get any answer with different dampings and what answers do you believe?

A: *Data on structural damping of wind turbine blades are lacking because little attention has been paid to such damping. When it is better known, the transient loads can be estimated more accurately.*

From: W.C. Walton

Q: 1) Should results be compared with "normal operating loads" or with design loads?

2) Please explain the term fixed axis.

A: *1) The transient loads are compared with normal operating loads because both must be taken care of as far as structural strength is concerned, although their fatigue effects are different due to the different numbers of cycles during the life of the wind turbine.*

2) The MOSTAB-HFW code assumes a rotor with a fixed axis in space. In other words, the rotor is assumed to be uncoupled from the other components of the wind turbine system. In contrast, the MOSTAS code considers the interaction between the rotor and the other components.

From: Anonymous

Q: How was damping incorporated into MOSTAB and what is required for input data to take this into account?

A: *Modal damping was introduced for each mode in the form of a viscous damping term. Damping ratio (percentage of critical damping) is assigned to each mode as input.*

From: Jack Hoffman

Q: Why did the flap loads go up with damping?

A: *The flapwise bending moment did not go up. With 2 percent damping, the moment was 69 percent of its value for zero damping.*

COMPARISON OF UPWIND AND DOWNWIND ROTOR OPERATIONS OF THE DOE/NASA 100-kW MOD-0 WIND TURBINE

John C. Glasgow
Dean R. Miller
Robert D. Corrigan

National Aeronautics and Space Administration
Lewis Research Center
Cleveland, Ohio

ABSTRACT

Tests have been conducted on a 38m diameter horizontal axis wind turbine, which had first a rotor downwind of the supporting truss tower and then upwind of the tower. Aside from the placement of the rotor and the direction of rotation of the drive train, the wind turbine was identical for both tests. Three aspects of the test results are compared: rotor blade bending loads, rotor teeter response, and nacelle yaw moments. As a result of the tests, it is shown that while mean flatwise bending moments were unaffected by the placement of the rotor, cyclic flatwise bending tended to increase with wind speed for the downwind rotor while remaining somewhat uniform with wind speed for the upwind rotor, reflecting the effects of increased flow disturbance for a downwind rotor. Rotor teeter response was not significantly affected by the rotor location relative to the tower, but appears to reflect reduced teeter stability near rated wind speed for both configurations. Teeter stability appears to return above rated wind speed, however. Nacelle yaw moments are higher for the upwind rotor but do not indicate significant design problems for either configuration.

INTRODUCTION

The Mod-0 100-kW Experimental Wind Turbine located near Sandusky, Ohio, has served as the major test facility for the U. S. Large Horizontal Axis Wind Energy Program since initial operation of the machine in 1975. The machine was designed, fabricated, and has been operated by the NASA Lewis Research Center as a part of the research and technology program under the direction of the U. S. Department of Energy. Many concepts in current use or planned for future use on wind turbines have been first evaluated on the Mod-0 machine.

The subject of this report, a comparison of upwind and downwind rotor operating characteristics, is the result of tests to describe the loads and operating characteristics of the teetered tip-controlled rotor with the rotor in turn downwind and upwind of the tower. Preliminary results of the downwind rotor configuration were presented previously in reference 1, but this report presents some new information for the downwind configuration and makes specific comparisons with the upwind rotor configuration.

The wind turbine test configuration was the same for both tests, only the direction of rotation was reversed when the rotor was put upwind of the tower; otherwise, the wind turbine and rotor were identical. Tests were conducted to determine loads and operating characteristics of each configuration and comparisons will be made of the following items: blade bending loads, teeter motion, and nacelle yaw moments.

TEST CONFIGURATION

The upwind and downwind rotor tests were conducted on the Mod-0 100-kW Experimental Wind Turbine in the teetered, tip-controlled rotor configuration described previously (Refs. 1 and 2). Toward the end of the downwind rotor test program and throughout the upwind rotor program a hydraulic motor was used for the nacelle yaw drive, replacing the electric motor drive and double reduction worm gears used previously for orienting the nacelle in yaw. This greatly simplified the yaw drive and provided an effective method of measuring nacelle yaw torque. Otherwise, the nacelle and rotor were unchanged from earlier tests. A schematic of the Mod-0 nacelle with the teetered rotor and hydraulic yaw drive is shown in Fig. 1. The rotor is either downwind or upwind of the tower and the nacelle is tilted $8\text{-}1/2^{\circ}$ to provide tower clearance for the unconed rotor. Wind speed and nacelle yaw angle are measured on the anemometer/windvane mounted atop the nacelle as shown in Fig. 1.

Drive train slip was 4.66% for the downwind rotor tests and only 2.32% for the upwind rotor tests, which resulted in a 33.0 rpm rotor speed at 100 kW for the downwind tests and a 32.6 rpm rotor speed at 100 kW for the upwind rotor tests.

Tower

The wind turbine is mounted on the Mod-0 open-truss tower; however, an adjustable spring base has been added to provide capability for simulating various tower flexibilities (Ref. 3). The tower first cantilever bending frequency for this test configuration was measured to be 1.6 to 1.7 Hz or 2.9 to 3.1 times the rotor speed at 33 rpm. The flexible tower base adds 1m to the rotor axis height placing it 31.4m above the ground at the tower centerline. Fig. 3 shows the wind turbine on the tower and also presents parameter definitions and sign conventions pertinent to the upwind and downwind rotor configurations.

Rotor

The teetered, tip-controlled rotor is depicted in Fig. 3. The rotor is unconed, the blades have a 23% root cutout, and the outer 30% of span is pitchable. The blade section is a NACA 23024 airfoil from root to tip, and speed and power control is achieved by pitching the blade tip about its 25% chord point. The tip is capable of pitch angle changes from $+10^{\circ}$ to the full feather

position at -90°. The tip is driven by a hydraulic actuator and the rotor is stopped by feathering the blade tip at a rate of 2° per second. Rotor and blade characteristics are presented in Table I.

Table 1 - Rotor Characteristics

Rotor diameter, m (ft)	37.95 (124.5)
Root cutout, % span	23
Tip control, % span	30
Blade pitch, inb'd section, deg.	Zero
Airfoil (root to tip)	NACA 23024
Taper	Linear
Twist, deg	Zero
Solidity	0.033
Precone, deg	Zero
Max. teeter motion, deg	±6
Rotor speed @ 100 kW, rpm	33 (approx.)
Drive train slip @ 100 kW, percent	
Upwind Rotor	4.66
Downwind Rotor	2.32
Blade mass, kg (lb)	1815 (4000)
Blade Lock number	6.56
Blade first cantilever bending frequency	
Flapwise - Hz	1.76
Edgewise - Hz	1.90

The teetered hub is depicted in Fig. 3; it was designed to mate with the Mod-0 low speed shaft at the original hub-shaft interface. The teetered hub provides capability for approximately ±6° of teeter motion with initial contact with the stop occurring at approximately ±5.8°. The stops were designed to be easily replaceable should they become damaged or worn during the test program; this feature has been used several times to date.

TEST RESULTS

Tests on the wind turbine in the upwind and downwind rotor configurations were designed to obtain loads and operating characteristics for each configuration and the items compared in this report include bending moments on the blades, rotor teeter response, and nacelle yaw moments. It was also desirable to define rotor aerodynamic performance but this was not possible using the nacelle wind speed measurement which was available for the tests.

Analysis of the test data makes use of the bins analysis techniques, (Ref. 4) that have been used extensively in the past in the evaluation of wind turbine operational data. The results presented in this paper will use terms that are common in this type of analysis and have been described in previous reports. These terms, such as mean and cyclic values and median value of a given "bin" of data, are described in Fig. 4 for the convenience of the reader. The test results are a statistical presentation of data that have been sorted into "bins" or specific intervals of an independent variable, such as nacelle wind speed or nacelle yaw angle. A single revolution of the rotor provides a data point, and typically anywhere from 2000 to 10,000 data points comprise a data set used in the bins analysis.

Rotor Power

The upwind and downwind rotor tests did not provide adequate data for a comparison of the rotor performance for upwind and downwind rotors as would be indicated by power output as a function of wind speed. The variation in rotor power between an upwind and a downwind rotor wind turbine has been predicted to be less than 5%, and the anemometer used in the Mod-0 upwind and downwind rotor tests was not accurate enough to distinguish differences this small; therefore, a comparison is not presented. Rotor performance as a function of the wind speed measured on the nacelle was obtained, and indicated a rated wind speed (i.e., wind speed at which 100 kW of alternator power is produced) of 9.4 m/s for the upwind rotor and 7.3 m/s for the downwind rotor. The rated wind speed values are not corrected for local interference effects and differences in slip in the drive train; therefore the actual values are unimportant as a basis of comparison of the two configurations. However, the rated wind speeds are important in understanding the data presented in the following sections comparing the configurations. These data are shown as a function of nacelle wind speed and different behavior is noted as the control system becomes active to regulate power. This makes rated wind speed an important point. Unfortunately, a comparison of rotor performance must wait for a more accurate wind measuring system.

A new array of wind instrumentation has recently been installed at the Mod-0 wind turbine site and rotor performance tests are planned for early spring 1981. Once operational, this system will make it possible to accurately define rotor performance.

Blade Bending Moments

Flatwise rotor blade bending moments at blade station 13.21 for the downwind and the upwind rotor are shown in Fig. 5 and Fig. 6. Station 13.21 is on the pitchable tip near the 70% span point of the blade and the data shown represents bending parallel and perpendicular to the chordplane of the blade, but not always aligned with the rotor plane. Flatwise bending moments are loads which produce blade deflections which are generally perpendicular to the rotor plane; chordwise bending moments produce deflections which are generally in the plane of the rotor. Mean flatwise bending moments increase as wind speed increases until rated wind speed is attained. At this point the control system is active and the blades are pitched toward feather to maintain a power level of 100 kW. Above rated wind speed rotor thrust is decreased as the wind speed increases; this is reflected in reduced blade bending moments. The trend appears to be the same for both the downwind and the upwind rotor (Fig. 5a and Fig. 6a) though the data sample for the upwind rotor did not contain enough high wind speed data to define the upwind rotor response at higher wind speeds. Mean bending loads peak at the same value and drop off at rated wind speed, indicating that both configurations are experiencing approximately the same level of rotor thrust at rated condition.

The main difference between upwind and downwind blade loads appears in the cyclic component of the bending moment (Fig. 5b and Fig. 6b). While mean bending loads are related to rotor thrust and decrease at wind speeds above rated conditions, cyclic flatwise bending loads are related to flow disturbances that occur as the rotor blade completes each revolution. In the cyclic blade bending data (Fig. 5b), the downwind rotor shows a trend that increases with wind speed while the upwind rotor (Fig. 6b) does not appear to indicate this trend. The tendency of the downwind rotor loads to increase with wind speed is consistant with the effects of tower shadow, which become more pronounced as wind speed increases. The upwind rotor does not experience this disturbance, as demonstrated by the data in Fig. 6b.

Three stations along the rotor blade were instrumented for blade bending, but problems with the instrumentaion unfortunately prevented obtaining reliable data from both configurations at other stations.

No differences were noted in blade chordwise bending and this data was not included in the paper.

Rotor Teeter Response

Rotor teeter response for downwind and upwind rotors are compared in Fig. 7 and Fig. 8. Cyclic teeter angles as a function of wind speed and yaw angle indicated on the nacelle are shown for both configurations.

The median values of teeter angle show no discernable trend with wind speed for either configuration (Fig. 7a and Fig. 8a), but the maximum values show a tendency to increase with wind speed until rated wind speed is reached, at which point the maximum values show a decreasing trend. We feel that this tendency of the rotor teeter response to peak at rated wind speed is associated with an approaching instability in the rotor as the blade stall margin decreases. Local stall occurs when the wind speed increases to the point that the local angle of attack on the blade exceeds the airfoil stall point. As the blade operates nearer the stall point, the rotor stall margin is reduced. At wind speeds above V-rated, the blade tips are pitched to reduce the blade angle of attack, which increases the stall margin of the tip of the blade and adds stability to the teetered rotor. We plan additional tests to verify this theory.

Teeter angle as a function of yaw angle, as indicated on the nacelle, is shown for the downwind rotor in Fig. 7b and for the upwind rotor in Fig. 8b. The downwind rotor case exhibits a slight tendency for teeter angle to increase as yaw angle increases, whereas the upwind rotor reaches a maximum value at a yaw angle of 10^{o} and shows a second peak at 35^{o}. The reason for this behavior around 10^{o} of yaw angle is not understood, but the increase at 35^{o} is consistent with similar behavior on the downwind rotor and appears to be connected with the rotor direction of rotation.

The rotor teeter response for the downwind rotor differs from that presented in an earlier report (Ref. 1). The teeter data shown in this report was taken from a data set which was tailored to resemble the data set which was yielded by the upwind rotor tests. The data set used in the earlier report contained more high wind data, and perhaps more importantly, data that were more turbulent in terms of wind speed and azimuthal variations and was not felt to be a proper basis for a comparison.

Nacelle Yaw Moment Tests

Tests were run on the wind turbine to determine the effect of yaw angle on nacelle yaw moment. To acquire the necesary data, the wind turbine was synchronized with the utility grid at 33 rpm with the yaw brake released, the machine was yawed out of the wind approximately 30^{o}, the yaw motor was deactivated, and data were taken for a period of 30 minutes, allowing only the variation in wind direction to vary yaw angle. This process was repeated for a mean yaw angle of -30^{o}, the data sets were combined, and bins analysis was performed to determine the effect of yaw angle on nacelle yaw moment. The tests were performed on both the upwind and the downwind rotor and the results are shown in Fig. 9 and Fig. 10. Yaw torque data were taken on the yaw shaft torque gage shown in Fig. 1, which have been converted to nacelle yaw moment for the convenience of the reader. Yaw angle was measured on the nacelle mounted wind vane.

Test results for the downwind rotor shown in Fig. 9 indicate that mean values of nacelle yaw moment remained relatively constant at -6900 N-m over the range of yaw angles from -30^{o} to 40^{o}. At -30^{o} the yaw moment increases and passes through zero at -53^{o}. The data point at $+45^{o}$ also indicates a trend toward zero yaw moment; however, the data set provided no information past this point. The point of zero yaw moment corresponds well with a "free yaw" equilibrium point of 50^{o}, which was obtained in free yaw tests on this configuration of the wind turbine and adds to our confidence in the validity of the yaw moment data.

Cyclic yaw moments show no particular trend except for the slight decrease in the median value around a yaw angle of -50^{o}, near the point of zero yaw moment. Both cyclic and mean yaw moments for the downwind rotor are very well behaved when compared with these terms for the upwind rotor, which tend to be more variable, i.e., have larger standard deviations in each of the bins.

For the upwind rotor, mean yaw moments (Fig. 10a), tend to increase with yaw angle and peak at a yaw angle of $+40^{o}$, where the trend appears to reverse with the yaw moments decreasing, as we approach the limits of the data set. The point of zero yaw moment occurs at a yaw angle of approximately -50^{o}, very near the point of zero yaw moment indicated for the downwind rotor. However we can place no particular significance on this coincidence.

The cyclic component of the nacelle yaw moment for the upwind rotor (Fig. 10b) shows the same trend as the mean component, i.e., increasing with increasing yaw angle. The two components, mean and cyclic, showed similar trends for the downwind rotor also. However, as mentioned above, the magnitude and the variability of the cyclic component indicates that the upwind teetered rotor is less well behaved when compared with a downwind rotor.

The median of the mean component of yaw moment for the downwind rotor was measured to be -6900 N-m for yaw angles between -30^{o} and $+40^{o}$. The yaw moment caused by the $8\text{-}1/2^{o}$ tilt of the nacelle while 100 kW is being produced by the rotor is -5350 N-m, which indicates that the major portion of the mean yaw moment measured on the downwind rotor machine was due to the tilt in the nacelle. These tests will be repeated later this year on a tubular tower with the rotor tilt removed, and the yaw moment and "free yaw" characteristics will again be evaluated.

The results of the yaw moment tests indicate that from the viewpoint of yaw forces, a downwind rotor is to be preferred over an upwind rotor. Both mean and cyclic yaw forces were higher for the upwind rotor, indicating the need for more power and damping in the yaw drive mechanism and the potential for increased fatigue. There was no indication that the upwind rotor presented particularly difficult design problems with respect to yaw loads, however.

CONCLUDING REMARKS

Tests have been conducted on a 100 kW horizontal axis wind turbine having first a rotor downwind of the supporting truss tower and then upwind of the tower. Aside from the placement of the rotor and the direction of rotation relative to the nacelle, the wind turbines tested were identical. Three aspects of the test results were compared: rotor blade bending loads, rotor teeter response, and nacelle yaw moments. Conclusions based on the comparisons are presented below:

1. Cyclic flatwise bending moments are higher for the downwind rotor and increase with wind speed, reflecting the flow disturbance created by the tower. Cyclic bending moments for the upwind rotor appear to be relatively unaffected by wind speed. Mean flatwise bending moments were the same for upwind and downwind rotors.

2. Rotor teeter response appears to indicate a tendency toward teeter instability near rated wind speed for both upwind and downwind rotors. Further testing is required to verify this conclusion. No significant differences were noted between upwind rotor and downwind rotor teeter response.

3. Nacelle yaw moments were smaller for the downwind rotor but the increased yaw loads on the upwind rotor do not indicate significant design problems.

References

1. Glasgow, J. C., and Miller, D. R., "Teetered, Tip-Controlled Rotor: Preliminary Test Results from Mod-0 100-kW Experimental Wind Turbine", DOE/NASA 1028-80/26, NASA TM-81445, 1980.

2. Glasgow, J. C., and Birchenough, A. G., "Design and Operating Experience on the U. S. Department of Energy Experimental Mod-0 100-kW Wind Turbine", DOE/NASA 1028-78/18, NASA TM-78915, 1978.

3. Winemiller et. al., "Design, Fabrication and Initial Test of a Fixture for Reducing the Natural Frequency of the Mod-0 Wind Turbine Tower", DOE/NASA 1028-79/24, NASA TM-79200, 1979.

4. Richards, T. R., and Neustadter, H. E., "DOE/NASA Mod-0A Wind Turbine Performance", DOE/NASA 1004-78/13, NASA TM-78916, 1978.

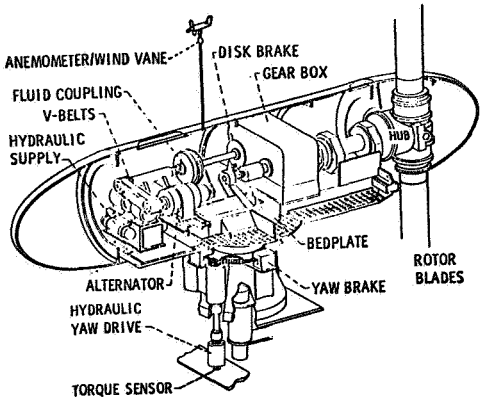

FIG. 1 - MOD-0 100 KW EXPERIMENTAL WIND TURBINE NACELLE INTERIOR

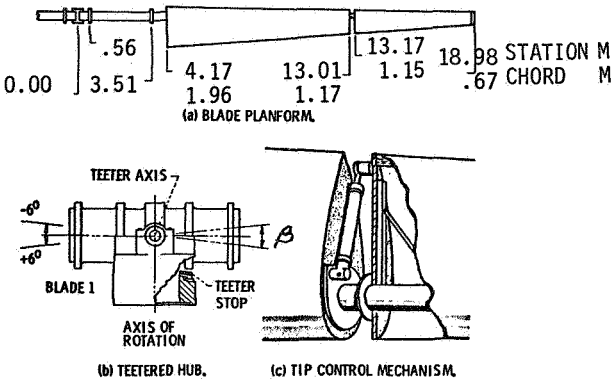

FIG. 3 - MOD-0 ROTOR DETAILS

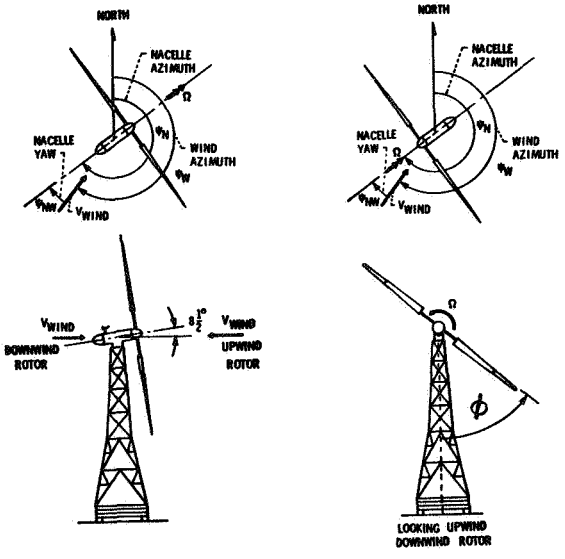

FIG. 2 - MOD-0 100 KW WIND TURBINE SIGN CONVENTIONS FOR UPWIND AND DOWNWIND ROTORS

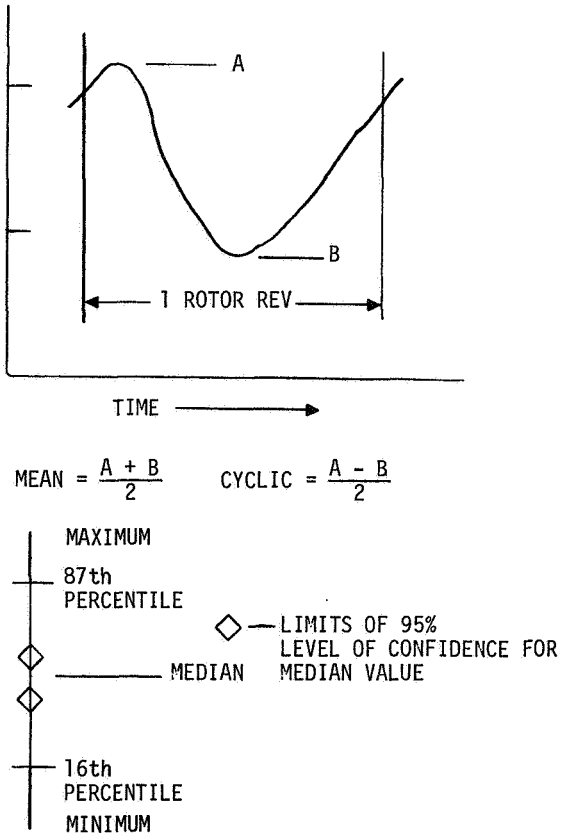

FIG. 4 - DEFINITION OF TERMS USED IN BINS ANALYSIS OF WIND TURBINE DATA

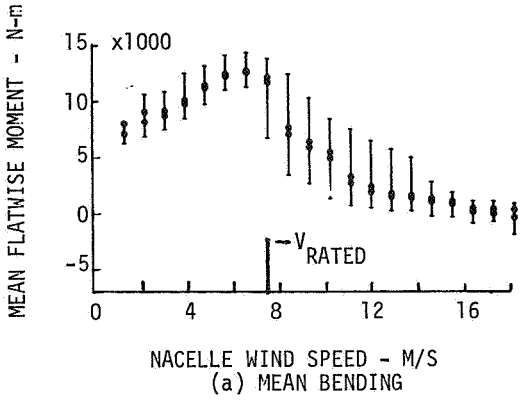

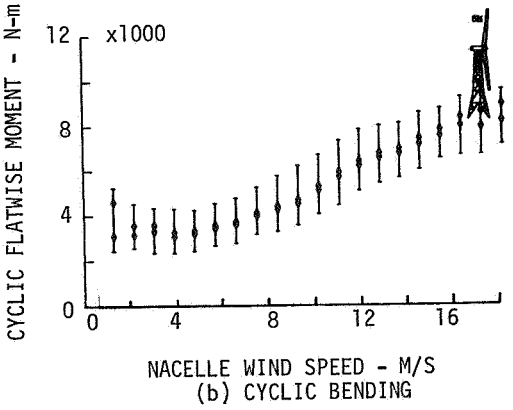

FIG. 5 - DOWNWIND ROTOR: FLATWISE ROTOR BLADE BENDING MOMENT AT STATION 13.21; MEAN BENDING, a, AND CYCLIC BENDING, b, VS. NACELLE WIND SPEED

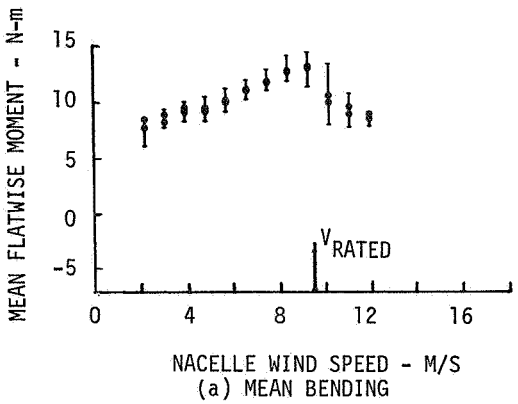

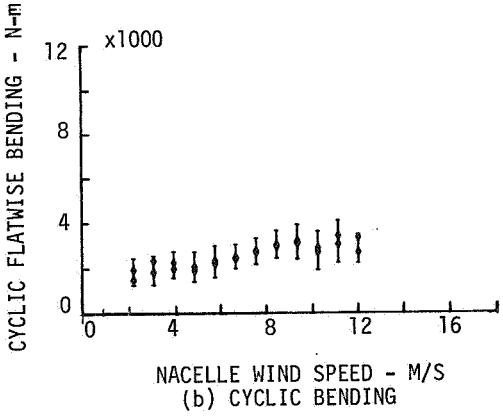

FIG. 6 - UPWIND ROTOR: FLATWISE ROTOR BLADE BENDING MOMENT AT STATION 13.21; MEAN BENDING, a, AND CYCLIC BENDING, b, VS. NACELLE WIND SPEED

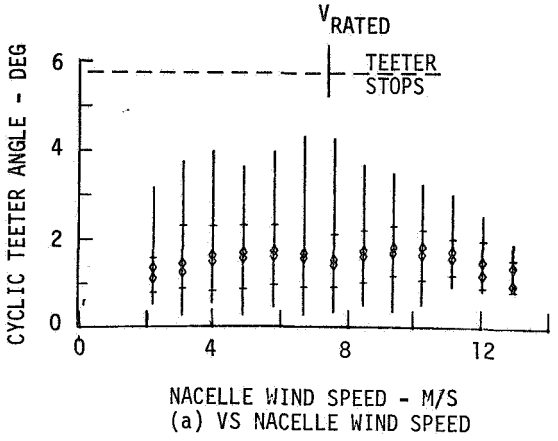

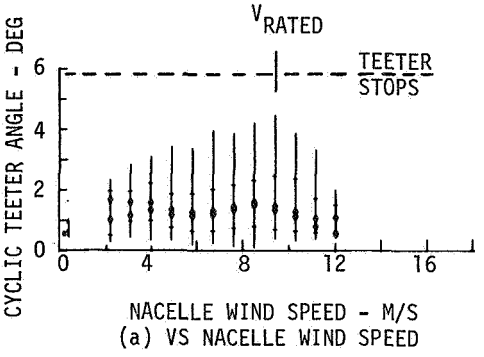

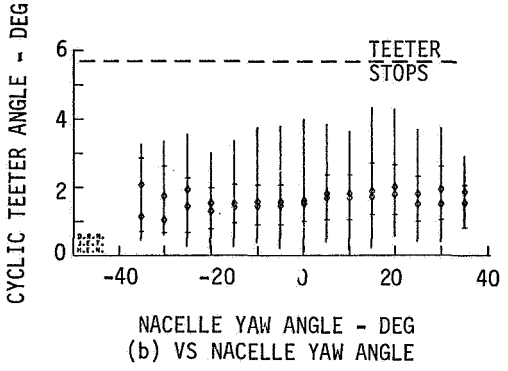

FIG. 7 - DOWNWIND ROTOR: CYCLIC TEETER ANGLE VS. NACELLE WIND SPEED, a, AND NACELLE YAW ANGLE, b

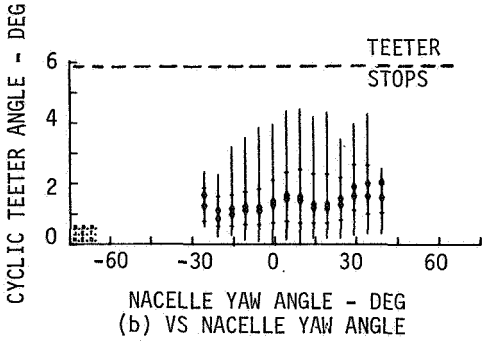

FIG. 8 - UPWIND ROTOR: CYCLIC TEETER ANGLE VS. NACELLE WIND SPEED, a, AND NACELLE YAW ANGLE, b

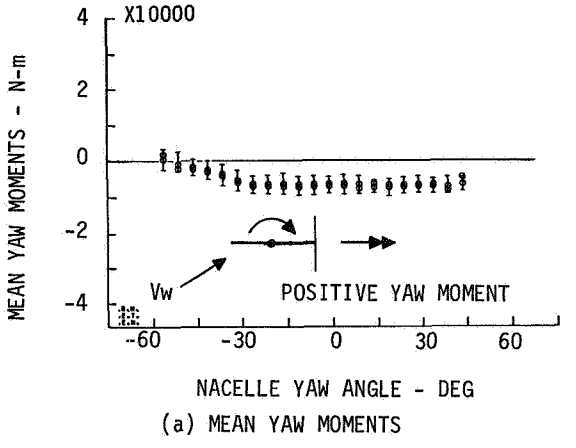

(a) MEAN YAW MOMENTS

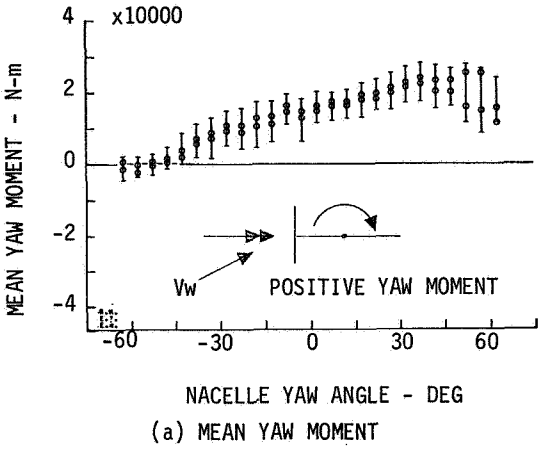

(a) MEAN YAW MOMENT

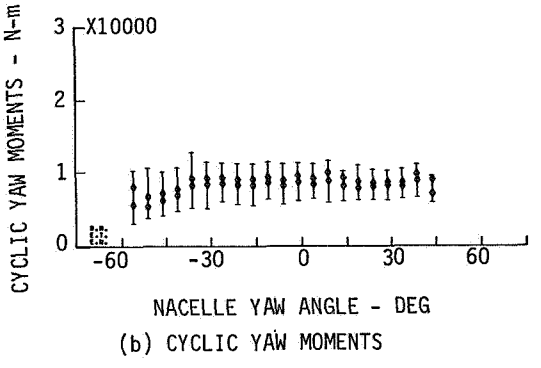

(b) CYCLIC YAW MOMENTS

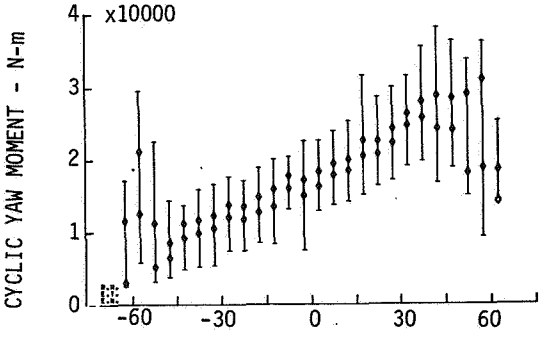

(b) CYCLIC YAW MOMENT

FIG. 9 - DOWNWIND ROTOR: MEAN NACELLE YAW MOMENTS, a, AND CYCLIC NACELLE YAW MOMENTS, b, VS. NACELLE YAW ANGLE

FIG. 10 - UPWIND ROTOR: MEAN NACELLE YAW MOMENTS, a, AND CYCLIC NACELLE YAW MOMENTS, b, VS. NACELLE YAW ANGLE

QUESTIONS AND ANSWERS

J.C. Glasgow

From: Mike Bergey

Q: What problems were encountered as a result of the inclined rotor axis?

A: *Aside from creating an unbalanced yaw force in our "free yaw" tests, no problems or peculiar behavior were noted as a result of the inclined rotor axis. We will have a chance to compare these results with tubular tower results later this year and we should then be able to say what the effects or rotor axis tilt was.*

From: W.C. Walton

Q: 1) What do you think is the main benefit of the teeter?

2) You show improvement in blade cyclic bending moments associated with the upwind configuration. Were the downwind cyclic bending moments a concern?

3) What aspect of design is affected by nacelle yaw moment?

A: *1) Reduced loads on blade, hub main drive shaft (bending) and yaw loads. Probably the most significant benefits are the reduced loads on the yaw drive and the rotor support (i.e., low speed shaft or main rotor support bearing).*

With a teetered rotor the response to gusts appears more benign than with a rigid two-bladed rotor.

2) No! Blades are usually designed by disaster type loads such as hurricanes, ice, or emergency shutdown.

3) Yaw drive and yaw mechanism -- also ability to attain "free yaw" alignment.

From: Anonymous

Q: What differences did you find in upwind and downwind readings of the anemometer?

A: *The effect of rotor placement on the anemometer is indicated by the differences in V_{RATED} - 7.3 m/s for downwind rotor and 9.4 m/s on the upwind rotor. How much of this is due to the interference of the rotor is not known. The agreement between nacelle wind speed and free stream wind speed does improve at values above V_{RATED}. We are studying this situation and should have more definitive answers about rotor interference on nacelle mounted anemometers in the near future.*

From: M. Gäbler

Q: What was your experience with the anemometer operating behind the blade with the machine upwind?

A: *For some strange reason, our nacelle measurements indicated that the flow was accelerated downwind of the rotor and retarded upwind of the rotor. The agreement with Free Stream Wind Speed improves above rated wind speed.*

From: W.E. Holley

Q: Why do you display results using "sigma-bins" method rather than "power-spectral-density" method?

A: *The "bins" method yields information which is more applicable to the questions which we have been asked to answer up to this point.*

There has not been a large demand for spectral data from wind turbine designers up to now.

From: Mel Snyder

Q: Do the graphs of yawing moment show a free yaw stability point of -60° for both wind and downwind rotors?

A: *I intended to cover this point: "Free yaw" tests showed that we had an equilibrium point at -50° for the downwind rotor. This same point, approximately -50° is indicated for the upwind rotor, but we did not run a "free yaw" test on the upwind rotors. See B. Brooks (Ham. Std.) paper for "free yaw" results.*

From: Don Meitson

Q: Were all the yaw moments at rated power?

A: *No. Some were at rated power of 100 kW, but most were not.*

SECOND DOE/NASA WIND TURBINE DYNAMICS WORKSHOP

Structural & Rotor Dynamics

Session Chairman - V.J. Weyers (NASA LeRC)

"A Review of Resonance Response in Large HAWT's"
T.L. Sullivan
(NASA LeRC)

"SWECS Tower Dynamic Analysis Methods and Results"
A.D. Wright
(Rocky Flats Plant)

"Guy Cables Damping for VAWT's"
T.G. Carne
(Sandia Labs.)

"North Wind 4 kW 'Passive' Control System Design"
H. Currin
(Foehn Consulting)

"Passive Cyclic Pitch Control for HAWT's"
G.W. Bottrell
(Ventus Energy Corp.)

"Dynamics of an Experimental Two-Bladed HAWT with Blade Cyclic Pitch Variation"
K. Hohenemser
A. Swift
(Washington University)

"Mod-0 Dynamics Test Correlation"
B. Brooks
(Hamilton Standard)

"The Effect of δ_3 on a Yawing HAWT Blade"
F. Perkins
R. Jones
(Kaman Aerospace)

Mod 2 Status Report (Verbal Presentation Only)
J.S. Andrews
(Boeing)

Mod 1 Failure Report (Verbal Presentation Only)
D.A. Spera
(NASA LeRC)

A REVIEW OF RESONANCE RESPONSE IN LARGE, HORIZONTAL-AXIS WIND TURBINES

Timothy L. Sullivan

National Aeronautics and Space Administration
Lewis Research Center
Cleveland, Ohio

ABSTRACT

Field operation of the Mod-0 and Mod-1 wind turbines has provided valuable information concerning resonance response in large, two-bladed, horizontal axis wind turbines. Operational experience has shown that 1 per rev excitation exists in the drive train, high aerodynamic damping prevents resonance response of the blade flatwise modes and teetering the hub substantially reduces the chordwise blade response to odd harmonic excitation. These results can be used by the designer as a guide to system frequency placement. In addition it has been found that present analytical techniques can accurately predict wind turbine natural frequencies.

INTRODUCTION

In any mechanical system, vibrations are undesirable and possibly dangerous if the vibratory motion becomes excessive. However, in a rotating system, like a wind turbine, vibrations are unavoidable. Hence, one of the keys to good design of wind turbines is to minimize vibrations. This is done by avoiding resonance.

Resonance is a phenomenon which occurs in a structure when an exciting or forcing frequency equals or nearly equals one of the natural frequencies of the system. It is characterized by a large increase in displacements and internal loads. In a rotating system the exciting frequencies are integer multiples of the rotational speed. In a wind turbine the important natural frequencies that must be considered are those associated with the blades, the tower (including yaw drive) and the drive train.

The purpose of this report is to review what has been learned about resonance response from operation of the Mod-0 and Mod-1 wind turbines. Based on this field experience, conclusions will be made concerning when resonance will occur in a two-bladed, horizontal-axis wind turbine. In addition analysis and design approaches to avoid resonance will be discussed.

ANALYTICAL APPROACH TO RESONANCE

A useful tool in the analysis of resonance potential of complex rotating systems is the frequency plot or Campbell diagram. A Campbell diagram for a hypothetical wind turbine, typical of wind turbines like the Mod-0 and Mod-1, is shown in Figure 1. In this diagram system natural frequencies are plotted versus rotational frequency. The radial lines are plots of integer multiples of the rotational frequency and represent exciting frequencies. Therefore, a potential for resonance exists whenever lines cross. This type of diagram is particularly useful for analyzing wind turbines designed to operate at variable rotational speeds.

System natural frequencies like those shown in Figure 1 can be calculated using finite element computer codes such as NASTRAN. Modeling considerations and natural frequency results for the Mod-0 tower, bed plate and blades are presented in reference 1 and for the Mod-0 drive train in reference 2. Experimental methods using vibration analyzers (ref. 3) are available for verifying calculations. Agreement between measured and calculated frequencies within 5 percent are not uncommon for the lower frequency modes that are of primary interest in wind turbines.

For a wind turbine with a single operating speed, another type of frequency diagram can be constructed and this is illustrated in Figure 2. This diagram was presented at the Mod-2 preliminary design review. The radial "per rev" lines of Figure 1 are now vertical lines with an avoid range applied. The required width of the avoid ranges is not precisely known. Here they were conservatively set at ± 0.5 per rev for the even harmonics and ± 0.25 per rev for the odd harmonics. Calculated system frequencies are also shown. All the system frequencies are clear of the avoid ranges except the off-line drive train frequency. Because the rotor is a node point for this mode, the rotor cannot excite it. Therefore it is permissible to be within the avoid range for this case.

The avoid ranges shown in Figure 2 are relatively wide, resulting in rather small windows for the designer to place system frequencies. Another point to note in this figure is that for the drive train no avoid range is shown for the odd harmonics. The significance of this will be discussed in the following section.

A similar diagram for the Mod-1 wind turbine for 35 rpm operation is shown in Figure 3(a). Here a slightly different approach to the avoid ranges was taken. The avoid ranges are not as wide, allowing the designer greater flexibility in frequency placement. The justification for the very narrow avoid range for the flatwise

blade mode is the high aerodynamic damping associated with this mode. Only odd harmonic avoid ranges are shown for the blade chordwise mode because no even harmonic excitation is expected. The theoretical basis for this can be found in reference 4. The blade torsion/pitch change mechanism (PCM) mode requires high stiffness to avoid flutter. The natural frequency of this mode should be designed to be so high that resonance is not a consideration.

Measured and calculated system frequencies are compared in Figure 3(a), showing the degree of correlation which can be expected. The calculated blade frequencies include the effect of centrifugal stiffening. The measured blade frequencies were obtained by applying an analytically derived correction factor to the measured non-rotating frequencies. In general the agreement between measured and calculated values is good, which is typical of experience to date. When differences do occur, they can usually be explained by modeling assumptions that were not realized in the as-built wind turbine. For instance, the difference in the off-line drive train frequencies comes from the assumption of no backlash in the drive train. The difference in the tower bending frequencies is related in part to the assumption of a flexible foundation, when the actual wind turbine was attached to bed rock.

A condensed version of Figure 3(a) is shown in Figure 3(b) for the present operating speed of the Mod-1, 23 rpm. The measured natural frequencies are clear of the avoid ranges except for the blade flatwise mode. Because of high aerodynamic damping, this is no concern. Note that the calculated drive train mode now is very close to 1 per rev. The implications of this are discussed in the following section.

FIELD EXPERIENCE WITH RESONANCE

Because it is a research machine the Mod-0 wind turbine has provided much experience with resonance. The Mod-1 has provided additional experience. In this section this experience will be reviewed for the drive train, rotor support (tower, yaw drive) and blades.

Drive Train

For a perfectly balanced rotor, only even harmonic excitation would be expected in the drive train of a two bladed rotor. For this reason avoid ranges in Figures 2 and 3 are shown only on the even harmonics. However, mass, stiffness or aerodynamic unbalance from blade to blade can cause odd harmonic excitation as well. This was vividly demonstrated when the Mod-1 rotor speed was reduced from 35 to 23 rpm which placed its natural frequency close to 1 per rev. The output power of a wind turbine can vary about a mean power level. Figure 4 compares the amplitudes of cyclic power variation for 23 and 35 rpm operations. Examination of the real time data for 23 rpm operation showed the cyclic frequency was close to 1 per rev. The source of the 1 per rev excitation in the drive train is presently being investigated. However, the response seen here is not peculiar to the Mod-1. Synchronous operation of the Mod-0 at 35 rpm placed its drive train natural frequency close to 1 per rev. A time history of output power is shown in Figure 5. The response here is very similar to that seen with the Mod-1.

The field experience described above provides strong evidence that wind turbine drive trains contain 1 per rev excitation. In addition, Mod-0 drive train resonance caused by even harmonic excitation is documented in reference 2. Therefore, drive train natural frequencies must avoid both even and odd harmonics until the source of the 1 per rev excitation is better understood and reduced or, hopefully, eliminated.

Rotor Support Structure

In its initial configuration the Mod-0 had a relatively flexible yaw drive. The natural frequency of the nacelle and rotor about the yaw drive was close to 2/rev at the operational speed of 40 rpm. This resonance resulted in large yaw oscillations which in turn resulted in an amplification of blade loads. This amplification was of major concern because, if allowed to continue, it would significantly decrease blade life. Modifications were, therefore, made to Mod-0 to increase its yaw stiffness. Figure 6 shows cyclic blade loads as a function of yaw drive stiffness. The measured data are compared to loads calculated using the MOSTAS-B computer code (ref. 5). The near 2 per rev resonance in the yaw drive caused both edgewise and flatwise blade load amplification. This amplification has been reduced by either softening the yaw drive (free yaw) or by stiffening it by means of a dual yaw drive (ref. 6) and by locking the bed plate to the tower with brakes.

Because it is a research machine, the Mod-0 has been modified in several ways primarily to support advanced wind turbine projects like the Mod-2. Among these modifications are reduction of the tower natural frequency by placing it on a spring fixture (ref. 7) and replacement of the rigid hub with a teetered hub (ref. 8). The effect of these modifications on resonance response will be described next.

The original Mod-0 tower had a first bending frequency of about 2.1 Hz and was characterized as being "stiff" because this frequency was greater than the blade passing frequency of 2/rev when operating at 40 rpm. Because of interest in more flexible towers, primarily for economic reasons, the frequency of the Mod-0 truss tower was reduced by placing the tower on a spring fixture. The details of this fixture are given in reference 7. With the fixture the tower bending frequency was reduced to about 0.8 Hz or 1.5/rev at the present operational speed of 31 rpm. Towers with bending frequencies

between 1/rev and 2/rev are classified as "firm" towers. One of the operational characteristics with firm towers is that the machine passes through a 2/rev tower resonance going up to and coming down from operation speed. The effect of this resonance on blade and tower loads was a concern.

Figure 7 shows the envelope of peaks from a time history of the response of the Mod-0 with a firm tower during a typical start-up, shut-down cycle. In summary, this test showed that when passing through the tower resonance, blade loads were not adversely affected and tower deflections were not excessive. More details of this test can be found in reference 9. Initial operation of the first Mod-2 wind turbine at Goldendale, Washington, confirms the results of the Mod-0 firm tower tests.

Blades

Blade resonance response can be determined by running a speed survey in which the wind turbine is operated over a wide range of rotor speeds. The results of a speed survey between 12 and 40 rpm for Mod-0 in the stiff tower configuration are shown in Figure 8. In general the chordwise loads respond to the odd harmonics as expected. Peak response was expected to occur very close to the odd per revs. However, the 5 per rev peak response occurs about 2 rpm higher than expected. The reason for this displaced response is not presently understood. The response to harmonics greater than 5/rev does not appear to be significant. Examination of flatwise blade loads during this same speed survey showed no load amplification at any rotor speed. High aerodynamic damping prevents the blades from responding in the flatwise direction.

The primary reasons for teetering a rotor is to reduce flatwise blade loads and torsional tower loads. As a result hub motions are reduced, which in turn should reduce the blade resonance response. This indeed is the case as shown in Figure 8 for a 5/rev resonance. The load amplification for the teetered hub was about half that for the rigid hub.

The data shown in Figure 8 have certain implications with respect to multispeed operation of a wind turbine. Operation on 5/rev and above for a teetered rotor and 7/rev and above for a rigid rotor could probably be tolerated. This is based on the fact that the load magnification for these resonances is less than 20 percent.

CONCLUSIONS

Based on the operation of the Mod-0 and Mod-1 wind turbines, the following conclusions concerning resonance response in large, two-bladed, horizontal axis wind turbines can be made:

1. The important natural frequencies of wind turbines can be calculated with reasonable accuracy.

2. Odd harmonic content is present in the drive train and can cause significant resonance response.

3. Resonance associated with yaw drive flexibility causes blade load amplification; resonance associated with tower bending flexibility does not cause blade load amplification.

4. Odd harmonic excitations up to and including 5/rev can cause significant blade chordwise resonance response; teetering the rotor will reduce this response substantially.

5. High aerodynamic damping prevents resonance response in the blade flatwise direction at all frequencies.

REFERENCES

1. Chamis, C. C. and Sullivan, T. L.: Free Vibrations of the ERDA-NASA 100 kW Wind Turbine, NASA TMX-71879, 1976.

2. Sullivan, T. L., Miller, D. R. and Spera, D. A.: Drive Train Normal Modes Analysis for the ERDA/NASA 100 kW Wind Turbine Generator, NASA TM-73718, July 1977.

3. Edgerly, Walter: Instant Replay for Vibration Analysis, Machine Design, November 22, 1979.

4. Den Hartog, J. P., Mechanical Vibrations, 2nd Edition, McGraw-Hill Book Company, New York, 1940, pg. 313.

5. Kaza, K. R. V., Janetzke, D. C. and Sullivan, T. L.: Evaluation of MOSTAS Computer Code for Predicting Dynamic Loads in Two-Bladed Wind Turbines; NASA TM-79101, 1979.

6. Spera, D. A., Janetzke, D. C. and Richards, T. R.: Dynamic Blade Loading in the ERDA/NASA 100 kW and 200 kW Wind Turbines, NASA TM-73711, 1977.

7. Winemiller, J. R., et al: Design, Fabrication and Initial Test of a Fixture for Reducing the Natural Frequency of the Mod-0 Wind Turbine Tower, NASA TM-79200, July 1979.

8. Glasgow, J. C. and Miller, D. R.: Teetered, Tip-Controlled Rotor: Preliminary Test Results from Mod-0 100 kW Experimental Wind Turbine, NASA TM-81445, 1980.

9. Keith, Jr., Theo G., Sullivan, Timothy L. and Viterna, Larry A.: Performance of a Steel Spar Wind Turbine Blade on the Mod-0 100 kW Experimental Wind Turbine, NASA TM-81588, Sept. 1980.

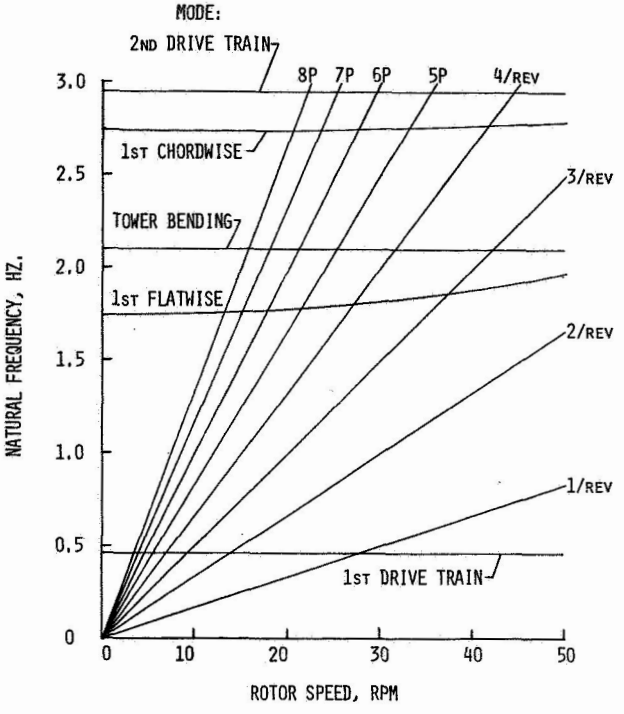

Figure 1 - Campbell diagram for a hypothetical wind turbine.

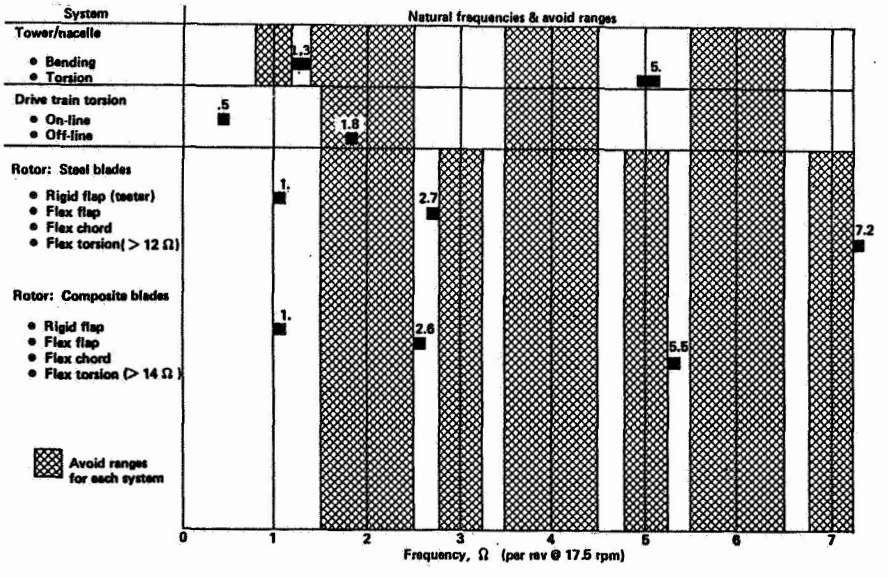

Figure 2 - System resonance avoidance -- the Mod-2 approach.

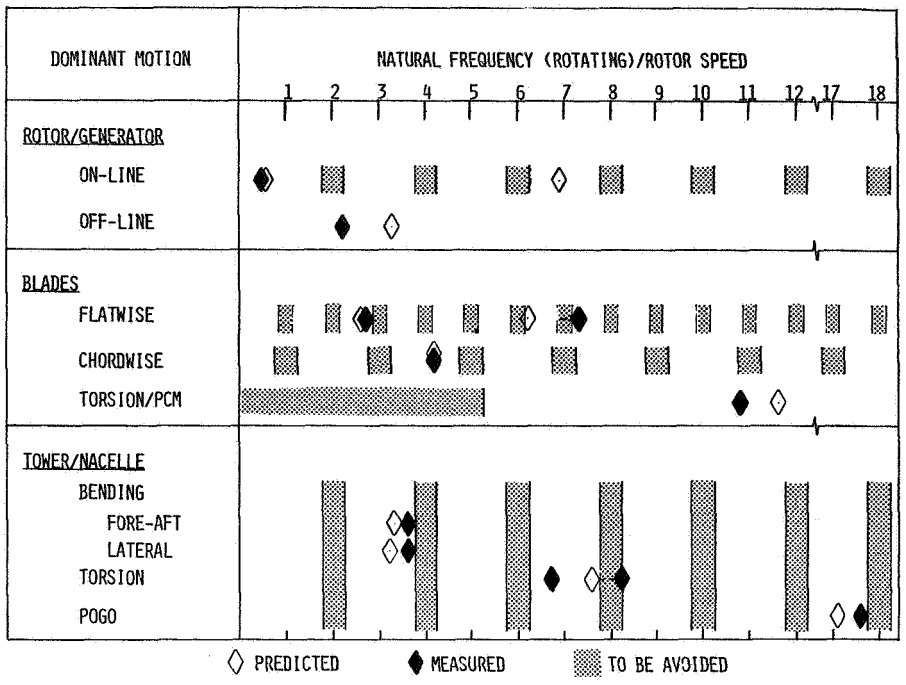

(a) 35 rpm

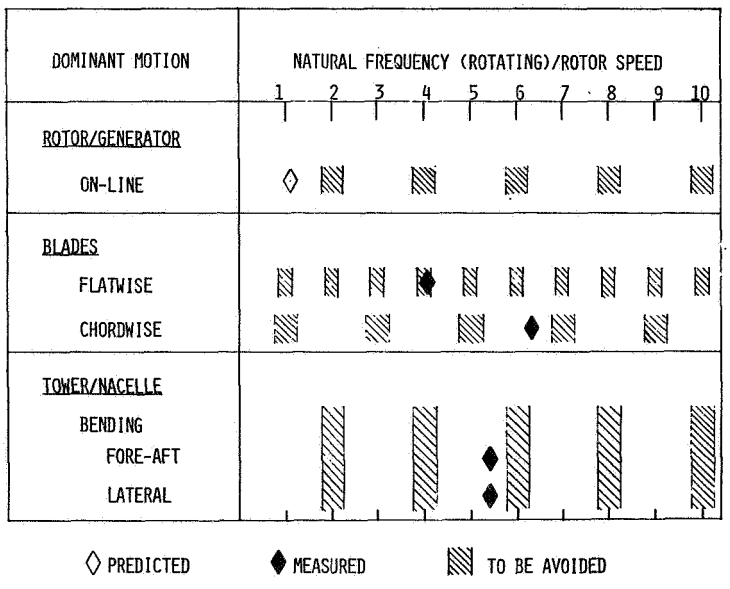

(b) 23 rpm

Figure 3 - Mod-1 system natural frequencies.

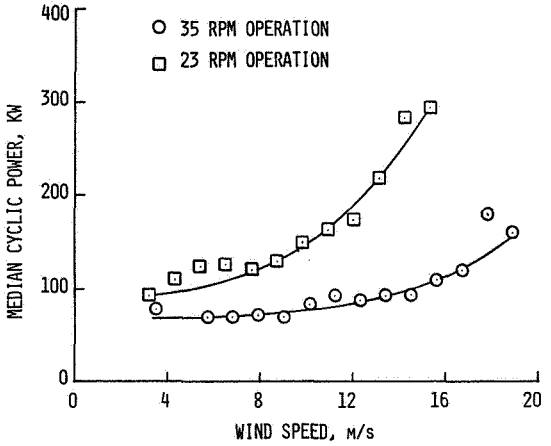

Figure 4 - Effect of drive train resonance on the amplitude of alternator power fluctions in the Mod-1.

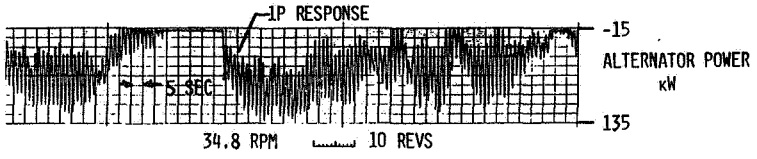

Figure 5 - Time history of a 1/rev drive train resonance in the Mod-0.

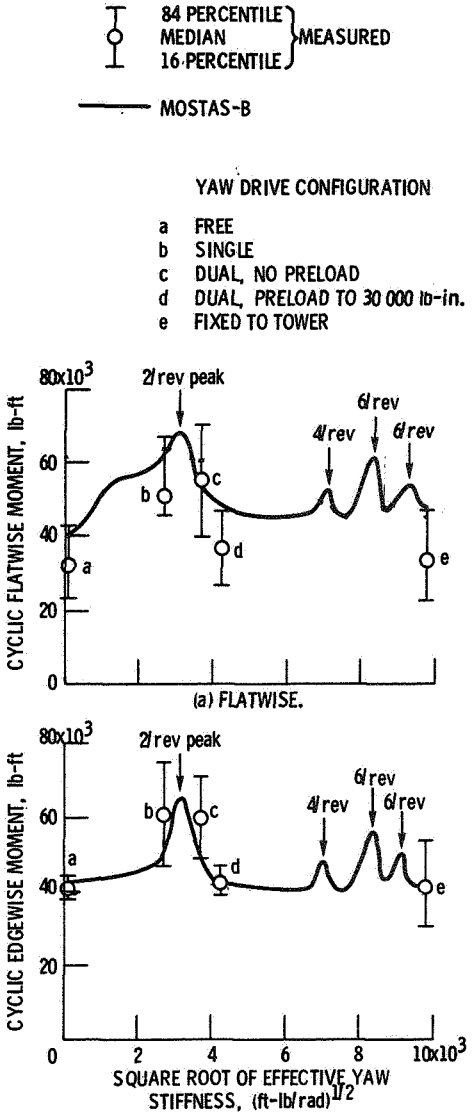

Figure 6 - Blade response to a yaw drive resonance in the Mod-0 (5% span).

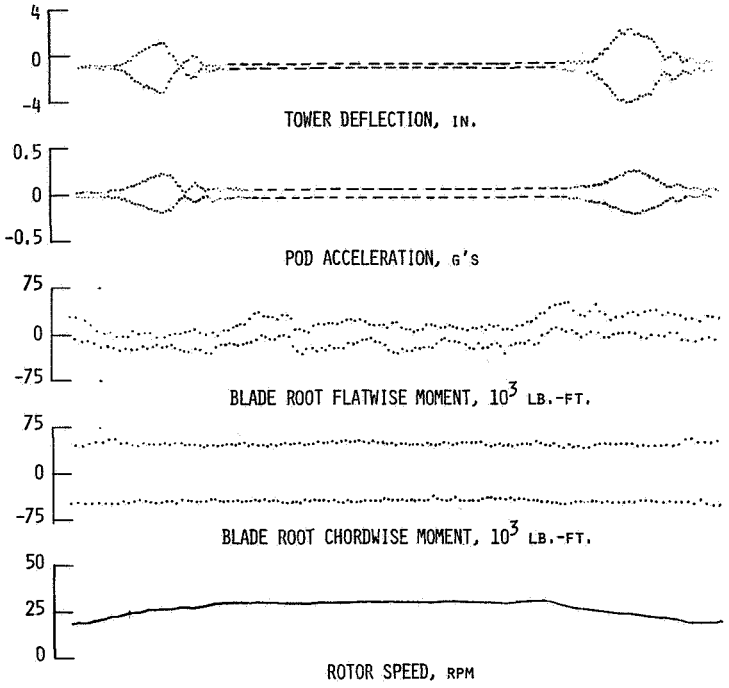

Figure 7 - Response of the Mod-0 when passing through a 2/rev tower resonance (envelope of cyclic peaks).

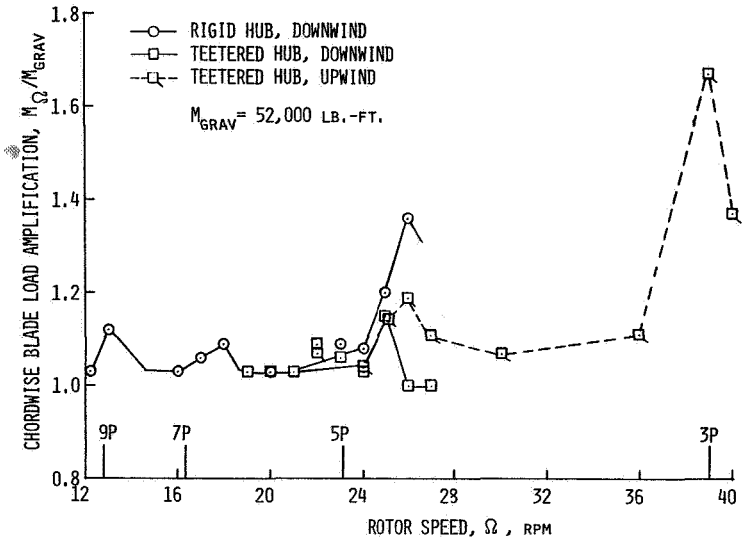

Figure 8 - Blade root chordwise response as a function of rotor speed for the Mod-0 tip-controlled blade.

QUESTIONS AND ANSWERS

T.L. Sullivan

From: K. Hohenemser

Q: Why did you not show the chordwise 3P for the rigid hub?

A: *We were afraid of damaging the blades if we ran the rigid hub up to 3P (40 rpm).*

From: W.C. Walton

Q: 1) Do blade dynamic characteristics (stiffness; natural frequencies) play any role in the 1P drive train resonance (i.e., do the blades just provide the rotational inertia)?

2) In the blooming of tower response (with no accompanying increase in blade loads) were the tower loads of any concern?

A: *1) For the fundamental drive train mode (which is the one of most concern) only the rotor inertia plays a role in the drive train natural frequency.*

2) Tower loads were not of concern. However, the loads in the spring fixture used to soften the tower were of concern. Hence, the spring fixture was strain gaged. These strains were within acceptable limits.

From: Anonymous

Q: What is the predominant frequency of the cyclic component of MOD-1 power output (at 23 rpm rotor speed)?

A: *Close to 1/rev.*

From: R. Perley

Q: What is the basis of establishing the avoidance ranges?

A: *Presently they are set rather arbitrarily. Heavily damped modes have narrow bands. Lightly damped modes have wider bands. Additional field experience and computer studies will allow us to set the avoid ranges more precisely.*

From: W. Sullivan

Q: What methods were used to compute MOD-1 and 2 resonant frequencies--are all rotating coordinate system effects included?

A: *The only rotational effect taken into account was centrifugal stiffening. This approach gives good agreement with measured data.*

SWECS TOWER DYNAMICS ANALYSIS METHODS AND RESULTS

Alan D. Wright, James H. Sexton and Charles P. Butterfield*

Rockwell International
Energy Systems Group
Rocky Flats Wind Systems Group
Golden, Colorado 80401

and

Robert W. Thresher
Professor of Mechanical Engineering
Oregon State University
Corvallis, Oregon

ABSTRACT

At the Rocky Flats Wind Systems Center, several different tower dynamics analysis methods and computer codes are used to determine the natural frequencies and mode shapes of both guyed and freestanding wind turbine towers. In this paper these analysis methods are described and the results for two types of towers: a guyed tower and a freestanding tower are shown. The advantages and disadvantages in the use of and the accuracy of each method are also described.

INTRODUCTION

The accurate prediction of tower vibration frequencies and mode shapes is important in avoiding unwanted vibration problems. At present, there is a variety of structural dynamic analyses covering a range of complexity and application. In this paper, some of the existing analyses and corresponding computer codes will be examined in order to determine those which can be of use to the SWECS industry.

A tower dynamics supporting research and technology project has been conducted at the Rocky Flats Small Wind Systems Center. The objective of this project has been to determine those analyses which are simple to use but give adequate results compared to test results. This paper will present some of the simpler tower dynamic analyses, their correct use and accuracy. The simpler analysis methods will be presented in order of increasing complexity and accuracy. The theory and use of the methods will first be described, as well as the accuracy of results for towers with various mass and stiffness distributions. The results from these analyses will then be compared to the test results for two types of towers at Rocky Flats: 1) a guyed tower with uniform mass and stiffness, and 2) a freestanding tower with uniform mass but tapered stiffness. It will be shown that accurate determination of the bending frequencies for towers with tapered stiffness is more difficult, using the simpler analyses. This will require the designer to use a more complex analysis, such as SAPIV. It should be emphasized that this paper deals specifically in determination of tower bending frequencies. The case of torsional frequencies or coupled bending torsional frequencies have not been analyzed, using the methods of this paper. The results for these frequencies may be the subject of a later paper.

*Now with Energy Sciences, Inc., Boulder Colorado.

THEORY AND USE OF THE METHODS

The Rayleigh Quotient

The Rayleigh Quotient forms the basis for some approximate methods: the Rayleigh Method and the Rayleigh Ritz Method, both to be described here. The system to be analyzed is shown in Figure 1. The freestanding tower has variable mass and stiffness distributions $\rho A(x)$ and $EI(x)$, respectively. A concentrated mass, M, is attached at the tower top at a height, L, above the ground.

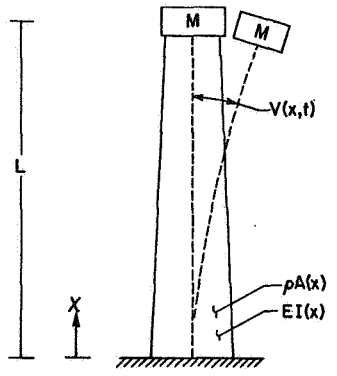

Figure 1: System to be Analyzed.

By assuming the deflection v(x,t) in the form:

$$v(x,t) = \phi(x) \sin pt$$

and equating the tower potential energy at maximum displacement to the kinetic energy at minimum displacement, the Rayleigh Quotient can be expressed:

$$p^2(\phi) = \frac{\int_0^L EI(x)\,[\phi''(x)]^2\,dx}{\int_0^L \rho A(x)\,[\phi(x)]^2\,dx + M[\phi(L)]^2} \qquad (1)$$

When ϕ is an exact vibration mode of the tower, p has the value of the corresponding exact natural frequency; also, p^2 is stationary with respect to variations in ϕ at each of these points (Ref. 3). This expression can be expected to give a good approximation to the frequency if a good approximation to the mode shape is used to evaluate Equation 1. A simple analysis can be formed for the special case of a tower with uniform or linearly tapered mass and stiffness distributions, in order to find the first bending frequency.

A Simple Analysis

For a freestanding tower with linear mass and stiffness distributions of the form:

$$EI(x) = EI_0\,(1 - \beta\, x/L)$$

$$\rho A(x) = \rho A_0\,(1 - \gamma\, x/L)^*$$

the approximate shape:

$$\phi(x) = \left(\frac{x}{L}\right)^4 - 4\left(\frac{x}{L}\right)^3 + 6\left(\frac{x}{L}\right)^2 **$$

can be used to evaluate Equation 1 with the result:

$$p^2 = \frac{EI_0}{\rho A_0 L^4} \cdot \frac{28.800 - 4.800\beta}{(2.311 - 1.854\gamma) + 9.00\mu} \qquad (2)$$

where μ is the ratio $M/\rho A_0 L$.

In those cases where exact frequencies for a cantilever beam with a tip mass have been calculated, the results from Equation 2 can be compared directly to give an indication of the accuracy. Table 1 shows the dimensionless frequency ratios:

$$W = \sqrt{\frac{\rho A_0 L^4}{EI_0}}\; p$$

obtained from Equation 1 compared to exact results calculated, using a power series method (Ref. 8).

*EI_0 and ρA_0 are the stiffness and mass distributions of the tower at the base. The case $\beta = 0$, $\gamma = 0$ is that of a uniform tower.

**The assumed mode shape should satisfy some or all of the cantilever tower boundary conditions. Here: $\phi(0) = 0$ and $\phi'(0) = 0$ are satisfied. The assumed mode shape should at least satisfy the base boundary conditions.

From Table I it can be seen that the accuracy of results from Equation 1 diminishes for towers with higher stiffness taper rates and larger tip masses because the assumed first mode shape $\phi(x)$, used in the above analysis, approximates the exact mode shape less accurately.

TABLE I: COMPARISON OF RESULTS OBTAINED FROM SIMPLE METHOD (W_s) TO EXACT RESULTS (W_e) FOR THE FIRST BENDING FREQUENCY RATIOS, FOR VARIOUS TAPERS AND TIP MASS RATIOS.

Uniform Stiffness, Uniform Mass: $\beta = 0.$, $\gamma = 0$

μ	W_e	W_s	% Error
1.0	1.56	1.60	2.6
2.0	1.16	1.19	2.6

Uniform Stiffness, Tapered Mass: $\beta = 0.$, $\gamma = .9$

μ	W_e	W_s	% Error
1.0	1.68	1.73	3.0
2.0	1.21	1.24	2.5

Tapered Stiffness, Uniform Mass: $\beta = .9$, $\gamma = 0$

μ	W_e	W_s	% Error
1.0	1.33	1.47	10.5
2.0	0.99	1.10	11.1

Limitations of the Method

This simple method is applicable to freestanding towers for mass and stiffness distributions varying approximately linearly. Only the first bending frequency can be found from Equation 2, although the second bending frequency might be estimated if the analyzer could evaluate Equation 1 with a good second mode shape approximation. Equation 2 is useful for obtaining a rough estimate of the first bending frequency of freestanding towers, without the use of a computer.

A Rayleigh Computer Code

A program developed at MIT, Program Rayleigh (Ref. 4), uses the Rayleigh procedure to evaluate the first bending mode for freestanding towers with nonlinear mass and stiffness distributions. The tower can be divided into N equal segments and constant values of mass and stiffness are input along each segment. Simpson's integration is then used to evaluate the integrals in the Rayleigh Quotient.

Both the Simple Method and the Rayleigh Program have the disadvantage that the user must input an assumed mode shape. The accuracy of the corresponding results depends on this one shape.

In a method to be described next, a linear combination of assumed shape functions is used to form the function $\phi(x)$ for use in the Rayleigh Quotient. This method is particularly useful for guyed towers, because the mode shapes are harder to approximate with a simple function, such as that used in the simple method above.

THE RAYLEIGH RITZ PROCEDURE

The Rayleigh Ritz method involves using a set of assumed shape functions $\psi_i(x)$ and combining them to form the mode shape:

$$\phi(x) = A_1\psi_1(x) + A_2\psi_2(x) + \ldots + A_N\psi_N(x) \qquad (3)$$

The A_i's are constants to be determined and the ψ_i's are a set of linearly independent functions, each satisfying some or all of the boundary conditions of the tower.*

For a guyed tower, Rayleigh's Quotient can be expressed:

$$p^2(\phi) = \frac{\int_0^L EI(x)\,[\phi''(x)]^2\,dx + Kc[\phi(a)]^2}{\int_0^L \rho A(x)\,[\phi(x)]^2\,dx + M[\phi(L)]^2} \qquad (4)$$

where Kc is the guy wire stiffness coefficient and a is the guy wire attachment height, shown in Figure 2. For three guy wires spaced 120° apart, Kc can be shown to be (Ref. 6):

$$Kc = \frac{3}{2}\left(\frac{A'E'}{\ell}\right)\cos^2\theta. \qquad (5)$$

While for four guy wires spaced 90° apart, the factor 3/2 in Equation 5 is replaced by a 2. These values of Kc are valid when the guy wires have been tensioned sufficiently so that there is no coupling between the guy wires and the tower (Ref. 1).

Substitution of the mode shape form in Equation 3 into Equation 4 gives:

$$p^2(\phi) = \frac{EI_o}{\rho A_o L^4}\,\frac{\sum_j\sum_i A_i A_j d_{ij}}{\sum_j\sum_i A_i A_j b_{ij}} \qquad (6)$$

Where:

$$d_{ij} = \int_0^1 f(\xi)\,\psi_i''(\xi)\psi_j''(\xi)d\xi + \overline{Kc}\,\psi_i(\xi a)\,\psi_j(\xi a)$$

$$b_{ij} = \int_0^1 h(\xi)\,\psi_i(\xi)\psi_j(\xi)d\xi + \mu\psi_i(1)\,\psi_j(1) \qquad (7)$$

$$i, j = 1, \ldots, N$$

and ξ, $f(\xi)$, $h(\xi)$, ξa, $\overline{Kc}$ and μ are the dimensionless distance, stiffness, mass distribution, guy level attachment, guy stiffness coefficient, and tip mass ratio, respectively, as defined in the nomenclature.

*The ψ_i functions should satisfy at least the geometric boundary conditions (Ref. 3).

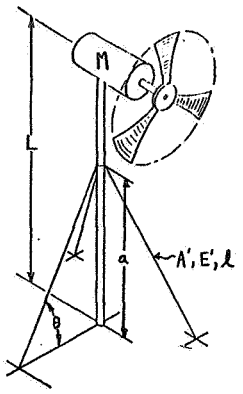

Figure 2: Guyed Tower to be Analyzed.

It is known that the Rayleigh Quotient is stationary with respect to variations in $\phi(x)$, when $\phi(x)$ is an exact mode shape for the tower. This can be shown to require that:

$$\text{Det}\,[d_{ij} - W^2 b_{ij}] = 0 \qquad \text{(Ref. 3).}$$

The problem is thus reduced to finding the N values of W^2 which make the determinant of this N x N matrix equal to zero. The N values of W give estimates for the first N frequencies of the tower.

Simple Analysis

A simple two-mode analysis for freestanding towers can be performed by using two approximating functions of the form:

$$\psi_1(\xi) = \xi^4 - 4\xi^3 + 6\xi^2$$
$$\psi_2(\xi) = 3\xi^5 - 10\xi^4 + 10\xi^3 \qquad (8)$$

The integrals d_{ij} and b_{ij} then are:

$$d_{11} = 28.800 - 4.800\beta$$
$$d_{12} = 24.000 - 6.857\beta$$
$$d_{22} = 34.286 - 12.857\beta$$
$$b_{11} = 2.3111 - 1.8540\gamma + 9.00\mu$$
$$b_{12} = 2.0698 - 1.6997\gamma + 9.00\mu$$
$$b_{22} = 1.8817 - 1.5732\gamma + 9.00\mu$$

when $\det [d_{ij} - W^2 b_{ij}]$ is evaluated, the polynomial $g(W^2)^2 - qW^2 + \ell = 0$ must be solved where:

$$g = b_{11}b_{22} - b_{12}^2$$
$$q = d_{11}b_{22} + b_{11}d_{22} - 2d_{12}b_{12} \qquad (9)$$
$$\ell = d_{11}d_{22} - d_{12}^2$$

Table II shows the results for various values of tip mass ratio and taper rates. This shows that the simple two-mode method becomes inaccurate for the second bending frequency ratios of towers with large stiffness tapers. This method gives more accurate results for the first bending frequencies compared to the results of the previous sections.

TABLE II: EXACT (W_{ie}) AND APPROXIMATE (W_{ia}) FIRST AND SECOND BENDING FREQUENCY RATIOS FOR A FREESTANDING TOWER. TWO-MODE RAYLEIGH RITZ PROCEDURE, FOR VARIOUS TAPERS AND TIP MASS RATIOS.

Uniform Stiffness, Uniform Mass: $\beta = 0$, $\gamma = 0$

μ	W_{1e}	W_{1a}	% Error	W_{2e}	W_{2a}	% Error
1.0	1.56	1.56	0.0	16.25	17.61	8.4
2.0	1.16	1.16	0.0	15.86	17.29	9.0

Unform Stiffness, Tapered Mass: $\beta = 0$, $\gamma = .9$

μ	W_{1e}	W_{1a}	% Error	W_{2e}	W_{2a}	% Error
1.0	1.68	1.70	0.6	22.37	23.56	5.3
2.0	1.21	1.21	0.0	22.17	23.00	3.7

Tapered Stiffness, Uniform Mass: $\beta = .9$, $\gamma = 0$

μ	W_{1e}	W_{1a}	% Error	W_{2e}	W_{2a}	% Error
1.0	1.33	1.37	3.0	11.81	15.36	30.1
2.0	0.98	1.02	4.1	11.53	15.06	31.0

This simple hand analysis can also be used for guyed towers, using these two approximating functions and including the guy wire stiffness effects in the terms d_{ij}. As an example, a single guyed tower with the dimensionless stiffness $\overline{Kc} = 200$ and guy level $\xi a = .8$ was examined for the first two bending frequencies. It was found that $W_1 \approx 20.16$ and $W_2 \approx 23.43$. These same results were calculated with a computer program, to be described in the next section, using a four-mode Rayleigh Ritz procedure with the results: $W_1 \approx 19.82$ and $W_2 \approx 22.45$. These results show that the simple two-mode Rayleigh Ritz procedure gives fair results for a guyed tower also.

As will now be shown, the use of more approximating ψ_i functions will improve the results of both the first and second bending mode frequencies and will also give results for the higher mode frequencies.

The Rayleigh Ritz Computer Program

The Rayleigh Ritz method can be used to determine any number of modal frequencies; however, the computational complexity increases greatly after the first two or three modes. For this reason, a computer code has been developed at Rocky Flats using four approximating functions of the form:

$$\psi_1(\xi) = \xi^4 - 4\xi^3 + 6\xi^2$$

$$\psi_2(\xi) = 3\xi^5 - 10\xi^4 + 10\xi^3$$

$$\psi_3(\xi) = 2\xi^6 - 6\xi^5 + 5\xi^4$$

$$\psi_4(\xi) = \xi^{10} - 2.5\xi^9 + 1.607\xi^8.$$

The program can be used for linear or nonlinear mass and stiffness distributions by dividing the tower into N sections (not necessarily equal) and inputting constant values of stiffness and mass along each section. Numerical integration techniques are then used to evaluate the integrals in the Rayleigh Quotient. Table III shows the improvement for the first and second bending frequency results, compared to the simple two-mode method of Table II.

TABLE III: EXACT (W_{ie}) AND APPROXIMATE (W_{ia}) FIRST AND SECOND BENDING FREQUENCY RATIOS FOR A FREESTANDING TOWER. FOUR-MODE RAYLEIGH RITZ PROCEDURE FOR VARIOUS TAPERS AND TIP MASS RATIOS.

Uniform Stiffness, Uniform Mass: $\beta = 0$, $\gamma = 0$

μ	W_{1e}	W_{1a}	% Error	W_{2e}	W_{2a}	% Error
1.0	1.56	1.56	0.0	16.25	16.26	0.1
2.0	1.16	1.16	0.0	15.86	15.88	0.1

Unform Stiffness, Tapered Mass: $\beta = 0$, $\gamma = .9$

μ	W_{1e}	W_{1a}	% Error	W_{2e}	W_{2a}	% Error
1.0	1.68	1.70	0.6	22.37	22.49	0.5
2.0	1.21	1.21	0.0	22.17	22.30	0.6

Tapered Stiffness, Uniform Mass: $\beta = .9$, $\gamma = 0$

μ	W_{1e}	W_{1a}	% Error	W_{2e}	W_{2a}	% Error
1.0	1.33	1.34	1.0	11.81	12.75	8.0
2.0	0.98	.99	1.0	11.53	12.45	8.0

The program can also be run for guyed towers, when the guy wire tension is large enough so that no coupling between the guy wire first mode and tower first mode occurs (Ref. 1).

Limitations of the Rayleigh Ritz Method

Both the simple hand method and the four-mode Rayleigh Ritz program can be used to calculate first and second mode bending frequencies for freestanding and guyed towers. The simple method gives poor results for the second bending frequencies of towers with high stiffness tapers. The more complex four-mode method can be used for towers having more complex nonlinear mass and stiffness distributions, and gives better results than the two-mode method, for highly tapered towers. The disadvantage of this method is that a computer must be used.

A code for a TI-59 programmable calculator has been developed to handle towers with nonlinear mass and stiffness distributions.

Program TUSF (Turbine System Frequencies)

The two-mode Rayleigh Ritz procedure covered above can only be used for towers which have approximately linear mass and stiffness distributions. For towers with nonlinear distributions, this method would be hard to use, because the integrals in the Rayleigh Ritz Method would be too hard to evaluate.

To circumvent this difficulty, a method similar to the Rayleigh Ritz procedure has been developed for towers with nonlinear mass and stiffness (Ref. 6). The tower can be divided into N sections and constant values of mass and stiffness are input along each sigment. Numerical integration techniques are then used to find the natural frequencies (Ref. 7).

In the techniques described previously, the nacelle and rotor were modeled as a single lumped mass at the tower top. This program includes the effects of rotor moments of inertia and nacelle-rotor C.G. location on the system frequencies. In addition, the effects of rotor spin rate on the natural frequencies are taken into account.

The program treats the tower as a flexible member and the nacelle and rotor as rigid bodies. It will be shown in the section on comparisons of analytical results to test results that the accuracy of results from this program are similar to the accuracy of results from the Rayleigh Ritz procedure, i.e., the results for the second bending frequencies are less accurate than the first bending frequencies.

In the approximate methods discussed above, an infinite degree of freedom structure is modeled as a beam having finite degrees of freedom. It can be shown that this causes the frequency estimates from these methods to be higher than the exact values (Ref. 6). A method using more degrees of freedom (such as SAPIV) gives more accurate frequency estimates.

In the next section, the test procedures and results for two types of towers will be presented. In the section on comparisons of analytical results to test results these simple methods, for these towers, will be compared. The results from more accurate structural codes (such as SAPIV) will also be shown. A recommendation as to which tower types can be analyzed, using the simple method, will also be given.

TEST PROCEDURES AND RESULTS

Objectives

This section deals specifically with the test methods and results for a Rohn 25G single guyed tower and a Rohn SSV freestanding tower. Impact tests were performed on each tower to determine the predominant modes of vibration and to compare the test results with various analytical methods.

Test Description and Theory

A technique currently being used at the Rocky Flats Test Center, for dynamic testing, is commonly known as impact testing. The structure can be excited with an impulse. This can be accomplished with the use of a hammer with a load cell attached, thereby exciting the structure with a known input, as shown in Figure 3.

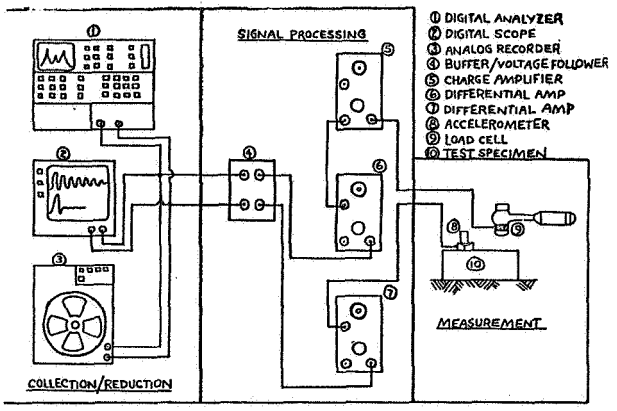

Figure 3.

With the load cell, the input force can be accurately measured; the response of the structure can be measured with the use of an accelerometer. Provided the input and response signals are fourier transformable (Ref. 2), the frequency response function can be computed.

In practice, better results are obtained by computing frequency response functions as a ratio of the cross spectrum between the input and output, to the power spectrum of the input (Ref. 2). This is useful in eliminating the effects of noise on the input and output signal measurements. If the input and output noise is noncoherent, the effects on the cross spectrum, involving the noise, will yield zero.

Test Specimens and Test Results

A Rohn 25G Single Guyed Tower

Figure 4 shows a Rohn 25G 40-ft guyed tower. The tower has constant mass and stiffness distributions as given in Table IV. The tower stiffness distribution was determined by first finding the moment of inertia of a tower cross section about the centroid, as shown in Figure 5. Because the distance between the tower legs remains constant, for various heights, the moment of inertia and thus the stiffness distribution remains constant. The mass distribution also is constant, since the weight and length of each tower section is the same. The effects of the cross braces have been neglected in the stiffness determination, but have been included in the mass distribution.

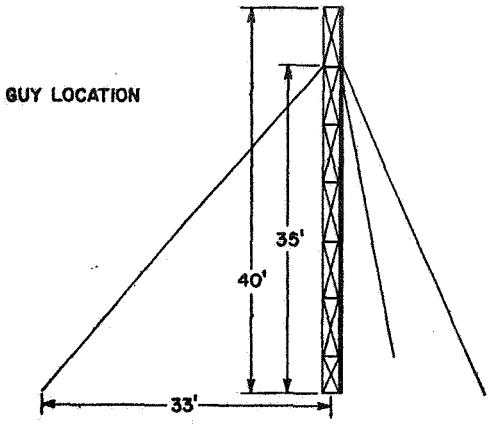

Figure 4.

TABLE IV: ROHN 25G PARAMETERS

Tower Height (L)	40.0 ft
Stiffness Distribution (EI)	3.14×10^6 lb-ft^2
Mass Distribution (ρA)	0.124 lb-s^2/ft^2
Tower Top Mass (M)	10.87 lb-s^2/ft^2
Guy Wire Attachment Level (a)	35.0 ft
Guy Wire Cross Sectional Area (A')	0.00015 ft^2
Guy Wire Elastic Modulus (E')	2.88×10^9 lb/ft^2
Guy Wire Length (ℓ)	48.45 ft
Guy Wire Stiffness Coefficient (Kc)	6365.76 lb/ft

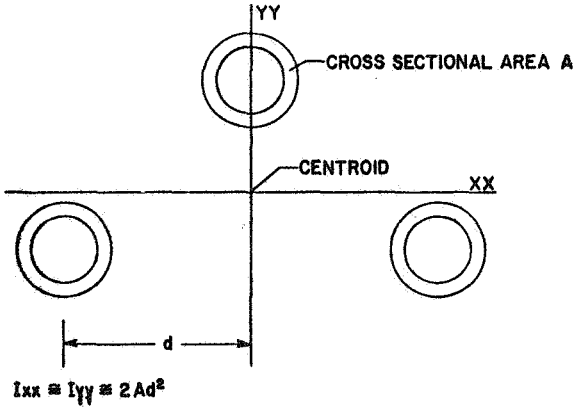

Figure 5.

The Rohn 25G was tested without a machine on top, but with the addition of 380 lb on the tower top. Table V shows the test results, using the impact testing methods. In this case, the three guy wires were tensioned sufficiently so that each had nearly the same fundamental frequency. As can be seen from Table V, the guy fundamental frequency was well separated from the tower first bending frequency, so that resonance between the guy wires and tower was not a problem (Ref. 1).

As will be shown in the next section, the simple methods can be used to get good estimates for the first bending frequencies for this tower.

TABLE V: ROHN 25G TEST RESULTS

First Mode Bending	2.6 Hz
First Mode Torsional	5.7 Hz
Second Mode Bending	7.8 Hz
Guy Wire Fundamental	6.9 Hz

A Rohn SSV Freestanding Tower

Figure 6 shows a 60-ft Rohn SSV freestanding tower. Unlike the Rohn 25G, the distance between tower legs decreases with increasing tower height. The stiffness distribution thus decreases from base to height. Figure 6 shows a plot of the mass and stiffness distribution for this tower. The mass distribution is nearly uniform, but the stiffness distribution tapers to 0.023 of the value at the tower base.

The Rohn SSV was tested without a machine on top but with a top plate of approximately 30 lb. As will be shown in the next section, accurate estimation of the first and second bending frequencies for this tower is difficult, using

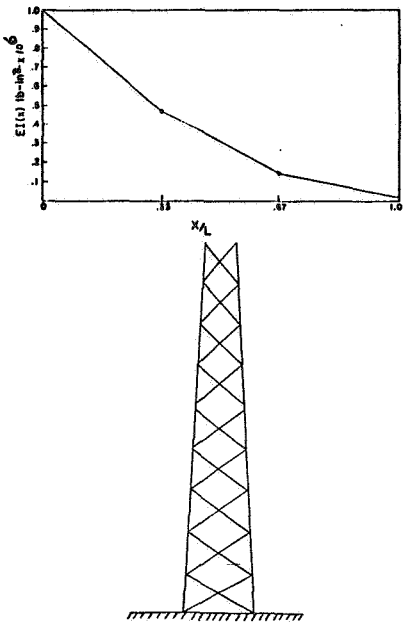

Figure 6.

the simple methods, because of the large stiffness taper. Also, the effects of the cross-members were neglected in the moment of inertia calculations, which poses further difficulties. Table VI shows the test results for the first two bending frequencies.

TABLE VI: ROHN SSV TEST RESULTS

First Mode Bending	3.3 Hz
Second Mode Bending	12.7 Hz

COMPARISONS OF ANALYTICAL RESULTS TO TEST RESULTS

In this section the results from the simple analysis methods and results from complex methods such as SAPIV (Ref. 5) will be compared to test results for the two towers presented in the previous section. A recommendation of the use and accuracy of the simple methods will be made.

Rohn 25G Results Summary

Table VII shows the results for the Rohn 25G. The simple two-mode Rayleigh Ritz method, a hand method, gives fair results for the first frequency (p_1), but poor results for the second frequency (p_2). The utility of this method is that it can be used to obtain a rough estimate, by hand calculations, for the first bending frequency of guyed or freestanding towers. This method gives less accurate results for towers with large stiffness tapers, however.

TABLE VII: ROHN 25G RESULTS SUMMARY

Method	p_1	Error	p_2	Error
Test	2.6	0.0%	7.8	0%
R-R-2 Mode	2.8	7.7%	9.0	16%
Program TUSF	2.6	0.0%	11.2	44%
R-R-4 Mode	2.6	0.0%	8.6	10%
MITGUY	2.6	0.0%	8.6	10%

Program TUSF, a hand calculator code, gives much more accurate results for the first mode. This code can also be used to determine the first bending frequency of towers with nonlinear mass and stiffness distributions, without use of a large computer.

The Rayleigh Ritz four-mode procedure, a small computer code developed at Rocky Flats, gives excellent results for the first mode and fair results for the second mode, while Program MITGUY (Ref. 4), a program utilizing matrix iteration methods, gives about the same results (to one decimal place).

The 10 percent inaccuracy in the second mode results is thought to be caused because of neglect of the cross-members in determination of the tower bending stiffness. This difficulty will be emphasized in the comparison of results for the Rohn SSV, to be shown next, in which use of the complex code SAPIV, which models the tower cross-members, is necessary.

Rohn SSV Results Summary

Table VIII shows the results for the Rohn SSV tower. The analysis of the Rohn SSV with the simple hand methods of the Rayleigh Method and Two-Mode Rayleigh Ritz Method is difficult, because the stiffness and mass distributions are nonlinear. For these analyses, the mass distribution was assumed constant, with a value equal to the base value. The stiffness distribution was approximated as linear, with a value of the taper rate β equal to 0.98. The resulting frequency estimates are too high, because the actual stiffness of the tower is less than what is given by this straight line approximation.

TABLE VIII: ROHN SSV RESULTS SUMMARY

Method	p_1	Error	p_2	Error
Test	3.3	0%	12.7	0%
Rayleigh	3.8	19%	--	--
R-R-2 Mode	3.6	12%	22.3	76%
Program TUSF	3.5	9%	16.3	28%
R-R-4 Mode	3.4	6%	15.5	22%
MITGUY	3.4	6%	14.8	17%
SAPIV	3.1	3%	13.0	2.4%

For towers with nonlinear mass and stiffness distributions, the program TUSF and the four-mode Rayleigh Ritz procedure can be used to find more accurate values of the first bending frequencies. The tower can be divided into N sections and constant values of mass and stiffness input along each segment. It was found that about 20 segments were needed in order to model the large stiffness taper correctly.

From Table VIII it can be seen that the second bending frequency results from: 1) the simple methods, and 2) the program MITGUY are in error by more than 17%. For this reason, the complex code SAPIV (Ref. 5) was used to model this tower, taking into account the effects of each cross-member. The improvement in the second bending frequency is very evident.

In the simple methods, as well as MITGUY, this tower was modeled as a beam, neglecting the effects of the cross-members in the bending stiffness. The cross-section moment of inertia was calculated, by taking into account the three legs only, as shown in Figure 5. The actual stiffness distribution of this tower is more complicated than this approximation because of the cross-members.

In the simple methods section it was shown that they give less accurate results for a beam with large stiffness tapers. For this truss-type of tower, this error is increased because the actual tower stiffness is more complicated than that of a beam in which the cross-members have been neglected.

CONCLUSION AND RECOMMENDATIONS

The simple methods can be used to determine good estimates of the first bending frequencies and rough estimates of the second frequencies of towers with uniform mass and stiffness distributions. Guyed towers can also be analyzed, using these methods, if the guy wire fundamental frequency is well separated from the tower first bending frequency so that guy wire-tower interaction will not occur.

For towers with high stiffness tapers, or stiffness distributions which are hard to determine accurately, more complex codes such as SAPIV may be needed, especially for accurate determination of the second and higher bending frequency.

REFERENCES

1. Butterfield, C. P., Pykkonen, K. R., and Sexton, J. H., Effects of Guy Wires on SWECS Tower Dynamics, Rockwell International, Rocky Flats, Technical Memorandum, July, 1980.

2. Halverson, W. G. and Brown, D. L., "Impulse Techniques for Structural Frequency Response Testing," Sound and Vibration, November, 1977, pp. 8-21.

3. Meirovitch, L., Elements of Vibration Analysis, New York, McGraw-Hill Book Company, 1975.

4. Miller, R. H., et. al, Wind Energy Conversion, Massachusetts Institute of Technology, ASRL-TR-184-7, Vol. 1.

5. SAP-IV, "A Structural Analysis Program for Static and Dynamic Response of Linear Systems," University of Southern California, Department of Civil Engineering.

6. Thresher, R. W. and Smith, C. E., "Free Vibration Approximations of Horizontal Axis Wind Turbines," Oregon State University, Department of Mechanical Engineering.

7. Thresher, R. W., "Inertia and Stiffness Coefficients of Wind Turbines," and "Natural Frequencies of Wind Turbine Systems," Oregon State University, Department of Mechanical Engineering.

8. Wright, A. D., et. al, "Vibration Modes of Centrifugally-Stiffened Beams," Journal of Applied Mechanics (to appear).

NOMENCLATURE

a	:	Guy wire attachment level.
A'	:	Guy cable cross-sectional area.
E'	:	Guy cable elastic modulus.
EI(x)	:	Tower stiffness at station x.
EI_0	:	Tower stiffness at the base.
$f(\xi)$	:	$EI(L\xi)/EI_0$
$h(\xi)$	:	$\rho A(L\xi)/\rho A_0$
Kc	:	Guy wire stiffness coefficient.
$\overline{Kc}$	:	Dimensionless form of Kc: $\overline{Kc} = \frac{KcL^3}{EI_0}$
L	:	Tower height.
ℓ	:	Guy cable length.
M	:	Lumped mass at tower top.
p	:	Bending frequency (rad/sec) or (Hz).
t	:	Time (sec.).
v(x,t)	:	Tower deflection.
W	:	Dimensionless frequency.
A_i	:	Coefficients in approximate mode shape.
ψ_i	:	Functions for approximating mode shapes.
β	:	Rate of decrease of linear stiffness.
γ	:	Rate of decrease of linear mass distribution.
ξ	:	X/L.
ξ_a	:	a/L.
θ	:	Angle guy cable makes with ground.
μ	:	Tip mass ratio: $M/\rho A_0 L$.
$\rho A(x)$	:	Mass distribution of tower at section x.
ρA_0	:	Mass distribution of tower at tower base.
$\phi(x)$	:	Tower mode shape.

QUESTIONS AND ANSWERS

A.D. Wright

From: G. Beaulieu

Q: 1) Don't you believe that direct solution of 4th order differential equation would give more accurate mode shape and frequencies?

2) Did you take into account the rotary inertia of the rather large top mass?

A: *1) The direct solution of the beam governing equation would probably give more accurate results. The main emphasis of this paper, however, has been the use of some simple methods, such as the Rayleigh-Ritz method as a hand calculator code, such as program TUSF.*

2) For the two towers presented in the paper, a Rohr 55V and a Rohr 25G, the rotary inertia effects were neglected in the analysis results. These effects could be easily taken into account, in the simple methods, by adding the appropriate term to the kinetic energy.

From: F.W. Perkins

Q: How do you determine a priori the location of nodes for higher mode analysis using Rayleigh's method?

A: *For towers with complex mass and stiffness distributions, the precise mode shape, a priori, is difficult if not impossible to determine. The nodal points are therefore unknown. In the Rayleigh or Rayleigh Ritz procedure we choose a shape which we hope approximates the true mode shape. If the resulting frequency estimate, using this assumed shape, is inaccurate compared to test results, a better mode shape approximation is needed.*

GUY CABLE DESIGN AND DAMPING FOR VERTICAL AXIS WIND TURBINES

Thomas G. Carne
Sandia National Laboratories
Division 5523
Albuquerque, New Mexico 87185

ABSTRACT

Guy cables are frequently used to support vertical axis wind turbines since guying the turbine reduces some of the structural requirements on the tower. The guys must be designed to provide both the required strength and the required stiffness at the top of the turbine. The axial load which the guys apply to the tower, bearings, and foundations is an undesirable consequence of using guys to support the turbine. Limiting the axial load so that it does not significantly affect the cost of the turbine is an important objective of the cable design. The lateral vibrations of the cables is another feature of the cable design which needs to be considered. These aspects of the cable design are discussed in this paper, and a technique for damping cable vibrations is mathematically analyzed and demonstrated with experimental data.

INTRODUCTION

Most vertical axis wind turbines use guy cable to support the top of a single, fully rotating central tower. Other designs, such a cantilevered tower or two concentric towers (one stationary to react cable loads) have been found to be, generally, less cost effective. The guy cables serve two primary functions while supporting the turbine. They provide the strength necessary to hold the turbine during hurricane winds, and they provide the stiffness at the top of the rotor. The strength and stiffness requirements are not competing design objectives, however, one or the other may "drive" the various parameters involved in the cable design.

There are two important consequences of using guy cables to support the rotor. First, since guys have an initial tension, the vertical component of the tension is reacted through the tower, the foundation and, in this case, the bearings. This axial load imposed by the guys impacts the cost of these components. The second consequence of the guy support is lateral vibrations of the cables. Cable vibration will be excited by the motion of the top of the turbine while it is operating. There is always excitation to the cables as long as the turbine is operating in wind. If the excitation frequency is near one of the cable natural frequencies, then the amplitude of vibration can be quite large. Large amplitude cable vibrations need to be avoided in order to reduce fatigue in the cables and their terminations and also to maintain a reasonable blade/cable clearance distance. Other aspects of the cable design, which include the cable sag, the required blade/cable clearance distance, thermal expansion effects, and cable anchors, are discussed in some detail in Ref. 1-5.

DESIGN GUIDELINES

There are a number of cable parameters which have to be chosen in order to establish the design for the guys. These parameters are the cross-sectional area of a cable, the number of cables, the length of the cables, the pretension of the cables, the cable elevation angle, and the cable material (density and modulus). All of these parameters affect the two key design requirements on the guys, their support strength and the stiffness they create at the top of the turbine [Ref. 3]. These cable parameters also affect the consequences of the cable design which include lateral cable vibrations, cable sag, and the resulting axial load on the turbine due to the tension in the guys [Ref. 3].

The strength requirement on the guys is the easiest to specify. The cross-sectional area of the cables must be sufficiently large to support the turbine during parked survival in hurricane winds without the tension in the cables exceeding their ultimate strength divided by a factor of safety. A factor of safety of at least three is recommended for cables with an expected life of thirty years. This factor of safety is not conservative when compared to other cable applications and should be increased if the turbine will be placed in an environment which is particularly harsh for corrosion. The tension in cables during the parked survival condition will be the initial tension plus the increase (or decrease) due to the wind drag on the turbine. Thus the value of the initial tension will affect the cable tension during parked survival unless the initial tension is sufficiently low that the downwind

cable goes slack during the hurricane winds.

The stiffness requirement for the guys is impossible to generalize for all turbine designs. The required stiffness will have to be chosen interactively with the rest of the turbine design. This is due to the fact that the stiffness at the top of the turbine affects the frequencies of the natural modes of vibration. However, these frequencies are also controlled by the whole turbine structure especially the blades and the tower. Consequently, depending on the desirable values for these modal frequencies, the operational frequency of the turbine, and the structural properties of the turbine, the guy cable stiffness will have to be chosen accordingly.

Figure 1 shows the variation in the modal frequencies with the guy stiffness for the 17-Meter Low Cost Turbine. Examining this figure, one can see that some of the modes are quite sensitive to the guy stiffness. Further, we can see that, in order to keep the modal frequencies away from the excitation frequencies, the guy stiffness is forced to be greater than three k.

Another consideration for choosing the cable stiffness is the allowable angle change for the bearings at the bottom of the rotor. If the bearing can only allow a small angle change of the rotor, then the cable stiffness will have to be sufficiently high to restrain the rotor from leaning. However, if a universal joint is used to protect the bearing or some more tolerant bearing design is used, then this constraint on the stiffness will not apply.

The frequencies of lateral vibrations of the guy cables are a consequence of the guy design, and they can place a constraint on the design. The natural frequencies of vibration of the cables are $f_n = n(T/\rho A)^{\frac{1}{2}}/2L$ [Ref. 3] where n is the mode number, L is the cable length, T is the guy tension, A is the cable cross-sectional area, and ρ is the mass density. In many designs these parameters cannot be chosen so that the first cable frequency is above the excitation frequency of 2.0/rev (for a two bladed turbine) since that would force the tension to be larger than would otherwise be desirable. Further, since the tension in the cables vary with the wind velocity and temperature, it may not be possible to completely avoid all cable resonances

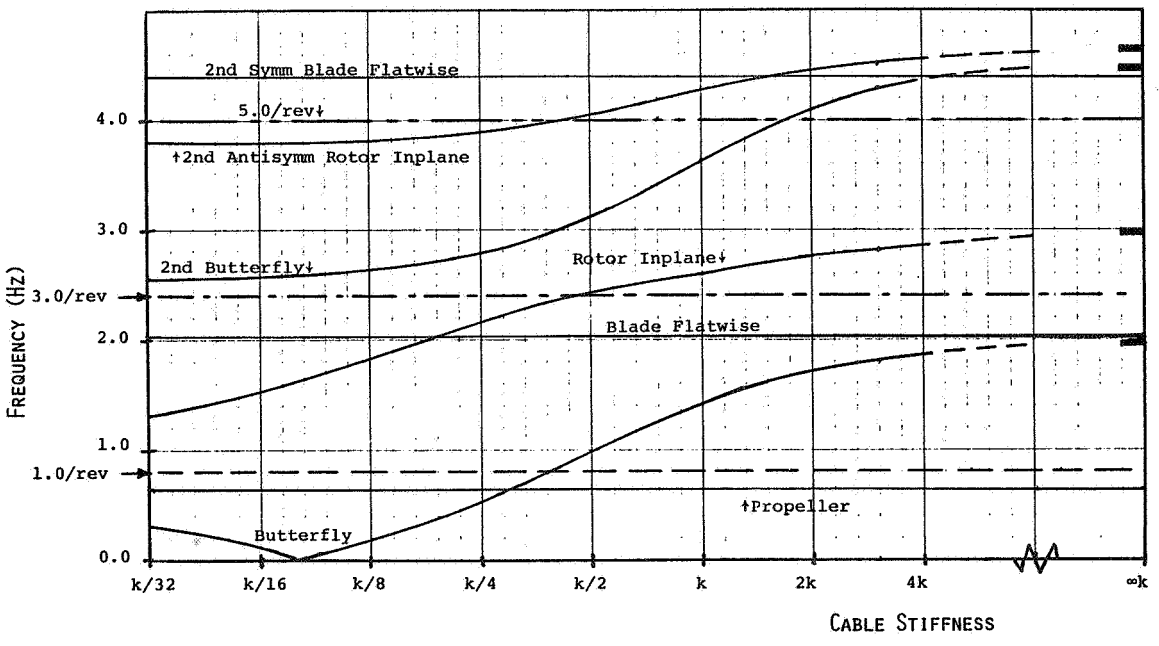

FIGURE 1 - MODAL FREQUENCIES VERSUS CABLE STIFFNESS
K = 4440 LBS/IN, SPEED = 48.1 RPM

in any case. The cable vibration problem is discussed in the last section of this paper and a technique for restraining the vibrations is analyzed and demonstrated.

The sag of the guy cables is another consequence of the guy design, and it must be evaluated and compared with the blades/cable clearance distance. If the sag is too large for available clearance, then the cable design will have to be changed. More discussion of the clearance requirements can be found in Ref. 3.

The axial load which is applied to the turbine by the guys can be the most serious consequence of the guy design. Reducing the axial load within the constraints of the design will reduce the cost of the turbine. Nellums in Ref. 6 has shown that reductions in the costs of the bearings and tower result from reducing the cable imposed axial load for a 150 foot tall turbine. Foundation costs would also be reduced.

The axial load is simply the total of the guy tensions times the sine of the cable elevation angle at the top of the turbine. Reducing either the tension or the elevation angle will reduce the axial load. However, both of these changes also decrease the guy stiffness, so the required stiffness will restrict the design choices. It can be shown that to obtain a minimum axial load, for a given stiffness, the elevation angle should be 35.3 degrees.

The axial load on the turbine will change as the guy tensions change, so during the hurricane survival the axial load may increase. Depending on the tower and bearings designs, an increase in the axial load during the parked survival condition may or may not affect the cost of these components.

In view of the requirements and consequences of the cable design, it is clear that the design process must be iterative and interactive with the total turbine design. The starting point for the cable design must be the strength requirement. Then, using an elevation angle of thirty-five degrees, determine a tension and an area for the stiffness requirement. This new area and tension will then be factored back into the strength requirment, and then the stiffness reevaluated, and during this design iteration the axial load, cable sag, and cable natural frequencies need to be computed and evaluated for acceptability.

CABLE VIBRATIONS

If the design of the guys results in the first cable frequency being less than n per rev where n is the number of blades, then lateral vibrations of the cables can result. Excessive cable vibration could cause a blade strike or fatigue the cable terminations or anchors. Excitation of the cables always exists since the top of the rotor moves while it is operating, and the cables have exceptionally low inherent damping (less than 0.2 percent of critical), so very high resonant responses can result. Experience has shown that if the first cable frequency is above the primary excitation frequency, n per rev, then there is no problem with cable vibrations. However, keeping cable frequencies that high can be costly, particularly for large turbines.

There are two direct solutions to alleviate the cable vibration problem. One is to constrain the cable so that the cable modes are shifted to a higher frequency. This can be done by forcing one or more nodal points along the span of the cable. The other solution would be to add damping to the cable so that resonant responses, when they occur, would be limited in magnitude.

The rest of this paper will discuss a cable damping system which was developed for this purpose.

The concept for the dampers utilizes Coulomb friction to dissipate the energy. It is simply a pair of weights which are suspended from the cable and slide on two inclined surfaces whenever the cable moves. The two surfaces are at right angles to each other and at right angles to the cable, thus they can damp the motion of any lateral cable vibration. The dampers can be placed near the anchors so that they are out-of-the-way. They can be built inexpensively and require no power to operate them. They could be designed to require very little maintenance and be very reliable. Figure 2 shows a diagram of the damping concept with just one friction surface shown, omitting the other for clarity purposes.

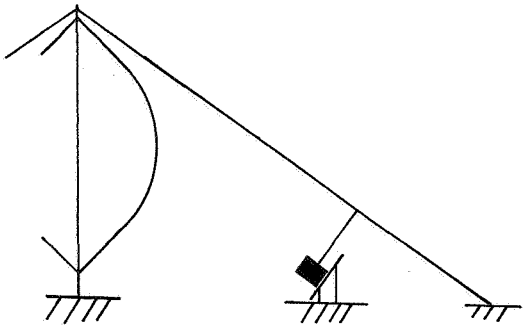

FIGURE 2 - DIAGRAM OF CABLE DAMPING CONCEPT

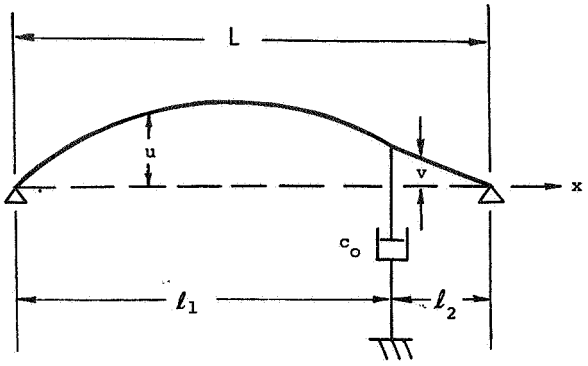

FIGURE 3 - DIAGRAM OF CABLE WITH DAMPER

In order to determine the size, weights, and spacing of this damping concept, an analysis for the damping was performed and is described very briefly below. Figure 3 shows a diagram of the physical system that will be anaylzed with the indicated notation. We will consider motion in only one plane since the out-of-plane motion is uncoupled. Our interest is the modal damping in the cable, so we can consider the homogeneous differential equation and boundary conditions.

$$\rho\ddot{u}(x, t) - T\, u''(x, t) = 0 \quad \text{for } 0 < x < \ell_1 \text{ and} \tag{1}$$

$$\rho\ddot{v}(x, t) - T\, v''(x, t) = 0 \quad \text{for } \ell_1 < x < L \ , \tag{2}$$

where ρ is the mass per unit length, T is the tension, u and v are the displacments, and the dots represent differentiation with respect to time and the primes with respect to x. The boundary conditions and continuity conditions are

$$u(0, t) = v(L, t) = 0 \ , \tag{3}$$

$$u(\ell_1, t) = v(\ell_1, t) \ , \tag{4}$$

and

$$T[v'(\ell_1, t) - u'(\ell_1, t)] = c_o\dot{u}(\ell_1, t) , \tag{5}$$

where c_o is the viscous damping coefficient. If we take ℓ_2 to be much less than ℓ_1, then v" can be approximated by zero; and the coupled differential equations can be reduced to one differential equation with an inhomogeneous boundary condition. Using separation of variables and assuming sinusoidal motion in the standard way leads to a transcendental equation for the eigenfrequencies, except in this case, the frequencies are complex because of the damping.

$$\frac{\ell_1}{\ell_2}\frac{\tan\beta}{\beta} + i\, c \tan\beta + 1 = 0 \ , \tag{6}$$

where

$$\beta = \frac{\omega}{\frac{1}{\ell_1}\sqrt{T/\rho}} \ ,$$

$$c = c_o/\sqrt{T\rho} \ ,$$

and ω is the natural frequency of vibration. Equation (6) can be solved approximately for the damping coefficient in the first mode, and we find

$$\zeta = \frac{\pi\, c\, \lambda^2}{1 + \pi^2\, c^2\, \lambda^2} \tag{7}$$

where

$$\lambda = \ell_2/L \ .$$

Equation (7) reveals some reassuring behavior. When c is zero or when c is infinity, the damping coefficient is zero as one would expect physically. Consequently ζ is a maximum at some intermediate value of c. This is easily computed and

$$\zeta_{max} = \lambda/2 \text{ at } c = 1/\pi\lambda \tag{8}$$

Figure 4 shows a series of plots of the damping coefficient ζ as a function of c for various values of λ. One can see the maxima of ζ shift as λ is increased. Also note that the curves become steeper near the maximum ζ with increasing λ.

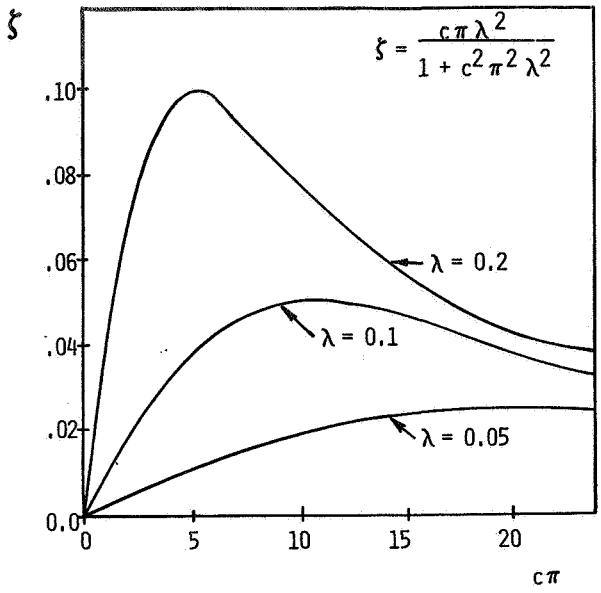

FIGURE 4 - THE VARIATION IN DAMPING FACTOR WITH VISCOUS DAMPING COEFFICIENT

The magnitude of the damping coefficient that can be obtained with this system appears quite attractive. With the damping system connected to the cable one-tenth of the distance along the cable ($\lambda = 0.1$), damping values as high as five percent of critical can be obtained. Even if only two percent damping were achieved, this still represents an increase by a factor of ten over the damping inherently in the cables.

The analysis of the cable damping was performed assuming viscous damping, but the actual damping mechanism is Coulomb friction. By equating the energy dissipated in one cycle of the viscous damper to that of the friction damper, a relationship between the viscous coefficient and friction coefficient can be obtained. The energy dissipated in one cycle is

$$U_D = \int_0^{2\pi/\omega} F_D \cdot \dot{u}\, dt$$

where F_D is the damping force. Evaluating U_D for both the viscous damping and the friction damping and equating the results, we find that the sliding weight W which must be suspended by the cable for the same energy dissipation is

$$W = \frac{c_o\, \pi\, \omega\, u(x_o)}{4\, \mu\, \cos\, \gamma} \qquad (9)$$

where μ is the friction coefficient, γ is the elevation angle of the friction surface, and $u(x_o)$ is the displacement of the cable at the attachment point. Equation (9) reveals the basic nonlinearity of friction damping as opposed to viscous damping; the weight required for equivalent damping is proportional to the displacement $u(x_o)$. Thus, the equivalent c_o goes down with increasing amplitude and goes up with decreasing amplitude. Consequently, an anticipated displacement $u(x_o)$ must be known before an equivalent weight W can be calculated. This nonlinearity also reveals itself when the cable motion is small, then the equivalent c_o is large, and the damper creates a large force relative to the elastic force at the connection. This force just drives a node point and the energy dissipation goes to zero.

This damping scheme was tested on the 17-Meter Research Turbine at Sandia National Laboratories in order to determine the effect of the damping on the cable vibrations. A single pair of friction dampers at right angles were connected to just one of the four guy cables four meters from the cable end ($\lambda = 0.1$). A pair of 18 kg weights were used as the sliding elements. The surfaces were inclined at thirty-five degree from the horizontal and had a friction coefficient $\mu = 0.20$. The size, mass, and location of these dampers were quite reasonable and should have yielded between two to five percent damping depending on the amplitude of the cable motion.

Acceleration measurements were taken on the cable in the horizontal and vertical directions while the turbine was operating in a variety of wind speeds. The acceleration data was analyzed using the Method of Bins [Ref. 7] so that the rms acceleration amplitude could be plotted as a function of wind speed. One would expect the cable vibrations to increase with wind speed since the excitation increases. Measurements were taken with and without the damping system connected and at three different cable tensions, T_1, T_2, and T_3.

The highest tension, T_1 = 80 kN, caused the first cable frequency to be about twenty percent higher than two per rev; the second tension, T_2 = 54 kN, produced a cable frequency very near two per rev; and the third tension, T_3 = 27 kN, created a cable frequency at about seventy percent of two per rev. The Bins data for the horizontal and vertical accelerations with the three tensions are shown in Figures 5-14. The first five figures are the horizontal acceleration plots:

Tension 1 without damping, Tension 2 without damping, Tension 2 with damping, Tension 3 without damping, and Tension 3 with damping. The last five figures are the vertical acceleration plots in that same order. Note the tremendous difference in the acceleration levels between Figs. 5 and 6, and then adding the damper in Fig. 7 brings the acceleration levels back down to the levels of Fig. 5. Figs. 8 and 9 are the undamped and damped cases for tension T_3. There is hardly any difference between the plots. This is the expected result since this case is not a resonant response, but merely a forced response, and damping does very little unless a resonance exists. Figs 10-14 show the same data but for the vertical direction. The same trends are exhibited in these figures.

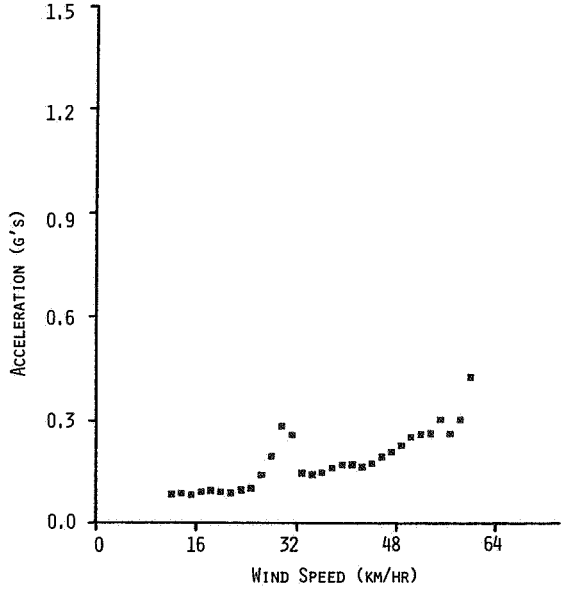

FIGURE 5 - CABLE HORIZONTAL ACCELERATION VERSUS WIND SPEED FOR TENSION 1, UNDAMPED

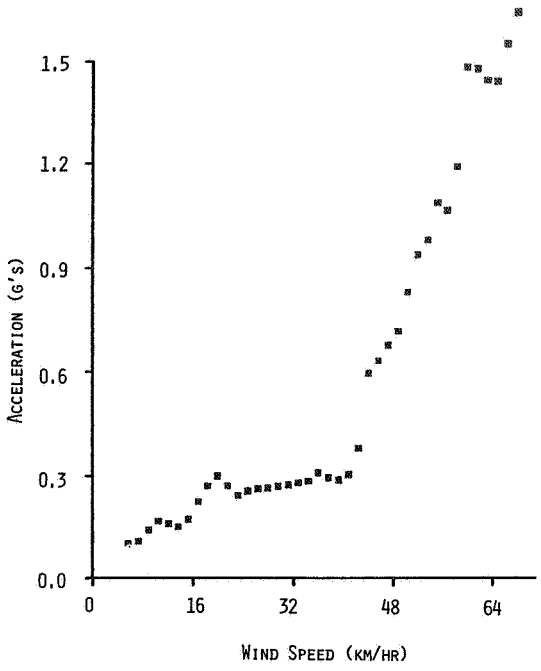

FIGURE 6 - CABLE HORIZONTAL ACCELERATION VERSUS WIND SPEED FOR TENSION 2, UNDAMPED

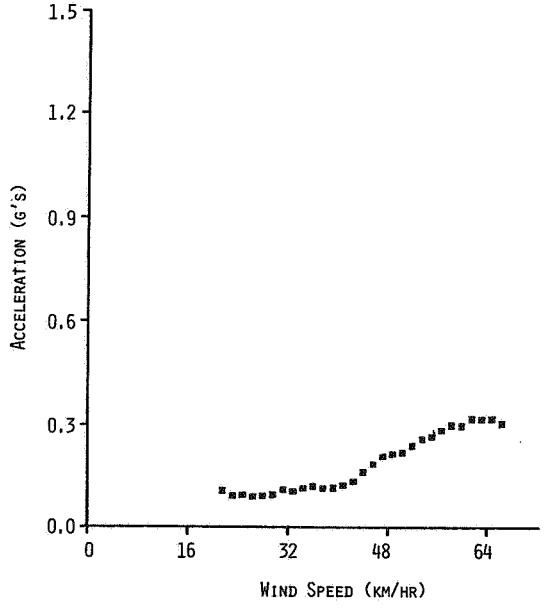

FIGURE 7 - CABLE HORIZONTAL ACCELERATION VERSUS WIND SPEED FOR TENSION 2, DAMPED

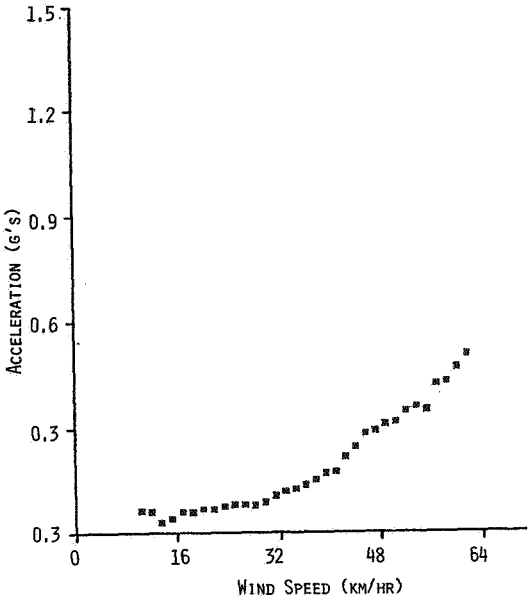

FIGURE 8 - CABLE HORIZONTAL ACCELERATION VERSUS WIND SPEED FOR TENSION 3, UNDAMPED

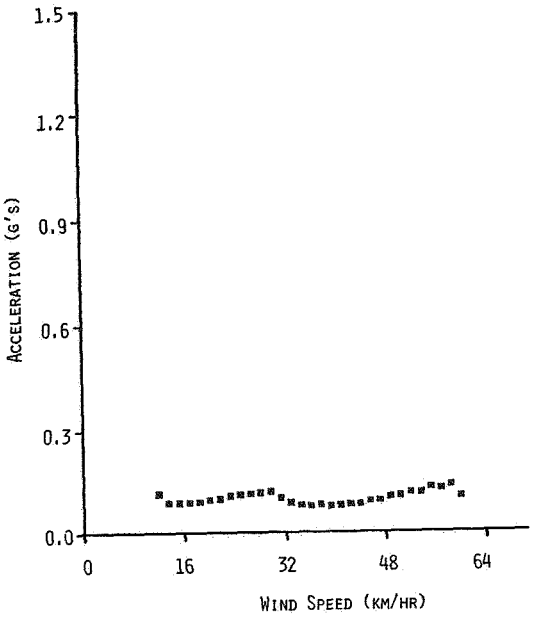

FIGURE 10 - CABLE VERTICAL ACCELERATION VERSUS WIND SPEED FOR TENSION 1, UNDAMPED

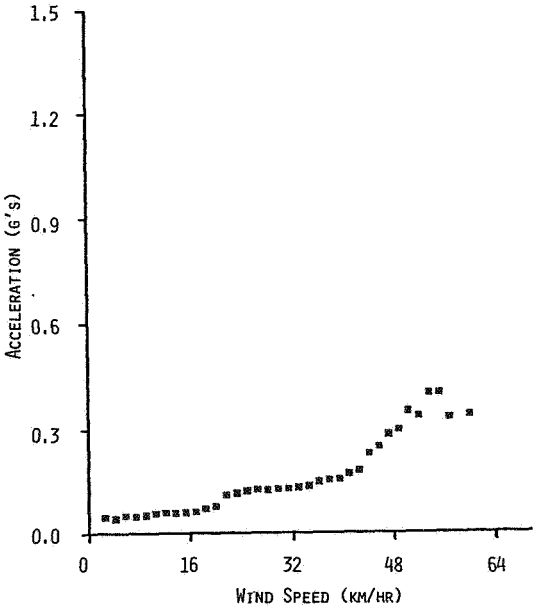

FIGURE 9 - CABLE HORIZONTAL ACCELERATION VERSUS WIND SPEED FOR TENSION 3, DAMPED

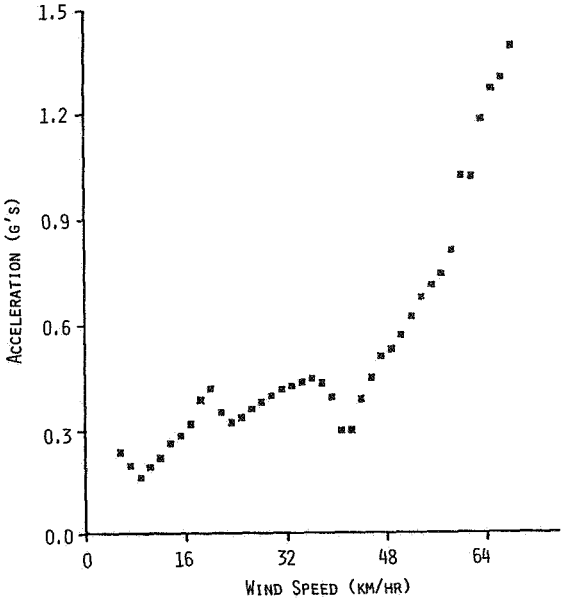

FIGURE 11 - CABLE VERTICAL ACCELERATION VERSUS WIND SPEED FOR TENSION 2, UNDAMPED

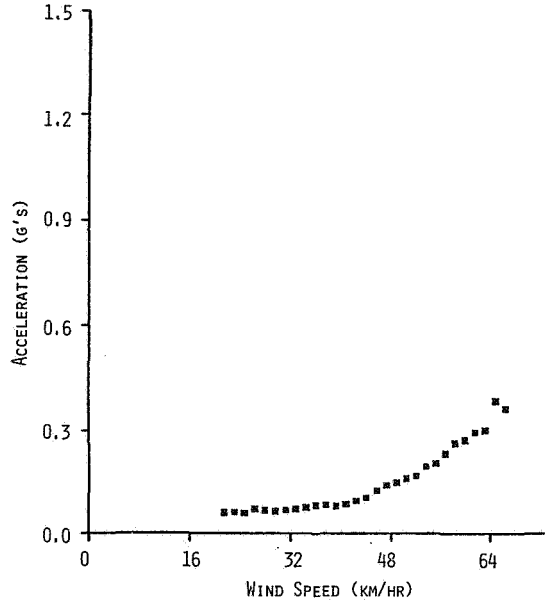

FIGURE 12 - CABLE VERTICAL ACCELERATION VERSUS WIND SPEED FOR TENSION 2, DAMPED

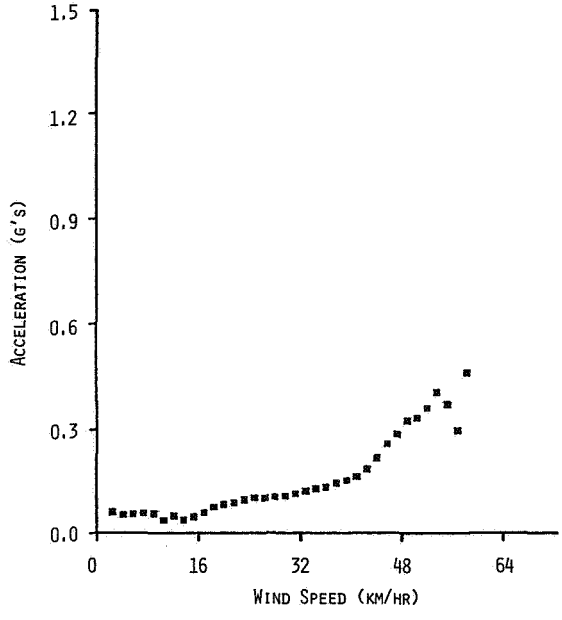

FIGURE 14 - CABLE VERTICAL ACCELERATION VERSUS WIND SPEED FOR TENSION 3, DAMPED

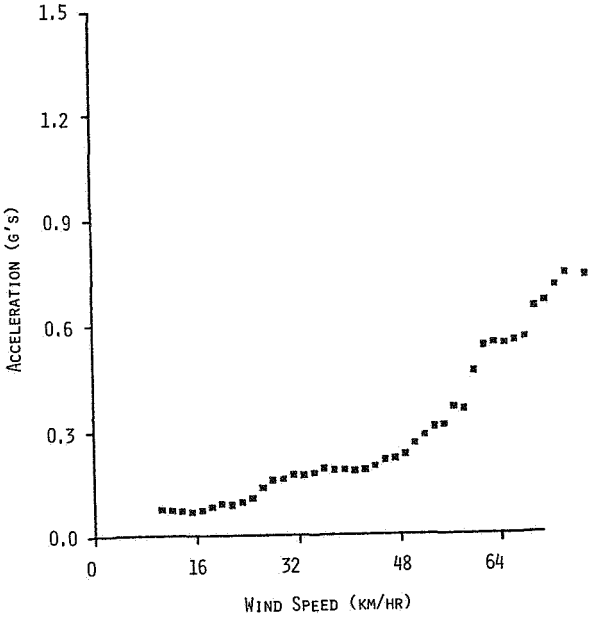

FIGURE 13 - CABLE VERTICAL ACCELERATION VERSUS WIND SPEED FOR TENSION 3, UNDAMPED

CONCLUSIONS

The design of the guy cables is not a straightforward process. It must be iterative since there are multiple requirements and constraints, and it must be interactive with the rest of the structural design since the cable stiffness affects the modal frequencies.

The cable damping concept demonstrated here appears to work quite well in reducing resonant vibrations of the cables. The system appears simple to design and install. Consequently, this system or something similar can be used to eliminate the constraint of cable vibrations on the design of the guys.

ACKNOWLEDGEMENTS

G. M. McNerney collected and processed all of the acceleration data for the Bins plots, and his contributions were essential to this work. R. O. Nellums' discussions with me were most helpful and are acknowledged.

REFERENCES

1. Reuter, R. C., Jr., Tie-Down Cable Selection and Initial Tensioning for the Sandia 17-Meter Vertical Axis Wind Turbine, SAND 76-0616 (Albuquerque, NM: Sandia National Laboratories, 1977).

2. Reuter, R. C., Jr., Vertical Axis Wind Turbine Tie-Down Design with an Example, SAND77-1919 (Albuquerque, NM: Sandia National Laboratories, 1977).

3. Carne, T. G., "Guy Cable and Foundation Design Techniques," SAND80-0984, Proceedings of the Vertical Axis Wind Turbine (VAWT) Design Technology Seminar for Industry,(Albuquerque, NM: Sandia National Laboratories, 1980).

4. Auld, H. E. and Lodde, P. F., A Study of Foundation/Anchor Requirements for Prototype Vertical-Axis Wind Turbines, SAND78-7046 (Albuquerque, NM: Sandia National Laboratories, 1979).

5. Lodde, P. F., Wind Turbine Foundation Parameter Study, SAND80-7015 (Albuquerque, NM: Sandia National Laboratories, 1980).

6. Nellums, R. O., "Economic Assessment of the Darrieus Wind Turbine," AIAA Paper 80-0614, Proceedings of the AIAA/SERI Wind Energy Conference, April 9-11, 1980, Boulder. Colorado.

7. Sullivan, W. N., "5-Meter Turbine Field Testing," SAND76-5586, Proceedings of the Vertical Axis Wind Turbine Technology Workshop, May, 1976 (Albuquerque, NM: Sandia National Laboratories, 1976).

QUESTIONS AND ANSWERS

T.G. Carne

From: D.J. Malcolm

Q: Why the odd effect of cable stiffness on first Butterfly frequency (first decrease, then increase)?

A: *There are actually two Butterfly modal frequencies. One is positive and one is negative. We have only shown the positive half of the frequency plane because the negative half is a mirror image. The cable stiffness for which the Butterfly mode has a zero frequency is the point where the frequencies are changing their signs. This feature is due to the fact that we are observing the modes in the rotating frame and is caused by the centrifugal softening and the coriollis effects.*

From: M.S. Chappell

Q: Will the dampers change characteristics with time, wear, weather conditions?

A: *We have seen the coefficient of friction change by ±50% for extreme weather conditions, but that magnitude of change does not alter the modal damping very much.*

From: Anonymous

Q: What is the maximum damping coefficient that you have measured experimentally? How do you include the effect of the weight (mass, used for friction) in your model?

A: *We have measured a five percent damping coefficient with the damping 4m from the end of a 40m cable. The mass can be included in the force equilibrium condition at the connection point.*

From: G.R. Frederick

Q: 1) Is cable stiffness due to cable only or some combination of cable and soil anchor stiffness?

2) What is the factor of safety against cable breakage?

3) What cable pretension to you use? Why cables instead of rods?

A: 1) *It is due only to the cable. but both the elastic deformation and changing the sag (see Ref. 3).*

2) One should use at least a factor of safety of three on the highest tensions imposed on the cables, more if the turbine is in a corrosive environment.

3) The pretension is one of the cable parameters which must be determined from the stiffness requirement, and considerations of the axial load, sag, and cable frequencies. Cables have a high breaking strength and are much easier to work with.

From: Anonymous

Q: How do you include time related (creep) changes in cable tension?

A: *By occasionally checking the tension in the cables and increasing it, if necessary, however, we have seen very little, if any, creep in the cables after installation.*

NORTH WIND 4KW 'PASSIVE' CONTROL SYSTEM DESIGN

Hugh Currin
Foehn consulting
Box 5123
Klamath Falls, OR 97601

An overview of a mechanical rotor control design is presented. Operation at constant RPM and rapid response are obtained by using blade pitch moments for both sensing control need and blade pitch actuation. The basic concept, static or equilibrium design, and dynamic analysis are briefly presented.

INTRODUCTION

The control system described here is part of a SWECS design done for North Wind Power Co. under a Rockwell/DOE contract. The machine, as now configured is a 10 meter, down wind, HAWT rated at 6KW @ 8m/s. It is a line interface unit using a direct drive syncronous alternator. The rotor is a two bladed, teetering system with delta three and uses solid laminated wood blades. The system is free yawing on a guyed wooden pole tower.

The rotor control is an all mechanical system which responds to blade aerodynamic loads and RPM. Power and load control is accomplished through blade pitching in the direction of feather with shut down being full feather. Starting comes from an inboard blade twist.

CONCEPT

The control system concept is to change blade pitch angle in response to blade pitch moment. The blades are then sensors transmitting control information, and also supplying control actuation force, via blade pitch moment. Pitch moment, through placement of the pitch axis, is made sensitive to aerodynamic and centrifugal forces. This control can thus be used with a rotor operating at constant, synchronous, RPM while still providing protection against overspeed conditions.

Figure 1 shows the pitch axis placement at one radial station. Aerodynamic Lift, the predominant blade force, will create a pitching moment through offset Xa. Equilibrium is obtained by applying the control moment Mc. For a given wind speed there is one equilibrium pitch angle θ. For example, assume θ is increased from an equilibrium position, then the airfoil angle of attack will decrease, reducing the coefficient of lift and thus Lift force. The aerodynamic moment is now less than the control moment which actuates a blade pitch, decreasing θ, until equilibrium is again reached. This aerodynamic restoring force maintains equilibrium.

For constant RPM operation a change in wind speed will move the system to a new equilibrium pitch angle. The predominant effect of an increase in wind speed is an increase in angle of attack which increases the lift coefficient and Lift force. This difference between aerodynamic and control moments will tend to increase the pitch angle until a new equilibrium point is reached.

The control moment Mc is a function of pitch angle and will determine the equilibrium pitch angle at each wind speed. The rotor power output, being dependant on wind speed and pitch angle, is determined by this Mc function.

Figure 1 also shows the blade center of gravity offset from the rotor axis. This gives a positive (+θ) pitching moment due to rotor angular velocity which results in sensitivity to rotor overspeed.

STATIC DESIGN

Static Design of this control system involves a trade-off between rotor geometry, control moment characteristics, desired power curve, and resulting unloaded equilibrium overspeed. Figure 2 represents the final geometric layout of the rotor.

To evaluate this analytically a Blade Element Theory for aerodynamic forces (ref 1) is combined with a simple rigid body model for rotational effects. A plot for constant rotor RPM is given in Figure 3. Here the pitch moment, or equilibrium control moment, is given as a function of pitch angle for constant wind speeds and rotor power outputs. Figure 4 presents the same type of plot for zero power output, representing the unloaded control response.

Equilibrium performance is determined by these plots. With control moment given as a function of pitch angle the resulting power, unloaded RPM, and blade pitch are defined as functions of wind speed. Assumed control moment curves are presented in Figures 3 and 4 as dotted lines.

Trade-offs to obtain desireable static performance characteristics involve adjusting rotor geometry, control moment function, and associated structure. Since these involve constraints such as manufacturability and conceptual design they don't lead to explicit evaluation.

AEROELASTIC

The torsional stiffness of this blade-hub system is inherently very low being predominantly from the aerodynamic restoring force mentioned earlier. Because of this the rotor is susceptable to aeroelastic instabilities.

Modes which involve in-plane motions shouldn't be excited due to the high natural frequencies in this degree of freedom. Following this reasoning, problems of ground resonance and whirl modes aren't anticipated. A teetering system with free yaw is not prone to these problems (ref 2).

This leaves pitch/flap instabilities which are of concern. By studying the rotor mode shapes and noting pitch deflections are concentrated at the pitch axis a single blade analysis can be justified.

Out-of-plane vibration modes can be classified into two groups as either involving or not involving teeter. Figure 5 shows the first four out-of-plane mode shapes for a teetering rotor. The first and third (5a, 5c) involve a teetering motion with the flap deflections of each blade opposite. Conversely, the second and third (5b, 5d) involve no teetering deflection and have identical flap deflections. Control pitch deflections, due to mechanical requirements of the pitch linkage, change the pitch angles of each blade by the same amount.

Pitch/flap instabilities involve an aerodynamic coupling of the above control pitch and out-of-plane deflections. The above then would require instabilities involving teeter motions to have a different mode shape for each blade. A 180 degree phase shift in pitch/flap deflections would have to occur. For this reason instabilities which involve a teetering motion are not anticipated. Other pitch/flap instabilities which involve cantilever deflections are however possible.

Note that pitch deflections due to a delta 3 angle, being directly coupled to teeter motions, are not independant degrees of freedom. This delta 3 effect will further stabilize modes which involve teeter motions (ref 3,4).

Three simple analytic models have been used to investigate pitch/flap aeroelasic stability. All involve rigid body, equivalent hinge representations. The first being a "classic" form derived from the helicopter industry. It incorporates Quasi-Steady, Theodorsen, aerodynamics with constant chord and twist (ref 5,6). The second uses the same formulation but assumes steady state aerodynamics. Figure 6 shows a representation of the first two models. The third model uses steady state aerodynamics but includes several geometric improvements over the first two. It includes twist and taper along with hinge offsets to better approximate geometric control characteristics. This model was derived for time domain investigations of control response. Figure 7 represents this model.

Each of these analytic models can be presented in matrix form as:

$$\frac{1}{\Omega^2}\begin{bmatrix}1 & m_{\ddot{\theta}}\\ M_{\ddot{\beta}} & M_{\ddot{\theta}}\end{bmatrix}\begin{Bmatrix}\ddot{\beta}\\ \ddot{\theta}\end{Bmatrix}+\frac{1}{\Omega}\begin{bmatrix}m_{\dot{\beta}} & m_{\dot{\theta}}\\ M_{\dot{\beta}} & M_{\dot{\theta}}\end{bmatrix}\begin{Bmatrix}\dot{\beta}\\ \dot{\theta}\end{Bmatrix}+\begin{bmatrix}m_{\beta} & m_{\theta}\\ M_{\beta} & M_{\theta}\end{bmatrix}\begin{Bmatrix}\beta\\ \theta\end{Bmatrix}$$
$$=\begin{Bmatrix}m_v\\ M_v\end{Bmatrix}V+\begin{Bmatrix}m_o\\ M_o\end{Bmatrix}$$

The stability derivatives, here the matrix elements, are given in Table I for each of the theoretical models. A numerical eigen value approach was used to solve the unforced equations for stability information.

A pitch/flap instability was predicted in each case. An attempt has been made to understand the parameters involved with this instability and eliminate it. In doing so some understanding of the system and the models used has been gained.

Various parameters were changed to determine which have a significant effect on this instability. This resulted in three parameters being flap natural frequency, RPM, and pitch damping. RPM is determined by the static design and was kept as small as reasonable. This leaves flap natural frequency and pitch damping for adjustment. Figure 8 shows stability plots for each of the three analytical models. These are calculated for running RPM and show flap natural frequency versus pitch damping. The three agree in general, predicting the instability, but differ quantitatively.

The flap natural frequency can be adjusted but, without a change in blade sructure, this parameter can not be varied enough to stabilize the system. Since pitch deflections are concentrated at the pitch axis damping can be added. This solution was adopted although a damper, being mechanical, can fail and allow the system to become unstable. A vibration shut down is required. For reliability, dampers are placed at the pitch shaft to avoid linkage wear and fatigue. Although having a minimal impact, pitch damping will slow gust response.

Some insight can be gained about the three analytical models from the stability plots in Figure 8. Note that the first two models compare well with the only difference due to aerodynamics. The similarity of these plots may be misleading due to the very low torsional stiffness which tends to slow the motions and minimize the differences between steady and Quasi-steady aerodynamics. The steady state assumption is the more conservative. The third model is considerably less stable than the first two. The modeling differences between these are the control offsets, taper, twist, and sweep but it is not known how much effect each has.

DYNAMIC RESPONSE

To assess dynamic control response the third model, with its forcing function, was solved in the time domain. A numerical solution was used to analytically model several wind gust cases.

Figure 9 shows pitch and flap response for a wind gust of 8 to 24 m/s in one second. This is felt to be an extreme gust which would be rarely encountered. The control system is responding within 1/4 second and the greatest out-of-plane load, corresponding to the greatest flap deflection, occurs at 1/2 second. This response is fast enough to relieve major blade loads. The largest out-of-plane load encountered is near one fourth the worst case load coming from high wind shut down conditions.

The rapid response is inherent with this control system. Translating blade loads into a control pitch involves only the pitch inertia.

Most control systems sense a condition, such as an RPM change, which involves a much larger inertia. Pitch damping, added for aeroelastic stability, does slow response time but is a minor effect. The plot presented in Figure 9 includes this damping.

CONCLUSIONS

Analysis of the control system is complex but results in a relatively simple mechanical system with control response rapid enough to relieve gusts. This complexity is due to the interdependance of rotor geometry, system loads, dynamic response and aeroelastic stability.

The simple aeroelastic models used are not in close agreement. These simple models are important in SWECS design where large computer codes are usually not cost effective. Investigations to determine the critical parameters in these models, and compare results with test data, or the large computer codes (ref 7), would be useful.

ACKNOWLEDGEMENT

Recognition is due Jito Coleman, North Wind Power Co. and Woody Stoddard, Stoddard Consulting for colaboration in this concept and design.

REFERENCES

1 Wilson,R.E., Lissaman,B.S., "Applied Aerodynamics of Wind Power Machines", Oregon State Univ., NTIS PB238594, July 1974.

2 Shue,D.T., "Effects of Tower Motion on the Dynamic Response of Windmill Rotors", MS Thesis, Dept. of Aero. & Astro., MIT, Feb. 1977.

3 Bramwell,ARS, "Helicopter Dynamics", Wiley & Sons, 1976.

4 Stoddard,F.S., "Structural Dynamics, Stability and Control of High Aspect Ratio Wind Turbines", Rockwell/DOE contract # PF 67025F, Dec. 1978.

5 Miller,R.H., Ellis,C.W., "Helicopter Blade Vibration & Flutter", Journal of the American Helicopter Soc., July 1956.

6 Loewy,R.G., "Review of Rotary Wing V/STOL Dynamic and Aeroelastic Problems", AIAA paper 69-202, Feb. 1969.

7 Spera,D.A., "Comparison of Computer Codes for Calculating Dynamic Loads in Wind Turbines", NASA-ERDA Structural Dynamics Workshop, Nov. 1977.

** "Developement of a 4KW SWECS", North Wind Power Company, Rockwell/DOE contract #PF08501C. (Forthcoming Design Reports for further information).

NOMENCLATURE

a - lift curve slope
c - chord
C_d - coef. of lift
d_1 - offset (Fig 2)
d_2 - offset (Fig 2)
I - I_e/I_b
I_b - flap moment of inertia
I_e - pitch moment of inertia
I_R - I_R/I_b
I_R - cross product of inertia
m - blade mass
r - local radius
R - radius
R_1 - inner blade radius
r_c - CG radius
V - gust wind velocity
V_o - equilibrium wind velocity
β - flap angle
γ - lock number
θ - pitch angle deflection
θ_o - equilibrium pitch angle
ρ - air density
x_A - quarter chord/elas. axis
x_2 - quarter chord/CG offset
Ω - rotor angular velocity
ω_β - flap natural frequency
ω_θ - pitch natural frequency

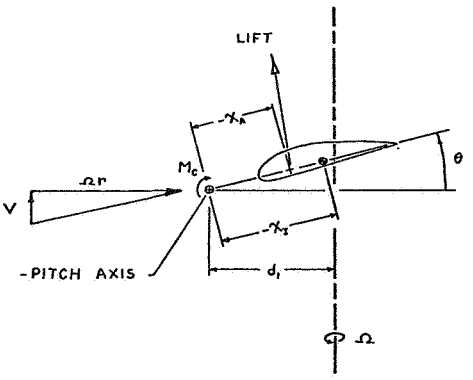

FIGURE 1 - CONTROL CONCEPT

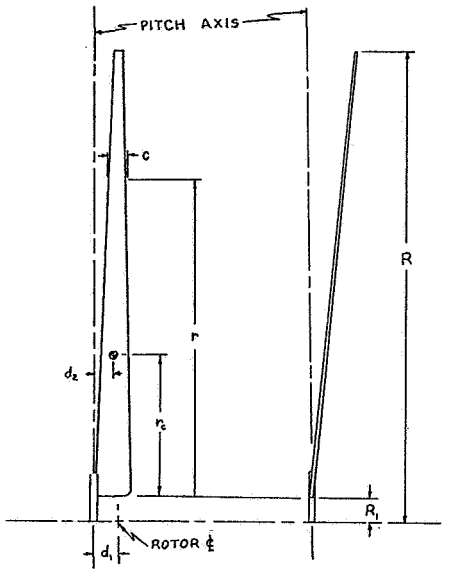

FIGURE 2 - ROTOR LAYOUT

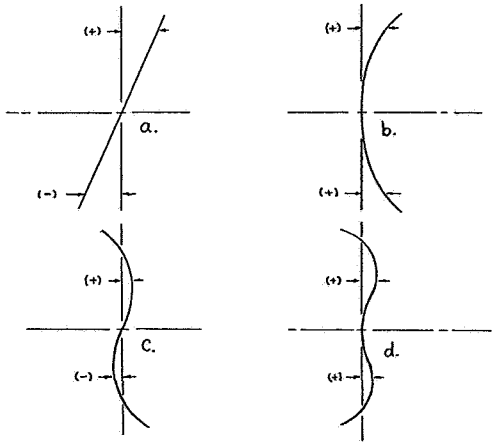

FIGURE 5 - TEETER MODES

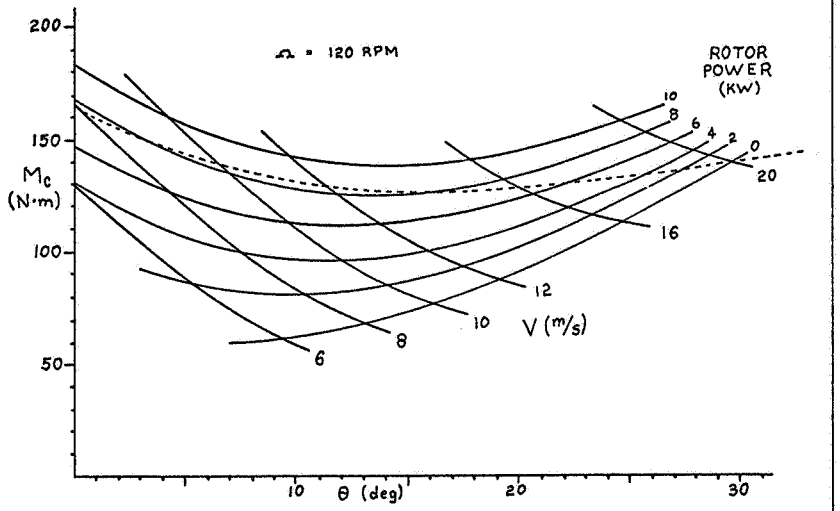

FIGURE 3 - STATIC PERFORMANCE

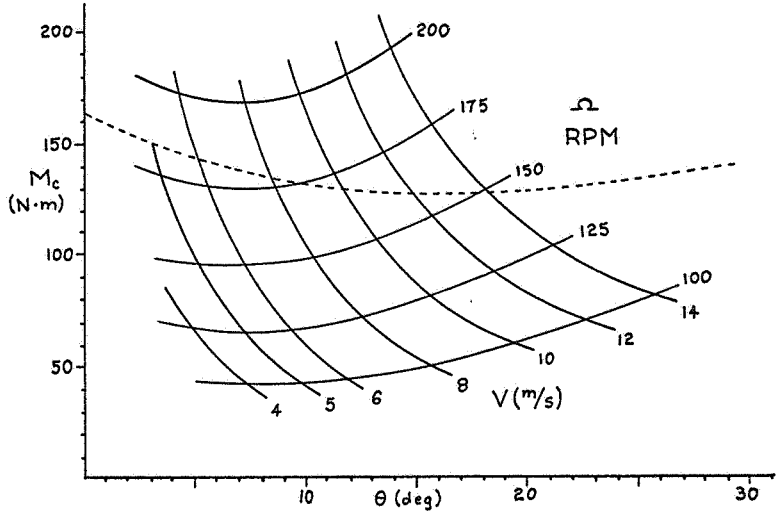

FIGURE 4 - UNLOADED OVERSPEED

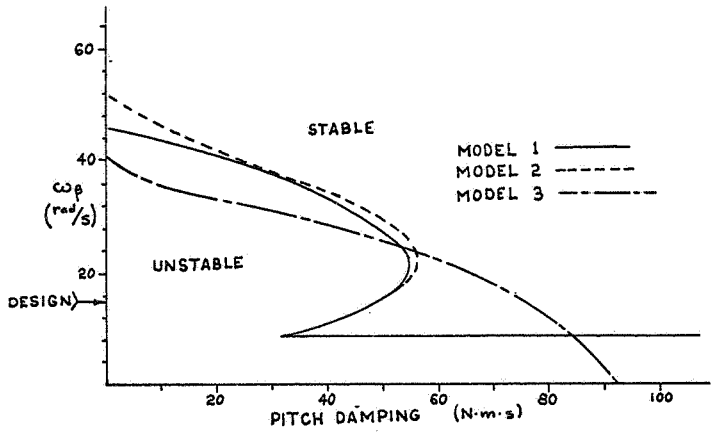

FIGURE 8 - STABILITY

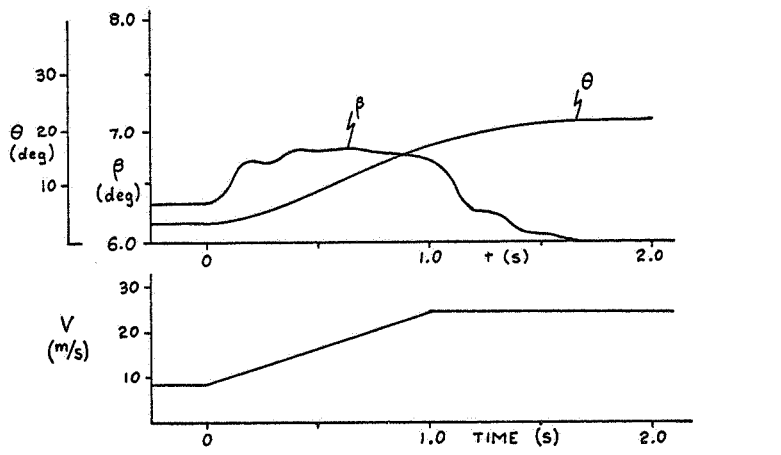

FIGURE 9 - GUST RESPONSE

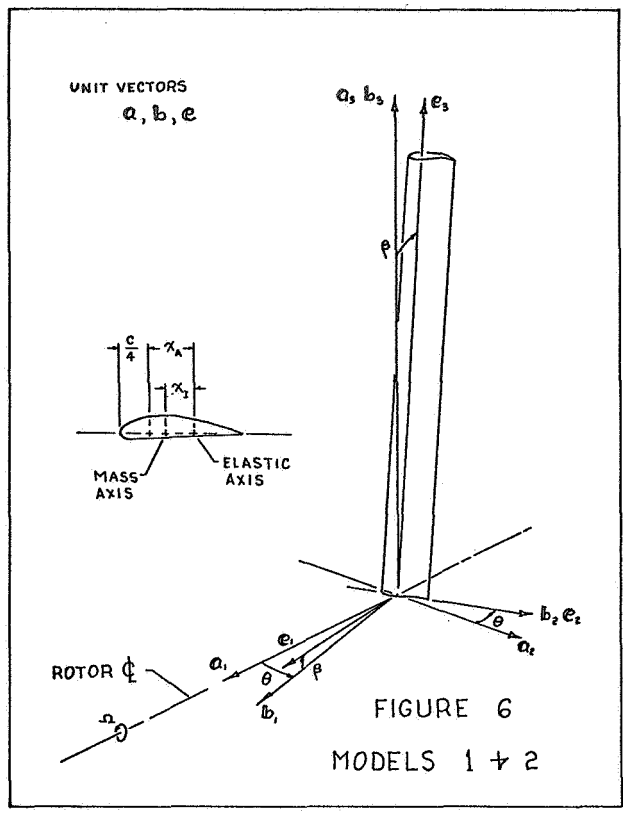

FIGURE 6

MODELS 1 + 2

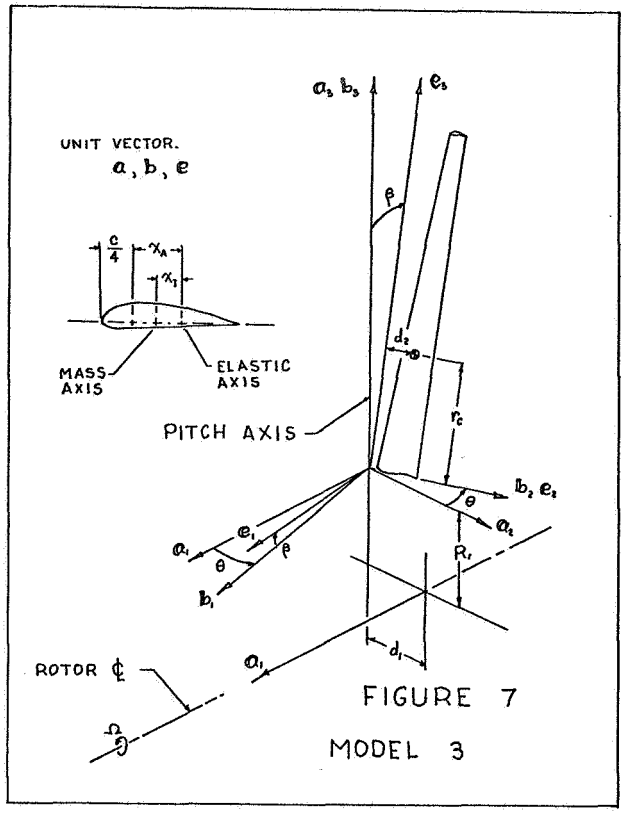

FIGURE 7

MODEL 3

TABLE I - STABILITY DERIVATIVES

	MODEL 1	MODEL 2	MODEL 3
$m_{\dot\beta}$	$\frac{\gamma}{8}$	$\frac{\gamma}{8}$	$\gamma\int_0^{R-R_1} c r^2 (R_1+r)(c\theta_0+\lambda s\theta_0)\,dr$
m_β	$1+\left(\frac{\omega_\beta}{\Omega}\right)^2$	$1+\left(\frac{\omega_\beta}{\Omega}\right)^2+\frac{\gamma\chi_A}{6R}$	$c^2\theta_0+\frac{m R_1 r_c}{I_b}+\left(\frac{\omega_\beta}{\Omega}\right)^2+\gamma\int_0^{R-R_1} c r (R_1+r)(d_1+\chi_A c\theta_0)(c\theta_0+\lambda s\theta_0)\,dr$
$m_{\ddot\theta}$	$-I_x$	$-I_x$	$-I_x$
$m_{\dot\theta}$	$\frac{\gamma}{6}\left[\frac{3c}{4R}-\frac{\chi_A}{R}\right]$	$-\frac{\gamma\chi_A}{6R}$	$-\gamma\int_0^{R-R_1} c r (R_1+r)\chi_A(c\theta_0+\lambda s\theta_0)\,dr$
m_θ	$-I_x+\frac{\gamma}{8}$	$-I_x+\frac{\gamma}{8}$	$-I_x c(2\theta_0)+\frac{m r_c d_1}{I_b}c\theta_0-\gamma\int_0^{R-R_1} c r (R_1+r)^2\left[(\lambda^2-1)c(2\theta_0)-2\lambda s(2\theta_0)\right]dr$
$M_{\ddot\theta}$	I	I	I
$M_{\dot\theta}$	$-\frac{\gamma}{2}\left[\frac{c}{8R}-\frac{\chi_A}{2R}\right]\left[\frac{\chi_A}{R}-\frac{c}{2R}\right]$	$\frac{\gamma\chi_A^2}{4R^2}$	$\frac{\gamma}{2}\int_0^{R-R_1} c(R_1+r)\chi_A^2(c\theta_0+\lambda s\theta_0)\,dr$
M_θ	$I\left[1+\left(\frac{\omega_\beta}{\Omega}\right)^2\right]-\frac{\gamma\chi_A}{6R}$	$I\left[1+\left(\frac{\omega_\beta}{\Omega}\right)^2\right]-\frac{\gamma\chi_A}{6R}$	$Ic(2\theta_0)-\frac{m d_1 d_2}{I_b}c\theta_0+I\left(\frac{\omega_\beta}{\Omega}\right)^2-\gamma\int_0^{R-R_1} c(R_1+r)^2\chi_A\left[2\lambda s(2\theta_0)+(1-\lambda^2)c(2\theta_0)\right]dr$
$M_{\ddot\beta}$	$-I_x$	$-I_x$	$-I_x$
$M_{\dot\beta}$	$-\frac{\gamma\chi_A}{6R}$	$-\frac{\gamma\chi_A}{6R}$	$-\gamma\int_0^{R-R_1} c r (R_1+r)\chi_A(c\theta_0+\lambda s\theta_0)\,dr$
M_β	$-I_x$	$-I_x-\frac{\gamma\chi_A^2}{4R^2}$	$-I_x c(2\theta_0)-\frac{m r_c d_1}{I_b}c\theta_0$ $-\gamma\int_0^{R-R_1} c(R_1+r)(c\theta_0+\lambda s\theta_0)\left[\chi_A(\chi_A c\theta_0+d_1)-\frac{c_d}{c_d+a}r(R_1+r)(c\theta_0+\lambda s\theta_0)\right]dr$

$\gamma=\frac{\rho a R^4 c}{2 I_b}$

$m_o=-\frac{1}{2}I_x s(2\theta_0)-\frac{m r_c d_1}{I_b}s\theta_0+\gamma\int_0^{R-R_1} c r (R_1+r)^2\left[\frac{1}{2}(\lambda^2-1)s(2\theta_0)+\lambda c(2\theta_0)-\frac{a}{c_d+a}\theta_r(c\theta_0+\lambda s\theta_0)^2\right]dr$

$M_o=-\frac{1}{2}I s(2\theta_0)+\frac{m d_1 d_2}{I_b}s\theta_0-\gamma\int_0^{R-R_1} c\chi_A(R_1+r)^2\left[\frac{1}{2}(\lambda^2-1)s(2\theta_0)+\lambda c(2\theta_0)-\frac{a}{c_d+a}\theta_r(c\theta_0+\lambda s\theta_0)^2\right]dr$

$m_v=\frac{\gamma}{\Omega}\int_0^{R-R_1} c r (R_1+r)\left[\lambda s(2\theta_0)+c(2\theta_0)\right]dr$

$M_v=-\frac{\gamma}{\Omega}\int_0^{R-R_1} c\chi_A(R_1+r)\left[\lambda s(2\theta_0)+c(2\theta_0)\right]dr$

$\gamma=\frac{\rho(c_d+a)}{2 I_b}$

$\lambda=\frac{V_o}{\Omega(R_1+r)}$

QUESTIONS AND ANSWERS

H. Currin

From: T.A. Egolf

Q: How does the nonlinearity of the actual unsteady lift response to rapid high angle of attack variations affect the control system response?

A: *Response should be rapid enough to avoid stall with any "real world" gust (an advantage of this control). Dynamic stall, if encountered, initially increasing lift would increase pitch response. Wihtout stall, I'd guess unsteady aero would slow response.*

PASSIVE CYCLIC PITCH CONTROL FOR HORIZONTAL AXIS WIND TURBINES

Gerald W. Bottrell

Ventus Energy Corporation
2442 Teasley St.
La Crescenta, California 91214

ABSTRACT

A new flexible rotor concept, called the balanced-pitch rotor*, is described. The system provides passive adjustment of cyclic pitch in response to unbalanced pitching moments across the rotor disk.

Various applications are described and performance predictions are made for wind shear and cross wind operating conditions. Comparisons with the teetered hub are made and significant cost savings are predicted.

INTRODUCTION

The two-bladed rotor with teetered hub has received almost universal acceptance as the most cost-effective configuration for multi-megawatt WECS. Despite this wide acceptance, the teetered hub has certain undesirable features which add to the cost and reduce reliability of the machine as a whole. These include:

- o Need for large tower clearances
- o Introduction of cyclic speed variations
- o Susceptibility to rotor damage during startup, shutdown, and survival conditions

The balanced-pitch rotor is expected to provide equal performance while avoiding these undesirable features. Savings on the order of 15 to 25 percent of rotor cost may be realized.

DESCRIPTION

The aerodynamically-balanced cyclic-pitch rotor (balanced-pitch rotor) is analogous to the teetered hub. Its main function is to reduce vibratory loads and improve yaw performance of wind turbine rotors. This is accomplished in the teetered hub by cyclic flapping in response to unbalanced thrust on the blades. In a similar manner, the balanced-pitch rotor produces cyclic pitch changes as a result of unbalanced pitching moments across the rotor disk.

The simplest balanced-pitch rotor configuration is shown in Figure 1. This is a two-bladed rotor with fixed collective pitch. The two blade root fittings are rigidly coupled together to form a single pitch shaft. This shaft is mounted in bearings so that the pitch axis of the two blades is free to rock back and forth. Blade airfoil and geometry are selected so that the blades pitch away from an increased angle of attack.

Also shown is an arm and bracket assembly rigidly fastened at right angles to the pitch shaft. This assembly couples the pitch axis to the rotor hub through the pair of springs shown, or through cushioned stops or dampers.

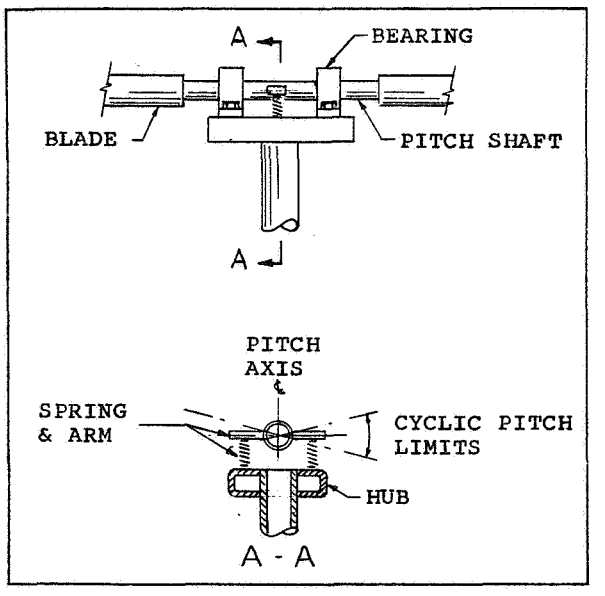

Figure 1 - Balanced-pitch rotor having two blades and fixed collective pitch.

WIND SHEAR EFFECTS

The schematic diagram, Figure 2, represents a conventional two-bladed rotor with rigid hub in the presence of wind shear. The rotor experiences high cyclic flapping, pitching, and yaw moments which have a large adverse effect on the cost and performance of horizontal axis wind turbines.

*Patent Pending

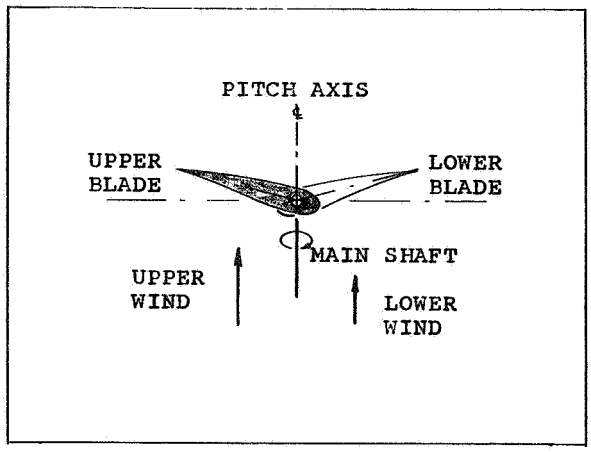

Figure 2 - Two-bladed rotor with rigid hub subject to wind shear

Figure 3 depicts the same wind shear conditions utilizing a balanced-pitch rotor. Areas of unequal wind velocity are seen to alter the pitch axis (not the fixed collective pitch) as the blades pass through. The result is a significant reduction or elimination of the cyclic loads and unstable yaw performance experienced by the conventional rotor with rigid hub. Tower shadow affects are expected to be compensated in a similar manner. This action also is expected to avoid the normal yaw angle deviation experienced by free yaw systems under wind shear conditions.

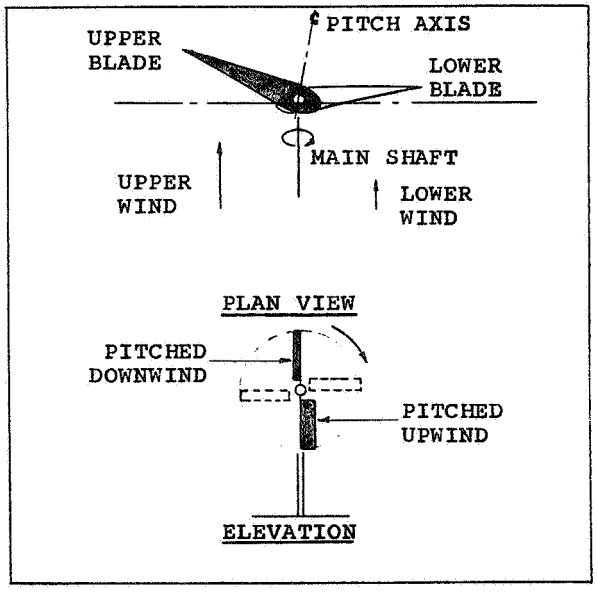

Figure 3 - Two-bladed balanced-pitch rotor subject to wind shear.

CROSS-WIND EFFECTS

As shown in Figure 4, the balanced-pitch rotor adjusts itself to cross-wind effects in much the same way it does under wind shear conditions. The result is expected to be a relatively small, steady yawing moment which, in a free-yaw system, aligns the turbine shaft to the new wind direction.

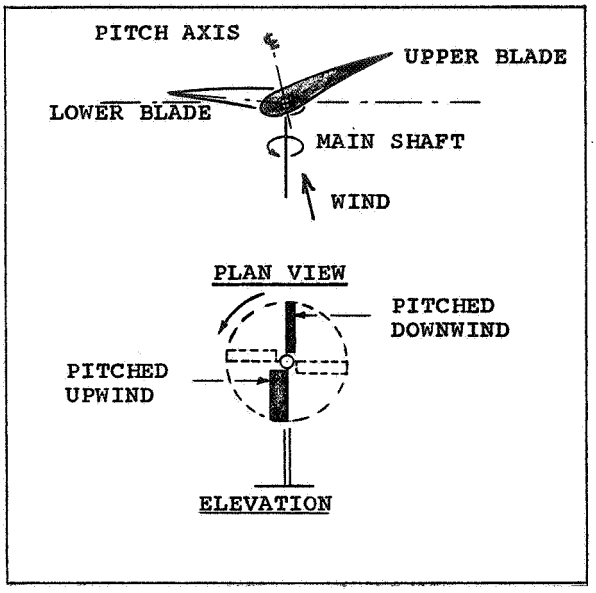

Figure 4 - Two-bladed balanced-pitch rotor subject to cross winds

APPLICATIONS

Fixed Pitch Configurations

As shown in Figure 1, the balanced-pitch rotor may easily be applied to fixed-pitch rotors simply by adding bearings at the hub. These bearings are not required to carry blade centrifugal loads. This same simple arrangement is applicable to rotors with partial-span collective pitch control. Pitch control linkages, of course, will have to be flexible where they pass between the hub and the rocking pitch shaft.

Variable Pitch With Rotating Actuators

The configuration shown in Figure 5 applies to units with full-span collective pitch control in which hub-mounted actuators are used. Passive cyclic pitch control is accomplished by interconnecting all actuators at a rocking yoke which is mounted in bearings and supported from an extension of the hub. Dampers are shown here which serve to limit the rate and extent of cyclic pitch excursions.

In most cases it is possible to design yoke geometry and that of the pitch linkage system to avoid substantial collective pitch changes through the full range of cyclic pitch excursions. In some cases, however, slight changes in collective pitch may be purposely introduced to effect turbine output power if cyclic pitch variations are extreme.

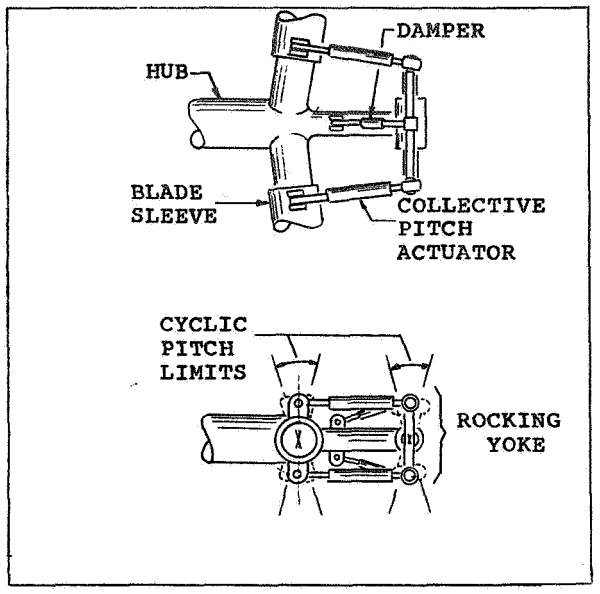

Figure 5 - Balanced-pitch rotor with rotating actuators for full-span collective pitch control.

Variable Pitch With Linear Actuators

Figure 6 shows an application utilizing a pitch control rod for full-span collective pitch control. Once again, it is only necessary to add a rocking yoke to which pitch control linkages are connected. In this design, cushioned stops are shown mounted on the pitch control shaft to limit the extent of cyclic pitch excursions.

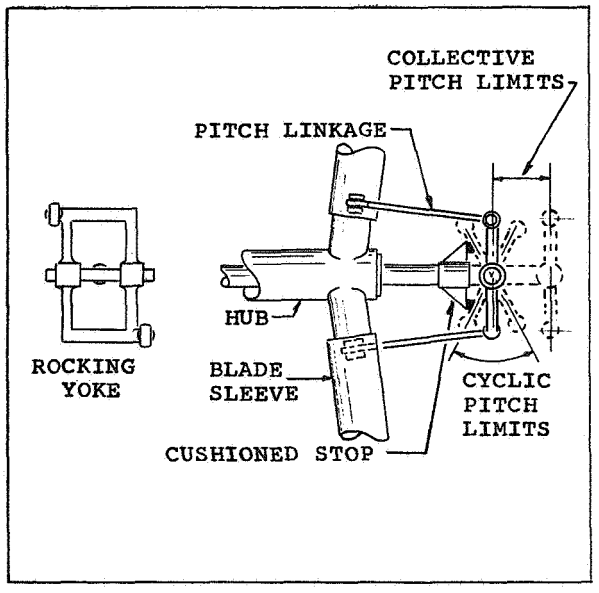

Figure 6 - Balanced-pitch rotor with linear actuator for full-span collective pitch control.

More Than Two Blades

For rotors having more than two blades, the rocking yoke shown in Figure 6 must be replaced with a ball joint or universal joint which is allowed to tilt in any direction. Blade linkages are then connected to arms extending around the periphery of the joint.

COMPARISON WITH TEETERED HUB

Tower Clearance

The teetered hub requires a very large distance between yaw axis and hub for adequate tower clearance at the blade tip. This distance is minimal for the balanced-pitch rotor, as shown by the comparisons of Figures 7, 8, and 9. Such a large overhang results in much higher costs for the low-speed shaft, bearings, nacelle and yaw structure.

Figure 7 compares configurations for a downwind rotor with coning. The teetered rotor does not gain much clearance from coning because of the need to gravity balance the rotor. This positions the teeter hinge far outboard from the intersection of the two blade axes.

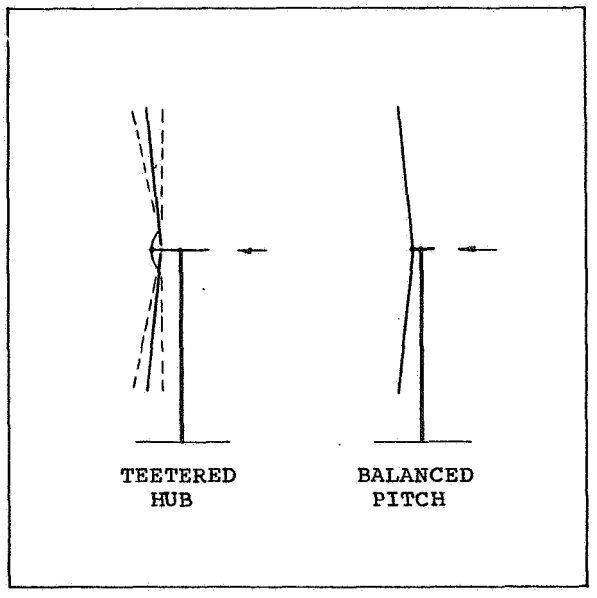

Figure 7 - Hub overhang with downwind rotors with coning.

Similarly, as shown in Figure 8, a tilted rotor provides extra clearance only if the normal wind direction is perpendicular to the tilted rotor disk. In the case of the balanced-pitch rotor, a tilt may be very effective regardless of the wind direction. Cyclic loads normally associated with such a tilt are greatly reduced or eliminated. Of course, any coning or tilt will cause a reduction in energy capture.

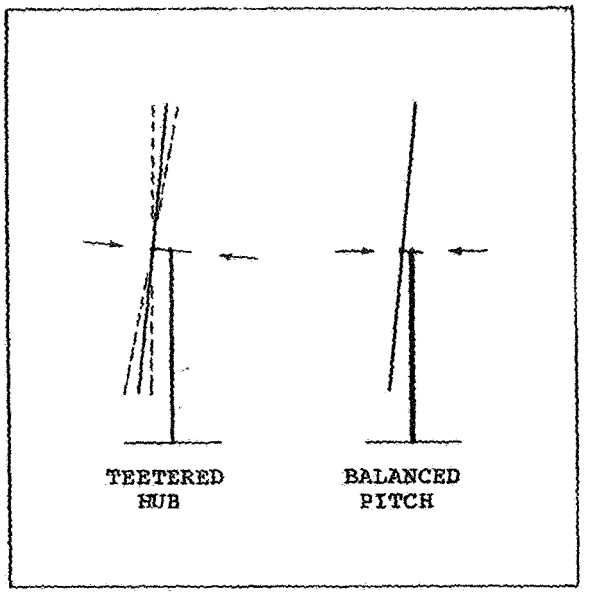

Figure 8 - Hub overhang with tilted rotors.

The unconed rotors shown in Figure 9 illustrate best the overhang advantage of the balanced-pitch rotor compared to the teetered hub.

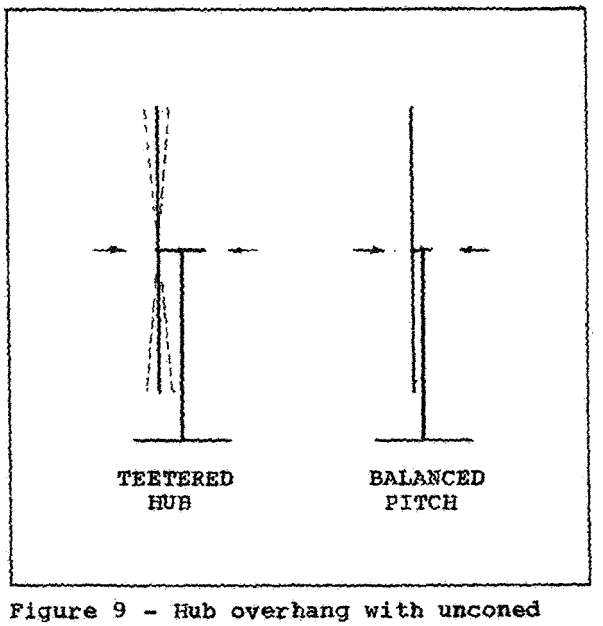

Figure 9 - Hub overhang with unconed rotors.

Cyclic Speed Variations

The teetered hub, in a sense, trades blade and hub cyclic loads for cyclic speed variations in the power train. These show up as large torque fluctuations in a constant speed machine. These torque fluctuations may be reduced to acceptable levels by means of a torsionally flexible low-speed shaft, flexible gear box mounting, or a slip coupling in the power train. These special features are costly in terms of capital investment and/or energy losses, and they all tend to increase maintenance costs and reduce reliability.

The balanced-pitch rotor is not expected to introduce any such speed or torque variations.

Survival Conditions

The teetered hub performs beautifully as long as aerodynamic and centrifugal loads are in balance. When not in balance, the huge teetered masses are very difficult to deal with. For this reason, all large WECS with teetered hubs must have brakes to prevent teeter operation during startup, shutdown, and parked conditions. These brakes are critical to the very survival of the unit and must be in operating condition through extended power outages.

No such startup, shutdown, or survival facilities are required with the balanced-pitch rotor.

Yaw Performance

The teetered hub and balanced-pitch rotor are expected to be equal in avoiding cyclic yaw moments. In a free-yaw system, however, the balanced-pitch rotor is expected to track more accurately than does the teetered rotor.

On the other hand, the teetered hub avoids cyclic gyroscopic forces while the balanced-pitch rotor does not.

CONCLUDING REMARKS

A new flexible rotor concept, called the balanced-pitch rotor, has been described and shown to be potentially equivalent to the teetered hub in performance. Certain advantages of the new concept have been pointed out, including reduced tower clearances, avoidance of cyclic speed variations, and superior survival characteristics. For two-bladed multi-megawatt wind turbines these features have been estimated to save some 15 to 25 percent of rotor cost and to increase reliability of the machine as a whole.

REFERENCES

1. Glasgow, J. C., and Miller, D. R.: Tip-controlled Rotor: Preliminary Test Results from MOD-0 100kW Experimental Wind Turbine, AIAA/SERI Wind Energy Conference, April 9-11, 1980, Boulder, Colorado.

2. Douglas, Richard R.: The Boeing MOD-2 - Wind Turbine System Rated 2.5 MW, NASA Conference Publication 2106, DOE Publication CONF-7904111.

QUESTIONS AND ANSWERS

G.W. Bottrell

From: L. Mirandy

Q: I can't see why the aero forces will automatically adjust the blade pitch in an optimum manner to reduce loads. Will you explain why?

A: *The system is only effective to reduce the difference in loads across the rotor disk. Load differences produce a differential pitching moment which increases the pitch of one blade and decreases that of the other until pitching moments are equal (assuming a frictionless system).*

From: F.W. Perkins

Q: What happens to your tower clearance when the rotor stalls? Why is this concept different from conventional pitch flap coupling?

A: *I would not expect blade deflection at rotor stall to be as large as that of a 6 degree teeter plus blade deflection. This concept and conventional pitch-flap coupling achieve the same results. We believe this concept will be far less expensive.*

From: Anonymous

Q: Does this concept also eliminate the pair of spindle thrust bearings in a normal two-bladed HAWT?

A: *No, not to my knowledge.*

From: G. Beaulieu

Q: What is the effect of this system on blade torsional frequencies? Is there any danger for blade flutter?

A: *I believe there is a danger of blade flutter and this will require further analysis. No flutter was observed in the limited tests performed to date.*

DYNAMICS OF AN EXPERIMENTAL TWO BLADED HORIZONTAL AXIS WIND TURBINE WITH BLADE CYCLIC PITCH VARIATION*

Kurt H. Hohenemser and Andrew H. P. Swift

Washington University
St. Louis, Missouri 63130

ABSTRACT

The horizontal axis wind turbine under study incorporates the combination of two features: The application of blade cyclic pitch variation and the use of yaw angle control for rotor speed and torque regulation. Due to its "emasculation" by passive cyclic pitch variation the rotor can be rapidly yawed without encountering gyroscopic and aerodynamic hub moments and without noticeable out-of-plane blade excursions. The two bladed upwind rotor is vane stabilized and of very simple and rugged design. The principle was first checked out with a small scale wind tunnel model and then tested in the atmosphere with a 7.6 meter diameter experimental fully instrumented wind turbine driving a 3 phase alternator. The rotor to tail vane furl angle was controlled through an electric actuator by a manually operated toggle switch overridden by an automatic rotor overspeed relay. The paper summarizes the test results with respect to structural dynamics and yaw dynamics.

NOMENCLATURE

A	Rotor disk area
A_T	Tail vane area
I_T	Machine moment of inertia about yaw axis
P	Rotor power
R	Rotor radius
T	Rotor Torque
V	Wind speed
C	Blade chord
$C_{L\alpha}$	Tail vane lift slope
C_P	Rotor power coefficient $(2P/\rho AV^3)$
C_Q	Rotor torque coefficient $(T/\rho AR(\Omega R)^2)$
α	Rotor angle of attack
α_T	Tail vane orientation
α_{TO}	Instantaneous wind direction change at tail vane
ζ	Damping ratio
λ	Tip speed ratio $(\Omega R/V)$
ρ	Air density
σ	Blade solidity ratio $(2C_{.7}/\pi R)$
τ	Cyclic pitch amplitude
Ω	Rotor angular speed
ω	Undamped natural yaw frequency
ω_n	Damped natural yaw frequency

INTRODUCTION

The bewildering variety of wind turbine configurations now in operation is a sign of a lack of maturity of this technology. In the course of time most of these configurations will undoubtedly fall by the wayside and only a few will survive. Meanwhile one more configuration of a horizontal axis wind turbine has been added and tested for several months in the atmosphere. Initial power-off test results are reported in Reference 1.

A selection of subsequent power-on test results with emphasis on structural and yaw dynamics are given in this paper. Continued testing is planned for the spring of 1981.

THE NEW CONFIGURATION

In order to place the new configuration within the frame work of preceding designs, let us first look at the various possible ways of power and rotor speed control for horizontal axis machines.

Power and RPM Limitation By

1. Blade stall, automatic brake
2. Blade feathering
3. Blade Unfeathering (enhanced stall)
4. Rapid rotor yawing, cyclic pitch

The first method is applicable if an induction generator is used with nearly constant RPM imposed by the electric grid. At fixed blade pitch setting and increasing wind speed the rotor power will reach a maximum and then decline leading ultimately to deep blade stall. In case of power cut-out the rotor will overspeed unless speed limited by an automatic mechanical or aerodynamic brake. While this system is simple it requires an over designed generator and drive system and a powerful brake.

The second method is widely used and effective for both power-on and power-off conditions. It needs variable pitch blades and an automatic pitch control mechanism. The implementation of this method is complex and costly.

The third method enhances blade stall both power-on and power-off. The power peak remains high and requires an over designed generator and drive system. The blade pitch varying mechanism adds to the complexity and cost.

The fourth method of rapid rotor yawing using cyclic pitch variation is the one to be discussed here. Let us now look at the various possible means of generating a yawing moment.

Yawing Moment By

1. Yaw gear, up or downwind rotor
2. Tail vane, upwind rotor
3. Rotor control, up or downwind rotor
4. Rotor self yawing, downwind rotor

The first method is used in many medium and large units. The yaw rate is low so that the rotor position lags behind wind direction changes. In some designs the yaw gear drive is powered by a paddle wheel with an axis perpendicular to

*Presented at the Second DOE/NASA Wind Turbine Dynamics Workshop, February 24-26, 1981 in Cleveland, Ohio.

the rotor axis. In other designs the yaw gear is driven by a servo motor receiving signals from wind direction pick-ups.

The second method is widely used for smaller units. Because of the gyroscopic and aerodynamic hub moments rapid wind following due to the tail vane can be a problem with respect to loads and vibrations, particularly for fast turning two bladed rotors. Our experimental wind turbine is tail vane stabilized and two bladed. It is subjected to high yaw rates. Due to the feature of passive cyclic pitch variation to be explained later, the rotor is "emasculated". Gyroscopic moments are balanced by aerodynamic moments from cyclic pitch variation and do not load up the hub or rotor shaft. The out-of-plane blade motions associated with the cyclic pitch variation are very small. There is no blade feathering mechanism.

The third method of yawing the rotor by active rotor cyclic pitch controls has been suggested in Reference 2 but has so far not been implemented.

The fourth method is limited to downwind rotors and has become quite popular. Its implementation requires a good understanding of rotor aerodynamics. Dynamic overshooting and large off-center equilibrium positions have been observed.

Figure 1 is a schematic plan view of the experimental wind turbine configuration with the definition of rotor angle of attack α, yaw angle $90^{\circ} - \alpha$ and furl angle. Though not quite correct, the furl angle, that is the angle between tail vane boom and rotor axis, has been assumed to be equal to the yaw angle. The furl angle could be varied between zero and almost 90° with the help of a linear electric actuator with a constant furl rate of 15 degrees per second. A toggle switch was used for starting, stopping and reversing the actuator motion. An automatic overspeed relay could override the manual switch in the direction of increasing furl angle. The actuator motion stopped when the overspeed condition terminated, or when the furl limit switch was tripped. Unfurling was then accomplished by manual operation of the toggle switch.

The 7.6 meter (25 foot) diameter turbine was driving a 3 phase alternator with a rectifier that produced up to 220 volt DC. A resistance load of 6.0 ohm resulted at 22 miles per hour wind velocity in an electric power output of 8.0 KW. The alternator torque input increases very closely with the second power of the RPM. Thus the wind turbine operated at all wind speeds and furl angles with a constant torque coefficient.

SMALL SCALE WIND TUNNEL MODEL STUDIES

The study of the new configuration began with some small scale wind tunnel model tests. Figure 2(a) shows an axial view of the model rotor. Figures 2(b) and 2(c) show side views. The hub can swivel freely about the two pins. The blades are attached to the hub with a small fixed prelag angle with respect to the swivel axis. The rotational deflection about the swivel axis is almost equal to the cyclic pitch deflection of the blade pair which is accompanied by a small out-of-plane teeter deflection. Because of the absence of any control mechanism the hub is very simple. The blades are retained by bending flexures. Only autorotational conditions could be tested. The following table gives the main data for the wind tunnel model and for the atmospheric test machine.

Table 1

Model and Full Scale Parameters

	Model	Full Scale
Rotor Diameter inch	17.2	300
Blade Chord, inch	1.0	12 to 4
Blade Solidity Ratio	.075	.032(at .7R)
Blade Twist, degrees	0	9.5
Blade Airfoil, NACA	0015	4425 to 4412
Blade Lock Number	6.4	7.0
Blade Prelag Angle	23°	23°
Cyclic Pitch Stops	$\pm 9^{\circ}$	$\pm 13^{\circ}$
Reference Rotor RPM	1800	225
Reynolds Number for .7R	50,000	640,000

Since blade Lock number and blade prelag angle are approximately the same for model and full scale rotor, blade cyclic pitch dynamics are, outside of the blade stall regime, the same despite the differences in geometry. The measured quantities were wind speed, rotor speed and yaw angle. The furl angle (see Figure 1) could only be changed between runs and not during operation. The model was tested both with tail vane (Figure 2(b)) and without tail vane (Figure 2(c)) at fixed yaw angles. Figure 3 shows the speed ratio $V/\Omega R$ vs. yaw angle in autorotation for about zero blade pitch angle setting. The model data are corrected for a .7R Reynolds number of 50,000 since not all tests were run at this Reynolds number. The results of the full scale power-off tests at a Reynolds number of 640,000 are also shown. The dash line refers to the results of NACA tests at zero blade pitch setting and with a Reynolds number of 620,000, Reference 3. The NACA test results represent a smooth continuation of the curve for our atmospheric test rotor. The model, due to the lower Reynolds number and higher blade solidity, operates at much higher speed ratio $V/\Omega R$ and exhibits at 50° yaw angle a discontinuity in the curve, which is apparently caused by blade stall. The small scale model tests demonstrated smooth operation of the two bladed rotor with passive cyclic pitch variation up to yaw angles of 50 degrees, good controllability of the RPM by yawing, easy starting up to 50° yaw angle, good damping of yaw transients and the capability of high yaw rate without noticeable vibrations.

In the original configuration of the model rotor an instability occurred with zero yaw angle at a wind speed of 24 miles per hour corresponding to 2100 RPM. Just prior to the onset of the instability the cyclic pitch amplitude was small and the rotor ran smoothly. Suddenly cyclic pitch stop pounding was observed with an estimated frequency of 10 to 20 Hz. The RPM rapidly dropped to about one-third and the

tip path plane was strongly warped indicating that the cyclic pitch frequency was different from the usual 1P. The condition persisted until the tunnel speed was reduced to 12 miles per hour. The onset of the instability was, in repeated tests, always exactly at 24 miles per hour.

It was suspected that the instability was related to the fact that, for the model, the blade coning frequency was quite low due to the blade retention flexures. These flexures were reinforced in order to appreciably raise the blade coning frequency. The model was then operated at zero yaw angle up to 28 miles per hour wind speed corresponding to 2500 RPM without encountering the instability. At 28 miles per hour the model was yawed whereby the rotor speed dropped at 45 degrees yaw angle to 1450 RPM. When yawing further beyond 50 degrees the stop pounding instability reoccurred but could be removed by yawing the rotor back to smaller yaw angles. The observed effect of the coning mode frequency on the instability proves that a coupling between the rigid body blade mode and the coning mode is involved. Blade stall must also be a contributor, otherwise the two modes could not couple, the coning mode being symmetrical, the rigid body mode being asymmetrical. The full scale rotor was tested up to 36 miles per hour wind speed and up to 80 degrees yaw angle without encountering the instability. Presumably it was not stalled in this test range. The coning frequency is high, see Figure 8.

The model instability may be related to a phenomenon observed with the NASA DOE MOD-0 machine in the configuration with teetering untwisted blades reported in Reference 4. The MOD-0 operated for these tests at substantially lower RPM than normal and closer to blade stall. Stop pounding of the teetering motion occurred repeatedly after encountering a gust. The stop pounding condition persisted after passing of the gust and could only be removed by feathering the blades. Stop pounding has also occurred in two bladed teetering helicopter rotors and has caused the destruction of rotors in flight. Conditions with deep stall should be avoided in teetering rotors.

ANALYSIS OF STEADY STATE YAW CHARACTERISTICS

The analytical studies were conducted in support of the design for the atmospheric test equipment. Figure 4 shows the effect of yaw angle on the power coefficient C_p. The curves are labelled according to the rotor angle of attack (90^o minus yaw angle, see Figure 1). The graphs have been estimated with the method of Reference 5, correcting for the opposite blade twist and for dynamic stall effects. Similar graphs based on analysis are given in Reference 6, based on tests in Reference 7. The cubic curve $C_Q/\sigma = .008$ represents approximately the power required coefficient for the 3 phase alternator. The operational points for the various yaw angles, indicated by circles, are the intersections of the power required and power available curves. At zero yaw angle ($\alpha = 90^o$) the machine operates with maximum power coefficient. The tip speed ratio $\Omega R/V$ is constant up to rated wind speed, the RPM then varies in proportion to the wind speed. Beyond rated wind speed the RPM and power is kept constant by yawing the wind turbine out of the wind. The power coefficient is now smaller and less than the maximum for a given yaw angle.

ANALYSIS OF YAW TRANSIENTS

Yaw transients are easy to compute since one can assume that the emasculated rotor does not resist a yawing motion. The undamped natural frequency in yaw depends only on the tail vane parameters.

$$\omega = (C_{L\alpha} q A_T h/I)^{\frac{1}{2}}$$

The yaw damping ratio is

$$\zeta = \omega h/2V$$

The natural frequency of the damped yawing motion is

$$\omega_n = (1 - \zeta^2)^{\frac{1}{2}}$$

For the test machine: $A_T = 12.5$ ft^2, $C_{L\alpha} = 3.0$ $I = 370$ slug ft^2, $h = 15.5$ ft. A wake factor of .7 was assumed to obtain the lift slope. For V = 21 miles per hour (9.5 meter per second) and standard sea level density one obtains

$$\omega_n = 1.31 \text{ rad/s}, \quad \zeta = .33$$

The yaw response to a unit step input of wind direction change is shown in Figure 5. The new wind direction is reached after 1.5 seconds and there is a 30% overshoot. After 4 seconds the machine is practically aligned with the new wind direction and stays aligned. The maximum yaw rate is $.6\alpha_{TO}$ rad/sec.

It is of interest to establish the effect of upscaling of the machine. From the given expressions it follows for geometric similarity and assuming that masses increase with the cube of the length dimension:

- The natural yaw frequency increases in proportion to wind speed.
- The natural yaw frequency is inversely proportional to the length dimension.
- The yaw damping ratio is independent of wind velocity and of scale.
- The damping ratio increases with $h(hA_T/I)^{\frac{1}{2}}$. For given geometry a light tail boom gives a high damping ratio.

One can easily show that for the rotor, assuming the cube law for the masses, the natural frequencies are also inversely proportional to the length dimension, and that damping ratios are independent of scale. Thus, the rotor scaling laws match those for the tail vane. A given step change in wind direction will lead, at the same wind speed, to the same cyclic pitch amplitude, no matter what the scale. Figure 5 shows also the time scale for a MOD-0A size machine with 5 times the diameter of the test rotor.

FURL TEST DATA

A number of power-off and power-on furling tests were conducted and several automatic furlings occurred in response to rotor overspeed. A particularly severe furling test consisted of a sudden power cut with simultaneous start of furling as it could occur by the blowing of a fuse in the alternator load circuit. Figure 6 shows the time history for such a case. The initial conditions were 16.5 miles per hour wind speed, 170 rotor RPM, 15° furl angle. The furl angle reached its maximum value of 80° after 4.3 seconds (15°/sec). The rotor speed reached the maximum of 225 RPM after 3.3 seconds. After 8 seconds a gust occurred increasing the wind speed to 20 miles per hour. At the same time the power was inadvertently cut in for 2 seconds. The RPM declined steadily. The overspeed ratio for this power cut-out case was 225/170 = 1.32. The rotor, the transmission system and the generator must be capable of occasionally sustaining such an overspeed. If the power cut-out should happen together with the beginning of a gust, the overspeed would be greater. A higher furl rate than 15°/sec would reduce the overspeed after power cut-out. The wind velocity was measured at 45 feet height, 15 feet below the rotor center.

VIBRATIONS AND DYNAMIC LOADS TEST DATA

The test machine is a modified Astral Wilcon Model 10B mounted on a free standing Unarco-Rohn S.S.V. 60 foot high tower which has been made tiltable to a near horizontal position to facilitate maintenance of the instrumentation. Vibration frequencies and damping ratios were first analyzed and then corrected from vibration test results at zero rotor speed. The effect of rotor speed on the blade natural frequencies as shown in Figures 7 and 8 was computed. The operational range is between 120 and 250 RPM. In this range there is a 3P resonance with the fundamental in-plane rotor mode. It was found to be hardly noticeable. The 2P coning mode resonance at an overspeed of 280 RPM is quite strong despite a high damping ratio of .21. Higher harmonic resonances with the higher modes were found to be weak. There is a wide separation between the in-plane mode frequency and the 1P line. The 1P gravity excitation is, therefore, not amplified and no 2P gravity hub loads exist. The asymmetrical rigid body mode (cyclic pitch) is placed between the 1P and 3P lines and shows little resonance excitation. This mode is furthermore well damped with a damping ratio of .26.

Of the various tower and tail boom modes only the 3 modes listed in Table 2 were found to be of any significance.

Table 2

Tower and Tail Boom Resonances

Excitation	First Tower	Vertical Boom	Second Tower
1P	112	160	--
2P	56	80	--
4P	28	40	180

The 1P tower excitation at 112 RPM was found to be mild. there is a 1P vertical tail boom excitation at 160 RPM which has an effect on almost all dynamic loads as seen in Figure 9, where the main harmonic contents is indicated for each graph. The yaw post bending moment is taken at the upper yaw bearing and peaks at the vertical tail boom 1P resonance of 160 RPM. The tail boom vertical root moment, not shown in Figure 9, is equal to the yaw post moment. It appears that the vertical tail boom resonance affects, in addition to the yaw post, also the blades. The stresses from these loads are quite small. The vertical and horizontal accelerations of the machine just aft of the hub are also small, not exceeding ±.15g even at the tower or tail boom resonances.

Table 3 shows the maximum measured dynamic transient loads at 3 furl angles for yaw post bending, for flap bending of the rotor center, and for rotor torque. The 1P in-plane bending amplitude at the rotor center is constant throughout and determined by gravity loads. Despite the two bladed rotor and despite rapid yawing the test machine is quite benign with respect to dynamic loads and vibrations.

Table 3

Maximum Transient Loads ± in-lbs

Furl Angle	RPM	Yaw Post	Flap Bend.	Torque
15°	200	4100	2500	1170
30°	200	3500	3100	1160
45°	144	3700	440	670

In-plane bending: 1800 in-lbs throughout

Analyses for several potential linear aeroelastic instabilities were performed. Bending torsion blade flutter up to 400 RPM cannot occur. A whirl instability of the two bladed rotor is predicted for equal rotor support stiffness in the vertical and horizontal direction. Due to the free yawing the horizontal rotor support stiffness is zero and analysis as well as tests showed that in this case no whirl instability exists. The Coleman type of mechanical instability from coupling of the in-plane blade mode with the rotor support mode was analyzed and found to occur far above 400 RPM. The rotor rigid body mode frequency coalesces with the in-plane mode frequency at about 350 RPM. A closed form approximate solution showed a slight negative damping ratio of the coupled mode. A more elaborate finite element analysis resulted in positive damping of this mode. One can conclude that the test machine is free of linear aeroelastic instabilities.*

STARTING TEST DATA

The wind velocity required for starting depends on the system friction torque and on the aerodynamics of the inner blade section. Due to

*The aeroelastic and vibration analyses were performed by the graduate students T.W.H. Ko and S.Y. Chen, under the supervision of Professor D.A. Peters.

the feathering mechanism of the Astral Wilcon Model 10B machine, 30% of the inner blade has no aerodynamic section but merely a circular shaft. Though the test rotor has no feathering mechanism and could have an aerodynamic section extending close to the hub, the available Model 10B blades were used to keep the cost of the test machine low.

Figure 10 shows a comparison of the test blade planform with a possible planform of a production blade, which would have, according to the analsis, twice the starting torque and a considerably improved performance. The measured contributions to the starting rotor torque were:

Rotor shaft and gearbox	3.5 foot lbs.
Alternator	1.0 foot lbs.
Alternator belt drive	1.0 foot lbs.
Total	5.5 foot lbs.

Figure 11 shows the time history of a starting test less belt drive, that is with 3.5 foot lbs. starting friction. The production type blade would have about the same characteristics with 7 foot lbs. starting friction. With 8 miles per hour average wind velocity the rotor accelerates steadily to 40 RPM within 40 seconds. It then takes off very rapidly and reaches 120 RPM in another 10 seconds. The cyclic pitch amplitude is initially large with an occasional stop contact at $\pm 11.5^{\circ}$ during the first few revolutions. Beyond 40 RPM the amplitude reduces to a small value of $\pm 2^{\circ}$. Starting tests were conducted up to a furl angle of 60°. Somewhat higher wind velocity is required for starting at higher furl angles.

STASTICAL TEST DATA

Due to the fluctuating wind velocities it is difficult to obtain data on steady conditions. The data points in Figure 12 of rotor power vs. rotor speed were obtained during brief periods of approximately steady wind. For both unfurled and 40° furl conditions the data follow closely the constant torque coefficient line $C_Q/\sigma = .008$, see also Figure 4. The highest two points were taken during gusts when the rotor was accelerating. The power from the torque meter reading was corrected for the accelerating torque. The total torque including the inertia torque is again on the $C_Q/\sigma = .008$ line.

The statistical data presented in Figures 13 to 18 were obtained with a microcomputer. For each dynamic variable 128 samples per second were taken. The computer then updated mean, standard deviation, overall maximum and overall minimum. After completing this task for all measured variables, the next set of 128 samples per second per quantity was taken. The intervals between the sample sets were about 3 seconds. For each sample set of one second duration the wind velocity was measured and the 1/2 meter per second wide velocity "bin" was determined for that particular set. Each run lasted for about one hour.

Figure 13 shows a typical distribution of sample sets. A logarithmic scale is used for the number of sample sets. Each wind speed "bin" between 2 and 6 meter per second contains about 100 sample sets, whereby each set contains 128 samples per measured quantity. The average power coefficient for each bin is shown in Figure 14. At low wind speed this coefficient is high because the inertia of the decelerating rotor adds to the shaft torque. At high wind speed the power coefficient is low because the inertia of the accelerating rotor subtracts from the shaft torque, see also Figure 12. If one weighs the average C_p value in each wind speed bin with the number of sample sets in this bin, and if one then takes the weighted average over all bins, one obtains the value of $C_p = .46$. This represents the ratio of the energy transmitted during the run to the shaft over the total wind energy flowing through the disk during the period of the run.

Figure 15 shows the distribution of the average power coefficient for 45° furl angle. The C_p values are now much lower, the weighted average over all bins is $C_p = .18$.

Figure 16 shows an example of the distribution of mean and standard deviation of the rotor RPM over the bins. For steady conditions the tip speed ratio λ should be independent of wind speed. Actually the tip speed ratio is higher at low wind speed, because the rotor runs faster than for equilibrium, the tip speed ratio is lower for high wind speed, when the rotor runs slower than for equilibrium.

Figure 17 shows an example of the mean, standard deviation, maximum and minimum of the cyclic pitch amplitude vs. rotor RPM "bins" at 30° furl angle. The vertical scale is in volt, whereby 1 volt = 5° cyclic pitch amplitude. For low RPM the mean cyclic pitch amplitude is $\pm 5^{\circ}$, for higher RPM it is about $\pm 2.5^{\circ}$.

Figure 18 shows an example of the effect of yaw rate on the cyclic pitch amplitude. Yaw rate "bins" of 3°/sec. width were used and the mean and standard deviation of the cyclic pitch amplitude in each bin was determined. For the case of Figure 18 the furl angle was 20°, and the yaw rates were obtained from the yaw post rotation due to wind direction changes. Only yaw rates in the furl direction were considered. For the opposite yaw rates the cyclic pitch amplitudes are about 30% smaller. A 14°/sec. yaw rate produces a mean cyclic pitch amplitude of $\pm 4^{\circ}$ which is in agreement with analytical estimates.

CONCLUSIONS

The test data taken with the experimental wind turbine during close to 100 hours of operation in winds up to 36 miles per hour have shown that the two bladed vane stabilized rotor with passive cyclic pitch variation can be continuously operated power-on at yaw angles up to 50° with a low level of dynamic loads and vibrations. The machine can also be rapidly yawed with with rates or more than 15°/sec without a noticeable increase in dynamic loads and vibrations. In partially furled conditions the rotor power can be held to a small fraction of the power when unfurled. With the present furl rate of 15°/sec

a sudden power loss results in 32% overspeed. So far automatic operation of the furl control was limited to overspeed furling. A fully automatic furl control is being developed.

REFERENCES

1. Hohenemser, Kurt H, and Swift, Andrew H.P., "The Yawing of Wind Turbines with Blade Cyclic Pitch Variation", SERI Second Wind Energy Innovative Systems Conference, December 3-5, 1980, SERI/CP-635-938, pp. 207-224.

2. Hohenemser, Kurt H., "Some Alternative Dynamic Design Configurations for Large Horizontal Axis WECS", Wind Turbine Structural Dynamics, Workshop held at Lewis Research Center, Cleveland, Ohio, November 1977, DOE CONF-771148.

3. Wheatley, J. B., and Bioletti, C., "Wind Tunnel Tests of 10 Foot Diameter Autogiro Rotors", NACA Report No. 552, October 1935.

4. Glasgow, J. C., and Miller, D. R., "Teetered Tip Controlled Rotor: Preliminary Test Results from MOD-0 100-KW Experimental Wind Turbine", AIAA/SERI Wind Energy Conference, April 9-11, 1980, Boulder, Colorado, pp. 261-268.

5. Gessow, A., and Tapscott, R. J., "Tables and Charts for Estimating Stall Effects on Lifting Rotor Characteristics", NASA TN D-243, May 1960.

6. Norton, J. H. Jr., "The Development and Testing of a Variable Axis Rotor Control System with 5 Meter Rotor and Direct Drive Alternator", Proceedings Small Wind Turbine Systems 1979 Workshop coordinated by Rockwell International and held at Boulder, Colorado, February/March 1979, Vol. 1, pp. 31-64.

7. Stoddard, F., Perkins, F., and Cromack, D., "Wind Tunnel Tests for Fixed-Pitch Start-up and Yaw Characteristics", Technical Report UM-WT-TR-78-1, NASA Lewis, June 1978.

The work was sponsored by the Solar Energy Research Institute in Golden, Colorado under Subcontract No. XH-9-8085-3 to Washington University Technology Associates (WUTA).

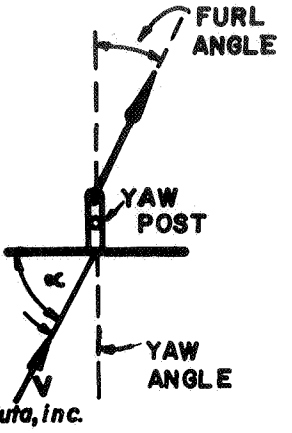

Figure 1—Schematic plan view

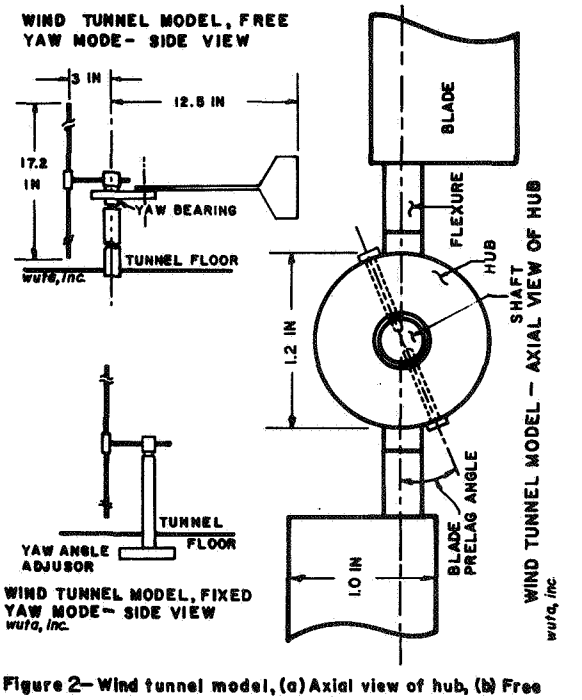

Figure 2—Wind tunnel model, (a) Axial view of hub, (b) Free yaw mode—side view, (c) Fixed yaw mode—side view.

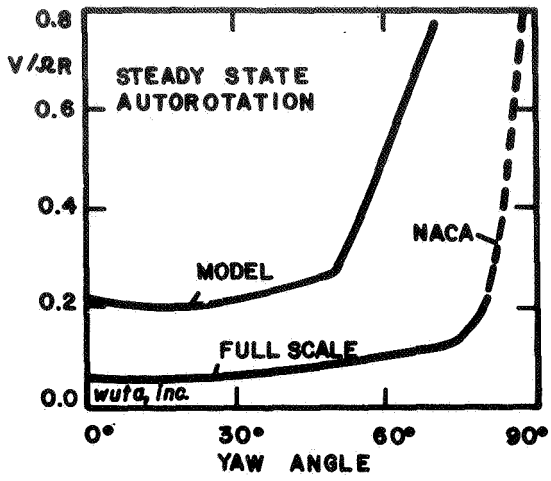

Figure 3— Test results, steady state model and full scale autorotation.

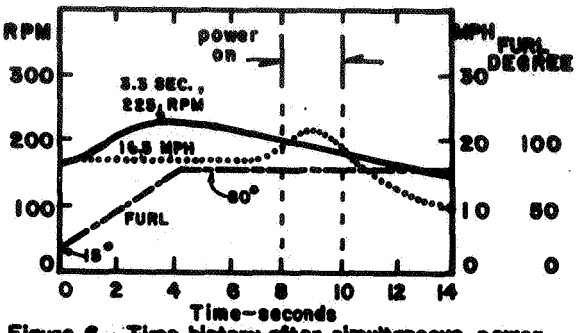

Figure 6— Time history after simultaneous power cut and initiation of furling.

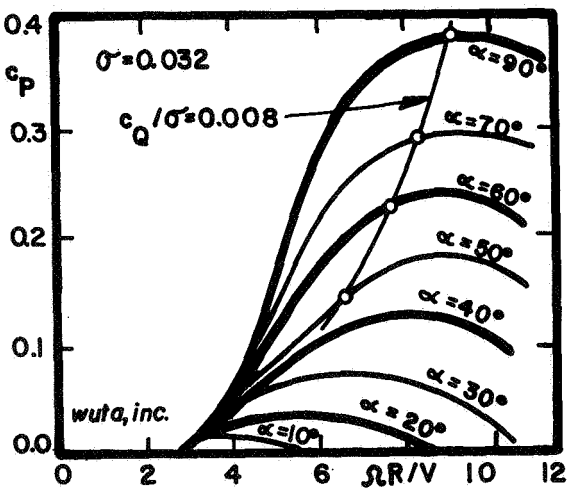

Figure 4— Power coefficient c_p vs tip speed ratio ΩR/V for constant rotor angle of attack values α.

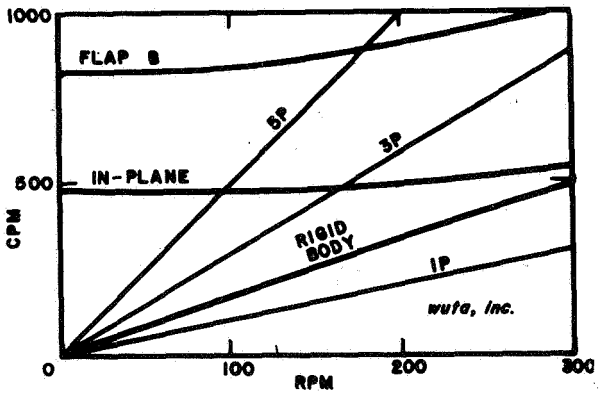

Figure 7—Asymmetrical rotor mode frequencies.

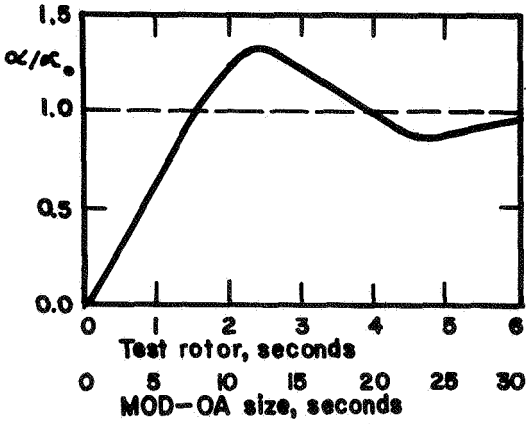

Figure 5— Yaw response to unit step input.

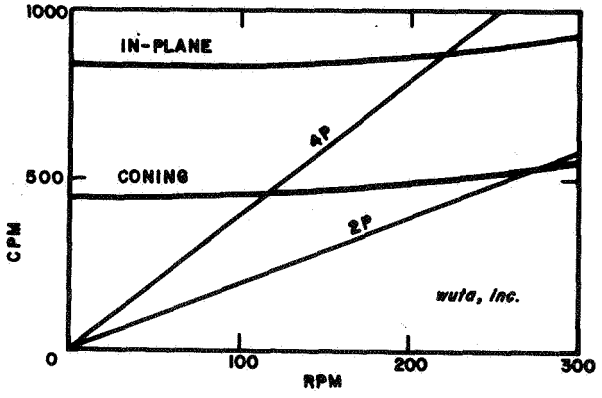

Figure 8—Symmetrical rotor mode frequencies.

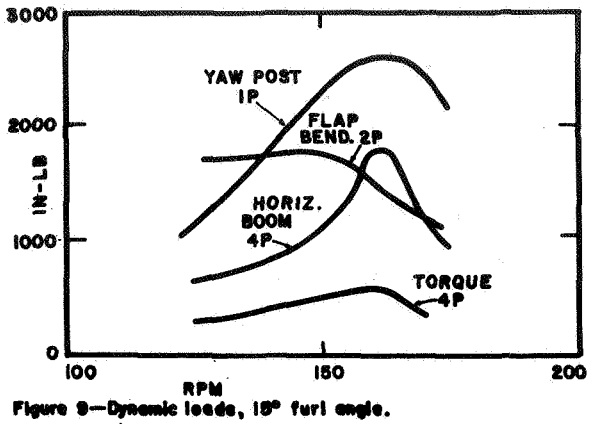

Figure 9—Dynamic loads, 15° furl angle.

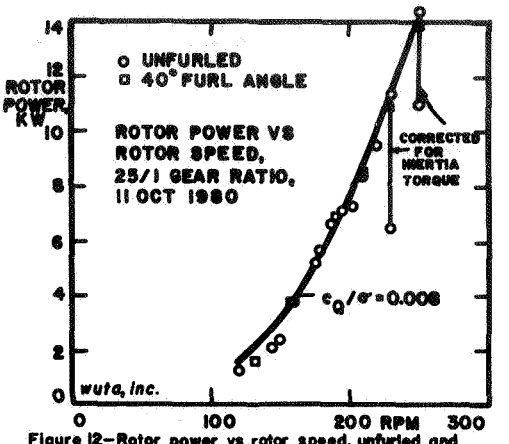

Figure 12—Rotor power vs rotor speed, unfurled and 40° furl angle.

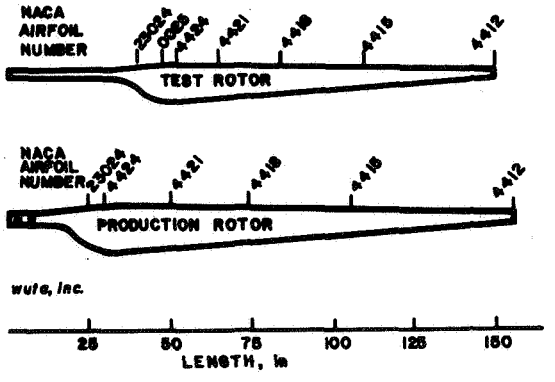

Figure 10—Test and production rotor.

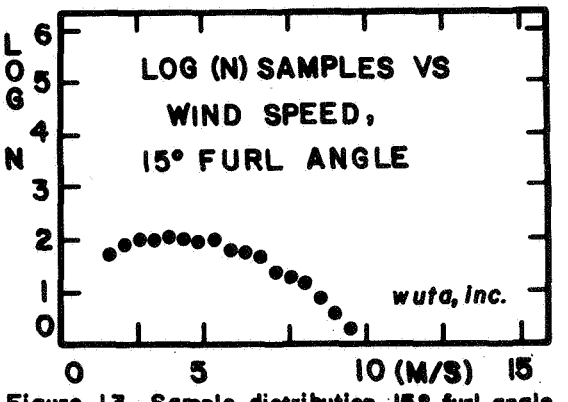

Figure 13—Sample distribution, 15° furl angle.

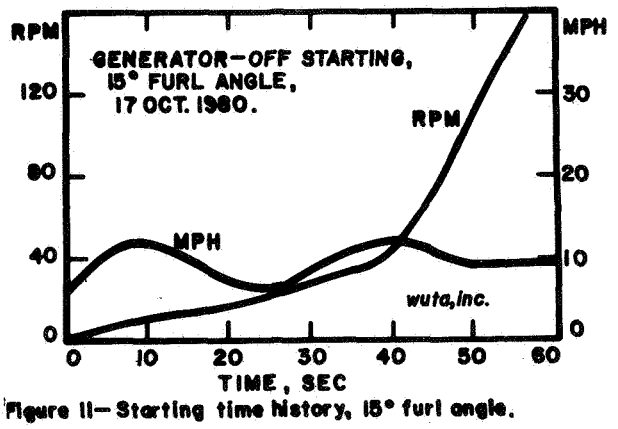

Figure 11—Starting time history, 15° furl angle.

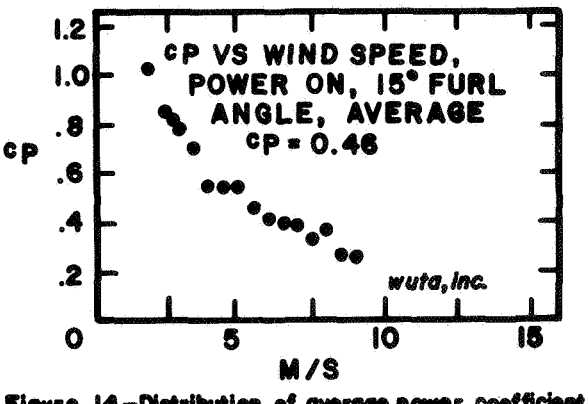

Figure 14—Distribution of average power coefficient, 15° furl angle.

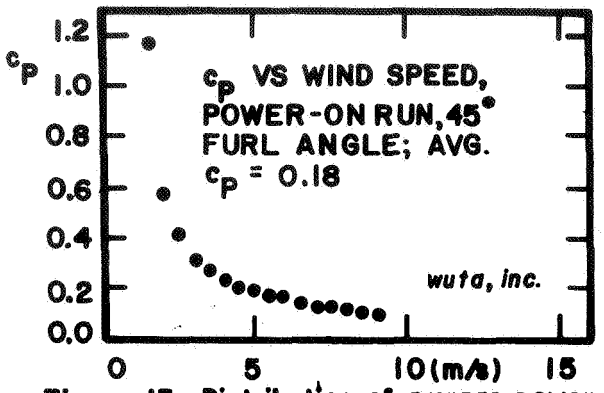

Figure 15—Distribution of average power coefficient, 45° furl angle.

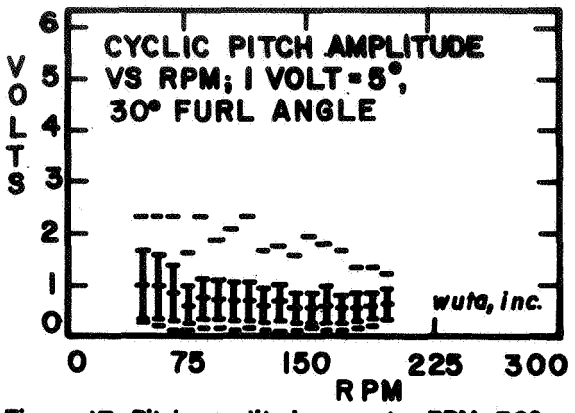

Figure 17—Pitch amplitude vs rotor RPM, 30° furl angle.

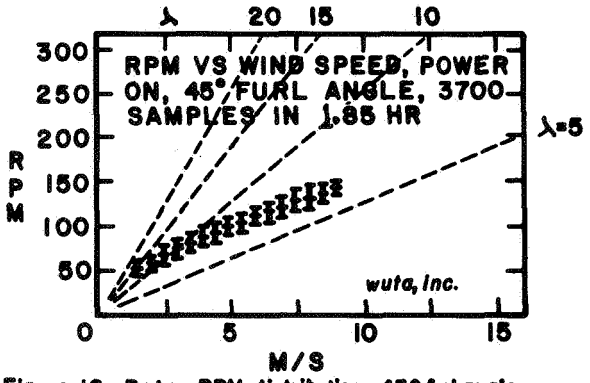

Figure 16—Rotor RPM distribution, 45° furl angle.

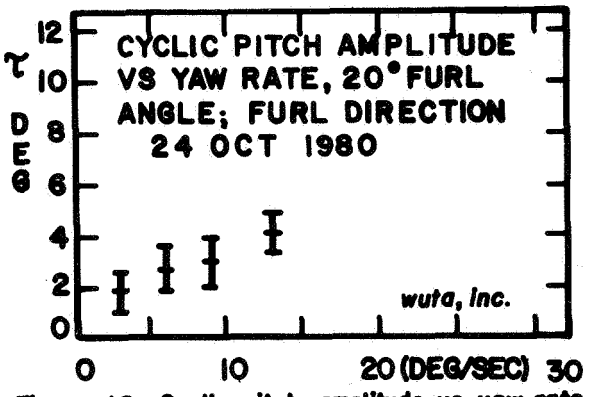

Figure 18—Cyclic pitch amplitude vs yaw rate, 20° furl angle.

QUESTIONS AND ANSWERS

K. Hohenemser

From: A. Smith

Q: Why such high Δ3 angles? And is the high rigid body frequency due to Δ3?

A: *Δ3 has been selected to place the frequency of the rigid body mode between 1 P and 3 P. This gives a Δ3 of about 20°.*

MOD-0 WIND TURBINE DYNAMICS TEST CORRELATIONS*

by

Bennett M. Brooks
Analytical Engineer

Hamilton Standard
Division of United Technologies Corporation
Windsor Locks, Connecticut

ABSTRACT

The behavior of the teetered, downwind, free yaw, MOD-0 wind turbine, as represented by NASA dynamic test data, was used to support confidence in the Hamilton Standard computer code simulations. Trim position, performance at trim, and teeter response as predicted by the computer codes were compared to test results. Using the computer codes, other possible configurations for MOD-0 were investigated. Several new test configurations are recommended for exploring free yaw behavior. It is shown that eliminating rotor tilt and optimizing coning and blade twist can contribute to good free yaw behavior and stability. The effects of rotor teeter, teeter gravity balance, inflow and other physical and operating parameters were also investigated.

INTRODUCTION

The 100 kW experimental MOD-0 wind turbine located near Sandusky, Ohio, (Plumbrook installation) has served as the test bed for the U.S. Large Horizontal Axis Wind Energy Program since its initial operation in 1975 (Reference 1). The MOD-0 installation is shown in Figure 1. In 1980, NASA conducted tests on the machine in downwind operation mode, with a teetered hub, and tip controlled blades. The tests covered the range of start-up, shut-down, and normal operation and focused on power control characteristics, and aerodynamic performance. Information in the strip chart data included such operating parameters as wind speed, yaw direction, generator power output, teeter angle, blade bending moments and bearing loads.

Since early 1979, Hamilton Standard has supported these aspects of the NASA MOD-0 SR and T Program with analytical studies using the F762 computer code simulation. The F762 program has been under development at Hamilton Standard for several years. This analysis is a teetering rotor computer program characterized by a rigorous modeling of the blade, and accounting for the nonlinear and time varying structural twist using modal response methods.

The tower response including yaw motions are described in the six degree of freedom equations of motion of the hub. The complete nonlinear response of the tower and rotor time history solutions are printed and/or plotted for harmonic analysis and transient aeroelastic response calculation purposes. The co-ordinate system for the wind turbine as defined in F762 is described schematically in Figure 2. Note, from the top-left drawing in Figure 1, that the difference between the nacelle yaw and the wind yaw is the angle that the nacelle makes with respect to the wind. This is known as yaw alignment.

This study of the MOD-0 test data had the following three objectives:

1. Confirm the behavior of the MOD-0 machine as represented by the NASA data using the F762 time history program.

2. Recommend to NASA a new test configuration for MOD-0.

3. Study yaw trim behavior as a function of blade twist, rotor cone, Δ3, inflow character, teeter, and other physical and operating parameters.

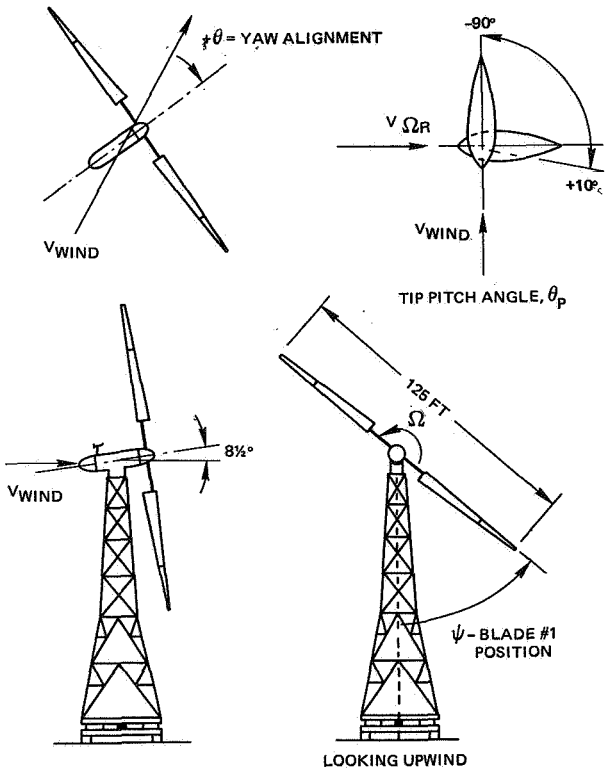

Figure 1 - MOD-0 kw wind turbine with teetered, tip control rotor

*Presented at the Second DOE/NASA Wind Turbine Dynamics Workshop, February 24-26, 1981 in Cleveland, Ohio.

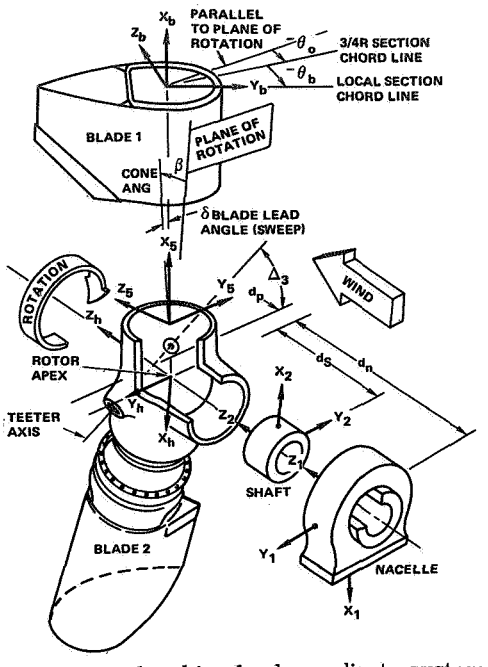

Figure 2 - Wind turbine load coordinate systems

The results of this study are summarized in this paper in two parts: one dealing with the correlation of test and calculations and the other dealing with optimized MOD-0 configurations.

Test/Analysis Correlation

Test data for the MOD-0 machine were compared with calculations for a model simulation using the F762 computer code time history results. A comparison of calculated and measured yaw behavior for the MOD-0 machine is shown in Figure 3. Both the test and calculations were for the MOD-0 operating at 33 RPM with no tip control. The calculations were made for a constant wind speed of 18 mph, whereas the test was conducted at varying wind conditions. The test was conducted at zero blade angle. The blade angle used for calculations was set at -4.5 degrees in order to produce the rated power at rated wind speed.

The MOD-0 machine was tested first in the fixed yaw mode with the yaw brake on. During subsequent test runs, the brake pressure was gradually bled off to zero so that the machine was allowed to yaw freely. The bottom curve in Figure 3 shows the tested yaw alignment vs. time. The yaw alignment for this run starts near zero but, as the yaw brake is released, the yaw alignment increases until it stabilizes at about -50 degrees. The variation from -50 degrees is due to the many changes in wind speed and direction which occurred during the test run. The results from the calculation are shown in the top curve. The model used in the calculation was started at a zero yaw position and allowed to yaw freely. The final yaw alignment settled at -65 degrees, approximately matching the test result. Note that the time for the calculation to reach trim is much less than the time observed during the test. The reason for this is unclear, but it is believed to be due to friction in the real system caused by drag on the yaw brake and in the yaw bearing.

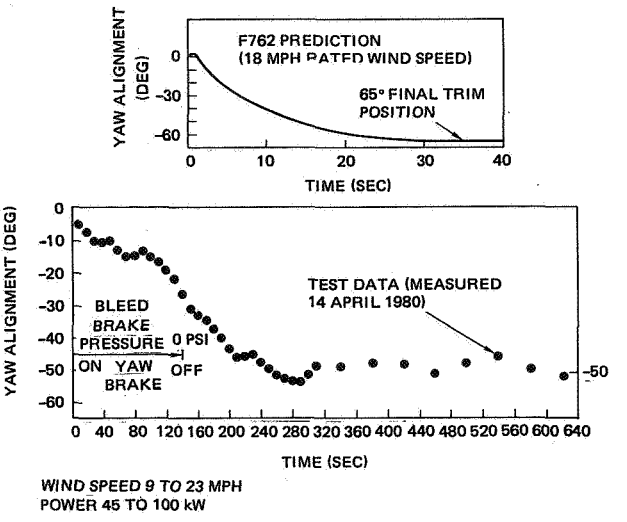

Figure 3 - Yaw behavior MOD-0 Plumbrook

A comparison of measured and calculated teeter angle time histories is shown in Figure 4. The measured teeter angle time history is shown in the top curve for a portion of the test run when the wind speed was steady at 18 mph ± 1 mph for about 10 seconds. The yaw alignment was -50 degrees varying little for this period and the teeter angle had reached steady-state. The corresponding F762 prediction is shown in the bottom curve. The time history calculations used in Figures 3 and 4 were started with no initial displacement at constant RPM. The rotor was therefore instantaneously immersed in the flow field. Thus, there was an initial transient response for an instantaneous 18 mph gust. The results are qualitatively equivalent to teeter gust responses observed in the measured data. In the calculation, this initial transient quickly decays, to the steady-state teeter response shown. The predicted teeter angle is of similar magnitude as that shown for the test data.

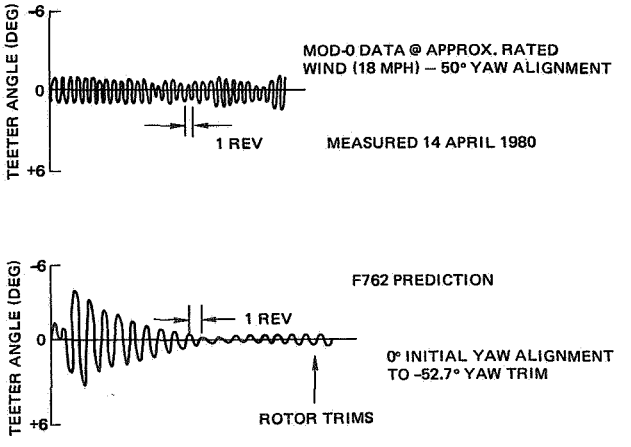

Figure 4 - MOD-0 teeter angle F762 vs. measured data

A comparison of the MOD-0 measured and calculated performance vs. wind speed is shown in Figure 5. The measured data represent the actual power output of the MOD-0 machine alternator, with the machine operating in free yaw at the approximate yaw trim position. This is within a few degrees of the -50 degree position as shown in Figure 3. The predicted performance was, for convenience, calculated using a computer code, which assumes a fixed yaw, rigid rotor. This computer code has basically the same aerodynamic formulation as in F762 and has been shown to give very similar performance results. The calculation assumed a fixed yaw position of -50 degrees and an alternator system efficiency of 80 percent (Reference 2). The sensitivity in the measured data of power output to wind speed at this extreme yaw position is well predicted by the calculation. The calculation is somewhat conservative for output power level at a given wind speed, which is possibly caused by the extreme yaw angle or by error in the assumed alternator efficiency, wind shear or other factors.

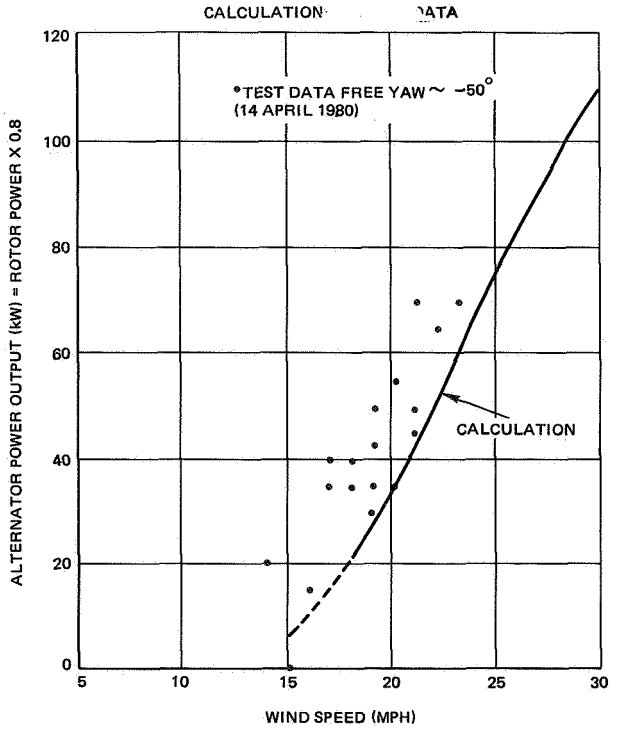

Figure 5 - MOD-0 performance at -50° yaw alignment 0° blade angle - calculations vs. test data

MOD-0 Configuration Studies

It was desired to design a new test configuration for the MOD-0 machine, one that was practical to build and that would provide better yaw behavior than the current design to achieve consistently full rated power. Using the F762 computer code, studies of various MOD-0 configurations were performed to accomplish this by investigating yaw trim behavior as a function of blade twist, coning, Δ3, teeter, and other basic parameters.

The effect of introducing aerodynamic blade twist to the MOD-0 base configuration is shown using the yaw trim diagram in Figure 6. The base configuration is the computer code model for the current MOD-0 machine described above at rated wind conditions. The investigated twist distributions are based on the Hamilton Standard twist distribution. The amount of twist at each radial station relative to the reference station (3/4 radius) is multiplied by a constant factor. Multiplying by 1.0 gives the Hamilton Standard twist, see Table 1, while a zero multiplier gives an untwisted blade. The base configuration has untwisted blades. The yaw behavior for the base case is shown at the far left of Figure 6. The zero twist case will yaw to the -65 degree position and trim (see Figure 3). The MOD-0 with Hamilton Standard aerodynamic twist will trim at -54 degrees yaw. Increasing the twist will cause the MOD-0 to trim closer to the wind.

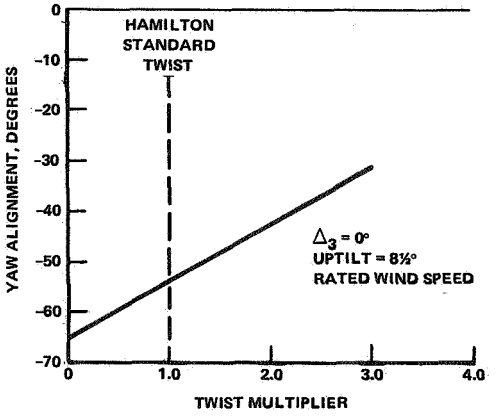

Figure 6 - Effect of twist on MOD-0 yaw trim calculated results, Plumbrook test configuration

Table 1

Hamilton Standard Wind Turbine - Blade Twist

	Radial Station	Twist (Degrees)
	0.0203	-12.5
	0.0751	-12.1
	0.146	-11.7
	0.217	-10.2
	0.289	- 7.80
	0.360	- 5.63
	0.431	- 4.14
	0.502	- 2.91
	0.573	- 1.94
	0.644	- 1.02
	0.715	- 0.31
Reference Station	0.750	0.00
	0.787	0.10
	0.858	0.53
	0.929	0.96
	0.982	1.22

Several configuration changes to the base model, without blade twist, were studied. The effect of coning the blades 6 degrees downwind on yaw trim behavior was examined. Coning the rotor without providing static balance causes the rotor to yaw further from the wind than the base case. Statically balancing the coned rotor, by placing the teeter pin at the rotor center of gravity, decreases the yaw rate somewhat. However, the trend is still to yaw further off wind. Finally, the addition of a 20 degree Δ3 angle to the teeter pin produces insignificant changes to the yaw behavior. Thus, none of these coning modifications to the base model produced satisfactory yaw behavior.

Since the base model has 8 1/2 degrees of uptilt, there is a significant component of the rotor torque in the yaw moment direction. Therefore, the effect of removing uptilt was examined. The results are shown in Figure 7, where the base case with 8 1/2 degrees uptilt is shown at the right. The base case without uptilt is shown at the left. By removing the uptilt, the yaw rate is greatly decreased, although a trim position is not found. It was therefore, decided to investigate further modifications with the uptilt removed.

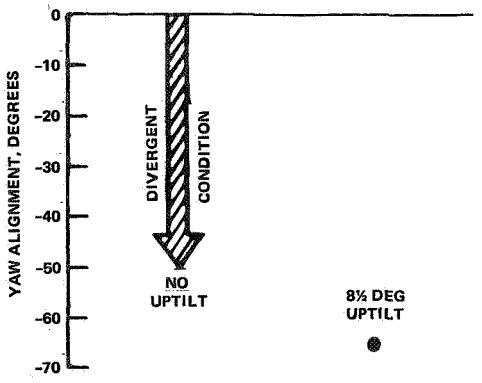

Figure 7 - Effect of uptilt on MOD-0 yaw trim untwisted rotor $\Delta_3 = 0^\circ$ rated wind speed

The effect of tilt removal and rotor static balance on the MOD-0 machine are shown in Figure 8. The configuration is identical to the base case except that the rotor is untilted and coned 6 degrees. The degree of rotor static balance can be varied by moving the teeter pin from the rotor apex to some fraction of the distance to the rotor center of gravity. The distance between the rotor apex and the teeter pin is called hub undersling. For the MOD-0 rotor coned 6 degrees, static balance is achieved with a hub undersling of 27.85 inches. The rotor is called half-balanced if the hub undersling is 13.925 inches.

As shown in Figure 8, there is no improvement in the yaw trim position for the fully statically balanced configuration over the base model. However, the half-balanced configuration shows some promise, trimming at about -45 degrees. The configuration with only 40 percent static balance shows further improvement, trimming at about -28 degrees. With less than 40 percent static balance the trim diverged. For these cases, if the time history is initialized with the rotor in the positive yaw position region, the rotor tends to move further off the wind, not toward the trim position. If the degree of static unbalance is increased, this behavior becomes worse.

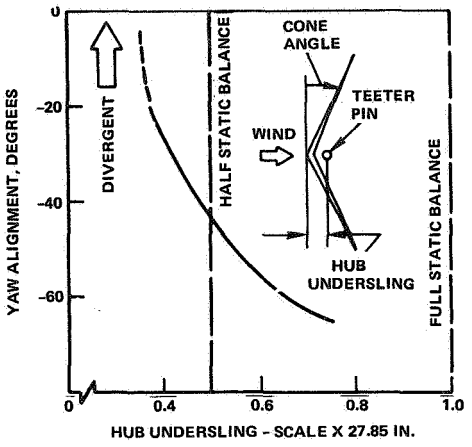

Figure 8 - Effect of rotor static balance on MOD-0 yaw trim, claculated results, untilted, untwisted rotor, $\Delta_3 = 0^\circ$ cone = 6° rated windspeed

It was apparent that a cause of this poor yaw behavior could be improper coning of the rotor blades. Since static balancing of the rotor affects yaw behavior, it seemed reasonable that the unbalancing effect of deflection in the loaded rotor, that is out-of-plane blade root bending, could also effect yaw behavior. Thus, a study was made to determine the cone angle that relieves out-of-plane (flatwise) blade bending moments. Since removing rotor uptilt and introducing blade twist improved the yaw behavior of MOD-0, these features were also included in the next study configuration. The results of the study are shown in Figure 9. The averaged out-of-plane blade root bending moments are plotted vs. rotor cone angle. These cases were statically unbalanced. The flatwise root moment is relieved for a cone angle of about 3.7 degrees, for the rated wind speed and power condition studied. The optimum cone angle would change for another wind speed since the balance of aerodynamic, structural dynamic and gravity forces would be different.

The free yaw behavior of the MOD-0 with optimum coning for rated wind speed was studied for several blade twist distributions. The results are shown in Figure 10. The configuration studied is untilted, with 3.7 degree coning, zero hub undersling and zero Δ3 angle. The blade twist distributions are multiples of the Hamilton Standard twist distribution. All of the models trim in yaw closer to the wind than the unconed, uptilted base configuration. The case with Hamilton Standard twist trims very near the wind. The cases with more twist trim more rapidly. Thus, it seems

that one way to insure rapid yaw trim behavior for the MOD-0 wind turbine is to provide highly twisted blades.

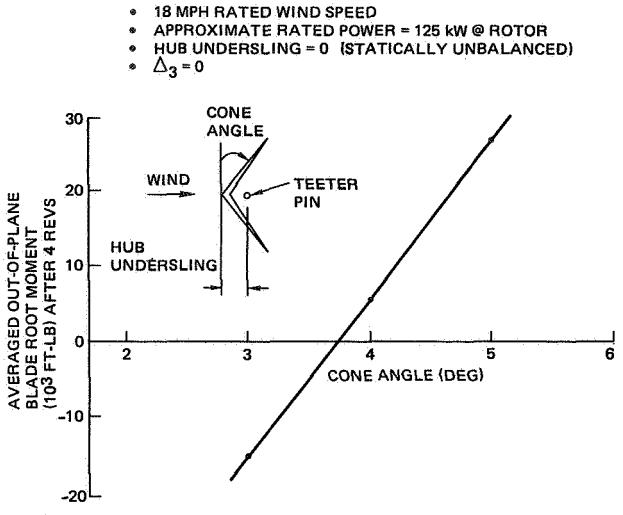

Figure 9 - MOD-0 optimum cone angle downwind untilted rotor with Hamilton Standard blade twist

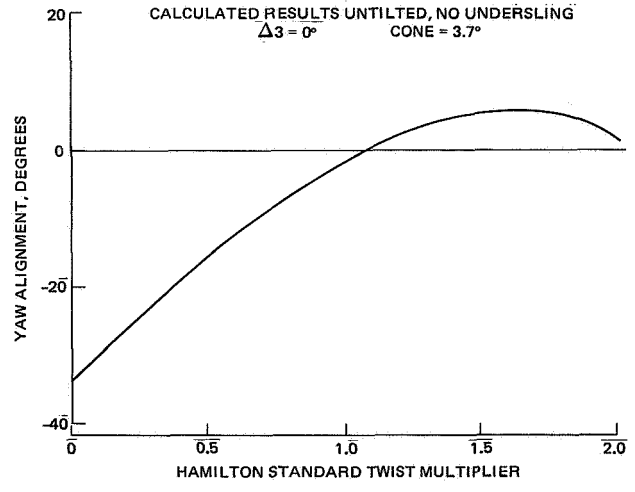

Figure 10 - Effect of twist on optimum MOD-0 yaw trim

Another way to modify yaw behavior is to include a $\Delta 3$ angle at the teeter pin. The effects of varying $\Delta 3$ for the MOD-0 configuration with optimum coning and Hamilton Standard twist are shown in Figure 11. The convention for positive $\Delta 3$ is shown in the diagram. It is also defined as teeter upwind, leading edge downwind. The case with zero $\Delta 3$ is repeated from Figure 10 so that the effects of twist and $\Delta 3$ can be compared. The models with large positive $\Delta 3$ trim in the positive yaw region at about +40 degrees. For negative values of $\Delta 3$, the trim position moves slightly off the wind.

The effect of wind speed on yaw behavior was examined for the MOD-0 configuration with no tilt, zero hub undersling, optimum coning, zero $\Delta 3$, and Hamilton Standard twist. Wind velocities higher than rated but less than cut-out were studied. For these conditions, blade angle was set to maintain rated power. The wind velocities were input to the calculation as gust factors, so the wind shear and tower shadow did not change. The higher velocities shift the yaw trim position somewhat, but do not seriously disturb the trim behavior. In addition, studies of yaw behavior using several different wind shear and tower shadow descriptions were made. The effect of these factors on yaw trim behavior is insignificant. Any configuration which is chosen for testing should be investigated for yaw behavior and stability at cut-in and cut-out wind velocities.

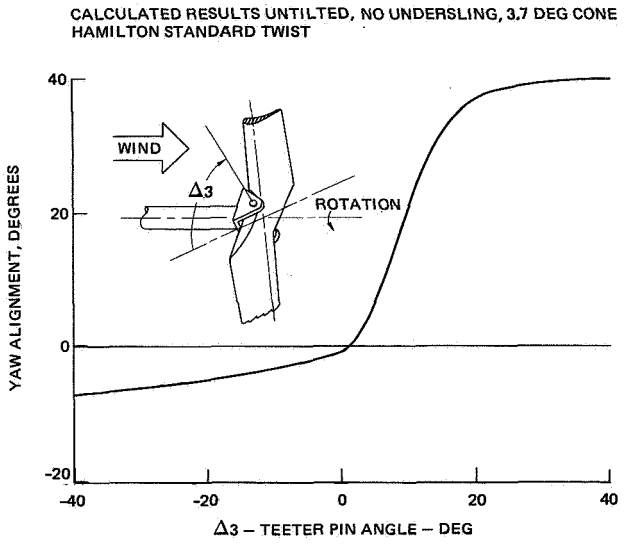

Figure 11 - Effect of $\Delta 3$ on optimum MOD-0 yaw trim

So far, the configurations presented which display satisfactory yaw behavior had blade twist, optimum coning, and static unbalance. The effect of introducing hub undersling at the teeter pin (see Figure 8) was studied next. For a cone angle of 3.7 degrees, the MOD-0 rotor is statically balanced with a hub undersling of 17.2 inches. When this was introduced to the model, it was seen that the yaw trim position shifts significantly off the wind.

The effect of $\Delta 3$ angle on this statically balanced configuration with optimum coning is shown in Figure 12. A positive value for $\Delta 3$ of 30 degrees provides excellent yaw behavior. The yaw trim position is within a few degrees of the wind and the configuration is quite stable. These results show that this type of configuration is successful in providing good yaw trim behavior for free yaw wind turbines.

Finally, the necessity of blade twist for good yaw behavior was confirmed using a MOD-0 configuration identical to that just discussed, but without blade twist. Without twist, yaw trim behavior for this configuration is unstable.

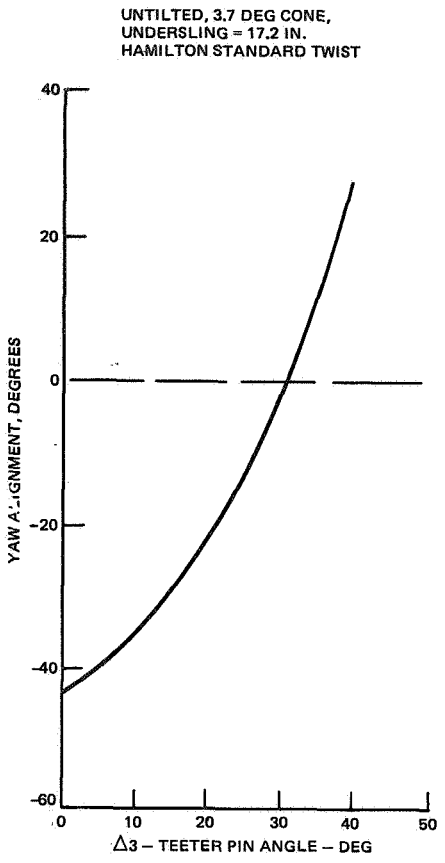

Figure 12 - Effect of Δ3 on the yaw trim of the MOD-0 balanced rotor

These studies demonstrate that it is possible to modify the MOD-0 to a configuration that balances the forces tending to yaw the rotor off the wind, and so achieve good yaw trim behavior. Essential elements of the design are an untilted rotor, optimum coning and blade twist. The value of Δ3 needed to insure good trim position with stability varies with the degree of static balance of the rotor.

CONCLUSIONS

The conclusions reached from this study are:

- The F762 computer code model provides a good representation for the behavior of the MOD-0 machine. Specifically, yaw trim behavior, performance at trim position and teeter angle are reasonably well predicted.

- Assuming that undersling is not possible, the modified free yaw MOD-0 configuration should include the following:

  - No uptilt, as this will reduce the yawing moment.

  - Optimum coning in order to relieve blade root moments and improve trim behavior.

  - Blade twist in order to improve trim stability and performance.

  Calculations show that this configuration would exhibit a final trim position within a few degrees of the wind direction. It is stable for yaw gusts to at least ± 60 degrees to the rotor shaft. The configuration is also stable for higher than rated wind speed and several different wind shear and tower shadow descriptions.

- In addition to the above factors, the effects of hub undersling (rotor static balance) and Δ3, and their interelation were investigated. A stable rotor either with or without hub undersling can be designed. However, the values of Δ3 needed for each case are different in order to insure good yaw behavior.

Acknowledgement

The author would like to thank the members of the Wind Energy Project Office at NASA-Lewis Research Center for their cooperation and assistance in providing the test data and other information necessary to conduct this study.

REFERENCES

1. Glasgow, J.C. and Miller, D.R., "Teetered, Tip-Controlled Rotor: Preliminary Test Results from MOD-0 100 kW Experimental Wind Turbine"; DOE/NASA/1028-80/26, also NASA TM-81445, 1980.

2. Glasgow, J.C. and Pawlas, G., "Drive Train Efficiency for MOD-0 in Teetered-Hub Tip-Control Rotor Configuration"; NASA-Lewis Research Center - Wind Energy Project Office, Project Information Release No. 137, 1980.

QUESTIONS AND ANSWERS

B. Brooks

From: Anonymous

Q: What is the "Hamilton-Standard" twist?

A: *This is the performance optimized nonlinear twist for the SVU configuration.*

From: W.C. Walton

Q: 1) Please explain the term "six-degree of freedom hub."

2) How is the tower represented in the analysis (1) by modes? (2) directly by finite element model?

A: *1) Six-degree of freedom is coupling between the rotor and the tower, 3 translations, 3 rotations.*

2) Indirectly by finite element coupled with the six-degree of freedom hub.

From: Anonymous

Q: How sensitive is yaw behavior to gust characteristics?

A: *The sensitivity of tested yaw behavior to variations in wind speed are shown in Figure 3. Large changes in wind speed produce small effects. Of course, a good machine will have yaw damping.*

From: Y.Y. Yu

Q: Is F762 code proprietary?

A: *Yes.*

THE EFFECT OF δ_3 ON A YAWING HAWT BLADE AND ON YAW DYNAMICS*

Frederick W. Perkins and Robert Jones

Kaman Aerospace Corporation
Old Windsor Road
Bloomfield, Connecticut 06002

ABSTRACT

A single degree of freedom aeroelastic computer model, WMSTAB3, has been employed to perform a parametric analysis of HAWT blade behavior during yaw maneuvers. Over 1,000 different combinations of δ_3 and normal frequency were analyzed.

The effect of δ_3 and flapping stiffness on flapping frequency, phase, and magnitude are discussed. The moments transmitted to the fixed system during yaw maneuvers are calculated and reduced to time constants of response to step changes in wind direction. The significance of the time constants for the configurations considered relative to yaw response rate and lag angle is discussed, along with their possible significance for large HAWT.

INTRODUCTION

The δ_3 hinge is a device which mechanically couples rotor blade pitching and flapping. The δ_3 hinge is typically employed to stabilize lifting rotors by increasing the flapping stiffness and reducing flapping. The stiffness increase also increases the flapping frequency, thereby allowing flexibility in blade tuning to avoid possible structural resonances.

Negative δ_3 is destabilizing. The effect of negative δ_3 is to reduce the flapping frequency, by virtue of reduction in flapping stiffness. The reduction in flapping frequency will be accompanied by increasing flapping as long as the flapping frequency is approaching 1.0 per rev. The phase of flapping response to yaw direction and rate excitations also changes with adjustment of frequency.

These qualitative observations of the effect of δ_3 on the magnitude and phase of flapping response to yaw inputs suggested a quantitative analysis to determine optimum operating configurations for spring restrained teetering type wind turbines. (The δ_3 hinge is easily incorporated in such a rotor by canting the teeter axis and the normal to the feathering axis, as in Figure 1.) Because of the large range of flapping frequencies and candidate δ_3 angles considered, a simple aeroelastic model, WMSTAB3, was developed which could be rapidly executed, yet which retained sufficient sophistication to be acceptable. More than 1,000 possible operating configurations were ultimately analyzed to develop the data reported herein.

The analysis indicates that it is possible to optimize rotor flapping with respect to magnitude or phase, or yaw performance, quantified by response time and/or restoring or damping moments. The operating conditions required for optimization are often contradictory. For example, it is possible to eliminate flapping in the direction of the tower due to either yaw position or rate excitations, but not both simultaneously.

ANALYTIC BACKGROUND

The equations of motion were derived from fundamental mechanics and a linear aerodynamic representation of the forcing function, paralleling Stoddard (Reference 1). The equation of motion of the flapping wind turbine blade is

$$I_b\ddot{\beta} + \Omega^2 I_b\left(K + \frac{G}{\Omega^2}\,\phi\,\Psi\right)\beta = \frac{I_b\gamma\Omega^2}{2}\left[\frac{1}{3}\left\{\mu_0 - \lambda_i - \frac{3}{4}\frac{q}{\Omega}\,\$\Psi - \left(\frac{3}{4} - \frac{e}{R}\right)\frac{\dot{\beta}}{\Omega} - \frac{3}{4}\left\{\beta\,\mathrm{Tan}\,\delta_3 + \frac{\theta_0}{5} - \theta_p\right\}\right\} - \bar{U}_0\,\phi\Psi\left\{\mu_0 - \lambda_i - \frac{2}{3}\left(\frac{\theta_0}{4} - \theta_p\right)\right\}\right] + 2I_b q\Omega\phi\Psi$$

where

$$K = 1 + \varepsilon + \frac{K_\beta}{I_b\Omega^2}$$

$$\varepsilon = \frac{M_b e X_g R^2}{I_b}$$

$$G = \frac{M_b X_g g R}{I_b}$$

*The work reported herein was done as part of a Kaman Aerospace Corporation in-house R & D program.

Substituting

$$\beta = \beta_0 + \beta_{1S}\$\Psi + \beta_{1C}\phi\Psi$$

$$\beta' = \frac{\partial\beta}{\partial\Psi} = \frac{\dot{\beta}}{\Omega}$$

$$\beta'' = \frac{\partial^2\beta}{\partial\Psi^2} = \frac{\ddot{\beta}}{\Omega^2}$$

into the equation of motion, neglecting products of β, α_y, $\bar{U}_0$ and their derivatives, and rewriting the equation of motion in the frequency domain, we have

$$\begin{bmatrix} K + \frac{\gamma}{8}\tan\delta_3 & \frac{G}{2\Omega^2} - \frac{1}{3}\bar{U}_0\tan\delta_3 & \frac{\gamma\bar{U}_0}{12} \\ \frac{G}{\Omega^2} - \frac{2}{3}\bar{U}_0\tan\delta_3 & K - 1 + \frac{\gamma}{8}\tan\delta_3 & \frac{\gamma}{8}\left(1 - \frac{4e}{3R}\right) \\ \frac{\gamma\bar{U}_0}{6} & -\frac{\gamma}{8}\left(1 - \frac{4e}{3R}\right) & K - 1 + \frac{\gamma}{8}\tan\delta_3 \end{bmatrix} \begin{Bmatrix} \beta_0 \\ \beta_{1C} \\ \beta_{1S} \end{Bmatrix}$$

$$= \begin{Bmatrix} \frac{\gamma}{2}\left[\frac{1}{3}\left(\mu_0 - \lambda_i\right) - \frac{1}{4}\left(\frac{\theta_0}{5} - \theta_p\right)\right] \\ -\frac{\gamma}{2}\bar{U}_0\left(\mu_0 - \lambda_i + \frac{\theta_0}{6} - \theta_p\right) - 2\bar{q} \\ -\frac{\gamma}{8}\bar{q} \end{Bmatrix}$$

where terms in harmonics of Ψ greater than the fundamental are neglected. This system of equations is solved in program WMSTAB.

The use of linear aerodynamics for the forcing function retains the essential features of a real wind turbine blade, including pitch angle, built-in twist, induced velocity, and blade mass, while sacrificing the accuracy of a more comprehensive aerodynamics analysis. Similarly, the single degree of freedom, flapping, retains the essential feature of a more comprehensive aeroelastic code, the mobility of the blade, while minimizing the computational difficulty. Because of the computational ease of the analysis, it is very useful for the reduction of a large number of candidate operating configurations into general trends.

The program WMSTAB uses the structural characteristics of the Kaman 40 kW wind turbine, where applicable, as the baseline. Those variables dependent on rotor size are proportioned for other radii as follows:

$$R \propto R^1$$

$$\Omega \propto R^{-1}$$

$$\gamma \propto R^0$$

$$e \propto R^1$$

$$M_b \propto R^3$$

$$I_b \propto R^5$$

$$K_b \propto R^5 \text{ (when flapping frequency is constant).}$$

Three rotor radii were analyzed to illustrate characteristics dependent on rotor size. These radii (4.88 m [16 ft]; 9.76 m [32 ft]; and 19.51 m [64 ft]) were taken to be representative of small, intermediate, and large wind turbines, respectively.

The equation of motion does not include an offset between the yaw axis and the rotor. This offset will have both aerodynamic and dynamic consequences, principally arising from three sources.

First, yaw motions impart an out-of-plane velocity component to the blade, given by

$$\underline{V}_y = \underline{q} \times \underline{r}$$

where the underscore denotes vector quantities. For small values of yaw offset, the magnitude of $\underline{r}$ is essentially equal to the blade radius at points where the aerodynamic forces are large. Hence, the effect of yaw offset on blade translations is second order, and is neglected.

Second, for very low normal frequencies, the tilt of the thrust vector will dominate yaw dynamics. For a true teetered rotor, there are no other yaw restoring or damping moments than those given by the product of the in-plane component of rotor thrust and the yaw offset. The magnitude of these moments depends on the exact value of the yaw offset so they cannot be calculated for a general case.

Third, the yaw offset will cause the inertia of the yawing system to be greater than the flapping inertia of the blades alone. The magnitude of the mass transfer effect again depends upon the magnitude of the yaw offset, and cannot be computed in general.

FLAPPING ANALYSIS

Because of the obvious difficulty in referring to both the actual flapping frequency and the stiffness of the flapping spring as some multiple of Ω, as is customary, the term "normal frequency" was coined to refer to the flapping frequency of the blade when $\delta_3 = 0$. Thus, increasing normal frequency refers to increasing spring stiffness, and a given normal frequency blade may have either increasing or decreasing flapping frequency, depending on δ_3.

Flapping is defined as the amplitude of the harmonic portion of the β deflections. WMSTAB3 includes only first harmonic flapping. It is probable that this harmonic would include the bulk of flapping energy in an actual wind turbine because the cyclic inputs leading to higher harmonic responses are generally lacking.

Figure 2 shows the dependence of flapping frequency on normal frequency, which is determined by the stiffness of the flapping spring, and on

δ_3 which greatly affects the strength of the aerodynamic spring. The range of normal frequencies was defined by practical considerations of rotor blade design. The relationship between decreasing flapping frequency and decreasing δ_3, and the converse, is apparent. Flapping instabilities are suggested by the rapid decay of flapping frequencies in the neighborhood of large negative δ_3 angles.

Figures 3 and 4 show the dependence of total flapping induced by yaw position and rate, respectively, on normal frequency and δ_3. A number of trends are evident. First, for $\delta_3 \geq 0$, increasing normal frequency decreases flapping. This is not necessarily so for $\delta_3 < 0$. Second, the total flapping is determined more by the proximity of the flapping frequency to 1.0 P than by normal frequency. In fact, the amount of flapping available to any normal frequency, given suitable δ_3, is essentially constant. The third item of major interest is that the flapping due to yaw position is independent of rotor size, but the flapping due to yaw rate increases linearly with rotor size for a fixed yaw rate. This is a consequence of the gyroscopic moments acting on the blade, and gives rise to the yaw dynamics effects discussed later.

Figures 5 and 6 present the phase angle of flapping response to yaw position and rate, respectively. Horizontal blade position corresponds to $\pm$ 90°. Consequently, flapping which takes place entirely in the horizontal plane has a phase angle of $\pm$ 90°. Comparison of Figures 5 and 6 indicates that it is not possible to totally eliminate flapping in the tower direction. Judicious selection of normal frequency and δ_3 can, however, insure that flapping in the direction of the tower will always be small relative to total flapping. Note that these phase angles are independent of rotor size, and depend only on the flapping frequency (and the pitch angles, a second order effect).

Finally, the flapping induced by yaw direction will depend approximately linearly on wind speed, while the yaw rate induced flapping is essentially independent of wind speed.

The data presented in this section may be used to estimate the yaw performance of a true teeter rotor (zero flapping spring) through the phase angles and flapping angles presented. Again, the results will depend on a particular design and are not included in this analysis.

YAWING BEHAVIOR

The yawing behavior of a wind turbine depends on three things: the aerodynamic spring rate, the total damping, and the yawing inertia. The governing equation of motion

$$I_y\ddot{\alpha}_y + C_y\dot{\alpha}_y + K_y\alpha_y = \text{yaw moments}$$

can be solved as discussed in many texts of elementary dynamics. The contribution of this study is the generation of linearized estimates for C_y and K_y and the solution of the homogeneous equation of motion, after setting $I_y = I_b$, from which time constants of yaw response to step changes in wind direction were calculated.

Figure 7 is an illustration of the aerodynamic spring constant, K_y, determined by imposing a yaw angle of 10°, and normalizing the result to a yaw angle of 1.0 radian. The peak of the spring rate occurs at the 1.0 P flapping frequency for all of the normal frequencies shown. Instability is suggested by the very large spring constants in evidence for high normal frequencies and large negative values of δ_3. The stabilizing effect of positive δ_3 is also evident by the convergence of spring constants for large positive δ_3, suggesting that δ_3 has come to dominate flapping dynamics. Note that the yaw spring constant is a linear function of rotor size. The spring rate is approximately linear with wind speed for fixed yaw angle.

The damping constant C_y is plotted in Figure 8. Much of what has just been described for Figure 7 is also true here. The most notable exceptions are that the damping rate was normalized to 1.0 radian/sec, and the peak damping occurs at δ_3 angles smaller (more negative) than for the corresponding spring rate. The yaw damping rate is independent (to first order) of wind speed.

The spring rates and damping rates are decoupled in this analysis.

The yaw dynamics behavior can be summarized by calculating the time constant of response to a step change in wind (yaw) direction, as discussed above. These data are assembled in Figure 9. Two trends, increasing time constant first with increasing δ_3, and second, with increasing normal frequency, are immediately obvious. The time constants also increase linearly with rotor size.

The time constant can be interpreted many ways. Also indicated on ordinate axes of Figure 9 are the time required to decay to 50% amplitude, and the time required to decay to 5% amplitude, which numbers are linear transforms of the time constant. Yet another interpretation is that the product of the time constant and the rate of change of wind direction equals the lag angle between the wind direction and the axis of rotation. Because the time constants increase with increasing rotor diameter, the data indicate that the lag angle for large rotors could be quite large, even if the rate of change of wind direction is quite small. Since this lag angle degrades performance, the evaluation of system productivity, particularly for large rotors in a variable wind, should be evaluated with respect to the lag (yaw) angles almost certain to be present.

CONCLUDING REMARKS

The incorporation of significant amounts of δ_3 into a horizontal axis wind turbine blade greatly increases the options available to the designer. The δ_3 hinge may be used to adjust magnitude or phase of the flapping response to either yaw rate or direction, thus controlling the mechanical and aerodynamic coupling with the fixed system degrees of freedom. The effect of δ_3 on flapping frequency can also be exploited to optimize system dynamics.

The reduction of the blade flapping data into yawing spring and damping constants allows the estimation of response time to changes in wind direction. The data indicate that large wind turbines may suffer large lag angles if operated where winds vary in direction. This may be a source of performance degradation previously overlooked.

REFERENCES

1. Stoddard, F. S.: "Structural Dynamics, Stability and Control of High Aspect Ratio Wind Turbines," PhD. Dissertation, Ocean Engineering, University of Massachusetts, Amherst, Massachusetts, February 1979.

2. Den Hartog, J. P.: Mechanical Vibrations, McGraw Hill (New York), Copyright 1947.

NOMENCLATURE

- a lift slope = 5.73/radian
- C chord
- C_y yaw damping rate
- $\cos$ cosine
- e offset/R
- g gravitational acceleration
- I_b flapping inertia
- I_y yaw inertia
- K_b flapping spring rate
- K_y aerodynamic yaw spring rate
- M_b rotor blade mass
- P division by Ω
- q yaw rate
- $\bar{q}$ q/Ω
- R rotor blade radius
- r distance from yaw axis to a point on the blade
- $\sin$ sine
- $\bar{U}_0$ crosswind/ΩR
- V_y out-of-plane velocity due to yaw rate
- X_g radius to c.g./R
- α_y yaw angle
- β flapping angle
- β_0 steady harmonic coefficient
- β_{1c} cosine harmonic coefficient
- β_{1s} sine harmonic coefficient
- γ lock number $\equiv \rho CaR^4/I_b$
- δ_3 angle between normal to feathering axis and teeter axis
- θ_0 built-in linear twist (total)
- θ_p pitch angle, + implies increasing thrust
- λ_i induced velocity/ΩR
- μ_0 wind velocity/ΩR
- ρ air density
- Ψ azimuth angle
- Ω rotational speed

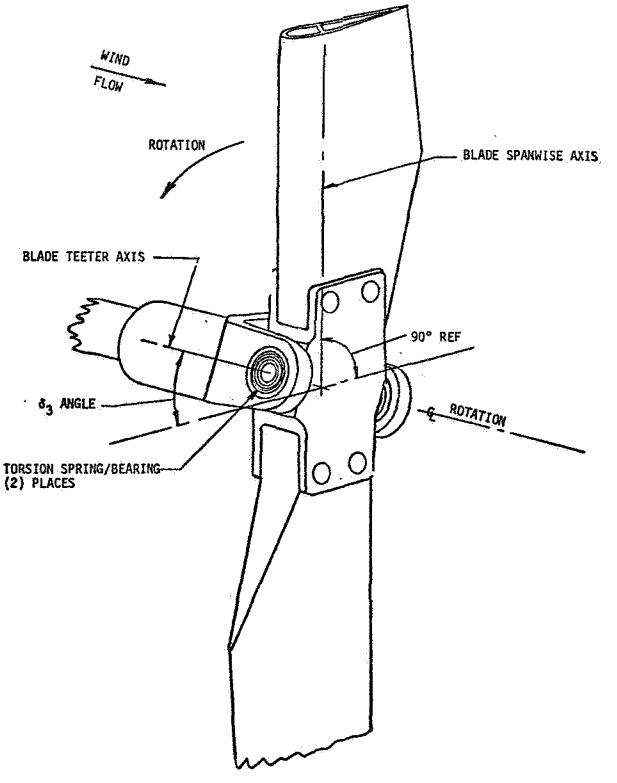

Figure 1 - Teetered rotor showing δ_3 due to offset between teeter axis and the normal to the feather axis.

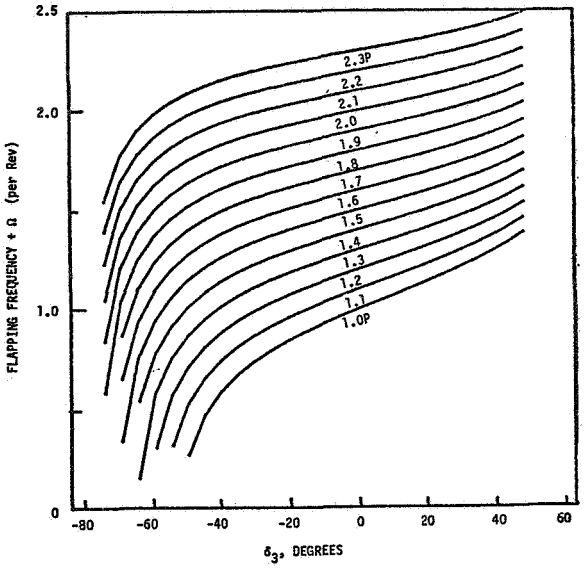

Figure 2 - Flapping frequency vs δ_3 for fourteen normal frequencies.

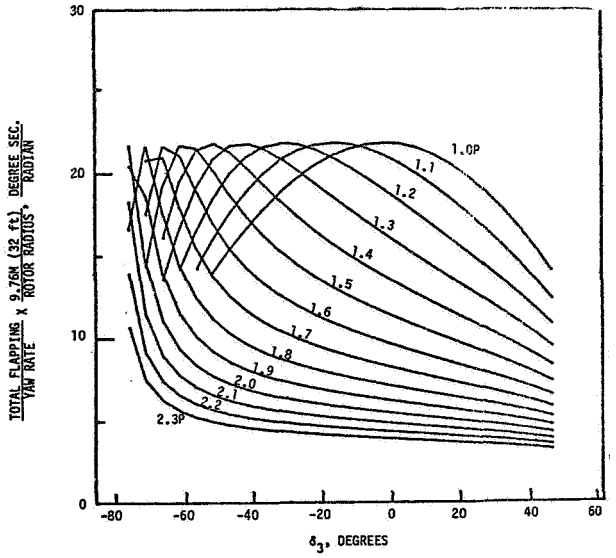

Figure 4 - Total flapping due to yaw rate vs δ_3 for fourteen normal frequencies.

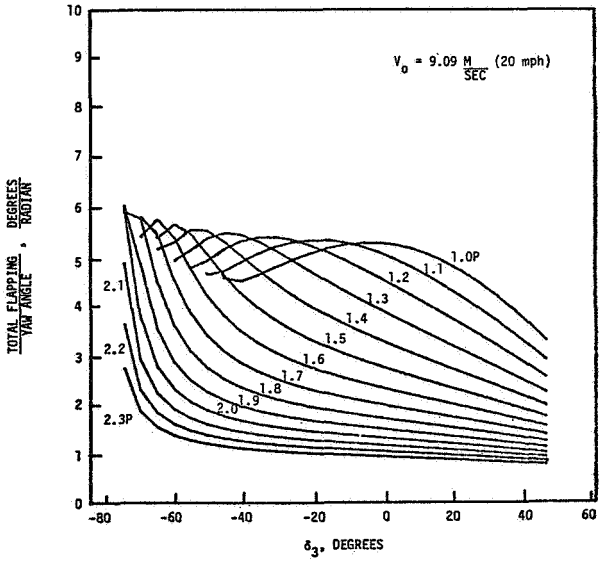

Figure 3 - Total flapping due to yaw angle versus δ_3 for fourteen normal frequencies.

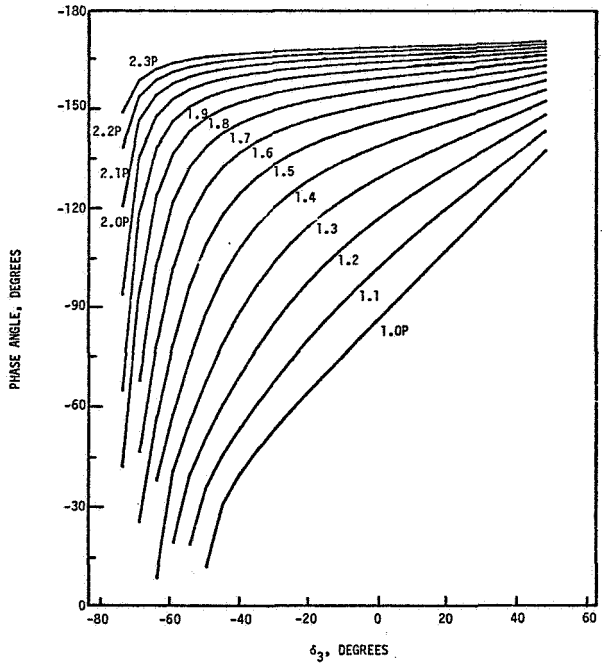

Figure 5 - Phase of flapping response to yaw position vs δ_3 for fourteen normal frequencies.

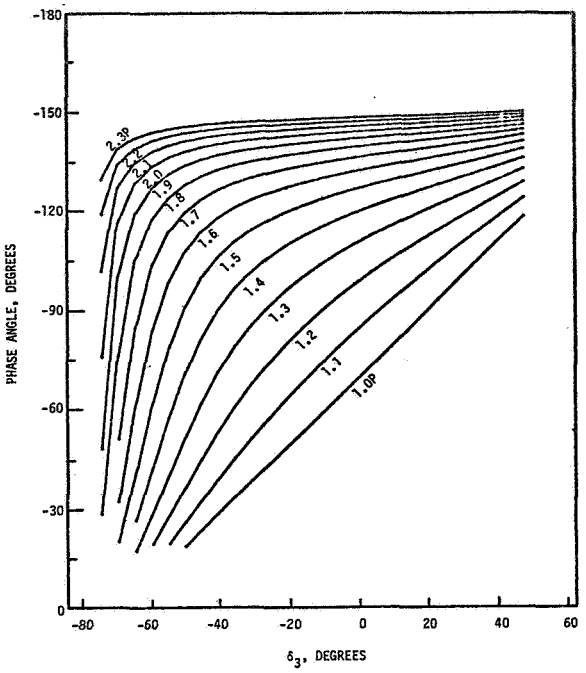

Figure 6 - Phase of flapping response to yaw rate vs δ_3 for fourteen normal frequencies.

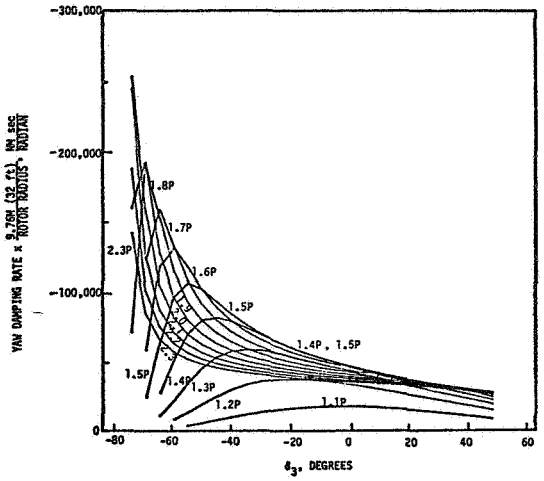

Figure 8 - Yaw damping rate vs δ_3 for thirteen normal frequencies.

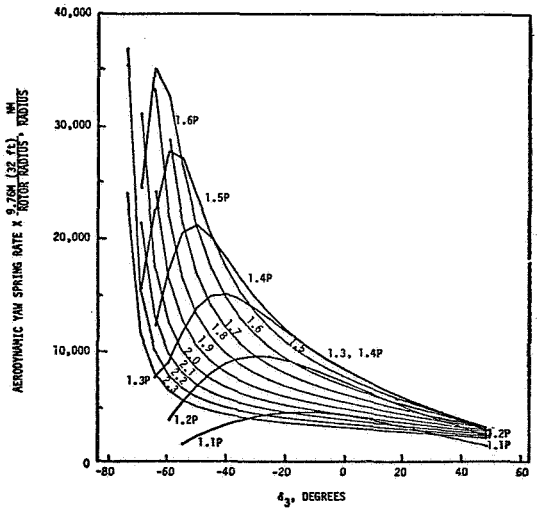

Figure 7 - Aerodynamic spring rate vs δ_3 for thirteen normal frequencies.

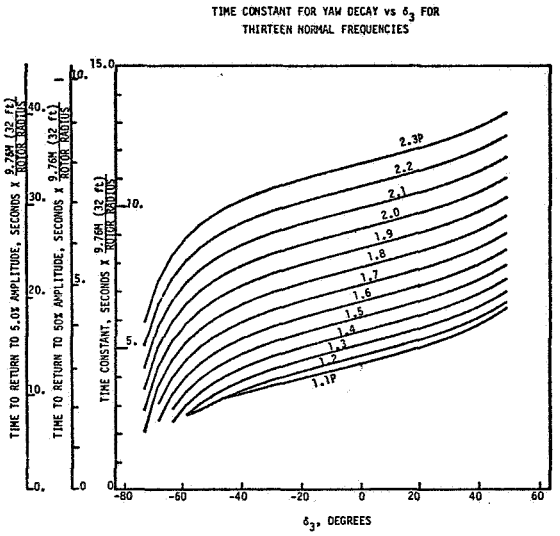

Figure 9 - Time constant for yaw decay vs δ_3 for thirteen normal frequencies.

QUESTIONS AND ANSWERS

F.W. Perkins

From: J. Cohem

Q: Can you physically explain the significance of 1.4 P, and its effect on yaw dynamics?

A: *1.4 P is just that normal frequency which maximizes the product of* K_β *and* β_{15} *which gives the yaw moment. Incerasing* K_β*, consequently the normal frequency, decreases* β_{15} *more rapidly than* K_β *increases.*

SECOND DOE/NASA WIND TURBINE DYNAMICS WORKSHOP

Electrical & Control Systems

Session Chairman - L.J. Gilbert (NASA LeRC)

"VAWT Drive Train Transient Dynamics"
D.B. Clauss
(Sandia Labs.)

"Dynamics & Stability of WTG's"
E.N. Hinrichsen
P.J. Nolan
(Power Tech., Inc.)

"Kaman 40 kW WTG - Control System Dynamics"
R. Perley
(Kaman Aerospace Corp.)

"Automatic Control Algorithm Effects on Energy Production"
G. McNerney
(U. of New Mexico)

"Effect of Wind Power Changes on Utility System Dispatch"
R.A. Schlueter
G.L. Park
(Michigan State Univ.)

VERTICAL AXIS WIND TURBINE DRIVE TRAIN TRANSIENT DYNAMICS

David B. Clauss and Thomas G. Carne
Division 5523
Sandia National Laboratories
Albuquerque, New Mexico 87185

ABSTRACT

Start-up of a vertical axis wind turbine causes transient torque oscillations in the drive train with peak torques which may be over two and one-half times the rated torque of the turbine. These peak torques are of sufficient magnitude to possibly damage the drive train; safe and reliable operation requires that mechanical components be overdesigned to carry the peak torques caused by transient events. A computer code, based on a lumped parameter model of the drive train, has been developed and tested for the Low Cost 17-Meter turbine; the results show excellent agreement with field data. The code has subsequently been used to predict the effect of a slip clutch on transient torque oscillations. It has been demonstrated that a slip clutch located between the motor and brake can reduce peak torques by thirty eight percent.

INTRODUCTION

Transient events during operation of Darrieus vertical-axis wind turbines can cause torque levels in the drive line which are unacceptable for many components. Start-up and braking in various ambient conditions are typical events during which peak torques may reach excessive magnitudes. Experience with research vertical axis wind turbines (VAWT) indicates that peak torques of 2 to 3 times rated torque are typical during starting and braking, which implies an undesired overdesign of drive-line components. The objective of the present investigation is to develop an analytical tool which can be used to predict drive-train behavior for several different loading conditions.

Analysis is needed to determine which starting and braking methods are most effective in reducing the peak torques seen in the drive-line. Areas deserving investigation include start-up in high winds, as well as electrical and mechanical methods (clutches) designed to achieve a softer start. The relative effectiveness of low speed vs. high speed braking, and definition of a braking rate which will decrease dynamic amplification to an acceptable level also merit study. Although this paper will deal primarily with turbine start-up in zero ambient wind speed and the effects of a slip clutch on transient response, the model can easily be adapted to study the problems mentioned above.

The model and the numerical results as well are based on experimental data obtained on the Low Cost 17M VAWT installed at Rocky Flats, CO, Figure 1. The method, however, is essentially general to all VAWT's. A Fortran program called DYDTA (DYnamic Drive Train Analysis) numerically evaluates the differential equations of motion and plots results.

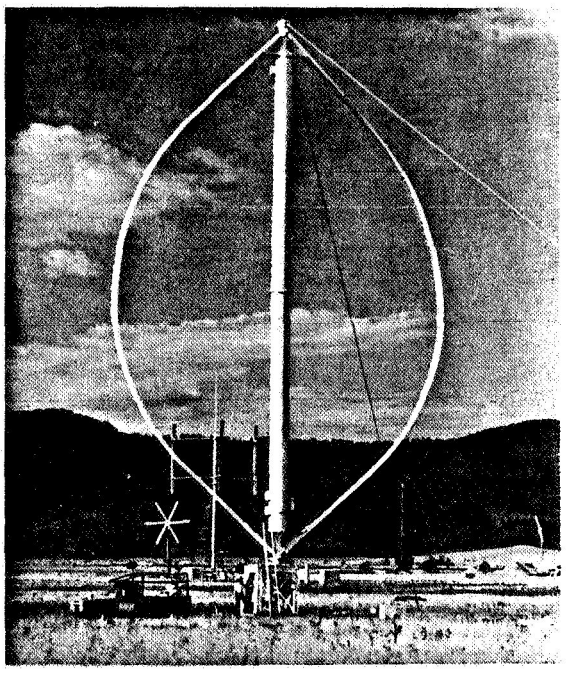

FIGURE 1. DOE/ALCOA LOW COST 17M VERTICAL AXIS WIND TURBINE INSTALLED AT ROCKY FLATS, CO.

THE DRIVE TRAIN MODEL

Typically, a VAWT drive train consists of the turbine rotor (blades and rotating tower), the transmission, a brake disc and an induction motor/generator which are connected in series by shafts and couplings. Additional mechanical components may be present, and the drive train topography may vary depending upon the specific turbine design. Additional components may include a timing belt (for incremental adjustment of turbine operating speed) and/or a slip clutch. The position of the brake relative to the

transmission and clutch, if present, is the most variable element in drive train topography. For instance on the Low Cost 17M turbine at Rocky Flats, Figure 1, the brake is on the high speed shaft, whereas earlier turbines have had the brake on the low speed shaft.

The transient response depends on the natural characteristics of the system and the functional form of the applied torques. The physical representation of the drive train is shown in Figure 2, along with physical values for the Low Cost turbine. For generality the model includes the slip clutch, as well as applied torques on each inertial element. Several assumptions are made, all of which may not be applicable to a given VAWT design. The low speed shaft is considered to be the only significant stiffness in the system since, in an equivalent system, it appears much softer than both the high speed shaft and the rotating tower. As larger turbines are built and tower height

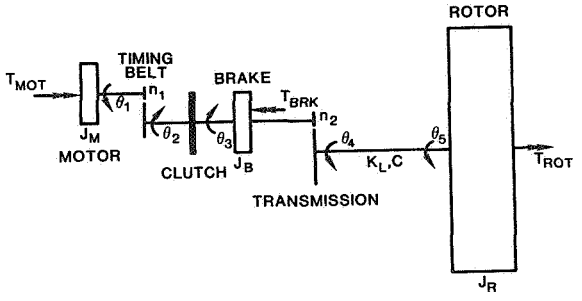

J_M = motor inertia = 1.291 lb-ft-s^2

J_B = brake inertia = 1.598 lb-ft-s^2

J_R = rotor inertia = 4.042 x 10^4 lb-ft-s^2

C = Viscous damping = 1.1 x 10^3 lb-ft-s

K_L = low speed shaft stiffness = 8.626 x 10^5 lb-ft

n_1 = timing belt ratio = 1, 40/38, 44/38

n_2 = transmission ratio = 35.07

T_{MOT} = motor torque, $T_{MOT}(\omega)$

T_{BRK} = brake torque, $T_{BRK}(t)$

T_{ROT} = aerodynamic torque, $T_{ROT}(\omega, t)$

FIGURE 2. PHYSICAL REPRESENTATION OF VAWT DRIVE TRAIN.

increases, the tower stiffness may approach the same value of stiffness as the low speed shaft, and at some point tower stiffness may have to be included in the model. On the other hand, the effect of the transmission's gear ratio on the equivalent stiffness of the high speed shaft seems to insure that the high speed stiffness will remain large relative to low speed stiffness, and thus the high speed shaft can be effectively modeled as a rigid element. The motor torque curve as specified by the manufacturer is modified by a constant scale factor less than one, which is related to the voltage drop in the line. For an induction motor/generator, torque is proportional to voltage squared, so that a 20% drop in voltage will cause a 36% reduction in motor torque. The assumption of a constant motor scale factor implies that the voltage drop, and thus the current drawn by the motor are independent of motor speed, which is only approximately true. Also, nonlinear effects such as Coulomb friction, aerodynamic damping, and drive slack are not treated. All losses are represented by viscous damping.

The equations of motions describing the torsional response of the drive train can be easily written by drawing free body diagrams for each inertial element, Figure 3, and equating the torque on each to zero. This method is preferred because it

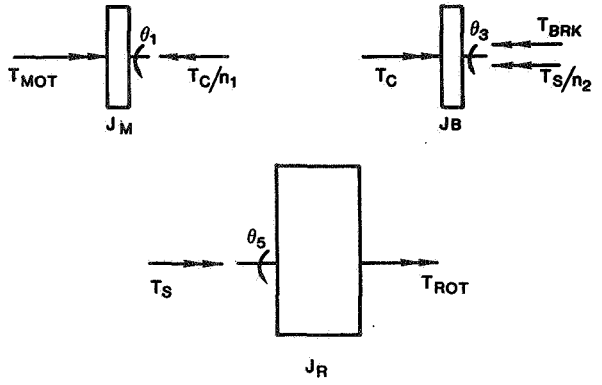

FIGURE 3. FREE BODY DIAGRAMS FOR WRITING EQUATIONS OF MOTION.

permits treatment of the nonlinear effect of the clutch in a simple way since torque through the clutch can be expressed explicitly. Referring to Figures 2 and 3, T_C and T_S are defined and calculated as follows:

T_S = torque transmitted through low speed shaft,

$$T_S = K_L(\theta_4-\theta_5) + C(\dot{\theta}_4-\dot{\theta}_5), \quad (1)$$

T_C = torque transmitted through slip clutch.

The equations of motion can now be written directly:

$$J_M\ddot{\theta}_1 = T_{MOT} - T_c/n_1, \quad (2)$$

$$J_B\ddot{\theta}_3 = T_c - T_{BRK} - T_s/n_2, \quad (3)$$

$$J_R\ddot{\theta}_5 = T_s + T_{ROT}, \quad (4)$$

where the clutch imposes a constraint of the form

$$|\ T_c\ | \leq T_{max}\ ; \quad (5)$$

T_{max} = maximum torque passed by clutch.

The slip clutch typically consists of two mating frictional surfaces which are connected to the driving and driven shafts, respectively. These frictional surfaces are compressed together by a spring, so that the normal force, surface area, and friction coefficients determine the maximum torque transmitted by the clutch. T_{max} can be adjusted by changing the spring deflection.

The clutch is always operating in one of two conditions; it is either engaged, in which case the velocities on either side of the clutch are equal, or it is slipping, in which case the velocities are unequal and the clutch torque is equal to $\pm T_{max}$. The torque speed characteristic of an ideal clutch is shown in Figure 4. Note that T_{max} is a restoring torque; that is, it is in a direction that will tend to re-engage the clutch.

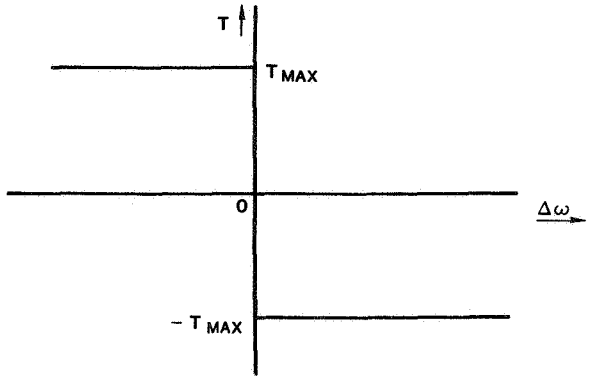

FIGURE 4. TORQUE VS. SPEED DIFFERENCE - IDEAL CLUTCH. ASSUMES STATIC FRICTION COEFFICIENT EQUALS DYNAMIC FRICTION COEFFICIENT.

With this understanding, two distinct sets of unconstrained equations of motion can be written corresponding to the two operating states of the clutch, which will be referred to as the engagement and slip equations, respectively.

Engagement of the slip clutch implies that $\theta_2 = \theta_3$, so that the motor and brake move together. Multiplying equation (1) by n_1 and summing the result with equation (2):

$$n_1 J_M\ddot{\theta}_1 + J_B\ddot{\theta}_3 = n_1 T_{MOT} - T_{BRK} - T_s/n_2. \quad (6)$$

The equations can be simplified by making the following variable transformation and taking advantage of gear relations

$$\psi_1 = \theta_2 = \theta_1/n_1\ , \quad (7)$$

$$\psi_2 = \theta_3 = n_2\theta_4\ , \quad (8)$$

$$\psi_3 = n_2\theta_5\ . \quad (9)$$

Thus the complete set of engagement equations can be written

$$(J_{ME} + J_B)\ddot{\psi}_1 = n_1 T_{MOT} - T_{BRK} - K_{LE}(\psi_2-\psi_3) - C_E(\dot{\psi}_2-\dot{\psi}_3)\ , \quad (10)$$

$$\ddot{\psi}_2 = \ddot{\psi}_1 \quad (11)$$

$$J_{RE}\ddot{\psi}_3 = K_{LE}(\psi_2-\psi_3) + C_E(\dot{\psi}_2-\dot{\psi}_3) + T_{ROT}/n_2\ ; \quad (12)$$

where

$$J_{ME} = (n_1)^2 J_M, \quad (13)$$

$$J_{RE} = J_R/(n_2)^2, \quad (14)$$

$$K_{LE} = K_L/(n_2)^2, \quad (15)$$

$$C_E = C/(n_2)^2. \quad (16)$$

Slipping of the clutch decouples the motor from the brake and rotor, so that the slip equations describe two independent systems as shown in Figure 5. Slip implies a velocity difference across the clutch and that the torque transmitted through the clutch is a constant $\pm T_{max}$. Again taking advantage of equations (7) - (9) and equations (13) - (16), and making the substitution

$$T_c = \pm T_{max} \quad (17)$$

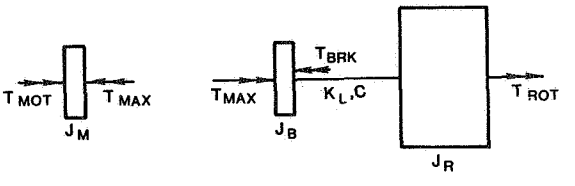

FIGURE 5. REPRESENTATION OF DRIVE TRAIN FOR CLUTCH SLIPPING.

the final form of the slip equations becomes

$$J_{ME}\ddot{\psi}_1 = n_1 T_{MOT} \mp T_{max} \quad (18)$$

$$J_B\ddot{\psi}_2 = \pm T_{max} - T_{BRK} - K_{LE}(\psi_2-\psi_3) - C_E(\dot{\psi}_2-\dot{\psi}_3) \quad (19)$$

$$J_{RE}\ddot{\psi}_3 = K_{LE}(\psi_2-\psi_3) + T_{ROT}/n_2 + C_E(\dot{\psi}_2-\dot{\psi}_3) \quad (20)$$

where T_{max} is positive for motor overspeed.

The conditions for initiation of slip and for re-engagement are somewhat more subtle, although intuitively simple. Assume that, at time equal zero, the clutch is engaged. Slip initiates when the clutch torque equals T_{max} and continued engagement would tend to violate the constraint, equation (5). Stated more rigorously the initiation of slip occurs when

$$T_{Ce} = T_{max} \quad (21)$$

and

$$\frac{dT_{Ce}}{dt} > 0 \quad (22)$$

where the subscript e indicates the result obtained from the engagement equations. If T_{Ce} is negative, then inequality (22) is directed in the opposite sense. Now assume that the clutch is slipping, so that $\dot{\theta}_2 \neq \dot{\theta}_3$. Re-engagement occurs when the velocities across the clutch become equal again:

$$\dot{\theta}_{2s} = \dot{\theta}_{3s} \quad (23)$$

and if

$$|T_{Ce}| \leq T_{max}$$

At re-engagement there must be a discontinuity in acceleration, which implies a discontinuity in the clutch torque. This is consistent with the characteristics of the clutch as shown in Figure 4, since when $\Delta\omega = 0$ (as it is at re-engagement), the clutch torque may be any value between positive T_{max} and negative T_{max}.

Thus, a basic algorithm would be to use the engagement equations until equations (21) and (22) are satisfied (slip initiates), and then to apply the slip equations until equation (23) is met (re-engagement), at which point the algorithm is applied recursively.

A great deal of insight can be gained from an examination of the natural characteristics of the system, especially in the case of start-up. The remainder of this paper will focus on start-up in a zero ambient wind speed. The motor torque-speed characteristic has a significant impact on the natural characteristics of the system. A typical induction motor curve is shown in Figure 6. It is important to realize that motor

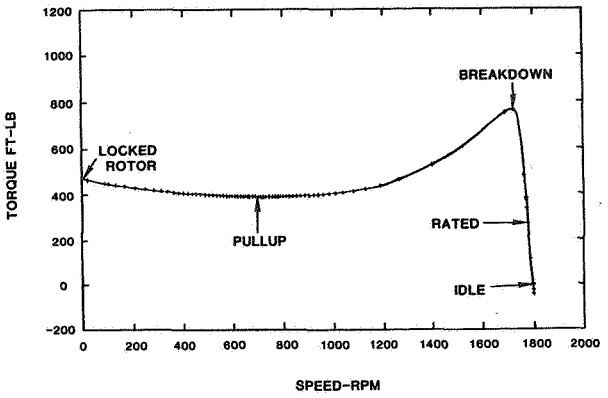

FIGURE 6. TORQUE-SPEED CHARACTERISTIC OF AN INDUCTION MOTOR.

torque is a function of motor speed, not of time. Torque ripple models developed[1] by Reuter have treated the induction motor/generator mechanically as an inertia connected to ground through a linear viscous damper. Referring to Figure 6 the torque-speed relationship is indeed linear for steady state operation ($1740 < \omega < 1860$ rpm). However, during start-up the motor speed goes from 0 to 1800 rpm and the torque-speed relationship cannot be represented as a linear element. From an intuitive standpoint, it is most clear to think of the motor torque characteristic as a non-linear damper, which has a coefficient dependent on rpm, superimposed on a step torque, though in the code and model it is treated as an applied torque. To be clear, the motor torque should not be considered to be an external torque because it is not independent of the state of the system. With this in mind, the free vibration characteristics of the drive train during start-up can be considered.

The natural characteristics of the system also depend on the operating state of the slip clutch. When the clutch is engaged, there is an effectively rigid connection between the motor and the brake so their respective inertias may be lumped together, and the system can be represented as shown in Figure 7. On the other hand, slipping decouples the motor and creates two independent systems, Figure 8. The latter case will not be treated in detail, however, it is apparent that the fundamental frequency of the decoupled system in 8(b) will be higher than that of coupled system in Figure (7), and that the isolated motor, Figure 8(a) moves as a rigid body.

Due to the nonlinearity introduced into the system by the motor and clutch, a linear eigenvalue analysis is not truly applicable. The equivalent motor damping changes continually so that the natural frequencies and mode shapes are a function

of speed. However, an approximate analysis can be done by considering two subcases based on motor speed less than or

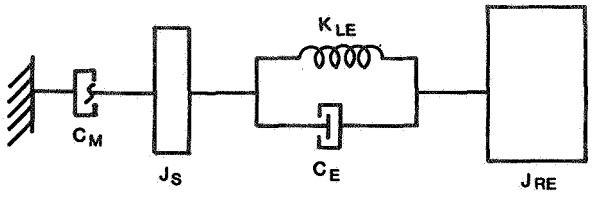

$J_S = n_1^2 J_M + J_B$

C_M = NONLINEAR DAMPING REPRESENTING MOTOR

FIGURE 7. SYSTEM REPRESENTATION WITH CLUTCH ENGAGED.

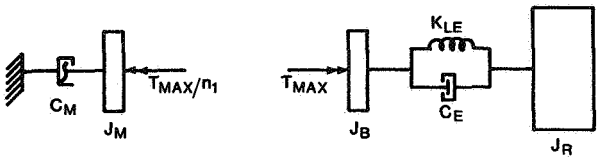

FIGURE 8. SYSTEM REPRESENTATION WITH CLUTCH SLIPPING.

greater than the motor breakdown speed, respectively. Up to the breakdown speed the maximum absolute instantaneous motor damping results in a critical damping of approximately minus nine percent, and consequently the damping does not greatly affect the natural frequencies up to breakdown speed. Note that negative damping has the same effect on frequency as positive damping (1 d.o.f., $\omega_d = \sqrt{1 - \zeta^2}\ \omega_n$), but the opposite effect on mode shape (in Figure 7, negative damping from the motor tends to increase the oscillations of the motor and brake relative to the rotor). Thus, up to breakdown, damping is negligible and the system can be viewed as shown in Figure 9(a). The natural frequencies and mode shapes of the

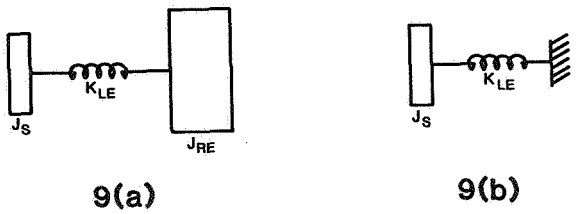

FIGURE 9. SYSTEM REPRESENTATION WITH CLUTCH ENGAGED AND MOTOR SPEED < 1720 RPM.

system in Figure 9(a) are easily determined. The results are

$$\omega = 0,\ \sqrt{\frac{K_{LE}(J_S + J_{RE})}{J_S J_{RE}}} \tag{24}$$

$$= 0,\ 2.586 \text{ HZ}$$

$$u^{(1)} = \begin{Bmatrix} 1.000 \\ 1.000 \end{Bmatrix},\quad u^{(2)} = \begin{Bmatrix} 1.000 \\ 1 - \dfrac{J_S + J_{RE}}{J_{RE}} \end{Bmatrix} \tag{25}$$

$$= \begin{Bmatrix} 1.000 \\ -0.083 \end{Bmatrix}$$

The mode shape indicates that the generator/brake is moving with much greater amplitude than the rotor, so that the mode basically represents the motor/brake winding up about the low speed shaft, Figure 9(b). Indeed, if $J_{RE} >> J_S$ (typically the case for VAWT's), equation (24) can be approximated by

$$\omega \simeq \sqrt{\frac{K_{LE}}{J_S}} \tag{26}$$

which corresponds to the frequency of the system in Figure 9(b).

As previously discussed, when the motor speed is greater than the breakdown speed, the torque is nearly a linear function of speed, with a very large negative slope. This slope, and thus the effective damping, is a function of the rated power, the synchronous speed, and the slip at rating for an induction motor/generator:

$$C_M = \frac{P_{rated}}{\Omega^2 S}\ , \tag{27}$$

as given in [2].

For the Low Cost turbine this corresponds to a critical damping factor of over 200%, which indicates that the generator/brake oscillation will be very small. As an approximation, the generator can then be considered to be fixed when the motor speed is greater than the breakdown speed, as shown in Figure 10, so that the first mode resembles the rotor winding up on the low speed shaft.

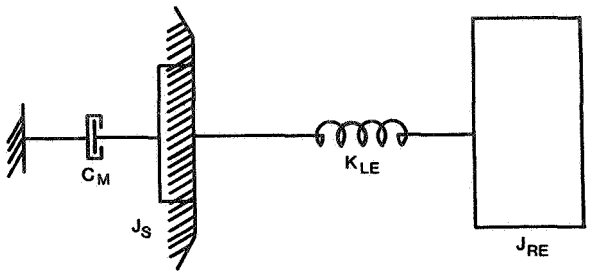

FIGURE 10. SYSTEM REPRESENTATION WITH CLUTCH ENGAGED AND MOTOR SPEED > 1730 RPM.

The frequency for the system in Figure 10 is simply

$$\omega \cong \sqrt{\frac{K_{LE}}{J_{RE}}} \quad . \tag{28}$$

EXPERIMENTAL RECORD - BASE CASE

The Low Cost 17M turbine at Rocky Flats is instrumented with a torque sensor located on the low speed shaft. A typical start-up record taken in zero ambient wind speed is shown in Figure 11. The experimental record was used to develop a base case which could be used to verify the predictive capabilities of the model, as well as to fix certain parameters that could not accurately be calculated analytically or experimentally. The parameters which were varied were the viscous damping coefficient and the motor scale factor. There are several characteristics which are typical of a start-up record: the initial overshoot and subsequent decay, and then the growth of torque oscillations to the largest peak torque, and the frequency shift that occurs just after the peak is reached. Note that the maximum torque (40,000 ft-lb) is over 2.5 times the rated turbine torque (15,000 ft-lb). The time to start is also an important characteristic. Several non-linear effects are apparent in the record as well; the decay envelope is not smooth, which indicates non-viscous damping, and gear slack is evident (note the 'notch' when the sign of the torque changes near the end of the record). The model does not attempt to explain or predict these non-linear effects.

DYDTA results for this base case are shown in Figures 12-15. Varying the motor scale factor changes the starting time and the magnitude of torque, while varying the viscous damping coefficient primarily affects the initial rate of decay and to a lesser extent the magnitude of torque oscillations. The final value for the motor scale factor is 0.665, which

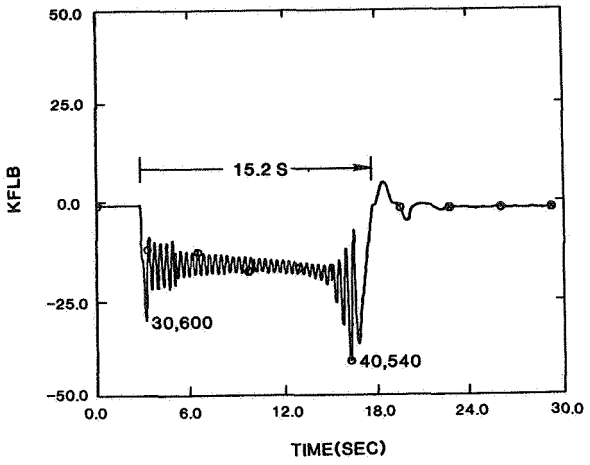

FIGURE 11. EXPERIMENTAL RECORD - LOW SPEED SHAFT TORQUE VS. TIME FOR THE LOW COST TURBINE START-UP IN ZERO WIND.

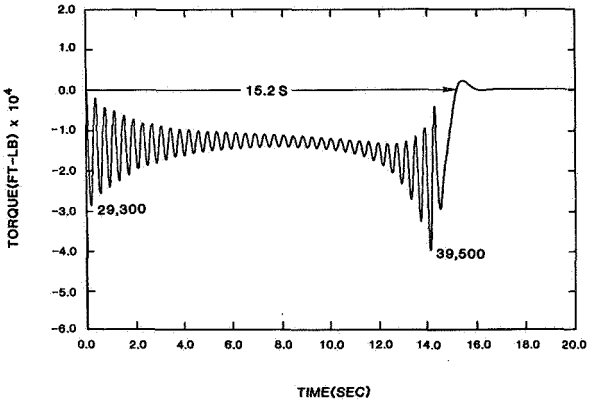

FIGURE 12. DYDTA PREDICTION - LOW SPEED SHAFT TORQUE VS. TIME DURING START-UP IN ZERO WIND - NO CLUTCH.

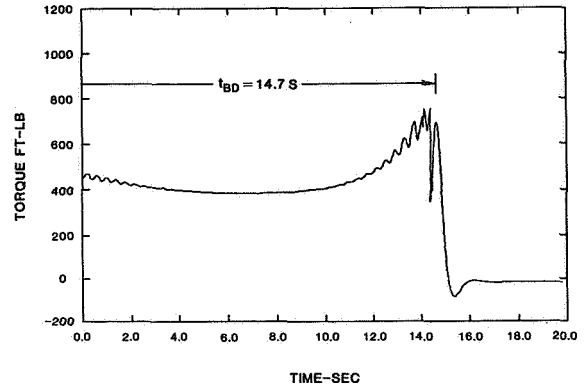

FIGURE 13. DYDTA PREDICTION - MOTOR TORQUE VS. TIME FOR START-UP IN ZERO WIND - NO CLUTCH.

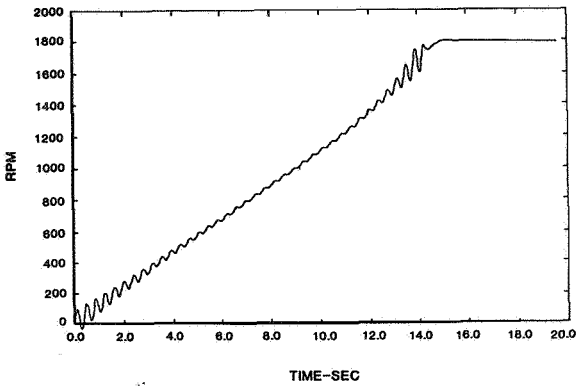

FIGURE 14. DYDTA PREDICTION - MOTOR SPEED VS. TIME FOR START-UP IN ZERO WIND - NO CLUTCH.

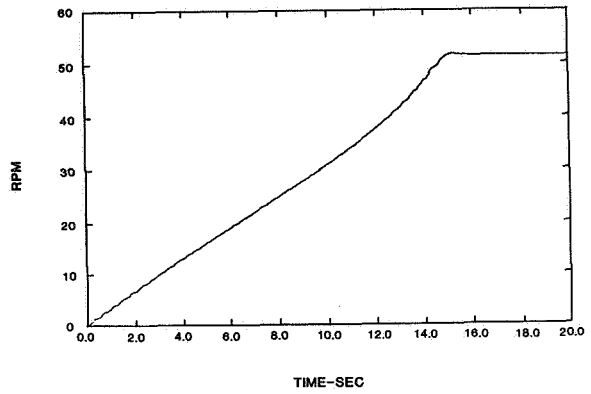

FIGURE 15. DYDTA PREDICTION - ROTOR SPEED VS. TIME FOR START-UP IN ZERO WIND - NO CLUTCH.

corresponds to an 18% voltage drop in the line. This is not unreasonable as the current drawn by the motor is rather high and the line is fairly long at the Rocky Flats site. Obviously the scale factor depends on the particular motor and electrical arrangement for a given VAWT design. The viscous damping coefficient was determined to be 1.1×10^3 lb-ft-sec, corresponding to a damping factor of approximately one percent. This is insignificant compared to damping provided by the motor and thus the influence of viscous damping due to the structure on the response is negligible.

The results from DYDTA, after adjustment of the scale factor and viscous damping coefficient, show excellent agreement with the field data (Figure 11), and the simple drive train model can be used to explain the characteristics typical of a VAWT start-up in zero wind. DYDTA correctly predicts the magnitude of the initial overshoot and the subsequent decay. The initial overshoot is due to the step in torque which occurs when the motor is turned on; the amplitude should be approximately twice the initial motor torque (locked rotor torque). When the motor speed is less than the pull-up speed (725 rpm) the motor contributes a small amount of positive damping, and together with the viscous damping due to the structure it causes the oscillations to decay in the typical envelope fashion. However, the rate of decay constantly decreases and eventually becomes zero as the damping from the motor goes from positive at locked rotor to zero at pull-up and becomes negative beyond that.

The growth of torque oscillations occurs when the damping produced by the motor becomes negative, an effect also predicted by DYDTA, Figure 12. Negative damping results in energy addition to the system, which causes an unstable growth in the amplitude of the torque oscillations. The maximum torque seen by the low speed shaft occurs at approximately the time the motor breakdown speed is reached, when the motor damping changes rapidly from negative to positive. As explained earlier, there is a frequency shift at this point as well: prior to breakdown, the total damping is relatively small, and thus it does not significantly affect the 1st fundamental frequency. Since the rotor inertia is much larger than the motor/brake inertia, the vibrational mode basically consists of the motor/brake winding up on the low speed shaft. Past breakdown the large positive damping produced by the motor effectively reduces the motor/brake vibration to zero, so that the first mode shape becomes the rotor oscillating about the low speed shaft. There is a significant decrease in the fundamental vibrational frequency past breakdown due to the large size of the rotor inertia relative to that of the motor/brake. Again, DYDTA is in very good agreement with field data with regard to these phenomena. DYDTA also matches experimental records on starting times, which essentially depends on rotor inertia and mean motor torque.

Figure 13 demonstrates the variation of motor torque as a function of time, which is another critical aspect of VAWT start-up. Up until breakdown the motor draws very high levels of current, and the motor can draw high power for only a short period of time. Past breakdown the current is reduced, so it is clearly advantageous to reduce the time to breakdown (t_{BD}) as much as possible. For the base case t_{BD} is about 14.7 seconds. Figures 14 and 15 show the speeds of the motor/brake and rotor, respectively as functions of time. They serve to verify that the turbine successfully comes up to speed, as well as to substantiate what has been said earlier in regard to the mode shapes (the rotor motion is almost entirely a rigid body mode whereas the motor contains a

significant amount of oscillation about the rigid body mode).

CONTROL OF TRANSIENTS WITH A SLIP CLUTCH

High torques experienced in the low speed shaft of the Low Cost 17M turbine resulted in the investigation of a slip clutch as a possibility for reducing peak torques. DYDTA has been used to analyze the effect of a slip clutch on torque levels during start-up. The results indicate a clutch could significantly lower the peak torques seen by the low speed shaft, with the following secondary benefit. The clutch also reduces the time to breakdown for the motor (t_{BD}), which reduces the current drawn by the motor and protects it from overload. It appears that an appropriately chosen clutch would be well within margins of safety with respect to heat dissipation and power absorption capabilities.

The characteristics of a typical slip clutch were discussed earlier; recall that the clutch passes torque uniformly up to some maximum value (T_{max}) which can be adjusted by changing the deflection of a compression spring. With this in mind a parametric study was done using DYDTA to determine what value or range of T_{max} would best reduce torque levels. Obviously T_{max} should be above the rated turbine torque, which is 427 ft-lbs (15,000 ft-lbs referred to the low speed shaft), or else power could be absorbed by the clutch during normal operation.

The optimum value for T_{max} for the Low Cost turbine appears to be 475 ft-lbs (16,700 ft-lbs referred to the low speed shaft), for which the results predicted by DYDTA are shown in Figures 16-21. With the clutch present, the maximum torque in the low speed shaft occurs during the initial overshoot, and its magnitude has been reduced 38% from 40,000 ft-lbs to 25,000 ft-lbs. The growth of torque oscillations does not occur because slipping of the clutch decouples the motor from the drive train, thereby isolating the low speed shaft from the negative damping produced by the motor. Note that the torque in the low speed shaft can exceed T_{max}, despite the clutch, because of the inertial reaction of the brake. This implies that the slip clutch should be located as close to the component needing protection as is physically possible.

The clipping action of the clutch is demonstrated in Figure 17; the torque transmitted through the clutch cannot exceed T_{max}. As discussed previously, a secondary benefit is that the clutch reduces t_{BD} for the motor. Figure 18 shows that the high torque part of the motor curve is sped through very rapidly, and t_{BD} is reduced to 12.6s from 14.7s for no clutch.

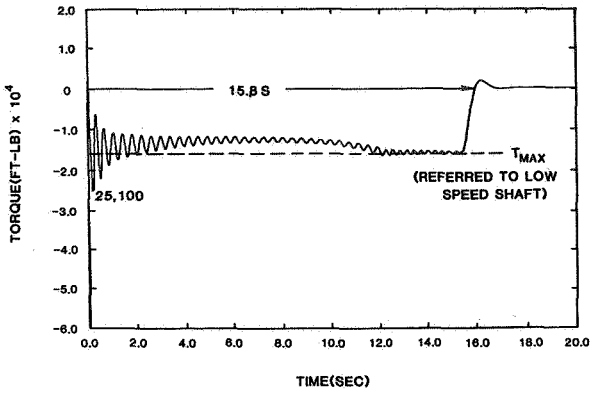

FIGURE 16. DYDTA PREDICTION - LOW SPEED SHAFT TORQUE VS. TIME DURING START-UP IN ZERO WIND WITH CLUTCH.

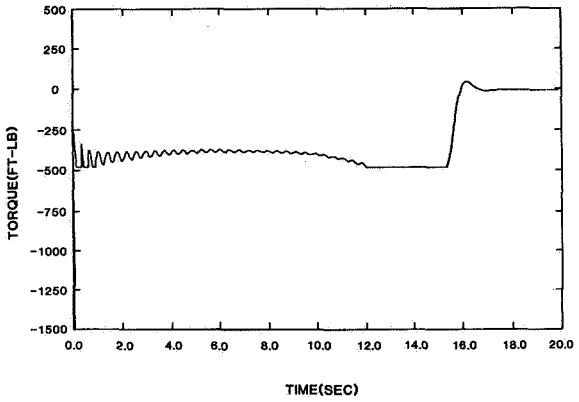

FIGURE 17. DYDTA PREDICTION - TORQUE TRANSMITTED THROUGH CLUTCH VS. TIME DURING START-UP IN ZERO WIND WITH CLUTCH.

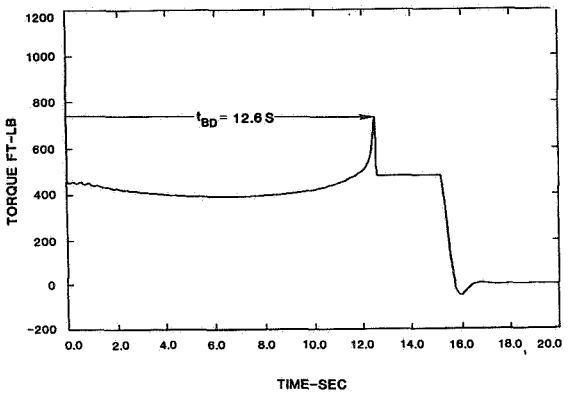

FIGURE 18. DYDTA PREDICTION - MOTOR TORQUE VS. TIME FOR START-UP IN ZERO WIND WITH CLUTCH.

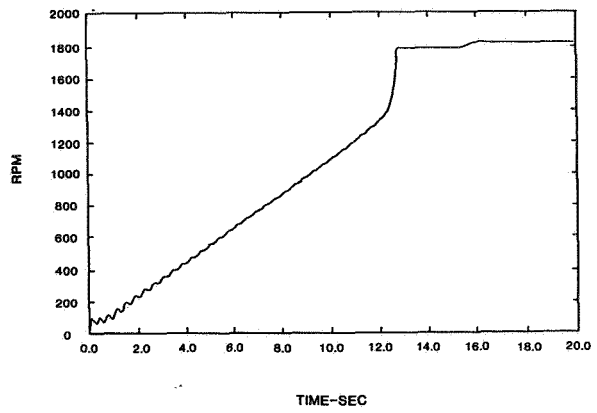

FIGURE 19. DYDTA PREDICTION - MOTOR SPEED VS. TIME FOR START-UP IN ZERO WIND WITH CLUTCH.

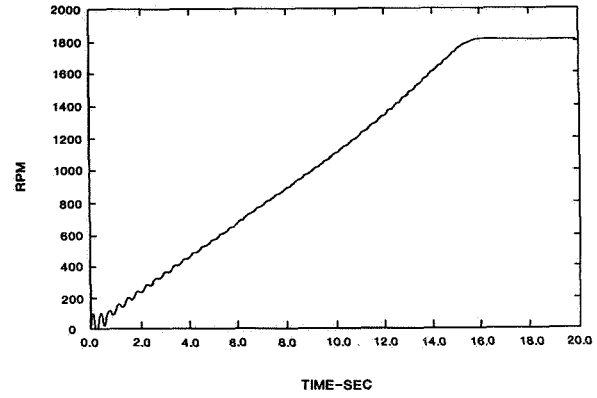

FIGURE 20. DYDTA PREDICTION - CLUTCH SPEED (ROTOR SIDE) VS. TIME FOR START-UP IN ZERO WIND.

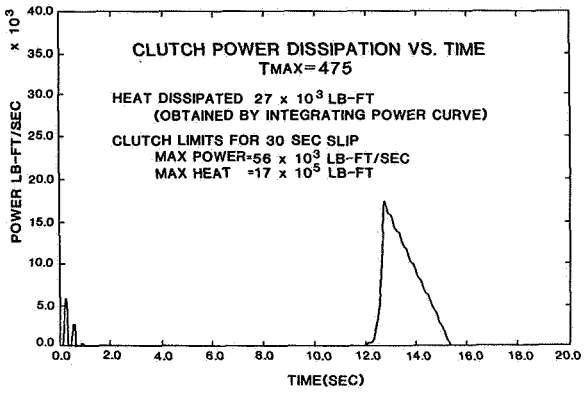

FIGURE 21. DYDTA PREDICTION - POWER DISSIPATED IN CLUTCH VS. TIME FOR START-UP IN ZERO WIND.

Figures 19 and 20 can be compared to determine at what times the clutch is slipping. The power dissipated in the clutch as a function of time, and the total heat dissipated (obtained by integrating the power curve) are shown in Figure 21.

CONCLUSIONS

DYDTA represents an initial step towards understanding and analyzing methods of controlling transient behavior in VAWT drive trains. Results for start-up in zero wind speed show exceptional agreement with experimental records on the Low Cost 17M turbine, thus providing verification of modeling accuracy. DYDTA is currently being used to predict responses for several different transient operations and possible design modifications intended to reduce transient torque levels. It is expected to become a versatile, easily implemented drive train design tool.

ACKNOWLEDGMENTS

The assistance of the following is gratefully acknowledged: T. M. Leonard for his programming ideas and support, P. S. Veers and K. W. Schuler for their help towards understanding and describing the slip clutch, and W. N. Sullivan for the initiation of this project.

REFERENCES

1. Reuter, R. C., "Torque Ripple in a Darrieus Vertical Axis Wind Turbine," Sandia National Laboratories Report No. SAND80-0475, September 1980.

2. Mirandy, L. P., "Rotor/Generator Isolation for Wind Turbines," Journal of Energy, Vol. 1, No. 3, May-June, 1977.

QUESTIONS AND ANSWERS

D.B. Clauss

From: I.P. Ficenec

Q: What value of damping was used for the transmission system and how was this established?

A: *The value of damping is 1.1 x 10^3 lb-ft-sec, and this was established by varying the damping coefficient in the code until the analytic results agreed well with observed data for start-up. I might add that this damping coefficient yields a critical damping of ∿1%, and consequently does not strongly influence the turbine response.*

From: G. Beaulieu

Q: 1) In order to have full automatic control of the turbine, would you also have a maximum power or maximum windspeed cut-off, at which time the turbine would be stopped?

2) Since you have introduced nonlinearities into your model, what numerical method of solution have you used in your computer code DYDTA?

A: *1) Studies involving this aspect of automatic control are in the planning stages.*

2) The equations of motion are numerically evaluated using a library routine which employs a variable order Adams method.

From: Mike Bergey

Q: Was the wind data for Oklahoma City from a National Severe Storms Lab report?

A: *Yes, the data was located for Sandia National Labs by James Connell of PNL. The National Severe Storm Labs had recorded the data in 1976 and transferred the data to the National Center for Atmospheric Research where Dennis Joseph provided magnetic tapes for dissemination.*

From: W.C. Walton

Q: You have treated the rotor as rigid. Do you think rotor elasticity has any bearing on the dynamic phenomena related to drive train stability and response?

A: *For VAWT's the size of the Low Cost N-M turbine, we are fairly confident that rotor elasticity does not strongly influence drive train stability or drive train response because the rotor structure appears much stiffer than the low speed shaft. This is, however, a question we will have to deal with for different turbines.*

From: P. Anderson

Q: Does the induction machine model include rotor electrical transients? What time step size was used for start-up simulations?

A: *The model does not include electrical rotor transients, nor am I certain of their influence on the mechanical system response. The step size is shown by the integrator based on the rate of change of the dependent variables, it varies tremendously depending on the smoothness and volatility of these functions.*

From: Rowley Camedav

Q: Have you seen reflection of torque spikes back into rotor structure during emergency braking?

A: *The model which has been used so far treats the rotor structure (turbine tower and blades) as essentially a rigid inertial element, so that analytically we have seen no such reflection . From a qualitative standpoint, however, there is certainly some reflection of torque spikes onto the rotor structure during emergency braking, although they are probably not as severe as in the low speed shaft.*

DYNAMICS AND STABILITY OF WIND TURBINE GENERATORS

E. N. Hinrichsen P. J. Nolan
Power Technologies, Inc.
Schenectady, NY

ABSTRACT

This paper describes the dynamic and stability properties of wind turbine generators connected to power systems. Both synchronous and induction generators are considered. A comparison is made between wind turbines, steam, and hydro units. The unusual phenomena associated with wind turbines are emphasized. The general control requirements are discussed, as well as various schemes for torsional damping such as speed sensitive stabilizer and blade pitch control. Interaction between adjacent wind turbines in a "wind farm" is also considered.

1. INTRODUCTION

The purpose of this paper is to provide an overview of the general dynamic characteristics of wind turbine generators in electric power systems and to discuss the impact of variations in system design and control.

Wind turbine generators possess some special characteristics not shared by steam and hydro units. The obvious one is the variability of the source of energy. Two others, which are less obvious, are the high turbine inertia and the low effective shaft stiffness between turbine and generator. These unusual torsional characteristics have several interesting consequences. First, WTGs have a low frequency (<0.5 Hz) torsional mode, which has to be damped, particularly if the turbine is equipped with blade pitch control. Second, the low stiffness shaft system gives WTGs very good transient stability properties. Third, matching of frequency, phase angle and voltage prior to synchronization is less important. Fourth, the two significant torsional modes are practically decoupled. One is determined by turbine inertia and effective shaft stiffness, the other by generator inertia and electrical stiffness. This has favorable implications for multi-machine installations. Interaction of low frequency torsional modes is very unlikely.

In most of the analysis presented here, attention is focused on single wind turbine generators supplying an infinite bus through an external impedance. This simple configuration facilitates system and control parameter variation over a wide range and provides insights into the general characteristics of wind turbine generators. It is subsequently shown how groups of wind turbine generators interact and how the results of the single machine case can be extended to the multi-machine case.

The material in the paper is organized as follows:

- The general characteristics of wind turbines as they relate to dynamics and control are described in Section 2. This section analyzes the significance of drive train configurations, discusses modal analyses and evaluates the differences between synchronous and induction generators.
- In Section 3 the general control requirements as well as actual turbine control systems are outlined and compared with those for steam and hydro turbine generators. Various methods of torsional damping are discussed and compared.
- Dynamic and transient stability properties are presented in Section 4.

The results reported in this paper are based on analytical work carried out for the Wind Systems Branch of the U.S. Department of Energy, the Wind Energy Projects Office of the National Aeronautics and Space Administration, and Sandia Laboratories.

2. CHARACTERISTICS OF WIND TURBINE GENERATORS

Figure 2.1 is the basic block diagram of a turbine generator system. The peculiarities of a WTG compared to conventional turbine generators lie in the variability of the energy supply, the characteristics of the wind turbine as an energy conversion device, and the geometry of the turbine, shafts, gears, and generator which comprise the torsional system.

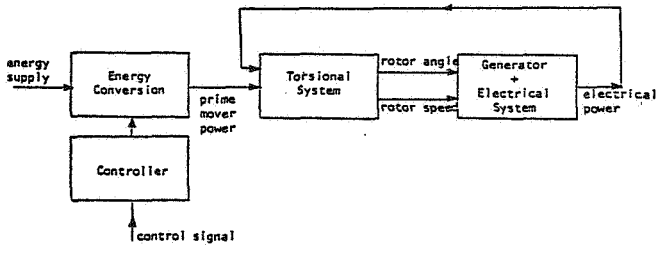

Figure 2.1 Turbine Generator System

At the present time, the horizontal axis propeller turbine and the vertical axis Darrieus turbine are the most likely choices for commercial electric power generation. (Figure 2.2). Both are low-speed machines with large diameter, high inertia rotors. Typical rotor speeds for large turbines (>1 MW) are 20-50 rpm. Typical per unit rotor inertias referred to turbine rating are 5-15 seconds. The large diameter, high inertia rotors are a result of the relatively low energy density of wind. Average wind energy densities in favorable locations are less than one thousand watts per square meter of area swept by the rotor. Both types of turbines achieve their best extraction efficiencies at

tip speed/wind speed ratios of 6-8. In that range, the efficiency is approximately 0.4. The theoretical maximum efficiency is 0.59. The large rotor diameter required for energy capture and the tip speed/wind speed ratio required for good efficiency determine rotor speed.

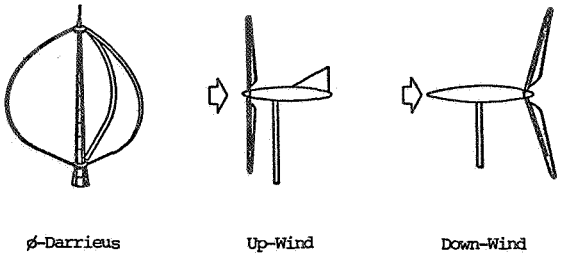

Figure 2.2 Wind Turbine Designs

Most large wind turbines operate at constant speed, driving standard three-phase ac generators. Synchronous as well as induction generators are used. Generators of suitable dimensions and reasonable cost are four- or six-pole machines with synchronous speeds of 1800 or 1200 rpm. The large difference between turbine and generator speeds makes gearboxes essential elements of wind turbine generator drive trains. The consequence of the gearbox in terms of drive train dynamics is low mechanical stiffness between generator and turbine when viewed from the generator. Figure 2.3 is a comparison of typical inertia-stiffness relationships in steam, hydro, diesel, and wind turbine generators. The unusual characteristics of WTG drive trains are evident from this comparison. The WTG is the only turbine generator in utility networks with a mechanical stiffness lower than the electrical stiffness (synchronizing torque coefficient) [2].

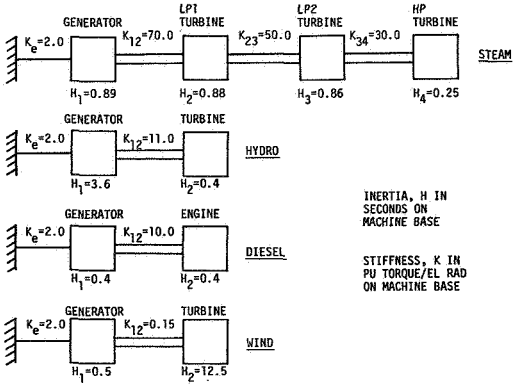

Figure 2.3 Comparison of Drive Trains of Typical Turbine Generators

For analysis of the mode shapes the electrical tie of the synchronous machine can be represented by a torsional spring (Figure 2.4.a). A low slip induction generator may be represented by the block diagram shown in Figure 2.4.b. This simplified representation includes the rotor dynamics of a single rotor circuit and embraces an algebraic solution of the network. T'_{dz} is typically 1 second and D lies in the range 50 to 500 p.u. It is evident that over the frequency range of interest the dynamics of both machines are similar, and that the induction generator can also be represented by an equivalent "synchronizing coefficient." Irrespective, therefore, of the type of generator, the torsional coupling between generator and synchronous frame has been represented as a torsional spring. Figure 2.5 shows mode shapes and modal frequencies of the 2.5 MW MOD-2 horizontal axis WTG designed by Boeing. Figure 2.6 shows the mode shapes and modal frequencies of the 2.0 MW MOD-1 horizontal axis WTG designed by General Electric, and Figure 2.7 depicts the same information for the 60 kW, 17 meter vertical axis Darrieus WTG designed by Sandia Laboratories. Even though the three machines are very different in size and design, the mode shapes are quite similar. The electrical stiffness selected for this analysis is 2.0 pu. This is a typical value for machine, network and loading in a WTG system. The lowest torsional mode in Figures 2.5, 2.6 and 2.7 represents oscillation of the turbine rotor through the shaft against generator and infinite bus equivalent of the electrical system. Since electrical stiffness is much higher than apparent mechanical stiffness, the relative torsional amplitude of the generator rotor is very small. It is evident that the frequency of this mode is almost entirely determined by turbine inertia and shaft stiffness, not by electrical parameters.

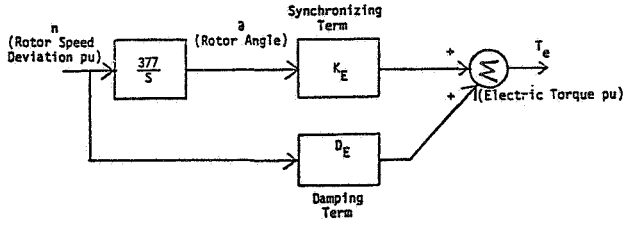

(a) Synchronous Generator

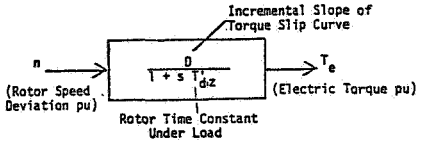

(b) Induction Generator

Figure 2.4 Simplified Block Diagrams for Synchronous and Induction Generators

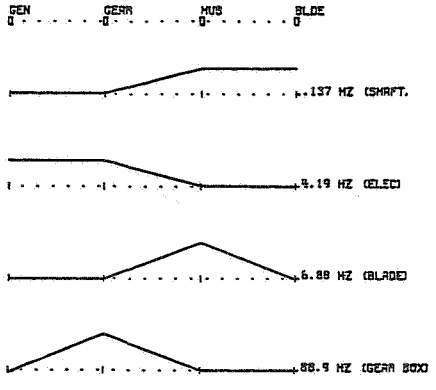

Figure 2.5 Mode Shapes of MOD-2 WTG

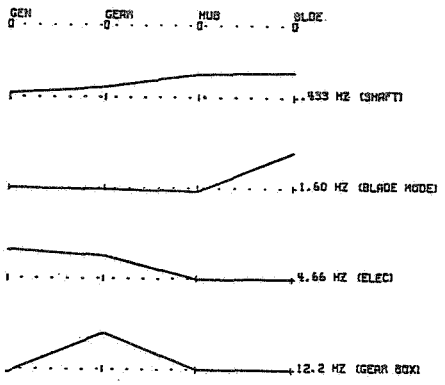

Figure 2.6 Mode Shapes of MOD-1 WTG

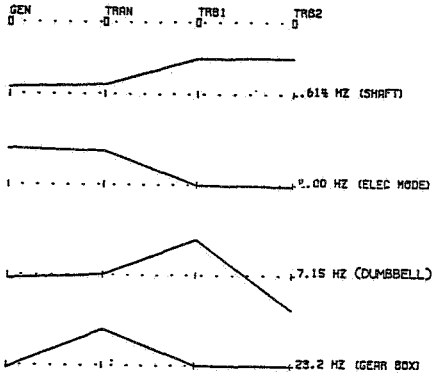

Figure 2.7 Mode Shapes of Sandia 17 M WTG

The second torsional mode in Figures 2.5 and 2.7 and the third mode in Figure 2.6 represent oscillation of the generator rotor through the electrical stiffness against the equivalent infinite bus. Turbine rotor participation in this "electrical" mode is insignificant. The frequency of this mode is primarily determined by generator inertia and synchronizing coefficient, which depends on loading, generator, and network characteristics. The frequency is essentially independent of turbine parameters.

For an analysis of the dynamics of WTGs connected to electric power systems, torsional modes other than the two discussed here can generally be neglected. They are either well damped or their frequencies are above the range of interest.

Figures 2.5, 2.6, and 2.7 further reveal that the first torsional mode is most easily stimulated by transients acting on the turbine, while the "electrical" mode responds primarily to stimulation acting through the generator.

The frequencies and mode shapes in Figures 2.5 and 2.6 describe the system without control. Blade pitch control with proportional action on electric power increases the frequency of the first torsional mode.

These mode shapes may be contrasted with those of a typical steam generator, where all the inertias move with almost equal amplitude at the low frequency system mode. The normal approximation for stability work is to combine all inertias into a single inertia connected to the electrical system through the equivalent electrical stiffness. In a WTG, by contrast, the generator inertia can be considered decoupled from the hub and blade inertias in the electrical mode. The effective stiffness between generator and turbine is very low. Relatively high "electrical" mode frequencies are then possible due to the nearly unconstrained motion of the generator inertia against the electrical system.

3. WIND TURBINE CONTROL

The overall linearized block diagram of a WTG, including pitch control, torsional system, generator, electrical system, and provisions for damping the first torsional mode, is shown in Figure 3.1.

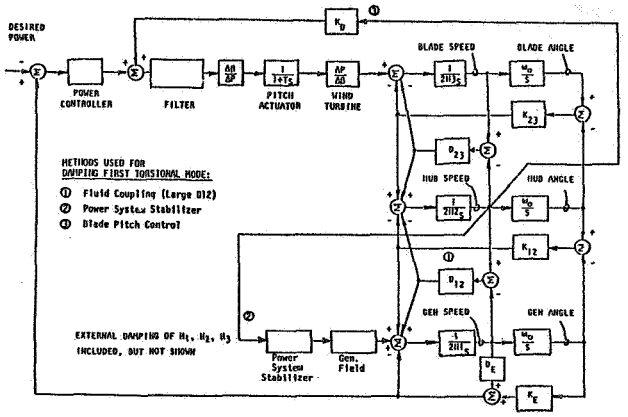

Figure 3.1 Linearized Model of WTG

In addition to drive train configuration, turbine blade pitch control has a significant impact on dynamic behavior. This type of control only exists in horizontal axis machines. Variable pitch turbines operate efficiently over a wider range of wind speeds than fixed pitch machines. Cost and complexity are higher. It is generally found that a sufficiently responsive pitch control system has a bandwidth that includes the frequency of the first torsional mode, i.e., this mode is stimulated by control action. Therefore, additional damping for the lightly damped first torsional mode is required. Three different methods of damping have been used in variable pitch turbines developed within the U.S. Federal Wind Energy Program:

- Generator damping either through the use of a power system stabilizer or by the inherent damping of an induction generator.
- Addition of a damping signal to the pitch controller.
- Fluid coupling between turbine and generator.

In the MOD-1 WTG, damping is achieved by a speed sensitive power system stabilizer. Turbine hub speed is used as the input. It can be seen qualitatively from the mode shapes of Figure 2.6 that the stabilizer operates on a relatively small component of generator motion in the first torsional mode, and can be expected to require large torques to influence shaft motion at this frequency. Loci of eigenvalues as function of stabilizer gain confirm the relative ineffectiveness of this means of providing damping to the first torsional mode.

A stabilizer can have a destabilizing effect on the "electrical" mode. This happens when there is a phase reversal between generator and hub displacements in the "electrical" mode.

In the MOD-2 WTG, a damping signal in phase with hub speed is summed with the output of the pitch controller. The time response plot of Figure 3.2 shows the effectiveness of this damping component. Figure 3.2 depicts the response of electrical power to a step change in wind power. The difference between the two traces marked "base design" and "no hub damping" is caused by the damping component. The third trace in Figure 3.2 marked "no control" shows the response without pitch control. It should be noted that in this case the addition of pitch control increases the frequency of the first torsional mode. The proportional component of power control introduces stiffness between turbine and generator inertias. Figure 3.3 shows the eigenvalues as wind speed changes. The variation in wind speed changes the incremental wind power/pitch angle relationship and thereby affects the transfer function of the control loop. It can be seen that the system is adequately damped over the whole wind speed range.

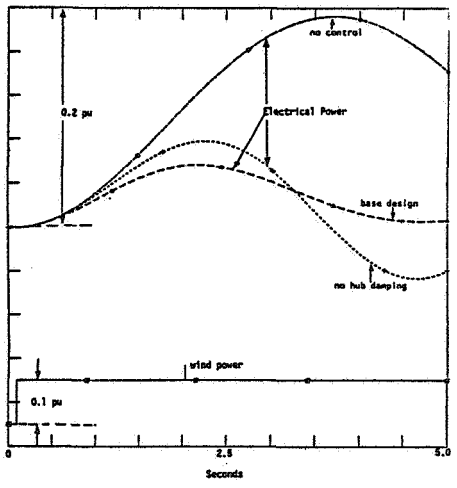

Figure 3.2 Effect of Damping with Pitch Control

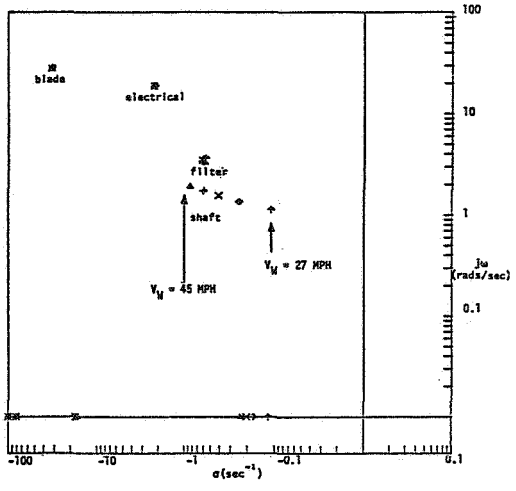

Figure 3.3 Effect of Varying Wind Speeds-MOD-2 WTG

Reference [1] describes a WTG control system which also uses pitch variations for introducing damping. A compensating network is included in the hub speed loop to offset servo lag.

Figure 3.4 shows that damping of the first torsional mode can also be introduced by a high slip induction generator. This would not be an effective mechanism in a WTG such as the MOD-2 because generator motion in the first torsional mode is extremely small (Figure 2.5). In a MOD-1 WTG, generator motion in the first torsional mode is larger (Figure 2.6). Damping with a high slip induction generator wouldbe more effective, however, losses would be high.

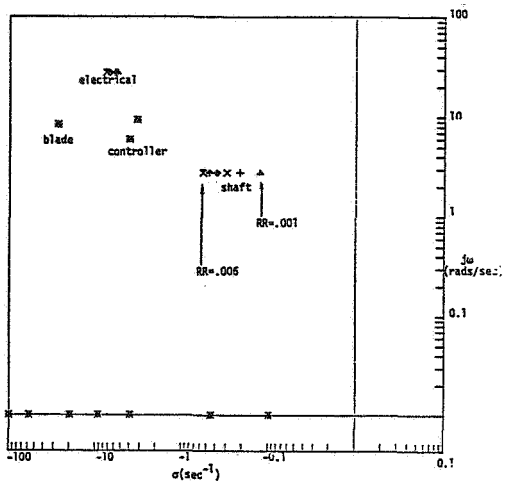

Figure 3.4 Effect of Varying Induction Generator Rotor Resistance, MOD-1 Drive Train

In the MOD-0 and MOD-0A, a fluid coupling is used. This is a very effective damping device but it introduces losses.

In addition to finding a suitable balance between control response and damping of the first torsional mode, the controlled variable has to be selected. For primary control, this can either be speed or power. Current WTGs use power. This selection has been based on the assumption that electric power systems are infinitely large compared to wind turbines and that constant power generated by WTGs can always be absorbed. There are two disadvantages:

- o WTGs using power control do not participate in load sharing.
- o The power controller cannot differentiate between changes it should respond to, i.e., changes caused by the turbine, and those it should not respond to, i.e., changes originating in the electrical system.

Use of turbine speed as the controlled variable would have three advantages:

- o Pitch control would not respond to system disturbances unless they affect turbine speed.
- o Speed is the controlled variable for turbine controllers of conventional turbine generators. Turbine speed controllers have proportional characteristics so that the speed droops slightly with load. This provides

load sharing capability. WTGs will not always be applied to systems infinitely large compared to their rating. They must be able to participate in transient load sharing.

- Speed control is dynamically superior to power control. Turbine torque excursions are integrated once and become speed excursions. They are integrated again before showing up as power angle and electric power excursions.

A combination of primary speed control and slower resetting type power control is traditional in power systems.

4. DYNAMICS AND STABILITY

The following issues were addressed:

- Dynamic stability of a single wind turbine generator connected to a strong system.
- Dynamic stability of a group of wind turbines synchronized to a common bus and connected to a strong system.
- Transient stability following disturbances at the mechanical end (wind speed changes) and at the electrical end (faults) of the WTG drive train.
- Shaft torque levels during disturbances.
- Synchronization.

Dynamic Stability of Single Wind Turbine

The dynamic stability of a single wind turbine generator was investigated by obtaining the eigenvalues of wind turbine systems for variations in the electrical system. In the case of a synchronous generator KE (the synchronizing coefficient) was modified to reflect these variations. Results are shown in Figure 4.1. In the case of an induction generator XE (the electrical system reactance) was modified to show the effect of variations in transmission strength. Results are similar to Figure 4.1. It is evident that only the electrical system mode is affected by these changes. It was noted earlier that this mode is nearly independent of the mechanical properties of the turbine.

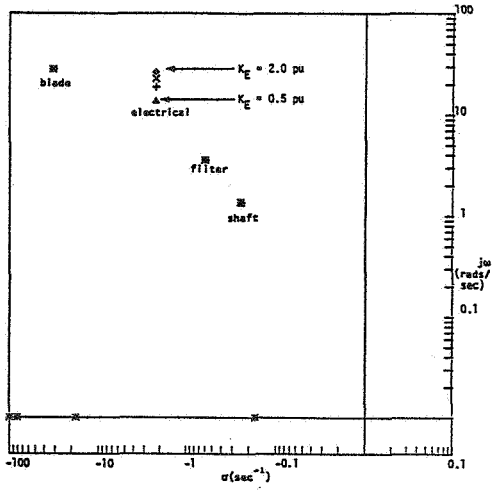

Figure 4.1 Effect of Varying Electrical Stiffness

Dynamic Stability of Groups of Wind Turbines

Most of the analyses presented so far have been based on systems with single WTGs connected to an infinite bus. In view of the variability of wind energy, there has been concern about interactions between adjacent wind turbine generators through the electrical network.

In the case of two identical wind turbines synchronized and connected to a stiff system, the dynamics comprise two sets of modes:

- Wind turbine generators move coherently with each other. These "in phase" modes are stimulated by wind speed disturbances of the same magnitude and sign applied to each machine. Electrical disturbances on the common transmission system also excite these modes.
- Wind turbine generators move against each other with equal and opposite magnitudes. It is not possible to excite these "anti-phase" modes by disturbances on the common electrical transmission. The bus at which the machines are synchronized represents a node for all anti-phase modes.

The dynamics of such a system can be analyzed in terms of two equivalents:

- A lumped equivalent machine swinging against the receiving end infinite bus.
- A single machine swinging against the bus at which the machines are synchronized.

It was concluded earlier that the first torsional mode is practically unaffected by the transmission system strength. Consequently, the natural frequency and damping of the first torsional mode is approximately the same for the single system and inter-system modes. It follows that a WTG designed for the first torsional mode in a single machine application will also satisfy damping requirements for intermachine first torsional modes in multi-machine applications.

The intermachine electrical modes are not particularly significant. There are three reasons:

- They generally have a higher frequency than the electrical system mode and are better damped.
- They are not stimulated appreciably by wind speed disturbances. This was shown earlier in the modal analysis of WTG drive trains.
- They are not stimulated by electrical disturbances common to all adjacent WTGs.

The analysis of interactions between WTGs has been explained in terms of a two machine system synchronized to a common bus. The results can be extended to the general case [3].

Transient Stability

Wind turbine generators are subjected to mechanical disturbances applied at the turbine when there are sudden wind speed changes. They are also subjected to electrical disturbances applied at the generator during electrical transients. While all the possible electrical disturbances are of the same nature for conventional turbine generators as for WTGs, the consequences of particular disturbances are different because the torsional system is different. Mechanical

disturbances of the drive train from the turbine end are a peculiarity of WTGs.

Figure 4.2 shows the response of a MOD-2 WTG to five successive 4 mph step changes in wind speed. Wind speed (mph), mechanical power at the blades (p.u.), electrical power (p.u.), and generator power angle (deg.) are plotted. Pitch control is active to provide power control and damping of the first torsional mode. It is interesting to note that damping of the first torsional mode increases with increasing wind speed. This corroborates the results of the eigenvalue analysis shown in Figure 3.3.

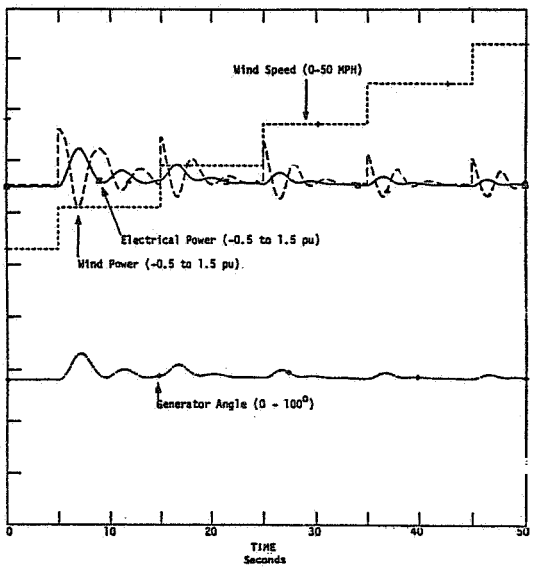

Figure 4.2 4 MPH Step Increases in Wind Speed

Figure 4.3 depicts the behavior of a MOD-2 WTG during and after a 0.1 sec. three-phase fault at the high side of the generator step-up transformer. The four traces in Figure 4.3B show airgap torque, low speed shaft torque, blade torque, and high speed shaft torque. The two frequencies dominating the response are the 60 Hz system frequency during the fault, and the frequency of the electrical system mode after the fault. Even though airgap torques reach 6 p.u., turbine torques are hardly affected by this transient.

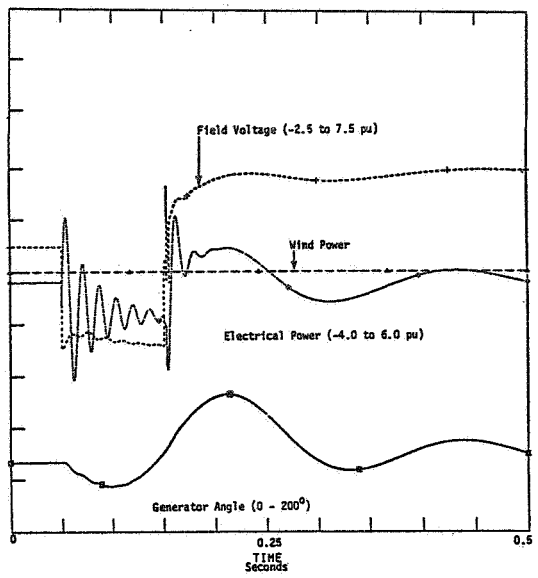

Figure 4.3A Three Phase Fault Near WTG for 0.1 Second

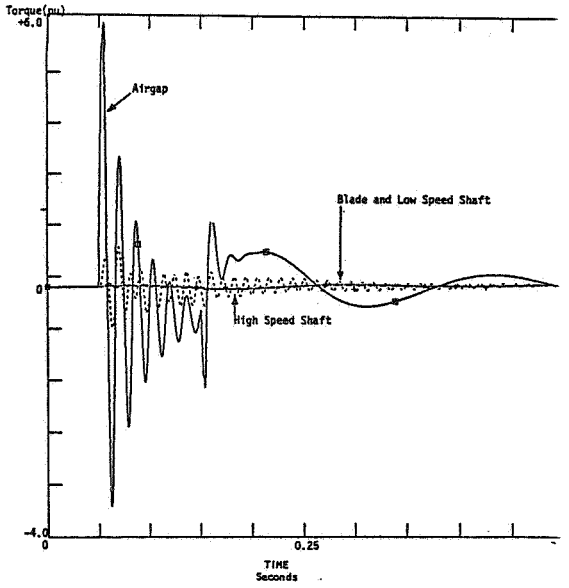

Figure 4.3B Torque Levels in MOD-2 Drive Train, Three Phase Fault Near WTG for 0.1 Second

Figures 4.4 shows the events occurring during and after a loss of electrical load for 0.5 seconds. The WTG is a MOD-2. The four traces in Figure 4.4A show generator speed, hub speed, blade speed, and gear speed. The generator rotor accelerates very quickly away from the synchronous reference frame, unwinding the turbine shaft and starting an oscillation with respect to the turbine. The generator rotor angle reaches 1000 degrees after approximately 0.5 sec. The turbine also begins to accelerate but at a much lower rate. As long as the turbine is still near synchronous speed, resynchronization is theoretically possible at any rotor angle. When the tie to the electrical system is restored at t=0.55 sec., the generator resynchronizes quickly at a rotor angle that differs from the original rotor angle by 1080 degrees (3*360). After the generator has been resynchronized, the turbine oscillates with respect to the generator at the frequency of the first torsional mode.

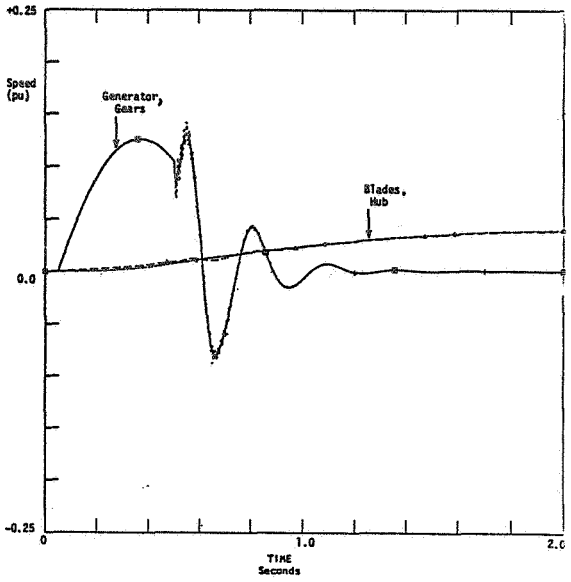

Figure 4.4A Speeds in MOD-2 Drive Train, Loss of Load for 0.5 Second

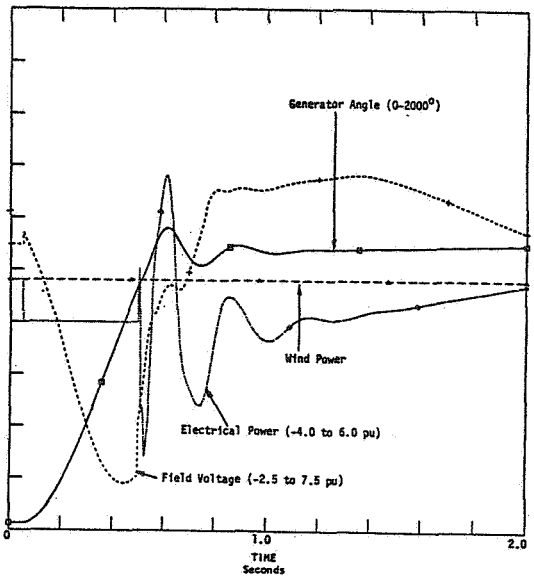

Figure 4.4B Loss of Load for 0.5 Second

Shaft Torque Levels

Figure 4.3B demonstrates another characteristic of the torsional system of wind turbine generators: low levels of shaft torque during disturbances. The mechanical limitation of WTGs during several electrical disturbances is not strength at shafts but rather the bracing of generator windings. The bracing required does not exceed conventional levels.

Synchronization

The unusual torsional dynamics of wind turbine generator drive trains can be used to advantage during synchronization. Turbine and generator are decoupled transiently by the apparent low shaft stiffness. This reduces the need for accurate matching of voltage, speed, and phase angle prior to synchronization. Speed errors of several percent and angle deviations of 30-40 degrees can be tolerated.

5. CONCLUSIONS

The dynamic and transient stability properties of wind turbine generators have been explored using eigenvalue and time response analysis. It has been shown that, unlike steam or hydro units, the dynamics of wind turbine generators are dominated by the torsional characteristics of the drive train. The most significant characteristic of such systems is the presence of an inherently poorly damped shaft mode having a frequency below 0.5 Hz.

Various schemes for introducing damping in the low frequency shaft mode are discussed. Inclusion of a hub speed damping signal in systems which have blade pitch control is shown to be particularly effective. The rationale for choosing electric power as the regulated variable is also considered and the advantages of choosing turbine speed instead of electric power are debated.

The unusual characteristics of the drive train are shown to have a decoupling effect on electrically and mechanically produced transients. Faults on the electrical side do not stimulate the low frequency shaft mode to any appreciable extent. Similarly, even large wind speed disturbances do not influence the electrical system mode.

Consistent with the above decoupling between the electrical and shaft modes, it is seen that electrically produced damping is not particularly effective in damping the first shaft mode. This implies that speed sensitive stabilizers operating on synchronous machine excitation, or induction generator damping will have limited effect on damping of the dominant shaft mode.

Further consequences of the unusual torsional system characteristics are the excellent transient stability properties and ability to synchronize a wind turbine through large phase and speed mismatches. Impact torque levels during fault and network switchings are lower than in typical steam units due to the inherent decoupling between generator and turbine.

From the viewpoint of network disturbances, both induction and synchronous machines exhibit a relatively high frequency oscillatory mode (typically 20 to 30 rads/sec.). This high frequency results from the lightness of the generator rotor and the softness of the torsional spring between generator and hub. Damping of the first torsional shaft mode and power control response do not vary appreciably with electrical system parameters.

No adverse interactions have been predicted for groups of wind turbines synchronized together. The only coupling is through the electrical system which is shown to have little influence on the power control loop or shaft mode damping. The main result of interconnection will be coupling between electrical modes. The intermachine electrical modes are not normally of concern as they are not stimulated by asymmetric wind disturbances (due to the soft shaft effect) and are not stimulated by electrical disturbances on the common transmission system.

The conclusions regarding the absence of interaction in the multi-machine case have been confirmed by carrying out detailed simulations of a three wind turbine system with each machine represented explicitly.

In addition to more detailed simulation to complement the results summarized in this paper the authors feel that further work in the following areas is warranted:

- The use of turbine speed as the regulated variable for pitch control systems. This would make wind turbine control functionally equivalent to steam and hydro turbine control.

- The limitation of using electrical power as the regulated variable in pitch control systems. The limitations will become apparent when WTGs are connected to noninfinite power systems.

- Other methods of damping the first torsional mode. Damping by pitch control is effective but is inactive at low wind speeds. Electrical damping is not particularly effective.

- Out of step synchronization WTGs are very tolerant to out-of-step synchronization. The usefulness of this characteristic for reclosing and synchronization should be evaluated.

6. REFERENCES

[1]. J. M. Kos, "On Line Control of a Large Horizontal Axis Wind Energy Conversion System and its Performance in a Turbulent Wind Environment," Proceedings of the 13th Intersociety Energy Conversion Engineering Conference, pp. 2064-2073, August, 1978.

[2]. F. P. deMello and C. Concordia, "Concepts of Synchronous Machine Stability as Affected by Excitation System Control," IEEE Trans. Power Apparatus and Systems, Vol. PAS 92, pp. 316-329, April, 1969.

[3]. R. T. Alden, P. J. Nolan and J. P. Bayne, "Shaft Dynamics in Closely Coupled Identical Generators," IEEE Trans. on Power Apparatus and Systems, Vol. PAS 77, No. 3, pp. 721-728, May/June, 1977.

QUESTIONS AND ANSWERS

E.N. Hinrichsen

From: D.L. Hughes

Q: a) Did you examine the effect of controlling the tips with any other form of feedback (e.g., torque/acceleration)?

b) Is rotor flexibility important in determining dynamic response of system with tip control?

A: *a) Yes. We examined the behavior of this system with primary turbine control based on power. We found that the sensitivity of pitch control to electrical disturbances was greatly reduced and the response to wind speed disturbances was essentially the same.*

b) We have not looked at rotor flexibility. It is unlikely that rotor flexibility affects the two modes which principally determine electrical system behavior.

From: Anonymous

Q: What is the sacrifice in energy capture as a result of controlling the pitch angle at lower wind speeds?

A: *No quantitative answer available.*

From: F.A. Stoddard

Q: I assume the aerodynamic model in your wind turbine $\Delta P/\Delta\beta$ is linear. Do you have any feeling for the effects of 1) dynamic stall and 2) quasi-steady or unsteady aerodynamics?

A: *The aerodynamic model is not linear. Figure 3.1 is a linearized version of the actual model. The actual model includes the full nonlinear representation of $c_p = f(\lambda, \beta)$. Unsteady aerodynamics are probably best treated as disturbances of the $\Delta P/\Delta\beta$ transfer function. Their principle effect would be stimulation of the first torsional mode.*

From: W.C. Walton

Q: a) The frequencies of the important modes - what ratio to nP?

b) Does blade elasticity influence the modes?

A: *a) At rated power (approximately):*

	MOD-1 (34 RPM)	MOD-1 (23 RPM)	MOD-2 (17.6 RPM)
First torsional:	*0.7*	*1.1*	*0.8*
Second torsional:	*8.3*	*12.4*	*16.5*

Since the frequency of the second torsional (electrical) mode is a function of electrical stiffness, its frequency varies with electrical system reactance. The values given here are for a stiff electrical system.

b) It is unlikely that blade elasticity affects the two modes important for electrical stability and control. It will create higher modes which probably lie outside the range of interest at pitch control and electrical system dynamics.

consideration of the utility configuration control loop requires a stiffness greater than 460,000 ft-lb/radian, which is important only at torque levels near rated torque.

CONTROL LOOP GAIN

A review of Figures 1 and 2 shows that the magnitude of the control loop gain is determined by the following:

No Load:

$$\text{Gain} = (A_C)\left(\frac{\partial T_R}{\partial \theta}\right)\left(\frac{1}{C_R + C_{GL}}\right)$$

Utility With Load:

$$\text{Gain} = (A_C)\left(\frac{\partial T_R}{\partial \theta}\right)\left(\frac{1}{C_R + C_{GL} + C_{GC}}\right)(A_G)$$

Standalone With Load:

$$\text{Gain} = (A_C)\left(\frac{\partial T_R}{\partial \theta}\right)\left(\frac{1}{C_R + C_{GL} + C_L}\right)$$

where:

A_C = Controller gain factor

$\frac{\partial T_R}{\partial \theta}$ = change in rotor torque per unit change in pitch angle

C_R = slope of the rotor torque-speed curve, C_{GL}, C_{GC}, C_L, as defined on Figure 2

A_G = a constant that relates generator power to generator slip speed

Two of these factors, $\frac{\partial T_R}{\partial \theta}$ and C_R, are derived from the rotor characteristics and vary considerably over the range of expected operating conditions. The slope of the torque-speed curve, C_R, increases from 170 ft-lb-sec/radian at 10 mph to 6254 ft-lb-sec/radian at 60 mph. The torque derivative with pitch, $\frac{\partial T_R}{\partial \theta}$, is zero when the maximum available power is being delivered (i.e., regulation is not possible). However, if power is restricted to the lesser of 40 kW or 80% of the maximum available, the torque derivative increases from 90 ft-lb/deg. to 1980 ft-lb/deg. as the wind increases from 10 to 60 mph. The three gain functions, normalized to their values at 20 mph are shown on Figure 7. The functions with load are based on the lesser of 40 kW or 80% of the maximum power available.

The loop gain in the no load case changes by a factor of almost 5. However, this case is primarily concerned with startup which takes place when the wind speed increases above 10 mph or decreases below 60 mph. The loop gains at these two points only differ by a factor of 1.5. More importantly, the control loop stability analysis indicated that a fixed controller gain could be selected that would provide adequate speed regulation at 10 and 60 mph and satisfactory overshoot characteristics at 20 - 25 mph. Test data has verified this projection up to 30 mph. Test data for startups above 30 mph have not yet been collected.

When the standalone configuration is operated with full load, the changes in the torque derivative are almost fully compensated by changes in the total damping and the loop gain is essentially constant. As the load is decreased, the curve approaches the no load curve. In this case also, the control loop stability shows sufficient gain margin to achieve adequate speed regulation and satisfactory overshoot characteristics under all of the wind speed and load conditions.

The utility configuration differs in two respects. First, the damping term is dominated by C_{GC}, the very steep slope of the induction generator torque-speed curve. Therefore, the change in loop gain is almost equal to the change in the torque derivative, a factor of 20 for 10 to 60 mph. Second, because of the added phase lag of the drive shaft dynamics, the gain margin available is much less than that available in the other modes. The result is that the controller gain that provides adequate power regulation at 20 - 25 mph causes instability at 60 mph. Therefore, the controller gain in this mode is made a function of the mean wind speed such that the total loop gain remains essentially constant.

RESPONSE TO WIND SPEED CHANGES

The ability of a variable-pitch wind turbine to maintain a given power level in the presence of wind speed changes is limited by the capabilities of the pitch change mechanism. Therefore, knowledge of the wind variability that must be accomodated is needed to establish the required capabilities of the pitch change mechanism.

To meet this need, the description of wind variability must relate the magnitude of wind speed changes to the time interval over which they are observed and the frequency with which they can be expected at the planned location of the wind turbine. The magnitude and time interval, with respect to the dynamic characteristics of the wind turbine, determine the impact on the wind turbine. The frequency determines whether or not they need to be accommodated. For example, wind speed changes that cause disruptions in the delivered power less frequently than once per month or once per year need not be accommodated. However, the system must accommodate wind speed changes that could cause damage more frequently than once per lifetime of the machine.

Cliff and Fichtl (Reference 1) have developed a description of wind speed changes based on turbulence theory. It allows the calculation of the root-mean-square (RMS) value of the change in wind speed over a time interval as a function of the mean wind speed, nature of the terrain (surface roughness), height above the surface, and the scale of the affected device. The RMS value and the characteristics of a Normal distribution determine the probability of exceeding a particular magnitude of speed change in any one time interval. The probability and the duration of the observation time interval determine the

KAMAN 40 kW WIND TURBINE GENERATOR - CONTROL SYSTEM DYNAMICS

Richmond Perley

Kaman Aerospace Corporation
Old Windsor Road
Bloomfield, Connecticut 06002

ABSTRACT

The Kaman 40 kW Wind Turbine Generator design incorporates an induction generator for applications where a utility line is present and a synchronous generator for standalone applications. A combination of feed forward and feedback control is used to achieve synchronous speed prior to connecting the generator to the load, and to control the power level once the generator is connected.

The dynamics of the drive train affect several aspects of the system operation. These have been analyzed to arrive at the required shaft stiffness. The rotor parameters that affect the stability of the feedback control loop vary considerably over the wind speed range encountered. Therefore, the controller gain was made a function of wind speed in order to maintain consistent operation over the whole wind speed range.

The velocity requirement for the pitch control mechanism is related to the nature of the wind gusts to be encountered, the dynamics of the system, and the acceptable power fluctuations and generator dropout rate. A model was developed that allows the probable dropout rate to be determined from a statistical model of wind gusts and the various system parameters, including the acceptable power fluctuation.

INTRODUCTION

Kaman Aerospace Corporation, under DOE sponsorship, has designed and fabricated a 40 kW, horizontal axis wind turbine generator. The work was part of the Small Wind Energy Conversion Systems (SWECS) program which is being directed by Rockwell International. The wind turbine is currently being evaluated in Rockwell's Rocky Flats, Colorado, test facility.

Three aspects of the control system dynamics are discussed in this paper. The first is the torsional characteristics of the drive train and factors affecting the selection of the drive train stiffness. Next is the effect that changes in rotor characteristics with wind speed have on the operation of the feedback control loop and the desirability of making the controller gain a function of wind speed. Finally, an analytical method for evaluating the adequacy of the control system design with respect to wind speed changes, or gusts, is discussed. The method is based on a statistical description of wind speed changes rather than on arbitrarily selected "worst gust" characteristics and, therefore, provides an objective means of assessing performance in a variety of locations.

SYSTEM DESCRIPTION

The wind turbine has a 64-foot diameter, two-blade, down wind rotor with a hub height of 75 feet. The unit has been designed to provide for direct conversion of wind power into regulated, 60 Hz, electrical power using either an induction generator for tie-in to a utility or a synchronous generator for standalone applications. The rotor operates at 69 rpm and a 1:26, two-stage, planetary gearbox provides a nominal generator speed of 1800 rpm. Cut-in wind speed is 10 mph; rated wind speed is 20 mph; and cut-out wind speed is 60 mph, at hub height.

Blade pitch is controlled to maintain the power level in the utility configuration and to maintain rotor speed, and thus frequency, in the standalone configuration. Both configurations also incorporate a feed forward control input based on wind speed.

The significant elements in the basic control loop are shown in Figure 1. The controller and the feed forward programmer are implemented in a microprocessor which also performs the startup and shutdown sequencing, as well as other monitoring and control functions. The microprocessor program includes provisions for integral control, but only proportional control is used. The output of the microprocessor is a voltage proportional to the desired blade pitch angle. A hydraulic position servo rotates the blades about the axles at the root ends. The feedback signal is proportional to rotor speed when either configuration is being brought up to the nominal operating speed and when the load is connected in the standalone (synchronous generator) configuration. The feedback signal is proportional to generator output power when the load is connected in the utility (induction generator) configuration. The distrubances to the system are changes in rotor torque due to changes in wind speed in either configuration and changes in load in the standalone configuration.

DRIVE TRAIN DYNAMICS

Several aspects of the drive train dynamics were considered in establishing the requirements for drive train stiffness: the avoidance of resonances as the rotor is brought up to operating speed; the magnitude of the rotor torque ripple that is transmitted to the load; and the impact of the drive train dynamics on the feedback control loop stability.

Drive Train Elements

A schematic representation of the drive train components with all elements referred to the rotor shaft speed is shown on Figure 2. The rotor is represented by the rigid-body inertia, I_R, and the slope of the torque-speed curve, C_R, at a particular operating condition. (The elastic modes of the rotor are high enough in frequency to be unimportant in these analyses.) The combined stiffness of the rotor shaft and the gearbox is included in K_S. There is an elastomeric coupling between the gearbox and the generator to accommodate shaft misalignment. Its inertia, I_C, is significant with respect to the other elements, but its stiffness, K_C, and damping, C_C, are not. The generator is represented by its mechanical losses, C_{GL}; rotor inertia, I_G; and the coupling to the load. The coupling of the induction generator, C_{GC}, is the slope of the torque-speed curve. The utility line connection is considered to be a zero impedance sink. The coupling of the synchronous generator appears as a stiffness, K_{GC}. In this case, the load impedance is finite, with a loss term, C_L, corresponding to 40 kW, as well as an inertia term, I_L, to account for large motor loads.

Resonances

The load is not connected while the rotor is being brought up to speed or during periods of rotor overspeed. (The control system limits overspeed to 125% of rated speed.) This results in a very underdamped resonance determined largely by the rotor shaft-gearbox stiffness, generator inertia, and generator mechanical losses. These resonant frequencies are plotted as a function of rotor shaft-gearbox stiffness on Figure 3. The synchronous generator configuration has lower resonant frequencies because of the higher generator inertia. The criterion for stiffness in this case is that the resonant frequency be higher than the two-per-rev frequency of the vibratory rotor torque at the 125% overspeed condition. Since rated rotor speed is 69 rpm, the resonant frequency should be greater than 2.9 Hz. This requires a stiffness greater than 120,000 ft-lb/radian.

Torque Ripple

The behavior of the two configurations in transmitting torque ripple from the rotor to the load is quite different because of the different load characteristics. The standalone configuration exhibits an underdamped resonance while the utility configuration is highly damped by the induction generator coupling characteristics and the zero impedance sink of the utility line. The torque transmissivity of each is shown on Figures 4 and 5 as a function of frequency and stiffness. The important criterion in this case is the torque transmissivity at the predominant rotor torque-ripple frequency of two-per-rev, or 2.3 Hz. This is shown on Figure 6 as a function of rotor shaft-gearbox stiffness.

For the standalone configuration, it is desirable that the torque ripple at the load be less than 10% of the actual load even when the system is lightly loaded (e.g., at 10% of rated load). Therefore, the torque ripple transmitted to the load should be less than 1% of rated torque. An analysis of the rotor indicates a two-per-rev vibratory torque at the rotor equal to about 13% of rated torque. Therefore, a torque attenuation of about 0.076 is desired. This requires a stiffness greater than 180,000 ft-lb/radian.

For the utility configuration, the torque transmissivity increases with increasing stiffness to a maximum value of 0.25. This would cause a ripple in the generator output equal to about 3% of rated load, or about 1.3 kW. Discussions with utility companies indicate that this would not be significant on a high capacity utility line. There will be a random phase relationship among two or more units connected to a common utility line, so their ripple components do not add directly. Therefore, this consideration does not put a constraint on stiffness.

Impact on Control Loop

During startup in either configuration, or when the load is connected in the standalone configuration, the feedback control loop is configured to control rotor speed. The feedback signal is rotor shaft speed measured at the node marked Ω_R on Figure 2. Because the admittance of the rotor inertia is very large in comparison to the other admittances at the frequencies of interest to the feedback control loop, the phase lag between rotor torque and rotor speed is essentially 90° and independent of reasonable values of rotor shaft-gearbox stiffness.

When the load is connected in the utility configuration, the feedback control loop is configured to control power level. The feedback signal is the power measured at the generator output. This corresponds to the node marked Ω_G on Figure 2. The phase lag between rotor torque and this point is the sum of the 90° lag noted above and the additional lag from Ω_R to Ω_G. The latter is largely determined by the stiffness, K_S, and C_{GC}, and decreases as the stiffness is increased. This additional lag is approximately 45° at a frequency corresponding to $K_S/(2\pi\ C_{GC})$. Since the frequencies of interest to the control loop stability are in the range of 1/2 to 3 Hz, a stiffness greater than 830,000 ft-lb/radian is desired.

Stiffness Selection

Each of the considerations above establishes a minimum constraint on rotor shaft-gearbox stiffness. The largest of these, 830,000 ft-lb/radian for the utility configuration control loop at rated load, was taken as the design requirement. Deflection measurements were made after the system was assembled. These measurements included the rotor shaft, gearbox, and coupling, and showed a stiffness of about 460,000 ft-lb/radian for low torque levels and 2,500,000 ft-lb/radian near rated torque. This level of stiffness is satisfactory because the constraint imposed by

consideration of the utility configuration control loop requires a stiffness greater than 460,000 ft-lb/radian, which is important only at torque levels near rated torque.

CONTROL LOOP GAIN

A review of Figures 1 and 2 shows that the magnitude of the control loop gain is determined by the following:

No Load:

$$\text{Gain} = (A_C)\left(\frac{\partial T_R}{\partial \theta}\right)\left(\frac{1}{C_R + C_{GL}}\right)$$

Utility With Load:

$$\text{Gain} = (A_C)\left(\frac{\partial T_R}{\partial \theta}\right)\left(\frac{1}{C_R + C_{GL} + C_{GC}}\right)(A_G)$$

Standalone With Load:

$$\text{Gain} = (A_C)\left(\frac{\partial T_R}{\partial \theta}\right)\left(\frac{1}{C_R + C_{GL} + C_L}\right)$$

where:

A_C = Controller gain factor

$\frac{\partial T_R}{\partial \theta}$ = change in rotor torque per unit change in pitch angle

C_R = slope of the rotor torque-speed curve, C_{GL}, C_{GC}, C_L, as defined on Figure 2

A_G = a constant that relates generator power to generator slip speed

Two of these factors, $\frac{\partial T_R}{\partial \theta}$ and C_R, are derived from the rotor characteristics and vary considerably over the range of expected operating conditions. The slope of the torque-speed curve, C_R, increases from 170 ft-lb-sec/radian at 10 mph to 6254 ft-lb-sec/radian at 60 mph. The torque derivative with pitch, $\frac{\partial T_R}{\partial \theta}$, is zero when the maximum available power is being delivered (i.e., regulation is not possible). However, if power is restricted to the lesser of 40 kW or 80% of the maximum available, the torque derivative increases from 90 ft-lb/deg. to 1980 ft-lb/deg. as the wind increases from 10 to 60 mph. The three gain functions, normalized to their values at 20 mph are shown on Figure 7. The functions with load are based on the lesser of 40 kW or 80% of the maximum power available.

The loop gain in the no load case changes by a factor of almost 5. However, this case is primarily concerned with startup which takes place when the wind speed increases above 10 mph or decreases below 60 mph. The loop gains at these two points only differ by a factor of 1.5. More importantly, the control loop stability analysis indicated that a fixed controller gain could be selected that would provide adequate speed regulation at 10 and 60 mph and satisfactory overshoot characteristics at 20 - 25 mph. Test data has verified this projection up to 30 mph. Test data for startups above 30 mph have not yet been collected.

When the standalone configuration is operated with full load, the changes in the torque derivative are almost fully compensated by changes in the total damping and the loop gain is essentially constant. As the load is decreased, the curve approaches the no load curve. In this case also, the control loop stability shows sufficient gain margin to achieve adequate speed regulation and satisfactory overshoot characteristics under all of the wind speed and load conditions.

The utility configuration differs in two respects. First, the damping term is dominated by C_{GC}, the very steep slope of the induction generator torque-speed curve. Therefore, the change in loop gain is almost equal to the change in the torque derivative, a factor of 20 for 10 to 60 mph. Second, because of the added phase lag of the drive shaft dynamics, the gain margin available is much less than that available in the other modes. The result is that the controller gain that provides adequate power regulation at 20 - 25 mph causes instability at 60 mph. Therefore, the controller gain in this mode is made a function of the mean wind speed such that the total loop gain remains essentially constant.

RESPONSE TO WIND SPEED CHANGES

The ability of a variable-pitch wind turbine to maintain a given power level in the presence of wind speed changes is limited by the capabilities of the pitch change mechanism. Therefore, knowledge of the wind variability that must be accomodated is needed to establish the required capabilities of the pitch change mechanism.

To meet this need, the description of wind variability must relate the magnitude of wind speed changes to the time interval over which they are observed and the frequency with which they can be expected at the planned location of the wind turbine. The magnitude and time interval, with respect to the dynamic characteristics of the wind turbine, determine the impact on the wind turbine. The frequency determines whether or not they need to be accommodated. For example, wind speed changes that cause disruptions in the delivered power less frequently than once per month or once per year need not be accommodated. However, the system must accommodate wind speed changes that could cause damage more frequently than once per lifetime of the machine.

Cliff and Fichtl (Reference 1) have developed a description of wind speed changes based on turbulence theory. It allows the calculation of the root-mean-square (RMS) value of the change in wind speed over a time interval as a function of the mean wind speed, nature of the terrain (surface roughness), height above the surface, and the scale of the affected device. The RMS value and the characteristics of a Normal distribution determine the probability of exceeding a particular magnitude of speed change in any one time interval. The probability and the duration of the observation time interval determine the

number of times the change is exceeded per hour of the mean wind speed. This can be combined with a mean wind speed distribution to determine the number of times the change is exceeded per year.

Figure 8 illustrates one form of the Cliff and Fichtl description using a particular mean wind speed distribution and a 64-foot diameter rotor 75 feet above terrain with a surface roughness of 0.05 meters (high grass). It describes the wind speed changes that occur during the 1.4 hours per year that the mean wind speed is between 50 and 60 miles per hour. It shows, for example, that if observations are made at one-second intervals, twenty changes greater than 12.5 mph will be seen, but changes greater than 18 mph will only be seen once in five years during 50 - 60 mph winds. On the other hand, if the observation interval is increased to 2.5 seconds, changes greater than 18 mph will be seen almost 20 times per year. This provides a satisfactory description of wind speed changes for determining the required capabilities of the pitch change mechanism. The method of using it is described below.

Figure 9 shows what happens to the rotor speed of a wind turbine with feed forward control when the wind speed changes at a rate faster than the pitch mechanism can follow. After a short delay, the pitch changes at its maximum rate. Since that is less than the rate required to compensate for the wind speed change, a torque unbalance develops and the rotor accelerates. Eventually, the proper pitch angle is reached and the rotor returns to the proper speed. The important parameter is the maximum change in rotor speed, $\Delta\Omega$, since this determines the maximum change in the delivered power. (The control system is configured to disconnect the load if some critical value is exceeded.)

Therefore, the dynamics of the wind turbine are analyzed to determine the wind speed changes (magnitude and time interval) that cause a rotor speed change equal to the critical value, Ω_c. This is shown on Figure 10 for two values of mean wind speed and a certain system configuration. The result is dependent on mean wind speed because the pitch change required by the rotor to compensate for a given wind speed change decreases with increasing mean wind speed. For wind speed changes above the curve, the rotor speed change is greater than the critical value. For the stand-alone synchronous generator application, a critical speed change of 10% was used, i.e., a 10% change in frequency and voltage. For the induction generator connected to a utility line, a critical speed change equal to the slip at rated power was used.

The 55 mph system characteristic is superimposed on the wind change characteristics for mean winds between 50 and 60 mph on Figure 11. This shows that the highest incidence of exceeding the critical speed change occurs for the wind speed changes that are observed over intervals of about one second. This occurs a little more than 0.2 times per year during the 1.4 hours per year that the wind is between 50 and 60 mph. If the pitch rate were only 3°/sec, instead of 6°/sec, it would occur much more frequently. The process illustrated on Figure 11 is repeated for each of the wind speed intervals necessary to cover the operating range of the wind turbine. The exceedance rates for each interval are then summed to determine the total number of times per year the critical speed change is exceeded. The result is shown in the top data set of Figure 12. The system parameters under the control of the designer are then adjusted until an acceptable exceedance rate is achieved.

The second and third data sets on Figure 12 illustrate the influence of the system characteristics in determining the critical wind speed characteristics. Although both systems have about the same exceedance rate, the synchronous generator configuration, with its longer time constant (ratio of inertia to damping), reacts with the larger wind speed changes seen with longer observation time intervals. While the induction generator configuration has 97% of its exceedances when the mean wind is between 50 and 60 mph, the comparable figure for the synchronous generator configuration is 81%. The fourth data set on Figure 12 gives the results when the maximum pitch rate is adjusted so that the critical speed is exceeded about 12 times per year for the induction generator configuration with a lag of 0.15 sec.

It should be noted that there is no "worst gust" that would produce the same results, even if the "worst gust" is a function of mean wind speed.

These results are based on a particular wind speed distribution. The distribution was chosen to represent the 95th percentile of the 138 geographical locations tabulated by Frost and Long (Reference 2). That is, the rate of exceeding the critical speed will be greater than that calculated at 5% of the locations and less than that calculated at 95% of the locations. The distribution is described at the 10 meter reference height by Weibull coefficients of 9.8 mph and 1.4.

REFERENCES

1. Cliff, W. C., and Fichtl, G. H., "Wind Velocity Change (Gust Rise) Criteria for Wind Turbine Design," DOE Report PNL-2526, July 1978.

2. Frost, W., and Long, B. H., "Engineering Handbook on the Atmospheric Environmental Guidelines for use in Wind Turbine Generator Development," NASA Report (Contract NAS8-32118), November 1977.

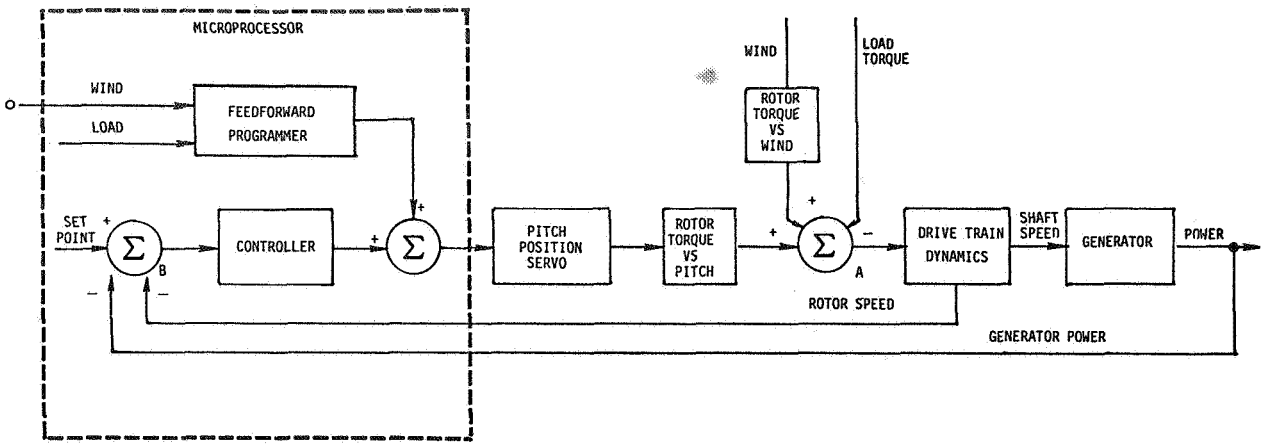

Figure 1 - Basic control loop.

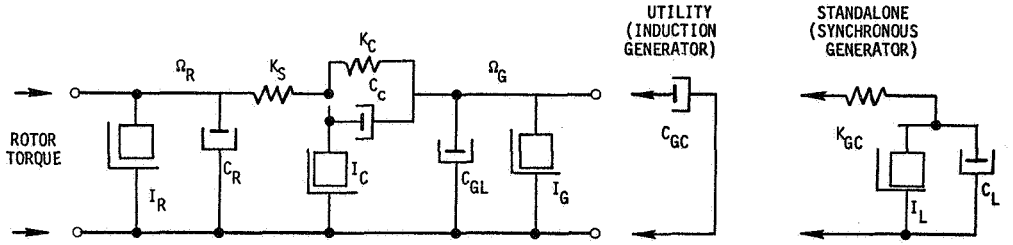

ROTOR:	I_R	6425	ft.lb.sec^2/rad.	UTILITY:	C_{GL}	26.4	ft.lb.sec/rad
	C_R	286	ft.lb.sec/rad.		I_G	189	ft.lb.sec^2/rad.
					C_{GC}	44,000	ft.lb.sec^2/rad.
COUPLING:	K_C	3.5×10^6	ft.lb./rad.	STANDALONE:	C_{GL}	26.4	ft.lb.sec/rad.
	C_C	15	ft.lb.sec/rad.		I_G	280	ft.lb.sec^2/rad.
	I_C	92	ft.lb.sec^2/rad.		K_{GC}	$.8 \times 10^6$	ft.lb./rad.
					C_L	1364	ft.lb./rad.
					I_L	189	ft.lb.sec^2/rad.

Figure 2 - Drive train elements.

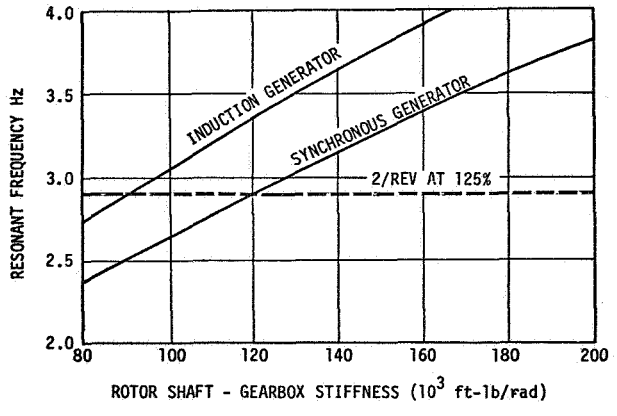

Figure 3 - No load resonant frequency.

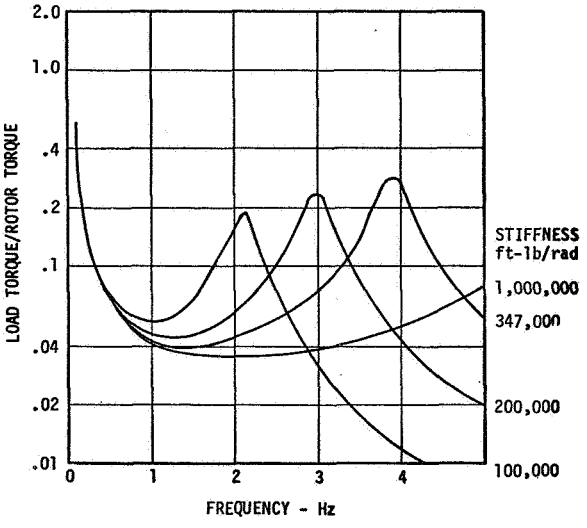

Figure 4 - Standalone configuration.

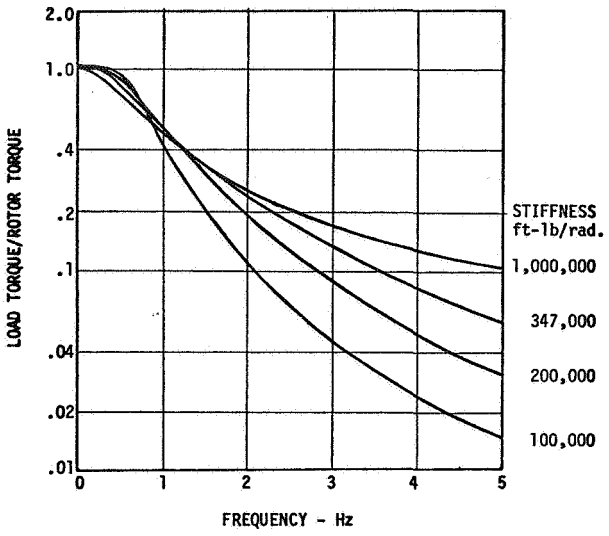

Figure 5 - Utility configuration.

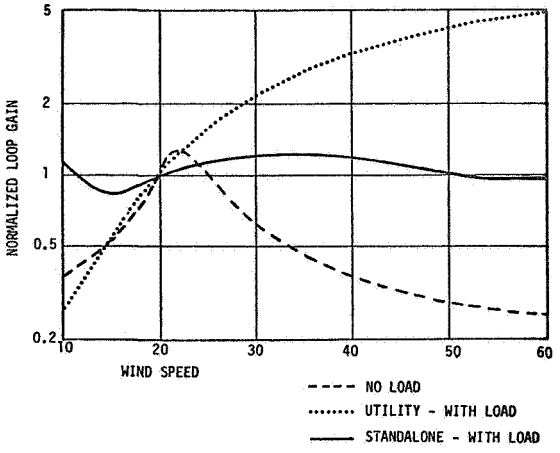

Figure 7 - Loop gain functions.

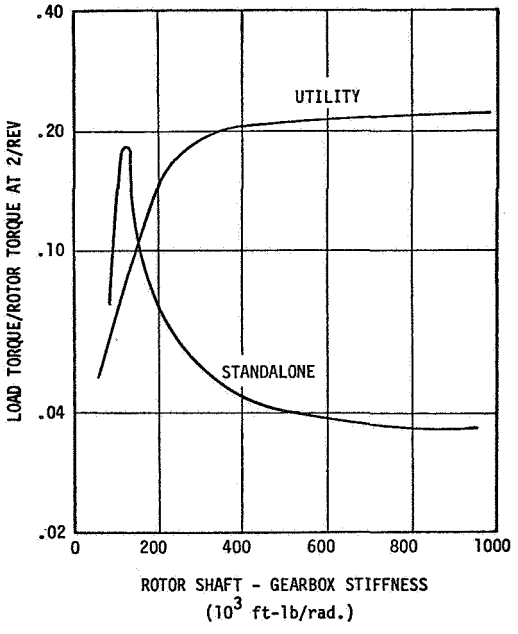

Figure 6 - Torque transmissivity.

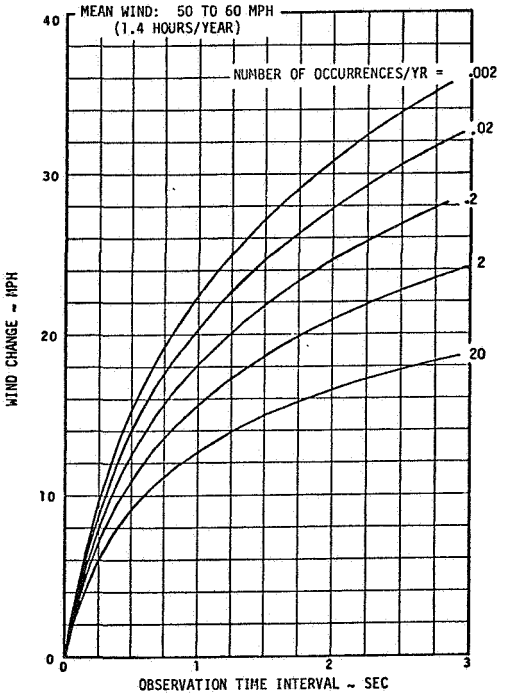

Figure 8 - Wind change characteristics.

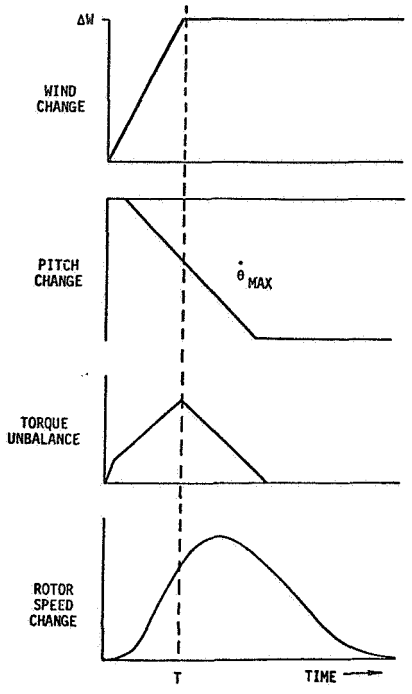

Figure 9 - Response to wind change.

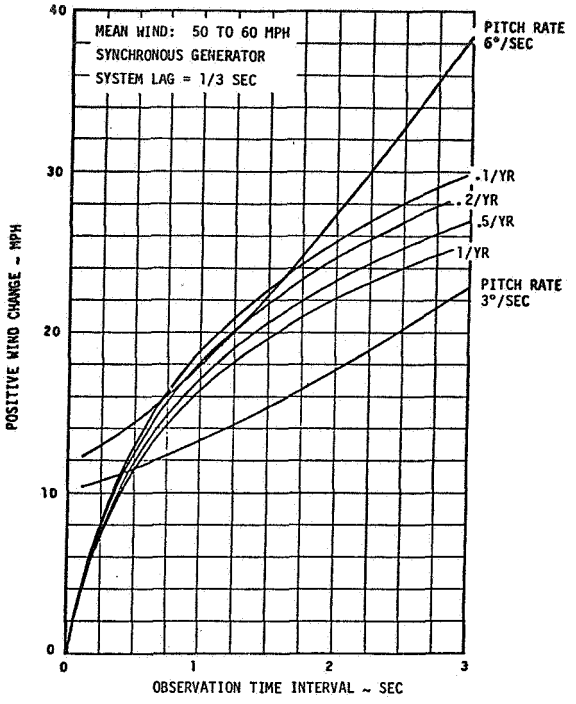

Figure 11 - Critical wind change.

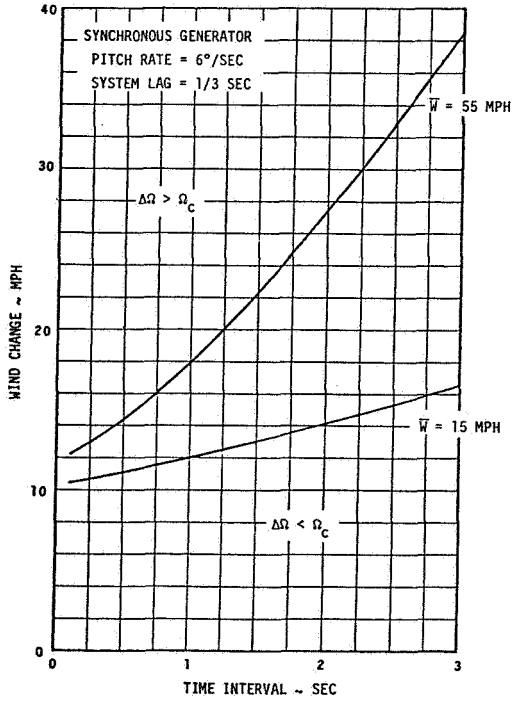

Figure 10 - System characteristics.

CENTER OF WIND SPEED INTERVAL (MPH)	SYSTEM TIME CONSTANT (SEC)	WIND CHANGE TIME INTERVAL (SEC)	WIND CHANGE MAGNITUDE (MPH)	NUMBER OF OCCURRENCES PER YEAR
SYNCHRONOUS GENERATOR:	Rate 6°/sec, Lag .33 sec			
15	5.06	---	---	0
25	4.65	2.3	16.3	.000
35	2.53	1.6	18.6	.000
45	1.55	1.2	18.5	.018
55	1.07	1.0	18.3	.256
			TOTAL	.274
SYNCHRONOUS GENERATOR:	Rate 4.2°/sec, Lag .15 sec			
15	5.06	4.3	16.3	.000
25	4.65	2.7	15.1	.000
35	2.53	1.9	18.3	.000
45	1.55	1.6	18.8	.174
55	1.07	1.3	18.9	.766
			TOTAL	.941
INDUCTION GENERATOR:	Rate 6°/sec, Lag .15 sec			
15	.35	---	---	0
25	.33	2.1	18.3	.000
35	.31	1.2	17.4	.000
45	.29	.9	15.5	.027
55	.27	.7	14.0	.971
			TOTAL	.998
INDUCTION GENERATOR:	Rate 4.2°/sec, Lag .15 sec			
15	.35	---	---	0
25	.33	2.5	16.8	.000
35	.31	1.5	16.0	.002
45	.29	1.1	14.1	1.600
55	.27	.8	12.8	9.191
			TOTAL	10.793

Figure 12 - Rate of exceeding critical speed change.

QUESTIONS AND ANSWERS

R. Perley

From: R.A. Edkin

Q: Why does an induction machine with only 1% slip exhibit a high damping characteristic?

A: *The damping term is inversely proportional to the slip at rated torque. The damping term is the ratio of a torque to the speed change necessary to produce that torque.*

AUTOMATIC CONTROL ALGORITHM EFFECTS ON ENERGY PRODUCTION

Gerald M. McNerney

University of New Mexico
Engineering Research Institute
Albuquerque, New Mexico 87185

ABSTRACT

Algorithm control strategy for unattended wind turbine operation is a potentially important aspect of wind energy production that has thus far escaped treatment in the literature. Early experience in automatic operation of the Sandia 17-m VAWT has demonstrated the need for a systematic study of control algorithms. To this end, a computer model has been developed using actual wind time series and turbine performance data to simulate the power produced by the Sandia 17-m VAWT operating in automatic control. The model has been used to investigate the influence of starting algorithms on annual energy production. The results indicate that, depending on turbine and local wind characteristics, a bad choice of a control algorithm can significantly reduce overall energy production. The model can be used to select control algorithms and threshold parameters that maximize long-term energy production. An attempt has been made to generalize these results from local site and turbine characteristics to obtain general guidelines for control algorithm design.

INTRODUCTION

A computer model has been developed using real data to simulate power production of a vertical axis wind turbine (VAWT). The purpose of the model is twofold. First, to develop guidelines in control algorithm strategies. This basic step was initially undertaken with using data particular to the Sandia/DOE 17-m VAWT. These initial results are very interesting and have been useful in the automatic control program for the 17-m.

The second purpose of the model is to provide more general information on the energy available to a VAWT that is lost in the automatic control process. This information will, in turn, be used in the economic selection process of VAWTs for site specific cases.

The automatic control simulation model is discussed in section 1, the algorithms on the Sandia/DOE 17-m turbine are described in section 2, and the first step results are presented in section 3. In section 4, the specific first step results are generalized in an attempt to be applicable in a turbine selection process.

THE COMPUTER MODEL

The computer model was originally designed to simulate the 17-m VAWT in automatic control in Albuquerque, New Mexico, and as such was based on two sets of experimental data. The first data set is the electric power versus windspeed data collected using the method of bins (Ref. 1) for the 17-m operating at 50.6 rpm. A plot of the power curve used appears in Fig. 1.

The second set of data used is a collection of 890 hours of .5 Hz time series data of windspeed over 43 periods recorded during weekends and nights of Summer-Fall 1979. The probability density function is plotted versus windspeed for the wind data in Fig. 2. The mean value of windspeed for the wind data is 11.1 mph which is above the actual Albuquerque mean annual windspeed.

The actual computer model is a Fortran program in which the electric power versus windspeed data are used to determine the power available at every point of wind data. If the turbine is stopped, the control algorithm will use this information to decide if the turbine should be started. If the turbine is running, the power is summed to determine the energy generated.

The overall energy output that is computed for a particular control algorithm depends on how long and when the turbine is running, as well as the number of starts. The number of starts is used by subtracting the energy consumed in all the starts from the calculated energy produced when the turbine is running. For the 17-m turbine, each start consumes approximately .6 kW-hr.

The output of the auto control simulator is given as an algorithm efficiency, and a number of starts occurring over the duration of the wind data. The notion of algorithm efficiency will be given a precise meaning following the preliminary notion of energy available to a wind turbine.

Energy Available. The energy available to a wind turbine is that amount of energy that would be produced by a turbine operating under an ideal algorithm. This quantity may be calculated from the electric power data directly by integrating the power produced over all times the power is positive, or by using the windspeed distribution function for positive powers.

Algorithm Efficiency. The algorithm efficiency is the percent the energy produced is of the energy available for a turbine operating under the algorithm control.

ALGORITHMS TESTED

Five different algorithms have been tested in parametric studies by the automatic control simulator. The first four algorithms have two parameters which are adjusted to find the optimum operating values. These two parameters are referred to frequently and will thus be formally defined.

Turn On/Off Threshold. The turn on/off threshold is the minimum value of average windspeed or average power that is required to start/stop the turbine by a decision loop of a control algorithm.

Test Window. The test window is the duration of the test period over which the average windspeed or power is calculated for comparison with the turn on threshold.

We may now name and describe the five algorithms tested as follows.

1) Discrete Windspeed Averages - At the end of each test window, the average windspeed over the test window is compared to the turn on threshold. If the test fails, a new average is begun and not tested again until the end of another test window. If the average windspeed is above the turn on threshold, the turbine is started. During turbine operation, the average windspeed is tested against the turn off threshold at the end of each test window for a stop decision.

2) Moving Windspeed Algorithm - After each point of windspeed data, a new average windspeed is calculated over the most recent test window. If the turbine is off, the average windspeed is tested against the turn on threshold to decide on a turbine start. If the turbine is on, the average is compared to the turn off threshold. After a start or stop, a 60 second blind period is introduced to simulate an actual start or stop.

3) Moving Power Algorithm - At each windspeed point, a value of power is read from the electric power versus windspeed data. From the power data, a running power average is calculated over the test window and compared to the turn or on turn off threshold for a start or stop.

4) Discrete, Double Power Algorithm - At the end of each test length, two power averages are calculated. One for the average over the entire test window, and second, for the last one-tenth of the test window. Both averages must be greater than the threshold value for a start to occur. Stops are based on a test of the average power over the entire test window.

5) Canadian Coast Algorithm - Certain Canadian VAWT systems have utilized a semi-mechanical control system with an overrunning clutch on the high speed shaft to permit the rotor to coast when below synchronous speed. This system could conceivably reduce motoring losses in low wind conditions and simplifies the turn off condition which can be based on a simple rpm measurement.

From a cold stop, one of the first four algorithms is used to decide if a start should be initiated by a starting motor which takes the turbine to some fraction of the synchronous rpm. The turbine is then allowed to coast until either synchronous speed is reached, at which time the generator engages, or 5 minutes has elapsed and the turbine falls below a turn off threshold value of rpm. If synchronization is reached, when the torque at the high speed shaft becomes negative, the generator disengages and the coast cycle begins again. Whenever the rotor is coasting, the system generator is assumed to motor without shaft load at synchronous speed. Windage losses in the generator are accumulated during the coast period. The only parameter is the turn off threshold rpm.

RESULTS OF PARAMETRIC STUDIES

The results of the parametric computer runs for the five algorithms are plotted in Figs. 3 through 7. The maximum curves from each of the algorithms are plotted together in Fig. 8 to facilitate comparing the results. The following points are clear from the figures.

1) For each algorithm, a choice of the parameters can be made which will maximize the algorithm efficiency, and minimize the number of starts or coast time.

2) The algorithms may be ranked according to the maximum algorithm efficiency as follows:

a) Canadian coast algorithm - 93.7%
b) Moving power algorithm - 93.4%
c) Discrete, double power algorithm - 92.8%
d) Discrete windspeed algorithm - 92.3%
e) Moving windspeed algorithm - 91.6%

3) A bad choice of parameters, particularly the test window, will greatly reduce the algorithm efficiency.

APPLICATIONS TO VAWT ECONOMICS

The algorithm control study of the previous sections is useful in maximizing energy production once a particular turbine and site have been selected. However, if a turbine is badly matched to a site, the maximum algorithm efficiency

may be as low as 72% as shown in an example below. It is clear then that control algorithm considerations will have an effect on the economics of wind energy production.

In order to utilize control algorithm properties in wind energy economics, it is necessary to determine if the maximum algorithm efficiency depends functionally upon a suitable composition of a local windspeed probability distribution function (PDF) with a turbine electric power curve (EPC). Since the windspeed PDF and the turbine EPC are both functions of windspeed, it is natural to construct the energy distribution function (EDF) from the two, which at any windspeed gives the fraction of the annual energy produced by the machine at that windspeed. The EDF is constructed as the normalized product of the PDF and the EPC. We will concentrate then on quantifying the dependence of the maximum algorithm efficiency upon the EDF.

The five types of algorithms discussed in section 2 were initially tested using the EPC from the Sandia/DOE 17-m VAWT. The EPC was determined experimentally by the method of bins, and the windspeed time series was recorded at the 17-m test site in Albuquerque, New Mexico. Clearly, a generally applicable relation between the maximum algorithm efficiency and the EDF cannot be found from the results of one specific set of turbine and windspeed time series data. Therefore, an expanded data base has been acquired including one additional set of windspeed time series data, and several other sets of turbine EPC's. The windspeed time series consists of a year of data recorded by the National Severe Storm Laboratory from the WKY tower in Oklahoma City, Oklahoma from October 1, 1976 to November 26, 1977. Most of the readings were taken at a sample rate of 0.1 Hertz. The data set includes windspeed, wind direction, temperature, and vertical velocity at 7 elevations, as well as pressure, wet bulb temperature, pyronometer, and rain gauge readings from selected elevations. The data were transcribed to 9 track magnetic tape and made available for dissemination by the National Center for Atmospheric Research. The windspeed data recorded at an elevation of 26 meters were used in the model since this elevation closest matches the equatorial elevation of VAWTs of interest. The PDF of the windspeed time series is closely approximated by the Rayleigh distribution with a mean windspeed of 10.4 mph (Fig. 9).

In addition to the Sandia/DOE 17-m EPC, two other types of EPC's have been used. The first type is generated by the computer code PAREP (Ref. 2) for a 17-m VAWT operating at 25, 30, 35, 40, and 45 rpm's. The second set of EPC's come from a one parameter family of piecewise linear curves defined by the function

$$P(V) = \begin{cases} -6\text{kW for } 0 \le V \le V_0 - 2.2 \\ 2.7*(V-V_0) \text{ for } V_0 - 2.2 \le V \le 3*V_0 - 6.6 \\ 5.4*(V_0 - 18) \text{ for } 3*V_0 - 6.6 \le V. \end{cases}$$

The parameter V_0 is the cut in windspeed, satisfying $P(V_0) = 0.0$. This family of EPC's was chosen to give a wide variation in turbine characteristics depending on only one parameter.

Automatic control simulator tests conducted subsequent to the introduction of the additional windspeed time series and turbine EPC's have been made using only the "moving power" algorithm since this algorithm so clearly outperformed the three other purely electronic control algorithms, and was nearly equal to the coast type algorithm.

The dependence of the maximum algorithm efficiency on the EDF may take any number of possible forms. After finding the maximum algorithm efficiencies for several cases by running many tests of the automatic control simulator corresponding to different data sets, plots were made of the maximum algorithm efficiency versus various properties of the EDF's. Two clear relationships emerged in the plots, either of which may be used to determine the approximate maximum algorithm efficiency corresponding to a given EDF. The first relationship is between the maximum algorithm efficiency and the slope of the EDF at the cut in windspeed, denoted E_0. The plot of the maximum algorithm efficiency versus E_0 appears in Fig. 10. The second relationship is between the maximum algorithm efficiency and the ratio

$$R = \frac{V_m - V_0}{V_0}, \qquad (1)$$

where V_m is the windspeed at the maximum EDF, and V_0, as before, is the cut in windspeed. The plot of the maximum algorithm efficiency versus R appears in Fig. 11.

From Figs. 10 and 11 it is apparent that the maximum algorithm efficiency may be given as a function of either E_0, the slope of the EDF at V_0, or the ratio, R, defined in Eq. (1). This functional relation may be used in a VAWT economic selection process for a given site, or more basically, in determining if a VAWT is badly suited controlwise for a turbine site, as the Sandia 17-m turbine is for Oklahoma City with a maximum algorithm efficiency of 72%.

REFERENCES

1. Akins, R.: Performance Evaluation of Wind Energy Conversion Systems Using the Method of Bins - Current Status, SAND77-1375, March 1978.

2. Leonard, T.: A User's Manual for the Computer Code PAREP, SAND79-0431, April 1979.

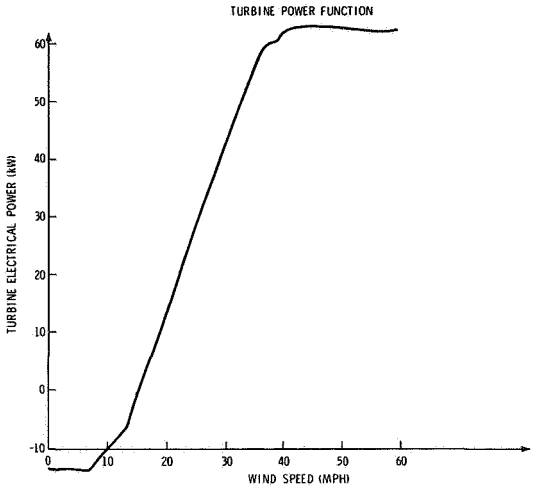

FIGURE 1

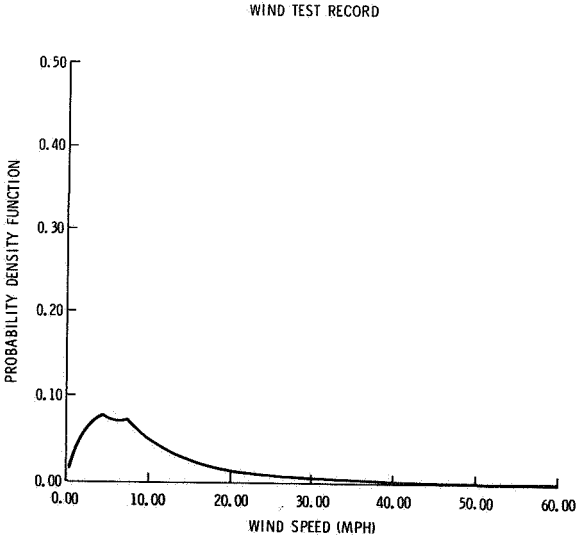

FIGURE 2

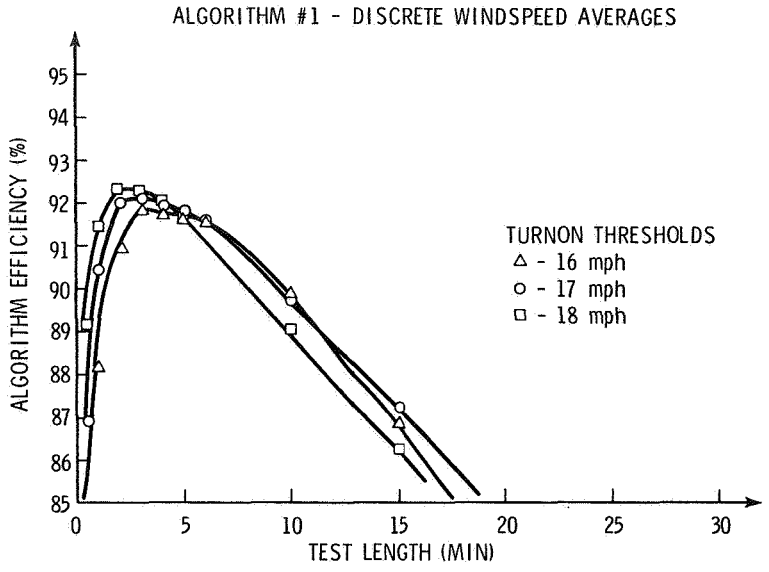

FIGURE 3

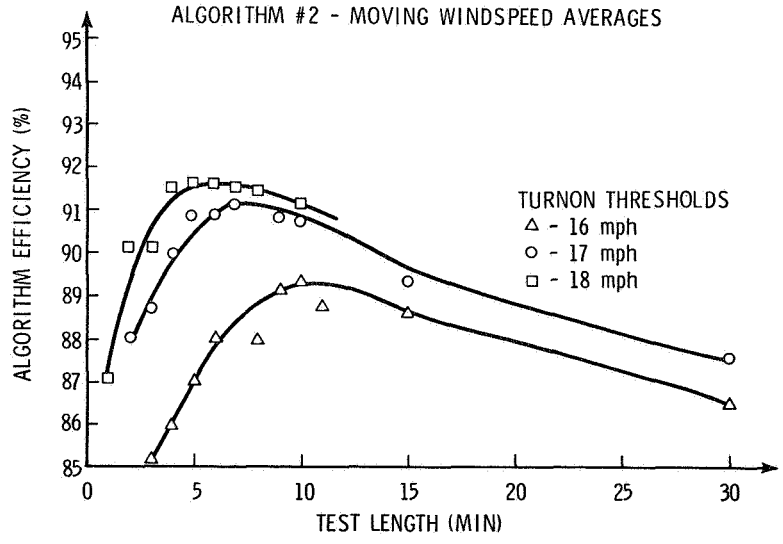

FIGURE 4

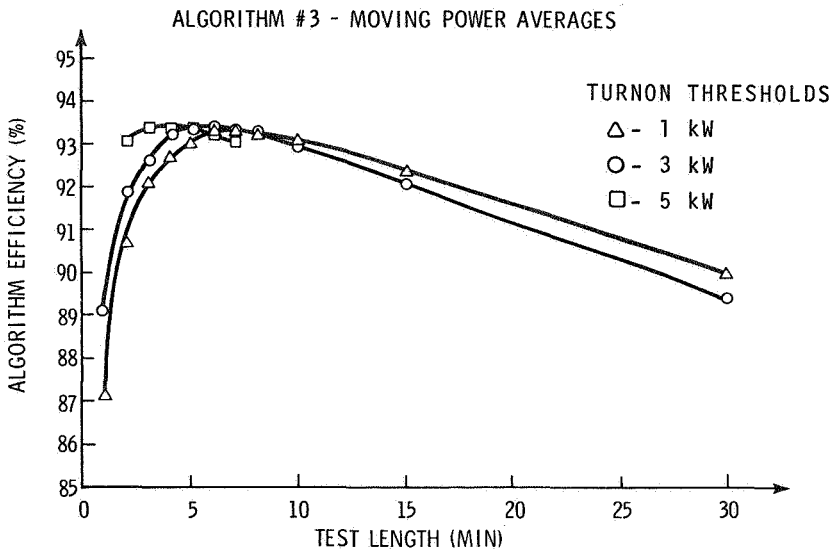

FIGURE 5

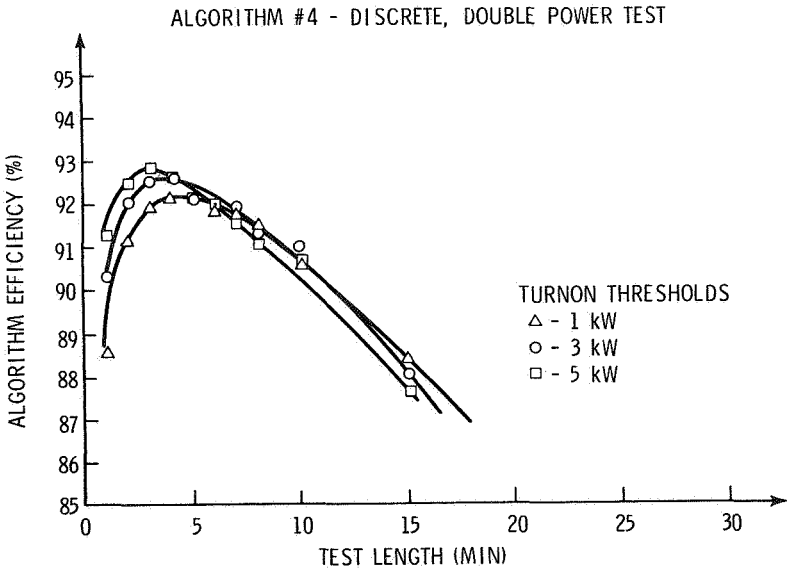

FIGURE 6

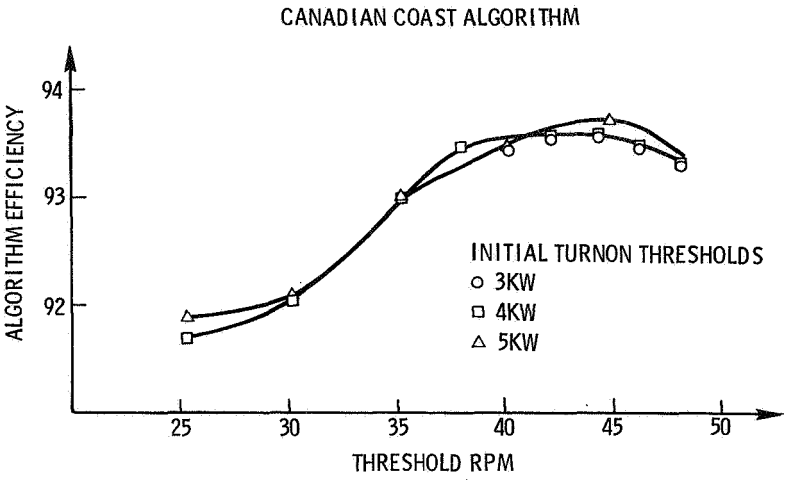

FIGURE 7

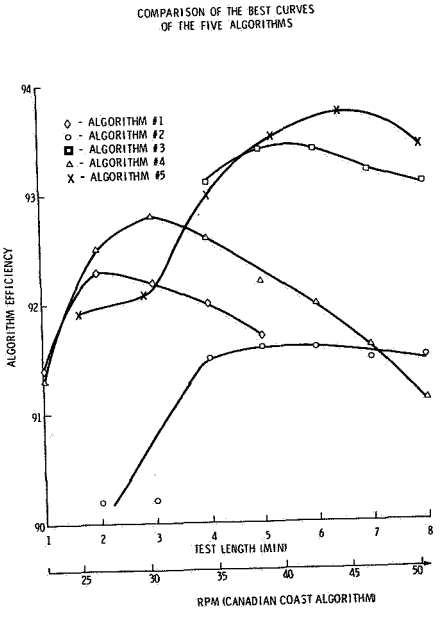

FIGURE 8

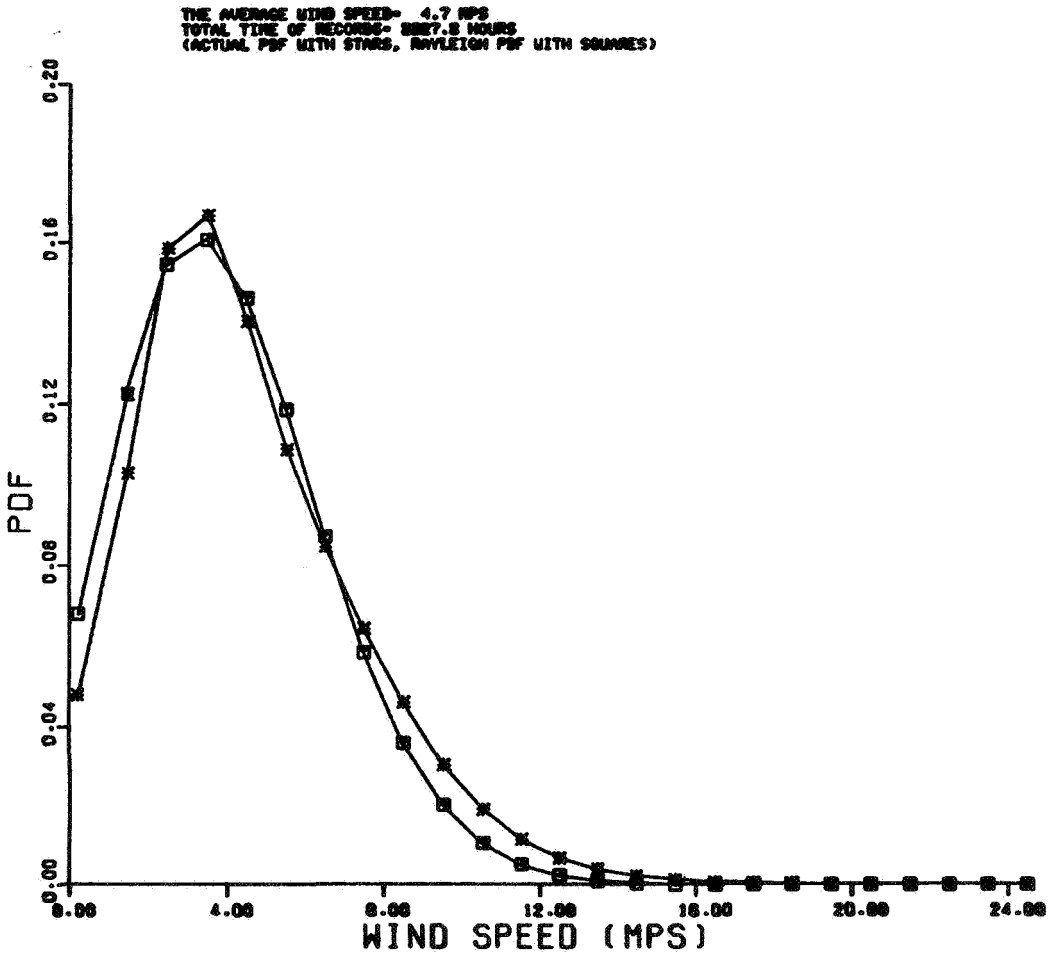

FIGURE 9 - Comparison of WKY Tower PDF with Rayleigh PDF

FIGURE 10

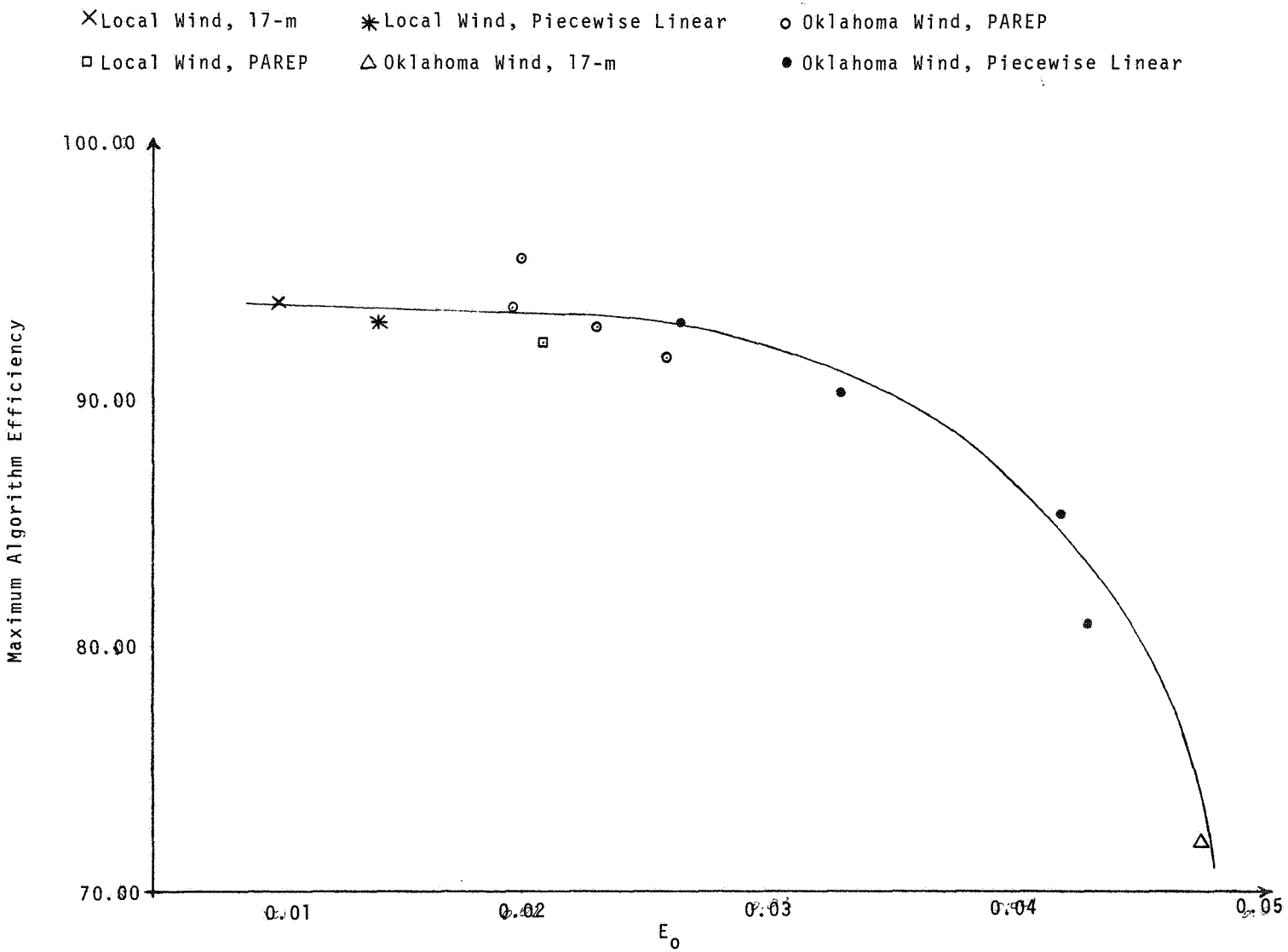

Maximum Algorithm Efficiency vs E_o

FIGURE 11

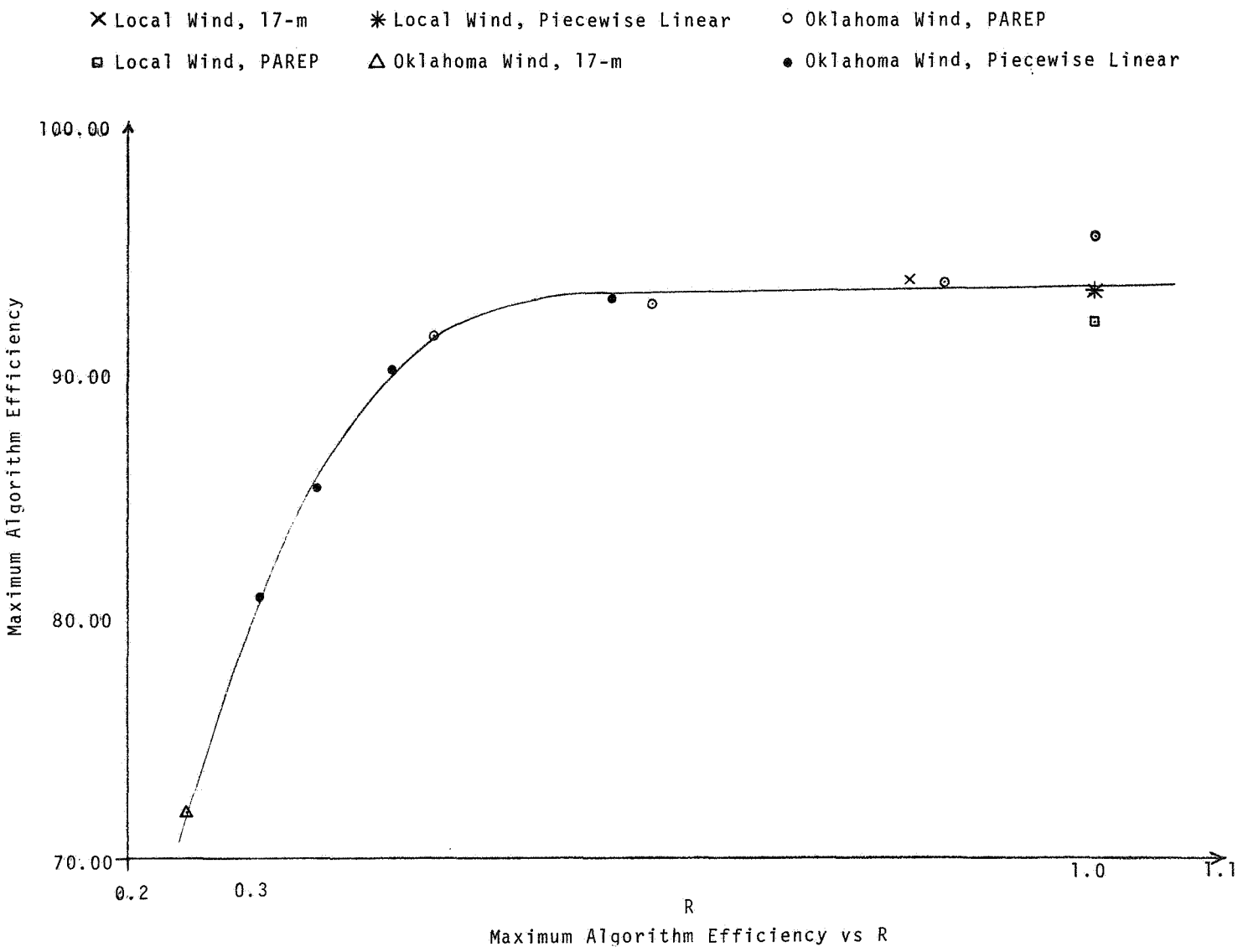

Maximum Algorithm Efficiency vs R

EFFECT OF WIND TURBINE GENERATOR MODEL AND SITING ON WIND POWER CHANGES OUT OF LARGE WECS ARRAYS

Schlueter, R.A., Park, G.L., Lotfalian, M.,
Dorsey, J., and Shayanfar, H.
Michigan State University

ABSTRACT

Previous results have [1,2,3], been concerned with establishing (1) whether operating problems could exist when WECS generation is significant and (2) the proper modification of unit commitment, regulation, and economic dispatch required to provide sufficient system security and alleviate the operating problems caused by WECS generation changes. This paper discusses methods of reducing the WECS generation change through selection of the wind turbine model for each site, selection of an appropriate siting configuration, and wind array controls. An analysis of wind generation change from an echelon and a farm for passage of a thunderstorm is presented to establish the factors concerning the wind turbine model and siting configuration that contribute to these variations. Detailed simulation results indicate more precisely how these factors can be exploited to minimize the WECS generation changes observed. Reduction of the wind generation change over ten minutes is shown to reduce the increase in spinning reserve, unloadable generation and load following requirements on unit commitment when significant WECS generation is present and the farm penetration constraint is satisfied. Controls on the blade pitch angle of all wind turbines in an array or a battery control are shown to reduce both the wind generation change out of an array and the effective farm penetration in anticipation of a storm so that the farm penetration constraint may be satisfied.

1. INTRODUCTION

The research reported in this paper is an extension of previous work [1,2,3]. The objectives of the earlier work was to determine:

(1) if operating problems could exist on automatic generation control (regulation and economic dispatch), frequency regulation, and unit commitment when wind generation capacity is significant;

(2) the penetration limits on wind generation capacity that would alleviate these operating problems.

The results indicated that there were two specific operating problems which could both be eliminated with proper penetration constraints:

(1) The automatic generation control will saturate for long periods when the total change in wind generation for passage of a thunderstorm front and simultaneous load change in a ten minute interval will require non-wind generation change that exceeds load following capability in a ten minute interval. This problem violates NAPSIC performance standards but can be eliminated by imposing a farm penetration constraint on the capacity of all wind turbine generators that can be affected by a single thunderstorm front.

(2) A cycling problem caused by simultaneous load and generation change that induce frequency deviations that exceed governor deadband. This continual cycling of steam turbine units is objectionable to generator operators and can cause increased maintainance costs, forced outage rates and ultimately reduce unit life. The cycling of nuclear units is of concern for safety reasons in addition to those mentioned above. The cycling problem can occur due to a storm front sweeping through a wind generator array causing large power variations on successive echelons. A echelon penetration constraint on the capacity of all WTGs that can experience simultaneous change in generation level will eliminate this cycling problem.

A subsequent study [3] was devoted to a detailed discussion of the modification of unit commitment, regulation, and economic dispatch when WECS generation is significant. A modified farm penetration constraint is determined that limits WECS generation to be less than the maximum first contingency loss of resource or commitment. A violation of this farm penetration constraint is shown to necessarily cause an increase in the maximum first contingency loss of resource or commitment to the level of the farm capacity and thus an increase in load following, spinning reserve, and unloadable generation requirements on unit commitment. A discussion of the methodology, costs and benefits of changing unit commitment, when WECS generation is significant and the farm penetration constraint is or is not violated, is included. A discussion of the methods for modifying unit commitment is also included. Detailed simulation results that document the reduction of the effects of significant WECS generation change through the modification of the unit commitment regulation, and economic dispatch is also presented.

A modified echelon penetration constraint is proposed which limits instantaneous change and rate of change of wind array generation that must be handled by frequency regulation and regulation controls. This constraint is imposed to limit cycling of units.

This paper presents both analysis and simulation results that show how to decrease the WECS generation change over a ten minute interval through selection of the wind turbine generator model at each site, the siting configuration, and controls on the power variation out of the array. These direct controls of power out of the array are shown to also permit reduction of the effective farm penetration below the farm penetration constraint level and thus make the increase in spinning reserve, unloadable generation, and load following requirement depend on the probable change in WECS generation over a ten minute interval rather than on the farm capacity, which would be the maximum first contingency loss of resource or commitment for a particular utility if the farm penetration constraint were violated.

2. ANALYSIS AND SIMULATION OF WIND GENERATION CHANGE FROM AN ECHELON AND A FARM

The purpose of this section is to:

(1) briefly describe the model and simulation of wind power change from an array of wind turbine generators for passage of a thunderstorm front;

(2) analyze the power change and rate of change from an echelon and a farm in terms of the factors that determine these changes;

(3) review the methodology for determining spinning reserve, unloadable generation, and load following requirements on unit commmitment and briefly discuss how the selection of wind turbine models, siting configuration and wind array controls can influence these requirements.

A model of a single MOD-1 WTG and an array of wind turbine generators is developed. The MOD-1 WTG model, given in [1], is a static nonlinear model that relates generation to wind speed if the wind speed does not exceed the cut out velocity for a sustained period, which causes shutdown to avoid damage. The dynamics of the shutdown startup sequence is also modeled since a thunderstorm can cause such a shutdown. A similar model of a MOD-2 wind turbine is discussed in section 3 of this paper in order to compare the changes from an identical siting configuration of MOD-1 and MOD-2 wind turbines experiencing the identical wind speed profile.

The farm model, which is common for every wind turbine model, assumes the motion of thunderstorm front is normal to each echelon. The power out of the first echelon is then just the generation out of a single generator in this echelon multiplied by the number of generators in this echelon. The generation out of the j^{th} echelon is the generation profile of this WTG in the first echelon (1) delayed by an interval (d_j/V_o) proportional to the distance between the first and j^{th} echelon and inversely proportional to the speed of the thunderstorm front, and (2) multiplied by the number of WTGs in the j^{th} echelon. The generation out of all echelons is simply summed to obtain the generation time profile for the farm for passage of a thunderstorm front.

The worst case change and rate of change from a coastal farm will now be determined. The results are derived based initially on simulation of a worst case coastal farm experiencing a worst case thunderstorm wind speed versus time profile.

The worst case MOD-1 siting configuration for a coastal farm [1], which is a farm located on the coast of a body of water, shows a 0.5 mi. spacing between 50 generators in each echelon and a 2 mi. separation between two echelons. The echelons are assumed sited normal to the motion of the thunderstorm front.

The wind speed profile of a worst case thunderstorm gust front on the WTGs in the first echelon is shown in Figure 1A. The initial wind speed increase is due to the leading edge outflow and the second segment of high wind speed is due to the trailing edge inflow. The wind speed increases from 13 km/hr. at t = 0 to 26.km/hr. at t = 50 causing the power on each WTG in the first echelon to increase from zero to capacity (1.5 MW) in that interval. The power remains at capacity for speeds in excess of 26 km/hr. due to blade pitch controls. The thunderstorm front was chosen with a 13 km/hr. initial wind speed to cause maximum power variations out of any WTG.

The power variation out of the coastal wind farm of MOD-1 WTGs, shown in Figure 1B, shows two 75 megawatt ramps each 50 seconds long which are the increases in generation due to the leading edge outflow passing over the two echelons. The two pronounced power decreases are due to the shutdown of WTGs on both echelons caused by sustained wind speed exceeding cutout velocity. The time interval between the successive increases or decreases on the two echelons is 240 seconds.

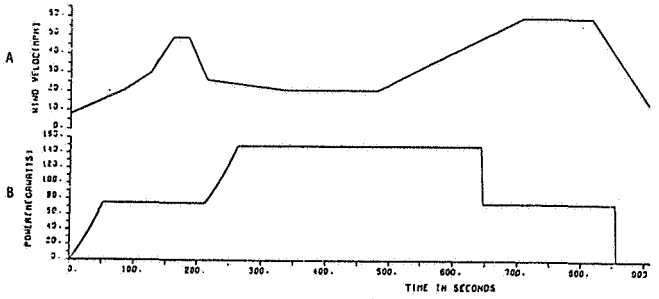

Figure 1 Simulation of Coastal Farm for a Thunderstorm Front

The logic for initiation of shutdown of a WTG requires the output of a one minute smoothed wind speed $W_{av}(k)$, to exceed 64 km/hr. Thus, a shutdown only occurs for the trailing edge inflow because the excessive wind speed for the leading edge outflow is not sustained long enough to trigger a shutdown.

The power out of any MOD-1 WTG does not decrease after the first 50 seconds of the leading edge outflow passes over (until the shutdown) due to the blade pitch control that maintains constant maximum generation over a wide range of wind velocities (26 km/hr. - 64 km/hr.).

An analysis of power variations out of an echelon and a farm is now performed to determine the factors that influence power increases and decreases for passage of a thunderstorm front. The analysis assumed all WTGs in a farm are similar, and arranged in straight parallel lines normal to the motion of the front. The analysis is not restricted to any particular WTG model if the parameter D is interpreted as the distance between the leading edge of the thunderstorm and the point where the wind speed reaches V_R, the wind speed at which that WTG model achieves rated generation. This maximum change and rate of change in generation is derived based on the additional assumption that the wind speed is below V_{ci}, the cut in velocity for the WTG before the front arrives.

The time in seconds for a particular WTG to change its generation from zero to capacity C_W for a thunderstorm front is

$$T_M = 3600\ D/V_o \text{ sec} \qquad (1)$$

where V_o is the velocity of the front and D is the distance from the very leading edge of the front to the point internal to the front at which wind speed first reaches V_R, the wind speed level just sufficient for maximum generation on that WTG model (C_W). Thus a thunderstorm front with a minimum value of T_M due to a minimum value of D and a maximum value of V_o,

would require a higher response rate for the governor frequency regulation and AGC regulation controls to handle this change in wind power generation without excessive or sustained change in frequency or area control error.

The time interval T_e between initiation of generation changes on two adjacent echelons is

$$T_e = \frac{3600\ d}{V_o} \text{ sec} \tag{2}$$

where d is the distance between echelons in miles. The distance d must be greater than D for the response of two adjacent echelons due to passage of the leading edge outflow not to overlap. The shorter T_e and d, the higher the response rate capability of the power system required to handle this generation change without excessive or sustained frequency or area control error changes.

The maximum change of generation from an echelon of N_e WTGs with rated capacity C_W is

$$\Delta P_e = N_e \times C_W$$

and the maximum average rate of change during period T_M required for passage of the leading edge outflow is

$$\frac{\Delta P_e^+}{\Delta t} = \frac{N_e \times C_W}{T_M} \tag{3}$$

The maximum average rate of change of power from an echelon during the period T_S required for shutdown during the passage of the trailing edge inflow of a thunderstorm front is

$$\frac{\Delta P_e^-}{\Delta t} = \frac{N_e \times C_W}{T_S} \tag{4}$$

The maximum power change out of a farm composed of N_f WTGs for passage of either the leading edge outflow or trailing edge inflow is

$$\Delta P_f = N_f \times C_W \tag{5}$$

The maximum average rate of change from the farm during the period $(N_f/N_e - 1)\ T_e + T_M$ required for the increase in generation during the passage of the leading edge outlfow is

$$\frac{\Delta P_f^-}{\Delta t} = \frac{N_f \times C_W}{\left(\frac{N_f}{N_e} - 1\right) T_e + T_M} \tag{6}$$

The maximum average rate of change from the farm during the period $(N_f/N_e - 1)\ T_e + T_S$ required for shutdown of all the echelons during passage of the trailing edge inflow of the thunderstorm front is

$$\frac{\Delta P_f}{\Delta t} = \frac{N_f \times C_W}{\left(\frac{N_f}{N_e} - 1\right) T_e + T_S} \tag{7}$$

The formulas for WECS generation change out of an echelon and farm for passage of the leading edge outflow are given by equations (3) and (6) where T_M and T_e satisfy equations (1) and (2) respectively. Results obtained in section 4, where generators in echelons are randomly sited in a strip D miles long rather than in straight lines normal to the motion of the front, indicated that the rate of change of WECS generation in an echelon for passage of a thunderstorm trailing edge inflow to be identical to that for the passage of the thunderstorm's leading edge outflow. Thus, the formulas for rate of change of power from an echelon (3) or a farm (6) are appropriate for passage of both the leading edge outflow or trailing edge inflow if the siting configuration is not in straight lines normal to the motion of the front which will generally be true.

These formulas will not be used to derive detailed expressions that indicate more precisely the factors that contribute to $\frac{dP_e}{dt}$ and $\frac{dP_f}{dt}$ so that the model WTG and siting configuration can be selected to keep these WECS power generation rates below that of the power system average response rate capability.

The power rate of change out of an echelon is quite different depending on whether the density of wind turbines in an array is or is not uniform; i.e., whether the density of wind turbine in an echelon, defined

$$\rho_E = \frac{N_e}{D \times D_o} \tag{8}$$

is or is not identical to the density in the farm

$$\rho_f = \frac{N_f}{(V_o T + D)\ D_o} \qquad T = \left(\frac{N_f}{N_e} - 1\right) T_e \tag{9}$$

where T is the time for the thunderstorm to move through the farm. The formula for power rate of change from an echelon (3) becomes upon substitution of (2) and (9)

$$\frac{dP_e}{dt} = \frac{\rho_f\ D_o\ V_o\ C_W}{3600} \tag{10}$$

if $\rho_f = \rho_e$ as it is more nearly in a low density midwestern farm siting configuration. Note that V_o and D_o are the velocity of the thunderstorm front and the width of the front respectively, C_W is the capacity in MW for the wind turbine model, and ρ_f is the uniform density of wind turbine in the farm in #/mi.[2] The rate of change of power out of an echelon is

$$\frac{dP_e}{dt} = \frac{\rho_e\ D_o\ V_o}{3600} \left(D\left[\frac{V_R - V_{CI}}{D}\right]\left[\frac{C_W}{V_R - V_{CI}}\right]\right) \tag{11}$$

if $\rho_e > \rho_f$, as in the coastal farm siting configuration. Note that in this case $\frac{dP_e}{dt}$ depend on

$\frac{C_W}{V_R - V_{CI}}$ - The slope of the power versus wind speed curve for a wind turbine model for the range of velocities $V_R - V_{CI}$ where power can change.

$\frac{V_R - V_{CI}}{D}$ - The slope of the wind speed profile of thunderstorm front for the distance D into the front.

D - The distance into a particular thunderstorm front where power will change on the WTG model considered or alternately the length of an echelon in the direction of motion of the thunderstorm front.

The formula for power out of a farm (6) has the form

$$\frac{dP_f}{dt} = \frac{\rho_f D_o V_o C_W}{3600} \tag{12}$$

upon subsititution (1,2, 9) into (6). Note when the density of an echelon is the same as that of the farm, the rate of change out of an echelon is the same as that out of the farm.

It is clear that the wind generation rates of change from an echelon (10,11) and farm (12) depend on the width (D_o), speed (V_o), and the slope $\frac{V_R - V_{CI}}{D}$ of the leading edge outflow for the thunderstorm front. The remaining parameters depend either on the WTG model (C_W, $\frac{C_W}{V_R - V_{CI}}$, D) or on the siting configuration (ρ_f, ρ_e, d). The effects of different WTG models and siting configuration characteristics on the change and rates of change from an echelon and a farm for different wind speed profiles will be demonstrated in the next two sections of the paper. The purpose of studying the effects of WTG models and siting configuration patterns is to analyze how such factors can be used to minimize WECS generation change and thus minimize any increase in load following, spinning reserve and unloadable generation requirements provided through unit commitment modification when WECS generation is present. These increased requirements add to fuel, operating, and maintainance costs but are required to maintain system security as discussed in [3]. Changes in regulation and economic dispatch (load following) controls must also be implemented [3] to take advantage of the increased response and response rate capability provided by the increased spinning reserve, unloadable generation, and load following capability, when WECS generation is present. Thus minimizing WECS generation change by WTG model and siting configuration selection can either dramatically decrease or possibly eliminate the need for modifying the unit commitment, regulation, and economic dispatch when WECS generation is present.

A brief discussion of spinning reserve, unloadable generation, and load following requirements and how they are affected by the magnitudes of the change and rate of change from an echelon and a farm is now presented. The two factors that determine the spinning reserve, unloadable generation, and load following requirements are the maximum probable rise ΔL_k^+ and drop ΔL_k^- in thermal load in ten minutes. These maximum probable changes are defined as

$$\Delta L_k^+ = \max\{(L_{k+1} - L_k)T + D_R + Q_{Wk}^+ + Q_{Lk}^+, 0\}$$
$$\Delta L_k^- = \max\{-(L_{k+1} - L_k)T + D_C + Q_{Wk}^- + W_{Lk}^-, 0\} \tag{13}$$

where

L_k - thermal load at the k hour

$(L_{k+1} - L_k)T$ - predicted change in thermal load in ten minutes

T = .1667 hour = ten minutes

Q_{Wk}^+ Maximum probable drop in WECS generation output in 10 minutes

Q_{Wk}^- Maximum probable rise in WECS generation output in 10 minutes

Q_{Lk}^+ Maximum probable rise in system load in 10 minutes

Q_{Lk}^- Maximum probable drop in system load in 10 minutes

D_R Largest single resource (generation or import) subject to failure

D_C Largest single commitment (export) subject to failure

The spinning reserve SR_k, unloadable generation SS_k, and load following capabilities LF_k for a unit commitment where

G_k Required load-following capacity

f Average minimum generation level of load-following units as a fraction of maximum capacity

g_k Average operating level of load-following units above level f($0 \le g_k \le 1 - f$)

r Average ramp rate of load-following units in % of rated capacity per minute

are defined as

$$SR_k = (1 - f - g_k)\, G_k$$
$$SS_k = g_k\, G_k \tag{14}$$
$$LF_k = 10r\, G_k$$

when there is no unconnected hydro or pumped storage units, interruptible load, and unused but connected base loaded generation to contribute to spinning reserve and unloadable generation capability. The requirements for security on the system are that

$$SR_k = (1 - f - g_k)\, G_k \ge \Delta L_k^+ \tag{15}$$

$$SS_k = g_k\, G_k \ge \Delta L_k^- \tag{16}$$

$$LF_k = 10r\, G_k \ge \max\{\Delta L_k^+, \Delta L_k^-\} \tag{17}$$

The presence of significant wind generation can affect the maximum first contingency loss of resource D_R and commitment D_C and the probable rise Q_{Wk}^- and drop Q_{Wk}^+ in wind generation in ten minutes. The farm penetration constraint [3] limits the maximum change in wind generation in an array for passage of a thunderstorm to be less than the minimum of the maximum first contingency loss of resource or commitment

$$N_F\, C_W \le \min(D_R, D_C) \tag{18}$$

where C_W is the capacity of each of the N_f wind turbines in the farm. If the farm penetration constraint is violated in some region due to favorable economics and limited siting availability due to wind, environmental or other factors, then either D_R or D_C or both must be increased to the farm capacity and $Q^+_{Wk} = Q^-_{Wk} = 0$. The logic for changing D_R, D_C or both is that the maximum first contingecny loss of resource or commitment is now the worst case changes in wind generation due to passage of the thunderstorm's trailing edge inflow and leading edge outflow respectively as indicated by the simulation results given earlier in this section. Q^+_{Wk} and Q^-_{Wk} are set to zero because the effect of wind generation has been already included in adjustment of D_R and D_C and thus ΔL^+_k and ΔL^-_k.

If the farm penetration constraint is not violated, D_R and D_C are not changed and values of Q^+_{Wk} and Q^-_{Wk} must be determined. These probable or predicted changes in wind generation (Q^+_{Wk}, Q^-_{Wk}) depend on the anticipated wind conditions, the wind turbine models in the array, the siting of wind turbines, and the correlation of wind speeds at the various sites. These factors and their effect on the probable change in WECS generation in ten minutes will be discussed in the next two sections.

Two methods for determining or setting Q^+_{Wk}, Q^-_{Wk} were discussed in [3]. The first method is based on reliability analysis that includes the statistics of WECS generation change on a particular array for anticipated wind conditions and can select ΔL^-_k in addition to ΔL^+_k. A second method would select Q^+_{Wk} and Q^-_{Wk} based on a weighted prediction of change of WECS generation change on a specific array and anticipated wind conditions. The weighting would depend on the operating procedure of the utility.

The proper selection of wind turbine models and the siting configuration can dramatically reduce Q^+_{Wk} and Q^-_{Wk} when the farm penetration constraint is satisfied. Thus the analysis of how the factors in the wind turbine model (C_W, $\frac{C_W}{V_R - V_{CI}}$, D) and the siting configuration (ρ_f, ρ_e, d) can be selected to reduce WECS generation change can provide guidelines for siting wind turbine generators and model selection.

The values of D_R and D_C (and thus ΔL^+_k and ΔL^-_k) can not be reduced by wind turbine model or siting configuration selection if the farm penetration constraint is violated since the $N_F\ C_W = D_R = D_C$ and the farm penetration level does not necessarily depend on the wind turbine model and siting configuration but on the total capacity of wind turbines in an area swept out by a thunderstorm. The effective farm penetration can be reduced if the farm penetration constraint is violated by the controls discussed in section 5. These controls would reduce D_R and D_C and thus spinning reserve, unloadable generation and load following requirements if the farm penetration constraint were violated.

3. EFFECTS OF THE WTG MODEL

The analysis in the previous section showed that the change and rate of change of wind generation out of an echelon and farm are dependent on the following wind turbine model parameters; capacity C_W, the slope of the change of power produced with wind speed $\frac{C_W}{V_R - V_{CI}}$, and the distance D into the leading edge outflow where the wind speed first reaches rated velocity V_R for the WTG model. The capacity C_W and distance D are much larger for a MOD-2 WTG than for a MOD-1 while the slope $\frac{C_W}{V_R - V_{CI}}$ is nearly identical for the two WTG models. Thus, the change and rate of change of generation for an echelon (10,11) and farm (12) of MOD-2 WTGs will be much larger than for an identical echelon and farm of MOD-1 WTGs.

A detailed model and simulation of the MOD-2 and the MOD-2 wind farm was developed and is discussed in [3]. The discussion of the detailed operation of the MOD-2 is omitted here. The simulation of the coastal farm of MOD-2 wind turbines experiencing the Mitchell storm front is presented and compared with similar results for the MOD-1 presented in section 2. These simulation results on the MOD-2 confirm the results of the above analysis of the differences in power change and rate of change from the MOD-1 and MOD-2.

The power out of a coastal farm of MOD-2 wind turbines experiencing the Mitchell storm front is shown in Figure 2. Note that the power increases are

$$\frac{dP^+_e}{dt} = 1.75 \text{ MW/sec.}$$

which is larger than for the MOD-1 and that the period over which power changes on each echelon is T_M = 80s rather than 50s for the MOD-1. Thus the total power change, the rate of change, and the period over which the change in power on an echelon of MOD-2 WTGs is significantly larger than for an identical ehcelon of MOD-1 WTGs experiencing the same Mitchell storm front as predicted from the analysis.

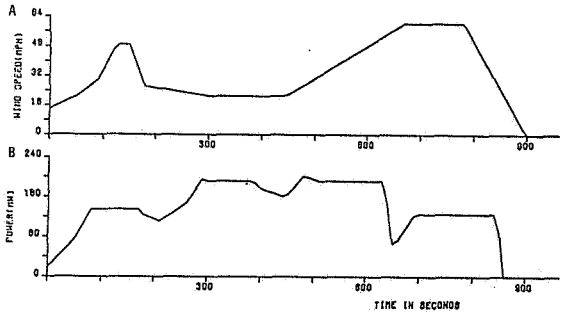

Figure 2 The Power Out of a Coastal Farm of MOD-2 Wind Turbines Experiencing The Mitchell Storm Front

The power output of the MOD-2 WTGs in the first echelon fall with the decrease in wind speed after passage of the very high winds of the leading edge outflow. The power output of a MOD-1 remains constant during this period because V_R = 18 mph is much lower on a MOD-1 causing the blade pitch controls to keep power output constant when wind speeds are above V_R.

The power increase out of the second echelon starts at T_e = 220s and is similar to that out of the first echelon. The power drop due to shutdown of the two echelons is quite rapid. The power decrease out of the first echelon is shown at t = 650 seconds followed almost immediately by a ramp increase in power on the second echelon due to increasing wind speeds for passage of the trailing edge inflow over this second echelon.

4. EFFECTS OF SITING CONFIGURATION ON WECS GENERATION CHANGE

The purpose of this section is to discuss how following factors affect the probable WECS generation change in ten minutes (Q^+_{Wk}, Q^-_{Wk}):

(1) density of WTGs in a farm ρ_f when $N_f C_W$ is held constant;

(2) uniformity of the farm siting configuration when $N_f C_W$ and ρ_f values are held constant;

(3) the wind speed characteristics of typical thunderstorms; and

(4) the correlation of wind speed characteristics at various sites in an echelon and farm.

This discussion will indicate how each of these factors affect probable changes in WECS generation for ten-minute intervals (Q^+_{Wk}, Q^-_{Wk}), and how one might attempt to minimize these probable changes and thus to minimize the changes in spinning reserve, unloadable generation, and load following capability required if the farm penetration constraint is satisfied. The siting configuration has no affect on the spinning reserve, unloadable generation, and load following requirements if the farm penetration constraint (18) is violated since the change in these requirements are embodied in changes in D_R and D_C to the farm capacity ($N_f C_W$) and not changes in Q^+_{Wk} and Q^-_{Wk}.

The effects of increasing ρ_f and not N_f or penetration $N_f C_W$ is indicated by simulating the WECS generation change out of a coastal farm of MOD-1 WTGs experiencing a Mitchell storm front when the distance between two echelons is decreased from 2 miles to 0.5 miles. The power change from this modified coastal farm, where the total number of WTGs is unchanged but the farm density is increased 2.5 times, is shown in Figure 3A. The average WECS power change as a function of the length of the interval over which the average is computed is plotted for the WECS generation change out of the modified coastal farm siting configuration in Figure 3B. Note that the average power system response rate capability curve is also included in Figure 3. The increased farm density has not increased the instantaneous rate of change in power from an array but held it at the level for 100s rather than 50s. The farm and echelon penetrations have to be reduced from 6% and 3%, respectively, to 4% and 2%, respectively, so that the average WECS generation change would not exceed power system response rate capability. If the density were increased as indicated, while holding the number of WTGs (N_f) and penetration ($N_f C_W$) constant, the peak frequency and area control error deviations would be larger and would not be reduced to low values as quickly because the system response and response rate capability are more severely stressed by the same total WECS generation change occuring in a shorter interval.

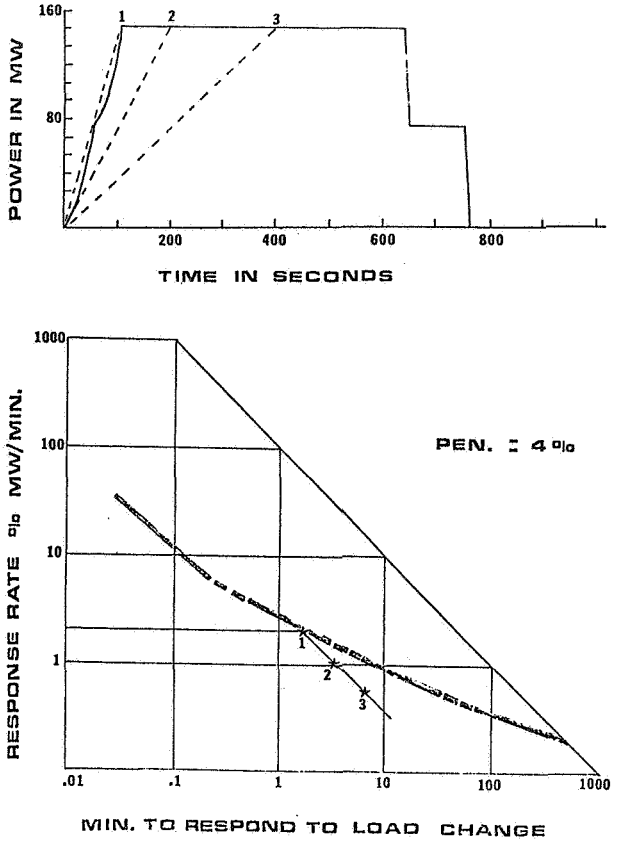

Figure 3 Power Change and Rate of Change from the Modified Coastal Farm of MOD-1 WTGs

The effects of reducing both farm and echelon siting densities without changing farm penetration is shown by simulating the WECS generation changes from the midwestern farm and coastal farms of MOD-1 WTGs as shown in Figures 4 and 5. The midwestern farm has the same 100 WTGs in 10 echelons of 10 WTGs each with separation between every WTG equal to 0.7 miles. The spreading out of generation, by reducing ρ_f and ρ_e and reducing ρ_e to values that more closely approach ρ_f

$$\rho_e = \begin{cases} 1.4\ \rho_f & \text{midwestern} \\ 4\ \rho_f & \text{coastal} \end{cases}$$

eliminates the saturation of area control error, reduces frequency and area control error deviations, and permits the utility to handle the WECS generation easily in a manner similar to load changes.

Thus, reducing farm and echelon density and maintaining echelon density at or near farm density levels (uniform low density farm siting patterns) could dramatically reduce WECS generation changes in ten minutes and the need to increase load following,

spinning reserve, and unloadable generation requirements. It should be noted wind speed characteristics, site availability, legal and environmental constraints seriously limit the ability to select uniform low density siting configurations. A coastal farm, where wind speeds drop as distance from the coast increases, is one example where higher non-uniform density configurations are likely.

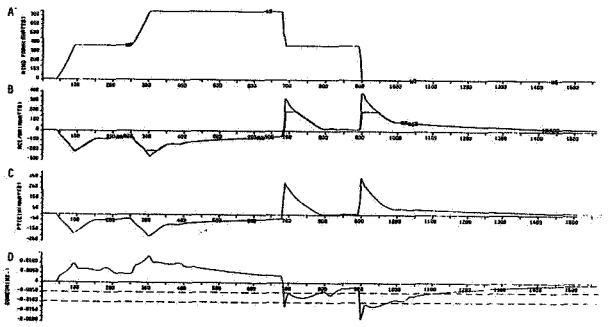

Figure 4 Effects of Power from a Coastal Farm on System Frequency and ACE

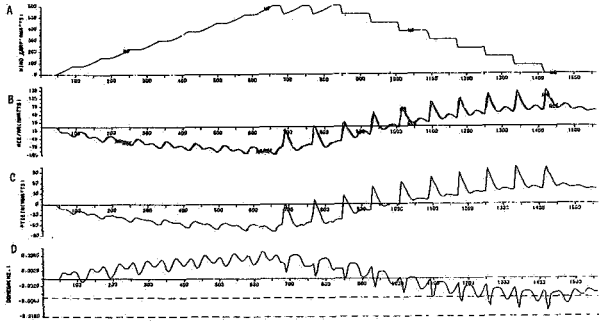

Figure 5 Effects of Power from a Midwestern Farm on System Frequency and ACE

The siting pattern assumed to this point is that all WTGs are sited in straight lines normal to the front although the definition of an echelon included all generation in strip D_o miles wide and D miles long in the direction of the motion of the storm front. The echelons were separated by a distance d which was greater than the MOD-1 or MOD-2 WTG value of D for the coastal and midwestern farm configurations. The effects of randomly siting WTGs in the farm maintaining a 0.5 mi. separation between WTGs, which avoids turbulence and loss of efficiency, was investigated for both coastal and midwestern farms. This random siting has the effect of making the density ρ_e of WTGs in every D x D_o area smaller and much closer to farm density levels. Thus, this random siting shows the effect of spreading out the siting within an echelon and the effects of reducing echelon density.

The coastal farm, with a d = 2.0 mile separation between echelons, was randomly sited by restricting all WTGs within the two mile strip but maintaining a 0.5 center band within this strip to satisfy the turbulence avoidance constraint. Note from Figures 1 and 6 for the original and randomly sited coastal farm, respectively, that randomly siting WTGs has smoothed out the power increases for passage of the thunderstorm leading edge outflow so that the rise is continuous with no intervals where WECS generation change has stopped. Random siting has made the drops in generation due to passage of the trailing edge inflow almost as smooth and continuous as the increases. This result indicates that the large almost instantaneous drops in generation, that could occur due to simultaneous loss of generation on an entire echelon, is not likely since the siting configuration is not likely to be perfectly straight lines normal to the motion of the thunderstorm front. The large frequency changes, which result due to the inability of frequency regulation to cope with such large instantaneous change, is also not likely.

The average response rate over a 70 second interval for this random sited coastal farm and the original farm are almost identical, as can be seen by comparing the power change on the two farms at t = 70s in Figures 6 and 1. This indicates random siting has virtually no effect on the average rate of change that must be coped for by frequency regulation and regulation in 60 seconds given by (10) for this Mitchell front. However, randomly siting the coastal farm would likely have greatly reduced the WECS generation changes for the O'Hare 6 wind speed profile, shown in Figure 7B, where adjacent echelons of the coastal farm had simultaneous increases. This random siting of echelons, which makes echelon densities smaller and more equal to farm density, could thus have decreased the changes in WECS generation out of the coastal farm. This result confirms that

(a) reducing echelon density and penetration, and

(b) making echelon density uniform by making it more nearly equal to farm density

decreases WECS generation change over ten minutes (Q^{+}_{Wk}, Q^{-}_{Wk}) as well as instantaneous rates of change which must be handled by frequency regulation and regulation controls.

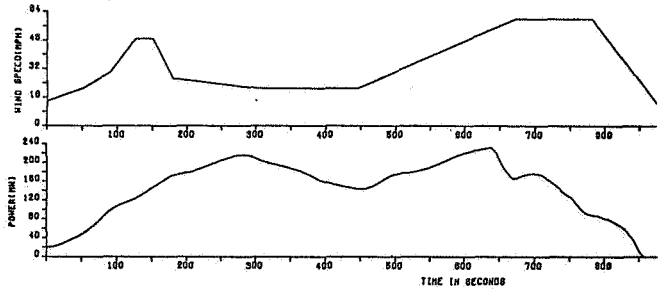

Figure 6 Random Sited Coastal Farm of MOD-2 WTGs with the Mitchell Storm Front

Wind speed time profiles during thunderstorms at Chicago's O'Hare International Airport and at Ludington, MI were measured and used at inputs to the original coastal farm siting configuration of MOD-2 WTGs, replacing the Mitchell storm front wind speed profile used exclusively up to this point. The power fluctuation out of this coastal farm for these various thunderstorm wind speed versus time profiles are given in Figures 7A-7D.

The actual measurements of wind speeds at these sites indicate there can be several peaks and lulls in a wind profile (Figures 7A-7C) and that the time interval between peaks can vary between 10 minutes to 40 minutes. The gradual buildup of wind speed for an advancing storm and the eventual peaks and lulls in the actual storm can be seen in Figure 7D.

The power from the coastal farm indicates that WECS generation changes can occur simultaneously on the two echelons which was not true for the Mitchell front. These WECS generation changes sometimes add giving short term (~ 1 minute) WECS generation change that is larger than can occur on a single echelon. This occurs at t = 300s and 1800s in Figure 7B where WECS generation changes reach 150 MW and 170 MW when the capacity of the echelon of MOD-2s is 120 MW. The repetition of these changes in wind speed and generation and the long duration of the thunderstorms (~ 1 hour) were not anticipated based on the Mitchell storm front data.

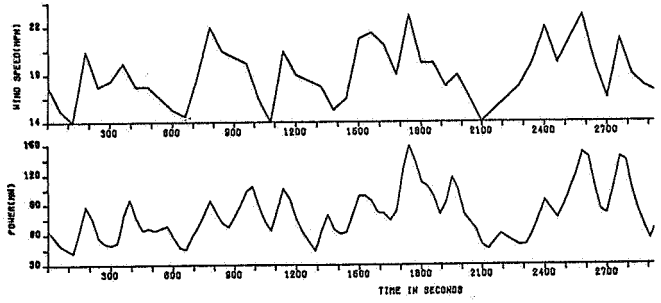

Figure 7A O'Hare 2 Storm Front on the Coastal Farm of MOD-2 WTGs

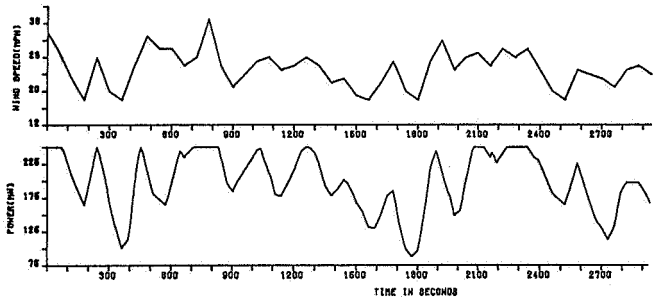

Figure 7B O'Hare 6 Storm Front on the Coastal Farm of MOD-2 WTGs

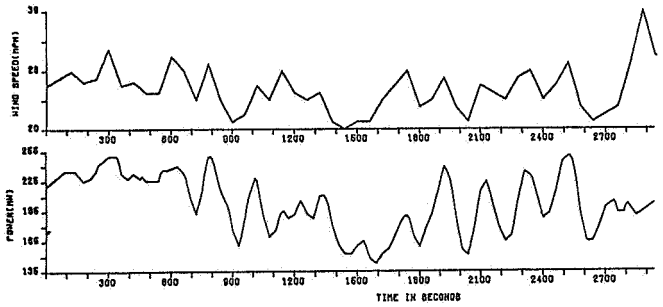

Figure 7C O'Hare 5 Storm Front on the Coastal Farm of MOD-2 WTGs

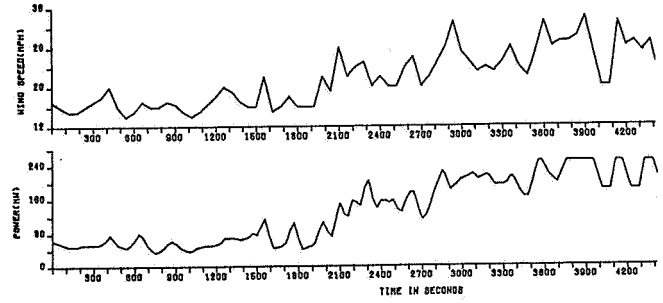

Figure 7D O'Hare 4 Storm Front on the Coastal Farm of MOD-2 WTGs

The effects of these large and cyclic power variations from the coastal farm of MOD-2s experiencing the O'Hare 6 wind speed versus time profile is shown in Figure 8. The simulation is performed on the 4000 MW system with 5% load following capability and experiencing ½%/min. load change for ten minutes in addition to these WECS generation changes on the 5.5% penetration coastal farm. The power variations from the coastal farm with O'Hare 6 wind speed profile is large and oscillatory. This is observed in large area control error and frequency deviations that reach peak to peak 150 MW and .03 hz respectively at t = 300s and approximately similar values at 1800s. The area control error saturated in both positive and negative directions within 100s in each case. Economic dispatch and economic dispatch/regulation units take on the load increase over the first 20 minutes and then respond to the overall cyclic (t = 800s) power changes in WECS generation, but not the faster changes seen on base and hydro units.

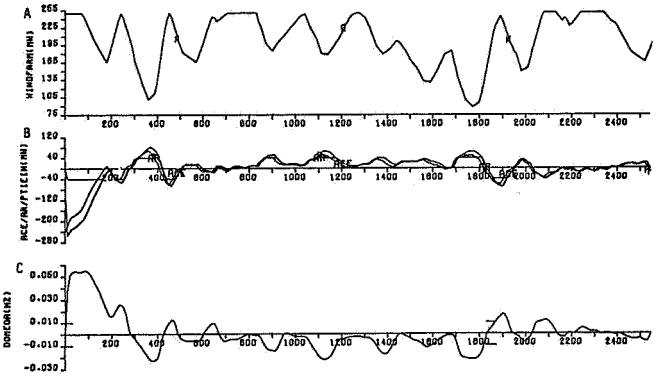

Figure 8 Effect of the O'Hare 6 Storm Induced WECS Generation Change on System Frequency and ACE

The large power changes from the coastal farm with O'Hare 6 wind speed profile are truly excessive for the 4000 MW system not only in size but also in terms of their repetition at t = 300, 1800 and 2700s and the duration of these changes (t = 3600). The size of these oscillations is due, in part, to the occasional overlapping of generation increases or decreases on different echelons. These large WECS generation changes can repeatedly cause saturation in area control error in both directions over a very short interval.

It would appear that reducing farm and echelon density without changing farm penetration would reduce the magnitude of these fluctuations. This is shown in Figure 9 where the O'Hara 6 wind speed profile is inserted into the midwestern farm configuration. Note that compared to coastal farm changes in WECS generation, shown in Figure 9b, the peaks and sharp valleys have been eliminated. The result indicates high echelon and farm density can have a major effect on the WECS generation changes over ten minutes as well as those over 60 seconds thus increasing spinning reserve, unloadable generation, and load following requirements as well as effecting the measures of operating reliability such as the average area control error and interval between area control error zero crossings.

It should be noted that the width of peaks and valleys, and duration between such peaks and valleys, probably are related to the very structure of a thunderstorm wind pattern. If statistics were determined on the width of peaks and valleys and duration between them, rules or principles for siting in coastal and midwestern farms could be developed that

would minimize WECS generation change out of an array. The analysis of wind speeds and the appropriate principles for siting WTGs is a subject for further research.

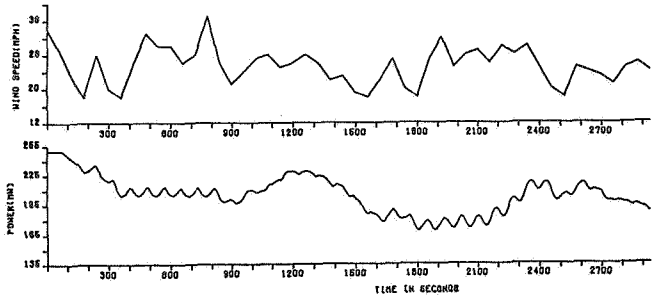

Figure 9 O'Hare Storm Front on the Midwestern Farm of MOD-2 WTGs

The analysis and simulation of thunderstorm induced WECS generation changes have assumed that the wind speed at every point along a straight line normal to the direction of front motion is identical and perfectly correlated and that the wind speed profile propagates at V_o so that each WTG observes the same wind speed profile. This may not be true in reality and thus an effort is made to assess what effect the assumption of perfect correlation of wind speed in an echelon and the assumption that the wind speed profile propagates from echelon to echelon unchanged has on the size of power variations from a farm. The present correlated echelon wind farm model works as follows.

The power out of a single WTG is multiplied by the number of WTGs in an echelon and then this echelon power output is delayed by $\frac{nd\ 3600}{V_o}$ to get the output of the nth echelon. The output of all echelons is then summed. This wind farm model assumed all wind speeds in an echelon are perfectly correlated and that the wind speed profile propagates from echelon to echelon. A second wind farm model assumes power out of each WTG is independent. If power out of each WTG is assumed to be a gaussian process, then if all wind turbines in a farm see independent identical stationary ergodic wind speed processes, a sample function of the power out of such a farm is

$$P_f(t) = N_f m_X + \sqrt{N_f}\left(P_W(t) - m_X\right) \qquad (19)$$

where $m_X = \frac{1}{t}\int_o^t P_W(t)dt$ and $P_W(t)$ is a sample function of the power out of a single WTG for this wind speed process. A perfectly correlated model of power out of a farm assumed the wind speed process at every WTG are an identical stationary ergodic gaussian processes which are perfectly correlated so that

$$P_f(t) = N_f P_W(t) \qquad (20)$$

The output of independent model, perfectly correlated model, and the perfectly correlated echelon wind farm model are shown for wind speed profiles measured during thunderstorms at O'Hare 5 and 6 in Figures 10 A-C, respectively and 11 A-C, respectively. Note that power variations out of the perfectly correlated model, perfectly correlated echelon model, and independent model are generally successively smaller. There are exceptions when the perfectly correlated echelon model has larger power variations than the perfectly correlated model, which occurs when power increases on different echelons simultaneously.

The assumptions concerning the correlation of wind speeds at various sites thus not only affect the magnitude of the variations over a one minute interval but also the variations over a ten minute interval. Thus, the correlation of wind speeds can significantly affect the statistics of the changes in WECS generation out of an array over a ten minute interval and thus the selection of (Q^+_{Wk}, Q^-_{Wk}) in the load following, spinning reserve, and unloadable generation requirements.

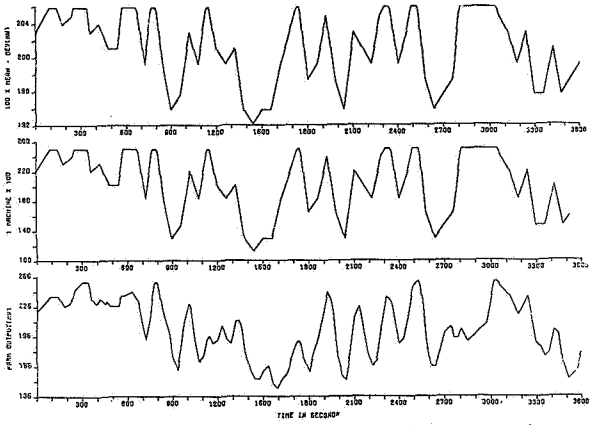

Figure 10 Independent, Correlated Farm, and Correlated Echelon Wind Speeds on WECS Generation from the Coastal Farm with O'Hare 5 Wind Speed Profile

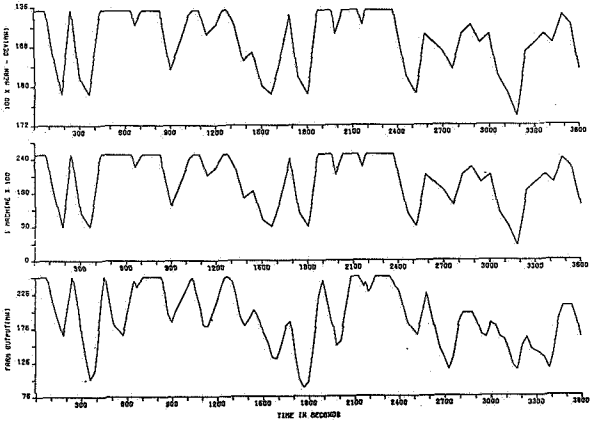

Figure 11 Independent, Correlated Farm, and Correlated Echelon Wind Speeds on WECS Generation from the Coastal Farm with O'Hare 6 Wind Speed Data

5. EFFECT OF WIND ARRAY CONTROLS

The previous two sections discussed factors, which depend on the WTG model (C_W, D. $\frac{C_W}{V_R - V_{CI}}$) and siting configuration (ρ_f, ρ_e, d), that affect probable WECS generation change (Q^+_{Wk}, Q^-_{Wk}). The selection of wind turbine models and siting configuration are often based on economics, wind conditions, site availabiltiy and other factors which do not permit the most favorable WTG selection and siting configuration combination. Moreover as WECS generation penetration increases no WTG model and siting configuration will reduce the probable changes (Q^+_{Wk}, Q^-_{Wk}) in WECS generation sufficiently to eliminate the need for increased spinning reserve, unloadable generation and load following requirements and the

appropriate modification of regulation and economic dispatch controls as described in [3]. Finally, WTG model and siting configuration selection only have effect on reducing the need for modifying unit commitment, regulation, and economic dispatch if the farm penetration constraint is satisfied.

The direct controls of WECS generation change, discussed in this section, can:

(1) reduce the effective farm penetration when thunderstorms are present and thereby make an array that would otherwise violate the farm penetration constraint effectively satisfy the constraint. This satisfaction of the farm penetration constraint thus makes the increase in spinning reserve, unloadable generation, and load following requirement depend on the probable change in WECS generation in ten minutes Q^{+}_{Wk} and Q^{-}_{Wk} and not on the modification of D_R and D_C to $N_F C_W$;

(2) significantly reduce the probable WECS generation changes in ten minutes (Q^{+}_{Wk}, Q^{-}_{Wk}) assuming that WTG model and siting configuration have been appropriately selected and that the effective penetration of the array with these controls present satisfies the farm penetration constraint.

Two direct controls limit the WECS generation change out of an array during any ten minute interval by coordinated control of blade pitch angles of all WTGs in an array. These controls would also reduce the apparent farm penetration during thunderstorms so that it meets the farm penetration constraint. One of these controls would clip WECS generation change in any ten minute interval and the other causes partial shutdown of each echelon in anticipation of the storm so that the effective farm penetration satisfies the farm penetration constraint and the WECS generation changes are capable of being handled by the unit commitment, regulation, and economic dispatch controls that are set when WECS generation is not present.

The partial shutdown of each echelon reduces both the ramp WECS generation increases and the sudden WECS generation drops on each echelon by 50%. The area control error, frequency, and tie line power deviations for each of these changes is thus decreased by approximately 50% also.

Frequency regulation is seen to be more capable of quickly reducing frequency deviations after the sudden drops of WECS generation on each echelon because they are smaller. Finally the saturation of area control error after the drop in WECS generation on the second echelon is reduced from 500s to 100s indicating the effectiveness of a partial shutdown in anticipation of the arrival of a thunderstorm front.

This partial shutdown would require wind speed monitors to detect the approach of a thunderstorm from any direction. Both clipping and partial shutdown would result in lost energy and that may somewhat reduce the economic attractiveness of the wind turbine arrays.

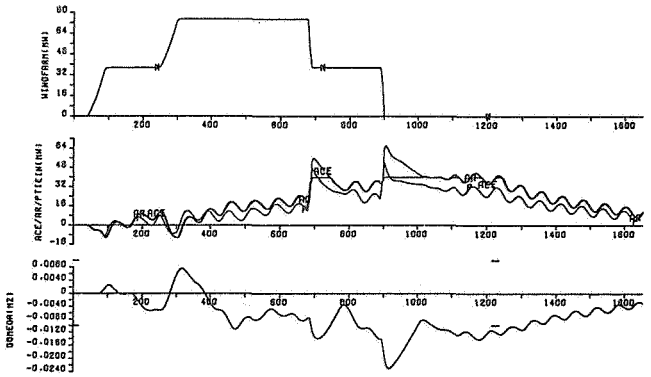

Figure 12 Effect of Partial Shutdown on ACE and Frequency Deviation

6. CONCLUSIONS

The paper discusses methods of reducing the wind generation changes from an array for passage of a thunderstorm by wind turbine model selection and site configuration selection. Coordinated blade pitch controls are also discussed and can be used to reduce the effective farm penetration level so that the farm penetration constraint is not violated. Satisfaction of this constraint implies that the added spinning reserve unloadable generation and load following requirement on unit commitment and the added response capability of AGC controls depends on WTG model selection and site configuration selection and not on the capacity of the farm. These coordinated blade pitch controls on each WTG in the array could also reduce the wind generation change out of an array much as wind turbine model and site configuration selection. The wind generation change after appropriate wind turbine model selection, site configuration selection, and coordinated blade pitch controls must be responded to by the units under AGC control. Limitation on site availability and wind turbine model selection and economic incentives for higher density siting may contribute to a rather significant change and rate of change in WECS generation especially during severe weather conditions. The adjustment of unit commitment to allow sufficient spinning reserve, unloadable generation, and load following capability and the adjustment of AGC controls to exploit the response capability available from unit commitment are discussed in [3].

7. REFERENCES

[1] Schlueter, R.A., Park, G.L., Modir, H., Dorsey, J., and Lotfalian, M., "Assessment of the Effects of Large Wind Generator Arrays on Power System Operation," IEEE Power Society, Winter Power Meeting, Paper A8D-110-7, February, 1980.

[2] Schlueter, R.A., Park, G.L., Modir, H., Dorsey, J., and Lotfalian, M., "Analysis and Simulation of Storm Induced WECS Generation Changes on System Operation," IEEE Winter Power Meeting, Paper WM-81-171-8, and accepted for IEEE Trans. on Power Apparatus and Systems.

[3] Schlueter, R.A., Park G.L., Lotfalian, M., Dorsey, J., and Shayanfar, H., "Operations Model for Utilities Using Wind Generator Arrays," Final report to U.S. Department of Energy Under Contract COO-23168-80/1, November 1980.

[4] Schlueter, R.A., Park, G.L., Modir, H., Dorsey, J., and Lotfalian, M., "Impact of Storm Fronts on Utilities with WECS Arrays." Final report to U.S. Department of Energy Under Contract EG-77-S-4450, COO/4450-79/2, September, 1979.

SECOND DOE/NASA WIND TURBINE DYNAMICS WORKSHOP

Acoustics

Session Chairman - J.P. Couch (NASA LeRC)

"Measured versus Calculated Characteristics of WTG Noise"
G. Greene
(NASA-Langley)

"Dynamics of Wakes Downstream of Wind Turbine Towers"
M.H. Snyder
W.H. Wentz, Jr.
(Wichita State University)

"Acoustic Noise Generation by the DOE/NASA MOD-1 Wind Turbine"
N.D. Kelley
(SERI)

"GE MOD-2 Noise Study"
R.J. Wells
(GE-Corp R&D)

"Refraction Focusing of Windmill-Produced Noise"
D.W. Thomson
(Penn. State Univ.)

"HAWT Noise"
W.L. Harris
(MIT)

"The NASA LeRC Wind Turbine Sound Prediction Code"
L.A. Viterna
(NASA LeRC)

"Noise Generation of Upwind Rotor WTGs"
R.H. Spencer
(Boeing Ventol)

"Status of Downwind Rotor HAWT Noise Prediction"
F.B. Metzger
R.J. Klatte
(Hamilton Standard)

"Wind Turbine Acoustic Standards"
D.G. Stephens
(NASA LaRC)

MEASURED AND CALCULATED CHARACTERISTICS OF WIND TURBINE NOISE

George C. Greene
NASA Langley Research Center
Hampton, Virginia 23665

ABSTRACT

This paper presents the results of an analytical and experimental investigation of wind turbine noise. Noise calculations indicate that for configurations with the rotor downwind of the support tower, the primary source of noise is the rapid change in rotor loading which occurs as the rotor passes through the tower wake. Noise measurements are presented for solid and truss-type tower models with both upwind and downwind rotors. Upwind rotor configurations are shown to be significantly quieter than downwind configurations. The model data suggest that averaged noise measurements and noise calculations based on averaged tower wake characteristics may not accurately represent the impulsive noise characteristics of downwind rotor configurations.

INTRODUCTION

One of the desirable characteristics of wind turbines is their minimal effect on the environment when compared to other methods of power generation. In particular, there is little evidence to suggest that wind turbines should be noisy. For example, reference 1 presented detailed noise measurements to show that the acoustic impact of a 38m (125 ft.) diameter, 100 kw wind turbine is minimal.

However, the noise resulting from the operation of a recently constructed 61m (200 ft.) diameter, 2000 kw wind turbine at Boone, North Carolina has caused concern for the community noise impact of very large wind turbines. The Boone wind turbine, designated the MOD-1, has caused nearby residents to complain of a periodic thumping sound. Noise calculations presented in reference 2 showed that for wind turbines such as the MOD-1 which have rotors downwind of their support towers, the dominant noise source can be the rapid change in rotor loading which occurs when the rotor passes through the tower wake. Because of the severity of the MOD-1 noise problem, an analytical and experimental investigation was conducted to identify promising noise control methods. The purpose of this paper is to present the results of that investigation and to provide some guidelines for designing wind turbines using both solid and truss-type towers.

NOISE CALCULATIONS

The noise calculations described herein were made using the technique described in reference 3. This is a "first principles" noise prediction technique which requires as input the detailed load distribution of the rotor as a function of time. It has been shown to give excellent results for propeller configurations where the blade loading is accurately known. Therefore, the principal difficulty in accurately calculating wind turbine noise is defining the rotor loading as it passes through the tower wake.

There are several options available for estimating rotor loadings for input to the noise calculations. One is to use wind tunnel measurements of tower wake characteristics such as those presented in reference 4. These are average wake characteristics and can be used to calculate average noise characteristics. Several researchers have made noise calculations using these wake characteristics and have obtained reasonably good agreement with average noise measurements on the MOD-1 wind turbine.

There has been no attempt to estimate the transient wake characteristics and rotor loadings which might be used for a more accurate noise prediction, and with good reason. As can be appreciated from figure 1, the MOD-1 rotor operates in a very complex wake which must vary considerably with wind speed (Reynolds number) and wind direction.

In addition, the wind turbine is situated in a small clearing surrounded by deciduous trees. The treetops, which can be seen in figure 1, are approximately the same height as the bottom of the rotor disk. Therefore, there can be a significant seasonal change in the turbine noise noise resulting from the change in the thickness of the atmospheric boundary layer. When the trees lose their leaves, the wind speed through the tower can be higher and therefore the rotor can experience a greater change in loading as it passes behind the tower.

Because of the complexity of the wake and since there were no rotor load measurements on the MOD-1 machine, initial calculations to understand noise mechanisms were made using very simplistic models of the rotor loading as it passed through the tower wake. Figures 2 and 3 show three assumed loading models and the corresponding time histories and spectra. The baseline case assumed no tower interference and resulted in no noise which would be visible at the scale used in figure 2. This case approximated the upwind rotor configuration. The level of the fundamental for this case is shown as the solid symbol in figure 3, all higher harmonics were insignificant.

The other two cases were single and double "notch" wake loadings to determine if the noise was due to the general existence of the wake or to the details of the wake structure. The single "notch" loading is seen to produce a single impulse time history while the double "notch" produces a double impulse as one would expect. The levels of the pressure impulses are approximately the same as are the overall noise levels. In the frequency domain it can be seen that the double "notch" loading causes the maximum noise levels to shift to a higher frequency. This results in a dramatic increase in the apparent loudness of the noise. Since the MOD-1 noise data contain multiple pulses, it was concluded that the MOD-1 noise problem was due primarily to the change in rotor loading caused by the individual tower leg wakes. It was also apparent that if the wake could be changed to produce a rotor loading more like the single notch, then the audible noise level could be reduced.

EXPLORATORY NOISE TESTS

A series of exploratory noise tests were conducted to determine if the trends which were predicted analytically could be duplicated in the wind tunnel. The cylindrical shapes shown in figure 4 were tested upwind of a model airplane propeller. Three of the cylinders were made of screens of varying porosity for comparison with a solid cylinder of the same diameter. In addition, two smaller cylinders were tested, one with a spiral strake and one plain.

Average noise spectra were generated for each of these configurations. These measurements confirmed the analytical trends in that the fine mesh and solid cylinders were significantly quieter than the more porous cylinders. A simple truss structure, shown in figure 5, was also tested. Average noise spectra were generated for both the basic tower configuration and with part of the tower taped to represent a solid surface. The taped portion of the tower was adjacent to the outer half of the rotor blade. Again, the average noise spectra indicated a significant reduction in noise.

MOD-1 MODEL TESTS

Based on the results of the exploratory tests, a model of the MOD-1 tower was constructed and tested in an anechoic wind tunnel. The overall installation in the anechoic wind tunnel is shown in figure 6(a) and a close-up of the tower is shown in figure 6(b). Tower details were carefully scaled in order to reproduce as nearly as possible the details of the tower wake. The geometric scale was 1:140 and the wind tunnel speed was 21 m/sec (70 ft/sec). This resulted in a model Reynolds number about 1/100 of the full scale value (depending on wind speed). The rotational speed of the rotor was chosen to match the model and full scale tip speeds. Because of the high rotational speeds, the model rotor had a straight blade (no coning) to minimize structural problems. The MOD-1 rotor planform and twist were modeled as closely as possible.

Because the model blade was straight, it was not possible to duplicate the rotor/tower spacing along the entire blade. The .75 radius position was chosen to match the spacing. Therefore, the outer portion of the blade operated closer to the tower than full scale and the inner portions were further away.

Noise measurements were made with a microphone located outside the wind stream at a slant distance of 1.8m (6 ft.). The microphone was downwind of the rotor plane at an angle of 56 degrees from the rotor axis and an azimuth position of 120 degrees, measured counterclockwise (facing upwind), from a zero degree position with the rotor blade tip at the base of the tower.

Figure 7 shows the average noise spectra for the MOD-1 model rotor without any flow interference other than the upstream influence of the streamlined rotor mounting strut. This represents the minimum noise level which could be achieved with the model rotor in the airstream. Since the model scale factor is 140:1, a full scale frequency of 20 Hz corresponds to a model frequency of 2800 Hz.

Figure 8 shows the average noise spectra for the MOD-1 upwind configuration with the wind perpendicular to the side of the tower. As expected, there was very little increase in noise since the upstream influence of the tower is not significant beyond a few diameters of the largest structural members.

The upwind results are quite different from the downwind configuration results shown in figure 9. The average spectra show the expected substantial increase in harmonic or rotational noise. The data, taken with the wind perpendicular to the face of the tower, are typical of the downwind data although the noise spectra varied considerably as the wind direction relative to the tower was changed. This is not surprising since the tower wake and the relative spacing of the rotor and tower change with wind direction. However, there were no wind directions where the noise levels approached the low levels experienced in the upwind configuration.

Since the exploratory tests showed a substantial difference between solid and open towers, tape was applied to the MOD-1 model to simulate a solid tower. Figure 10 shows the average noise spectra for the tower with tape applied to the portion of the tower adjacent to the outer half of the rotor. As predicted by both the analysis and the exploratory tests, the periodic or rotational noise was essentially eliminated and replaced with what appears as broadband noise above a frequency of about 2800 Hz (20 Hz full scale). Since the primary MOD-1 noise complaint was a periodic thumping rather than broadband noise, the solid tower averaged data suggested that a significant noise reduction might be possible.

TRANSIENT EFFECTS

All of the results presented thus far, both calculations and measurements, assumed that the noise problem can be characterized in an average sense. In this section we will examine that assumption in terms of model noise measurements. Before discussing the model measurements it is appropriate to describe the difference in the way people percieve low and high frequency periodic noise. It should be pointed out that this is not a well understood subject and that these comments are based only on the author's experience.

A noise spectra contains a subset of the information contained in the time history. A spectra describes the frequency content of the signal but contains no information on the impulsive or nonimpulsive nature of the signal. This is not a problem for most of the frequency range since the infinite number of time histories which can be generated from a given spectra will all sound the same, whether impulsive or not. However, for very low frequency noise, such as that generated by the MOD-1 wind turbine, the "character" of the time history can be important and, in particular, whether or not the signal is impulsive. The ear can discern each pressure impulse or thump from the MOD-1 and therefore the "character" of each thump is important. Since the pressure pulses can be influenced by random wake characteristics, they will not in general be exactly the same and therefore some thumps may sound louder than others. If the noise is averaged, the high frequency characteristics of the individual impulses tend to be lost. This may result in an underestimation of the noise actually generated.

Figure 11 shows an average noise spectra for a model configuration identical to the nominal MOD-1

configuration except that the rotor was positioned approximately four tower leg diameters further downwind. When compared with the average spectra for nominal spacing, figure 9, there does not appear to be a significant difference due to the increased spacing.

The time histories for the nominal and increased spacing are shown in figure 12. The wake structure is obviously very different for the two cases as evidenced by the complete change in character of the noise time histories. Although it is not possible to describe how these would sound if extrapolated to full scale, it seems probable that the alternating single and double pulses of the nominal spacing time history would sound different than the double pulses of the increased spacing time history or an average time history. The difference in the time histories shown in figure 12 is typical of the changes which occurred each time the tower configuration, wind direction or rotor spacing was changed. In general, it was not possible to look at the average noise spectra and estimate the character of the time history.

Another way of demonstrating the variability of the noise signal is to compare the averaged time histories. Figure 13 shows the average time histories for the taped-over or "solid" MOD-1 model at both the nominal tower/rotor spacing and with the spacing increased by approximately 2/3 of the overall tower "diameter." The rotor tachometer signal was used as a trigger to begin each signal average at the same shaft position. This technique enhances periodic signals and averages out the random components. The data in figure 13 are the result of 32 averages.

The nominal-spacing average time history shows the very consistent single pulse caused by the solid tower wake. In sharp contrast is the signal resulting from increasing the tower/rotor spacing. The time history of the impulse is highly variable and apparently random in nature since the average time history shows no periodic content.

The data in figure 13 are not typical although the same phenomena occurred for another configuration. In general, the averaged signal was still periodic with the pressure pulses being less distinct and more rounded than a single impulse. In the frequency domain this would correspond to a loss of the higher frequency portion of the signal which might significantly affect the apparent loudness of the noise. Therefore one should be very careful in interpreting averaged measurements of an unsteady low frequency noise.

12 SIDED TOWER TESTS

Tests were also conducted using the 2 cm diameter, 12 sided tower shown in figure 14. Figure 15 shows the average noise spectra for the configuration with the rotor located 2 diameters upwind of the center of the tower. The noise levels are not significantly different from the no-tower data of figure 7 or the MOD-1 upwind data of figure 8.

The average noise spectra for the downwind configuration ($x/D = 2.8$) is shown in figure 16. The harmonic noise falls off very rapidly compared to the MOD-1 downwind results of figure 9. These average spectra suggest that a small solid tower would not have a noise problem. However, when viewed from the time domain there is some uncertainty as to how noisy this tower might be.

Figure 17 presents a comparison of time histories for the MOD-1 and 12 sided towers with downwind rotors. Note the occurrence of multipeaked pulses in addition to the expected single-peaked pulses in the solid tower time history. It is not known whether or not these multipeaked pulses would exist for a full scale wind turbine. If they did exist, they might produce a thump about as loud as the MOD-1 thump. Since they do not occur periodically, an averaged measurement might not show their existence.

CONCLUDING REMARKS

The MOD-1 "thump" is the result of the interaction of the turbine rotor and the complex tower wake. Detailed calculations of the noise would require a detailed description of the rotor loading as it passes through the complex tower wake and would be difficult to make with certainty. However, average noise calculations using average wake characteristics are in general agreement with average noise measurements.

Calculations and model tests indicate that placing the rotor upwind of the support tower minimizes the noise risk. It is difficult to extrapolate model results for the downwind configuration to full scale since all the parameters which affect the wake affect the generated noise. The inherent unsteadiness of wake flows may produce noise which is louder than would be expected from average measurements or calculations based on average wake characteristics.

REFERENCES

1. Balombin, J. R.: An Exploratory Survey of Noise Levels Associated with a 100 kw Wind Turbine. NASA TM 81486, April 1980.

2. Greene, George C.; and Hubbard, Harvey H.: Some Calculated Effects of Non-Uniform Inflow on the Radiated Noise of a Large Wind Turbine. NASA TM 81813, May 1980.

3. Nystrom, P. A., and Farassat, F.: A Numerical Technique for Calculation of the Noise of High Speed Propellers with Advanced Blade Geometry. NASA TP 1662, 1980.

4. Savino, J. M.; and Wagner, L. H.: Wind Tunnel Measurements of the Tower Shadow on Models of the ERDA/NASA 100 kw Wind Turbine Tower. NASA TMX 73548, November 1976.

Figure 1.- DOE/NASA 2000 kw experimental wind turbine.

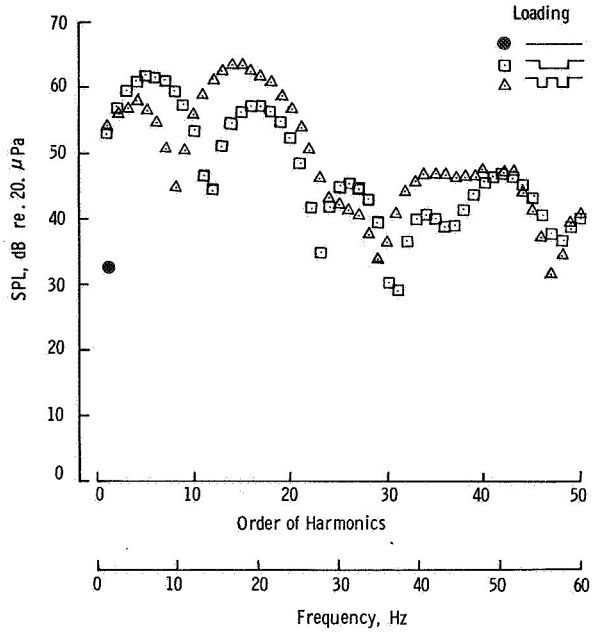

Figure 3.- Calculated noise spectra for three turbine inflow conditions.

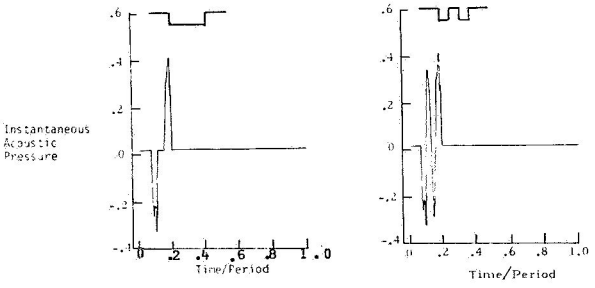

Figure 2.- Calculated noise signatures for single and double notch rotor loadings.

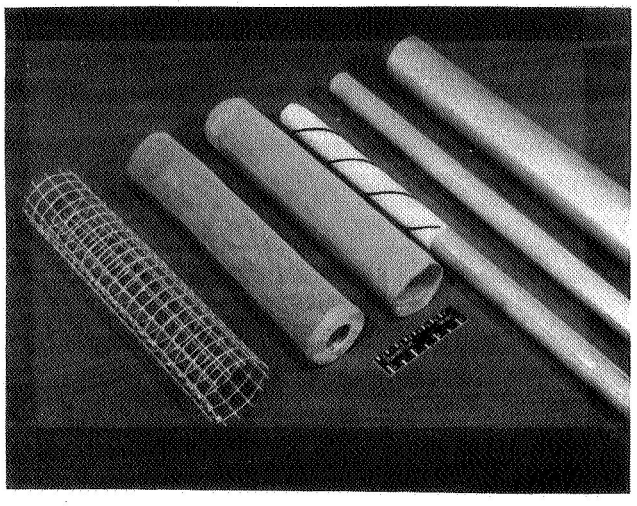

Figure 4.- Cylindrical models used in exploratory noise studies.

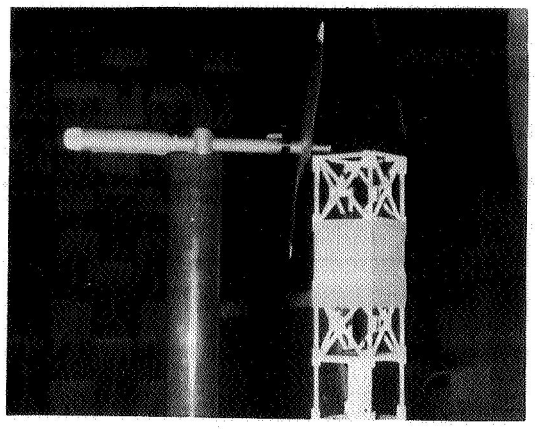

Figure 5.- Tower model (with partial tape covering) used in exploratory noise studies.

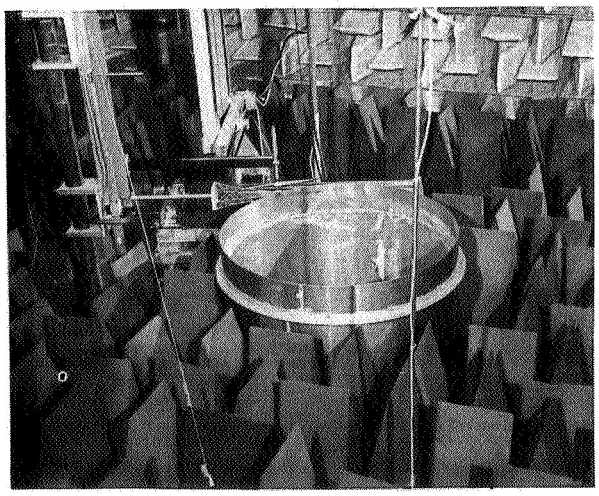

Figure 6(a).- Model installation in anechoic wind tunnel.

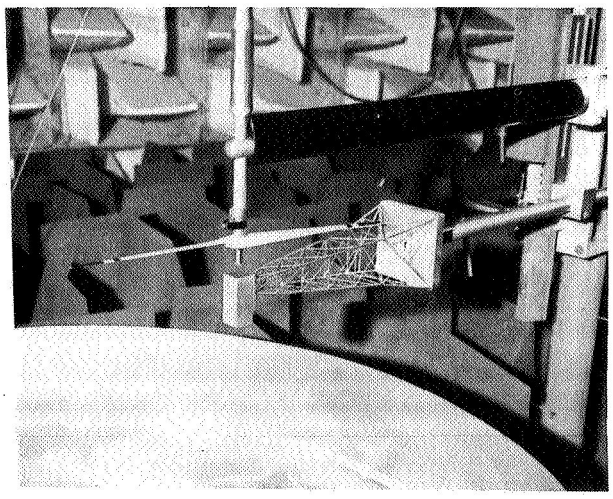

Figure 6(b).- MOD-1 tower model.

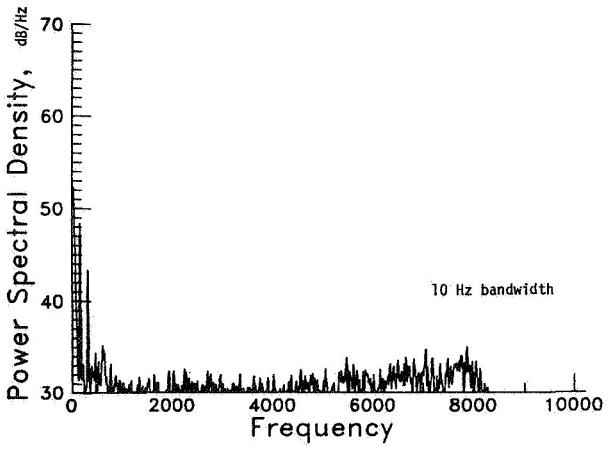

Figure 7.- Average noise spectra for MOD-1 model rotor with no support tower.

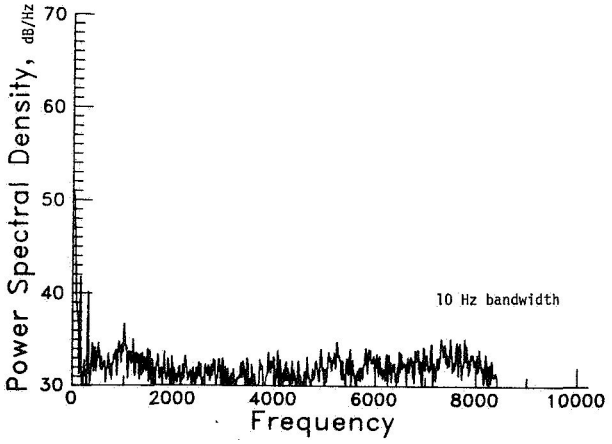

Figure 8.- Average noise spectra for MOD-1 model in the upwind configuration.

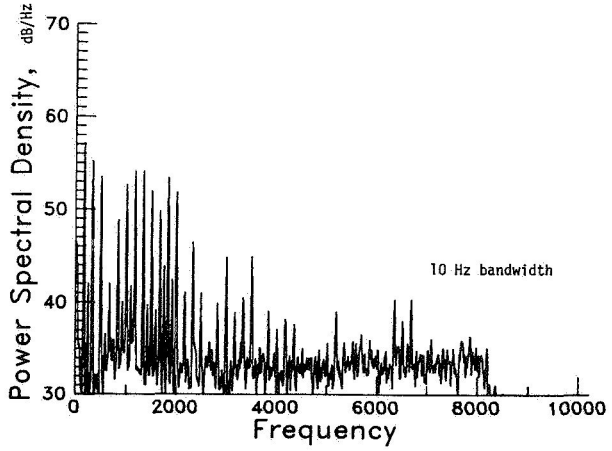

Figure 9.- Average noise spectra for MOD-1 model in the downwind configuration.

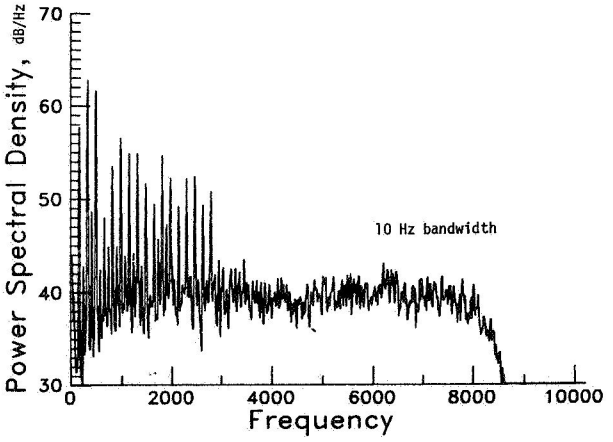

Figure 10.- Average noise spectra for MOD-1 "solid" tower model.

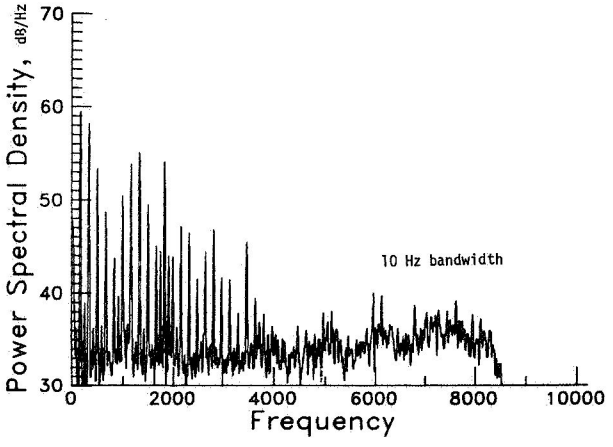

Figure 11.- Average noise spectra for MOD-1 tower model with the rotor approximately 4 tower leg diameters further downwind.

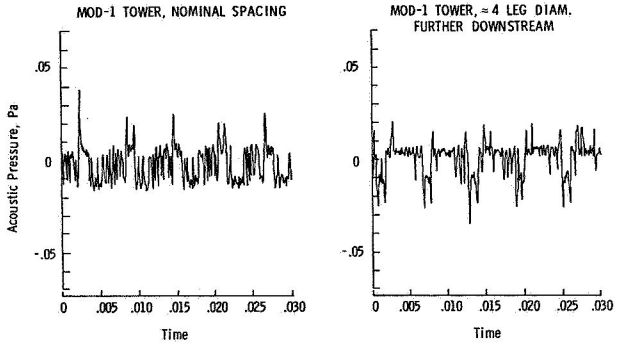

Figure 12.- Effect of tower/rotor spacing on the character of the noise time history.

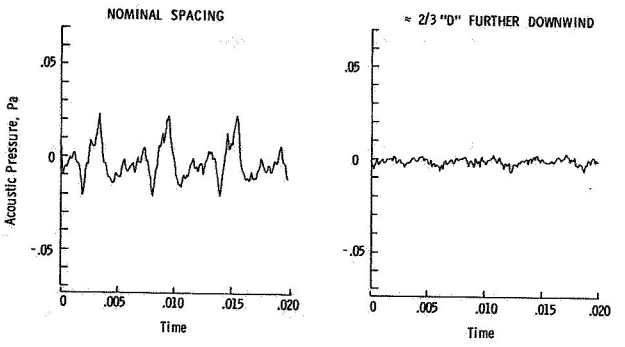

Figure 13.- Effect of tower/rotor spacing on the average time histories for the MOD-1 "solid" tower model.

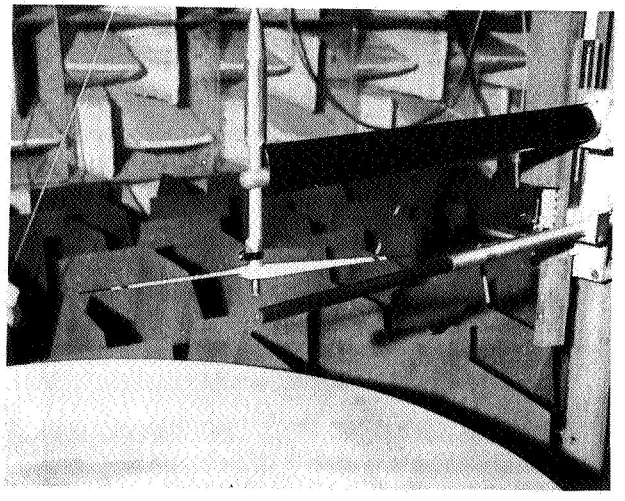

Figure 14.- Twelve-sided tower installed in the anechoic wind tunnel.

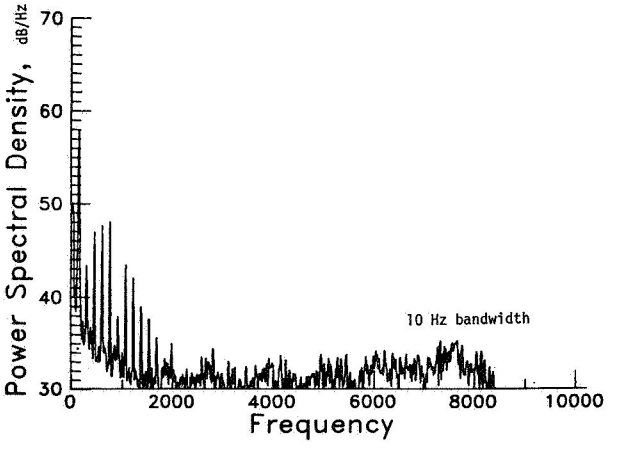

Figure 15.- Average noise spectra for the 12-sided tower model with the rotor located 2 tower diameters upwind.

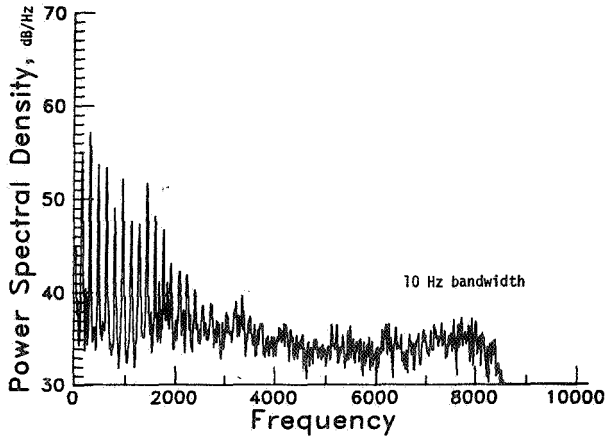

Figure 16.- Average noise spectra for the 12-sided tower with the rotor located 2.8 tower diameters downwind.

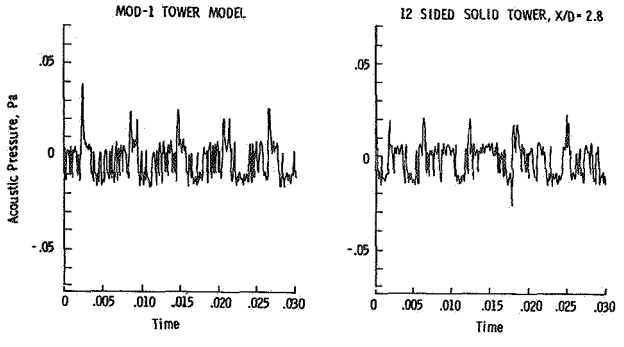

Figure 17.- Comparison of time histories for the MOD-1 and 12-sided tower models in the downwind configurations.

QUESTIONS AND ANSWERS

G. Greene

From: G.P. Tennyson

Q: Have measurements or calculations been made to determine the effects of blade planform and twist on noise? (Optimum diametrical loading should reduce shear, particularly at the blade tips and hence, noise.)

A: *Only for propeller noise, i.e., studies by OSU and MIT.*

From: R.J. Templin

Q: Did you investigate the effect of blade speed on noise, and if so, what was the effect?

A: *Did not investigate.*

DYNAMICS OF WAKES DOWNSTREAM OF WIND TURBINE TOWERS

Melvin H. Snyder* and W.H. Wentz, Jr.*
Wind Energy Laboratory
Wichita State University
Wichita, Kansas 67208

ABSTRACT

The near-field wakes downstream of circular cylinders and of 12-sided cylinders were surveyed in a wind tunnel. Local velocity and velocity deficit diagrams are presented. The variation of turbulence in the wake was surveyed and the frequency of the periodic component of wake motion was determined. Differences between wakes of circular cylinders and of 12-sided cylinders are discussed. Also effects of strakes, orientation of the 12-sided cylinders, and rounding of the corners are noted.

SYMBOLS

D	Diameter of cylinder (or of circumscribed circle)
f	Frequency of periodic component of wake motion
N	Number of samples taken at data point
q	Dynamic pressure, $1/2\,\rho\,V_\infty^2$
r	Radius of curvature of corners of 12-sided cylinders
R	Cylinder radius = D/2
Re	Reynolds number = $\rho VD/\mu$
S	Strouhal number = fD/V_∞
u_{mean}	Average local velocity
$\bar{u}$	u_{mean}
u_x	x-component of local velocity
u'_{rms}	Standard deviation (see text)
u_1	$1 - (u_x/V_\infty)$
V_∞	Freestream velocity
x	Streamwise distance downstream measured from centerline of cylinder to plane of survey in cylinder diameters
y	Distance along the cylinder axis
z	Distance normal to the x-z plane and measured from x-z plane passing through cylinder centerline
z_R	Half-width of wake
α	Orientation of 12-sided cylinder, see text
σ	Standard deviation = u'_{rms}

*Professors of Aeronautical Engineering

BACKGROUND

Wind turbine towers are often composed of cylinders, either as components of truss-type towers or as single column towers. Two types of towers and tower elements in use are circular cylinders and 12-sided cylinders. In the cases of turbines operating with rotors downwind of towers, there have been some undesirable results of the blades passing through the tower wake. These results include unwanted noise, as well as fluctuating loads on the blades resulting in transient torque and thrust loads.

The wake produced by separation of the flow from a cylinder is marked by velocity deficiency, i.e., decreased kinetic energy, and by unsteady behavior. The unsteady behavior has two components--"turbulence," by its nature random; and a regular periodic part, described by Roshko as "organized motion." These "organized" vortices shed from the cylinder are superimposed on the background of general turbulence (reference 1 and 2).

There is uncertainty regarding just what it is about the nature of the wake which causes the noise and other effects mentioned above, i.e., is it the (1) periodic structure of the wake, (2) velocity deficit, or (3) turbulence of the wake?

To obtain a model of the wake, wind tunnel tests were conducted in the Walter Beech Memorial Wind Tunnel of Wichita State University. The tests were surveys of wakes downstream of circular cylinders and of 12-sided cylinders.

MODELS

Four models were tested. Two models were circular cylinders, 0.17 m (6.7 in.) diameter and 0.508 m (20 in.) diameter. There were also two 12-sided cylinders; the smaller had a diameter of circumscribed circle of 0.182 m (7.17 in.), and the larger had a 0.508 m (20 in.) diameter circumscribed circle. The smaller models were mounted horizontally across the 2.13 m x 3.05 m (7 x 10 ft) tunnel test section (Fig. 1), and the larger models were mounted vertically.

The wake of the cylinders was surveyed at various stations downstream. Most published details regarding cylinder wakes are for long distances downstream (e.g., Schlichting: velocity deficit at greater than 50 diameters downstream--ref. 3;

see also ref. 4). Most downwind wind turbine blades will be operating in the range of 3 to 6 diameters downstream of the centerline of the cylinder producing the wake. Surveys were conducted at stations in the range from 2 diameters to 9 diameters downstream of the cylinder centerlines.

INSTRUMENTATION AND DATA PROCESSING

Pressure Probe Survey

Two types of instrumentation were used. Pressure measurements were made using a 5-tube probe (Fig. 2) to determine local velocity. Pressure data were processed on-line to determine local velocity magnitude and direction and all components.

Hot-Film Anemometer

The second phase of testing of each model was a survey of the wake using a hot-film anemometer. Figure 3 diagrams this data system. Linearized voltage signals from the hot-film anemometer were fed directly into the minicomputer; 6000 measurements were made at each station at a rate of 400 Hz, for a total sampling time of 15 seconds. These data were processed in about 40 to 45 seconds per station.

Voltage measurements were digitized, stored, and converted to velocity values. The velocity values were processed to determine the sample mean and standard deviation (σ). The standard deviation of a velocity sample is the turbulence intensity, when non-dimensionalized by a reference velocity. Local turbulence intensity was calculated, based on local mean velocity, and global turbulence intensity was calculated based on the remote freestream velocity.

$$u_{mean} = \bar{u} = \frac{\sum_{i=1}^{N} u_i}{N} \qquad [m/s \text{ (fps)}]$$

where N is total number of samples.

$$\text{Standard deviation} = \sigma = u'_{rms} = \sqrt{\frac{\sum_{i=1}^{N}(u_i - \bar{u})^2}{N}} \qquad [m/s \text{ (fps)}]$$

$$\text{"Global Turbulence Intensity"} = TI = \frac{u'_{rms}}{V_\infty}$$

$$\text{"Local Turbulence Intensity"} = TIL = \frac{u'_{rms}}{\bar{u}}$$

Velocity distribution was determined using a method of bins. A series of seven bins are used for determination of the sample histogram. The central bins are of σ width, centered about the mean, and the 1st and 7th bins are the "tails" for data respectively below and above the central bins. The entire sample is sorted into these bins to determine the distribution of the sample. The number printed for each bin is a fraction of the total number of samples.

Spectral Analysis

The signal from the hot-film anemometer was also fed to an analog spectrum analyzer (Hewlett-Packard model 3580A). Results were recorded in the form of photos of an oscilloscope trace of the power spectral density (psd). Figure 4 shows a typical photo obtained during these tests. For signals for which significant periodicity is present, the frequency or frequencies at which peaks in the psd appear are tabulated, non-dimensionalized, and presented in the form of Strouhal numbers ($S = fd/V_\infty$).

CIRCULAR CYLINDER TESTS

Testing

The smaller (0.17 m dia.) cylinder was mounted horizontally as shown in Figure 1. The wake was surveyed at stations x = 300%, 450%, 600%, 750%, and 900% using the 5-tube pressure probe. Measurements were taken every half-inch from z = -10 inches to z = +10 inches. Tunnel dynamic pressures ranged from 8.14 N/m^2 to 3.11 kN/m^2 providing Reynolds numbers from 174000 to 758000.

Survey of the wake using the hot-film anemometer was performed completely at x = 300% and for a more limited number of z-positions at the other stations. Frequency of the periodic component of the wake was determined at all stations and for a complete range of Reynolds numbers.

Two sets of spiral strakes were attached to the 17 cm circular cylinder and the wake was surveyed using the 5-tube probe at stations x = 300% and 600%. The strakes were fabricated from sheet aluminum, were 1.6 cm high (approximately 10% of diameter), and made an angle of 30° with the cylinder centerline (Fig. 5). Initial testing was done with the strakes in the 90° position in the plane of the survey (x-z plane), as in Figure 5. The cylinder was rotated 90° on its axis putting the strakes at the 0° and 180° position, in the plane of survey.

The large (0.508 m dia.) circular cylinder was tested only briefly after all of the 12-sided cylinder tests had been completed. It was mounted vertically in the wind tunnel to provide as much clearance between the cylinder and side wall as possible. Only the hot-wire anemometer was used at x = 300%.

Test Results

The results presented in Figures 6 and 7 are only sample runs. Complete results are presented in References 5 and 6.

Reversed flow, which results from separation of the boundary layer from a circular cylinder, was not found to be present in the range of 3 to 9 diameters downstream at any of the test Reynolds numbers ($.17 \times 10^6 < Re < .76 \times 10^6$). Apparently the reversed flow region is confined to the region between the cylinder and the x = 300% station (Fig. 6).

Figure 7 more clearly shows the nature of the velocity defect in the wake. u_1 is plotted at five stations in the wake, where $u_1 = 1 - (u_x/V_\infty)$. As expected, the velocity deficit profile is affected by the nature of the separation from the cylinder. Critical Reynolds number is approximately 400,000. At less than critical Reynolds number, the laminar boundary layer separates at about the 90° position on the cylinder. At greater Reynolds numbers the boundary layer is turbulent and separates downstream of the 90° point resulting in a narrower wake which should be characterized by more turbulence but with a smaller velocity deficit at a given station because of the more effective mixing in the wake.

Figure 8 summarizes these expected effects of Reynolds number on the velocity deficit profiles at x = 300% and 750%. Note that at Reynolds number of 420,000, the wake is not symmetrical on the centerline. This lack of symmetry is apparently due to turbulent separation on one side and laminar separation on the other side of the cylinder. Apparently there was a small difference in the cylinder smoothness so that critical Reynolds number was slightly different for the two sides. Oil dot tests to visualize the separation point appeared to confirm unsymmetrical separation at about $Re = 0.42 \times 10^6$.

The shape of the wake velocity defect was nondimensionalized by plotting $u_1/u_{1_{max}}$ vs. z/z_R, where z_R is the semi-width of the wake. The resulting profiles are compared in Figure 9 with the profile which Schlichting defines at a long distance downstream (greater than 50 diameters--see ref. 3). Figure 9a is for the subcritical wake ($Re \approx .17 \times 10^6$), and Figure 9b is the profile at $Re \approx .76 \times 10^6$. The non-dimensional profiles are quite sensitive to the wake width which is chosen. In both cases the profile approaches the "standard shape" as the wake progresses downstream.

Growth of the wake is indicated in Figure 10. The locus of 50% $u_{1_{max}}$ position spreads at an included angle of about 3° (1.5° to centerline) for the subcritical wake. The supercritical wake (Fig. 10b) starts narrower and the 50% $u_{1_{max}}$ lines diverge at only about 2 degrees.

Turbulence intensity is plotted at the x = 300% station for various cylinder Reynolds numbers in Figure 11. Highest levels of turbulence correspond to high subcritical Reynolds numbers. It is also apparent that turbulence intensity has a double peak--corresponding to the mixing regions. Highest turbulence intensity corresponds to highest $(\partial u/\partial z)$ and lower values of turbulence are at $(\partial u/\partial z) \to 0$ (at the center of the velocity deficit profile and at the edges of the wake).

Turbulence intensities are mapped in Figures 12a and 12b.

As described above, a periodic structure is superimposed on the general turbulence of the wake (or vice-versa). The frequency of this periodic structure is represented in Figure 13 by Strouhal number, where Strouhal number = $S = (fD/V_\infty)$. The variation of Strouhal number with Reynolds number agrees very well with that reported by McCroskey (ref. 2), i.e., below critical Reynolds number, S ≈ 0.2; above Re = 400,000, S increases to greater than 0.4.

In Reference 1, Roshko illustrates the tendency for vortices in a wake to combine, stretching the length of the periodic structure as it moves downstream. This action should change the frequency of the wake in a way which may be significant to the perceived noise of the wake. Figure 14 indicates some shift in the wake frequency as the instrumentation is moved downstream.

When strakes were added, two important results were noticed. The reversed flow (deadwater) region was increased in size extending beyond the 300% station when the strakes were at ±90° (in plane of measurements--see Fig. 15a). Also, the periodic structure of the wake was weaker, or else the general turbulence was stronger, so that any periodic motion was completely immersed in the random turbulence so that no dominant frequency could be measured.

The fact that the reversed flow region extended beyond the 300% station downstream of the ±90° strakes (Fig. 15b) but did not reach 300% downstream of strakes at 0° and 180°, indicates that spiral strakes produce a fairly strong 3-dimensional motion to the wake.

12-SIDED CYLINDER TESTS

Testing

The mounting and testing of the 12-sided cylinders was the same as that of the circular cylinders. The large [0.508 m (20 in.) dia. circumscribed circle, 0.491 m (19.32 in.) dia. inscribed circle] cylinder was tested first. It was immediately obvious that the periodic component of the wake was quite strong. The buffeting wake forced the tunnel dynamic pressure to be limited to less than 1 kN/m² to prevent structural damage to wind tunnel control room windows. Similarly, the strength of the periodic component of the wake of the smaller [18.2 cm (7.17 in.) dia. circumscribed circle, 17.7 cm (6.95 in.) dia. inscribed circle] 12-sided cylinder was greater than for the similar sized circular cylinder. The dynamic pressure of those tests was limited to 2.15 kN/m² because of model and test section wall vibration. Table I lists test ranges.

TABLE I 12-SIDED CYLINDER TESTS

Dynamic Pressure, q [N/m² (psf)]	Reynolds Number (Large Cylinder)	(Small Cylinder)
71.8 (1.5)	0.52×10^6	0.19×10^6
143.6 (3.0)	0.72×10^6	---
87.3 (6.0)	0.98×10^6	0.36×10^6
574.6 (12.0)	1.32×10^6	0.49×10^6
957.6 (20.0)	1.59×10^6	0.60×10^6
1436.4 (30.0)	---	0.68×10^6
2154.6 (45.0)	---	0.77×10^6

The cylinders were tested in two positions with respect to freestream wind direction. With flat sides parallel to the freestream direction (i.e., a flat at the stagnation point) the position was defined as $\alpha = 0°$. Rotated 15°, with a point at the stagnation point, the position was defined as $\alpha = 15°$.

Following testing of the small 12-sided cylinder with sharp corners, it was modified to permit testing with rounded corners to simulate production utility poles. Two sizes of round corners were tested: small radius corners, r = 8.4 mm, r/R = 4.6%, and large radius corners, r = 16.8 mm, r/R = 9.2%.

Test Results

The complete set of wake velocity diagrams and velocity-deficit diagrams are presented in Reference 5; Figures 16 and 17 are representative of the results. The reversed flow region is upstream of x = 200% and considerable velocity recovery occurs between the 200% and 300% stations. Wake growth is shown in Figures 18 and 19. Apparent from these figures is a higher rate of spreading than in the case of a circular cylinder.

Also, the nature of the wake and the rate of wake spreading is more affected by orientation of the cylinder than by Reynolds number. On a circular cylinder the nature of the boundary layer (laminar or turbulent, energy level, etc.) is a function of the Reynolds number. Because of this dependency, the point of boundary layer separation is a function of the Reynolds number; the point of separation is the primary factor affecting the wake geometry.

In the case of the 12-sided cylinder (probably any cylinder having a polygon cross-section), the point of separation is fixed by the corner, not primarily by Reynolds number. The corner, which produces an adverse pressure gradient, will be the point of separation. Thus, the geometry of the wake is fixed by geometry, and is relatively insensitive to Reynolds number. This hypothesis is reinforced by the graph of the Strouhal number presented in Figure 20. The Strouhal number is not a function of Reynolds number; it is approximately constant for given orientation. Turbulence intensity of the 12-sided cylinder wake is of the same order of magnitude as that of the wake of a circular cylinder. However, the strength of the periodic component of the wake motion is much greater for the 12-sided cylinder than for the circular cylinder.

Rounding the corners of the 12-sided cylinder produces two effects: (1) the strength of the periodic component of wake motion appears to be reduced (observed qualitatively, not measured), (2) some dependency on Reynolds number is produced (see Fig. 21).

SUMMARY OF RESULTS

The results may be summarized:

1. The wake downstream of a cylinder has three characteristics which may affect a wind turbine blade passing through the wake:
   a. A velocity deficit compared to the freestream wind,
   b. Random turbulence of wide frequency range and moderate strength,
   c. Low frequency (less than 100 Hz) periodic vibrations.
2. The velocity deficit profile for the near-field is different than the published far-field profiles (e.g., ref. 3).
3. The turbulence associated with the mixing has highest values on both sides of the wake centerline, where (du_1/dz) values are highest.
4. The magnitude of turbulence is about the same for 12-sided cylinders as for circular cylinders.
5. The strength of the periodic component of the wake structure is greater for a 12-sided cylinder than for a circular cylinder.
6. The separation point and geometry of the wake of a 12-sided cylinder is independent of Reynolds number (unlike a circular cylinder).
7. Rounding the corners of the 12-sided cylinder causes some dependence on the Reynolds number and reduces the strength of the periodic motion.
8. Spiral strakes on a circular cylinder can eliminate the periodic motion of the wake--at the expense of increased velocity deficit and turbulence of the wake.

REFERENCES

1. Roshko, A.: "Structure of Turbulent Shear Flows: A New Look," Dryden Research Lecture, AIAA Journal, vol. 14, no. 10, October 1976.
2. McCroskey, W.J.: "Introduction to Unsteady Aspects of Separation in Subsonic and Transonic Flow," AGARD.
3. Schlichting, H.: Boundary Layer Theory, McGraw-Hill, New York.
4. Schetz, J.A.: Injection and Mixing in Turbulent Flow, Volume 68, Progress in Astronautics and Aeronautics, AIAA, 1980.
5. Snyder, M.H., and Wentz, W.H., Jr.: "Characteristics of the Wakes Downstream of Circular Cylinders and 12-Sided Cylinders, as Determined by Wind Tunnel Tests," WER-13, Wind Energy Laboratory, Wichita State University, January 1981.
6. Snyder, M.H., and Wentz, W.H., Jr.: "Wind Tunnel Data--Characteristics of Wakes of Circular Cylinders and 12-Sided Cylinders," WER-13A, Wind Energy Laboratory, Wichita State University, January 1981.

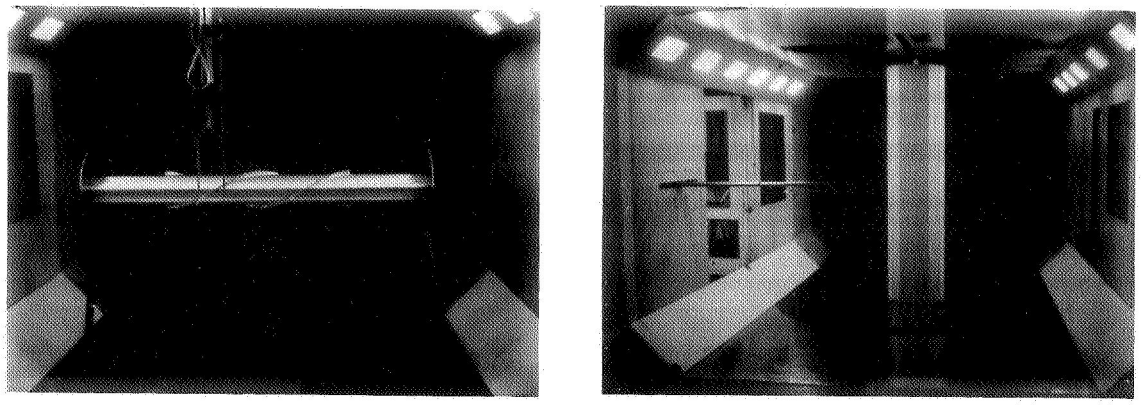

Fig. 1. Cylinders Mounted in Wind Tunnel.

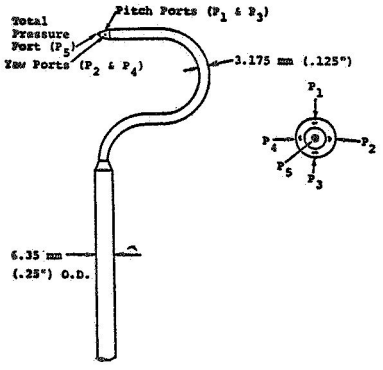

Fig. 2. Five-Tube Probe.

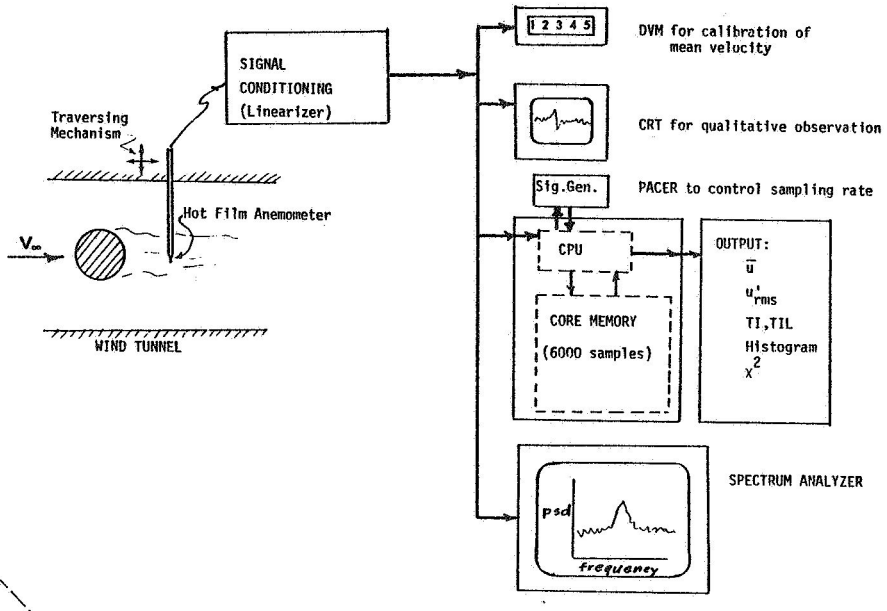

Fig. 3a. Hot Film Data Processing System.

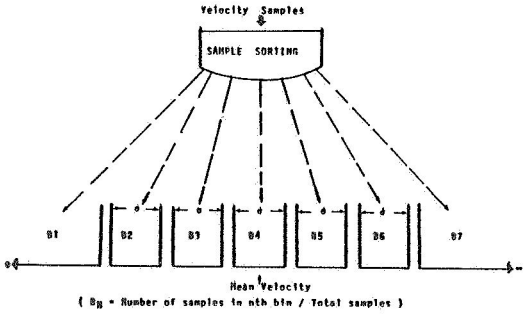

Fig. 3b. Method of Bins.

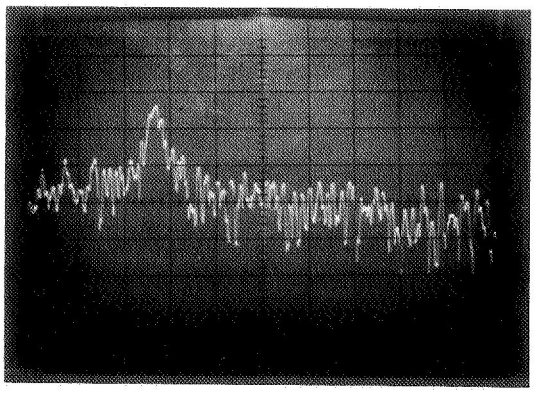

Fig. 4. Typical Spectrum Analyzer Output.

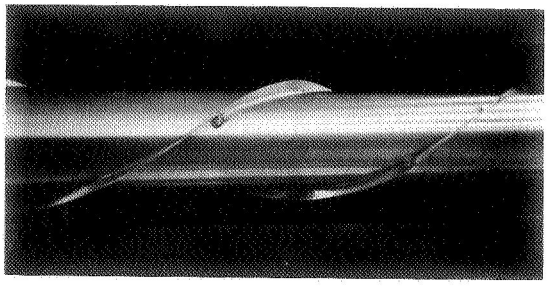

Fig. 5. Strakes on Circular Cylinder.

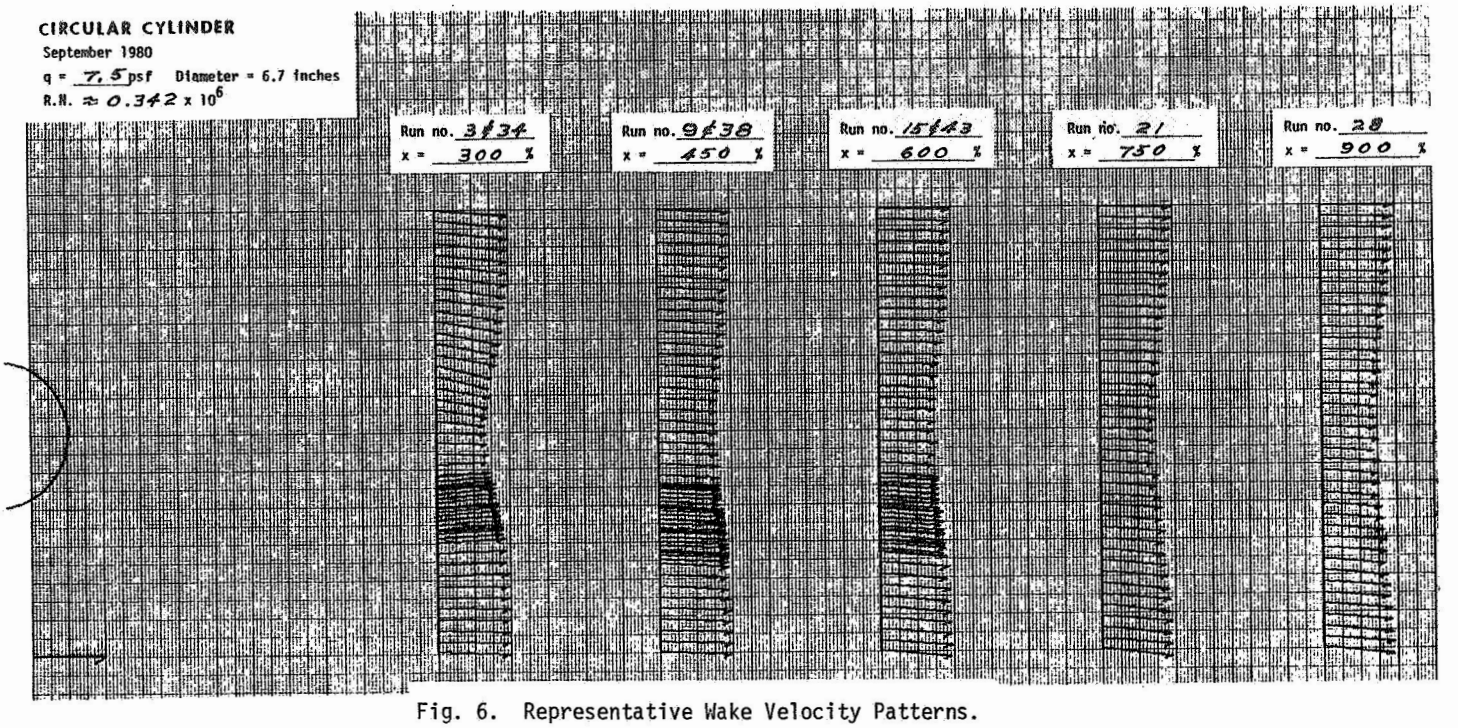

Fig. 6. Representative Wake Velocity Patterns.

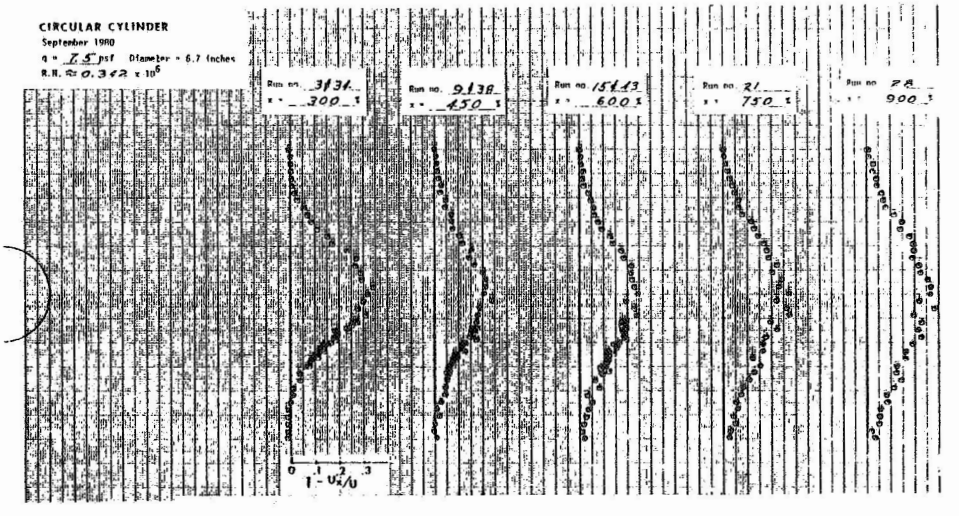

Fig. 7. Representative Wake Velocity Deficits.

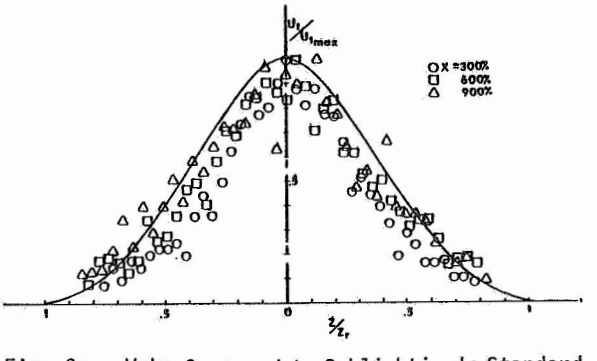

Fig. 9a. Wake Compared to Schlichting's Standard, Re = 0.17 x 10^6.

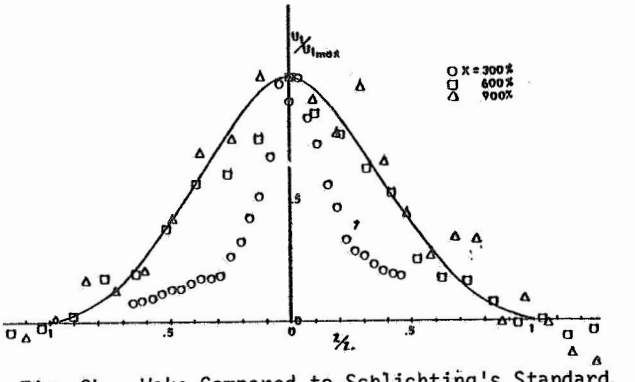

Fig. 9b. Wake Compared to Schlichting's Standard, Re = 0.76 x 10^6

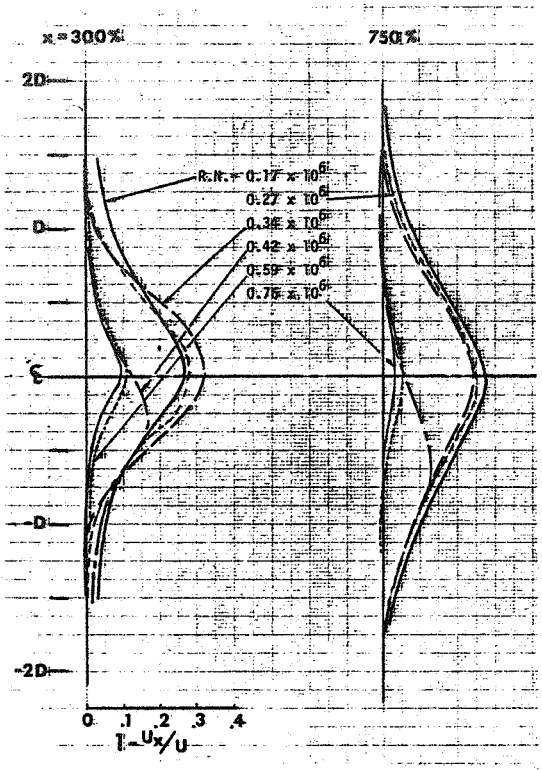

Fig. 8. Circular Cylinder Wake Velocity Deficits.

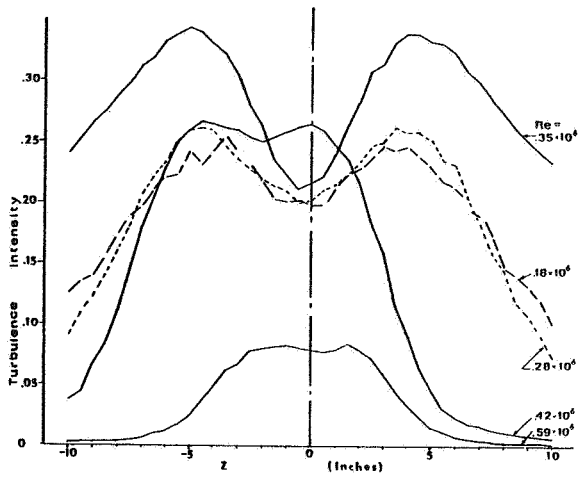

Fig. 11. Circular Cylinder Wake Turbulence Intensity at x = 300%.

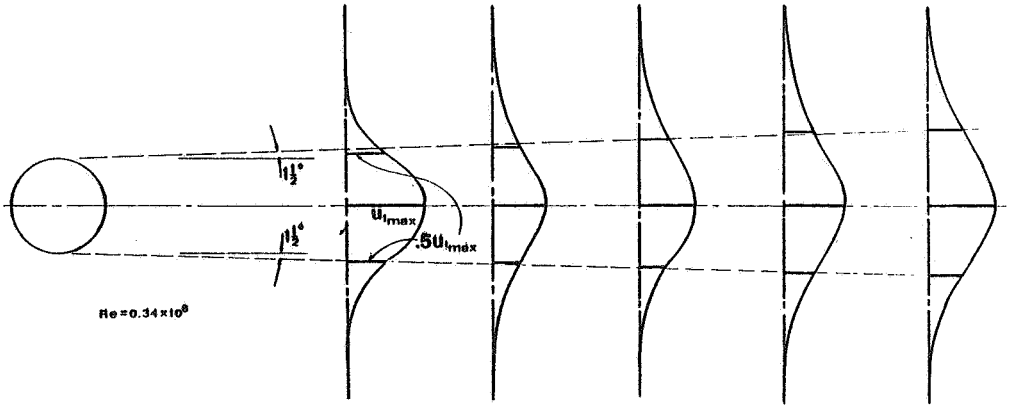

Fig. 10a. Subcritical Wake Growth.

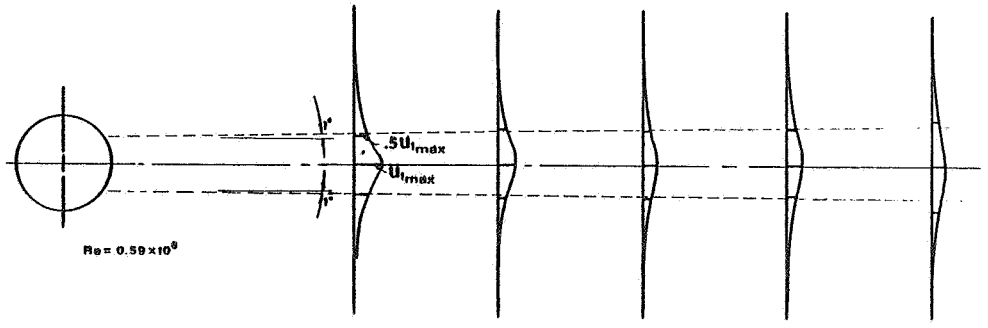

Fig. 10b. Supercritical Wake Growth.

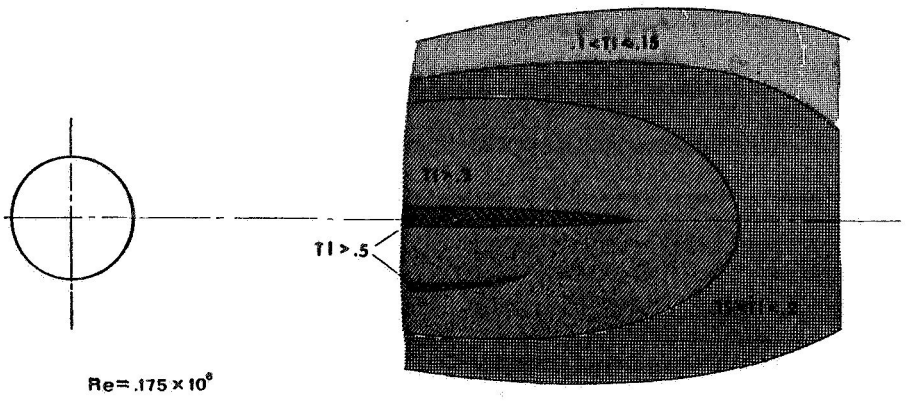

Fig. 12a.

Wake Turbulence Intensity.

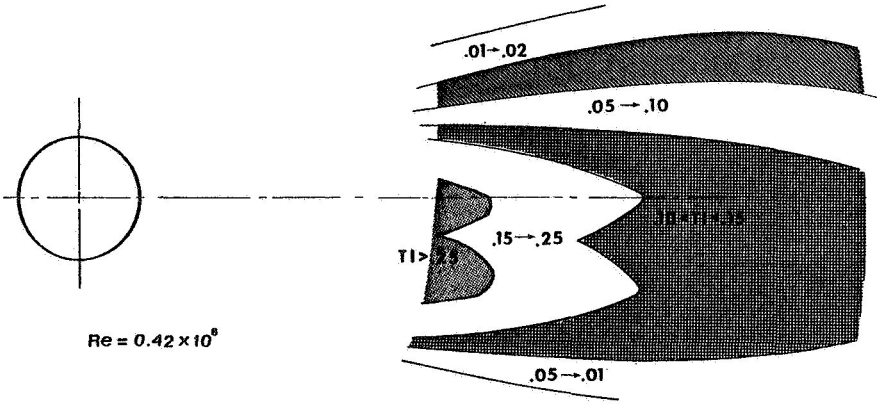

Fig. 12b.

Wake Turbulence Intensity.

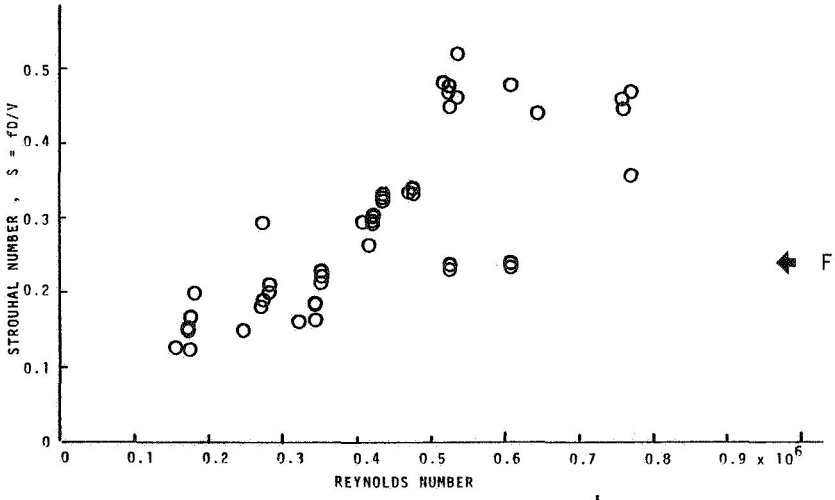

Fig. 13. Circular Cylinder.

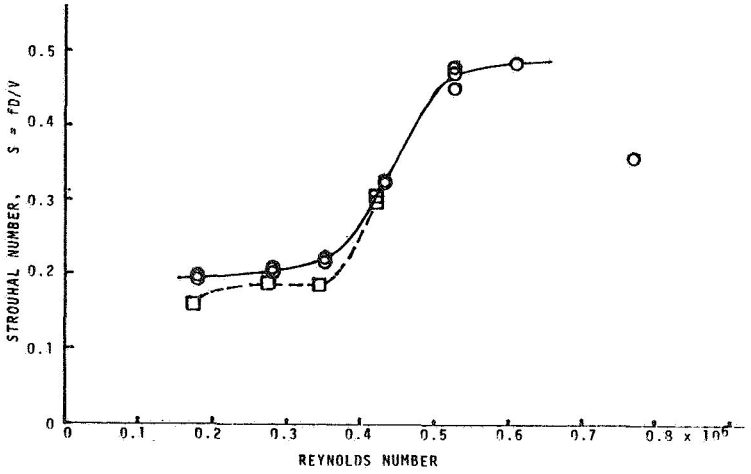

Fig. 14.

Circular Cylinder Wake. Solid curve is at x = 300%, dotted curve at x = 600%.

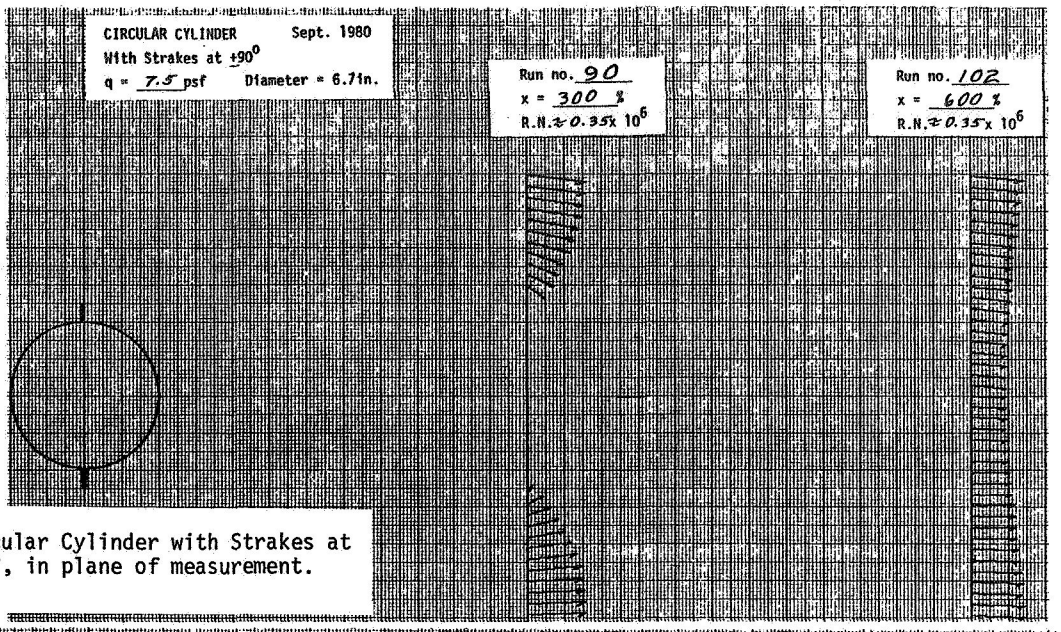

Fig. 15a. Circular Cylinder with Strakes at ±90°, in plane of measurement.

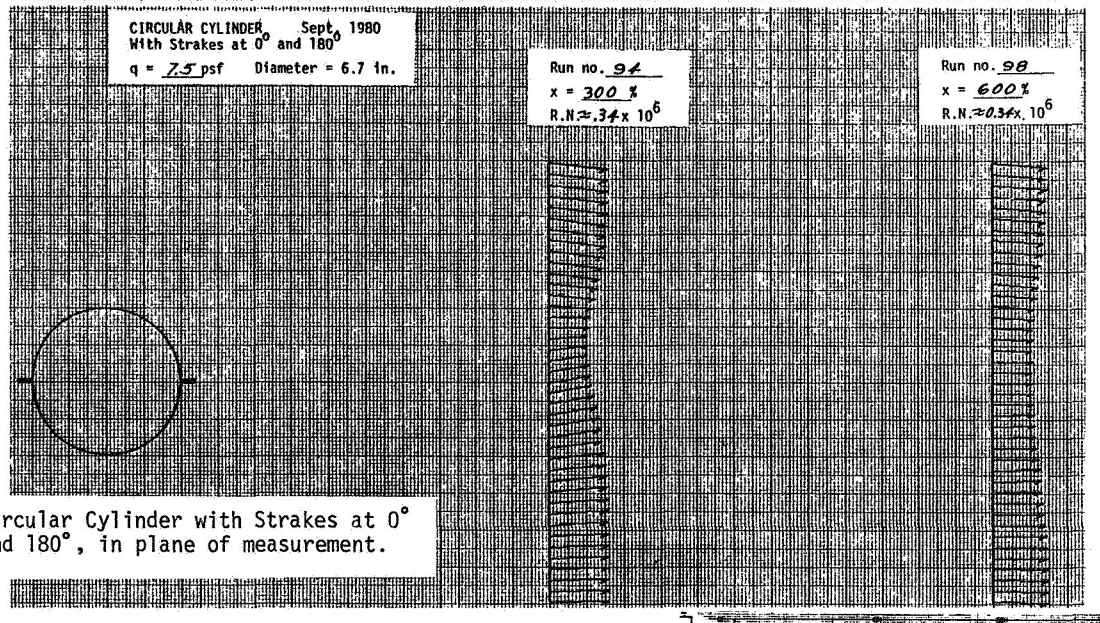

Fig. 15b. Circular Cylinder with Strakes at 0° and 180°, in plane of measurement.

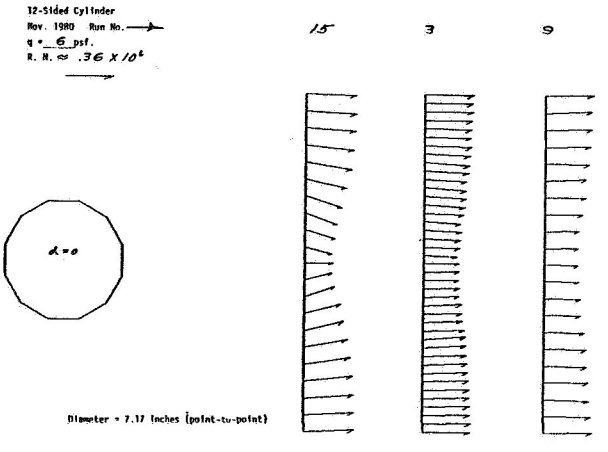

Fig. 16. Velocity Pattern Example.

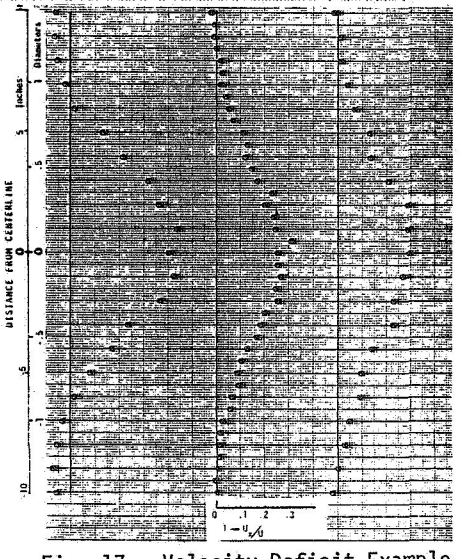

Fig. 17. Velocity Deficit Example.

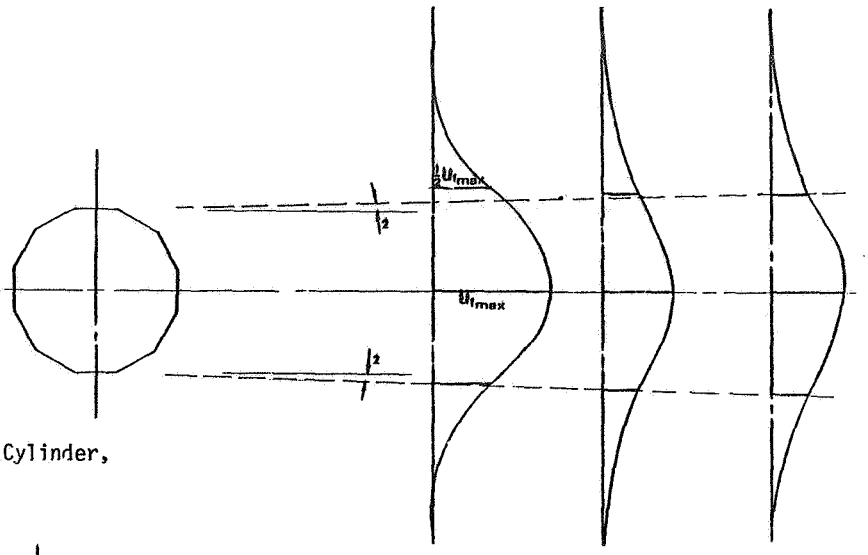

Fig. 18. Wake Spreading, 12-Sided Cylinder, $\alpha = 0$, $Re = .36 \times 10^6$.

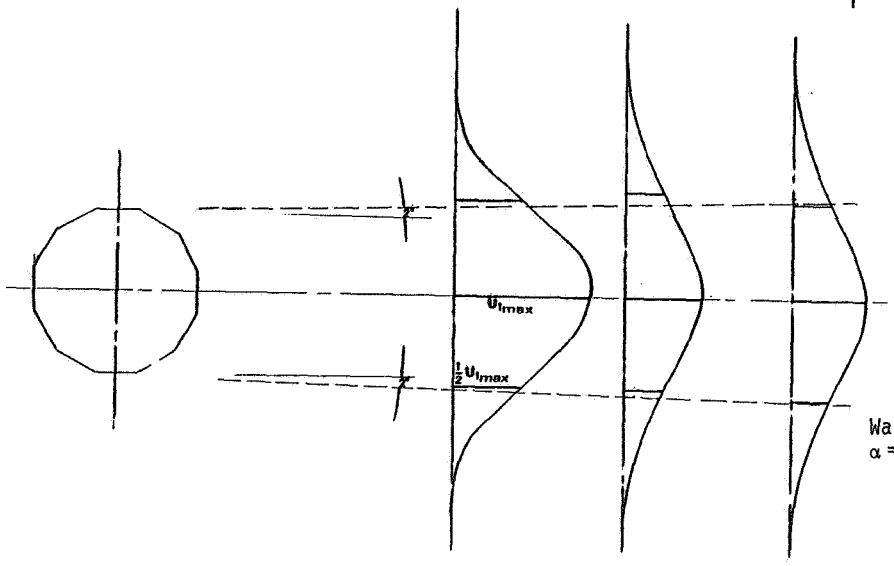

Fig. 19.

Wake Spreading, 12-Sided Cylinder, $\alpha = 0$, $RE = .59 \times 10^6$.

Fig. 20. Strouhal Number for 12-Sided Cylinder.

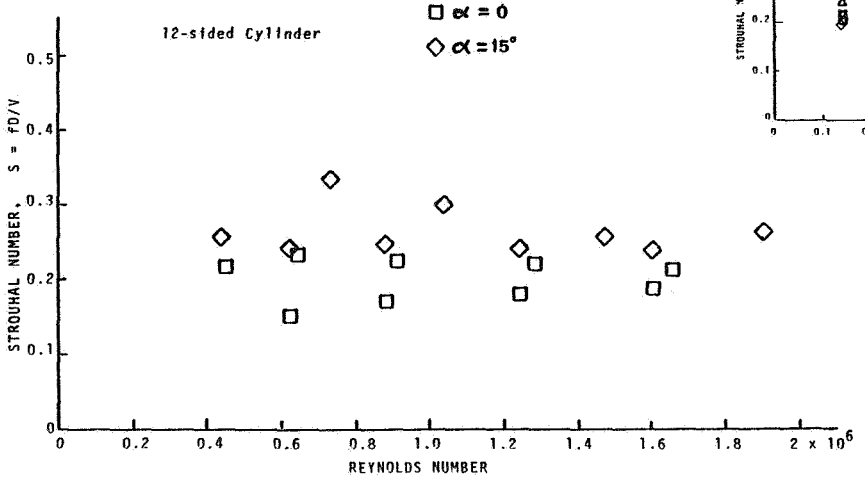

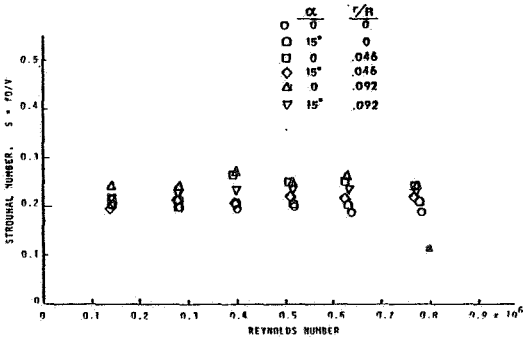

Fig. 21.

Effects of Rounding Corners

QUESTIONS AND ANSWERS

M.H. Snyder

From: R. Spencer

Q: What maximum wake deficit was found downstream of the circular cylinder?

A: *Maximum value of 1 - u_x/u was 1 at the end of the reversed flow region. Had we used a double-film anemometer we could have made measurements in the reversed flow region (possibly as high as 1.2). The high deficiency region smooths out rather quickly--in most cases, by 3 cylinder diameters downstream.*

From: A.C. Hansen

Q: Can you comment on the importance of free stream shear and turbulence to the periodic vortex shedding?

A: *No, we made no measurements in sheared flow. All tests were in the wind tunnel which has a relatively low turbulence factor.*

Some years ago, some of my students worked on problems of pressure distribution on cylinders in sheared-flow fields (analytically and experimentally). There was significant alteration of pressure distribution and streamline pattern. Therefore, I expect that shear will affect vortex shedding. I have not yet tried to apply these results to this problem.

From: Anonymous

Q: Was the low frequency periodic vibration measured on a circular cylinder related to the Strouhal vortex shedding frequency at that Reynolds number?

A: *Yes.*

From: Anonymous

Q: Did you vary the height of the strakes and what is the typical ratio of strake dimension to diameter?

A: *No, we only had time to test one set of strakes, 0.10 high. I plan to do further testing.*

ACOUSTIC NOISE GENERATION BY THE DOE/NASA MOD-1 WIND TURBINE

Neil D. Kelley

Wind Energy Branch
Solar Energy Research Institute
Golden, Colorado 80401

ABSTRACT

The results of a series of measurements taken over the past year of the acoustic emissions from the DOE/NASA MOD-1 Wind Turbine has shown the maximum acoustic energy is concentrated in the low frequency range, often below 100 Hz. The temporal as well as the frequency characteristics of the turbine sounds have been shown to be important since the MOD-1 is capable of radiating both coherent and incoherent noise. The coherent sounds are usually impulsive and are manifested in an averaged frequency domain plot as large numbers of discrete energy bands extending from the blade passage frequency to beyond 50 Hz on occasion. It is these impulsive sounds which are identified as the principal source of the annoyance to a dozen families living within 3 km of the turbine. The source of the coherent noise appears to be the rapid, unsteady blade loads encountered as the blade passes through the wake of the tower structure. Annoying levels are occasionally reached a nearby homes due to the interaction of the low-frequency, high energy peaks in the acoustic impulses and the structural modes of the homes as well as by direct radiation outdoors. The peak levels of these impulses can be enhanced or subdued through complex propagation.

INTRODUCTION

Background

During the fall of 1979, as the DOE/NASA MOD-1 Wind Turbine was undergoing a series of engineering shakedown tests, a number of sporadic and totally unexpected noise complaints were received from a few homeowners living within a 3 km radius of the installation atop Howard Knob near Boone, North Carolina. These complaints came as a surprise since a series of earlier sound measurements taken at the 100 kW MOD-0 wind turbine near Sandusky, Ohio indicated acoustic emissions associated with the machine operation were indistinguishable from the wind-dominated background at distances greater than 200 m (ref. 1). These early reports associated with the MOD-1 were very puzzling since complaints were not received each time the turbine was operated and attempts to correlate the type and location of the complaints with machine operating modes proved inconclusive. It was at this point the NASA Wind Energy Project Office and the SERI Wind Energy Branch entered into a cooperative effort to document and establish the source of the annoyance with the ultimate objective being the implementation of a suitable mitagation procedure as soon as practical.

The Nature of the Complaints

It should be pointed out, while the general character of the complaints has not changed materially from the initial reports received, the total number of families known to be affected has not increased above the dozen identified within the first few months, even though more than 1000 families live within the 3 km radius. Thus it is many of the same families being annoyed at various times, some more often than others. Figure 1 shows the location of the complainant homes with respect to the wind turbine and also indicates those locations reporting a higher frequency of annoyance.

Most homeowners describe the annoyance as consisting of periodic "thumping sounds and vibrations" similar to the sensation of having someone walk heavily across a porch or hearing a heavy truck passing with a flat tire. Some have reported the rattle of loose picture frames or small objects and most agree the noise level is greater inside their homes than out. Most complainants site the periodicity of the sounds and vibrations as being the most annoying aspect with the level becoming louder and more consistent during the evening and nighttime hours.

The SERI Program

In cooperation with NASA, the SERI Program has had as its objectives the identification of the physical mechanisms responsible for the generation of the noise, its propagation to the homes below, the resulting subjective responses and development of suggestions for methods to mitagate the annoyance. These resulting mechanisms must adequately explain the following questions regarding the perceived characteristics of these sounds:

1. Why is it the noise does not reach annoying levels each time the turbine is operated?

2. Why are some families annoyed more often than others and why does the situation confine itself to such a tiny fraction of the overall population potential?

3. Why does the noise appear more noticable inside the homes and why does it become more consistent and perhaps louder during the evening and nighttime hours?

The purpose of the SERI effort goes beyond the specific noise situation associated with the MOD-1 and the knowledge gained will be applied to provide definitive noise evaluations and predictions for sound levels and annoyance potentials for a number of generic wind turbine designs.

THE PROCEDURE OF THE INVESTIGATION

As a result of the initial assessment of the situation, it was recognized the problem has three major components; i.e., the actual noise generation process which was suspected to be aeroacoustic in origin, the propagation of low-frequency sound in complex terrain, and the annoyance-generating mechanisms in the affected homes. Efforts were initiated with the MIT Department of Aeronautics and Astronautics for development of analytical techniques for assessing the physics of the sound generation and the Pennsylvania State University for investigating the propgation aspects. The initial results of these activities are being reported separately (refs. 2 and 3).

The need for a definitive set of physical measurements which documented the acoustics characteristics of the sounds, the atmospheric structure present and controlling the propagation, and the structural and ground motions of affected houses was recognized and considerable effort has been mounted towards this end. Further, the scope of these activities has extended beyond the MOD-1 and additional measurements have been performed using the MOD-0 and a small wind turbine installed at the Rocky Flats Test Center near Golden, Colorado in order to obtain important supporting data.

Measurements

Two major field studies have been accomplished during the past year. The first (March 1980) acquired both near- and far-field acoustic and house structural motions data during an actual annoyance episode. In addition, two acoustic sounders and two tethered balloon systems were employed to gain information on the vertical structure of the atmosphere to assess the propagation of the turbine sounds. The locations of this equipment is shown in Figure 1. The second study investigated the acoustic emissions at both 35 and 23 rpm under loaded conditions but only in the acoustic near-field (June 1980).

Data Reduction and Analysis

The supporting turbine operating data; i.e., blade pitch, rotor position, and nacelle yaw angles, generator output, and hub-height wind speed, were digitized and stratified into 2-3 minute records which exhibited relatively stationary statistics. The near-field acoustic data corresponding to these periods were analyzed by both frequency and time domain methods. The former was accomplished using a standard 800-line, narrowband FFT spectrum analyzer. Impulses found in the acoustic signal were analyzed with the spectrum analyzer in the time domain mode and under computer control to process sample estimates of various waveform criteria such as pulse risetime, riserate, total energy content, and peak overpressure. The dual-channel, 400-line mode of the analyzer was used to study the dynamic interactions between the pressure fields and the house structural motions.

RESULTS

Turbine Acoustic Emissions

Analysis of the near-field acoustic signals has shown the emissions can be composed of at least three types of acoustic energy which can exist in different proportions depending on the characteristics of the winds blowing by the turbine. Figure 2 illustrates a sound pressure frequency spectrum in which two of the three posible types of acoustic emissions are represented. This spectrum is composed of mostly broadband, incoherent rotor noise with a few discrete tones out to about 10 Hz and two distinct tones at 60 and 79 Hz whose source are the mechanical and electrical equipment of the turbine. The low frequency discrete tones are the reflection of unsteady loading on the blades as they move around the rotor disk and are brought about by such factors as wind shear and tower shadow induced velocity gradients (refs. 2 and 4). Figure 3 depicts the corresponding pressure-time plot of a portion of the period used to obtain the average of Figure 2. The period represented encompasses two complete rotor revolutions and two passages by the tower for each blade. The wind speed at hub height was 9 m/s (20 mph) and rather steady in character.

The existence of strong, highly coherent impulses imbedded in the normal, broadband rotor noise is illustrated in Figures 4 and 5. Figure 4 displays the pressure-time history plotted over two blade revolutions. Compare the sharpness and the higher peak overpressures of these pulses with Figure 3. Figure 5 plots the corresponding averaged, sound pressure spectrum for this period. Note the many, many discrete tones extending all the way out to 100 Hz! The wind speed during this period was approximately 11 m/s (25 mph) and was more gusty than the wind characteristic for the period of Figures 2 and 3. Figures 6 and 7 increase the time resolution for these same pressure-time plots allowing a comparison of the waveforms in greater detail. The more gentle trace of Figures 3 and 6 was made when the rotor was parallel to the SE flat of the support tower; that of Figures 4 and 7, as the blade passed slightly closer to the tower leg while perpendicular to the tower N-S diagonal. The blade came slightly closer to the tower leg (5 leg diameters) while near the N-S axis as compared with the 7.5 diameters while parallel to the tower flat.

Figure 8 illustrates a pressure-time history similar to Figures 4 and 7 but this impulse was received outside of House #8 which is about 1 km to the ESE and about 300 m lower in elevation than the turbine. The home at this time was experiencing what was described by SERI personnel in the house as "very heavy thumping" and confirmed by the residents, two of which were present. The rotor was slightly oriented closer to the south leg of the tower but almost parallel to the SE flat as in Figures 2 and 3. The wind at the turbine site was 11-13 m/s (25-30 mph) and gusty. Notice this plot shows two major downward-traveling pulses. If one measures the time delay between them (81 msec) and computes the linear distance corresponding to this delay for a tip speed of 111 m/s (35 rpm) is 9.3 m (31 ft). The tower leg separation at this point is 9.5 m (31 ft).

From the preceeding, whatever is producing these large excursions in the acoustic pressure field is taking place in the lee of the 0.5 m diameter tower legs and the source of the low-frequency "thumping" sounds reported by the residents. Coherent pulses of this type are best evaluated using energy techniques which involve analysis in both the time and frequency domains. The time domain is used to establish waveform characteristics of the impulses; i.e., the risetime, riserate, total energy content, and peak overpressure. The frequency domain allows the determination of the frequency distribution of the impulse energy. Figure 9 plots the energy distribution with frequency for the time history shown in Figure 8.

A total of over 75 series of impulses have been processed using the SERI time domain program and the results correlated with turbine operating parameters. The results of this analysis can be summarized as follows:

1. The peak overpressure and riserates are most highly correlated with windspeed, rotational speed (rpm), and the blade-to-tower leg distance.

2. Little or no correlation could be found with generator output (machine loading) since peak overpressures could be found which were as high or higher unloaded.

Figure 10 summarizes the variation of impulse peak overpressure as a function of wind speed. Note the tendency for two groupings of data points about 10 dB (re 20 μPa) apart. Many of the points representating data taken at 35 rpm lie near the upper curve and those at 23 rpm near the lower, but not all!

Propagation

The Penn State work has concluded the following (ref. 3):

1. Due to the extremely low atmospheric attenuation for sound frequencies below 100 Hz, high levels of such noise generated by wind turbines which are "unacceptably" above local ambient may produce unacceptably high noise levels in the far field due to meteorologically dependent atmospheric refraction.

2. The intensity, duration, and location of enhanced (or subdued) far-field noise levels cannot be predicted without very high resolution meteorological data (wind speed and direction, vertical shear, and thermal parameters) and therefore suppression of the noise source appears to be the only, long-term, viable solution.

3. The conditions responsible for optimum power generation at the MOD-1 site are also the ones most likely to produce adverse noise propagation.

4. Airborne propagation controlled by atmospheric refraction is the primary transmission mechanism to the homes below and surface and ground propagation is negligible.

House Acoustics and Vibration

In order to address the manifestation of both low-frequency sounds and vibration, a detailed analyis of recorded acoustic and vibration data taken at two of the residences during the March 1980 tests has been accomplished. These homes include a double-wide, mobile structure (House #7 in Figure 1) and a two-story, frame building (House #8). These particular homes were chosen in view of the high frequency of annoyance reported by the families. Acoustic measurements using special, low-frequency microphones were taken simultaneously inside and closeby outside. Vibration data using seismic-range sensors included both vertical and horizontal floor and single-axis window accelerations. The measurements in each home were located in the room in which the residents had decided the noise was most noticeable. Both homes were equipped with storm windows but the frame house was substantially tighter.

From the description of the complaints, it was suspected the "thumping" sounds heard inside the houses were being re-generated by the interaction of the acoustic impulses from the turbine and the physical structure of the house. It also has been suggested the sounds heard are largely the result of the direct radiation in the 20-50 Hz band. To establish the acoustic absorbtivity as a function of frequency the cross-correlation of the inside and outside sound pressure levels was established using the technique of coherent power (coherent power = coherence x autospectral density of indoor sound pressure signal, ref. 8). Figure 11 shows the major coupling through the walls and support structure of House #7 occurs in the 7-14 and 20-26 Hz bands with a narrow band at 62 Hz. In contrast, House #8 exhibits the maximum direct coupling only in the lower 7-14 Hz band, as indicated in Figure 12.

The structural resonances of the homes were determined by either exciting the structure through a rapid door close or by recording background vibration levels for several hours. Tables 1 and 2 summarize the major normal and cross-coupling resonances in the 0.2 to 100 Hz range. The confirmation that most sounds were being re-generated by the structure under impulsive acoustic loads was accomplished by measureing the time delay between the arrival of the peak impulse at the outside microphone and the initial onset of sound energy peaks in the 10-20 Hz, 31.5, 63, and 125 Hz octave bands measured in the subject room. The physical separation between the outdoor microphone and the indoor was about 23 m with the outdoor closer to the wind turbine. This separation would account for approximately a 73 msec delay between microphones at this altitude and air temperature. The actual delay, which is illustrated in Figure 13 for the 63 Hz octave vibration band, has been determined to be in the range of 120-125 msec or about 40% longer than would be expected from propagation in air alone. Thus much of the acoustic energy impacting the house and not being initially reflected is being stored in the structure as stresses, a portion of which is subsequently re-radiated as sound at frequencies where the modal damping is small. The coherent power plots of Figures 11 and 12 indicate the transmission of sound energy into the house is dispersive due to the

frequency dependency of the transmission and not simply pure delay. The peak re-radiated sound pressure level has been found at 65 Hz for House #8 which corresponds to a very lightly damped mode as is shown in Table 2. The maximum instantaneous vibration levels have been found to be in the 8-20 Hz band corresponding to the two lowest frequency modes in Table 2.

Whether or not the structural modes listed in Tables 1 and 2 will be excited under impulsive, acoustic loads depends on the frequency distribution of the impulse energy impacting the structure. Figure 9 depicts the actual energy distribution of a single impulse recorded during a period which was described to be highly annoying, a time when the turbine was operating at 35 rpm. It should be noted the major spectral peaks of Figure 9 reside at 10.8 and 25.1 Hz both of which correspond to the broad 8-12 and 26 Hz modes in Table 2. Thus, the positioning of these spectral peaks and their respective amplitudes are very important in determining what modes may be excited and contribute to the coherent generation of both sound and vibration levels. Using pulse analysis techniques and a typical, average sound pressure frequency distributions for 35 and 23 rpm spectra, a list of the preferred spectral peak frequencies has been determined and is listed in Table 3. It is interesting to note that many of the structural resonances found in Homes #7 and #8 agree quite closely with four frame test houses used as part of sonic boom and aircraft fly-over noise investigations (ref. 7).

DISCUSSION AND CONCLUSIONS

The lowering of the turbine rotational speed from 35 to 23 rpm, as is indicated in Table 3, primarily results in a shifting of the preferred spectral peaks to lower frequencies. From pulse analconsiderations, the relative distribution of energy or the positioning of spectral peaks of such energy is controlled by the pulse width or duration. The repetition frequency,or blade-passage frequency in this case (which is determined by the rotational speed) has very little effect. A typical pulse width for a series of short impulses at 35 rpm typically lasts about 100 msec and increases to 123 msec at 23 rpm. The relative distribution of energies or peak amplitudes is determined by the combination of peak value or overpressure and the risetime; i.e., riserate. Thus the downward shift in frequency and the reduction in peak energies in some of the higher frequency modes is due to:

1. the increased residence time of the blade in the tower leg wake which increases the pulse duration, and
2. the reduction in the peak overpressure is due to a smaller aerodynamic loading of the blade as a result of the slower rotational speed and decreased static lift and therefore smaller maximum values to interrupt by a still undefined unsteady aerodynamic process.

The magnitude of the riserate, when viewed in terms of unsteady aerodynamics, reflects the change in lift above static values due to rapid, local attack angle fluctuations (refs. 5 and 6). Thus the pressure-time history of the acoustic signals may be thought to indicate the characteristics of the rapid changes in blade loads (and therefore in acoustic radiation) as the blade cuts through intense horizontal velocity gradients in the wake of the tower legs. The existence of such intense gradients has been verified by hot-wire anemometer measurements in a tower wake of similar dimensions belonging to a small wind turbine which is also capable of producing impulsive sounds under certain turbulent inflow conditions not yet fully understood.

The plot of peak overpressures against windspeed in Figure 10 suggests that some form of a bimodal process or forcing is taking place since it is possible for an impulse at a given rotational speed and wind velocity to assume either a higher or lower level separated by about 10 dB. Thus impulses which may not be causing any annoyance at one point in time may suddenly change levels at the same windspeed and begin to bother some homes. This has been observed to occur during the measurements of March 31, 1980. This would indicate stronger, transient velocity gradients are occassionally superimposed on the much weaker, mean velocity deficit flow field. Work by Sato and Kuriki (ref. 9) on the wake transition of a thin, flat plate in parallel uniform flow has shown the existence of three distinct subregions for transition regime flow. They found the intensity of the velocity fluctuations in a wake could be amplfied exponentially when artificial excitation at predominant shedding frequencies was introduced in what they describe as the linear and nonlinear transitional subregions. If true for a cylinder, this excitation could be a predominance of turbulent eddies in the inflow whose dimensions correspond to a frequency near the Strouhal shedding frequency of the tower legs. This possibility has not been able to be confirmed with the MOD-1 due to the upper frequency response limitations of the wind sensing equipment, but visual evidence in comparing the impulse and turbulence characteristics does indicate some connection. Since the small wind machine at Rocky Flats exhibits some of the same characteristics, hot-film measurements of the inflow and wake regions will be undertaken in the near future to examine this hypothesis.

From the above discussion and the observations of Figure 9, the impulses being generated in the tower leg wake must be the result of time-dependdent velocity gradients and not just a pure deficit since by definition such a deficit should be only a function of the upstream velocity. The MIT calculations have shown impulse-type sound pressure fluctuations can be predicted by using a mean wake as determined from wind tunnel tests, but the model fails to reproduce the important rapid riserates observed. What is important, however, is the model confirms impulses can be produced by the tower wakes (ref. 2) but a more realistic velocity distribution is necessary to reproduce the actual observations.

In summary, the following conclusions are drawn from the analysis of the collected acoustic and structural data:

1. The primary source of annoyance of nearby residents are the short bursts of acoustic energy associated with impulses being generated by a yet-to-be-defined unsteady aerodynamic process. This process involves the turbine blade interaction with a transient level of wake instability and resulting intensity of velocity fluctuations and horizontal gradients in the wakes of the legs.

2. The impulses are propagated entirely through an airborne path and subjected to atmospheric refraction effects which can enhance (or suppress) the level over normal, geometric spreading due to strong vertical and horizontal gradients of wind velocity and atmospheric thermal parameters.

3. The primary annoyance mechanism in the houses affected is the coupling of low-frequency impulse energy to lightly damped structural modes and the resulting vibration and re-generated acoustic emissions at the excited modal frequencies. From all appearances, the annoyance generated in House #8 is composed of a coherent excitation of low-frequency vibration at the 8-10, 14, and 26 Hz frequencies simultaneously with audible acoustic radiation at 60 and 65 Hz.

4. The potential for annoyance appears to be greater for House #7 due to the poorer acoustic absorption or increased transmissivity and the number of lightly damped structural modes.

5. From the evidence compiled to date, the only sure way to stop the annoyance under all conditions is to prevent any impulses generated from reaching annoying levels. This would mean reducing the tower wake velocity gradients to a point where the result would be similar to the spectral pressure-time plots of Figures 2 and 3. From the evidence at hand, it is necessary to destroy the organized, two-dimensional vortex flows thought to be developing in the lee of the tower legs by some form of aerodynamic spoiling device.

ACKNOWLEDGEMENTS

The cooperation and assistance of the NASA Wind Energy Project Office, the General Electric Company, and the Blue Ridge Electric Membership Corporation is gratefully acknowledged. Special thanks are given to the residents of Boone, North Carolina and specifically the residents near the MOD-1 who aided us in this investigation. The efforts of the SERI staff: Ed McKenna, Carol Etter, Dick Garrelts, Stan Thues, Chris Linn, Bob McConnell, and Jane Ullman contributed significantly. Ben Bell is acknowledged for his development of the time domain analysis program. The work was supported by the DOE Wind Energy Systems Division.

REFERENCES

1. Balombin, J.R.: An Exploratory Survey of Noise Levels Associated with a 100 kW Wind Turbine. NASA TM-81486, Lewis Research Center, Cleveland, OH. 1980.

2. Martinez, R., S.E. Widnall, and W.L. Harris: Predictions of Low-Frequency Sound from the MOD-1 Wind Turbine. FDRL Report No. 80-5, Massachusetts Institute of Technology. 1980, 77p.

3. Thomson, D.W.: Analytical Studies and Field Measurements of Infrasound Propagation at Howard's Knob, NC. Department of Meteorology, The Pennsylvania State University. 1980, 36p.

4. Homicz, G.F., and A.R. George; Broadband and Discrete Frequency Radiation from Subsonic Rotors. Journal of Sound and Vibration, Vol. 36 (2), 1974, pp 151-177.

5. Wright, S.E.: Discrete Radiation from Rotating Periodic Sources. Journal of Sound and Vibration, Vol. 17(4), 1971, pp 437-498.

6. Ericsson, L.E. and J.P. Reding: Unsteady Airfoil Stall Review and Extension. Proceedings of AIAA 8th Aerospace Sciences Meeting. AIAA Paper No. 70-77, New York, NY, 1970, 10p.

7. Carden, H.D. and W.H. Mayes: Measured Vibration Response Characteristics of Four Residential Structures Excited by Mechanical and Acoustical Loadings. NASA TN D-5776. Langley Research Center, Hampton, VA. 1970, 59p.

8. Bendat, J.S. and A.G. Piersol: Engineering Applications of Correlation and Spectral Analysis. Wiley (New York), 1980, p. 68.

9. Sato, H. and K. Kuriki: The Mechanism of Transition in the Wake of a Thin Flat Plate Placed Parallel to a Uniform Flow. Journal of Fluid Mechanics, Vol. 11, 1961, p. 351.

TABLE 1

MAJOR NORMAL AND COUPLED STRUCTURAL MODES OF HOUSE #7

Frequency (Hz)	Floor Modal Damping Characteristics Vert	Horiz	Cross	Window Mode Damping	Cross[a]
8.6*	L[b]	M	M[c]	M	M
20	M	L	S	L	S+
30	L	VL	S+	M	S+
59	L	M	M	L	M
79	L	M	M	L	M
89	VL	M	S	L	S
96	VL	M	M	M	M

TABLE 2

MAJOR NORMAL AND COUPLED STRUCTURAL MODES OF HOUSE #8

Frequency (Hz)	Floor Modal Damping Characteristics Vert	Horiz	Cross	Window Mode Damping	Cross
8.9*	L	L	S	VL	S+
14	L	L	S		
21	M	L	S		
26	L	L	S		
32				L	W
50	VL	VL	S+	L	M
60	VL	VL	S+	L	S+
65	L	VL	S+		

*estimated to be house fundemental resonant frequency

[a]Cross coupling with floor vibrations

[b]Damping: VL = very light, L = light, M = moderate

[c]Degree of cross-coupling: W = weak, M = moderate, S = strong

TABLE 3

PREFERRED SPECTRAL PEAKS FOR TYPICAL IMPULSES

35 RPM

Frequency (Hz)	Relative Level (dB)
6.25	0
16.25	-9
26.25	-23
45.0	-39
62.5	-47
81.3	-51
97.3	-55

23 RPM

4.4	0
10.6	-9
17.5	-15
25.6	-29
30.6	-38
38.8	-44
51.9	-47
65.0	-55

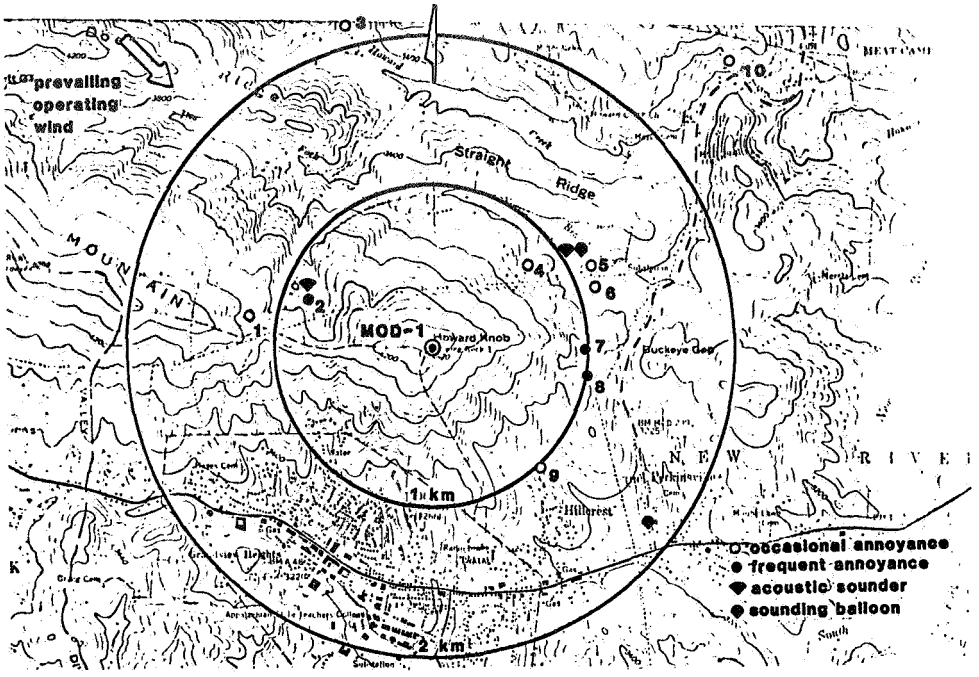

Figure 1. Map showing area surrounding MOD-1, complainant homes, and location of atmospheric measuring equipment for March 1980 test series.

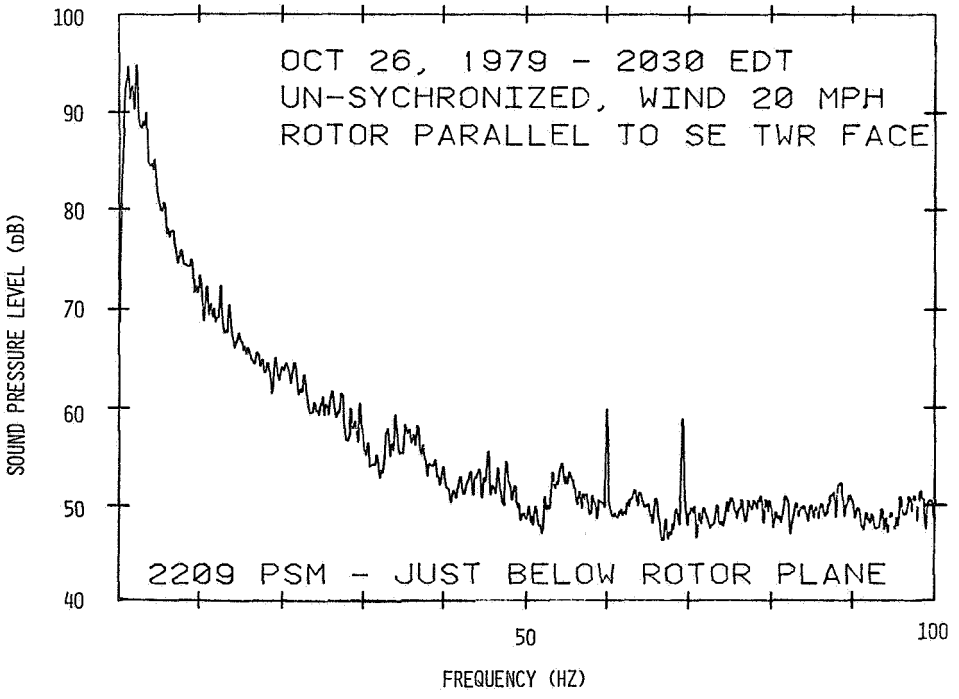

Figure 2. Sound pressure spectrum of MOD-1 acoustic emission with no impulse present.

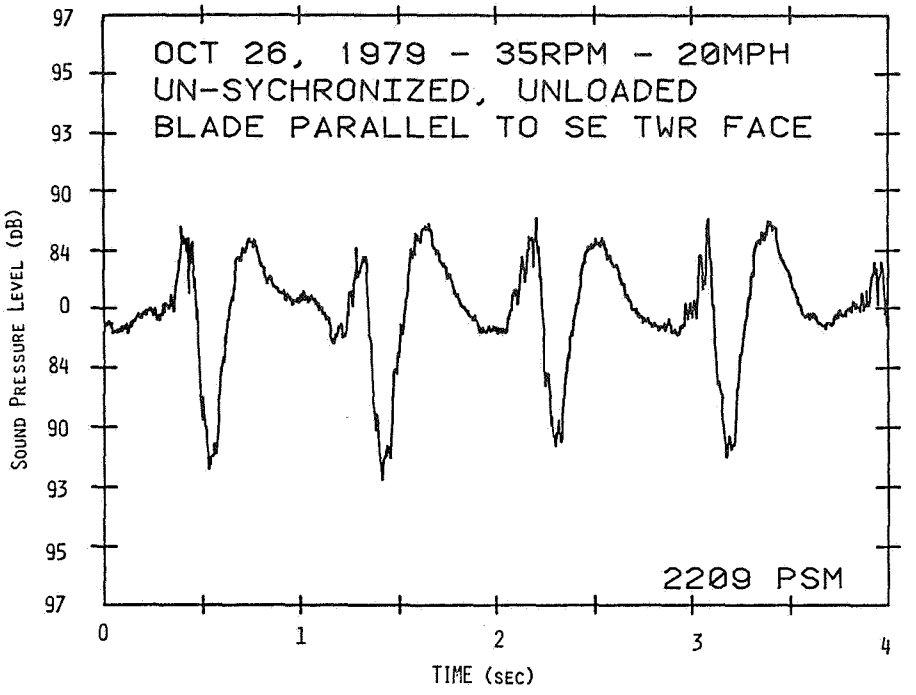

Figure 3. Pressure-time history of acoustic signal of Figure 2. Two complete rotor revolutions.

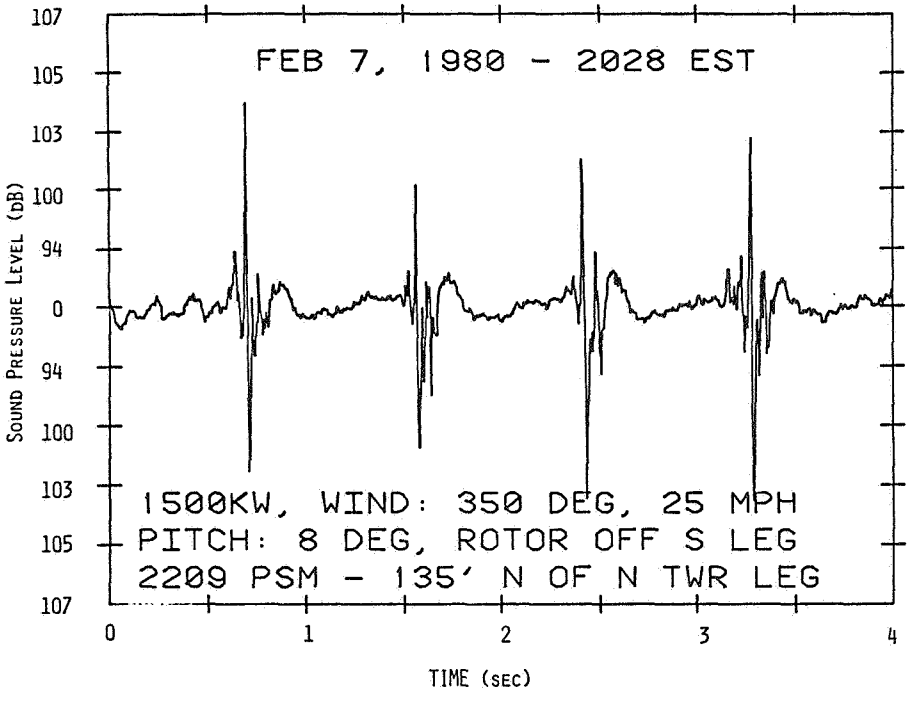

Figure 4. Pressure-time history of strong impulses. Two complete rotor revolutions.

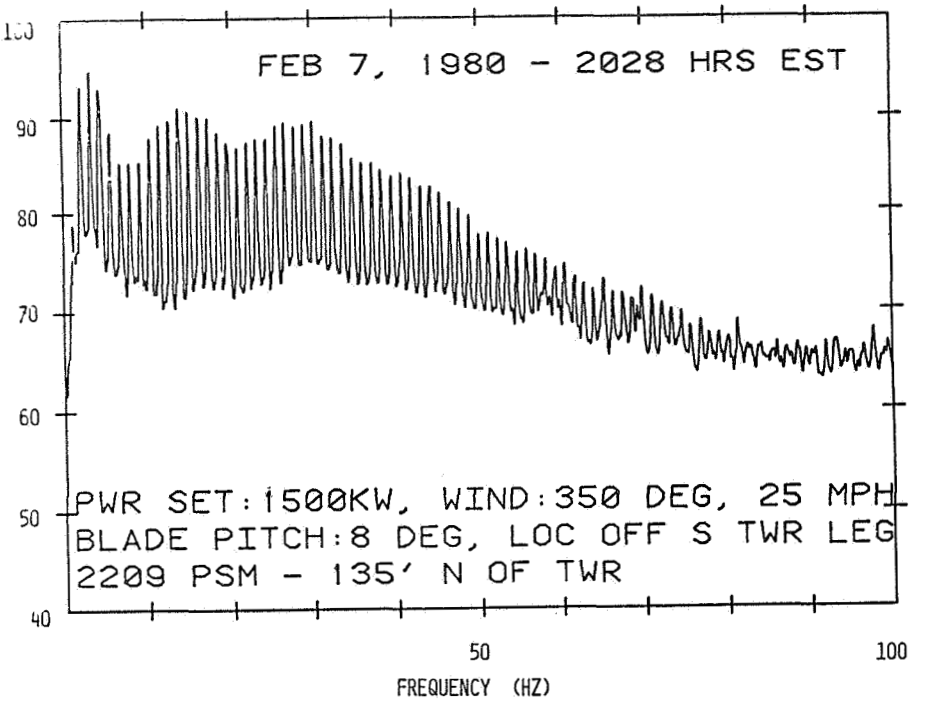

Figure 5. Sound pressure spectrum of MOD-1 acoustic containing strong impulses of Figure 4.

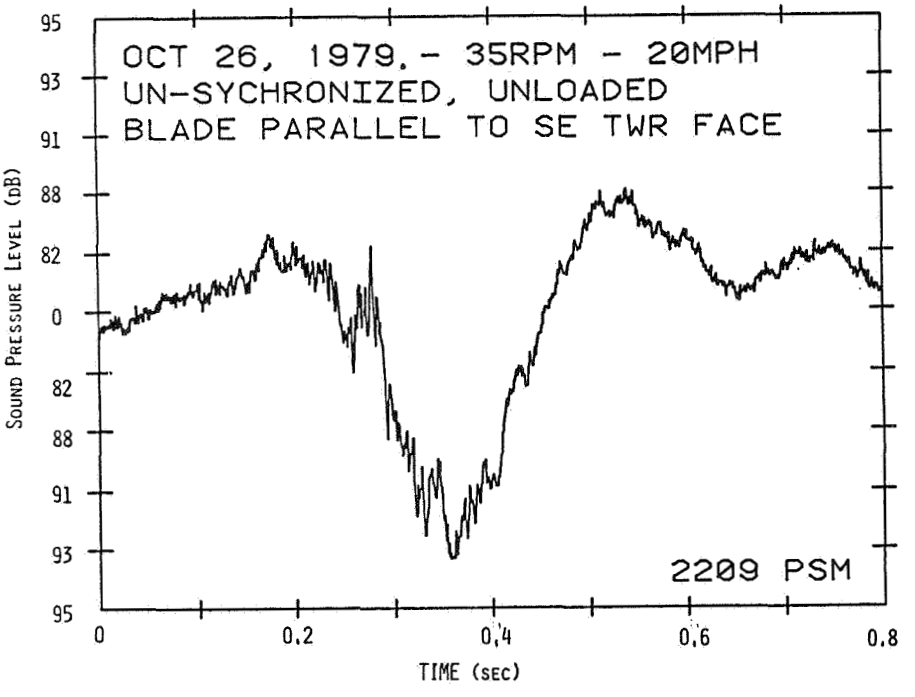

Figure 6. Detail of pressure-time history of Figure 3 for a single blade passage by the tower.

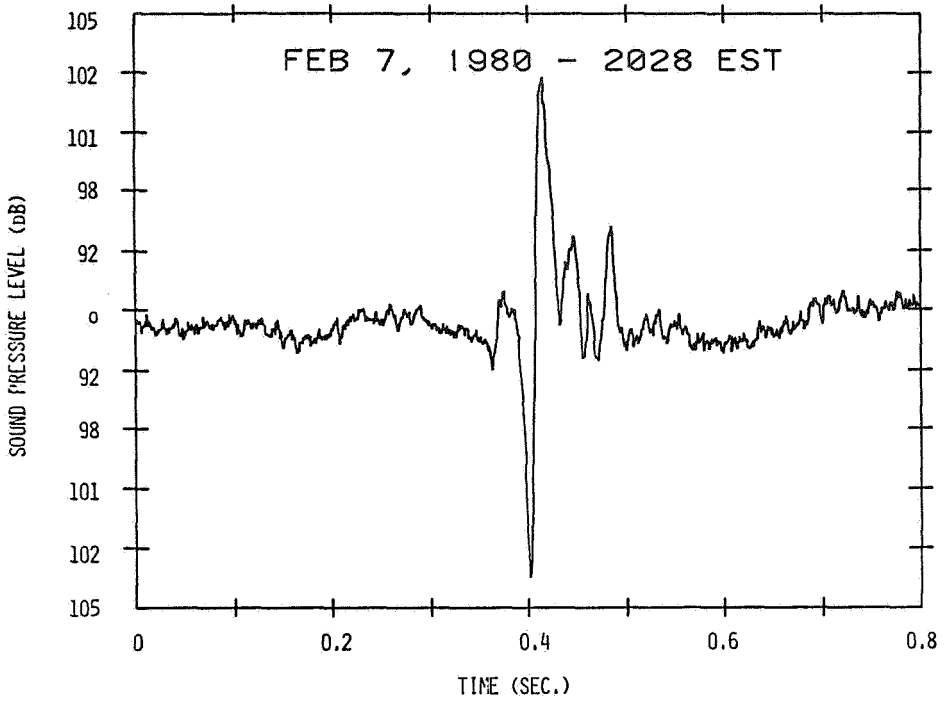

Figure 7. Detail of pressure-time history of Figure 4 for a single blade passage by the tower.

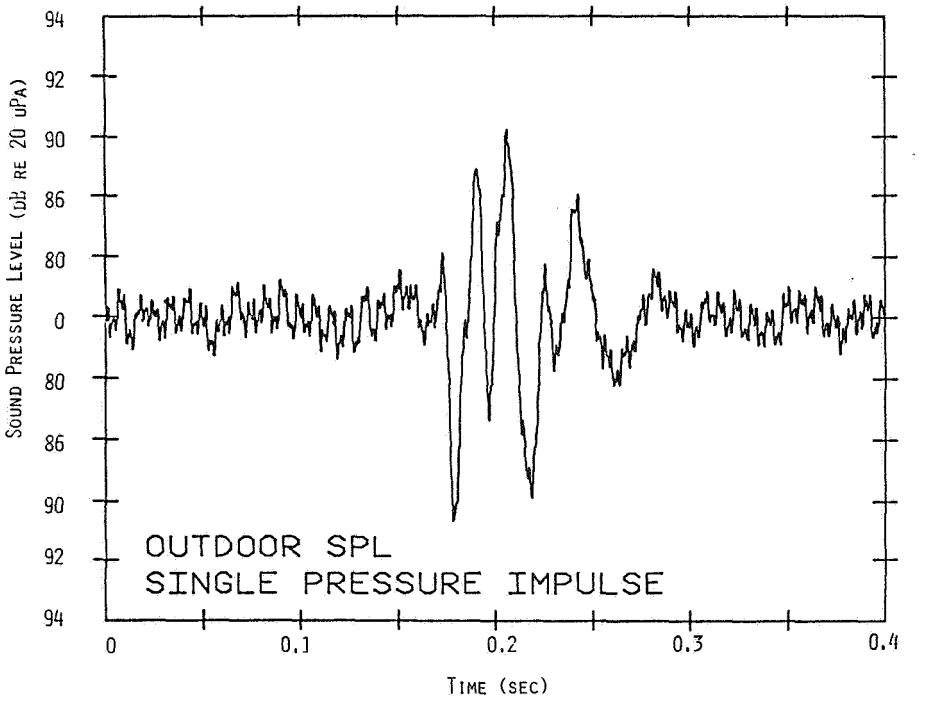

Figure 8. Far-field pressure-time history of strong impulse received at House #8 on March 31, 1980.

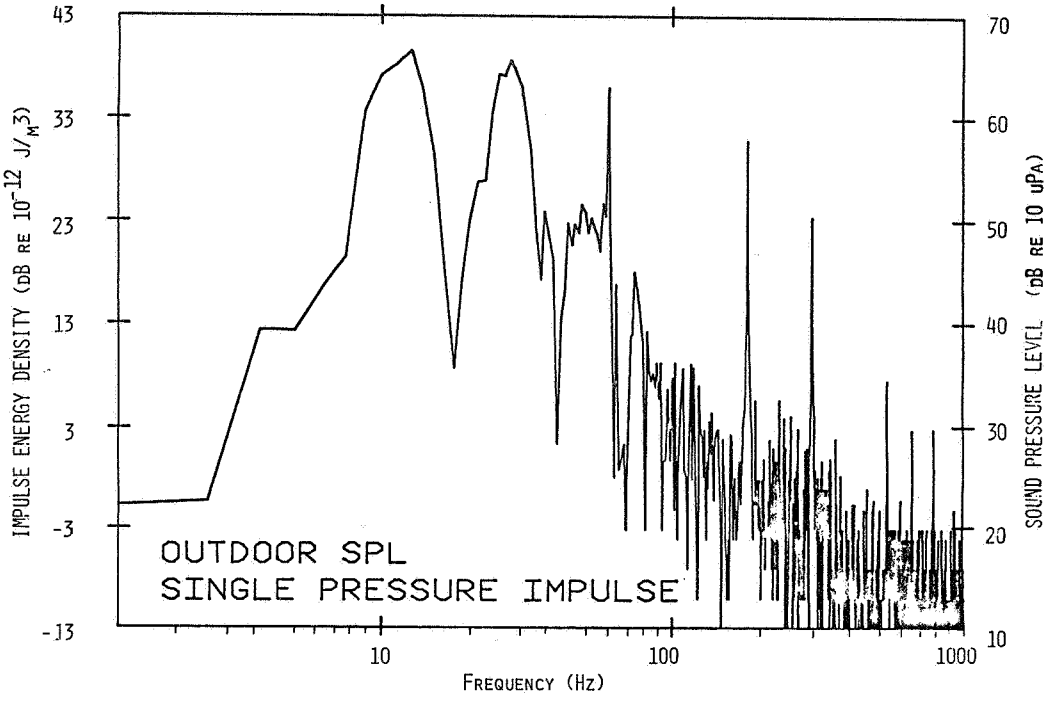

Figure 9. Energy distribution of single impulse of Figure 8 received at House #8.

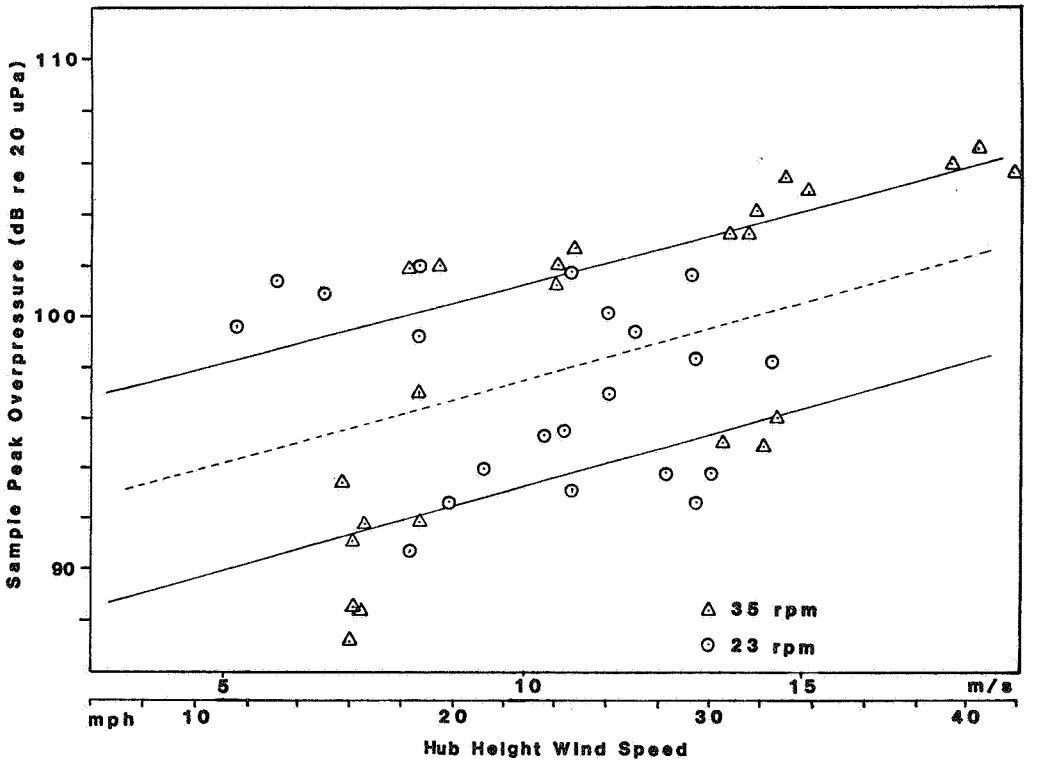

Figure 10. Plot of sample peak impulse overpressure versus windspeed in acoustic near-field.

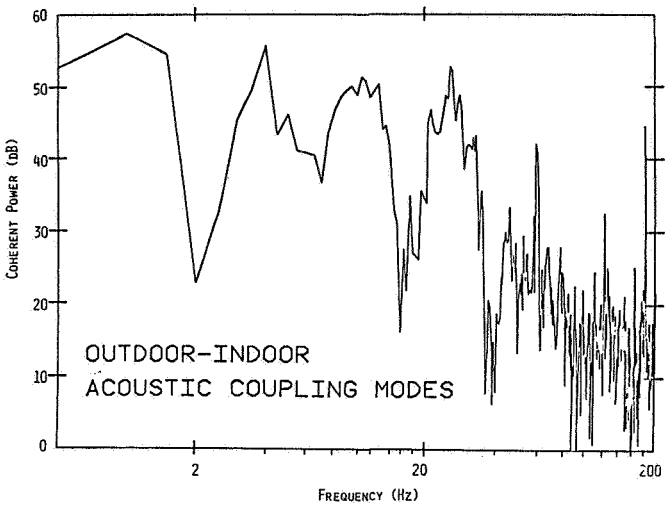

Figure 11. Plot of direct acoustic coupling to the interior of House #7.

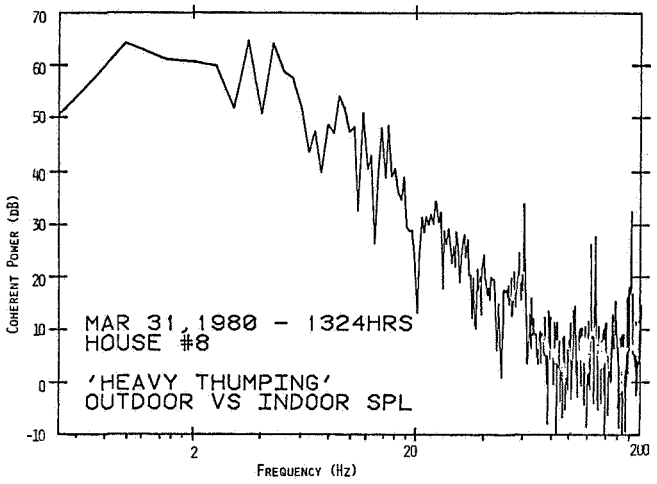

Figure 12. Plot of direct acoustic coupling to the interior of House #8.

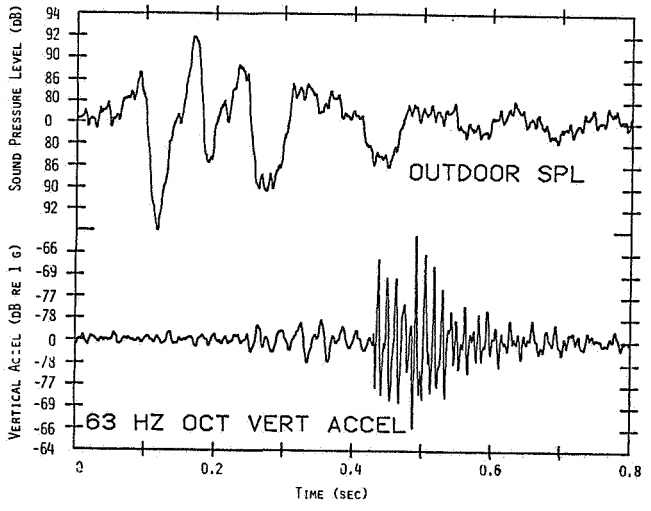

Figure 13. Example of time delay in forced vibration (and acoustic emissions) due to impulsive acoustic loading of House #8.

QUESTIONS AND ANSWERS

N.D. Kelley

From: Anonymous

Q: Were you able to correlate some of your data scatter to any gust intensity measurements?

A: *Only qualitatively. We have made some attempts at this with mixed results. We suspect the answer lies in turbulent eddies whose dimensions are close to the equivalent Strouhal shedding frequencies of the tower legs. The available wind data does not reach these frequencies.*

From: W.K. Wentz

Q: What is the future of large downwind rotors?

A: *I believe the downwind rotor is still viable if the tower wakes can be smoothed sufficiently to preclude the generation of large amounts of noise, particularly impulse noise.*

From: F.W. Perkins

Q: Is the time delay between excitation and response of a house related to house dimensions?

A: *I do not know. I refer the questioner to the work by Carden and Hayes at NASA Langley on aircraft sonic boom and fly-over noise.*

From: P.M. Abbot

Q: At 23 rpm, 10 mph, the SPC was over 100 lbs and higher than for 35 rpm. Is reduction to 23 rpm a solution to the problem?

A: *No, not entirely, only control of the tower leg wake appears to offer a complete solution.*

From: G.P. Tennyson

Q: Has there been found any similarity to the Smith Putnam noise experience?

A: *I am not aware of any such information. I have heard local residents who were living there at the time say that it was not noisy.*

From: P.M. Moretti

Q: Is there a correlation of the noise to the exact wind direction?

A: *Yes, we believe this is due to the propagation, machine orientation, and terrain.*

GE MOD-1 NOISE STUDY

R. J. Wells

General Electric Company
Corporate Research and Development
Schenectady, New York 12301

ABSTRACT

Noise studies of the MOD-1 Wind Turbine Generator are summarized, and a simple mathematical model is presented which is adequate to correlate the sound levels found near the machine.

A simple acoustic measure is suggested for use in evaluating far field sound levels. Use of this measure as input to a currently available sound complaint prediction program is discussed.

Results of a recent statistical survey relative to the far field variation of this acoustic measure because of atmospheric effects are described.

INTRODUCTION

For more than a year, the General Electric Company has been actively studying the problem of adverse community reaction to the noise of the MOD-1 Wind Turbine Generator at Boone, North Carolina. Sound measurements were made near the machine itself and at some of the residential locations from which complaints originated.

Early data were confusing from the standpoint of variability - especially in the far field. Much of this variability was recognized to be due to atmospherical focusing of the sound waves because of wind and temperature gradients, etc. However, the noise also varied widely with different modes of wind turbine operation, and an early need was felt for a simple mathematical model which could be employed to correlate the data.

The question of selecting a suitable simple acoustic measure with which to correlate complaints was also of concern. Wind turbine noise is characteristically different from that of any other machine. All of the noise of interest is confined to low frequencies. In fact, the highest peaks in a noise spectrum are typically below 10 Hz; and during the early stages, the problem was often considered to be purely infrasonic in nature. Because of the frequency range involved, commonly used acoustic measures such as dB(A), and perceived noise level (PNL), were recognized to be inapplicable.

The general statistical variation of sound propagation through the atmosphere was also recognized as important.

A SIMPLE MATHEMATICAL MODEL

Dimensional Arguments

Wind turbine noise appears to be largely due to blades cutting the turbulent wakes introduced by the tower structure. This should produce a dipole source of noise. Morse and Ingard (ref. 1) have shown that for such sound sources the acoustic power can be approximately expressed in the form

$$W_A = K_1 f_x^2 f_o^2 \qquad (1)$$

where f_x represents the strength of the dipole and f_o is the acoustic frequency. (The quantity, K_1, contains other dimensional parameters to be taken as constant for these considerations.)

Now f_x must be the fluctuating force induced on the blade and can be roughly approximated by one-half the difference between the force acting on the blades outside the wake, and the force acting within the wake. Aerodynamic reasoning of this nature leads to the expression

$$f_x = K_2 \, cD \, v_t v_w \qquad (2)$$

where c is blade chord (75% span), D is blade diameter, v_t is tip speed, and v_w is wind velocity. (Again K_2 contains other dimensional parameters which are neglected for simplicity.)

Also

$$f_o \sim \frac{v_t}{D} \qquad (3)$$

for a given order of blade harmonic, and substitution of (2) and (3) into (1) yields

$$W_A = K_3 c^2 v_t^4 v_w^2 \qquad (4)$$

applicable to each harmonic and hence to the total rotational noise.

Hence, the square of the on-axis sound pressure at a given distance, R, may be expressed as

$$p^2 = Kc^2 v_t^4 v_w^2 R^{-2} \quad (5)$$

Principles of Scaling

Note that (5) is consistent with the generally accepted concept of scaling as applied to similar fans, etc. - under the assumption of constant tip Mach number, or constant v_t. Thus, if we have two machines of similar design, we may write

$$p_1^2 = K c_1^2 v_{t_1}^4 v_w^2 R_1^{-2}$$
$$p_2^2 = K c_2^2 v_{t_2}^4 v_w^2 R_2^{-2} \quad (6)$$

and assuming

$$v_{t_2} = v_{t_1} \quad (7)$$

and geometrical scaling - with a ratio s - so that

$$c_2 = s.c_1 \; ; \; R_2 = s.R_1 \quad (8)$$

we find

$$p_2^2 = p_1^2 \quad (9)$$

For example, if the second machine has twice the diameter and twice the blade chord of the first machine (and is rotating at half the rpm to preserve tip Mach number), one would expect to find the same overall sound pressure if measured at the same distance in terms of blade diameters. The spectral components would all be shifted downwards in frequency by a factor of 2, however, in accordance with (3).

A Generalized Curve

For a given machine, it should be possible to correlate on-axis sound pressure spectra obtained under different conditions of operation in a manner similar to that which has been employed for fan noise (ref. 2, 3). Thus, the sound spectral density may be considered as

$$s(f) = \frac{p^2(f)}{\Delta f} \quad (10)$$

and this quantity may be determined experimentally as a function of frequency. It then follows that

$$p^2 = \int s(f)df = Kc^2 v_t^4 v_w^2 R^{-2} \quad (11)$$

from (3). Since

$$v_t \sim N.D \quad (12)$$

where N = RPM, (11) may also be expressed as

$$p^2 = \int s(f)df = Kc^2 N^4 D^4 v_w^2 R^{-2} \quad (13)$$

Now, we may introduce a nondimensional variable, X, a form of Strouhal number, defined by

$$X = \frac{f}{N} \quad (14)$$

and it may be shown that (13) can be put into the form:

$$\int \left(\frac{R^2 s(f)}{c^2 N^3 D^4 v_w^2}\right) dX = K \quad (15)$$

This yields a normalization concept which may be employed to correlate wind turbine sound data. Such a procedure may be carried out in decibel notation.

Assuming sound levels are measured in one-third octave bands, they may be converted to sound spectrum levels (generally analogous to s(f) above) by subtracting 10 log (Δf) from each band level. Here Δf represents the effective bandwidth of the individual one-third octave bands. Then, the spectrum levels are normalized by subtracting the quantity

$$20 \log_{10}(c) + 30 \log_{10}(N) + 40 \log_{10}(D)$$
$$+ 20 \log_{10}(v_w) - 20 \log_{10}(R) \quad (16)$$

from each value. Finally, plotting these normalized values vs. $\log_{10}(f/N)$ would be expected to yield some degree of data collapse. Figure 1 shows an average regression line fit of this nature to a large group of different MOD-1 sound spectra (ref. 4). (In this calculation, conventional dimensions of inches, rpm, feet, mph, and feet were employed for c, N, D, v_w and R respectively, as consistency of units was not of concern.) The standard deviation of this data fit was about 1.6 dB, and it was possible to reduce this value to about 1.5 dB by including regression against parameters of secondary effect - such as pitch angle and load.

Actually, in the data analysis described above the sound levels were not measured on the wind turbine axis, but rather at a wide variety of angles and corrected to on-axis by means of the approximate directivity pattern shown in Figure 2 and based on previously published information (refs. 5-7). Figure 2 also agrees in general with recent calculations using the NASA LeRC Wind Turbine Sound Prediction Code.

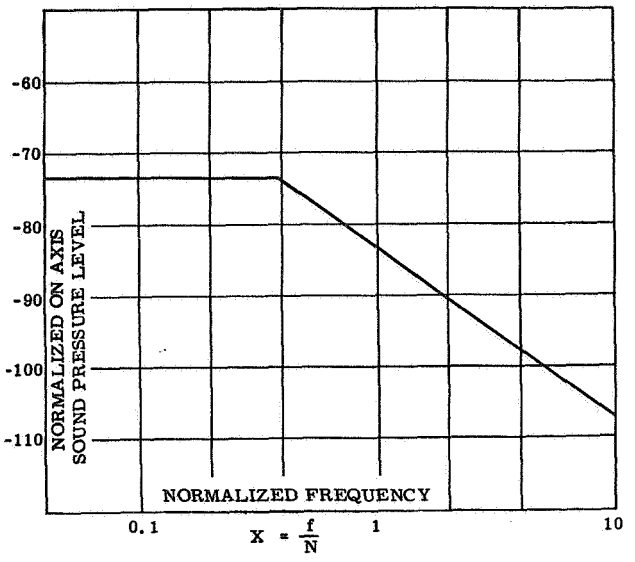

Figure 1: Generalized Wind Turbine Noise Curve

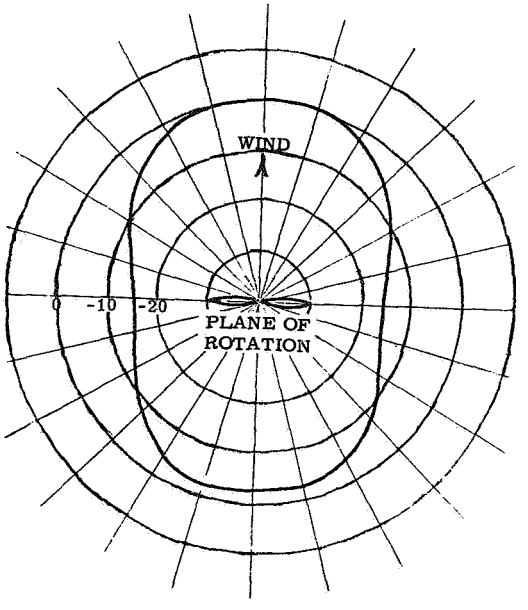

Figure 2: Estimated Directivity Index Pattern of Wind Turbine Noise

It should be noted that the plot of Figure 1 cannot be expected to apply to all possible wind turbine designs. However, it should apply to similar designs - where all dimensions are varied by the same factor and tip Mach number held to reasonable limits. Inherently, direct application of Figure 1 also assumes similarity in tower design, in minimum clearances between blades and tower, and downwind machine operation with but two blades. It is believed, however, that changing such basic design parameters would not invalidate the general concept, but rather simply result in a generalized curve different from that of Figure 1.

The data of Figure 1 included many cases of both 35 RPM operation and 23 RPM operation, both with and without a resistive load bank. The data collapse was sufficient to allow the simple curve to fit both 35 and 23 RPM sets about equally well. These tests also predicted about a 10 dB reduction in noise (except at very low frequencies) when the original 1800 RPM generator was replaced with a 1200 RPM unit. Recent tests with the new generator have confirmed this prediction.

COMMUNITY REACTION TO THE NOISE

A Suitable Noise Measure

During studies carried out about a year ago, both sound and vibration levels were examined at one of the residences about 1 kilometer from the MOD-1 site (ref. 8). Although it was found that both sound and vibration spectra did show predominant peaks at frequencies of the order of 5-10 Hz, neither were at levels sufficiently high to be considered objectionable based on current literature of this subject (refs. 9-12).

However, at somewhat higher frequencies, notably of the order of 20-70 Hz, sound levels were occasionally found which were high enough to be of more concern. In particular, it was noticed that - for 35 RPM at least - the condition often referred to as "thump" seemed to be characterized by a spectral peak in the 20-30 Hz range (ref. 8). Quantitatively, it was also noted that when thump was said to exist, the outdoor sound level in the 25 Hz one-third octave band was typically of the order of 65 dB or more.

Figure 3 shows typical wind turbine noise outside of this residence (based partially on the generalized curve concept) versus a typical ambient spectrum and an approximate threshold of audibility (refs. 11, 12). In many instances, there has been a rather narrow frequency range where the sound levels were above both the ambient levels and the threshold of audibility. Yet complaints have arisen, and general experience confirms, that some reaction to noise will usually occur if an intrusive sound is audible and appreciably above the normal ambient. (Studies relative to the actual amount of this excess above ambient were conducted at General Electric some years ago (ref. 13).)

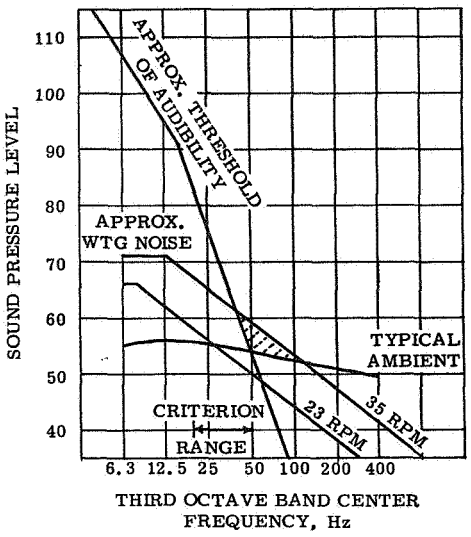

Figure 3: Wind Turbine Noise vs. Ambient and Threshold of Hearing

In Figure 3, the frequency range from 20 to 50 Hz has been labeled the "criterion range". This range was chosen for several reasons:

- It includes at least the lower frequency portion of the range where sound levels are likely to exceed both ambient and threshold levels.
- Experience shows that the presence of sound an octave or so above this range correlates well with the presence of sound in this range, though instantaneous variations may be greater at the higher frequencies.
- Levels at 60 Hz should be excluded from such a criterion because of possible electrical noise interference.
- Historically (in gas turbine noise studies, for example) the range from 20 to 40 Hz has been a "problem range", both with regard to audible sound and acoustically induced house vibration.

With regard to the latter point above, it might be added that a 31.5 Hz octave band level approaching 70 dB would usually give rise to noise complaints, while a level above 75 dB in this band almost always did.

It is well known that the human ear may be considered as analogous to a sound analyzer with an effective bandwidth which increases as frequency is reduced. In the frequency range under consideration, the typical ear has a bandwidth several octaves wide - and any spectral components below 20 Hz are not likely to be even audible. For these reasons, the character, or shape of the noise spectrum at these low frequencies cannot be critical.

Consideration of all of the above has led to the conclusion that the total sound level within the range from 20 to 50 Hz is a suitable measure of wind turbine sound for our purposes. A simplified measure, more suitable for most commercial sound measuring equipment, and yet still adequate for the purpose, is provided by the 31.5 Hz octave band level. This was recently employed in tests described later.

Noise Complaint Prediction

About ten years ago, a computer program was devised at the General Electric Company for the purpose of estimating the numerical probability of complaints due to excessive noise. As an example, this program has been widely used for gas turbine power plant installations as a means of defining the necessary acoustic treatment for exhaust stacks. With but minor modifications, the program may be extended to the wind turbine generator.

The basic input to the program is the measure of wind turbine noise just described, viz the total sound pressure level in the frequency range from 20 to 50 Hz - or alternatively, in the 31.5 Hz octave band.

In general, the computer program employs a cumulative normal distribution function as representative of expected complaints from a specific community of homes. The ordinate of the curve is percent probability of a serious complaint. The abcissa of the curve is related to the difference between noise level and normal ambient level. Different curves of the same family are used for different numbers of homes in the community, and the concept may be modified to include structures other than homes.

The time period during which operation takes place also has an effect on reaction to the noise. The computer program includes this factor by the introduction of a time period category as specified below.

Period	Category
Weekdays:	
7 a.m. - 6 p.m.	C
6 p.m. - 10 p.m.	B
10 p.m. - 7 a.m.	A
Saturdays and Sundays:	
7 a.m. - 10 p.m.	B
10 p.m. - 7 a.m.	A

One merely estimates the number of operation hours per week in each category and enters such data as A, B, C in the program. (For A and B categories, one hour is considered as the minimum time for any period of operation.) The computer program basically makes an effective correction, T, to the actual sound levels as defined below:

$$T = 10 \log_{10} \frac{1}{21} \{A + \frac{B}{10^{.25}} + \frac{C}{10^{.50}} \}$$

T is an additive quantity, in decibels, normalized to three hours per day of category A for T = 0. Other time periods are considered in similar fashion with 2.5 dB more tolerance assumed for category B, and 5 dB more for category C. These latter values are derived from many noise complaint case histories in several departments of General Electric and elsewhere.

In addition, the general class of homes, and other details of the environment affect the prediction. In essence, the computer program also makes a correction of 5 dB multiplied by the code numbers listed below:

District	Code
Very expensive homes	-1
Middle class homes	0
Low cost housing	1
Substandard housing	2
Schools and hospitals	-1
Motels, hotels, stores	1
Light and medium industry	1
Heavy industrial area	2

In summary, for each area of concern the following items must be specified:

- Wind turbine generator sound pressure levels in area by one-third octave bands from 20 Hz through 50 Hz, or alternatively in the 31.5 Hz octave band.
- Normal ambient noise (wind turbine generator not running) in above frequency range.
- Number of building units (homes) in area. For apartments or other building complexes, each individual apartment, store, etc., to be considered as a building unit.
- District code number.
- Operation hours per week by category.

Calculations were made with this program for several cases relevant to the MOD-1 operation. Twenty homes were assumed - as typical of the Boone situation, the district code number being taken as 0. For one set of computations, typical operation was assumed to be for 40 hours per week with two-thirds of this between 10 p.m. and 7 a.m., the remaining one-third being weekdays during the day; for the second set the assumed hours of operation were increased to 60 - with the same percentages relative to time period. For all cases, a typical ambient of 59 dB in the 31.5 Hz octave was assumed. Three values for wind turbine noise in this band were used: 69 dB as typical of 35 RPM operation during times "thump" was reported, 60 dB as typical of 23 RPM operation with comparable atmospheric sound propagation, and 65 dB as an intermediate value. The computed probabilities of complaint were as tabulated below:

Assumed Level in 31.5 Octave Band - Due to WTG Noise Alone (Ambient = 59 dB)	Assumed Time Category Values A = 26.7 B = 0 C = 13.3	A = 40 B = 0 C = 20
69	60.1	78.9
60	4.7	11.8
65	22.6	40.9

The predicted 60.1% seems to correlate well with case histories at Boone. The 4.7% figure suggests that complaints would have been minimal if operation had been confined to 23 RPM. Of course, now that people have been sensitized to this noise, it is not unlikely that some may continue to complain for 23 RPM operation.

A Statistical Noise Study

During January 1981, a brief statistical study was carried out at the MOD-1 site. Although magnetic tape sound recordings were made, primary evaluation has been confined to acoustic levels in the 31.5 Hz octave band. For this purpose, a General Radio Model 1945 Community Noise Analyzer was employed. This instrument automatically computed exceedance levels - such as L1, L10, L50, L90 and L99 - for sound in this frequency range. (L10, for example, is defined as the sound level which was exceeded 10% of the time for the duration of a specific short test period.)

Short test periods of one-half hour duration were used, and statistical determinations were made in the near field, about 270 feet from the machine, and at selected locations near areas of complaint. For the entire study period of about two weeks' duration, the wind turbine was confined to normal on-line 23 RPM operation whenever weather permitted; and primary data analysis has been confined to periods when the wind turbine was

on-line for a full thirty minute short period. Individual statistical curves were then combined (in a proper statistical fashion) in specific groups of interest.

The top curve of Figure 4 shows the result of such a procedure for fifteen cases of on-line operation with the wind predominantly from the west - blowing almost directly toward one of the residences of concern. (The microphone position was essentially upwind from the machine - this being selected due to the fact that the terrain dropped sharply downwind.) The L50 value for this curve is 71 dB; and the flatness of the curve should be noted - L10 was less than 74 dB and L90 was nearly 69 dB. The lower curve of Figure 4 is simply the lowest of several individual one-half hour determinations when the wind turbine was not operating.

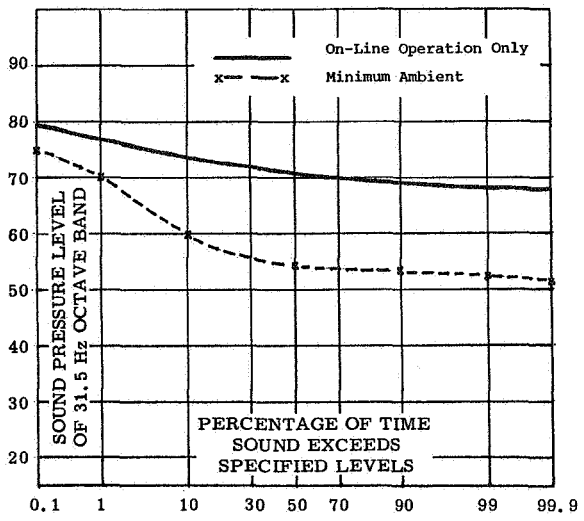

Figure 4: Sound Level Distribution at Position 1, 270 Feet from Center of Tower

During part of the time represented by the data of Figure 4, a strong noise complaint was received from the downwind residence. Excessive levels were noted there during an overall period of 2-3 hours. Three successive one-half hour statistical evaluations were obtained there during this period, and the combined evaluation is presented as the upper curve of Figure 5. Note that L50 for this curve is nearly 64 dB and L10 more than 72 dB. There is little doubt that the levels here actually exceeded the levels at 270 feet occasionally. With normal spherical divergence, one would have expected more than a 21 dB reduction in sound relative to the near field - thus bringing the expected L50 down to about 50 dB.

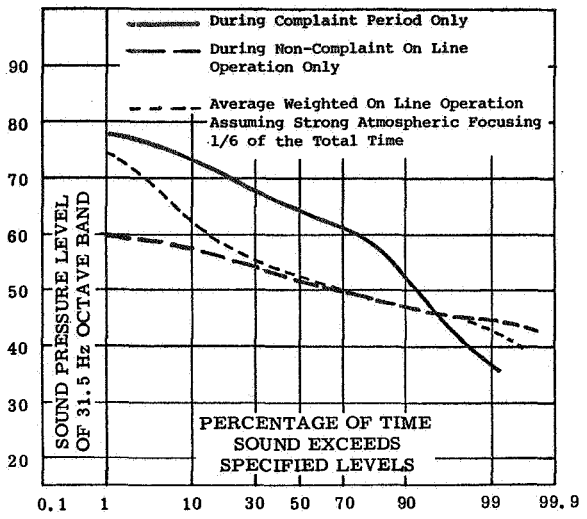

Figure 5: Sound Level Distributions at Residence of Concern

The lower curve of Figure 5 is a similar evaluation at this residence for other periods of on-line operation when complaints were not received. Note that for this curve, L50 is 51 dB - in close agreement with expectations. However, as shown by the upper curve of Figure 5, there were occasions during the complaint period when the sound levels were more than 25 dB in excess of what should have been expected on the basis of simple spherical divergence.

The middle curve of Figure 5 is a combination of the other two curves shown here made under the rough assumption that atmospheric conditions leading to such acoustic focusing might occur perhaps one-sixth of the total time. In this event, 31.5 Hz octave band levels of 65-70 dB might be expected to occur about 3-7% of the time.

It would be possible to combine a statistical level evaluation with the complaint prediction program previously discussed, but no attempt has yet been made in this direction.

CONCLUSIONS

The results of these studies indicate that for a given type of wind turbine design, the mathematical model concept presented should provide a useful tool for estimating wind turbine noise.

An acoustical measure consisting of the total sound level within the frequency range from 20 to 50 Hz seems to be suitable for correlating wind turbine noise with possible complaints. The use of the 31.5 octave band level is believed to be

satisfactory as a rough approximation to this measure.

A previously developed computer program seems to provide reasonable agreement with complaints relative to MOD-1 noise, when used with the above measure as input.

The brief statistical study indicates that there are occasions when atmospherical focusing is sufficient to increase MOD-1 sound levels to more than 25 dB higher than would be expected with simple spherical divergence.

REFERENCES

1. P. M. Morse and K. U. Ingard, "Theoretical Acoustics," McGraw-Hill, 1968.

2. H. C. Hardy, "Generalized Theory for Computing Noise from Turbulence in Aerodynamic Systems," ASHRAE Journal, pp. 95-100, January 1963.

3. R. Parker, "New Fan Law for Sound," ASHRAE Journal, October 1967, pp. 83-85.

4. R. J. Wells, "MOD-1 Wind Turbine Generator Noise Studies," Vol. I: Basic Data, Vol. II: Evaluations, Corporate Research and Development, GE Report, October 1980.

5. C. L. Morfey, "Rotating Blades and Aerodynamic Sound," JSV, 28, No. 3, p. 587 (1973).

6. J. W. Leverton, "The Noise Characteristics of a Large Clean Rotor," JSV, 27, No. 3, p. 357 (1973).

7. J. W. Leverton and J. S. Pollard, "A Comparison of the Overall and Broadband Noise Characteristics of Full Scale and Model Helicopter Rotors," JSV, 30, No. 2, p. 135 (1973).

8. R. J. Wells, "MOD-1 Wind Turbine Generator Preliminary Noise Evaluation," Corporate Research and Development, GE Report, May 1, 1980.

9. CHABA Working Group 69, "Guidelines for Preparing Environmental Impact Statements on Noise," National Academy of Sciences, 1977.

10. Draft Addendum ISO 2631/DAD1, ISO TC 108, "Guide to the Evaluation of Human Exposure to Vibration and Shock in Buildings, Addendum 1: Acceptable Magnitudes of Vibration," 1980.

11. W. Tempest, "Infrasound and Low Frequency Vibration," Academic Press, Inc., 1976.

12. N. S. Yeowart and M. J. Evans, "Thresholds of Audibility for Very Low Frequency Pure Tones," J. Acous. Soc. of Amer., Vol. 55, pp. 814-818, April 1974.

13. R. J. Wells, "Noise Complaint Potential: Ambient Noise versus Intrusive Noise," Proc. 7th International Congress on Acoustics, Budapest, 1971.

ENHANCEMENT OF FAR-FIELD SOUND LEVELS BY REFRACTIVE FOCUSING

Dennis W. Thomson and S. David Roth

Department of Meteorology
The Pennsylvania State University
University Park, PA 16802

ABSTRACT

The enhancement of sound pressure levels resulting from refractive focusing has been calculated for meteorological conditions representative of those observed at the MOD-1 site near Boone, N.C. The results show that 10 to 20dB enhancements can occur over ranges of several hundred meters. Localized enhancements in excess of 20dB can occur but will probably be of limited duration as a consequence of normal temporally varying meteorological conditions.

INTRODUCTION

Refractive propagation of sound which produces zones of enhanced and diminished audibility at varying distances from the source has been of intermittant interest since the turn of the century. In fact prior to rocket soundings, analysis of the so-called anomalous propagation provided Whipple (1923) and others with one of few available means for studies of upper atmosphere temperature profiles.

Although there have been a number of studies of refractive propagation resulting from wind and temperature gradients in the atmosphere's planetary boundary layer (the lowermost one to two km), the results of these studies ought now to be reviewed in the light of our recently, vastly, improved knowledge of meteorological boundary layer structure and processes. The lack of adequate supporting meteorological measurements, for example, greatly diminishes the value of the otherwise careful 13.5 Hz measurements and analysis by Chung (1972). In retrospect the author and his colleagues (Greenfield et. al., 1974) should have included evaluation of the contribution by wind shear in elevated temperature inversions to their analysis of 200 Hz refractive propagation. Artillery sound ranging errors have also been extensively evaluated (see e.g. Lee, 1969). However, results from case studies appear to be either lacking or not readily available.

About one year ago, the meteorological acoustics group at Penn State assisted SERI with field measurements and began analysis of the noise disturbances associated with the MOD-1 WECS situated at Boone, N.C. Results of the preliminary studies are available in the technical report by Thomson (1980) which is currently in press at SERI. These studies clearly established that refractive focusing of the sound by wind shear in the vicinity of the MOD-1 WECS could have contributed to unacceptably high noise levels at several of the locations from which complaints had been registered. The results of this paper include recently completed estimates of the enhanced sound pressure level (relative to spherical spreading) of a caustic, the domain of which has been set to conform to typical dimensions of a residential unit.

MODELING TECHNIQUE

The motion of the acoustic wave front $s(\vec{x},t)$ is described by the Eikonal equation

$$2\nabla\theta_n\cdot\nabla s + \left\{ \nabla^2 s - \frac{1}{c^2}\frac{\partial^2 s}{\partial t^2} \right\} \theta_o = 0$$

where θ_n are the series coefficients in the expansion of the potential velocity, c is the phase velocity and θ_o the initial angle of a specified ray.

The Eikonal equation is numerically solved for nonhomogeneous, anisotropic media, i.e. for wind speed and temperature varying (externally specified) with height. A unique aspect of the computer program is the inclusion of the tracking of rays which have undergone reflection at a complex terrain (non-horizontal slope) surface. Figure one illustrates such a ray trace including focusing near one of the MOD-1 impacted homes.

The exact location of a focus point, caustic, is critically dependent upon meteorological conditions at the mountain site. Variations in the time scale of a few minutes in the vertical wind speed profile near the mountain top can easily displace a caustic several 10's or even hundreds of meters. To evaluate the temporal variability factor we hope shortly to be able to produce "tracks" of caustic positions using processed micrometeorological data from the Univ. of Virginia and Pacific Northwest Labs tethersonde flights. In order to evaluate the sound pressure level at an arbitrary receiver location, we use an eigenray routine which searches a range of angles and employs a bisection method to zero in on the initial angles of rays at the source. Corrections are made for spherical spreading and both ground reflection and atmospheric absorption losses. In their present form the eigenray programs are not yet able to be used for predicting actual sound pressure levels for complex terrain locations.[1] We recognize, however, the substantial community interest in knowing the approximate magnitude of enhanced sound levels resulting

[1]The necessary modifications are scheduled as a part of a larger research effort to be performed by us for SERI

from refractive focusing and, therefore used the currently operating ray trace and eigenray routines for homogeneous terrain to produce figures 2 and 3.

RESULTS

The environmental vertical sound velocity profile on the right of Fig. 2 corresponds to a nocturnal situation characterized by a weak thermal inversion capped by an elevated (mountain top) region of strong wind shear. At higher altitudes we assume a weak temperature lapse and negligible wind shear. Figure 3 is a plot of the noise enhancement (above spherical spreading) as a function of distance from the source. The principal curve corresponds to 10m source and receiver heights, respectively. For comparative purposes a few points are included for a 30m source height. As indicated earlier the receiver domain was set in both cases to be 20m in horizontal extent. Noise level enhancements of order of 10dB are thus easily realized and 10 to 20dB and even higher can occur.

In theory, the sound pressure level at an incremental caustic can be infinite. The actual spatial and temporal properties of caustics resulting from atmospheric focusing have not, to our knowledge, yet been examined. Consequently, our future studies will include detailed analysis of the characteristics of points such as the indicated 27dB enhancement present at 1.25 km on Fig. 3.

REFERENCES

1. Chung, A.C., (1972): The variabilities of wind and temperature structures in the lower troposphere as revealed by an infra-sonic wave probe, Int. Tech. Rep., Mass. Inst. Tech., Contract: U.S. Army DA-31-124-ARO-D-431.

2. Greenfield, R.J., M. Teufel, D.W. Thomson and R.C. Coulter (1974): A method for measurement of temperature profiles in inversions from refractive transmission of sound, J. Geophy. Res., 79, No. 36, pp. 5551-5554.

3. Lee, R.P., (1969): A dimensional analysis of the errors of atmospheric sound ranging, U.S. Army Elect. Command Rep. ECOM-5236.

4. Thomson, D.W., (1980): Analytical studies and field measurements of infrasound propagation at Howard's Knob, N.C., Final Rep. to SERI, in press.

5. Whipple, F.J.W., (1923): The high temperature of the upper atmosphere as an explanation of zones of audibility, Nature, III, No. 2780, p. 187.

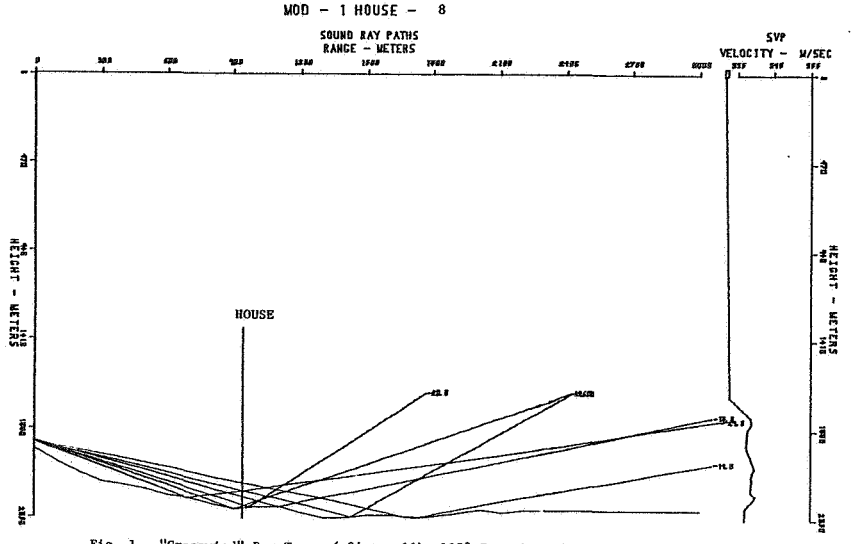

Fig. 1. "Crosswind" Ray Trace (-24 to -16), 105° Terrain and Bearing, Univ. of Virginia Profile 8.

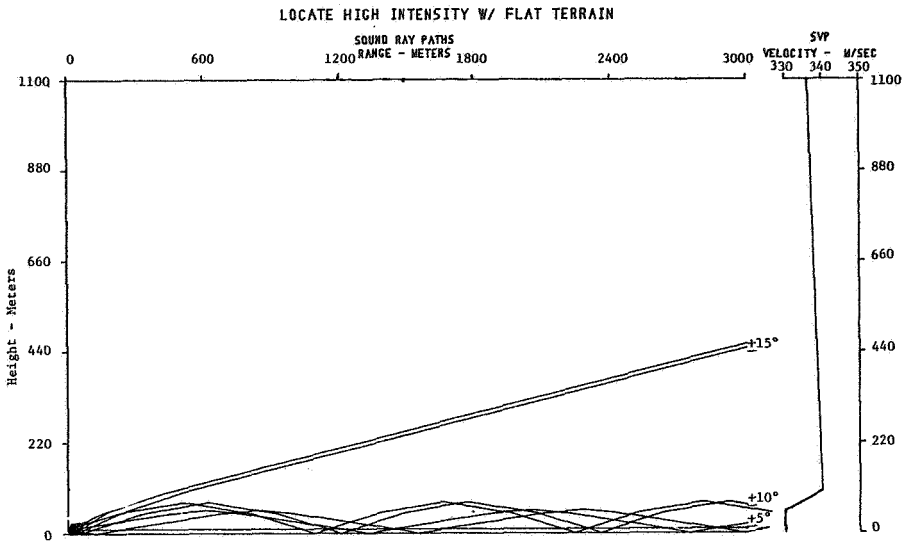

Fig. 2. Ray trace for following sound pressure level enhancement case.

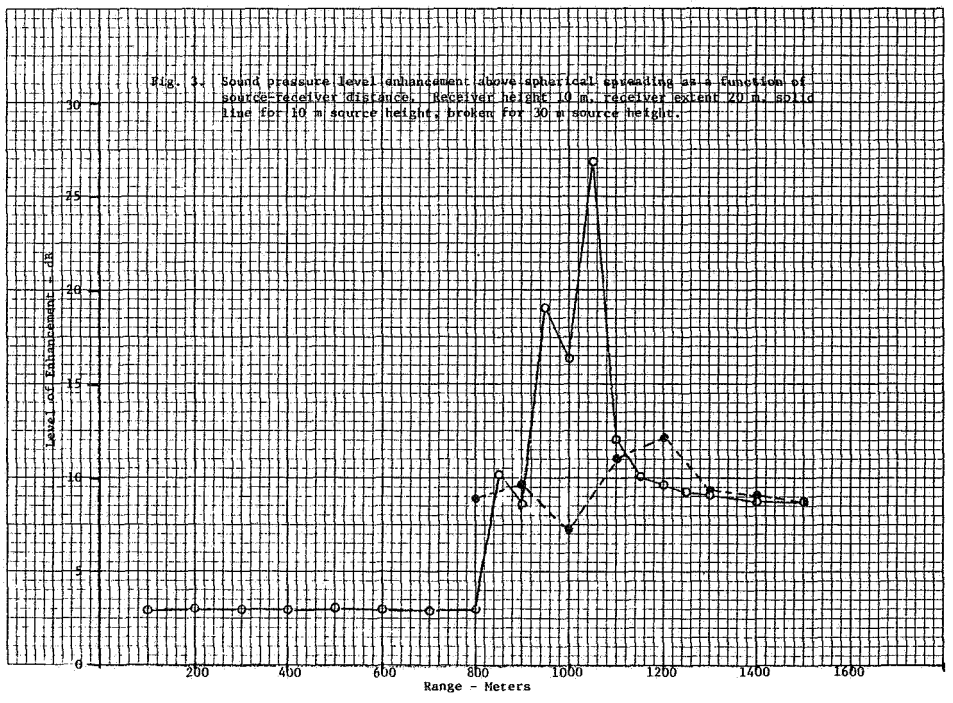

Fig. 3. Sound pressure level enhancement above spherical spreading as a function of source-receiver distance. Receiver height 10 m, receiver extent 20 m; solid line for 10 m source height, broken for 30 m source height.

QUESTIONS AND ANSWERS

D.W. Thomson

From: S. Quraeshi

Q: What, in your opinion, would be the effect of location of HAWTG on a hill or in a valley (effect on noise, propagation, amplification, distance)?

A: *Flow convergence near a hilltop will tend to increase downwind sound levels. Flow divergence downwind of a valley or channel location will tend to reduce downwind noise levels.*

From: Anonymous

Q: What was relative enhancement of upwind versus downwind?

A: *Upwind: 3-7 dB*
Downwind: 10-20 dB

From: Anonymous

Q: Is the primary mechanism responsible for refractive focusing the wind shear or temperature (density) gradient?

A: *It is the wind shear by about an order of magnitude.*

From: J.R. Connell

Q: What effect would you expect for vertical profiles of wind (at a mountain top) which have reduced on negative shear?

A: *Reduced downwind noise levels or even refraction of the sound upward if the negative shear profile is sufficiently large to overcome the temperature gradient (inversion) contribution to the vertical sound velocity profile. However, for isolated peaks the work of Hunt at Cambridge and Mason and Sykes of the English Met Office indicate that 3-dimensional flows will enhance downwind focusing.*

From: G.P. Tennyson

Q: If we can provide fairly good wind profiles, directions, velocities, etc., can you forecast noise focusing so as to evaluate a site ahead of time?

A: *Yes, but as far as I know, the wind and temperature profiles which are needed for acoustic propagation analysis are not currently made in site evaluation studies.*

From: G. Greene

Q: Are you suggesting the problem is totally due to refraction or just enhanced?

A: *The problem is only aggravated by refraction. The only solution is suppression of the noise at the source. Even a "relatively quiet" machine may produce occasionally annoying levels due to refractive focusing.*

From: F.W. Perkins

Q: What climate types will have most and least focusing? Hot and dry versus cold and wet, for example.

A: *Climate in the sense of say, desert versus coastal fog conditions, is not the principal factor. What is important is local terrain and the diurnal structure and evolution of the atmosphere's planetary boundary layer. Generally, the worst case conditions will be associated with complex terrain where strong shear (wind) is generated by the underlying surface and nighttime conditions where the atmosphere tends to be dynamically stable and hence, acres of large wind shear can exist in the lowest 100 to 500 m height.*

PREDICTIONS OF LOW-FREQUENCY AND IMPULSIVE SOUND RADIATION FROM HORIZONTAL-AXIS WIND TURBINES

Rudolph Martinez, Sheila E. Widnall, and Wesley L. Harris

Massachusetts Institute of Technology
Cambridge, Mass. 02139

ABSTRACT

This paper develops theoretical models to predict the radiation of low-frequency and impulsive sound from horizontal-axis wind turbines due to three sources: (1) steady blade loads; (2) unsteady blade loads due to operation in a ground shear; (3) unsteady loads felt by the blades as they cross the tower wake. These models are then used to predict the acoustic output of MOD-1, the large wind turbine operated near Boone, N.C. Predicted acoustic time signals are compared to those actually measured near MOD-1; good agreement is obtained.

INTRODUCTION

The possibility of satisfying some fraction of our energy needs with wind power has recently received serious consideration. As a result, a number of experimental vertical- and horizontal-axis wind turbines have been constructed under DOE sponsorship and are presently being tested. In this paper we present aerodynamic and acoustic models developed or adapted to predict sound radiation from horizontal-axis wind turbines due to the following three acoustic sources: (1) steady blade loads, (2) unsteady blade loads due to wind shear, and (3) unsteady loads acting on the blades as the latter pass through the tower wake.

Below, we describe the mathematical models used to predict noise due to these sources and apply these models to calculate the acoustic output of the DOE/NASA MOD-1 wind turbine (for which some tower wake data and sound measurements are available) under typical operating conditions: a free stream of 35 MPH and rotor speeds of 23 and 35 RPM. Although possibly an important cause of impulsive low-frequency sound radiation under certain operating conditions, cross flow into the rotor was not studied here due to difficulties in aerodynamic modeling similar to those met in non-rigid wake analyses for helicopter rotors (ref. 1). Study of this mechanism should be part of future theoretical and experimental research on wind turbine noise. In the present preliminary study we are mainly concerned with modeling the rotor aerodynamics in order to determine the strength and frequency content of sources of sound on the rotor disk; we do not consider terrain and atmospheric effects on the propagation of such sound once it has been created. So, the models developed here for mechanisms (1)-(3), above, do not take into account the presence of the ground plane or the effects which the wind profile or an atmospheric temperature gradient will have on acoustic propagation.

The acoustic models used to predict sound due to (1), steady blade forces and (2), unsteady blade forces to ground shear are based on, respectively: the classical Gutin propeller noise theory (ref. 2); and its generalization for the case of unsteady blade sources (ref. 3). In both studies we used lifting-line theory coupled with a vortex-lattice-wake model to calculate loads at chosen radial stations for each blade. The wake was assumed to be semi-rigid in that it was allowed to move with the local wind velocity (ref. 4). We did not assume compactness of acoustic sources on the rotor disk which would have simplified the analysis somewhat.

To investigate the acoustic effect of (3), blades cutting through the tower wake, we applied the blade-slap theory of ref. 5. Here. the unsteady airloads acting on a blade passing through the mean profile of the tower wake were obtained using Filotas' linear, unsteady aerodynamic theory (ref. 6). The wake data used in the calculations is that given in ref. 7 for a 1/40th-scale model of MOD-1. Predictions of sound are in good agreement, both quantitatively and qualitatively, with field measurements.

FORMULATION

A. Sound due to Steady Blade Loads (Gutin noise)

Even if the tower and rotor wakes did not interact with the turbine blades, and ground shear and cross flows were absent, sound would radiate from a wind turbine due to the rotary motion of steady blade loads. The model used here to study the contribution of this source mechanism to the total far-field signal is based on an adaptation of the classical Gutin propeller noise theory (ref. 2); propagation of sound was assumed to take place in a stationary medium and the acoustic effect of the presence of a ground plane was neglected. The source representation for each blade did not take advantage of acoustic compactness in either the chordwise or radial directions. Instead, we constructed a distributed source region for the rotor plane (zero coning angle) by using values of blade thrust and in-plane forces for six radial stations. Furthermore, at each station these values of force were distributed along the local chord assuming a flat-plate loading distribution.

The actual calculations of blade forces were performed using the lifting-line aerodynamic numerical model described in detail in ref. 4. The model uses curved grids or lattices of trailing and shed vortices to represent the wake behind a turbine rotor in a nonuniform incident free stream. Each lattice has its origin at the trailing edge of a rotor blade and is allowed to change shape as each of its grid points is convected with the local value of the nonuniform free stream velocity; such a wake is "semi-rigid" in current aerodynamic terminology. The blade loads are calculated using an iterative procedure. The code, named US-2I by its original developers (ref. 4), outputs values of blade forces around the rotor for an input ground shear; it can calculate steady blade loads for the special case of a uniform rotor inflow. Although based on potential theory, US-2I incorporates some

viscous effects in the aeroacoustic model by computing values of local skin-friction drag from knowledge of the calculated potential flow field and the drag coefficients for each local blade section. Figure 1 shows the coordinate system used in the acoustic model for the steady loads; since the Gutin sound field is axisymmetric, only the angle ψ is needed to describe the predicted directivity patterns.

In the classical theory of Gutin noise (ref. 2) the pressure level P_s at the s^{th} harmonic of the blade-passage frequency is given by the following expression:

$$P_s(r,\psi) = -\frac{i}{2r} e^{\frac{isB\Omega r}{c_o}} (-i)^{sB} \left\{ \frac{sB\Omega\cos\psi}{c_o} \int_o^R dr' r' T(r') \cdot A_s(r') J_{sB}\left(\frac{sB\Omega r'\sin\psi}{c_o}\right) + sB \int_o^R dr' I(r') A_s(r') J_{sB} \cdot \left(\frac{sB\Omega r'\sin\psi}{c_o}\right) \right\} \quad (1)$$

where r,ψ define the observer's position in the axisymmetric (in γ) Gutin sound field; B stands for the number of blades, c_o for the speed of sound, and Ω and R for the rotor's speed and radius, respectively. $T(r')$ and $I(r')$ denote the values in pounds per linear foot of steady thrust and in-plane forces, respectively, computed by US-21 at six radial stations for each blade; r' is the distance separating each station from the hub. We chose stations located at 20, 30, 40, 60, 75, 85, and 95% of the rotor radius. At each, we distributed the values of the calculated forces along the local chord $c(r')$ using a flat-plate loading shape $\Delta p \sim \sqrt{(x+x_{te})/(x-x_{le})}$; the Fourier coefficients of the load shape functions are designated $A_s(r')$ in (1). With $\gamma_o(r')$ indicating the position of the trailing edge of each blade section for each radial station relative to that of $r' = 0.2R$, we have, for the thrusts (the in-plane forces were treated similarly)

$$\Delta p(r',\gamma) = \begin{cases} \frac{T(r')}{\pi c(r')/2} \sqrt{\frac{\gamma-\gamma_o(r')}{\gamma-\gamma_o(r')-c(r')/r'}} \\ \qquad \text{for } \gamma_o(r') < \gamma < \gamma_o(r') + \frac{c(r')}{r'} \\ 0 \quad \text{otherwise} \end{cases} \quad (2)$$

and so, by Fourier's theorem,

$$\Delta p(r',\gamma,t) = T(r') \sum_{s=-\infty}^{\infty} A_s(r') \exp[2\pi i s(\gamma-\Omega t)/\Gamma] \quad (3)$$

Here Γ is $2\pi/B$; for the two-bladed MOD-1, $\Gamma = \pi$.

Having calculated the harmonics by means of (1), we obtain the acoustic signal p using

$$p(r,\psi,t) = \sum_{s=-\infty}^{\infty} P_s(r,\psi) e^{-isB\Omega t} \quad (4)$$

where t is time.

A Fast-Fourier Transform routine calculated the $A_s(r')$ coefficients in (3) and the time signal from (4). A sample size of 2048 points was used to represent the load-shape functions for every radial station. The same number was used to obtain the time signal from the calculated harmonics.

B. Low-Frequency Sound due to Operation in a Ground Shear

Since the turbine operates in the earth's boundary layer, the actual free stream can be far from uniform and the associated acoustic field far from axisymmetric. Low-frequency sound then has two origins: (1) the steady loads in rotary motion, as for uniform flow; and (2) the unsteadiness due to the variation of blade forces around the rotor.

As in the Gutin noise study, the acoustic model we used to investigate the effect of wind shear does not take advantage of compactness of acoustic sources on the rotor. The distributed source representation was constructed as previously described, that is, blade loads (thrust and in-plane) were calculated at six radial stations and at each such station their local values were distributed across the local chord using the flat-plate loading shape. The acoustic theory used is the standard generalization of the Gutin model to allow blade forces to vary around the rotor (ref. 3). We assumed that sound propagates in an infinite stationary medium with no ground plane. Program US-21 calculated the blade loads for the turbine operating cases of interest.

We considered an example of a free stream with a shear linear in profile constructed from the sum of a uniform 35 MPH free stream and a linear function with a magnitude of 8 MPH at the highest and lowest points on the rotor. Such a model for shear, besides approximating well most free-stream profiles, enabled us to compare the predicted acoustic fields to those obtained here using Gutin's theory because, for the small blade-pitch cases considered here, the pressure far field for linear ground shear contains approximately the same amount of Gutin noise as its uniform-flow counterpart. This allowed us to isolate the acoustic effect of unsteadiness due to the nonuniformity of the incident rotor inflow.

The standard generalization of Gutin's theory for nonuniform incident inflows contains the following expression for the harmonics of the acoustic signal in the far field (ref. 3):

$$P_s(r,\gamma,\psi) = -\frac{i}{2r} e^{\frac{isB\Omega r}{c_o} + isB\gamma} \sum_{q=-\infty}^{\infty} \left\{ (-i)^{(sB+q)} \left[\frac{sB\Omega\cos\psi}{c_o} \int_o^R dr' r' B_q^T(r') A_s(r') J_{sB+q}\left(\frac{sB\Omega r'\sin\psi}{c_o}\right) + (sB+q) \int_o^R dr' B_q^I(r') A_s(r') J_{sB+q}\left(\frac{sB\Omega r'\sin\psi}{c_o}\right) \right] \right\} e^{\frac{2\pi iq\gamma}{\Gamma'}} \quad (5)$$

where, since the flow into the rotor is not uniform, the thrust and in-plane forces T and I become functions also of γ, the in-plane rotor angle. We then write, for the thrust,

$$\Delta p(r',\gamma)= \begin{cases} \dfrac{T(r',\gamma)}{\pi c(r')/2}\sqrt{\dfrac{\gamma-\gamma_o(r')}{\gamma-\gamma_o(r')-c(r')/r'}} \\ \qquad \text{for } \gamma_o(r')<\gamma<\gamma_o(r')+\dfrac{c(r')}{r'} \\ 0. \\ \qquad \text{or otherwise} \end{cases} \tag{6}$$

so that in place of (3) we now have

$$\Delta p(r',\gamma,t)= \sum_{q=-\infty}^{\infty} B_q^T(r') e^{\frac{2\pi i\gamma q}{\Gamma'}} \sum_{s=-\infty}^{\infty} A_s(r') \cdot \exp[2\pi i s B(\gamma-\Omega t)/\Gamma] \tag{7}$$

where the substitution $T(r',\gamma)= \sum_{q=-\infty}^{\infty} B_q^T(r') e^{\frac{2\pi i q\gamma}{\Gamma'}}$ has been made. Here, $\Gamma' = 2\pi$, and the $B_q^T(r')$'s are the Fourier coefficients of $T(r',\gamma)$, calculated numerically for each radial station using a Fast-Fourier Transform routine. Equations similar to (6) and (7) were also used to express the in-plane forces $I(r',\gamma)$. $T(r',\gamma)$ and $I(r',\gamma)$ changed around the rotor only very gradually for the case of linear shear studied here; so we found that they and their transforms could be adequately represented by 24 sample points.

The time signal is still given by eq. (4).

C. Impulsive Sound due to the Passage of the Blades through the Tower Wake

In order to investigate sound radiation due to the tower wake we applied a modification of the helicopter-blade slap theory of ref. 5. Briefly, the present model performs the following sequence of calculations: (1) the measured mean tower-wake velocity profile is expressed as a sum of upwash gusts by the Fourier transform theorem; (2) the unsteady force acting on a blade passing through a single gust is determined using Filotas' aerodynamic theory; (3) the unsteady force acting on a blade as it encounters the tower wake is obtained by superposition of solutions from (2); (4) spanwise superposition of solutions of (3) is applied to model the three-dimensional effects of blade rotation and finiteness in span; (5) the wave equation in an infinite stationary medium (with no ground plane) is solved with the aerodynamic forces as boundary condition.

In step (1) above, we used the wake profile approximately at the 74% rotor radius station to represent the profiles at all radial positions. The actual tower wake data for the numerical calculations was taken from ref. 7, where the 74% radial position corresponds to a height of 23.2" from the base of a 1/40th-scale model of MOD-1. The mean wake velocity measurements were made at points downstream of the rotor which were at a distance from the tower-center line of 13.13" (43.77 feet in scale); we assumed these did not differ greatly from those on the actual rotor plane, which for the model is at a distance of 9.10" (or 30.33 feet in scale) from the tower-center line. Two sets of calculations were performed, one using a rotational speed of 35 RPM and the other 23 RPM. In each we investigated wakes for free streams oriented at 0°, 20°, and 45° with respect to the tower structure; for convenience, computer generated reconstructions of these velocity profiles normalized by the free stream are presented in figs. 2a-c. In each, the abscissa, which represents the distance across the tower wake normal to both the tower and the free stream, has been scaled to actual MOD-1 dimensions.

To calculate the local unsteady load acting on a blade section passing through the tower wake, we use Filotas' linear two-dimensional aerodynamic theory (ref. 6). The model is adapted from ref. 5, where it was used to predict noise due to blade-vortex interaction in helicopter rotors. Its application here is justified by the following two conditions on turbine operation and tower wake characteristic, respectively, which generally are met by wind turbines: (1) small advance ratio (small ratio of rotor inflow velocity to rotor tip speed); and (2) small sector of rotor azimuth occupied by the tower wake.

We assumed the wake was two-dimensional, that is, that the same wake profile existed at all positions along the tower height. Also, we used a local two-dimensional model for the blade unsteady aerodynamics. Later, we incorporated some three-dimensional effects of blade rotation and finiteness of blade length into both aerodynamic and acoustic models.

Let w(y) denote the upwash felt by a blade passing through the tower wake; the variable y measures the distance normal to the radial direction on the rotor plane. By Fourier's theorem, we express w(y) as a sum of sinusoidal gusts of varying amplitude W(s)

$$w(y) = \int_{-\infty}^{\infty} ds\, W(s)\, e^{isy} \tag{8}$$

The unsteady load $\bar{L}(t,s)$ acting on the blade due to the interaction with a single gust is obtained applying Filotas' aerodynamic theory:

$$\bar{L}(t,s)=\left[\frac{\pi\rho(\Omega R)^2}{\sqrt{1+2\pi s}}\, c \exp\left(1-\pi^2/(2+4\pi s)\right)\right] W(s) e^{-ist} \tag{9}$$

where ρ is the background air density, Ω and R the rotor speed and rotor radius, respectively, and c the blade chord. We shall refer to the term in brackets in (9) as $L_o(s)$. From (9), and using superposition, we obtain the unsteady blade loading

L(t) due to the passage through the tower wake

$$L(t) = \int_{-\infty}^{\infty} ds\, \bar{L}(t,s) \qquad (10)$$

The expression above (valid for a locally two-dimensional flow) has been derived for a blade of infinite length traveling rectilinearly. The three-dimensional aerodynamic and acoustic effects of blade rotation and finiteness of blade length are modeled as follows: the acoustic pressure p satisfies the three-dimensional stationary medium wave equation; the unsteady loads on the blade passing through the tower wake are taken to be equal to the two-dimensional sectional load given in (10) with the local blade velocity (and thus the magnitude of the loading) varying linearly from hub to tip. Given the assumption we have made here about the tower wake being the same for all points along the vertical (from blade tip to hub), such a model for the actual three-dimensional loading on a rotating blade, which sees a relative free stream linearly increasing in the tip direction, should be reasonably accurate except at a small region near the tip; here it overestimates the actual dipole strength since the latter must vanish as $\sqrt{R-r'}$. We solve the three-dimensional wave equation subject to the boundary condition

$$\Delta p(r',y) = \begin{cases} \frac{r'}{R} L(t)\,\delta\{\frac{c}{2}(y-t)\} & \text{for } 0 < r' \le R \\ 0 & \text{for } r' > R \end{cases} \qquad (11)$$

where, as before, r' stands for the radial distance from the hub measured on the rotor plane. All spatial variables have been normalized by the blade semichord c/2, and time by $(c/2)/\Omega R$.

The solution of the above boundary value problem has the following form in the far field:

$$p(r,\tfrac{z}{r},\tfrac{y}{r},\tfrac{r'}{r};t) = \frac{iMR}{2\pi rc}\int_{-\infty}^{\infty} ds\, s\, L_o(s) D(s;\tfrac{z}{r},\tfrac{y}{r},\tfrac{r'}{r}) \cdot \exp\left[is(Mr-t)/(1-M\tfrac{y}{r})\right] \qquad (12)$$

with

$$D(s;\tfrac{z}{r},\tfrac{y}{r},\tfrac{r'}{r}) = \frac{z}{r}\cdot\frac{1}{(1-M\frac{y}{r})^2}\cdot\frac{1}{R}\left\{\frac{\exp[-isRM(r'/r)/(1-M\frac{y}{r})]-1}{R\,[M(r'/r)s/(1-M\frac{y}{r})]^2} + \frac{i\exp[-isRM(r'/r)/(1-M\frac{y}{r})]}{s[M(r'/r)/(1-M\frac{y}{r})]}\right\} \qquad (13)$$

Here, r is the distance between the observer in the far field and the turbine hub, and z is the projection of this distance on a plane normal to that of the rotor. M is $\Omega R/c_o$, the tip Mach number.

The directivity factor D(s;z/r,y/r,r'/r) in (13) reaches a maximum in magnitude when r'/r = 0, that is, at points in the acoustic field which coincide with the rotor axis. Naturally, for a given r there are two such points -- one upstream of the turbine and one downstream. The fourier transform W(s), of the tower-wake upwash on the blade, was computed numerically with 2048 sample points using a Fast-Fourier Transform routine; so was the acoustic pulse in the far field as given by (12).

DISCUSSION OF RESULTS

A. Predictions of Gutin Noise

Figure 3 shows predicted directivity patterns at one kilometer from MOD-1 for the first three harmonics of the acoustic pressure for an operating condition of 35-RPM rotor speed and a 35-MPH free stream; the sound pressure level had a maximum value of 56 dB in the direction $\psi = 65°$. Figure 4 corresponds to the 35-MPH free stream, 23-RPM condition, for which the maximum level was 50 dB. A value of zero pitch at the blade tips was used in both sets of calculations.

For both uniform-flow operating conditions studied here we found that the predicted spectrum had the expected feature of containing only a few harmonics of significant level; therefore, the time signals (not shown here) were essentially pure sine waves at the blade passage frequency. Also as expected, the predicted Gutin directivity patterns indicated zero on-axis sound and a preference for radiation in the upstream direction of the turbine. Finally, we also confirmed that the case of lower rotational speed (23 RPM) radiates less overall Gutin noise than that of 35 RPM.

B. Predictions of Sound due to Ground Shear

Because the ground shear produces unsteady blade loads that vary with position around the rotor disk, the sound field is a function of both the angle ψ and angle in the rotor plane γ. Normally, for an observer on the ground far from the rotor, γ will be essentially 90°. However, if the observer is at a position in the field which is close to the rotor or much higher or lower than the horizontal plane of the turbine's base, acoustic predictions at other values of γ may be of interest. Our numerical results indicated however that the dependence on γ is very weak.

Figure 5 shows the predicted directivity pattern at one kilometer from MID-1 for the first three harmonics of the acoustic pressure for $\gamma = 90°$; the maximum sound pressure level was found to be about 58 dB in the direction of $\psi = 65°$. The operating condition for the turbine was a 35-RPM rotor speed, zero blade tip pitch, and the previously described linear-shear free stream. Figure 6 shows similar predicted results for the operating condition of 23 RPM, zero blade tip pitch, and the

same ground-shear profile. The maximum sound pressure level was found to be about 52 dB for this case.

In conclusion, in contrast to the acoustic directivity patterns for Gutin noise, those for ground shear indicated non-zero values of on-axis sound levels, due mostly to the higher harmonics. This relative growth of the higher part of the spectra is apparent also at the field points where the calculated sound pressure levels had maximum values in that the shapes of the acoustic signals there (not presented here) had slightly steeper slopes than those for Gutin noise. Accordingly, the maximum sound levels were higher than those obtained for uniform rotor inflow; the difference came from the added contribution to the sound field of the unsteadiness of blade forces, an acoustic source which of course is absent when the incident rotor inflow is uniform.

C. Predictions of Sound due to Tower-Wake/Blade Interaction

Figures 7a-c for 35 RPM show predicted acoustic signals at one kilometer from MOD-1 for the wind-tower angles of 0°, 20°, and 45°, for which we obtained predicted sound levels of 85, 83, and 84 dB respectively, at the field point of maximum acoustic pressure (0° azimuth). These values are in good agreement with the amplitude of the measured signal shown in Fig. 8 (ref. 8). The signal in Fig. 8 was recorded approximately one kilometer from MOD-1 and at a position in the field 24° in azimuth off the turbine's axis (see Fig. 10 below); by definition the direction of the wind corresponds to a 0° azimuth. The predicted time signals for the 23-RPM case were qualitatively similar to those shown here for 35 RPM but with the substantially lower values for maximum amplitude of 74, 72, and 73 dB for wind-tower angles 0°, 20°, and 45°, respectively. Figure 9 shows the predicted sets of spectra of these computed acoustic signals for the two cases of 35 and 23 RPM. Figure 10 shows the predicted simple acoustic dipole directivity pattern at one kilometer for the case of 35 RPM and wind-tower angle of 0°; the position in the field corresponding to that where the acoustic measurement in Fig. 1 was taken is indicated.

CONCLUSIONS

Based on the predictions of the models, we conclude that neither steady blade loads nor loads due to operation in ground shear contribute substantially to the acoustic signal from a wind turbine such as MOD-1. However, comparison of the theoretically predicted signal for noise from interaction with the mean wake (Fig. 7a) for a 35-RPM rotational speed, 35-MPH wind speed, 0° wind-tower angle, and the measured one shown in Fig. 8 indicates a close resemblance, both quantitatively and qualitatively. The conclusion to be drawn from this that high level impulsive sound could radiate from MOD-1 due to the interaction of its blades and tower wake.

The results for the 23-RPM case suggest that a possible way to reduce a turbine's acoustic output is to operate at a lower rotor speed. Instead, dramatic noise reduction could be achieved without compromising performance by changing the structural configuration of towers to have smoother wakes. To accomplish this, the relationship of complicated tower geometries and their wakes will have to be investigated experimentally in follow-on studies. Earlier we had pointed out that cross flows into the rotor might have significant acoustic effects. Investigation of this possibility should also form part of future experimental and theoretical research.

ACKNOWLEDGEMENTS

This work was supported by the Solar Energy Research Institute, purchase order number AH-0-9161-1. We wish to acknowledge the assistance of Mr. Neil Kelley of the Solar Energy Research Institute.

REFERENCES

1. Miller, R. H.: Unsteady Air Loads on Helicopter Blades, J. Royal Aeronaut. Society, Vol. 68, April 1964, pp. 217-229.

2. Gutin, L.: On the Sound Field of a Rotating Propeller, NACA TM 1195, 1948.

3. Morse, P. M., and Ingard, K. U.: Theoretical Acoustics, McGraw-Hill, 1968, pp. 737-747.

4. Miller, R. H.: Wind Energy Conversion, Vol. II, ASRL TR-184-8, Dept. of Aero- and Astronautics, M.I.T., September 1978.

5. Wolf, T., and Widnall, S. E.: The Effect of Tip-Vortex Structure on Helicopter Noise due to Blade-Vortex Interaction, Fluid Dynamics Research Lab. Rep. 78-2, M.I.T., 1978.

6. Filotas, L. T.: Theory of Airfoil Reponse in a Gusty Atmosphere - Part I, Aerodynamic Transfer Function, UTIAS Rep. 139, University of Toronto, October 1969.

7. Savino, J. M., Wagner, L. H., and Nash, M.: Wake Characteristics of a Tower for the DOE-NASA MOD-1 Wind Turbine, DOE/NASA/1028-78/17, NASA TM-78853, April 1978.

8. Kelley, N. D.: Review and Status of Noise Measurements and WECS, SERI Task 3532.55, presented to Wind Systems Branch DOE, May 21, 1980.

NOMENCLATURE

A_s	Fourier components of the flat-plate load shape functions, Eq. (1)
B	number of blades - two for MOD-1
$B_q^{I,T}$	Fourier coefficients of I, T, respectively, given in Eq. (5)
C	local blade chord
c_o	sound speed
D	directivity factor, Eq. (13)
I	magnitude of computed in-plane blade force
J_n	Bessel function of order n
$\bar{L}$	unsteady lift acting on a blade passing through a gust, Eq. (9)

L_o magnitude of unsteady lift due to blade/gust interaction given by Filotas' theory, term in brackets in Eq. (9)

M blade tip Mach number

p acoustic pressure

P_s harmonics of the acoustic pressure signal p

r distance of observer in the far field from turbine hub

r' radial distance measured on the plane of the rotor disk

R rotor radius

s harmonic counter

T magnitude of computed thrust blade force

t time

W Fourier transform of w

w downwash felt by the blades as they cross the tower wake

y distance measured across the tower wake normal to the free stream direction and tower centerline

z distance normal to rotor disk

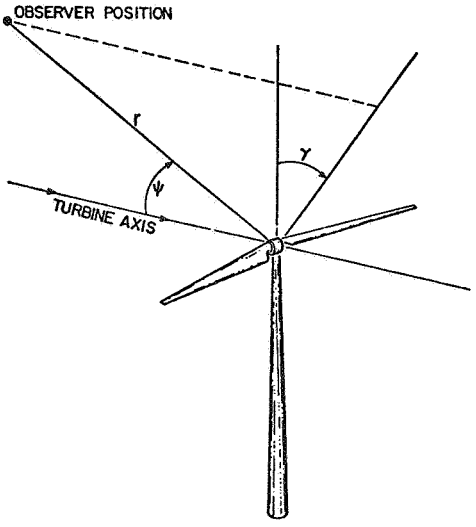

Figure 1: Coordinate system used in the Gutin and ground-shear models.

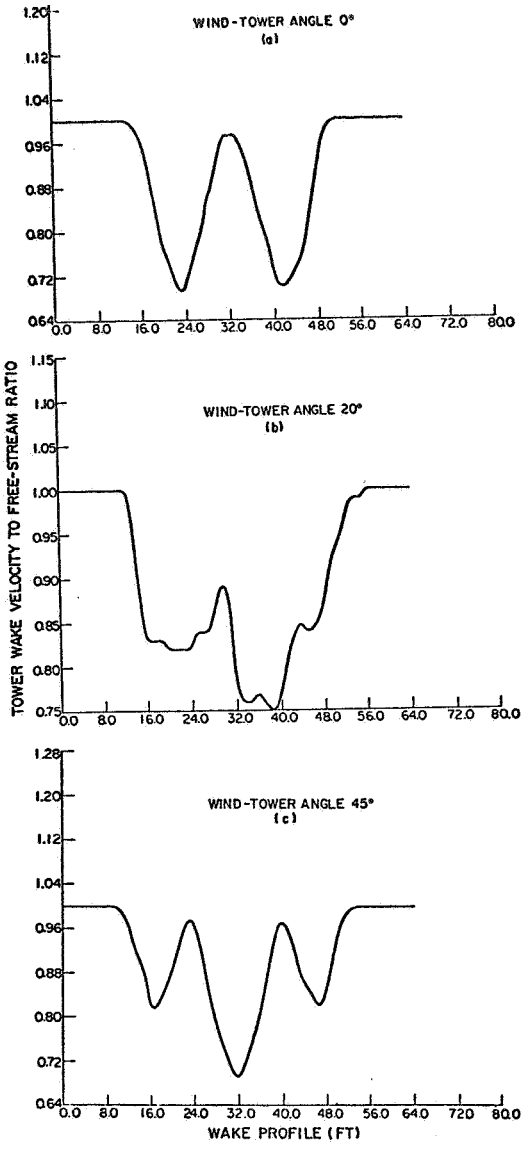

Figure 2a-c: Tower-wake velocity profiles from ref. 7. Abscissa has been scaled to actual MOD-1 dimension.

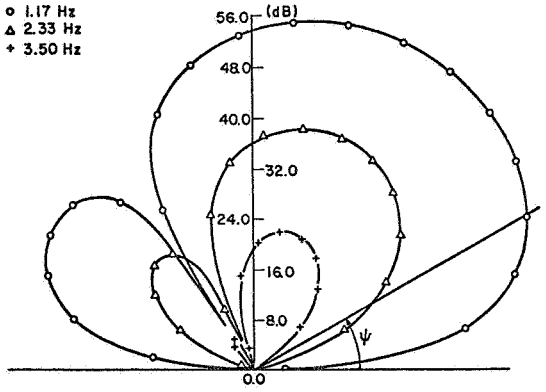

Figure 3: Directivity pattern at 1 Km of first three harmonics of Gutin noise for free stream of 35 MPH, $\Omega = 35$ RPM.

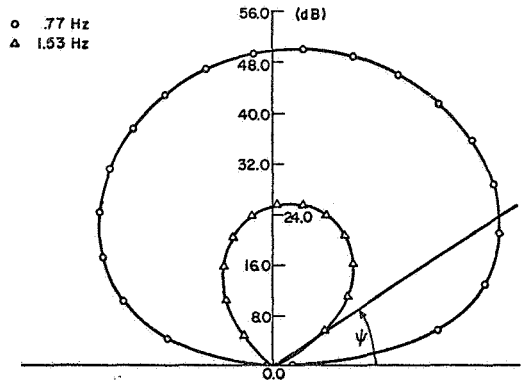

Figure 4: Directivity pattern at 1 Km of first three harmonics of Gutin noise for free stream of 35 MPH, $\Omega = 23$ RPM.

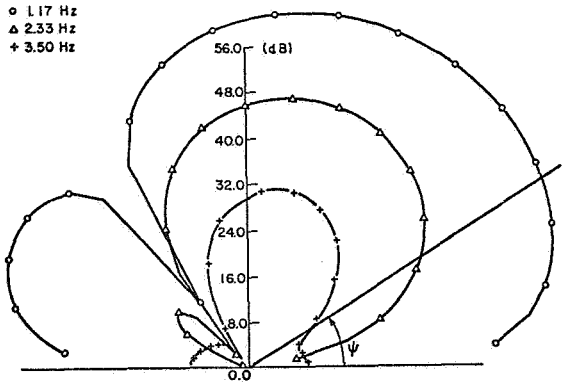

Figure 5: Directivity pattern for $\gamma = 90°$ at 1 Km of first three harmonics of acoustic signal due to operation in a linear Ground Shear of 8 MPH for free stream of 35 MPH, $\Omega = 35$ RPM.

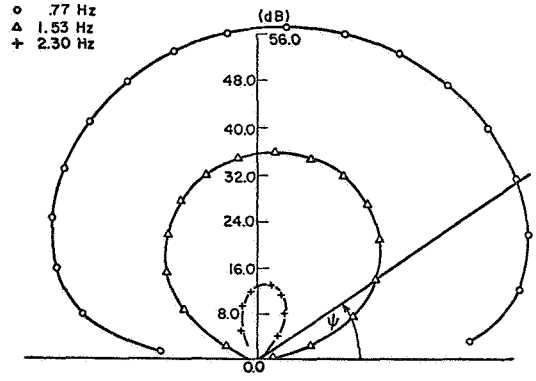

Figure 6: Directivity pattern for $\gamma = 90°$ at 1 Km of first three harmonics of acoustic signal due to operation in a linear Ground Shear of 8 MPH for free stream of 35 MPH, $\Omega = 23$ RPM.

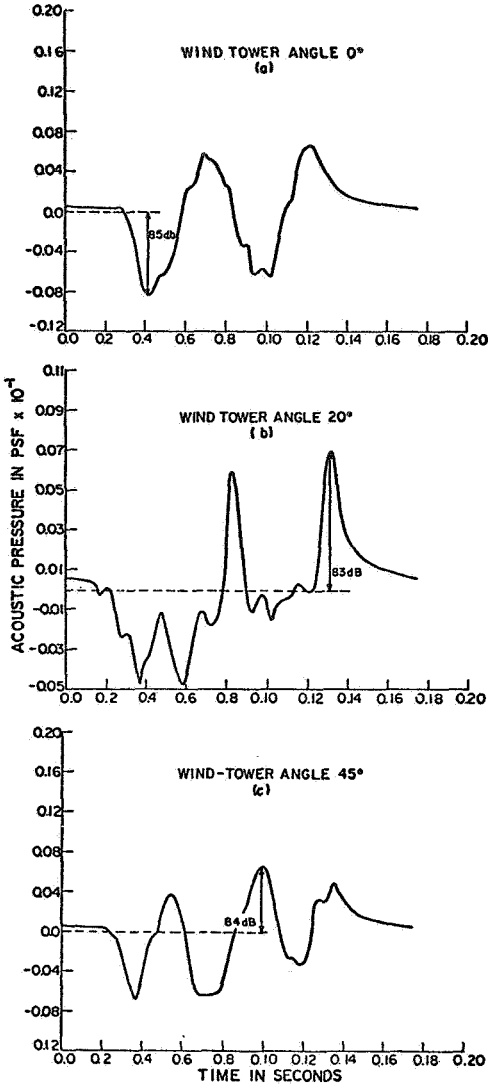

Figure 7a-c: Predicted acoustic signals at 1 Km at field point where sound pressure level was maximum for free stream of 35 MPH, $\Omega = 35$ RPM.

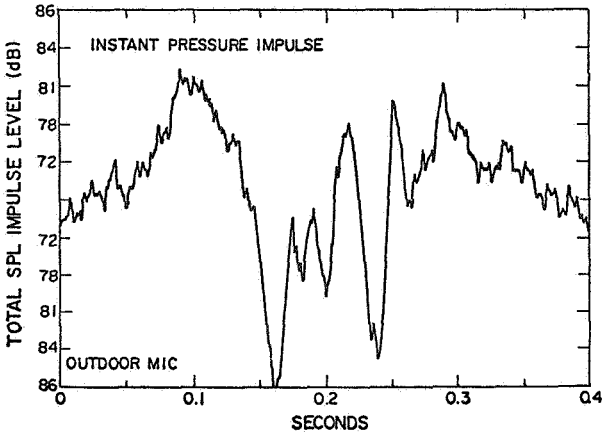

Figure 8: Measured acoustic signal at 1 Km, 24° off turbine axis for $\Omega = 35$ RPM (from ref. 8).

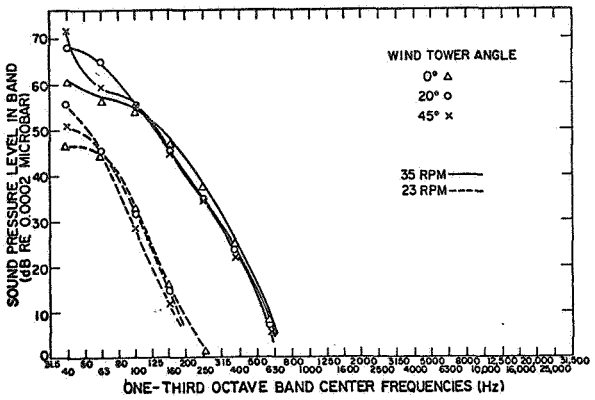

Figure 9: Spectra of predicted acoustic signals at 1 Km for $\Omega = 23$, 35 RPM; wind-tower angles 0°, 20°, 45°.

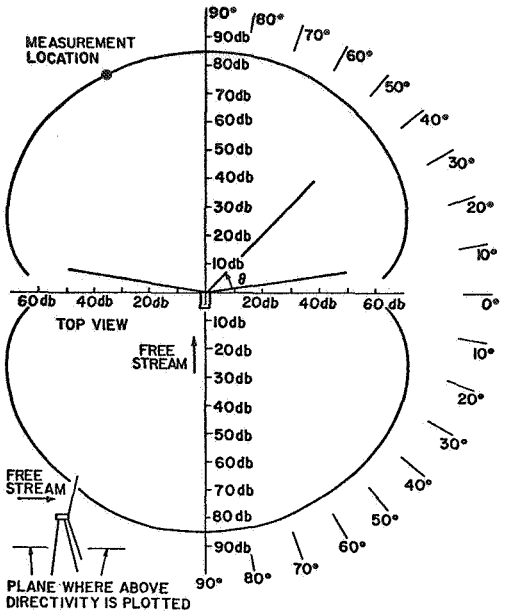

Figure 10: Predicted acoustic directivity pattern for tower-wake model for wind-tower angle of 0°. Location of measurement is indicated in the acoustic field.

QUESTIONS AND ANSWERS

W.L. Harris

From: F.W. Perkins

Q: Will any internal structural changes to the blades reduce impulsive noise significantly?

A: *No. Structural changes in the blades, within limitations of maintaining reliable blades, will not influence the tower wake. A small reduction in the amplitude of impulsive noise may be observed if a "softer" blade is used.*

THE NASA-LeRC WIND TURBINE SOUND PREDICTION CODE

Larry A. Viterna
National Aeronautics and Space Administration
Lewis Research Center
Cleveland, Ohio

ABSTRACT

Since regular operation of the DOE/NASA Mod-1 wind turbine began in October 1979 about 10 nearby households have complained of noise from the machine. Development of the NASA-LeRC wind turbine sound prediction code began in May 1980 as part of an effort to understand and reduce the noise generated by Mod-1. Tone sound levels predicted with this code are in generally good agreement with measured data taken in the vicinity Mod-1 wind turbine (less than 2 rotor diameters). Comparison in the far field indicates that propagation effects due to terrain and atmospheric conditions may be amplifying the actual sound levels by about 6 db. Parametric analysis using the code has shown that the predominant contributors to Mod-1 rotor noise are (1) the velocity deficit in the wake of the support tower, (2) the high rotor speed, and (3) off-optimum operation.

INTRODUCTION

Since regular operation of the Mod-1 wind turbine began in October 1979 about ten households have complained of noise from the machine. The character of the noise is described as an audible "thump" at a repetition rate equal to the blade passing frequency. In some instances, low frequency acoustic energy has resulted in complaints of vibrations within the homes.

Since January 1980, efforts have been directed at identifying the causes of the noise and methods of reducing it. One effort has been the development of computer prediction codes and obtaining experimental data to verify these codes. The objective of this effort is to understand the noise generated by Mod-1 and to prevent it from being a problem on advanced machines. Development of a wind turbine sound prediction code began at the NASA-LeRC in May 1980. This report presents (1) measured data that characterize the noise problem at Mod-1, (2) the analytical method used in the NASA LeRC code, (3) validation of the code using experimental data from Mod-1, and (4) applications of the code to the Mod-1 situation.

SUMMARY

Measured data taken at the Mod-1 site show that the impulsive character of the noise is composed of harmonics of the blade passing frequency. While some of these harmonics exist below the audible frequency range (about 20 to 20,000 Hz), many are above the nominal audible threshold of 20 Hz.

A computer program (WTSOUND) has been developed for calculating the intensity and frequency characteristics of sounds generated by wind turbines in a non-uniform wind flow field. The results calculated with this code are generally in good agreement with Mod-1 measured sound spectra. However, propagation effects due to terrain and atmospheric conditions have complicated the amplitude correlation with Mod-1 data in the far field. These effects have been estimated by the code to cause an amplification of 6 dB or more at a home that has registered complaints.

The WTSOUND code has been used to determine the source of the noise generation from Mod-1 as well as identifying operating conditions associated with the highest noise levels. Modeling of the wind flow field characteristics shows that the predominant source of noise from Mod-1 is the wind velocity deficit in the wake of the tower. Because the rotor plane is downwind of the tower, this deficit produces changes in the aerodynamic forces on the blades resulting in sound pressure variations in the acoustic field. The level of the sound pressure variations is most strongly a function of rotor speed and wind speed. Reducing the rotor speed from 35 to 23 rpm is predicted to reduce sound levels by about 11 dB. The increase in sound levels with windspeed is expected to be about 12 dB between cutin and rated windspeeds. Variation in sound level with power is not clear-cut since high sound levels can occur during both high and low power conditions.

MOD-1 MEASURED DATA

In January 1980, the Solar Energy Research Institute (SERI) and the General Electric Company under DOE funding began visiting the Mod-1 site to investigate the noise problem. During those visits, tape recordings of the sound pressures were made both near the Mod-1 and at residences that had complained of noise.

A good example of the recorded time history of the pressure variation near the Mod-1 recorded by SERI is shown in Figure 1. The impulsive nature is clearly apparent as each blade passes behind the tower structure. The passage of the blade through the wake of each leg of the tower is seen as the two upper peaks approximately 0.075 seconds apart.

To better understand the character of the pressure impulse, spectrum analyses were performed on the measured data. One sample spectrum of the sound near the Mod-1 is shown in Figure 2. This was recorded when the machine was generating a heavy "thumping" sound at a residence. From this analysis, it is obvious that the impulsive character is composed of harmonics of the blade passage frequency (1.16 Hz). While the highest amplitude harmonics

are in the sub-audible frequency range (less than about 20 Hz), tones are apparent in the audible frequency range above 20 Hz.

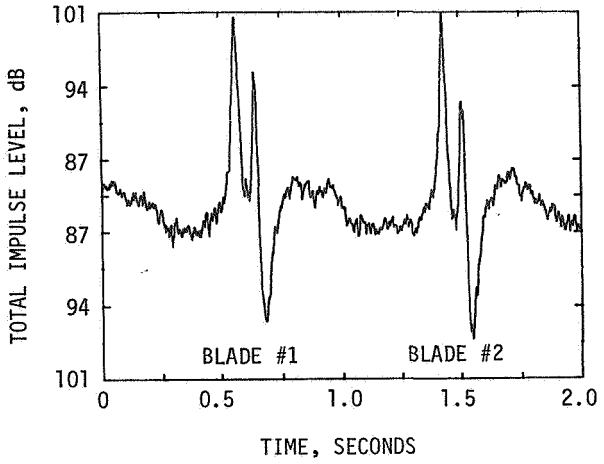

Figure 1 - Time history of the sound pressure variation near the Mod-1

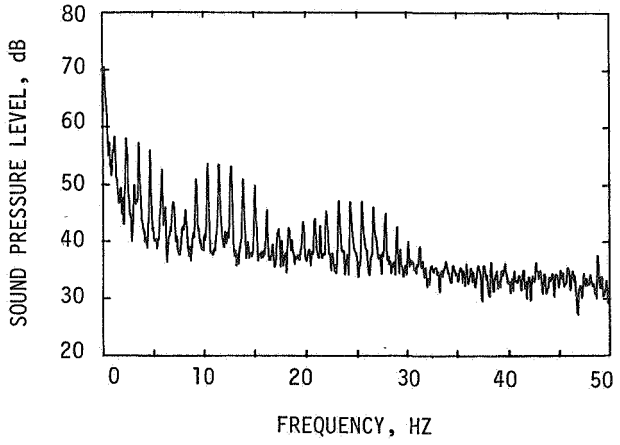

Figure 2 - Spectrum Analysis of sound variation near the Mod-1

ANALYTICAL METHOD OF THE SOUND CODE

The approach used in developing the wind turbine sound prediction code, WTSOUND, was to apply an available theory used for calculating noise from conventional aircraft propellers. The development of such theories goes back to 1937, when Gutin first successfully calculated the noise from a propeller in a uniform flow field (ref. 1). Since then, Gutin's theory has been extended to include the effects of non-uniform flow fields (ref. 2) and applied to helicopters and turbomachinery as well as propellers. The WTSOUND code was written using this theory to provide a means of calculating sound intensity and frequency characteristics specifically for wind turbines in non-uniform flow fields.

The predominant sound produced by a wind turbine is associated directly with the aerodynamic pressures on the blades. These pressures can be related for convenience to the thrust and torque forces on the rotor. The thrust and torque forces have components that are both steady and unsteady in time. The steady forces produce sound called rotational noise, which consists of pressure variations in the acoustic field at the blade passing frequency with harmonics of rapidly decreasing magnitude. The unsteady forces may be either periodic (i.e. tower shadow and windshear) or random (i.e. gusts). Noise due to periodic unsteady forces may be dominant over rotational noise and generated higher harmonics of amplitude comparable to that of the fundamental.

The method used to determine the sound pressure levels in the acoustic field is described by the flow chart in Figure 3. This procedure can be summarized as follows: (1) calculation of the steady aerodynamic blade forces, (2) variation in these forces due to unsteady aerodynamics, (3) Fourier analysis of the force variation, and (4) calculation of sound pressure levels in the acoustic field. These steps are explained in more detail in the following sections.

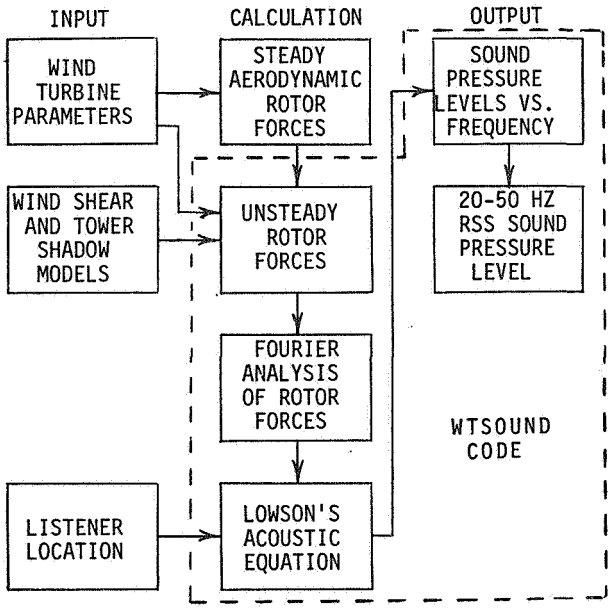

Figure 3 - Flow chart of sound pressure level calculation

Steady Aerodynamic Blade Forces

The total thrust force and torque on a rotor in uniform flow is determined from blade element-momentum theory. The reader is referred to reference 3 for development of this theory. There are several computer programs available that use blade element-momentum theory,

including the PROP code (ref. 3). The PROP code requires modeling of the wind turbine characteristics and operating conditions (i.e. planform, twist, rpm, windspeed, etc) to calculate the steady torque and thrust force on the rotor. The total torque and thrust on the rotor can then be resolved into equivalent forces acting on each blade at a single point. The point used in this analysis is the 75 percent radius of the blade. That radial location is also used when modeling the unsteady aerodynamic variation.

Unsteady Aerodynamic Blade Forces

Once the steady forces have been determined, the unsteady forces are obtained through perturbation with non-dimensional force coefficients. Figure 4 shows the the wind velocity and force vector diagram of an airfoil element of chord length c. This airfoil is operating at a pitch angle θ with respect to the plane of rotation. The velocity of the wind at the rotor plane, V_W, combines with the velocity due to rotation, V_Ω, to give the relative velocity vector, V_R. The relative velocity vector acts at an angle of attack α with respect to the airfoil chord line. The relative velocity and angle of attack are given by

$$V_R = \left(V_w^2 + V_\Omega^2\right)^{1/2} \tag{1}$$

and

$$\alpha = \tan^{-1}\left(\frac{V_w}{V_\Omega}\right) - \theta \tag{2}$$

The airfoil lift and drag coefficients are shown as the heavy line vectors in Figure 4.

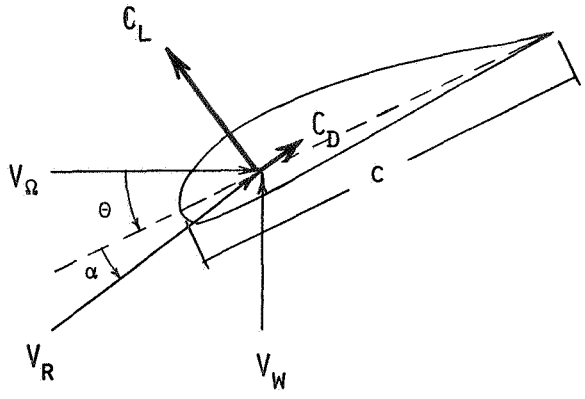

Figure 4 - Wind velocity and force vector diagram

These coefficients can be transformed into a thrust force coefficient, C_T, acting perpendicular to the rotor plane and a torque force coefficient, C_Q, acting parallel to the rotor plane where

$$C_T = C_L \cos(\alpha + \theta) + C_D \sin(\alpha + \theta) \tag{3a}$$

and

$$C_Q = C_L \sin(\alpha + \theta) - C_D \cos(\alpha + \theta) \tag{3b}$$

The thrust and torque coefficients can now be used to determine the unsteady forces associated with periodic variations in the wind velocity, V_W. Such a periodic variation will occur as the blade rotates through wind shear or behind the wind turbine support tower. The quasi-steady state values of blade thrust force, T^Ψ, and torque force, Q^Ψ, at any rotor azimuth position, ψ, are given by

$$T^\Psi = \frac{C_T^\Psi}{C_T^s} T^s \tag{4a}$$

and

$$Q^\Psi = \frac{C_Q^\Psi}{C_Q^s} Q^s \tag{4b}$$

in which the superscript s denotes the steady forces and coefficients respectively.

Fourier Analysis of the Force Variation

The next step is to a perform a Fourier analysis of the blade force variation. The complex Fourier coefficients for the thrust and torque forces respectively are given by

$$a_p^T = \frac{\Omega}{2\pi} \int_0^{2\pi/\Omega} e^{ip\Omega\tau} T^\Psi(\tau)\, d\tau \tag{5a}$$

and

$$a_p^Q = \frac{\Omega}{2\pi} \int_0^{2\pi/\Omega} e^{ip\Omega\tau} Q^\Psi(\tau)\, d\tau \tag{5b}$$

in which Ω is the rotor speed.

These coefficients are determined in the program using the IBM subroutine FORIT. FORIT gives real Fourier coefficients A_p and B_p for the cosine and sine terms respectively. The transformation to complex coefficients is

$$a_p = A_p + iB_p \tag{6a}$$

or

$$a_{-p} = A_p - iB_p \tag{6b}$$

for

$$p \geq 0$$

A correction to the quasi-steady state analysis can now be made by including the effects of unsteady aerodynamics. The approach used here to determine the response of the airfoil was developed by Sears (ref. 4). The correction is

given by a simple expression called a Sears function, which is used as a factor to the Fourier coefficients. The expression used to approximate the Sears function is

$$S(\sigma) \simeq \frac{\exp\left\{-i\sigma\left[1 - \frac{\pi^2}{2(1 + 2\pi\sigma)}\right]\right\}}{(1 + 2\pi\sigma)^{1/2}} \qquad (7a)$$

for $\sigma \geq 0$

where $$\sigma = \frac{p\Omega c}{2V_R} \qquad (7b)$$

The coefficients a_p and a_{-p} in Equations (6) are multiplied by the Sears factor before use in calculating sound pressure levels.

Sound Pressure Levels in the Acoustic Field

The mathematical relationship for calculating the sound pressure levels from the Fourier coefficients of the blade force variation was obtained by Lowson (ref. 5). The RMS pressure variation of the n^{th} harmonic of the blade passage frequency is given by the following equations:

$$P_n = \frac{k_n\sqrt{2}}{4\pi s}\sum_{p=1}^{\infty}\left[e^{-ip(\phi-\pi/2)}J_{nB-p}(k_n r_m \sin\gamma)\times\left(a_p^T\cos\gamma - \frac{nB-p}{k_n r_m}a_p^Q\right)\right. \qquad (8a)$$

$$\left. + e^{ip(\phi-\pi/2)}J_{nB+p}(k_n r_m \sin\gamma)\times\left(a_{-p}^T\cos\gamma - \frac{nB+p}{k_n r_m}a_{-p}^Q\right)\right]$$

$$+ J_{nB}(k_n r_m \sin\gamma)\left(T^s\cos\gamma - \frac{nB}{k_n r_m}Q^s\right)$$

and $$k_n = \frac{nB\Omega}{C_o} \qquad (8b)$$

in which

- B is the number of blades
- S is the distance from the rotor
- γ,ϕ are azimuth and altitude angles to the listener
- r_m is the blade radius where the thrust and torque forces are assumed to act
- J is the standard Bessel function
- Co is the speed of sound

VALIDATION OF THE WTSOUND CODE

To verify the accuracy of the WTSOUND code, measured data from the Mod-1 wind turbine were used. The data presented here were taken from references 6 and 7.

Correlation with the Mod-1 Measured Data

On June 10, 1980 at 12:36 a.m. sound levels were being measured with a microphone located about 240 ft from the Mod-1. The wind turbine was operating at 34.6 rpm in a 30 mph wind and generating about 750 kw into a load bank. The measured sound spectrum is shown in Figure 5 and has been designated case GE 180. These measured sound levels consist of both tones and broad-band noise. The tone levels, shown as the narrow peaks, are generated by the wind turbine. The broad-band level, shown as the flat areas of the spectrum, is composed of ambient wind noise as well as blade vortex noise.

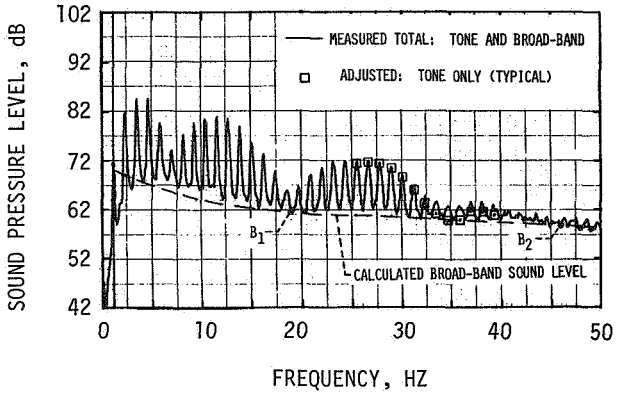

Figure 5 - Mod-1 measured sound levels for case GE 180

Since the WTSOUND code calculates tone sound pressure levels, the effect of the broad-band noise on the spectrum must be removed for comparison with the code. To do this, two points on the spectrum were chosen that were believed to be at the broad-band noise level (B_1 and B_2 in Figure 5). The broad-band levels throughout the spectrum were calculated using the following empirical model:

$$L_f^b = \left(\frac{L_2^b - L_1^b}{\log\frac{f_2}{f_1}}\right)\log\left(\frac{f}{f_2}\right) + L_2^b \qquad (9)$$

where

- L_f^b is the broadband sound level in dB at frequency f
- L_1^b, L_2^b are the broadband sound levels in dB at points B_1 and B_2
- f_1, f_2 are the frequencies corresponding to points B_1 and B_2

The tone-only levels were then determined by

$$L_f^t = 10 \log\left(10^{L_f^m/10} - 10^{L_f^b/10}\right) \qquad (10)$$

where

L_f^t is the tone sound level in dB at frequency f

L_f^m is the measured total sound level in dB at frequency f

Some typical adjusted tone-only sound pressure levels are shown as the squares in Figure 5. Note that this correction is small and can only be seen in areas where the tone and broad-band levels are comparable.

An analytical model of the Mod-1 wind turbine was developed for case GE 180. Steady thrust and torque forces, required input for the WTSOUND code, were calculated using the PROP performance code. The wind velocity deficit in the wake of the tower was approximated as an average of the velocity profiles at the 69, 75, and 81 percent blade radius. The velocity profiles were taken from scale model wind tunnel tests of the Mod-1 tower (ref. 8). Figure 6 shows the measured wake velocities as well as the analytical wake model assumed. Note that the measured and assumed profiles were taken at different distances downwind of the tower. No correction to the wake for distance appears to be required, and none was made.

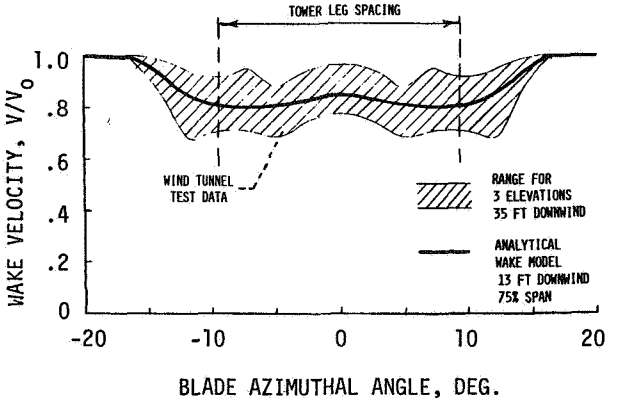

Figure 6 - Mod-1 tower shadow

Lowson's equation gives free-space sound pressures with no effect of reflection from nearby solid bodies. A 6 dB increase has been included in the WTSOUND code analysis to account for reflection when using microphones near the ground. This correction is common practice when calculating airplane propeller noise at ground level (ref. 9).

Figure 7 shows the comparison of measured and predicted sound levels. The squares are the same as those shown in Figure 5. The vertical lines are the tone levels predicted by the WTSOUND code. In general the code predicts the amplitudes of the highest harmonics very well. Also the roll-off rates (amplitude decreasing with frequency) of the harmonics compare favorably. The differences that do exist are believed to be associated with the tower shadow model mentioned earlier.

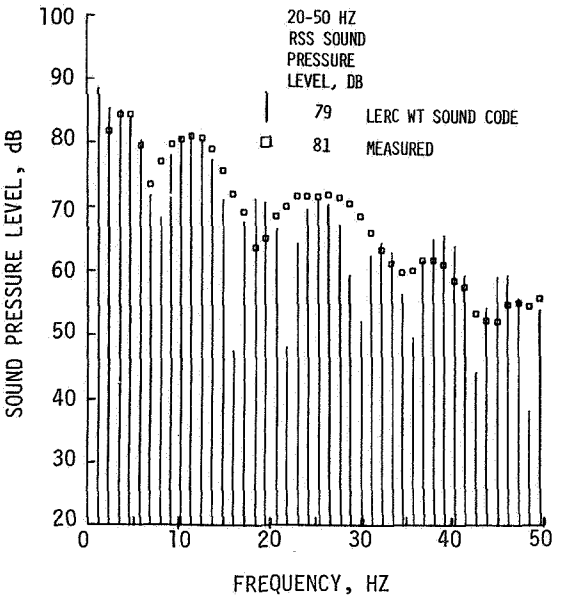

Figure 7 - Comparison of theoretical and measured sound spectra for case GE 180

To more conveniently characterize the overall sound level of this spectrum, the root sum square (RSS) of the harmonics between 20 and 50 Hz was calculated. The lower end of this range was chosen as the nominal threshold of hearing. The upper bound was chosen because the tone levels above this frequency fall below the broad-band noise. As shown in Figure 7 the 20-50 Hz RSS sound pressure level given by the WTSOUND code is 2 dB lower than the measured data. This agreement is felt to be very good.

Table 1 summarizes the results from GE 180 as well as two other examples, cases GE 140 and GE 1B. These two cases were chosen to test the ability of the code to predict changes in rotor speed and distance from the machine.

GE 140 documents the sound levels near the Mod-1 on June 9, 1980 at 9:22 p.m. The wind turbine was operating at a reduced speed of 22.7 rpm while again generating 750 kw. The wind speed of 26 mph was lower than the 30 mph wind of GE 180. The measured RSS sound level for GE 140 is 17 dB less than GE 180. Note that this reduction is exactly the same as predicted by the code.

GE 1B documents the sound levels at some distance from the Mod-1 (3100 ft. downwind) on March 31 at 12:26 pm. This location is near a residence that has complained of noise from the

machine. At this time the Mod-1 was operating at 34.7 rpm in a 30 mph wind and producing about 1850 kw into the utility grid. The measured 20-50 Hz RSS sound level is 21 dB lower than GE 180. The predicted level, however, was 27 dB lower. Thus the actual level is about 6 dB higher than predicted by normal spherical dispersion. This 6 dB increase is believed to be associated with focusing of the sound due to terrain and atmospheric conditions. Though the amount of amplification may vary, this case demonstrates the use of the code to quantify the effects on sound propagation.

Table I - Summary of Mod-1 sound data cases

NEAR FIELD (1.3 D)

CASE	RPM	WIND SPEED, MPH	20-50 HZ RMS SOUND PRESSURE LEVEL, DB		
			CODE	MEASURED	DIFFERENCE
GE 180	34.6	30	79	81	-2
GE 140	22.7	26	62	64	-2

FAR FIELD (15.5 D)

GE 1B	34.7	30	52	60	-8

APPLICATION OF THE SOUND CODE

After gaining confidence in the ability of WTSOUND to predict the sound characteristics of wind turbines, the code was used to investigate the Mod-1 problem. In particular, studies were made of (1) the contribution to the sound level by characteristics of the flow field, and (2) the operating conditions that affect the Mod-1 sound problem.

Effect of Flow Field Characteristics

The WTSOUND code was used to determine the relative contribution to the sound level by the characteristics of the flow through the rotor. Figure 8 shows the effect of the uniform flow, wind shear, and tower shadow. As stated earlier, the uniform flow field contribute significantly only to the fundamental blade passing frequency. Similarly, wind shear, which is essentially a 1/rev. variation, contributes only to the first few harmonics. However, with the addition of tower shadow, many harmonics are introduced that have high amplitudes up into the audible frequency range. Thus, the predominant contribution to the noise problem of Mod-1 is the wind velocity deficit in the wake of the tower.

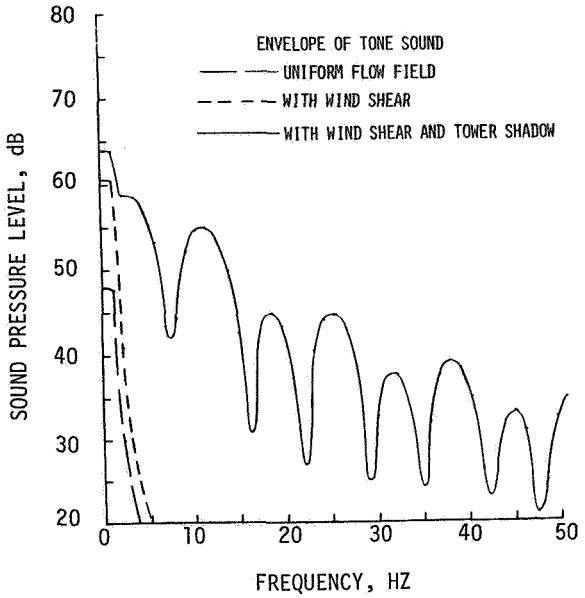

Figure 8 - Effect of wind shear and tower shadow on wind turbine sound level (Mod-1 case GE 1B)

Effect of Operating Conditions

In an effort to better understand the conditions under which the highest sound levels are produced, the WTSOUND code was used to study the effects of various operating parameters. In particular, the effects of power, rotor speed, wind speed, and direction were investigated.

Figure 9 shows the predicted sound levels versus power output for both 35 and 23 rpm operation. The solid line shows normal operation as the wind speed varies from cutin through rated to cutout wind speed (6, 15, and 20 m/sec respectively). This analysis shows about a 12 dB increase in sound level from cutin to rated wind speeds for both 35 and 23 rpm operation. This agrees reasonably well with empirical modeling of the measured data (ref. 7) that indicates a variation of about 14 dB over those wind speeds.

During normal operation at 23 rpm, the sound levels predicted in Figure 9 are about 11 dB lower than those for 35 rpm. This also agrees well with measured data taken in June 1980. During those tests, the Mod-1 was operated at various speeds into a load bank. Analysis of these data showed a reduction of about 10 dB at a rotor speed of 23 rpm (ref. 7).

The shaded area in Figure 9 represents operation below the available power in the wind for wind speeds less than rated. Operation in this region is characterized as off-optimum. Under this situation the pitch of the blade is increased toward feather, to limit power below the rating of the machine. The shaded area shows that high sound levels may be produced even at low power levels. This conclusion seems to be supported by the fact that GE 180 (750 kw, 30 mph) is further from normal operation than GE 140 (750 kw, 26 mph) and is higher in sound

level than the 11 dB difference associated with rpm only.

The sound levels at off-optimum operation above rated have not been determined. Improvements in the unsteady aerodynamic force calculation in the WTSOUND code are being incorporated to analyze this area of operation.

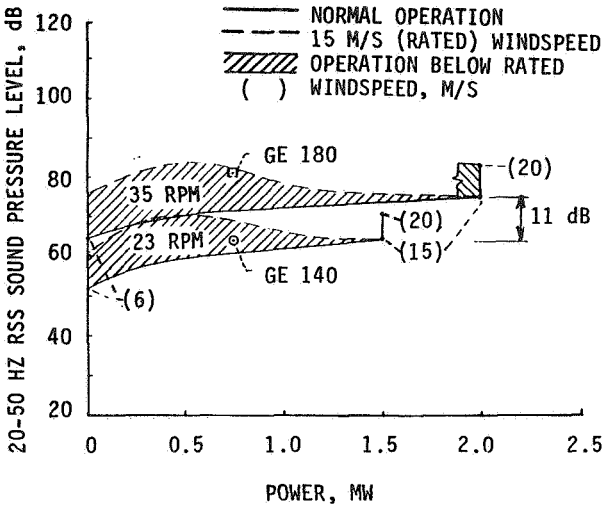

Figure 9 - Effect of power, rpm, and windspeed on Mod-1 wind turbine sound levels

The WTSOUND code can also be used to calculate the directivity pattern of the sound. Figure 10 shows the directivity pattern in a plane 1100 ft. below the Mod-1 hub height. The direction of highest sound pressure is directly downwind; however, it is nearly as high upwind. Minimum sound generation occurs in the rotor plane where levels are about 18 dB lower than downwind. This compares reasonably well with measured data in the near field showing about 15 dB variation (ref. 7).

CONCLUSIONS

The WTSOUND computer code shows generally good agreement with sound spectra measured in the vicinity of a wind turbine. In the far field, however, correlation of the absolute amplitude of the sound level is complicated by propagation effects. For the case in this study, terrain and meterological conditions caused an increase of about 6 dB.

Analysis using the SOUND code shows that the predominant contributor to the noise problem of Mod-1 is the wind velocity deficit in the wake of the tower. Changes in the aerodynamic forces, as the blades pass through the deficit, produce sound pressure variations in the acoustic field.

The level of the sound pressure variations are most directly affected by rotor speed and windspeed. Reducing the rotor speed from 35 to 23 rpm is predicted to reduce sound levels by about 11 dB. The increase in sound levels with windspeed is predicted to be 12 dB between cutin and rated.

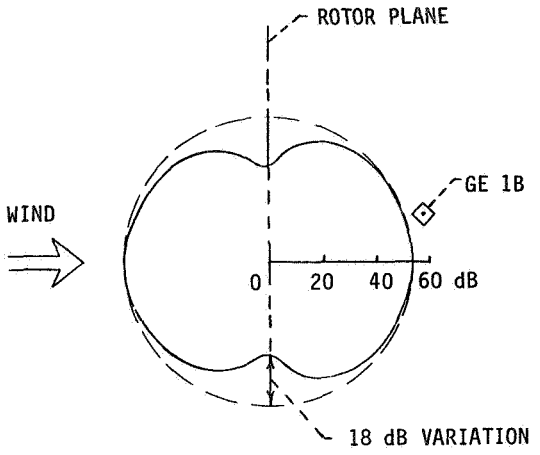

Figure 10 - Predicted sound directivity pattern in a plane 1100 ft. below the Mod-1

REFERENCES

1. Gutin, L.: On the Sound Field of a Rotating Propeller. NACA TM 1195, 1948.

2. Goldstein, M. E., Aeroacoustics, Mc-Graw-Hill (New York), 1976.

3. Wilson, R. E., and Lissaman, P. B. S.: Applied Aerodynamics of Wind Power Machines, Oregon State University, May 1974.

4. Sears, William R.: Some Aspects of Non-Stationary Airfoil Theory and its Practical Applications, J. Aeron. Sci, 8, 3, 1941.

5. Lowson, M. V.: Theoretical Analysis of Compressor Noise. J. Acoust. Soc. Am., 47, 1 (part 2), 371-385, 1970.

6. Wells, R. J.: Mod-1 Wind Turbine Generator Preliminary Noise Evaluation. General Electric Company Report, May 1980 (unpublished).

7. Wells, R. J.: Mod-1 Wind Turbine Noise Studies, General Electric Company Report, October 1980 (unpublished).

8. Savino, J. M., Wagner, L. H., and Nash, M.: Wake Characteristics of a Tower for the DOE-NASA Mod-1 Wind Turbine, NASA TM-78853, April 1978.

9. Regier, A. A., Hubbard, H. H., Lassiter, L. W.: Propeller Noise, Technical Aspects of Sound, E. G. Richardson, ed., Elsevier (New York), 1957, p. 338.

QUESTIONS AND ANSWERS

L.A. Viterna

From: G. Greene

Q: What was the averaging time of the data you used for comparison?

A: *Approximately 5 minutes.*

From: D.W. Thomson

Q: Are you working on a code for f < 20 Hz? The observational data seemed to strongly support structural excitation as a major source of annoyance.

A: *The code predicts harmonics starting at the blade passage frequency (∿ 1 Hz). We are using the 20-50 Hz RSS sound level to characterize audible annoyance.*

From: N.D. Kelley

Q: Why does your model predict so many spectral peaks between blade passage and 50 Hz compared to OBS?

A: *This is due to the actual tower wake shape being different than the assumed wake based on scale model wind tunnel tests. We feel however, that the assumed wake is adequate to acceptably predict the spectrum characteristics.*

NOISE GENERATION OF UPWIND ROTOR WIND TURBINE GENERATORS

R. H. Spencer

The Boeing Vertol Company
P.O. Box 16858
Philadelphia, PA 19142

ABSTRACT

Noise sources of wind turbines with rotors upstream of the support structure are discussed along with methodology for sound level prediction. Estimated noise levels for the MOD-2 wind turbine are presented operating in both the upwind and downwind configurations. Results indicate that upwind rotor configurations may be advantageous from an acoustical standpoint.

INTRODUCTION

Wind turbine installations in the past generally have had low acoustic signatures that ranged from unobtrusive to those which generated some annoyance in the immediate vicinity of the turbine while not dominating the ambient signature of the surrounding area. With the operation of the MOD-1 system, however, a more active interest in the noise of wind turbines took place. The acoustic signature of this rotor surprised engineers involved with the program as well as those who became associated as a direct result of the operation of the MOD-1 system. The predominant source of noise for this downwind rotor configuration appears now to be fluctuating airloads arising from interaction of the rotor and the wake trailed by the tower support structure. Upwind rotor configurations do not experience the same magnitude of airload fluctuations as the blade passes upstream of the tower, and other noise sources dominate. The subject paper discusses sources of noise on upwind rotor configurations and, in particular, the Boeing MOD-2 system.

SOURCES OF NOISE

Wind turbine generator systems may be classified into two categories with respect to the position of the rotor relative to its support tower structure: (1) rotors which operate upwind and (2) those which operate downwind of the support structure. Rotors which are positioned closely downstream of the tower experience airload fluctuations as the blades pass through the disturbed wake of the structural members. Noise sources for wind turbines consist of rotor periodic and non-periodic components as well as those due to mechanical, hydraulic and electrical components housed within the hub, although these latter sources are negligible beyond a few rotor diameters. Figure 1 presents the components of rotor noise classified with respect to their time domain characteristics. The periodic elements consist of thrust, drag and radial forces on the blade which arise from the steady and fluctuation airloads, wind shear effects, and periodic airload disturbances resulting from the tower wake on a downwind rotor, the aerodynamic reflection of the tower on an upwind rotor, or possible interactions with the trailed vortex system.

Nonperiodic components of rotor noise consist of (1) random load fluctuations resulting from atmospheric turbulence ingested into the rotor, and (2) the shear stress effects of a viscous medium. Noise arising from rotating blades ingesting disturbances in the flow has been investigated previously by researchers interested in the effects of axial flow fans[1,2,3]. More recently, atmospheric turbulence effects on propellers and helicopter rotors were studied, among others, by Hanson[4], George and Kim[5] and Humbad and Harris[6]. This research showed that

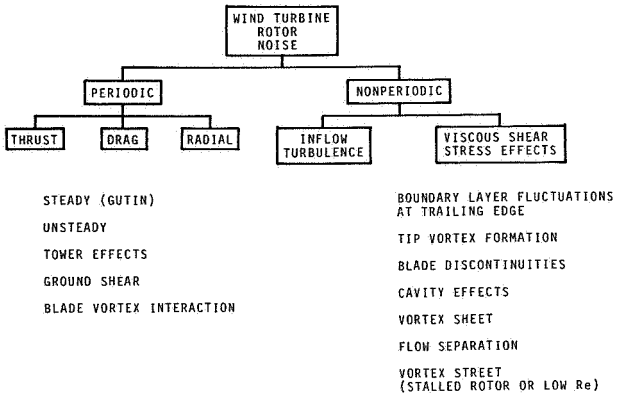

Figure 1 - Wind turbine generator noise sources

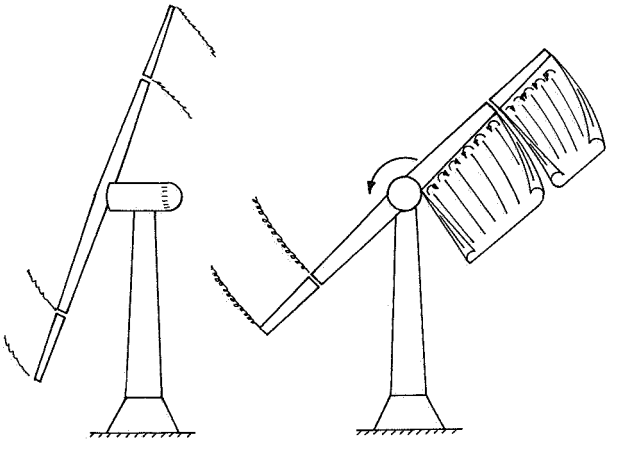

Figure 2 - Trailing vortex sheet and filaments

sources which can arise from shear stresses in the viscous medium are (1) turbulent boundary layer noise, (2) trailing edge noise resulting from unsteady flow, (3) noise of trailed vortex filaments on the tip and other blade discontinuities, such as the joint of a segmented rotor, and (4) the trailed vortex sheet arising from the spanwise loading gradient, as well as loading fluctuations at each blade station which gives rise to a sheet of vortex filaments shed along the blade span. This vortex sheet rolls up within a few chord lengths into the trailed filaments at the tip and into a weaker system at the root. The blade discontinuity of a segmented rotor gives rise to an additional filament (Figure 2).

In a recent paper presented at the HAA/NASA Advanced Rotorcraft Technology Workshop[7] Raney, Hood and Biggers compared the contribution of the unsteady nonperiodic sources. This is reproduced here as Figure 3 and shows that turbulence ingestion appears harmonic in content, but in reality is random atmospheric turbulence modulated at blade passage frequency.

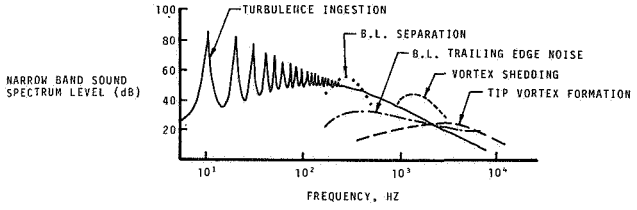

Figure 3 - Noise from unsteady loading sources

NOISE PREDICTION METHODOLOGY

The method of Lowson and Ollerhead[8] was used to determine the periodic forces on the rotating blade. Harmonic amplitudes of rotational noise can be determined from

$$C_n = \sum_{\lambda=0}^{\infty} k \cdot \frac{T}{R \cdot r_\lambda} \left\{ nM \sin C_{\lambda T} J_1' - C_{\lambda D} J_2' + (nM \cos\theta C_{\lambda C}) J_3' \right\} \quad (1)$$

Two methods were evaluated to account for tower wake effects. The first was Lowson's noncompact source theory, Eq. 2, which may be used to predict periodic components of rotational noise if spanwise and azimuthal distribution of airloads and velocity are known.

$$p = \frac{1}{4\pi a_0^2} \int \left[\frac{x_i - y_i}{a_0 r (1-M_r)} \frac{\partial}{\partial t} \left(\frac{F_i}{r(1-M_r)} \right) \right] d\eta \quad (2)$$

Airloading near the tower structure was modified by wake velocity and incidence effects. This procedure showed that using 11 spanwise airloading stations and 180 azimuthal stations, harmonics of rotor noise up to approximately 40 could be determined. An alternate method of including wake effects was investigated in an attempt to improve the higher harmonic prediction. Wright[9] expanded Lowson's theory to include the response to a vortex. In the form written by Pegg[10], the expression is,

$$P_{mB} = \frac{\Delta L}{L_0} E \rho_w K_T mB \frac{\sin \pi (ft_0 - 1)}{4(ft_0 - 1)} - \frac{\sin \pi (ft_0 + 1)}{4(ft_0 + 1)} \quad (3)$$

This was evaluated for the MOD-1 turbine using the wake structure downstream of the tower as measured by Savino[11] on a wind tunnel model. These results, shown in Figure 4, indicate reasonable agreement with measured data at 35 and 23 RPM. Prediction of harmonic components of rotor noise are reliable provided airloads and wake structure are known.

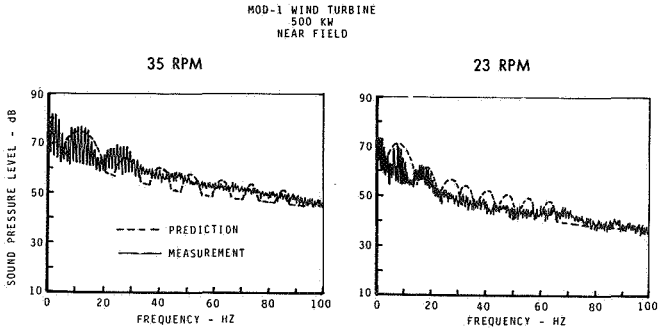

Figure 4 - Comparison of measured and predicted MOD-1 noise levels

Prediction of the nonperiodic sources of rotor noise on the other hand is less exact. For example, the spectrum, scale length and intensity of random atmospheric turbulence is not known nor have pressure fluctuations in the boundary layer been thoroughly documented. Detailed knowledge of the structure of the wake of the rotor is required to estimate tip vortex noise and trailing edge noise and this information is not available. As a result, estimation of the noise due to viscous shear effects has been predominantly empirical. Airframe noise prediction procedures are currently empirically based in that analytic methods have not been adequately correlated with data. Fink[12], for example, describes the noise of fixed wind aircraft airframes, leading edge devices, trailing edge flaps and landing gear by empirical trends.

Since the noise due to nonperiodic sources results from viscous effects rather than from turbulent inflow, the noise signature can be related to profile drag of the rotor. Trends developed by Boeing Vertol during the Heavy Lift Helicopter program showed that broadband noise above 300 Hz was related to rotor profile power by

$$SPL_{2KHz} = 20 \text{ Log } p - 10 \text{ Log } \frac{A_b}{\cos^2 \gamma + 0.1} + K + 20 \text{ Log } \frac{110}{r} \quad (4)$$

Broadband noise profile power trends based on a helicopter rotor are shown in Figure 5. The K term derived for helicopter rotors (-3 to -13) appears to be too large for wind turbines and preliminary data from the MOD-0 unit indicates that a K of -26 gives good agreement. There is some indication that for a given profile power, increased blade area, A_b, reduces broadband noise. This would indicate that reduced turbulence intensity on and in the wake of the blade reduces the nonperiodic noise. Directivity is accounted for in the angle between the thrust line and the observer, γ, and distance effects in the last term. A spectum slope of 6db per octave appears to give good agreement for segmented rotors.

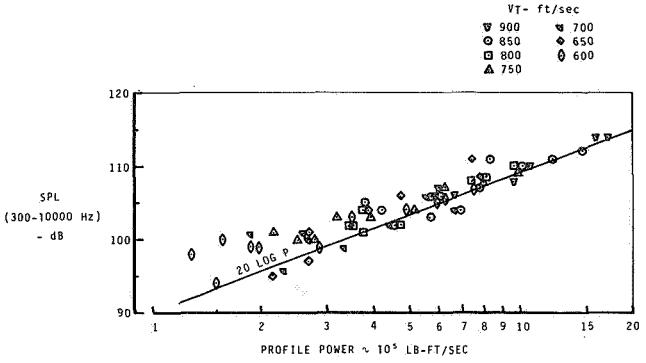

Figure 5 - Broadband noise profile power trends

PREDICTION OF MOD-2 NOISE

Noise levels of the MOD-2 turbine were estimated (Figure 6) using the methods of the previous section including Wright's theory for the tower wake response. As an upwind system, the velocity profile of the tower reflection shown in Figure 7 was included. This profile was developed using theory for flow around circular cylinders [13] as well as measured profiles behind model towers. Ground shear was considered to be insignificant and was not included in the airloading. Broadband noise was determined using Equation 4. Note that broadband noise for MOD-2 establishes

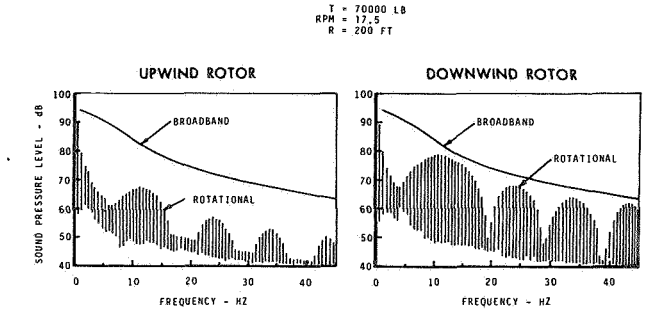

Figure 6 - Predicted MOD-2 noise levels

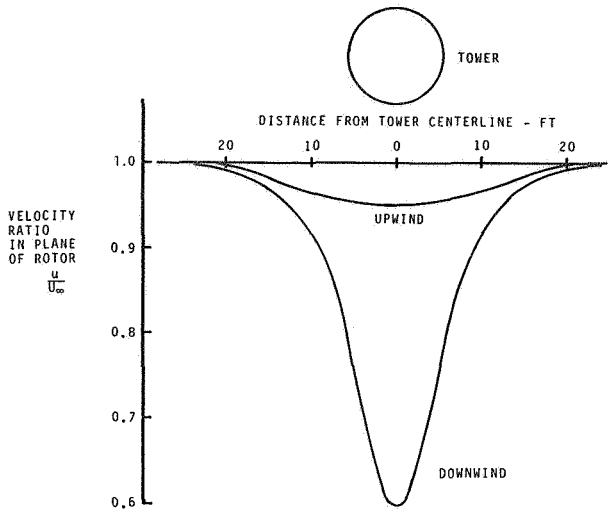

Figure 7 - Wind velocity profile used in analysis

the signature, while for MOD-1 (Figure 4) harmonic levels dominate. Broadband levels also dominate the MOD-0 rotors.

An estimate of the rotational noise of the MOD-2 turbine was made assuming it was operating as a downwind rotor. In this case, the downwind velocity profile of Figure 7 was used. The marked increase in higher harmonic sound level illustrates the benefit which results from rotors that operate in undisturbed air.

CONCLUSIONS AND RECOMMENDATIONS

Upwind rotor wind turbines, which produce only nonperiodic sources of noise such as generated by random atmospheric turbulence, a turbulent boundary layer or the formation of a trailed tip vortex filament result in a nonimpulsive acoustic signature that is characterized by a swishing, rather than a thumping sound. These sources of noise tend to have low radiation efficiencies and broadband spectra which are more acceptable than discrete tonal noise components. Any device which reduces the disturbed wake behind the tower structure of a downwind rotor will also improve the acoustical signature of a downwind rotor.

Upwind rotors appear to have an advantage over downwind rotors from an acoustical standpoint. Predictions for the MOD-2 turbine indicate that the noise signature will be of a broadband nature. Although noise measurements have not been made on the MOD-2 turbine to date, comments from observers indicate that the predominant noise is a swishing sound characteristics of a broadband noise source. Levels between 60-65 dBA have been predicted for MOD-2 at a distance of 200 ft, similar to those near a freeway with moderate traffic at an equivalent distance.

Improved prediction methods for broadband, nonperiodic sources of noise are required in order to estimate the acoustic signature of new turbine generators with confidence. The existing

empirical broadband methodology lacks a rigorous analytical understanding which must be developed from an adequate data base in order to accurately quantify these sources. Additional measurements should be made to verify the unsteady loading noise theory as it is developed.

ACKNOWLEDGEMENT

Substantial technical and programming assistance for this paper was contributed by Byung K. Oh of Boeing Computer Services. The author gratefully acknowledges this contribution particularly in the area of harmonic noise component prediction.

REFERENCES

1. Sharland, I.J., "Sources of Noise in Axial Fans", J. Sound and Vibration (1971) 17

2. Mani, R., "Noise Due to Interaction of Inlet Turbulence with Isolated Stators and Rotors", J. Sound and Vibration, (1971) 17

3. Morfey, C.L., "Broadband Sound Radiated from Subsonic Rotors", 1970 International Symposium on the Fluid Mechanics and Design of Turbomachinery, Pennsylvania State University

4. Hanson, D.B., "The Spectrum of Rotor Noise Caused by Atmospheric Turbulence", Presented at the Spring Meeting of the Acoustical Society of America, New York City, April 23-26, 1974

5. George, A.R. and Kim, Y.N., "High Frequency Broadband Rotor Noise", AIAA 34d Aeroacoustics Conference, Palo Alto, California, July 20-23, 1976

6. Humbad, N.G. and Harris, W.L., "Model Rotor Low Frequency Broadband Noise at Moderate Tip Speeds, AIAA 6th Aeroacoustics Conference, Hartford, Connecticut, June 4-6, 1980

7. Raney, J.P., Hood, D.R., Biggers, J.C., "Overview of NASA's Rotorcraft Acoustics Program", a paper presented at the HAA/NASA Advanced Technology Rotorcraft Workshop, Palo Alto, California, Dec. 3-5, 1980

8. Lowson, M.V. and Ollerhead, J.B., "Studies of Helicopter Rotor Noise", USAAVLABS TR68-60, Jan. 1969

9. Wright, S.E., "The Acoustic Spectrum of Axial Flow Machines" J. Sound and Vibration (1976) 45(2) 165-223.

10. Pegg, R.J., "A Summary and Evaluation of Semi-Empirical Methods for the Prediction of Helicopter Rotor Noise" NASA TM 80200 Dec. 1979.

11. Savino, J.M., Wagner, L.H. and Nash, M., "Wake Characteristics of a Tower for the DOE-NASA MOD-1 Wind Turbine", NASA TM-78853, April 1978

12. Fink, M.R., "Airframe Noise Prediction Method", FAA Report FAA-RD-77-29, March 1977

13. Schlicting, Herman: Boundary Layer Theory, McGraw-Hill Book Co. Inc., 6th Ed., 1968.

NOMENCLATURE

A_b	total blade area
c	speed of sound
C_n	amplitude of nth harmonic at specified field point
$C_{\lambda T}$, $C_{\lambda D}$, $C_{\lambda C}$	thrust, drag and radial force harmonic coefficient
E	number of interactions per revolution
F_i	aerodynamic force components
J_i	complex collection of Bessel functions of argument (nMcosθ)
k	airload decay constant
K	constant, nonperiodic equation
K_T	thrust constant
$\frac{\Delta L}{L_o}$	fractional steady load change per blade
M	rotational Mach number
M_s	source Mach number in direction of observer
n = MB	harmonic number x number of blades
P	rotor profile power
p(t)	instantaneous near-field acoustic pressure
r	distance between rotor center and field point
R	radius of action of blade forces
s	blade loading harmonic number
S	distance between source and observer
T	thrust
x_i	observer coordinates
y_i	source coordinates
θ	angle between disc plane and field point
γ	angle between thrust axis and field point
λ	air loading harmonic number
ρw	load solidity (fraction of the effective disc annulus occupied by the unsteady loading region
χs	blade loading spectrum function

QUESTIONS AND ANSWERS

R.H. Spencer

From: G. Greene

Q: Did you identify any source for MOD-2 which would not also be present in a downwind machine?

A: *No. It appears that the broadband sources are present on upwind and downwind rotors. On downwind rotor wind turbines, the periodic components dominate the acoustic spectrum--at least at frequencies below 200-300 Hz.*

STATUS REPORT

ON

DOWNWIND ROTOR HORIZONTAL AXIS WIND TURBINE NOISE PREDICTION

BY

F. B. Metzger and R. J. Klatte
Hamilton Standard Division of United Technologies Corporation

ABSTRACT

NASA and industry are currently cooperating in the conduct of extensive experimental and analytical studies to understand and predict the noise of large, horizontal-axis wind turbines. This effort consists of (1) obtaining high quality noise data under well-controlled and documented test conditions, (2) establishing the annoyance criteria for impulse noise of the type generated by horizontal-axis wind turbines with rotors downwind of the support tower, (3) defining the wake characteristics downwind at the axial location of the plane of rotation, (4) comparing predictions with measurements made by use of wake data, and (5) comparing predictions with annoyance criteria. This report briefly summarizes the status of work by Hamilton Standard in the above areas which was done in support of the cooperative NASA and industry studies.

INTRODUCTION

Work is now under way at NASA and in industry to understand wind turbine noise generation mechanisms. All aspects of this problem are complex, so the progress has been limited. The information in this report describes the work done at Hamilton Standard with the assistance of NASA and other investigators in industry. It is emphasized that the statements made in this report are in many cases tentative and subject to change as more information becomes available.

Annoyance Problem

In the past, many wind turbines have been built and operated with no indication of a noise problem significant enough to prompt an investigation or apply any noise control measures. This is also true of all currently operating wind turbines except for the MOD-1 at Boone, North Carolina. The noise heard at the Boone site has been described as a thumping noise which is annoying, mainly when heard indoors. As shown in Figure 1, the complaints have been received from residents within 1 1/4 miles of the MOD-1 site. Also, it is of interest to note that the complaints are received from residents outside the towns in the area. This indicates that the very quiet background noise at less populated locations may allow even low levels of wind turbine noise to be heard. It can also be seen from the topographic information in Figure 1 that many of the compliants are received from sites 1000 ft. below the height of the MOD-1. Thus it is possible that high wind velocities could exist at the MOD-1 location, but the wind velocity at the complaint site might be negligible. This would also lead to a very quiet ambient background noise in which even faint sounds from a wind turbine might be heard. In a fairly level site the nigh winds that drive a wind turbine would also raise the background noise at a residence, so the wind turbine noise would tend to be inaudible.

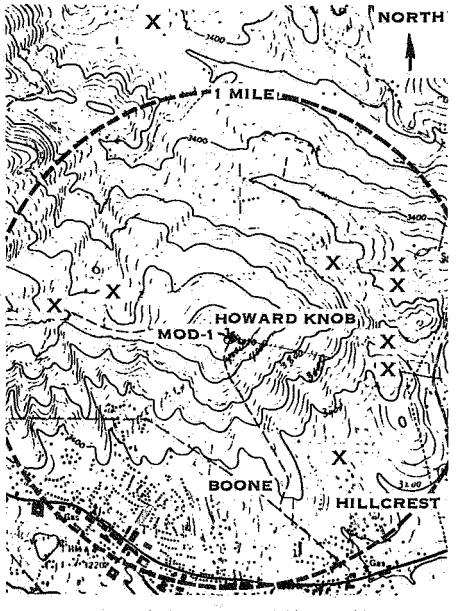

Figure 1 - Complaint locations at MOD-1 site

The characterization of the annoying noise as a "thump" rather than a "swish" indicates that it is impulsive in nature and due to interaction of the wakes from the tower legs with the rotor, i.e., the wake velocity deficit downwind of a tower leg causes a sharply flutuating lift on the rotor which is radiated as impulse noise. A sample of these impulses is shown in Figure 2. Here the sound pressure level as a function of time is plotted at a location outside a house at Boone where complaints were generated. Each of the sharp pulses of Figure 2 are caused by the passage of a rotor blade through the tower wake. Spectrum analysis of characteristics of the noise in the near field, 205 ft. from the MOD-1, outdoors at a complaint location 3000 ft. from the MOD-1, and inside a complainant's house are shown in Figure 3. Figure 3 shows that the impulse character of the noise is found only below 31 Hertz as evidenced

by the multiple humped envelope of the spectrum shape seen at the upper left. Above 31 Hertz it is not possible to identify the character of the sound and it is conjectured that the impulse character of the noise is confined to frequencies below 31 Hertz. In fact, it is even more difficult to identify impulse character in the far field outside or inside a complainant's house. It should also be noted that Figure 3 is typical of the data from MOD-1 which has been analyzed.

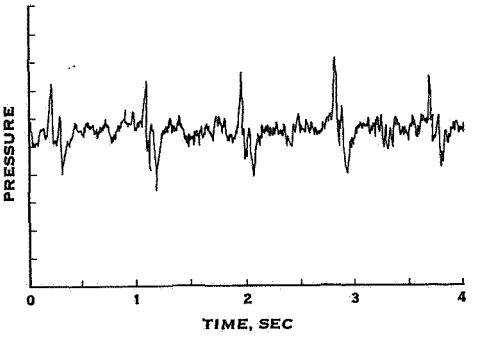

Figure 2 - Pressure impulse sequence recorded outside of complainant's home (data from unpublished NASA Langley Report Jan 26, 1980)

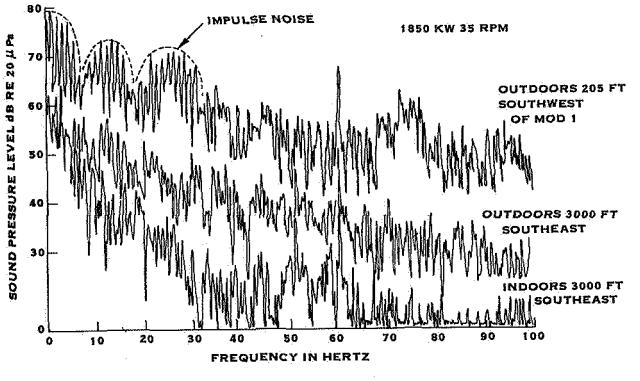

Figure 3 - MOD 1 noise spectra

Prediction Method

In order to predict the noise of a wind turbine Hamilton Standard has adapted the theoretically-based methodology used for predicting propeller noise. This method uses an extension of the theory contained in (ref. 1). A block diagram for this methodology is shown in Figure 4. This methodology calculates tone noise due to steady loading associated with the volume of the blade, and unsteady loading caused by the wind shear and tower wake defect. Broadband noise due to turbulence at the trailing edge of the blade or due to interaction of the blade with inflow turbulence is also calculated. The method is capable of evaluating the influence of ground reflection on measured noise, but this feature has not yet been considered necessary for wind turbine predictions.

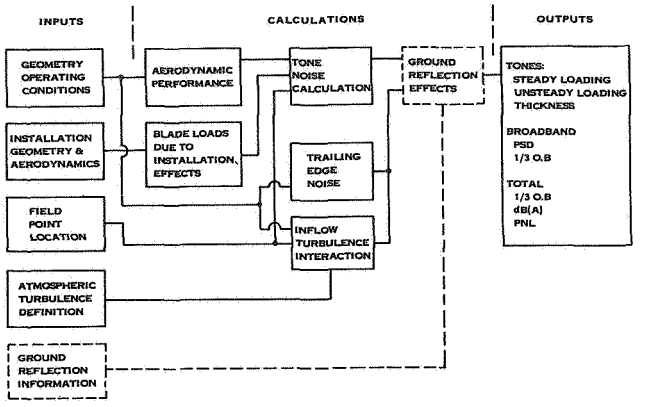

Figure 4 - Far-field rotor noise calculation procedure

The method is computerized and is a far-field time domain method, i.e., it will calculate noise only at locations a minimum of several rotor diameters from the wind turbine, and the output of the calculation is a frequency spectrum. In order to run cases, the performance of the rotor is calculated, and the characteristics of wake velocity defect and wind shear are used to calculate unsteady blade loads. These two sets of input information are used to calculate the tone noise components of the noise spectrum. The impulse character of the noise due to the wake defect is calculated by the tone noise program. For the present annoyance studies, broadband noise due to trailing edge or inflow turbulence has not been considered.

Correlation of Measurement and Prediction

An indication of the accuracy of the method can be seen in Figure 5 where the outdoor far-field spectrum of Figure 3 is compared with an envelope of harmonics predicted by the method of Figure 4. As input, this calculation used wake definition derived from the model tests of (ref. 2). It can be seen that the impulse character of the spectrum up to about 30 Hertz is fairly well predicted. However, above this frequency the prediction falls below the measurement and it is not possible to identify the character of the measured spectrum.

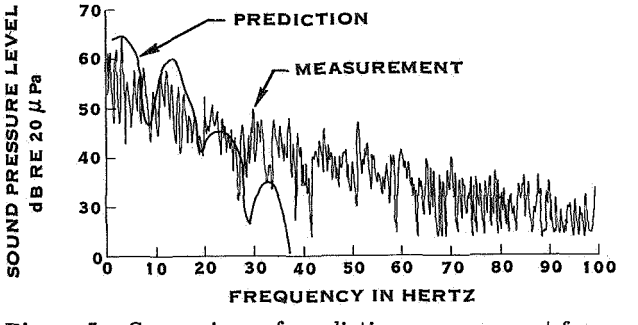

Figure 5 - Comparison of prediction measurement for MOD-1

The lack of agreement between prediction and measurement is believed due primarily to the specification of the tower wake which causes the fluctuating lift on the rotor. As indicated above, the wakes used for the predictions of Figure 5 were derived from wind tunnel model tests of a MOD-1 tower. To use this data the wake characteristics of the full-scale tower had to be inferred from measured wakes in model scale obtained at a distance downwind of the tower which differed from the full-scale, tower-to-rotor spacing. Also, it was assumed that the Reynold's number of the flow in model and full-scale were similar. Therefore, it can be seen that the disagreement between predictions and measurements might be considerably improved if full-scale wake data were available for noise calculations.

The lack of wake data in the literature obtained at distances downstream of the tower at rotor-to-tower clearances being used in wind turbine design has prompted NASA to sponsor model wind tunnel tests at Wichita State University. Wake definition as a function of Reynold's number at several downwind distances close to the tower will be established for smooth cylinders having various radii on the corners. This data will be particularly valuable for noise predictions of wind turbines with single-shaft towers. Analysis of this data is not yet complete but early results indicate that the published wakes (ref. 3) for cylinders may not be reliable as the basis of wake definition for noise calculations. The deficiency in the published wake data appears to be due to the use of measurements obtained in the far wake, 10 or more diameters downstream of a cylinder. When this data is extrapolated to locations closer to the tower, wake width and wake velocity deficit do not appear to agree with Wichita State data.

Noise Annoyance Criteria

Annoyance caused by noise from any source is a problem which has been addressed by municipal and federal governments with increasing emphasis in recent years. Noise control ordinances have been written in many communities to insure that the noise of mechanical equipment used in everyday life does not compromise the character of the living environment. There are many methods for evaluating the annoyance potential of a sound. However, these methods have primarily addressed sounds with a broadband character or ones with pure-tone components. Impulse noise is addressed, but impulse noise corrections may not be applicable to the impulse characteristics of wind turbine noise.

Therefore, NASA-Langley has conducted limited psychoacoustic tests in an attempt to identify annoyance criteria for wind turbines. The following discussion makes use of the NASA-Langley results plus other available information in order to establish some tentative noise annoyance criteria for wind turbine noise. It is recognized that NASA-Langley is continuing psychoacoustic research and that there is a limited understanding of the character of wind turbine noise spectra. Therefore, the criteria below should be considered tentative and the starting point for further development.

NASA-Langley, in unpublished reports, has taken the position that wind turbine impulse noise will probably be unacceptable if it can be heard. This is a very stringent criteria and one which has not been accepted in establishing the annoyance of other noise sources. In general, the rating systems such as ISO R 1996 (ref. 4) allow some exceedance of the criteria before sporadic complaints are expected. However, it is certainly true that wind turbine noise that is inaudible will be completely acceptable. Therefore, the NASA-Langley work will be used as a starting point for development of the tentative criteria discussed below.

Figure 6 shows the basis for the proposed tentative criteria. The curve labelled 'Impulse Noise Criteria' was obtained by drawing a line through the spectrum of a wind turbine impulse noise where the spectrum shape was adjusted such that it could just barely be heard in a quiet background noise in an anechoic test chamber. Since listeners in real life environments do not listen to wind turbine noise in completely quiet background noise, the two curves of Figure 6 for wind noise at 20-30 mph and 0-10 mph as heard indoors were developed by applying the assumed noise attenuation at the bottom of Figure 6 to measured outdoor wind noise spectra. Also, it has been stated earlier that the character of wind turbine noise above 31 Hertz cannot be clearly identified as impulse in nature, so another line for minimum audible field for tones or broadband noise is required. For this, the minimum audible field lines in Figure 6 were plotted. The upper curve is one contained in an unpublished NASA-Langley report of June 26, 1980 and the lower curve is one contained in ISO R 226 (ref. 5). The higher of these two curves will be used as the basis for further discussion in this paper. However, it is certainly subject to change as the character of wind turbine noise becomes better understood and additional psychoacoustic tests are conducted.

Based on the above discussion, several criteria are suggested in Figure 6:

1. If the noise is impulsive in nature it must exceed the line marked 'Impulsive Noise Criteria' at some point in the 1/3 octave band spectrum. However, if the impulse noise is heard in a background noise caused by wind at 20-30 mph, the impulse noise must also exceed the line marked 'Indoor Wind Noise Estimate 20-30 mph'. If the background noise is due to wind at 0-10 mph, then the impulse noise would be audible if at some point it exceeded the curve marked indoor wind noise estimate 0-10 mph.

2. If the wind turbine spectrum is not impulse in nature, then noise levels that do not exceed the curve marked minimum audible field (whole body) are considered acceptable.

From the above discussion it is clear that the nature of the various portions of the wind turbine noise spectrum must be understood to apply the criteria. This will require further work.

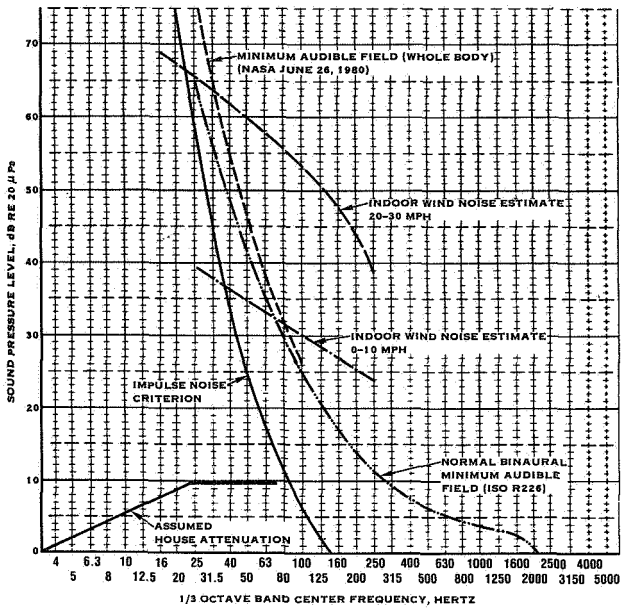

Figure 6 - Basis/or tentative annoyance criteria

Application of Tentative Noise Criteria

Figure 7 demonstrates the application of the tentative noise criteria. Here a 1/3 octave band spectrum at an operating condition of 1850 kW and 35 RPM, measured in a complainant's home, is plotted. This is a 1/3 octave band version of the narrowband spectrum plotted in Figure 3. Since the complainant's home was in the valley below the MOD-1 site, it will be assumed that the 0-10 mph wind criterion applies. Also, as indicated earlier in the discussion of Figure 3, the noise at frequencies greater than 31 Hertz is not believed to be impulsive. Figure 7 shows that the measured spectrum exceeds the impulse criteria and the 0-10 mph wind criteria only by a small amount of 40 Hertz. Also, the prediction of Figure 5 has been converted to 1/3 octave bands, the house attenuation of Figure 6 applied, and the result plotted in Figure 7. Relatively good agreement with measurements is shown at frequencies below 31.5 Hertz. From Figure 7 it is tentatively concluded that annoyance at the complainant's house, due to MOD-1 operation, should be negligible. If, on the other hand, the annoyance at the complainant's house is indeed considered significant, then the tentative criteria discussed in this report must be revised.

Noise Reduction Concepts

Figures 6 and 7 indicated that annoyance can be eliminated by minimizing the high-frequency components of wind turbine noise. Also, if the measurements and predictions of Figure 7 are typical of the wind turbine noise problem, then only a small change in configuration may be required to eliminate the problem.

One possibility for reducing noise at higher frequencies is to reduce rotor design RPM. For the MOD-1, the design speed was originally 35 RPM. A reduction in design speed to 23 RPM is expected to reduce noise by about 10 dB, particularly at higher frequencies. On the basis of the measurements in Figure 7, such a reduction should eliminate the annoyance problem on MOD-1. There is, however, some energy capture penalty for such a modification.

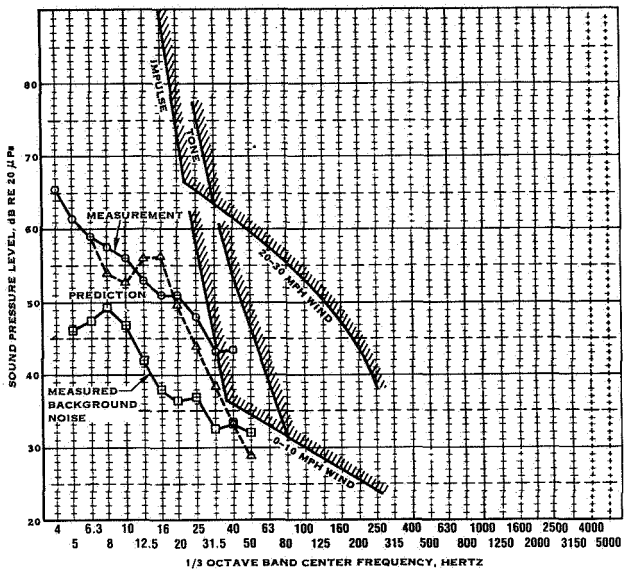

Figure 7 - Evaluation of predictions and measurements relative to tentative annoyance criteria

Other alternatives which may have no energy capture penalty are modifications to the tower. Guidance for beneficial changes to wind turbine support towers is contained in Figures 8 and 9. These figures are based on a simplified analytical study of wind turbines with downwind rotors and cylindrical towers. In Figure 8 it can be seen that a narrow wake with a large wake defect is the worst case for producing high-frequency noise. If the velocity defect is minimized, then the noise at all frequencies is reduced. If, in addition, the width of the wake is increased, then the high-frequency noise is suppressed.

Figure 9 indicates the best shape for a wake defect from a noise reduction standpoint. The shape derived by Schlicting from test data on smooth cylinders (ref. 3) is seen to cause the highest level of high-frequency noise. A wake with cosine-squared shape produces less noise and, surprisingly, a Gaussian wake produces no high-frequency noise. The message from Figure 9 is that high-frequency noise might be eliminated if the tower could in some way be modified to produce a Gaussian wake. Also, very small differences in the wake shape assumed for a noise calculation can have a large effect on the high-frequency components of noise predicted. The implied sensitivity of the calculation procedure to small changes in wake definition indicates the need for additional work to correctly model full-scale tower wakes.

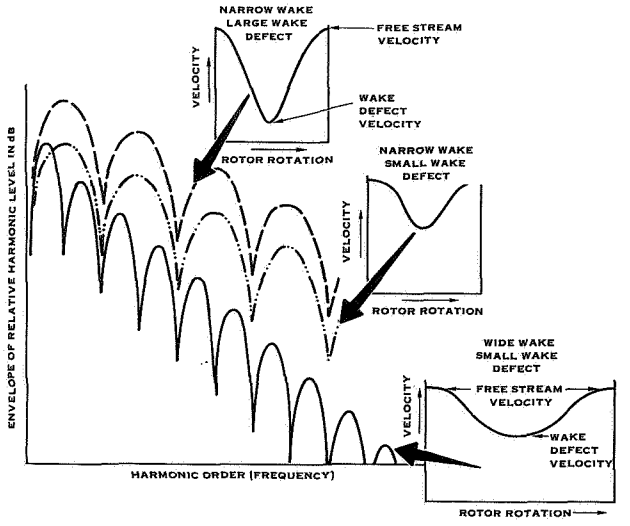

Figure 8 - Effect of wake defect amplitude and width on noise spectrum shape

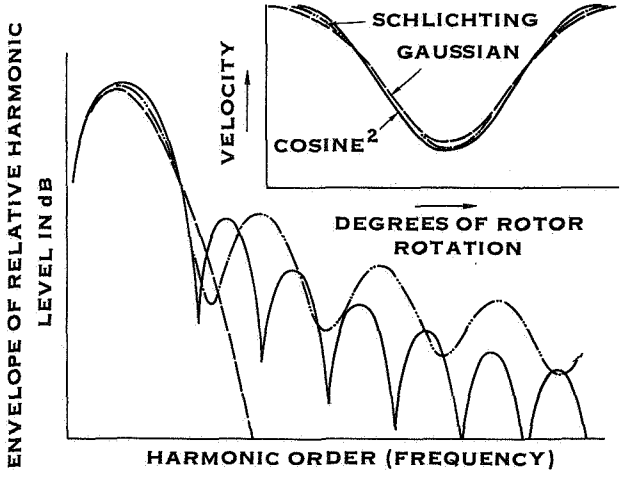

Figure 9 - Effect of wake velocity defect shape on noise spectrum shape

CONCLUDING REMARKS

At present there is a limited understanding of the annoyance problem at the MOD-1 site. This problem appears to be unique as there have never been any annoyance problems due to operation of other wind turbines. However, in order to prevent such problems at future turbine sites it is important that the MOD-1 noise is completely understood. Evaluation and control of noise of future wind turbines requires further work in three areas: (1) noise annoyance criteria which correctly reflect the actual annoyance response of residents living around existing wind turbines, (2) accurate noise prediction procedures for use in predicting noise of new wind turbine designs and for conducting analytical noise control studies, and (3) definitive noise measurements of sample wind turbines for use in testing prediction methods and annoyance criteria.

At the present time there are deficiencies in all three areas. Noise annoyance criteria for impulsive noise must be developed and their accuracy must be established. Noise prediction procedures such as that described in this paper appear capable of accurate predictions, but substantial work is needed to define the wakes as input to the calculation procedure. Finally, additional reference wind turbine noise measurements are needed which have been obtained under carefully controlled conditions in the far acoustic field at test sites with terrain and vegetation that does not cause unpredictable changes in the data.

Acknowledgement

The authors gratefully acknowledge the support of NASA-Lewis, NASA-Langley, Solar Energy Research Incorporated, and Wichita State University in providing data used in preparation of this report.

REFERENCES

1. Hanson, D.B.: Helical Surface Theory for Harmonic Noise of Propellers in the Far Field, AIAA Journal, Vol. 18, No. 10, October 1980, p. 1213.

2. Savino, J.M., et al, Wake Characteristics of a Tower for the DOE-NASA MOD-1 Wind Turbine, DOE/NASA/1028-78/17, NASA TM-78853, April 1978.

3. Schlichting, H., Boundary Layer Theory, McGraw-Hill, 1968.

4. International Organization for Standardization, ISO/R 1996-1971 (E), Assessment of Noise With Respect to Community Response.

5. International Organization for Standardization ISO/R 226-1961E, Normal Equal-Loudness Contours for Pure Tones and Normal Threshold of Hearing Under Free Field Listening Conditions.

QUESTIONS AND ANSWERS

F.B. Metzger

From: F.W. Perkins

Q: Would a swept tip on the blade effectively broaden the wake, and reduce impulsive noise?

A: *Yes. However, it is not clear how much sweep is required and how much of the blade must be swept to cause a significant reduction.*

From: P. Abbot

Q: Do you believe that the wake deficit is the sole problem of the low frequency noise and if so, why don't we see this occurring (always) from the data? What is your feeling about the turbulence on the wake?

A: *Yes. There are nonrepetitive characteristics of the wake and atmospheric variations which may prevent noise generation from being consistent. Turbulence in the wake would lead to less annoying random or broadband noise generation.*

WIND TURBINE ACOUSTIC STANDARDS

David G. Stephens, Kevin P. Shepherd*, and Ferdinand Grosveld*

National Aeronautics and Space Administration
The Bionetics Corporation*
Langley Research Center
Hampton, Virginia 23665

ABSTRACT

A program is being conducted to develop noise standards for wind turbines which minimize annoyance and which can be used in design specifications. The approach consists of presenting wind turbine noise stimuli to test subjects in a laboratory listening chamber. The responses of the subjects are recorded for a range of stimuli which encompass the designs, operating conditions, and ambient noise levels of current and future installations. Results to date have established the threshold of detectability for a range of impulsive stimuli of the type associated with blade/tower-wake interactions. The status of the ongoing psychoacoustic tests, the subjective data, and the approach to the development of acoustic criteria/standards are described.

INTRODUCTION

The development of wind turbines which are acoustically acceptable to the community requires an understanding of the human perception of, and response to, wind turbine noise and any noise induced building vibrations resulting from their operation. Subjective data on wind turbine operations, however, are virtually nonexistent with the exception of a few cases of reported annoyance with the MOD-1, a 2000 kw downwind machine located at Boone, North Carolina. Furthermore the noise associated with wind turbines, and in particular the low frequency blade/tower-interaction noise, have temporal and spectral characteristics which are in a range where very little subjective data and/or experience are available (ref. 1). Thus, a laboratory study has been initiated to better understand wind turbine type noise to provide guidance in the design and siting of future machines.

The factors which are believed to be important to the development and application of wind turbine noise criteria are shown schematically in figure 1. As indicated, the turbine may produce noise through several source mechanisms which may result in both impulsive characteristics due to blade/tower-wake interactions ("thumping") and nonimpulsive ("swishing") noise due to unsteady flow over the blades. These source characteristics are modified before reaching the receiver due to atmospheric propagation and terrain effects. Finally, the effects of wind turbine noise on the receiver may be modified by many factors such as the background or ambient noise level, the time of day, the activity and location of the receiver (indoors/outdoors), and the presence of any perceptible house vibrations induced by the noise. To assess the impact of the noise, criteria must be developed which consider the receiver's perception of, and response to, the acoustical factors (noise level and frequency, for example) and nonacoustical factors (e.g. time of day) associated with the operation of the wind turbine. These criteria must include the various source and path effects both separately and in combination in order to be useful for the design and siting of future machines.

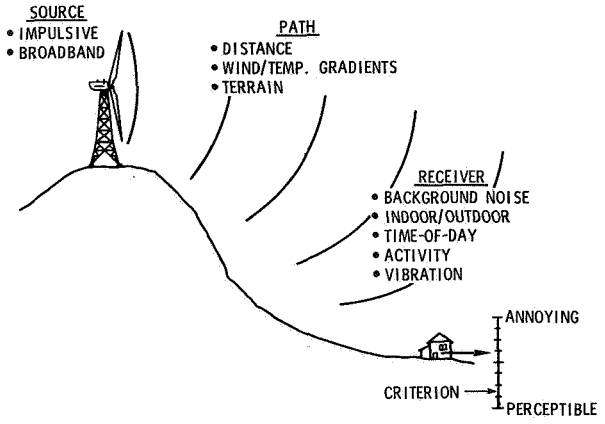

Figure 1 - Wind turbine noise factors.

This paper is a status report of an ongoing program to develop noise criteria to be applied at the receiver location. Emphasis to date has been on the determination of the perception threshold of wind turbine spectra covering the range of anticipated designs and operating conditions. It should be noted that building vibration, despite the fact that it has received considerable attention in the case of the MOD-1 operation will not be considered in this report for two reasons. First, the levels recorded to date suggest that the building response is below the human (whole-body) threshold of detectability and, secondly, it is believed that any noise standards resulting from these studies will yield noise levels low enough to preclude perceptible building vibration (refs. 2 and 3).

PROCEDURE

Tests were conducted to determine the threshold of detectability for the impulsive "thumping" sounds which result from blade/tower-wake interactions. This stimulus is believed to be the dominant source of annoyance in large downwind machines such as the MOD-1 configuration. Although the thump resulting from the blade passing the wake of the tower is uniquely defined by the time history of the pressure pulse, it is more common to define the noise by a frequency spectrum which, with information on the phase relationship between harmonic components, completely describes the noise signature. Since phase information is not always available from

measurements or calculations, a preliminary study was conducted to examine the importance of phase to the subjective detectability of the noise. Four phase conditions were examined; three having coherent phase relationships and one being random. For the first three (nonrandom) conditions, the threshold of detectability was found to be independent of phase and lower in level than that found for the random phase condition. For this reason, the sounds used in this study had a coherent phase relationship between harmonic components.

Test stimuli were computer generated and consisted of a fundamental frequency (blade passage) and up to 250 harmonics for which amplitude and phase were defined. Since the sound amplification/reproduction system introduces phase and amplitude distortion, the transfer function between the output from the computer and a microphone placed at the location of the test subject's ear was calculated. This transfer function was incorporated in the noise generation software, enabling the desired spectra and time histories to be produced in the anechoic test facility, figure 2. This facility has dimensions of 4m x 2.5m x 2.5m (cutoff frequency of 150 Hz) and is equipped with two loudspeakers having a frequency response of 5 Hz to 20 kHz.

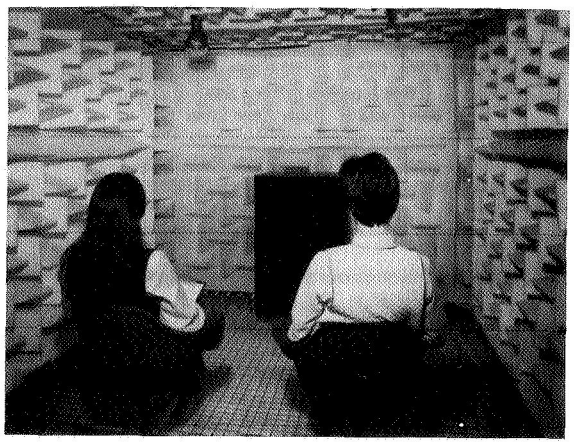

Figure 2 - Anechoic test facility.

Each subject was seated in front of the loudspeakers and instructed to press a hand-held switch when they heard the sound (fig. 3). This switch activated a light which indicated to the test conductor that a given sound was heard. The sound pressure level of the sound was slowly reduced until no longer detectable and then slowly raised until detectable again. This process was repeated until consistent ascending and descending thresholds were achieved. The mean of these two values was considered to be the threshold of detectability.

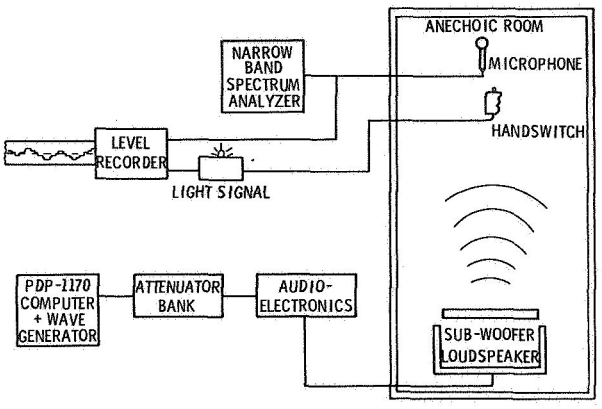

Figure 3 - Stimuli presentation and subjective response system.

RESULTS AND DISCUSSION

The primary objective of the study to date has been the determination of the threshold of detectability for impulsive turbine noise having a variety of spectra in the frequency range from 20 to 110 Hz. Frequencies below 20 Hz, were considered to be unimportant due to the extreme insensitivity of the ear to wind turbine noise levels in this low frequency region. These spectra were synthesized based on measured data from the MOD-1 site as well as calculations of the spectra resulting from blade/tower-wake interactions (refs. 4 and 5). No broadband ("swishing") noise has been included nor have ambient noise effects been studied.

Ten spectra, having a fundamental frequency of either 1.0 Hz or 0.5 Hz, were designed to be dominated, subjectively, by harmonics at different frequencies. Those having a 1.0 Hz fundamental were dominated by components at 20, 40, 60, 80 and 100 Hz and those having a 0.5 Hz fundamental were dominated by components at 30, 50, 70, 90 and 110 Hz. Detectability thresholds were determined for each of the 10 sounds using nine test subjects, none of whom had significant hearing loss. The standard deviations of the threshold measurements were found to be typically 2.5 dB, with a tendency for the spectra having 0.5 Hz fundamental to have the higher standard deviations.

The narrowband spectra at the mean threshold level are presented in figure 4. Tangential curves were fitted to these spectra and are presented in figure 5 for comparison. Due to the higher harmonic density, the curve for the spectra having 0.5 Hz fundamental is lower than the 1.0 Hz case. Also shown in the ISO pure tone or minimum audible field (MAF) threshold (ref. 6) which has the same general shape. The difference in level between the turbine curves and the MAF curve may be attributed to the critical bandwidth of the human ear (ref. 7) which is far greater than the bandwidth used in the spectral analysis.

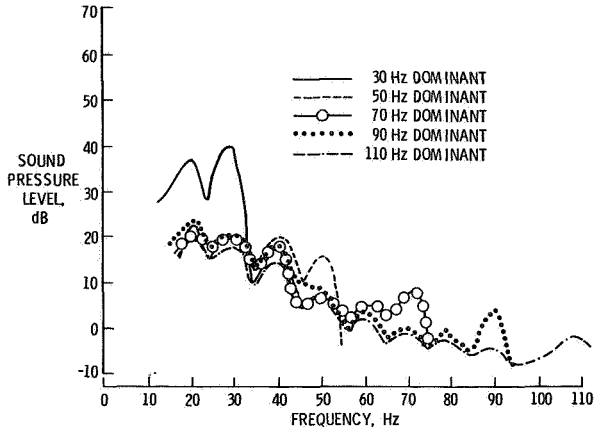

a) 0.5 Hz fundamental

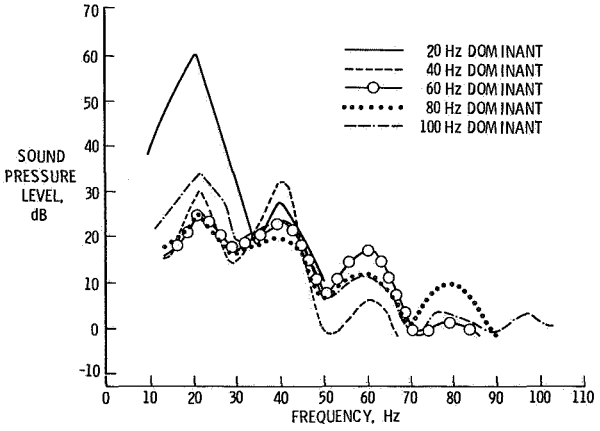

b) 1.0 Hz fundamental

Figure 4 - Narrowband spectra at the mean threshold level

The data (fig. 5) suggest that the frequency of the fundamental is a significant variable. It is recommended that the 1 Hz fundamental curve be used and then an adjustment made on a logarithmic (energy) basis for the actual fundamental blade passage frequency. Thus, the curve for 0.5 Hz fundamental would be 3 dB lower and the curve for 2 Hz would be 3 dB higher than the 1 Hz fundamental curve. Furthermore, the frequency analysis bandwidth should be less than the fundamental frequency. The use of 1/3 octave or octave band analysis is not recommended due to the steep slope of the threshold curves.

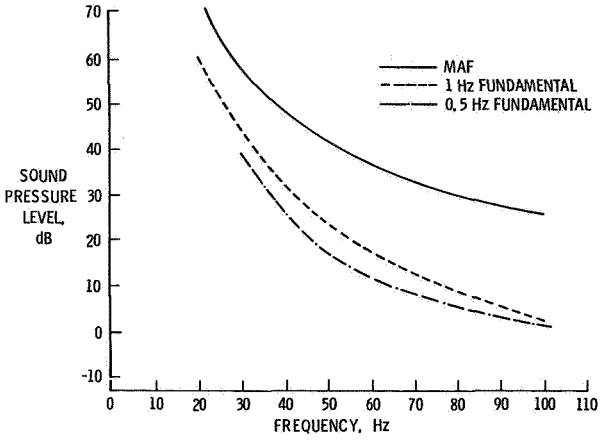

Figure 5 - Thresholds of detectability

Certain limitations of the preceding results need to be considered. Mean threshold data have been presented and consequently many people will be able to detect sounds at lower levels. Also these tests were conducted in an anechoic environment with extremely low background noise (masking by higher levels of background noise will be considered in the near future). The spectra used to generate the threshold curves were specifically designed such that detectability was achieved over a narrow frequency range. The threshold level of sounds which have components at or near the threshold curve over a wider frequency range is unknown at this point in time, but will be studied in future testing.

CONCLUDING REMARKS

The thrust of the program is to develop the psychophysical functions relating human response to each of the wind turbine noise components such as "thumping" and swishing." Furthermore, the variation or dependence of these functions on other acoustical factors such as ambient noise will be examined. This will enable assessment of the acceptability of a predicted or measured noise condition at a receiver location. For example, if "thumping" is the dominant noise source in a low ambient noise situation, the ideal solution would be to design for noise levels below the threshold of detectability for impulsive noise (fig. 5). However, if the measured or predicted spectrum exceeds the detection threshold, annoyance may result. The degree of annoyance cannot be predicted at the present time due to absence of subjective data under actual operating conditions but an indication of the growth of annoyance may be found in classical loudness studies which show that the growth of loudness is frequency dependent as shown in Table 1.

Frequency	dB/doubling of loudness
20	4.5
50	6.1
100	7.2
500	8.6
1000	10.0

Table 1 - Growth of loudness

Exceeding the threshold of detectability at 20 Hz has more serious consequences than at higher frequencies. In general, the major use of the psychophysical relationships will be to guide the designer/operator in pinpointing the exact frequency components and hence source mechanisms which may cause problems with wind turbine operations.

REFERENCES

1. Tempest, W.: Infrasound in Transportation. Infrasound and Low Frequency Vibration, W. Tempest, ed., Academic Press, 1976, pp. 19-36.

2. Vibration and Shock Limits for Occupants in Buildings. ISO Standard 2631, 1974.

3. Stephens, D. G. and Mayes, W. H.: Aircraft Noise-Induced Building Vibrations. Community Noise, Peppin and Rodman, eds., Am. Society for Testing and Materials, 1979, pp. 183-194.

4. Wells, R. J.: MOD-1 Wind Turbine Generator Noise Studies. General Electric Company, 1980.

5. Greene, George C. and Hubbard Harvey H.: Some Calculated Effects of Non-Uniform Inflow on the Radiated Noise of a Large Wind Turbine. NASA TM 81813, 1980.

6. Normal Equal-Loudness Contours for Pure Tones and Normal Threshold of Hearing Under Free Field Listening Conditions. ISO Recommendation R 226, 1961.

7. Kryter, Karl D.: The Effects of Noise on Man. Lee, Hewson, and Okun, eds., Academic Press, 1970.

QUESTIONS AND ANSWERS

D.G. Stephens

From: Anonymous

Q: Have you varied the background ambient noise level in your test room to simulate that at a residence?

A: *No, but we intend to.*

From: W. Beans

Q: From test subjects did you obtain the standard deviation due to subject age?

A: *No. All subjects used in the test had good hearing and consequently were relatively the same young age.*

From: D.W. Thomson

Q: Have you considered setting the individual subjects on a shaker table driven from your synthesizer system so as to provide "body" input? Another possibility would be to include a loaded china closet in the chamber which might pick up the vibrating stemware source.

A: *No answer was provided.*

SUMMARY OF STATE-OF-THE-ART DISCUSSIONS

Following are the summary reports made by the Session Chairmen. During all of the discussion sessions, participants were asked to focus on the following three questions:

1. Are the state-of-the-art analysis tools satisfactory for designing the next generation of wind power systems?

2. Are state-of-the-art analysis tools being used satisfactorily by designers?

3. What important verifications of theory are lacking or inadequate?

In the summary reports, the Session Chairmen have attempted to report the general context of the discussions rather than specific comments. The discussion sessions were described as controlled, but were diverse and inconclusive. In most areas, there was no consensus opinion with regard to the answers to the above questions.

AERODYNAMICS SESSION REPORT

by

J.M. Savino and J.C. Estes
NASA Lewis Research Center

A meeting with the authors of the aerodynamics session of the Dynamics Workshop revealed diverse opinions on the adequacy of current working technology. There was definitely no consensus.

A substantial minority voiced the opinion that current working knowledge is entirely sufficient to design the next generation of wind turbines. It was stated that wind turbines operation and maintenance costs are well controlled. It was also pointed out that vibratory loads do not appear to be an important wind turbine design driver so that improved loads computation methods are unnecessary.

Several members of the audience argued for less costly analysis methods. Extensive computer analyses are said to be simply too expensive to be economically justifiable for small wind turbines. There was some sentiment expressed for a "make-em and break'em" trial and error approach. Manufacturers of small machines would prefer to have a small library of analysis programs which could be run on hand calculators. One author noted that small wind turbines are less complicated than large trucks and should, therefore, cost less per pound. One contributor asked if wind turbine costs could not be reduced by reducing performance requirements sufficiently to eliminate sophisticated aerodynamic and structural analyses.

Some questioned the adequacy of communications within the wind turbine community. It was suggested that acceptable analytical techniques may be available but are unknown or unavailable to some of those who need them. One person felt that the aerodynamic, performance, and loads specialists do not discuss their requirements sufficiently with one another.

Among those calling for improvements in state-of-the-art analyses, the following points were made:

1. The widely used PROP computer program predicts rotor performance well over most of the operating range, but it gives unsatisfactory results and is difficult to extend to high tip-to-wind speed ratios.

2. Greater standardization in predictive techniques is desirable to minimize the present wide variation in answers.

3. Present aerodynamic predictions for small wind turbines seem inadequate to forecast extreme conditions.

4. Some commonly used loads programs do not predict well, but it is unclear whether this is due to deficiencies in the programs themselves or to their aerodynamic inputs.

The following comments were made in the area of test verification:

1. Small wind turbines require increased emphasis on the comparison of analysis and tests.

2. Field measurements and their analysis deserve higher priority and increased publication.

3. Additional controlled (wind tunnel) testing would help to verify the aerodynamic predictions. (However, scaling problems frequently cause wind tunnel results to overpredict full-scale responses.)

4. Greater attention is needed for the comparison of predicted versus observed wind turbine energy capture.

ACOUSTICS SESSION REPORT

by

James P. Couch
NASA Lewis Research Center

Sounds generated by a wind turbine during its operation are a relatively new concern to wind turbine designers. None of the earlier machines, dating from the Smith-Putnam machine of the early forties through the DOE/NASA Mod-0/Mod-0A's, generated sounds that were loud or disturbing enough to be noted by any observer. This is not the case for the DOE/NASA Mod-1 machine installed at Boone, North Carolina. From the time the Mod-1 first began regular operations in October, 1979, some of the residents living near the wind turbine (within 1 km) started complaining about the sound generated by the machine. The sound has two general characteristics: (1) a steady swishing sound produced by the aerodynamic disturbances around the blade, like tip vortices and turbulences; and a thumping or beating sound which is produced each time one of the blades passes through the wake of the tower. This thumping sound has been the source of most of the complaints. To date, about a dozen households of the hundred or so nearest the machine have complained at least once, some several times. The topography around the Mod-1 is a significant factor in the local sound perception of the machine. The wind turbine is installed on top of a 1347m mountain. Most of the homes where complaints have originated are located in narrow, heavily wooded valleys about 310m below the wind turbine. The background sound level of these valleys is very quiet.

All of the papers in the Acoustics Session deal with sound generated and propagated by large, horizontal axis wind turbines. Some measurements have been made of the sound generated by vertical axis wind turbines by the Solar Energy Research Institute, but these data are not yet available. The Session contained ten papers: two dealt with wind tunnel experiments, two dealt with sound measurements taken around the Mod-1 site, one dealt with the effects of propagation on perceived sound at Boone, four dealt with analytical approaches to calculating wind turbine sound generation, and the final paper dealt with the establishment of a criteria or standard for acceptance of wind turbine noise.

Many factors influence whether the sound generated is objectionable or not, and not all authors agree on which factors are more significant. Most agree that the analytical tools seem to define the theory adequately. Some feel better agreement between analysis and experimental data could be obtained if more detailed information were available on the structure of the air stream entering the rotor, especially for downwind rotor machines. Other authors feel that the variability of the wind will make such detailed analyses of limited practical use, and they have adopted some sort of averaging approach and empiricism in their analyses to get results. This difference in approach shows up in other areas. Those who are concerned about the details of the wake structure tend to be the same people who do detailed analyses of sound measurements resulting from a single passage of one blade behind the tower legs. Each blade passage then becomes an event which may or may not produce a thump which is loud enough to disturb people. The other workers prefer to accumulate, and average in some way, a great many of these individual events. These sound levels would than be compared against a complaint history or against an accepted standard.

An additional complicating factor is the effects of topography and meteorological conditions on the propagation of sound from the wind turbine to the listener. Various authors showed that propagation in the area around Mod-1 could amplify sound by 6 to 25 dB at distances of about 1 km.

Finally, each Session was asked to focus on three questions: 1) Are state-of-the-art analysis tools satisfactory for designing the next generation of wind power systems? 2) Are state-of-the-art analysis tools being used satisfactorily by the designer? 3) What important verifications of theory are lacking or inadequate? Since sound generation is a relatively new concern for wind turbine designers (and even then only for designers of horizontal axis wind turbines), the analysis tools are also relatively new and untested. Very little verification work has been done on these analysis tools and much work in this area needs to be done. It is not yet known whether or not large vertical axis wind turbines generate sounds that will prove to be disturbing to nearby residents.

ELECTRICAL AND CONTROL SYSTEMS SESSION REPORT

by

Leonard J. Gilbert
NASA Lewis Research Center

General agreement was indicated by the participants of the Electrical and Control Systems Session that given the configuration and parameter values of the machine, the state-of-the-art analysis tools are satisfactory for designing the controls for an individual wind turbine system. Some areas of the technology are still not well defined. For example, the improvement of wind modeling and the method of applying a given wind model is one feature that warrants attention. A second phenomenon that needs clarification is the dynamics of the yaw motion of a HAWT. Generally, however, the analysis tools are available and are being satisfactorily used. Similarly, the analysis integration with the utility network is an area of the technology wherein greater understanding must be achieved.

The consensus of the participants was that the establishment of compatibility between wind machine technology and power system technology and requirements is the necessary objective of research and development efforts in the electrical and control systems area of WECS. An appreciation of this requirement is present and increasing in the wind turbine and power system technical communities, and the cooperation between utilities and machine designers is improving as each technology acquires a better understanding of the performance requirements of the other. This situation is true for SWECS as well as WECS.

To make an impact on the quantity of electrical power generated wind turbines must be operated in sizable clusters. Among the several parameters which affect the performance of the cluster, the key parameter may be the array design--the configuration of the array and manner in which it is tied into the network. Research and development studies targeting the effect of array designs should be undertaken promptly.

WECS are being designed and built emphasizing energy capture and cost of electricity. Possible trade-offs between these considerations and the response desired, and required by the utility, should be recognized. There must be a rationalization between the cost of utility usage and the cost of generation.

The full integration of WECS into the power network was recognized as a complex problem. Nevertheless, with appropriate analytical studies and the increasing development of operating clusters on networks, the technology is building toward a complete understanding of the problem.

STATE OF THE ART SUMMARY

STRUCTURAL DYNAMICS AND STRUCTURAL

AND ROTOR DYNAMICS SESSIONS

The session chairmen, authors of papers and other interested attendees held a discussion on Wednesday, February 25 which attempted to answer the following three questions:

1. Are state-of-the-art analysis tools satisfactory for designing the next generation of wind power systems?

2. Are state-of-the-art analysis tools being used satisfactorily by designers?

3. What important verifications of theory are lacking or inadequate?

The discussion was lively and produced a diversity of conflicting opinions representing the experience and personal beliefs of the participants. Nevertheless, there did emerge a general consensus of opinion. The following is an attempt to summarize that overall consensus regarding these three questions.

Regarding the use of state-of-the-art analysis tools, the overall opinion was that these tools are satisfactory for predicting design loads, steady state response and performance. The existing tools have shortcomings in analyzing transient loads and hardware response at resonant or near-resonant conditions. In particular, it was pointed out that the existing methods are deficient in their ability to predict free yaw behavior in horizontal axis wind turbines, and to provide an adequate description of wake aerodynamics for vertical axis machines. The current practice is to take great pains to avoid operating near critical resonances. It was believed by most present that this practice, augmented by the judicious use of structural or mechanical damping, will prove to be adequate to design satisfactory and safe wind turbines. It was noted that the NASA Mod-0 experimental wind turbine at Plum Brook Ohio is providing valuable empirical data to verify and expand theory.

Finally, there was wide disagreement concerning the need for, and value of, stochastic studies.

Discussion of the second question produced more of a concensus of opinion. Simply stated, it was felt that some designers are using state-of-the-art analytical tools, and some aren't. Obviously, among the users are the large manufacturers - invariably from the aerospace field - already in possession of helicopter rotor codes, sophisticated finite-element computer codes, etc. In contrast, some of the small designers prefer the approach which uses high safety factors, and engineering judgment in combination with simpler analysis in producing wind turbines to be qualified by a try 'em/bust 'em/fix 'em approach. This somewhat sanguine attitude, while not always without merit, is perhaps offset by the large number of fatigue failures experienced by small machines at the Rocky-Flats test site. A case in point, however, that the use of sophisticated analytical tools alone does not guarantee anything, may be made by the experience of some of the large wind turbines, where drive shaft failures, blade fatigue cracks, etc. have occurred. Large manufacturers also have had their problems.

In the case of the third question, there was virtually unanimous agreement that the most important verifications of theory that are lacking are correlations of theory with data from the long term operation of wind turbine systems over the complete spectrum of design conditions - including transient conditions.

Specifically, three areas were singled out, in which experimental and/or actual operational data verification is needed, as follows:

- Free yaw performance

- Verification of soft tower designs (i.e. natural frequencies less than the turbine shaft speed)

- Actual demonstration of long-term reliable performance

☆U.S. GOVERNMENT PRINTING OFFICE: 1981-0-777-084/69

1. Report No.	2. Government Accession No.	3. Recipient's Catalog No.
NASA CP-2185		SERI/CP-635-1238

4. Title and Subtitle	5. Report Date
WIND TURBINE DYNAMICS	May 1981
	6. Performing Organization Code

7. Author(s)	8. Performing Organization Report No.
	10. Work Unit No.

9. Performing Organization Name and Address	11. Contract or Grant No.
National Aeronautics and Space Administration Lewis Research Center Cleveland, Ohio 44135	13. Type of Report and Period Covered Conference Publication

12. Sponsoring Agency Name and Address	14. Sponsoring Agency ~~Code~~ Report No.
Department of Energy Division of Wind Energy Systems Washington, D.C. 20585	CONF-810226

15. Supplementary Notes

Robert W. Thresher, Oregon State University, Corvallis, Oregon, Editor.

16. Abstract

The Second DOE/NASA Wind Turbine Dynamics Workshop was held in Cleveland, Ohio, February 24-26, 1981. Papers were presented on the dynamic behavior of large and small horizontal-axis and vertical-axis wind turbines. The objective of the Workshop was to present recent progress in the analysis and prediction of the dynamic behavior of wind turbine generators. Discussions followed each technical session in which the participants were asked to focus on the following questions:

1. Are state-of-the-art analysis tools satisfactory for designing the next generation of wind power systems?
2. Are state-of-the-art analysis tools being used satisfactorily by designers?
3. What important verifications of theory are lacking or inadequate?

A total of 48 papers were contributed and are included in this proceeding. Contributors include universities, manufacturers, government laboratories, and private research organizations. The papers discuss a variety of topics including aerodynamics, structural dynamics, electrical system dynamics, control dynamics, and acoustics. Summaries of the informative discussions held at the workshop as well as the questions and answers which followed each paper are documented in the proceedings.

17. Key Words (Suggested by Author(s))	18. Distribution Statement
Wind power; Wind turbine; Structural dynamics; Aerodynamics; Electrodynamics; Controls; Acoustics	Unclassified - unlimited STAR Category 44 DOE Category UC-60

19. Security Classif. (of this report)	20. Security Classif. (of this page)	21. No. of Pages	22. Price*
Unclassified	Unclassified	450	A19

* For sale by the National Technical Information Service, Springfield, Virginia 22161

National Aeronautics and
Space Administration

Washington, D.C.
20546

Official Business
Penalty for Private Use, $300

SPECIAL FOURTH CLASS MAIL
BOOK

Postage and Fees Paid
National Aeronautics and
Space Administration
NASA-451

NASA

POSTMASTER: If Undeliverable (Section 158
Postal Manual) Do Not Return